Vibrational dynamics of formic acid and its dimer: FTIR and Raman jet spectroscopy and theory

DISSERTATION
zur Erlangung des mathematisch-naturwissenschaftlichen Doktorgrades
"Doctor rerum naturalium"
der Georg-August-Universität Göttingen

im Promotionsprogramm Chemie
der Georg-August University School of Science (GAUSS)

vorgelegt von
ARMAN NEJAD
aus Münster
Göttingen 2022

Betreuungsausschuss

- Prof. Dr. Martin A. Suhm (Georg-August-Universität Göttingen, Institut für Physikalische Chemie, Göttingen)
- Prof. Dr. Jörg Behler (Georg-August-Universität Göttingen, Institut für Physikalische Chemie, Göttingen)
- Prof. Dr. Deborah L. Crittenden (University of Canterbury, School of Science, Christchurch, Neuseeland)

Mitglieder der Prüfungskommission

- Referent: Prof. Dr. Martin A. Suhm (Georg-August-Universität Göttingen, Institut für Physikalische Chemie, Göttingen)
- Korreferent: Prof. Dr. Jörg Behler (Georg-August-Universität Göttingen, Institut für Physikalische Chemie, Göttingen)

Weitere Mitglieder der Prüfungskommission

- Prof. Dr. Ricardo A. Mata (Georg-August-Universität Göttingen, Institut für Physikalische Chemie, Göttingen)
- Prof. Dr. Daniel A. Obenchain (Georg-August-Universität Göttingen, Institut für Physikalische Chemie, Göttingen)
- Prof. Dr. Dirk Schwarzer (Max-Planck-Institut für biophysikalische Chemie, Göttingen)
- Prof. Dr. Dietmar Stalke (Georg-August-Universität Göttingen, Institut für Anorganische Chemie, Göttingen)

Datum der Disputation: 15.03.2022

Meiner Mutter

Without sensibility no object would be given to us; and without understanding no object would be thought. Thoughts without content are empty; intuitions without concepts are blind. Hence it is just as necessary that we make our concepts sensible (i. e., that we add the object to them in intuition) as it is necessary that we make our intuitions understandable (i. e., that we bring them under concepts).

(Immanuel Kant, *Critique of Pure Reason*, B 75)

Ohne Sinnlichkeit würde uns kein Gegenstand gegeben, und ohne Verstand keiner gedacht werden. Gedanken ohne Inhalt sind leer, Anschauungen ohne Begriffe sind blind. Daher ist es ebenso notwendig, seine Begriffe sinnlich zu machen, (d. i. ihnen den Gegenstand in der Anschauung beizufügen,) als seine Anschauungen sich verständlich zu machen (d. i. sie unter Begriffe zu bringen).

(Immanuel Kant, *Kritik der reinen Vernunft*, B 75)

Danksagung

Die vorliegende Arbeit wurde im Januar 2022 als Dissertation an der Fakultät für Chemie der Georg-August-Universität Göttingen eingereicht. Diese Arbeit hätte nicht entstehen können ohne den entscheidenden und prägenden Einfluss auf meinen wissenschaftlichen Werdegang durch meinen Erstgutachter und Mentor Prof. Dr. Martin Suhm, der mich von einer Promotion im Fach Chemie überzeugt hat und das interdisziplinäre Verknüpfen von Physik und Chemie, Experiment und Theorie ermutigte und förderte sowie mir stets mit Rat und Tat zur Seite stand. Ihm gilt mein ganz besonderer Dank. Für die Übernahme des Zweitgutachtens möchte ich Prof. Dr. Jörg Behler danken sowie Prof. Dr. Ricardo Mata, Prof. Dr. Daniel Obenchain, Prof. Dr. Dietmar Stalke und Prof. Dr. Dirk Schwarzer, die sich freundlicherweise die Zeit genommen haben, als Mitglieder der Prüfungskommission zu wirken. Schließlich möchte ich dem Drittgutachter für seine konstruktiven und hilfreichen Anmerkungen danken.

Der Gegenstand dieser Arbeit – die schwingungsspektroskopische Untersuchung der Ameisensäure – hat inzwischen Tradition in Göttingen und so konnte ich auf wichtige experimentelle Vorarbeiten von Dr. Zhifeng Xue, Dr. Franz Kollipost und Dr. Katharina Meyer zurückgreifen. Den beiden Letztgenannten gilt zudem mein Dank für die Erlaubnis zur Reproduktion einiger ihrer gemessenen Spektren.

Viele der dargelegten experimentellen und theoretischen Untersuchungen wurden befruchtet und vorangetrieben durch die Unterstützung von vielen, denen ich zu Dank verpflichtet bin: Prof. Dr. Deborah Crittenden, ein Vorbild, auch einmal gegen den Strom zu schwimmen, die maßgeblich zur Entstehung von Abschnitt 2.1.4 beigetragen und freundlicherweise Teile des Manuskriptes kritisch durchgesehen hat; Prof. Ricardo Mata für Unterstützung im Navigieren durch das ‘Minenfeld’ der politischen Wissenschaft; Prof. Dr. Edit Mátyus, Prof. Dr. Edwin Sibert und Prof. Dr. David Tew für viele lehrreiche Diskussionen zur theoretischen Schwingungsspektroskopie; Dr. Benjamin Schröder für das Bereitstellen seines VPT2-Programms und viele anregende Diskussionen zur störungstheoretischen Behandlung von Schwingungen; Dr. Robert Medel für sehr interessante Unterhaltungen zum Tunneleffekt in Alkoholen, die unter anderem zu den Untersuchungen in Abschnitt 5.3.2 geführt haben; Dr. Maxim Gawrilow für lehrreiche Diskussionen rund um den Smekal-Raman-Effekt, aus denen die Idee zur Rotationssimulation von HCOOD in Abbildung 2.6 geboren wurde; Prof. Dr. Zlatko Bačić und Prof. Dr. Tucker Carrington für meine Teilnahme an der Tagung “Spectroscopy and Dynamics of Coupled Anharmonic Vibrations of Floppy Molecular Systems” im Jahr 2019, die einen entscheidenden Einfluss auf den weiteren Verlauf meiner Promotion gehabt hat; den Entwicklern des Programmpaketes CFOUR, die ihr Programm der Wissenschaftsgemeinschaft frei zur Verfügung stellen und insbesondere Prof. Dr. Devin Matthews und Prof. Dr. John Stanton, die mir bei Fragen zur Bedienung des Moduls GUINEA stets hilfreich zur Seite standen. Dr. Katharina Meyer gilt mein ganz besonderer Dank für ihre Unterweisungen an den experimentellen Apparaturen, ihre Unterstützung an zahlreichen langen Messtagen und ihre kritischen sowie wertvollen Anmerkungen zu vielen Teilen des Manuskriptes.

Ich möchte mich herzlich beim Fonds der Chemischen Industrie für ein zweijähriges Kekulé-Promotionsstipendium bedanken, das mir viele Freiheiten im Verfolgen meiner Projekte gewährt

hat. Des Weiteren gilt mein Dank der Deutschen Forschungsgemeinschaft für finanzielle Unterstützung vor, während und nach dem Kekulé-Stipendium, insbesondere um die benötigten Mengen von deuterierter Ameisensäure für die spektroskopische Untersuchung des Monomers (Projekt-Nr. 389479699) und Dimers (Projekt-Nr. 388861488) anzuschaffen und die Projekte voranzubringen und abzuschließen, sowie dem Graduiertenkolleg 2455 “BEnch” für das Ermöglichen und Fördern des wissenschaftlichen Austausches.

Schließlich gilt mein Dank meinen beiden Eltern, die mir ein Leben in Deutschland ermöglicht haben und meiner Partnerin Dr. Rahel Micklich, ohne deren unermüdliche Unterstützung ich dieses Buch nicht hätte abschließen können.

Würzburg, im Dezember 2022
Arman Nejad

Contents

Preface

This work has been submitted as a dissertation to the Faculty of Chemistry at the Georg-August University of Göttingen in January 2022. Parts of this work have been previously published open access in peer-reviewed journals (Refs. [28, 91, 109, 130]). Respective sections and paragraphs have been rewritten to the best of my abilities. But especially when describing theoretical background and employed methods or assigning vibrational bands, there are just so many ways one can rephrase the same content. As such, there might be overlapping content in this work that is not explicitly marked as a citation.

As the title suggests, the topic of this work is the vibrational spectroscopy of formic acid and its cyclic dimer from a combined experimental and computational perspective. In recent years, in particular the computational vibrational dynamics of formic acid and its dimer have gained renewed interest. While there are extensive experimental vibrational and rotational reference databases for diatomic molecules, the situation is much more mosaic and scattered for larger polyatomic molecules, particularly for formic acid and its cyclic dimer whose experimental literature spans more than half a century. For example, despite several high-resolution vibrational spectroscopic studies on formic acid in the past two decades, still obsolete and incorrect values that date back several decades are being used in some research papers. Similarly for the dimer, one finds studies where obsolete room temperature low-resolution gas phase data are used to compare to nuclear vibrational structure calculations that usually do not take thermal shifts into account – a test quantum chemistry is bound to fail. Agreement with experiment might be for the wrong reasons, disagreement, however, not necessarily an indication for shortcomings in the calculations. As we all struggle with a complete coverage of the state of the art, it is desirable to overcome the scatter of the vibrational literature on these systems. To make a first step towards this goal, I have compiled and updated gas phase or jet-cooled high-resolution and jet-cooled low-resolution vibrational Raman and IR band centres of formic acid from the literature, focussing on the wavenumber region below 4000 cm^{-1} (Table 4.8, pp. 91). While this database is far from complete, I hope that I have not missed important contributions. In an effort to make this database more useful to researchers, in particular for future benchmarking endeavours, it has additionally been published online (https://qmbench.net) where the data can be downloaded in an easily accessible data table format. Moreover, the online database can be extended to incorporate new results. The digitalisation of the dimer and trimer databases in Chapter 7 will follow soon.

Since the submission of this work, several new experimental and high-level computational investigations of formic acid and its cyclic dimer have been published with further studies in preparation. Newly published literature has been included in the citations and is referenced in appropriate places. Of particular importance to this work are the new variational vibrational $J = 0$ energy levels of HCOOH on the Tew and Mizukami potential by Mátyus and co-workers. These GENIUSH-Smolyak values are essentially exact and near-fully converged. As such, Chapter 5 has been reworked to incorporate these new results. Rewardingly, the proposed (re-)assignments and main conclusions in Chapter 4 remain valid in light of these new variational calculations.

List of abbreviations and acronyms

Formic acid conformers and clusters

*c*F	Higher-energy *cis*-formic acid monomer
*t*F or F	Global minimum *trans*-formic acid monomer
(FF) or FAD	Global minimum cyclic formic acid dimer
FF	Higher-energy polar formic acid dimer
F(FF)	Global minimum formic acid trimer

Electronic structure theory

aVXZ	Dunning's augmented correlation-consistent basis sets (aug-cc-pVXZ)
B3LYP-D3(BJ)	Becke-3-LYP with Grimme's D3 correction and Becke-Johnson damping
CBS	Complete basis set limit
CCSD(T)	Coupled-cluster with singles, doubles, and perturbative triples
DFT	Density functional theory
HF	Hartree-Fock
MP*n*	*n*th-order Møller-Plesset perturbation theory
PES	Potential energy (hyper)surface
QB-PES	Formic acid dimer PES by Qu and Bowman [23]
RC-PES	Formic acid monomer PES by Richter and Carbonnière [22]
TM-PES	Formic acid monomer PES by Tew and Mizukami [21]
VXZ-F12	Correlation-consistent basis sets optimised for F12 methods (cc-pVXZ)

Nuclear vibrational structure theory

CVPT*n*	*n*th-order canonical Van Vleck perturbation theory
DMC	Diffusion Monte Carlo
DVPT*n*	*n*th-order deperturbed vibrational perturbation theory
ICPH	Internal coordinate path Hamiltonian
MCTDH	Multiconfiguration time-dependent Hartree
QFF	Quartic force field expansion of the PES
SFF	Sextic force field expansion of the PES
SOF	Sum-of-fundamentals (p. 17)
SOF+*x*	SOF with additional VPT2 corrections (p. 17)
VCI	Vibrational configuration interaction
VMP*n*	*n*th-order vibrational Møller-Plesset perturbation theory
VPT*n*	*n*th-order vibrational perturbation theory
VPT2+F	VPT2 with third-rank resonance treatment (pp. 20)
VPT2+K	VPT2+F including second- and fourth-rank resonances (pp. 22)
VSCF	Vibrational self-consistent field
ZPVE	Zero-point vibrational energy

Chapter 1

Introduction

In a recent essay, Mata and Suhm critically reviewed the paradigm shift in chemistry between experiment and theory that has set in over the past 30 years in light of the increasing accuracy of electronic structure methods, advocating more experimental benchmarks to evaluate theory [1]:

> "Over the last years a subtle but profound change has taken place in chemical research. Electronic structure calculations have become ubiquitous, with much of the work published in the field today making use of theoretical results. [...] We find ourselves at a perceived turning point where quantum chemical calculations are believed by many to be on par with experimental methods. [...] In contrast to other fields of science, where a model is mostly used as a framework to break down and understand complex systems, electronic structure methods are regarded as quantitative-data providers. [...] We chemists dare to believe that our theoretical models will be able to provide us with a reaction mechanism involving hundreds of atoms. This line of thought is fertile ground for illusions of grandeur, and calls for a critical analysis of the relation between experiment and theory in chemistry."

The primary concern in the field of quantum and computational chemistry nowadays is the efficient implementation of the exact or approximate theories into computer code in order to extend the applicability of these programs to larger and more complex systems [1]. Most quantum chemical applications are conducted in the framework of the adiabatic Born-Oppenheimer approximation where the electronic and nuclear degrees of freedom are treated separately [2]. Thus, the nuclear vibrational problem is divided into three parts with the experiment on one side and solutions of the electronic Schrödinger equation on the other side which are bridged by nuclear ro-vibrational dynamics [3–14]. In this work, the focus is on comparing vibrational wavenumbers between theory and experiment which is particularly fruitful as these can be benchmarked quite rigorously [1].[1]

A decade ago, Császár *et al.* proclaimed that after three ages of developments in electronic structure methods, the new fourth age of quantum chemistry had begun – under the sign of nuclear structure methods [7].[2] This work is intended to contribute to the development and further advancement of nuclear vibrational methods at the frontiers of size and dimensionality. It is dedicated to the rotationless ($J = 0$) vibrational spectroscopy of the formic acid molecule and its doubly hydrogen-bonded cyclic dimer (Fig. 1.1). The experimental and theoretical vibrational spectroscopy of both systems has seen new impulses in recent years. In particular, full-dimensional coupled-cluster-quality or transfer-learned potential energy functions have become available for both systems [21–25] (even a dipole moment surface for the dimer [26]) which is

[1] Vibrational spectroscopy can also be used to benchmark the relative electronic energy preferences of different conformers where it may be possible to neglect (anharmonic) zero-point vibrational differences [15–17].

[2] Since the quality of the nuclear vibrational calculation critically depends on the accuracy of the Born-Oppenheimer potential energy, the recent advances in explicitly correlated F12 theory are particularly noteworthy. For details, see for example Refs. [18, 19] and references cited therein. In a vibrational context, see also the benchmark in Ref. [20].

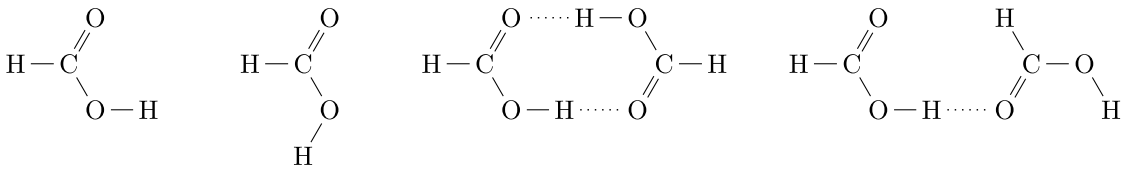

Figure 1.1 Schematic Lewis structures of the conformational isomers of formic acid and its dimer. F and (FF) are the respective equilibrium structures of formic acid monomer and dimer. The parentheses represent a closed hydrogen bond pattern. In the literature, (FF) is often referred to as *the* formic acid dimer and abbreviated to FAD.

a fertile ground to test and extend the nuclear vibrational methodologies for these systems. Indeed, several nuclear vibrational structure calculations have been published in recent years that utilise these potentials [21–25, 27–33]. To further push theory and uncover shortcomings in the currently 'best' calculations, it is now the experimental spectroscopists' turn. While the experimental vibrational spectroscopic research of formic acid and its thermally stable cyclic dimer is spanning over several decades, there are some gaps and errors in the experimental database of the former and an urgent need of updating and reanalysing the database of the latter. Utilising the *reciprocal* relationship between experimental and theoretical vibrational spectroscopy, the objective of this work is twofold: The experimental database is first reviewed and updated. It is then used for benchmarks in order to reveal weaknesses in the theoretical description of the formic acid monomer and dimer in order to advance our understanding of these prototypical model systems.

1.1 Experiment meets theory

In order to meet theory at the most basic level, the following requirements should be met by an experimental design that is aiming at providing benchmark-quality reference data [1]:

1. No environmental effects (molecules in the diluted gas phase).
2. No thermal effects (temperature as close as possible to 0 K).
3. Suitable molecular system.

Let us start with the first two points. Matrix isolation spectroscopy facilitates the study of metastable or short-lived species that are difficult to prepare in the gas phase [34]. The second obstacle mentioned above is overcome but the chemical environment induces shifts on the vibrational band centres that can vary in size and direction. While helium nanodroplet spectroscopy is less perturbing than matrix isolation techniques, it nonetheless introduces a weakly perturbing environment [35]. Until the size and direction of the environmental shifts can be modelled reliably for different environments and molecular vibrations, such techniques are less suitable for the purpose of vibrational benchmarking. The most accurate vibration-rotation data can be obtained by rotationally-resolved high-resolution [6, 36] supersonic jet or thermal gas phase spectroscopy. Supersonic jet spectroscopy[3] has the advantage of a simplified rotational fine structure through jet cooling and enhanced aggregation, facilitating the study of molecular complexes [38]. As such, low-resolution supersonic jet spectroscopy provides a straightforward and fully sufficient approximation to the required rotationless band centres.

As for the third point, there are no strict requirements for molecules or molecular systems to serve as benchmarking references except perhaps easy accessibility for experiment and theory.

[3] For an introduction to supersonic jet spectroscopy and its applications, see for example Refs. [37–39].

There are, however, some additional points one might consider. As an entry point, it would be desirable to reduce the dynamical complexity, i.e. 'floppiness' and delocalisation over several minima, as far as possible. But, the system should still offer some complexity and not be too harmonic, e.g. exhibit some anharmonic resonances. To allow for diversity, the ability to systematically increase the difficulty, e.g. through chemical substitution, would be very desirable.

The formic acid molecule and its cyclic dimer are such reference systems that are particularly suitable for the purpose of vibrational benchmarking. From the experimental side, the high volatility of formic acid and the thermodynamic gas phase stability of its cyclic dimer [40] make them easily accessible for gas phase spectroscopy while they also allow for a systematic and controlled increase in complexity through chemical C–H substitution.[4] From the theoretical side (as will be shown in this work), the moderate size and simultaneous semi-rigidity of the monomer and the dimer (through the strong hydrogen bonds) make them accessible to more widespread single-reference models that utilise rectilinear normal mode coordinates, as opposed to the hydrogen fluoride dimer [44] and even more so the water dimer [45]. Both formic acid systems exhibit additional characteristics that introduce further complexity, such as multi-well character and strong vibrational resonances that gradually increase in importance as functions of vibrational excitation and excitation wavenumber.

1.2 Theory meets experiment

The sheer dimensionality of the 'vibrational problem' requires certain approximations to be made in order to facilitate computations of medium-sized systems in realistic time frames. This has resulted in "different variants of quantum chemical nuclear motion theory [that] coexist and they often serve different purposes" [7]. Two very general distinctions are particularly useful: Which coordinate system is used to expand the ro-vibrational Hamiltonian and is a perturbative ansatz or the variational principle employed?

Behind the coordinate choice – tellingly also referred to as the "coordinate dilemma" [7] – is the reasoning to use a representation that best describes the curvilinear nuclear movements, thus making the zeroth-order description as separable as possible [7]. However, it may also be advantageous to use a less 'physical' description, e.g. rectilinear coordinates. In layman's terms, the coordinate impact on the kinetic and potential energy components of the nuclear vibrational Hamiltonian is somewhat inversely proportional where rectilinear coordinates yield a much more concise form of the kinetic energy operator whereas the molecular potential energy usually converges much faster in appropriate curvilinear coordinates. Generally, the coordinate dilemma is a choice between Scylla and Charybdis as there is no *a priori* superiority of one over the other since much depends on the molecular system and energy regime of interest. The practical implications and parallels to electronic structure theory were illustrated by Sibert III *et al.* [46] who stress that

> "exact implementations of the curvilinear and rectilinear descriptions are strictly equivalent. However, a key practical point is that they are not equivalent in low orders of approximation. A useful comparison here is with valence bond and molecular orbital theories of chemical bonds. When carried out to high levels of approximation, these two theoretical bonding frameworks naturally predict the same physics. In contrast, the physical pictures painted by the two descriptions differ considerably at low orders of approximation."

As to the question of how to solve the nuclear vibrational Schrödinger equation, there are several possible formulations that adhere to the variational principle.[5] Popular approaches include

[4] See also Refs. [41, 42] for other carboxylic acid homologues or Ref. [43] for mixed carboxylic acid-alcohol complexes.

[5] See for example the review by Bowman *et al.* [5] or the perspective by Császár *et al.* [7].

the multiconfiguration time-dependent Hartree method [47] (MCTDH) or the vibrational self-consistent field (VSCF) and its vibrational correlation extensions that are very similar to their electronic structure theory analogues.[6] Out of the possible post-VSCF methods, the vibrational configuration interaction (VCI) method is of particular importance to this work. There are formulations where the VCI wavefunction is expanded either as a linear combination of harmonic oscillator product functions or using VSCF modals.[7] In theory, these methods are independent of the coordinate choice but for this work, the more widespread implementations that utilise the rectilinear normal coordinate Watson Hamiltonian or Watsonian [57] are of particular interest.[8] To account for the distinct curvilinearity of certain modes, there are modifications to the Watsonian,[9] e.g. the internal coordinate path Hamiltonian which, for example, was employed to study the formic acid molecule [21, 29].

There are also different formulations of perturbation theory which are in principle again independent of the coordinate choice. There is no strict nomenclature, but usually, VPT (vibrational perturbation theory) refers to variants based on the harmonic oscillator whereas VMP (vibrational Møller-Plesset perturbation theory) builds on VSCF and is methodologically similar to its electronic structure counterpart. There are different methods to derive[10] the working equations of VPT, including the contact transformation or (canonical) Van Vleck perturbation theory and Rayleigh-Schrödinger perturbation theory. Due to its hierarchical structure, perturbation theory provides an inherent connection between the perturbative order and coordinate completeness. The inadequateness of rectilinear coordinates, for example, can in principle[11] be remedied by going to higher orders of perturbation theory which "account for effects associated with the nonlinear transformation between curvilinear and rectilinear coordinates as much as any profound anharmonicity *per se*" [73].

The oldest, best-known, and arguably most popular[12] variant of perturbation theory is second-order vibrational perturbation theory (VPT2) in conjunction with rectilinear normal coordinates [64]. There is a rift within the theoretical spectroscopy community regarding the approximate method of choice to solve the nuclear vibrational Schrödinger equation and especially VPT2 is a divisive subject. Matthews *et al.* [77] addressed this over a decade ago as follows:

> "The fact that VPT2 is exact for the Morse oscillator is surprisingly poorly appreciated in the theoretical chemistry community; the merits of VPT2 in the treatment of vibrational anharmonicity are undoubtedly more greatly appreciated by experimentalists than most quantum chemists. Indeed, statements about the 'need' for variational calculations of vibrational levels – and with them, a tacit acknowledgement of the supposed superiority of variational methods – are often made, even when VPT2 is working extremely well."

Apart from being the cheapest anharmonic nuclear structure model, one of the appealing features of VPT2 is that it utilises the same language that is used by spectroscopists, providing a simplistic and often surprisingly accurate picture to understand vibrational resonances, progres-

6 See for example Refs. [12, 48–51] and also Ref. [4] and references cited therein.

7 The VSCF modals are often but not necessarily contracted harmonic oscillator functions. See for example Refs. [21, 52]. Multimode [52], Molpro [51, 53, 54], and Dynamol [55] use VSCF modals whereas in PyVCI a harmonic oscillator basis is implemented [56].

8 For curvilinear VSCF and post-VSCF methods, see for example Ref. [58] and references cited therein.

9 See Refs. [59, 60] and for related models also Refs. [61–63].

10 For further reading, see for example Refs. [64–74] and references cited therein.

11 A well-known problem in electronic structure theory is the behaviour of the Møller-Plesset method (which is based on Rayleigh-Schrödinger perturbation theory) as a function of the perturbative order. Such expansions are not always necessarily convergent [75]. Similar results were found by Christiansen who investigated the convergence properties of its vibrational analogue [76].

12 The widespread popularity of VPT2 for polyatomic systems can particularly be credited to Barone and his implementation in the Gaussian program [70], facilitating the computation of anharmonic energy levels and intensities in a fully automated black-box manner (mind Appendix C).

sions of hot/difference bands, or anticipate positions of overtone/combination bands. Certainly, the perturbed harmonic oscillator is less useful to understand exotic molecules such as protonated methane [78] but these are rather the exceptions to the rule.

In the age of big data with ever-increasing supplemental appendices and data repositories, new community guidelines for publishing experimental and computational chemical results would be welcome. Mata and Suhm formulated some insightful ideas for experiment and theory meeting each other. Before *theory meets experiment*, one might add in the context of theoretical vibrational spectroscopy: *theory checking VPT2* – in analogy to long-established practices of experiment checking experiment, e.g. linear/action spectroscopy or IR/Raman in the absence of inversion symmetry. Harmonic wavenumbers are already regularly reported whenever anharmonic vibrational energy levels are published. Editors and reviewers should invite and encourage researchers who use sophisticated variational vibrational models, higher orders of vibrational perturbation theory, or perhaps more sophisticated coordinate systems to additionally include VPT2 predictions on the same potential. A critical reader might interject there are situations where VPT2 clearly fails and that there might be no point or even harm in publishing such results. "Theoreticians should", as Mata and Suhm [1] stress, however, "not only mention the 'successful' methods, but also take the opportunity to address the approaches that fail, in particular those with wide acceptance in the community." Indeed, we can learn from the limitations of theoretical models and it goes without saying that the publication of 'inadequate' results necessitates a disclaimer and proper discussion to prevent the propagation of wrong conclusions. Whereas there is no (sizeable) additional computational cost,[13] the scientific community will certainly profit from an extension of the well-established harmonic/anharmonic juxtaposition to such a triumvirate. Especially for experimentalists trying their hand at VPT2, these data will provide useful guidance on when and "how to VPT2" [11] – and when not to. An attractive byproduct of such a new mentality, i.e. publishing VPT2 wavenumbers alongside harmonic and more 'sophisticated' results, might be the occasional early discovery of shortcomings of the latter. As we will see, the stories of formic acid and its cyclic dimer are certainly such cases, where a comparison of harmonic, VPT2, and VCI term values could have revealed shortcomings[14] in the latter.

1.3 Formic acid – Current state of research

The formic acid molecule

The formic acid monomer has two conformational isomers, *cis*-formic acid and *trans*-formic acid (Fig. 1.1),[15] that are connected by rotation around the C–O bond which corresponds to the OH torsional vibration ν_9. Both conformers are planar, near-prolate asymmetric tops [80–82]. The nine vibrations are schematically illustrated for the *trans* conformer in Fig. 1.2.

Vibrational spectroscopic characterisation of the higher-energy *cis* rotamer is lagging behind

[13] From the point of view of any anharmonic vibrational model, it is a trivial and cheap task to compute harmonic wavenumbers. These arguments similarly extend to obtaining a semi-diagonal quartic force field and thus VPT2 wavenumbers when variational or higher-order perturbative calculations are feasible – if an analytic potential is available, this task is trivial and when *ab initio* single-point energies are used, the cost associated with additional displacements necessary for VPT2 is usually negligible in comparison. Ramakrishnan and Rauhut even demonstrated how accurate semi-diagonal quartic force fields can be retrieved from multi-mode expansions of the potential [79], obviating the need for additional energy calculations.

[14] This refers to specific VCI calculations on these systems that have been published in the literature and does not extend to the VCI method in general which, from a theoretical and conceptual perspective, is superior to VPT2.

[15] To distinguish between both rotamers, the *cis*/*trans* prefixes are used, which refer to the relative position of the H atoms about the C–O bond. If this distinction is not made, the global minimum *trans* conformation is implied. Note that also the IUPAC classification is used in the literature where the labels are interchanged.

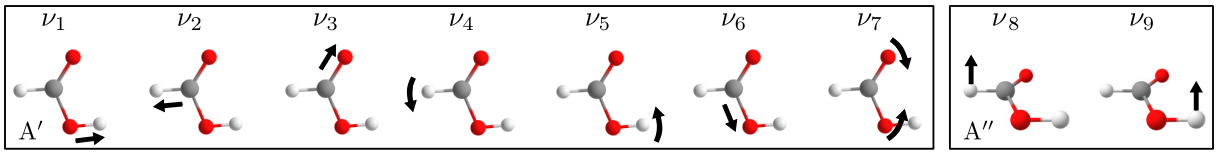

Figure 1.2 Schematic drawing of the nine *trans*-HCOOH fundamental vibrations. Adapted from Ref. [28] (published under a Creative Commons Attribution license, CC BY 4.0).

that of the *trans* species due to the high energy difference[16] and thus low *cis* population of approximately 0.1% at room temperature. In order to probe the vibrational dynamics of *cis*-formic acid, matrix isolation has been the method of choice until recently[17] but as mentioned earlier, the vibrational shifts on the band centres render them unsuitable for benchmarking purposes (see Ref. [87]). Gas phase vibrational data on *cis*-formic acid were first reported in 2006[18] and after a decade of stagnation, the number of environment-free vibrational *cis*-formic acid band centres has considerably increased since 2019 [86, 87, 89, 90],[19] even extending to deuterated isotopologues [86, 91]. The first Raman spectroscopic gas phase detection of *cis*-formic acid was pioneered by Meyer and Suhm by employing thermal excitation as a means to enhance the *cis* population, followed by rapid jet-cooling of the molecules in a supersonic expansion [87, 89].

The vibrational dynamics of the global minimum *trans* rotamer, on the other hand, have been characterised quite extensively in the gas phase.[20] The highest-wavenumber fundamental is located slightly below 3600 cm^{-1} but this spectral window has not been investigated exhaustively and some gaps remain. The experimental literature predominantly contains IR spectroscopic studies of the main isotopologue, the complementary Raman spectroscopic characterisation, in general, and the vibrational characterisation of the deuterated isotopologues, in particular, lagging behind. Throughout this work, we will see how additional Raman spectroscopy and deuteration are important aids in unravelling vibrational resonances – of which there are many in the *trans*-formic acid molecule – and cross-checking combination/overtone band assignments.

The high-level computational anharmonic vibrational literature on the formic acid molecule was relatively compact and has considerably grown since 2016.[21] Particularly noteworthy for the main isotopologue are the works of Demaison *et al.* [99] (perturbative effective Hamiltonians), Tew and Mizukami [21] (variational; including *trans-cis* delocalisation) and Richter and Carbonnière [22] (variational; single-well) in which many experimental assignments and analyses were meticulously examined and potential misassignments pointed out. Moreover, all these works have provided the scientific community with coupled-cluster-quality force fields [99] and full-dimensional potential energy functions [21, 22] of the formic acid monomer. Martín Santa

[16] The energy difference was measured in the 1970s by Hocking using microwave spectroscopy who reported 1365(30) cm^{-1} or equivalently 16.3(4) kJ mol^{-1} [81]. There does not seem to have been another experimental study attempting to reproduce this value. Recent variational calculations on CCSD(T)-F12-quality potentials yield 16.9-17.0 kJ mol^{-1} [21, 22, 29].

[17] The first vibrational characterisation of *cis*-formic acid was achieved in 1997 by Pettersson *et al.* using a solid argon matrix [83]. In subsequent years, the vibrational spectroscopy of *cis*-formic acid was extended to other isotopologues and matrix hosts, e.g. [84, 85]; see also references cited in Ref. [86].

[18] Until 2019, ν_9 was the only *cis* vibration that had been characterised in the gas phase, facilitated by the large spectral separation of ν_9 between both rotamers (147 cm^{-1}, Ref. [88]).

[19] Note that in addition to the OH stretching band, Doney *et al.* furthermore reported band centres for two additional Coriolis-coupled states (see supplementary material of Ref. [90]).

[20] See Refs. [92–96] and references cited therein. See also references cited in Section 4.6 of this work and cited in Ref. [86].

[21] Very recently, the published anharmonic vibrational studies of formic acid have been reviewed in Ref. [97]. See also Refs. [21, 22, 27–30, 98, 99] and Refs. [24, 55, 100–105] where the formic acid monomer is of secondary interest or used as a benchmarking reference.

Daría *et al.* [29] have recently published the so far most rigorous vibrational calculation of formic acid, utilising the exact 9D potential from Ref. [21] and including *trans-cis* delocalisation effects.

Some unresolved issues concerning the fundamental region below 4000 cm^{-1}, most of which are addressed in this work, include:

1. *The OH bend-torsion resonance*. In *trans*-HCOOH, there is a very strong and important Fermi resonance between the OH in-plane bending fundamental (ν_5) and OH torsional overtone ($2\nu_9$). It was long assumed that the fundamental corresponds to the lower-wavenumber band of this doublet, but based on recent theoretical and experimental evidence,[22] it is now widely accepted that ν_5 is centred at 1306.14 cm^{-1} [95] and $2\nu_9$ correspondingly at 1220.83 cm^{-1} [110]. In hindsight, the $\nu_5/2\nu_9$ 'controversy' could have easily been resolved if complementary, cluster-free Raman spectra of formic acid would have been available early on. This was recently demonstrated by Meyer who compared the IR and Raman jet spectra of HCOOH [86]. When defining a polyad quantum number[23] for this resonance, $N_5 = n_5 + n_9/2$, ν_5 and $2\nu_9$ correspond to $N_5 = 1$. Combination states that are partly excited in this polyad are known to perturb the C=O (ν_3) and C–H (ν_2) stretching fundamentals [96, 99] but little is experimentally known about how this resonance polyad progresses; up to $N_5 = 1.5$, this polyad has experimentally been characterised, starting with $N_5 = 2$, however, experimental data are sparse.[24]
2. *Delocalisation effects between the trans and cis wells*. So far, only two (full-dimensional vibrational) studies explicitly accounted for the double minimum along the torsional coordinate [21, 29]. These calculations indicate wavefunction mixing between both wells to start with $n_9 = 6$-7, corresponding to $N_5 = 3$-3.5 in the bend-torsion polyad. Such effects still need to be observed experimentally.
3. *Resonance perturbations of the OH stretching fundamental*. The OH stretching fundamental (ν_1) remains the only *trans*-HCOOH fundamental whose rotationally-resolved gas phase spectrum, which was reported already in 2000 by Hurtmans *et al.* [114], has not been analysed. The authors reported a higher than expected density of lines [114], usually indicative of additional resonance perturbations. Shortly after, Madeja *et al.* reported an analysis of the rotationally-resolved ν_1 band in helium nanodroplets. They obtained three vibrational band centres for the O–H stretching fundamental at 3570.66, 3568.63, and 3566.35 cm^{-1} [115]. They ascribed the two perturbers to $\nu_2+\nu_7$ (A′) and $\nu_2+\nu_9$ (A″). While Freytes *et al.* noted similarities between the room temperature gas phase and he-

[22] To get an overview of the history of the experimental $\nu_5/2\nu_9$ assignment, see Refs. [86, 93–95, 106–108]. For brevity, the bands at ∼1300 and ∼1220 cm^{-1} are hereafter referred to as ν_{high} and ν_{low}, respectively. Since ν_{low} is more visible in the IR [94, 95], it was observed early on (see Ref. [92] and references cited therein). While ν_{high} was observed already in the 1970s by Hisatusune and Heicklen [106], this was not realised by the authors who incorrectly attributed ν_{high} to the CH in-plane bend ν_4. ν_{high} is much more visible in the Raman spectra (see Section 4.2) and it was later observed by Bertie and Michaelian [93]. Since ν_{low} accidentally overlaps with a strong Raman-active fundamental of the dimer [109], it was not realised that ν_{high} is by far more Raman-active than ν_{low} which might have led to a critical reexamination of the $\nu_5/2\nu_9$ assignment already in the 1980s. Building on the previous IR assignment of ν_5 to ν_{low}, Bertie and Michaelian consequently ruled out an assignment to ν_5 and proposed $2\nu_9$ as an assignment for ν_{high}. With gas phase IR spectroscopy, ν_{high} was then again observed by Freytes *et al.* [94]. Its assignment to $2\nu_9$ was subsequently corroborated by Baskakov *et al.* who analysed $2\nu_9-\nu_9$ type hot bands [95]. Triggered by the theory-guided proposal to reassign ν_5 to ν_{high} [21, 22], Hull *et al.* [107] reexamined the hot band transitions in 2019 and refuted the assignment by Baskakov *et al.* Note that incompatibility of the pre-2019 assignment with theory was already pointed out one decade earlier by Demaison *et al.* who used perturbative effective Hamiltonians [99].

[23] On the concept of polyads in vibrational spectroscopy, see for example Refs. [111–113].

[24] See Refs. [94–96] and reassignments to bands this polyad in Refs. [21, 22]; mind $\nu_5 \leftrightarrow 2\nu_9$ label switch in the pre-2019 literature.

lium nanodroplet spectrum [94], the gas phase ν_1 band remains unanalysed to this day.[25] Since states from the OH bend-torsion polyad ($N_5 = 3$) are expected in the vicinity of ν_1, a clear assignment of the gas phase perturbers is of great significance, especially in view of items 1 and 2.

4. *Recent theory-guided reassignments.* In light of conflicting results for the computed $J = 0$ spectrum of *cis*-HCOOH in Refs. [21, 22] which similarly apply to higher-excited torsional states of *trans*-HCOOH [28], there is a need for an independent review of the recently proposed reassignments and analysis of the cause of these discrepancies.[26]
5. *Vibrational spectroscopy of deuterated trans-formic acid.* Generally, the vibrational gas phase spectroscopic characterisation of deuterated *trans*-formic acid[27] is – by far – not comparable to that of the main isotopologue, lacking studies similar to Refs. [94–96]. In order to guide and critically examine assignments for the highly anharmonic main isotopologue (item 4), deuteration information can be of great value [117].
6. *Raman spectroscopy of trans-formic acid.* Raman spectroscopy yields complementary information which can help to identify resonance situations and guide IR assignments. Raman spectroscopic studies of monomeric formic acid [28, 86, 87, 91, 93, 118, 119] are generally sparse in comparison to the predominant IR literature. There is especially a need for monomer-optimised, cluster-free Raman spectra of formic acid in the full fundamental range. The full fundamental range was measured and reported for all four H/D isotopologues by Bertie *et al.* in the thermal gas phase [93, 118] and more recently by Xue using jet-cooling [119]. However, these studies were primarily concerned with the formic acid dimer and were therefore carried out at higher acid concentrations, so that many monomer bands remained hidden under the cluster bands.

The cyclic formic acid dimer

The formic acid dimer has $2\times9 = 18$ internal degrees of freedom that correspond to intramolecular vibrations. Since both monomers move in concert and thus behave like a single molecule, six additional intermolecular pair or van der Waals vibrations are generated that correspond to hindered relative translations and rotations of the paired molecules. The global minimum cyclic dimer is planar [80] and the two equivalent *trans* monomers are arranged in a way that gives rise to inversion symmetry (Fig. 1.1). The energetically next higher-energy structure, the C_s symmetric polar dimer (Fig. 1.1), has been previously prepared in helium nanodroplets [120, 121] and matrix isolation [122–124] but eludes detection in the gas phase.[28]

For pairs of equivalent inter- and intramolecular vibrations, the inversion symmetry of the cyclic dimer leads to an excitonic or Davydov splitting into a symmetric (in-phase) and antisymmetric (out-of-phase) combination. Due to the rule of mutual exclusion, the cyclic dimer vibrations are exclusively Raman-active (A_g, B_g) or IR-active (A_u, B_u) [128]. Thus, each Davydov pair consists of one IR- and one Raman-active mode. Common IR and Raman splitting patterns directly point at wavefunction mixing for single bright modes which can and will be

[25] Just recently, the first high-resolution jet-cooled measurement of the first OH overtone ($2\nu_1$) has been published [116].

[26] The recent calculations by Martín Santa Daría *et al.* [29] and the analysis presented in Section 5.3.1 of this work suggest that the main source of discrepancies is due to convergence errors of excited torsional states in Ref. [21].

[27] See for example references cited in Section 4.6.

[28] See Refs. [125, 126] where possible assignments of FF are discussed in the jet-cooled gas phase spectra of HCOOH. Note that Balabin postulated the detection of FF in the gas phase Raman spectrum of HCOOH [127] but, so far, this result has not been confirmed by other gas phase spectroscopic studies. Similarly, his proposed assignment [127] of the Raman-active OH torsion of (FF) appears doubtful [109].

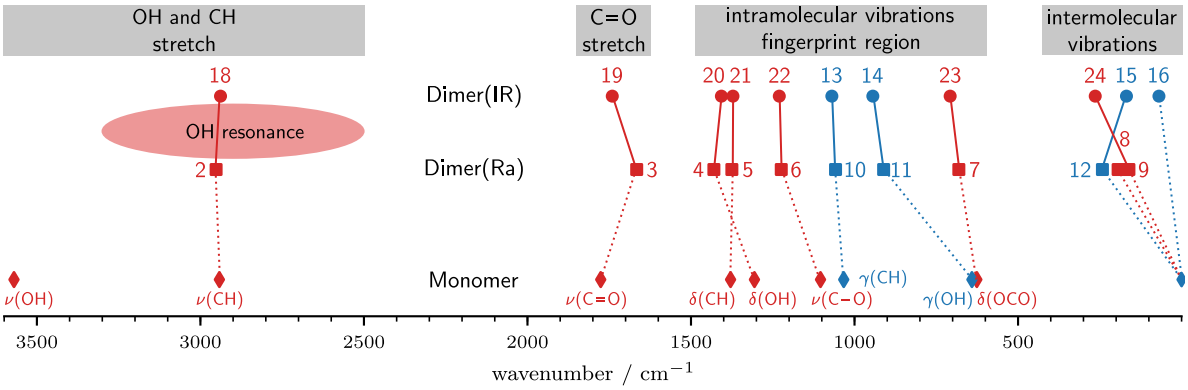

Figure 1.3 The fundamental vibrations of the cyclic formic acid dimer. Davydov pairs of IR-active (disks) and Raman-active (squares) vibrations are connected and further linked to the corresponding monomer transitions (diamonds) by dotted lines. In-plane vibrations are visualised in red and out-of-plane modes are in blue. Band centres are from Tables 3.2 and 7.5 and Refs. [119, 129]; for ν_3, ν_{14}, and ν_{22}, the centroid of the resonance is used. The limits of the resonance-broadened OH stretch are roughly estimated from published jet-cooled spectra [119, 129]. Note that the division into these four spectral ranges is also valid for all three symmetrically deuterated isotopologues. This figure is inspired by and an extension of Fig. 2 in Ref. [109].

exploited for the formic acid monomer. The inversion symmetry of the cyclic dimer removes this resonance assignment aid, making the excitonic analysis particularly important [109]. Four pair modes and all intramolecular modes are grouped in such pairs, leaving the dimer stretch (ν_8, A_g) and dimer twist (ν_{16}, A_u) which do not have a vibrational Davydov partner (Fig. 1.3).

The cyclic formic acid dimer is a prototype for double hydrogen bonding. Two aspects of its vibrational dynamics have sparked particular interest in the past. The Raman-active symmetric OH stretching mode promotes a concerted exchange of the two bound protons that leads to a tunnelling splitting already in the vibrational ground state. This splitting has attracted considerable attention and attempts to compute its time scale.[29] The experimental value of the full ground state tunnelling period has evolved over time and is now seen to amount to 3 ns [131] – corresponding to a ground state splitting of only 0.011 cm^{-1} – whereas it was long thought to be close to 2 ns [130]. At the other end of the time scale, in the sub-ps domain, are the high-frequency hydride stretches. It has long been known that the OH (and OD) stretching fundamentals of formic acid dimer and other carboxylic acid dimers give rise to complicated, resonance-rich structures that span several hundreds of cm^{-1} [93, 129]. Similarly, there have been many attempts to model these highly anharmonic spectra and understand the underlying dynamics [23, 132–137].

The vibrational ground state splitting is so small, that at present one can only hope to correctly predict its order of magnitude; for reduced-dimensional models that quantitatively agree with experiment, the question of the extent of fortuitous success always arises. The OH stretching spectra, on the other hand, are so complex, that the meaningfulness of assigning all individual bands in this spectral region – assuming this is even possible – is a questionable endeavour from the perspective of *quantitatively* challenging theory. In-between these two time scales are the van der Waals pair and slow fingerprint modes of the cyclic dimer which, in comparison, have received less attention from the theory side. However, they constitute a much more robust benchmarking target where the theory-experiment agreement is possible to within 1%.

Theoretical investigations into the resonance-rich OH stretching spectrum have yielded many valuable insights so far. In order to acquire a more profound – and perhaps *quantitative* – understanding of the underlying dynamics in the enigmatic OH stretching range, future endeavours can only bear fruits if they build on the foundation of a rigorous understanding of the internal dynamics of the skeletal modes in the isolated molecule and its hydrogen-bonded cyclic dimer.

[29] See for example Ref. [31] and references cited in Ref. [130].

While the systematic vibrational characterisation of the cyclic dimer has been completed long ago in the thermal gas phase [93, 118, 138, 139], an update using jet cooling or high-resolution spectroscopy is essential for reliable band centres and the identification of local resonances. In the past two decades, there have been several isolated efforts but this task still remains rather incomplete.[30]

Building on the completed update of the van der Waals vibrations below 600 cm^{-1} – at least for the main isotopologue[31] – it is the aim of this work to revisit the jet-cooled spectra in the slow fingerprint region between 600 and 1500 cm^{-1} and complete the experimental characterisation of the dimer in this range, including all three symmetrically deuterated isotopologues. Unresolved issues in the fingerprint region, that will all be addressed in this work, include:

1. *Resonance perturbations of $(HCOOH)_2$ fundamentals.* The IR-active C–O stretch, ν_{22}, is split into a triplet with perturbed band centres located between 1220 and 1234 cm^{-1}. Despite several (experiment-focussed) investigations [110, 145, 146, 149], there is no consensus regarding the assignment of both perturbers. While it appears to be accepted that one perturber corresponds to the binary combination $\nu_{10}+\nu_{15}$, Goroya *et al.* and Kollipost showed that an assignment of the second perturber to $\nu_{12}+\nu_{14}$, as proposed by Ito [145], is less likely and that this combination band is most likely located below 1200 cm^{-1} [110, 149], suggesting a ternary (or higher) state assignment.
2. *IR-active combination/overtone bands of the cyclic dimer.* Disregarding low-resolution gas phase spectroscopic investigations, Kollipost presented the so far only systematic IR spectroscopic investigation of the full fingerprint spectrum of the cyclic dimer [149]. In addition to the main isotopologue, he measured all three deuterated isotopologues and presented a very detailed analysis of the jet-cooled IR spectra. He was able to assign a selected number of bands to combination bands of the cyclic dimer but the assignment of some bands remains unclear since possible contributions from larger ($n > 2$) clusters must be checked.
3. *The Raman jet spectrum below 750 cm^{-1}.* Building on Raman jet spectroscopic work by Zielke and Suhm [140], Xue and Suhm extended the systematic vibrational characterisation of $(HCOOH)_2$ and its symmetrically deuterated isotopologues up to 750 cm^{-1} [141]. They were able to assign almost all spectral features down to the noise level to the formic acid monomer and its (symmetrically and asymmetrically deuterated) cyclic dimer but the assignment of a few weaker spectral features remains unclear.
4. *The Raman jet spectrum beyond 750 cm^{-1}.* Xue extended the Raman jet spectroscopic characterisation of the formic acid dimer to the full fundamental wavenumber range up to 3300 cm^{-1} [119]. In contrast to the IR jet spectra [149], the Raman jet spectra presented in Ref. [119] reveal a much higher complexity. Xue assigned several bands to overtone/-combination bands of the cyclic formic acid dimer which have so far not been confirmed independently.

The current reexamination of the jet-cooled formic acid spectra profits from and builds on recent advances in the experimental characterisation of larger formic acid clusters ($n > 2$), particularly the detection of the formic acid trimer.[32] Fig. 1.4 illustrates the close relationship between the

[30] For Raman spectroscopic studies, see Refs. [89, 119, 125, 140, 141]; for IR investigations, see Refs. [110, 129, 142–150].

[31] See Refs. [129, 130, 140, 141, 148]. Note that the two IR-active A_u pair modes (ν_{15} and ν_{16}) are still awaiting an update from jet-cooled or high-resolution gas phase spectroscopy for the symmetrically deuterated isotopologues. The experimental data for the twist (ν_{16}) might reveal interesting quantum effects, similar to the dimer stretch (ν_8) [140].

[32] Neill reported the first gas phase spectroscopic detection of the formic acid trimer in 2011 and confirmed its

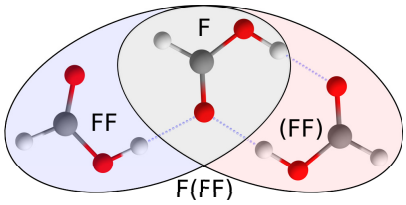

Figure 1.4 Connectivities of the *trans*-formic acid monomer F, cyclic dimer (FF), polar, acyclic dimer FF, and trimer F(FF). F, (FF), and F(FF) are close to the equilibrium structures of formic acid monomer, dimer, and trimer, respectively. (FF) is C_{2h} symmetric while the others are C_s symmetric. The parentheses represent a closed hydrogen bond pattern. Reproduced from Ref. [109] (published under a Creative Commons Attribution license, CC BY 4.0).

global minimum[33] trimer configuration and its constituents – F(FF) can either be thought of as an open dimer FF that forms a double hydrogen-bonded ring with another monomer F or alternatively a monomer F that docks onto a cyclic dimer (FF). Indeed, as a byproduct of the dimer analysis, several new vibrational formic acid trimer bands have been observed and assigned in this work, paving the way for future gas phase searches for the still rather elusive polar formic acid dimer FF.

planarity by means of microwave spectroscopy [151]. More recently, Meyer and Suhm were able to show that the global minimum trimer is present in significant amounts in supersonic jet expansions by utilising a multi-spectroscopic approach. They were able to identify the trimer on the basis of its carbonyl stretching vibrations [125]. Subsequently, Oswald *et al.* reported detection of the trimer in the OH stretching range, facilitated by the use of N_2 as a molecular sensor [126].

[33] The conformational landscape of formic acid trimer was computationally explored by Roy and Thakkar [152]. As Meyer pointed out, based on predicted energy differences only the global minimum trimer is expected in significant amounts in jet-cooled experiments [86, p. 124].

Chapter 2

Theoretical background and methods

2.1 Theoretical treatment of vibrational energy levels

The exact vibration-rotation Hamiltonian in rectilinear normal mode coordinates (Q_i) and conjugated momenta ($\hat{P}_i$),[34] the Watson Hamiltonian or Watsonian, has the following form[35] for non-linear[36] molecules [57]

$$\hat{H}^{\mathrm{rv}} = V + \frac{1}{2}\sum_i \hat{P}_i^2 - \frac{\hbar^2}{8}\sum_\alpha \mu_{\alpha,\alpha} + \frac{1}{2}\sum_{\alpha,\beta}\mu_{\alpha,\beta}\left(\hat{\pi}_\alpha\hat{\pi}_\beta + \hat{J}_\alpha\hat{J}_\beta - 2\hat{J}_\alpha\hat{\pi}_\beta\right), \tag{2.1}$$

where $\hat{J}_\alpha$ and $\hat{\pi}_\alpha = \sum_{i,j}\zeta^\alpha_{i,j}Q_i\hat{P}_j$ are components of the total and so-called[37] vibrational angular momentum around axis α of the body-fixed frame, $\zeta^\alpha_{i,j}$ components of the Coriolis coupling constant, $\mu_{\alpha,\beta}$ components of the effective reciprocal inertia tensor, and V is the (Born-Oppenheimer) potential energy. The (diagonal) sum over $\mu_{\alpha,\alpha}$ is called the Watson U term and is a potential-like contribution that depends on the normal coordinates.

As the individual rotational transitions are not experimentally resolved in this work, we shall continue the following discussion for the pure vibrational Hamiltonian

$$\hat{H}^{\mathrm{vib}} \equiv \hat{H}^{\mathrm{rv}}(J=0) = V + \frac{1}{2}\sum_i \hat{P}_i^2 - \frac{\hbar^2}{8}\sum_\alpha \mu_{\alpha,\alpha} + \frac{1}{2}\sum_{\alpha,\beta}\mu_{\alpha,\beta}\hat{\pi}_\alpha\hat{\pi}_\beta. \tag{2.2}$$

This Hamiltonian does not include terms that are formally classified as vibration-rotation interaction terms but this does not mean there is no inherent coupling since rotation and vibration are not fully separable. Even for the $J = 0$ case, centrifugal coupling is mediated through the dependence of $\mu_{\alpha,\beta}$ on the normal coordinates [67, p. 6].

2.1.1 Second-order vibrational perturbation theory (VPT2)

In the following, the working equations of second-order vibrational perturbation theory (VPT2) are discussed, focussing on the description of energy levels[38] for the most general case – a non-linear, polyatomic asymmetric top.

[34] The rectilinear normal coordinates are defined as linear combinations of mass-weighted Cartesian displacement coordinates. For further reading, see Ref. [153].

[35] The original arrangement in Ref. [57], $(\hat{J}_\alpha - \hat{\pi}_\alpha)\mu_{\alpha,\beta}(\hat{J}_\beta - \hat{\pi}_\beta)$, is simplified using the commutator relationship $\hat{\pi}_\alpha\mu_{\alpha,\beta} = \mu_{\alpha,\beta}\hat{\pi}_\alpha$ [57]. The two cross terms between $\hat{J}$ and $\hat{\pi}$ can also be condensed [67, p. 6].

[36] See Ref. [154] for the linear molecules.

[37] The point was made early on that $\hat{\pi}_\alpha$ – unlike its classical analogue – also contains an additional rotational contribution [57, 155] that arises from the inequality of $\hat{P}_i$ and $\dot{Q}_i$ in a quantum mechanical treatment [153, Section 11.2]. Thus, the description of $\hat{\pi}_\alpha$ as *vibrational angular momentum* is strictly speaking not correct [57].

[38] The derivation of the working equations and computation of infrared intensities in VPT2 is much more complex than for the energy levels. For further reading, see for example Refs. [156–159].

The vibrational Hamiltonian

In the perturbative vibration-rotation literature [66, 67], the total Hamiltonian is usually expanded in powers of the vibrational (m) and rotational (n) operators

$$\hat{H}^{\mathrm{rv}} = \sum_{m,n} \hat{H}_{m,n}, \tag{2.3}$$

the perturbative order of the Hamiltonian being $k = m + n - 2$.[39] Terms where one of the two indices is zero correspond to the pure vibrational ($n = 0$) or pure rotational ($m = 0$) components, whereas explicit vibration-rotation coupling is mediated by cross or "Coriolis" [67] terms. Instead of working with mass-weighted normal coordinates and conjugated momenta, it is convenient and common practice to first convert these into dimensionless normal coordinates and conjugated momenta

$$\begin{aligned} q_i &= \gamma_i^{1/2} Q_i, \\ \hat{p}_i &= \frac{\hat{P}_i}{\gamma_i^{1/2}\hbar}, \end{aligned} \tag{2.4}$$

with the conversion factor [67, 153]

$$\gamma_i = \frac{\lambda_i^{1/2}}{\hbar} = \frac{hc\omega_i}{\hbar^2} = \frac{4\pi^2 c\omega_i}{h}. \tag{2.5}$$

ω_i is the harmonic wavenumber and should not be confused with the angular frequency. Expanding the purely vibrational Watson Hamiltonian (Eq. 2.2) in these dimensionless normal coordinates and conjugated momenta through second-order ($m \leq 4$, $n = 0$) yields

$$\begin{aligned} \hat{H}_{\mathrm{VPT2}} =& \frac{hc}{2} \sum_i \omega_i \left(\hat{p}_i^2 + q_i^2\right) && \Big| \ \hat{H}^{(0)} \Rightarrow \hat{H}_{2,0} \\ &+ \frac{hc}{6} \sum_{i,j,k} \phi_{i,j,k} q_i q_j q_k && \Big| \ V^{(1)} \Rightarrow \hat{H}_{3,0} \\ &+ \frac{hc}{24} \sum_{i,j,k,l} \phi_{i,j,k,l} q_i q_j q_k q_l && \Big| \ V^{(2)} \Rightarrow \hat{H}_{4,0} \\ &+ hc \sum_\alpha \tilde{B}_e^\alpha \left(-\frac{1}{4} + \sum_{i,j,k,l} \zeta_{i,j}^\alpha \zeta_{k,l}^\alpha \sqrt{\frac{\omega_j \omega_l}{\omega_i \omega_k}} q_i \hat{p}_j q_k \hat{p}_l \right), && \Big| \ \hat{T}^{(2)} \Rightarrow \hat{H}_{4,0} \end{aligned} \tag{2.6}$$

where i, j, k, l are vibrational indices that run from 1 to $3N_{\mathrm{atom}} - 6$ and α is a principal axis of rotation in the Eckart frame [57, 153, 155].[40] The Coriolis coupling constant $\zeta_{i,j}^\alpha$ mediates

[39] In the usual perturbative expansion, the Hamiltonian is expressed in a power series

$$\hat{H} = \sum_k \lambda^k \hat{H}^{(k)},$$

where λ is the perturbation parameter. This expression is related to Eq. 2.3 via

$$\hat{H}^{(k)} = \sum_{m,n} \hat{H}_{m,n}.$$

The sum over m and n is restricted to all combinations that satisfy $m + n = k + 2$.

[40] The correct orientation of the body-fixed frame is very important because the Coriolis constants depend on the reference frame [66, p. 43]. For small and light molecules, these contributions in $\hat{T}^{(2)}$ can be several (tens of) cm^{-1} [53, 160, 161]. Previously reported [162, 163] numerical sensitivities of VPT2 computed with Gaussian have partly to do with the orientation of the body-fixed frame. This is discussed in Appendix C.1.

coupling between vibrations i and j via rotation around axis α, $\tilde{B}_e^\alpha$ is the equilibrium rotational constant around axis α, and $\phi_{i,j,k}$ and $\phi_{i,j,k,l}$ are the cubic and quartic force constants, respectively. The potential energy parameters (ω_i, $\phi_{i,j,k}$, $\phi_{i,j,k,l}$) are related to derivatives of the potential energy as follows

$$V = V_{\text{eq}} + \frac{1}{2}\sum_i \underbrace{\left.\frac{\partial^2 V}{\partial q_i^2}\right|_{\text{eq}}}_{=hc\cdot\omega_i} q_i^2 + \frac{1}{6}\sum_{i,j,k} \underbrace{\left.\frac{\partial^3 V}{\partial q_i \partial q_j \partial q_k}\right|_{\text{eq}}}_{=hc\cdot\phi_{i,j,k}} q_i q_j q_k + ..., \tag{2.7}$$

when the potential energy is expanded as a Taylor series about the minimum in dimensionless normal coordinates using an unrestricted summation [66]. Due to the nature of normal coordinates [153], the first and mixed second derivatives are zero.

At second-order of perturbation theory, the Watson U term is merely a sum over the rotational constants but it is usually counted to $\hat{T}^{(2)}$ [73]. The lowest-order contribution from the U term is therefore not always included in VPT2 implementations as it merely acts as a constant shift on all levels and thus cancels for experimentally accessible transitions between two vibrational levels.

Second-order corrections to the vibrational energy

An important advantage of choosing the harmonic oscillator as the zeroth-order basis is the availability of analytic solutions to all integrals that appear in the VPT2 equations [11].[41] Once the VPT2 equations for the energy levels are solved,[42] they are usually sorted by powers in the vibrational quantum numbers, yielding the familiar expression for the term values

$$\frac{E(\mathbf{n})}{hc} \equiv G(\mathbf{n}) = g_0 + \sum_i \omega_i \left(n_i + \frac{1}{2}\right) + \sum_i \sum_{j\geq i} x_{i,j}\left(n_i + \frac{1}{2}\right)\left(n_j + \frac{1}{2}\right), \tag{2.8}$$

where $\mathbf{n} = \{n_1, ..., N_{\text{vib}}\}$ is the vibrational excitation array, ω_i is the harmonic wavenumber, $x_{i,i}$ and $x_{i,j}$ are the well-known diagonal and off-diagonal anharmonicity constants, and g_0 is a constant. 2

The anharmonicity matrix is symmetric ($x_{i,j} = x_{j,i}$) and diagonal terms ($i = j$) account for diagonal anharmonicity along mode i whereas off-diagonal terms ($i \neq j$) mediate binary mode coupling between two vibrations i and j. Expressed in terms of the potential parameters, we obtain [11, 72, 73] for all anharmonic parameters in Eq. 2.8

$$x_{i,i} = \frac{\phi_{i,i,i,i}}{16} - \frac{5\phi_{i,i,i}^2}{48\omega_i} - \sum_{k\neq i} \frac{\phi_{i,i,k}^2\left(8\omega_i^2 - 3\omega_k^2\right)}{16\omega_k\left(4\omega_i^2 - \omega_k^2\right)}, \tag{2.9}$$

$$\begin{aligned} x_{i,j} =& \frac{\phi_{i,i,j,j}}{4} - \frac{\phi_{i,i,i}\phi_{i,j,j}}{4\omega_i} - \frac{\phi_{i,i,j}\phi_{j,j,j}}{4\omega_j} - \frac{\phi_{i,i,j}^2\omega_i}{2\left(4\omega_i^2 - \omega_j^2\right)} - \frac{\phi_{i,j,j}^2\omega_j}{2\left(4\omega_j^2 - \omega_i^2\right)} \\ &- \sum_{k\neq i,j}\left(\frac{\phi_{i,i,k}\phi_{j,j,k}}{4\omega_k} + \frac{\phi_{i,j,k}^2\omega_k\left(\omega_i^2 + \omega_j^2 - \omega_k^2\right)}{2\Omega_{i,j,k}}\right) + \sum_\alpha \tilde{B}_e^\alpha\left(\zeta_{i,j}^\alpha\right)^2\left(\frac{\omega_i}{\omega_j} + \frac{\omega_j}{\omega_i}\right), \end{aligned} \tag{2.10}$$

[41] Useful harmonic oscillator integrals are tabulated in Appendix III of Ref. [153].

[42] The literature on VPT2 is immense and its derivation for polyatomic asymmetric top molecules shall therefore not be repeated here. For a contemporary introduction to VPT2 and applications, see the recent review by Franke *et al.* [11]. See also for example Ref. [72]. Amongst the classic reading materials on this topic are the seminal works by Nielsen [64] or Papoušek and Aliev [66].

$$g_0 = \sum_k \left(\frac{\phi_{k,k,k,k}}{64} - \frac{7\phi_{k,k,k}^2}{576\omega_k} \right) - \frac{1}{4} \sum_\alpha \tilde{B}_e^\alpha \left(1 + \sum_k \sum_{l \neq k} \left(\zeta_{k,l}^\alpha \right)^2 \right) + \sum_k \sum_{l \neq k} \frac{3\phi_{k,k,l}^2 \omega_l}{64 \left(4\omega_k^2 - \omega_l^2 \right)} + \sum_k \sum_{l \neq k} \sum_{m \neq l} \frac{\phi_{k,l,m}^2 \omega_k \omega_l \omega_m}{24\Omega_{k,l,m}}, \tag{2.11}$$

where

$$\Omega_{i,j,k} = \left(\omega_i + \omega_j + \omega_k \right) \left(\omega_i + \omega_j - \omega_k \right) \left(\omega_i - \omega_j + \omega_k \right) \left(-\omega_i + \omega_j + \omega_k \right). \tag{2.12}$$

Resonance denominators appear in all three parameters (Eqs 2.9-2.11) that lead to divergences in the perturbational expansion if two states become close in energy. It is common practice to deperturb these resonances by removing the offending terms and to account for the strong coupling *post hoc* (see Section 2.1.2). Since vibration-rotation cross terms, which also include the Coriolis constants $\zeta_{i,j}^\alpha$, do not appear in the Hamiltonian or energy expression for $J = 0$, it has a mnemotechnical advantage to simply refer to the vibrational angular momentum contributions in Eq. 2.10 as Coriolis terms which is done throughout this work.

The zero-point vibrational energy

By setting all vibrational quanta in Eq. 2.8 to zero, we obtain the ground state or zero-point vibrational energy at second-order of perturbation theory

$$\frac{\mathrm{ZPVE}}{hc} \equiv G(0, ..., 0) = g_0 + \sum_i \frac{\omega_i}{2} + \sum_i \sum_{j \geq i} \frac{x_{i,j}}{4}. \tag{2.13}$$

Unlike excited vibrational states, the VPT2 ZPVE is or rather must be[43] resonance-free which can be shown by rearranging[44] the above expression to (unrestricted summations)

$$\frac{\mathrm{ZPVE}}{hc} = \sum_i \frac{\omega_i}{2} + \sum_{i,j} \frac{\phi_{i,i,j,j}}{32} - \sum_{i,j,k} \left(\frac{\phi_{i,i,k}\phi_{j,j,k}}{32\omega_k} + \frac{\phi_{i,j,k}^2}{48(\omega_i + \omega_j + \omega_k)} \right) + \sum_\alpha \tilde{B}_e^\alpha \left(-\frac{1}{4} + \sum_{i,j} \left(\zeta_{i,j}^\alpha \right)^2 \frac{(\omega_i - \omega_j)^2}{8\omega_i\omega_j} \right). \tag{2.14}$$

The above formulation is much more useful and appealing as it avoids resonance denominators.

For accurate ZPVE predictions, quantum diffusion Monte Carlo is a very popular method because it essentially yields the exact ground state energy on a given potential V [166, 167]. In order to compare the perturbational ZPVE predictions to diffusion Monte Carlo, care must be taken that constant contributions that cancel for transition wavenumbers are included, such as g_0 in general[45] (Eq. 2.8) and the Watson U contribution[46] to g_0 in particular (Eq. 2.11).

[43] On similar grounds – "the ground state is non-degenerate and its treatment by perturbation theory should therefore be free of potential singularities" [164, p. 290] –, the vibrational ground state rotational constants are (Coriolis) resonance-free in VPT2.

[44] The correctness of Eq. 2.14 was verified by comparison to numerical results with GUINEA (see also note 46, p. 16). Note that the resonance-free ZPVE expression in Ref. [165, Eqs. 7-8] contains an error in Z_{kinetic}.

[45] This applies in particular if resonance denominators are removed from the anharmonicity constants. In these instances, the same resonant terms must be removed from g_0.

[46] Gaussian 16 Rev. A.03 [70, 159, 168, 169] includes the Watson U term, whereas in GUINEA version 3.0 [170, 171], this term is not included in the Hamiltonian (Eq. 2.6). Thus, in ZPVE calculations with the latter one must subtract $0.25hc \sum_\alpha \tilde{B}_e^\alpha$ from the computed ZPVE.

Table 2.1 Useful SOF+x expressions for binary ($\Delta n = 2$) up to quaternary ($\Delta n = 4$) vibrational excitation wavenumbers. The second-order perturbation theory expressions are derived from Eq. 2.17.

Δn	n_i	n_j	n_k	n_l	$G_0(..., n_i, n_j, n_k, n_l, ...)$
2	1	1	0	0	$\tilde{\nu}_i + \tilde{\nu}_j + x_{i,j}$
2	2	0	0	0	$2 \times (\tilde{\nu}_i) + 2x_{i,i}$
3	1	1	1	0	$\tilde{\nu}_i + \tilde{\nu}_j + \tilde{\nu}_k + x_{i,j} + x_{i,k} + x_{j,k}$
3	2	1	0	0	$2 \times (\tilde{\nu}_i) + \tilde{\nu}_j + 2x_{i,i} + 2x_{i,j}$
3	3	0	0	0	$3 \times (\tilde{\nu}_i) + 6x_{i,i}$
4	1	1	1	1	$\tilde{\nu}_i + \tilde{\nu}_j + \tilde{\nu}_k + \tilde{\nu}_l + x_{i,j} + x_{i,k} + x_{i,l} + x_{j,k} + x_{j,l} + x_{k,l}$
4	2	1	1	0	$2 \times (\tilde{\nu}_i) + \tilde{\nu}_j + \tilde{\nu}_k + 2x_{i,i} + 2x_{i,j} + 2x_{i,k} + x_{j,k}$
4	2	2	0	0	$2 \times (\tilde{\nu}_i) + 2 \times (\tilde{\nu}_j) + 2x_{i,i} + 2x_{j,j} + 4x_{i,j}$
4	3	1	0	0	$3 \times (\tilde{\nu}_i) + \tilde{\nu}_j + 6x_{i,i} + 3x_{i,j}$
4	4	0	0	0	$4 \times (\tilde{\nu}_i) + 12x_{i,i}$

Sum-of-fundamentals (SOF) form of the VPT2 equations

For most applications, it is convenient to subtract the ZPVE (Eq. 2.13) from Eq. 2.8 and slightly rearrange the terms [172]

$$G_0(\mathbf{n}) = \sum_i \left[\left(\omega_i n_i + x_{i,i}(n_i^2 + n_i) + \frac{n_i}{2} \sum_{k \neq i} x_{i,k} \right) + \sum_i \sum_{j>i} x_{i,j} n_i n_j \right]. \tag{2.15}$$

The expression in parenthesis can be simplified by inserting the VPT2 expression for a fundamental transition wavenumber

$$\tilde{\nu}_i = G_0(n_i = 1, 0, ..., 0) = \omega_i + \delta_{i,\text{anh}} = \omega_i + 2x_{i,i} + \frac{1}{2} \sum_{k \neq i} x_{i,k}. \tag{2.16}$$

Replacing the corresponding terms in Eq. 2.15 with $\tilde{\nu}_i$ yields

$$G_0(\mathbf{n}) = \underbrace{\underbrace{\sum_i \tilde{\nu}_i n_i}_{=\text{SOF}} + \sum_i x_{i,i}(n_i^2 - n_i) + \sum_i \sum_{j>i} x_{i,j} n_i n_j}_{=\text{SOF+}x}, \tag{2.17}$$

where some of the diagonal and off-diagonal anharmonicity is absorbed into the anharmonic fundamental $\tilde{\nu}_i$ – the SOF form of the VPT2 equations or simply SOF+x. These two different formulations of $G_0(\mathbf{n})$ are strictly equivalent if $\tilde{\nu}_i$ is computed from Eq. 2.16. The advantage of the formulation in Eq. 2.17 is that we are not restricted to VPT2 but can insert $\tilde{\nu}_i$ values that were otherwise obtained, be it theoretically[47] or experimentally. If, for example, a reliable experimental database of the fundamental transitions of a molecule or molecular complex is available, it is advantageous to use experimental values for $\tilde{\nu}_i$, for the purpose of assigning experimental spectra, especially if only a lower-level *ab initio* treatment is computationally feasible.[48] Useful SOF+x expressions for binary up to quaternary vibrational excitation wavenumbers are reported in Table 2.1.

[47] In Section 5.4, this ansatz is combined with reduced-dimensional variational calculations to account for anharmonic contributions from the inactive degrees of freedom.

[48] In Sections 4.3 and 7.2, the assignments of monomeric and dimeric formic acid bands are guided by semi-experimental SOF+x with affordable MP2/aVTZ anharmonicity constants.

Higher-order corrections to the vibrational energy

Gong *et al.* recently reported algebraic expressions for VPT4 [73] which is also implemented in GUINEA, a stand-alone module in the most recent release of CFOUR [170, 171]. The fourth-order expression for the term values is given by

$$\begin{aligned} G_{\mathrm{VPT4}}(\mathbf{n}) =& g_0' + \sum_i \left(\omega_i + \tilde{\omega}_i\right)\left(n_i + \frac{1}{2}\right) + \sum_i \sum_{j\geq i} x_{i,j}\left(n_i + \frac{1}{2}\right)\left(n_j + \frac{1}{2}\right) \\ &+ \sum_i \sum_{j\geq i} \sum_{k\geq j} y_{i,j,k}\left(n_i + \frac{1}{2}\right)\left(n_j + \frac{1}{2}\right)\left(n_k + \frac{1}{2}\right), \end{aligned} \tag{2.18}$$

where g_0' contains additional fourth-order contributions to g_0 (Eq. 2.11), $y_{i,i,i}$, $y_{i,j,j}$, and $y_{i,j,k}$ are higher-order anharmonicity constants, and $\tilde{\omega}_i$ is linear in $n_i + 1/2$ and therefore a higher-order correction to the harmonic wavenumber ω_i. The fourth-order corrections to the energy depend on additional potential energy ($\phi_{i,j,k,l,m}$, $\phi_{i,j,k,l,m,n}$) and rotational ($a_i^{\alpha,\beta}$) parameters. $a_i^{\alpha,\beta}$ is proportional to the first derivative of the inertia tensor with respect to normal coordinates and appears higher-order expansions of the vibrational angular momentum [73].[49]

Reduced-dimensional VPT*n*

Reduced-dimensional VPT*n* expressions for 1D ($n = 2, 4$) and 2D ($n = 2$) fundamental term values are reported here for future reference. The 1D term value for a fundamental transition is given by

$$\begin{aligned} \tilde{\nu}_i^{\text{1D-VPT2}} &= \omega_i + 2x_{i,i}^{\text{1D}}, \\ \tilde{\nu}_i^{\text{1D-VPT4}} &= \omega_i + 2x_{i,i}^{\text{1D}} + \tilde{\omega}_i^{\text{1D}} + \frac{13}{4} y_{i,i,i}^{\text{1D}}, \end{aligned} \tag{2.19}$$

where

$$x_{i,i}^{\text{1D}} = \frac{\phi_{i,i,i,i}}{16} - \frac{5\phi_{i,i,i}^2}{48\omega_i}, \tag{2.20}$$

$$\tilde{\omega}_i^{\text{1D}} = \frac{1}{1152}\left(5\phi_{i,i,i,i,i,i} - \frac{19\phi_{i,i,i}\phi_{i,i,i,i,i}}{\omega_i} - \frac{67\phi_{i,i,i,i}^2}{8\omega_i} + \frac{153\phi_{i,i,i}^2\phi_{i,i,i,i}}{4\omega_i^2} - \frac{385\phi_{i,i,i}^4}{24\omega_i^3}\right), \tag{2.21}$$

$$y_{i,i,i}^{\text{1D}} = \frac{1}{288}\left(\phi_{i,i,i,i,i,i} - \frac{7\phi_{i,i,i}\phi_{i,i,i,i,i}}{\omega_i} - \frac{17\phi_{i,i,i,i}^2}{8\omega_i} + \frac{75\phi_{i,i,i}^2\phi_{i,i,i,i}}{4\omega_i^2} - \frac{235\phi_{i,i,i}^4}{24\omega_i^3}\right). \tag{2.22}$$

At second-order, the 1D analogue of VPT2 is exact for the Morse potential and yields the same energy levels [173, 174]. Extending the perturbational treatment to include coupling to one other mode j, we obtain

$$\tilde{\nu}_i^{\text{2D-VPT2}} = \omega_i + 2\left(x_{i,i}^{\text{1D}} + x_{i,i}^{\text{2D}}\right) + \frac{1}{2}\left(x_{i,j}^{\text{2D}} + x_{i,j}^{\text{Cor}}\right), \tag{2.23}$$

where

$$x_{i,i}^{\text{2D}} = -\frac{\phi_{i,i,j}^2\left(8\omega_i^2 - 3\omega_j^2\right)}{16\omega_j(4\omega_i^2 - \omega_j^2)}, \tag{2.24}$$

[49] When requesting a vibrational frequency and intensity calculation in the usual double, i.e. mechanical and electrical, harmonic approximation ("VIB" directive), CFOUR version 2.1 automatically computes all necessary rotational parameters. $\zeta_{i,j}^{\alpha}$ and $a_i^{\alpha,\beta}$ are directly written to separate files ("coriolis.joda" and "didq.joda") in a format that can straightforwardly be used in VPT calculations with GUINEA.

$$x_{i,j}^{\mathrm{2D}} = \frac{\phi_{i,i,j,j}}{4} - \frac{\phi_{i,i,i}\phi_{i,j,j}}{4\omega_i} - \frac{\phi_{i,i,j}\phi_{j,j,j}}{4\omega_j} - \frac{\phi_{i,i,j}^2\omega_i}{2\left(4\omega_i^2-\omega_j^2\right)} - \frac{\phi_{i,j,j}^2\omega_j}{2\left(4\omega_j^2-\omega_i^2\right)}, \tag{2.25}$$

$$x_{i,j}^{\mathrm{Cor}} = \sum_{\alpha} \tilde{B}_e^{\alpha}\left(\zeta_{i,j}^{\alpha}\right)^2\left(\frac{\omega_i}{\omega_j}+\frac{\omega_j}{\omega_i}\right). \tag{2.26}$$

The algebraic VPT4 expressions beyond 1D are cumbersome (see supplementary material of Ref. [73]) and not repeated here but can 'easily'[50] be evaluated numerically with GUINEA by setting the corresponding force constants and Coriolis coupling constants to zero. Combining all of the above equations, we obtain

$$\begin{aligned}
&\tilde{\nu}_i^{\text{1D-VPT}n} = && (2.27)\\
&+\omega_i && \text{Harm}\\
&+\frac{\phi_{i,i,i,i}}{8} - \left[\frac{5\phi_{i,i,i}^2}{24\omega_i}\right]_{(i)} && \text{PT2(1D)}\\
&+\frac{\phi_{i,i,i,i,i,i}}{64} - \frac{\phi_{i,i,i,i}^2}{32\omega_i} + \left[-\frac{55\phi_{i,i,i}\phi_{i,i,i,i,i}}{576\omega_i} + \frac{47\phi_{i,i,i}^2\phi_{i,i,i,i}}{192\omega_i^2} - \frac{215\phi_{i,i,i}^4}{1728\omega_i^3}\right]_{(i)}, && \text{PT4(1D)}
\end{aligned}$$

and

$$\begin{aligned}
&\tilde{\nu}_i^{\text{2D-VPT}n} = && (2.28)\\
&+\omega_i && \text{Harm}\\
&+\frac{\phi_{i,i,i,i}}{8} - \left[\frac{5\phi_{i,i,i}^2}{24\omega_i}\right]_{(i)} && \text{PT2(1D)}\\
&+\frac{\phi_{i,i,i,i,i,i}}{64} - \frac{\phi_{i,i,i,i}^2}{32\omega_i} + \left[-\frac{55\phi_{i,i,i}\phi_{i,i,i,i,i}}{576\omega_i} + \frac{47\phi_{i,i,i}^2\phi_{i,i,i,i}}{192\omega_i^2} - \frac{215\phi_{i,i,i}^4}{1728\omega_i^3}\right]_{(i)} && \text{PT4(1D)}\\
&-\left[\frac{\phi_{i,i,j}^2\left(8\omega_i^2-3\omega_j^2\right)}{8\omega_j\left(4\omega_i^2-\omega_j^2\right)}\right]_{(j)} && \text{PT2(2D,ii)}\\
&+\frac{\phi_{i,i,j,j}}{8} - \left[\frac{\phi_{i,i,i}\phi_{i,j,j}}{8\omega_i} + \frac{\phi_{i,j,j}^2\omega_j}{4\left(4\omega_j^2-\omega_i^2\right)}\right]_{(i)} - \left[\frac{\phi_{j,j,j}\phi_{i,i,j}}{8\omega_j} + \frac{\phi_{i,i,j}^2\omega_i}{4\left(4\omega_i^2-\omega_j^2\right)}\right]_{(j)} && \text{PT2(2D,ij)}\\
&+\frac{1}{2}\sum_{\alpha}\tilde{B}_e^{\alpha}\left(\zeta_{i,j}^{\alpha}\right)^2\left(\frac{\omega_i}{\omega_j}+\frac{\omega_j}{\omega_i}\right) && \text{PT2(Cor)}\\
&+\ldots && \text{PT4(2D)}\\
&+\ldots && \text{PT4(Cor)}
\end{aligned}$$

"PT4(Cor)" and "PT4(2D)" are introduced as collective terms for all fourth-order 2D terms that depend on the Coriolis constants and force constants, respectively. The correctness of Eqs. 2.27-2.28 was validated numerically with GUINEA. Note that due to symmetry, force constants are zero if the number of indices for at least one non-totally symmetric mode is odd. "$[...]_{(k)}$" indicates if such a term in Eqs. 2.27-2.28 becomes zero because $\Gamma(q_k)$ is not totally symmetric for a

[50] For comparison, the evaluation of the energy of a single vibrational state takes less than a second for the formic acid dimer with VPT2. With VPT4, it takes a few seconds for the 9-dimensional monomer and several hours for the 24-dimensional dimer. The calculations were run on one core with an Intel Core i7-8700 CPU.

vibrational mode k.[51] "(2D,ii)" and "(2D,ij)" are separate to distinguish between contributions from the diagonal and off-diagonal anharmonicity constants. For the molecules studied in this work, the fourth-order Coriolis contributions, PT4(Cor), are negligible.[52]

2.1.2 Accidental degeneracies: Vibrational resonances in VPT2

Following Aliev and Watson [67], we shall classify near-degeneracies on the basis of their *rank*, defined as

$$r = \sum_i |n_i|, \tag{2.29}$$

where a set of integers n_i exists (which can be positive, negative, or zero) that satisfy the necessary resonance condition

$$0 \approx \sum_i n_i \omega_i. \tag{2.30}$$

The interaction between two near-degenerate levels of rank r can be described to lowest-order by components of the vibrational Hamiltonian where the power of the vibrational operators (Eq. 2.3) equals the rank of the vibrational resonance, i.e. $m = r$.[53] Third-rank resonances are referred to as type I ($\omega_k \approx 2\omega_i$) and II ($\omega_i \approx \omega_j + \omega_k$) Fermi resonances. The classical Darling-Dennison resonance between two overtones [175] is a fourth-rank resonance and can be described to lowest-order in VPT4. An extension of canonical VPT2 to additionally treat fourth-rank resonances with a quartic force field has been coined "VPT2+K" [11, 72, 77]. For distinction, canonical VPT2 with only third-rank resonance treatment is referred to as "VPT2+F".

Third-rank resonances: VPT2+F

In VPT2, Fermi resonance denominators appear in the expressions of the diagonal and off-diagonal anharmonicity constants (Eqs. 2.9-2.10). Not only *can* third-rank resonance interactions be described by VPT2 but rather *must* be accounted for as strong Fermi resonances lead to small denominators and therefore divergences in the perturbational expansion of the energy.

The usual procedure [11, Section 3.1] to deal with Fermi resonances in VPT2 is to first remove the offending terms, yielding deperturbed VPT2 or DVPT2. This deperturbation of the anharmonicity constants and term values is usually indicated by an asterisk ($x \to x^*$, $\nu \to \nu^*$). By expanding the affected terms in the anharmonicity constants as partial fractions, the diverging terms can easily be identified.

$$x_{i,i} \Leftarrow -\frac{\phi^2_{i,i,k}}{32}\left(\frac{1}{\omega_k + 2\omega_i} + \frac{4}{\omega_k} + \frac{1}{\omega_k - 2\omega_i}\right) \tag{2.31}$$

[51] Since the normal coordinates transform like irreducible representations of the molecular point group, it follows that any force constant $\phi_{i,j,k,\ldots}$ can only be non-zero if $\Gamma(q_i) \times \Gamma(q_j) \times \Gamma(q_k) \times \ldots \supseteq \Gamma(\text{t.s.})$, i.e. if the symmetric product of the appropriate normal coordinates contains the totally symmetric species [3]. For the special case of non-degenerate point groups, we can write $\Gamma(q_i) \times \Gamma(q_j) \times \Gamma(q_k) \times \ldots = \Gamma(\text{t.s.})$.

[52] For formic acid and its cyclic dimer, the total Coriolis contributions – second- through fourth-order terms that depend on $\zeta^{\alpha}_{i,j}$ – to fundamental term values are only 1-10 and 1-2 cm^{-1}, respectively. The second-order contributions (sum over α in Eq. 2.10) are about two orders of magnitude greater than the fourth-order contributions. For example, the fourth-order corrections are below 0.1 cm^{-1} for fundamentals of *trans*-HCOOH and even smaller for $(\text{HCOOH})_2$.

[53] Usually, at this stage in the perturbational treatment of the vibration-rotation problem, the Hamiltonian has been transformed using the Van Vleck contact transformation ($H_{m,n} \to \tilde{H}_{m,n}$) to obtain a new representation that preserves the eigenvalue spectrum where couplings are reduced. In this formalism, it is the transformed Hamiltonian $\tilde{H}_{m,n}$ that mediates the resonance couplings. For further reading, see for example Refs. [64–67, 69].

$$x_{i,j} \Leftarrow -\frac{\phi_{i,j,k}^2}{8}\left(\frac{1}{\omega_i+\omega_j+\omega_k}-\frac{1}{\omega_i+\omega_j-\omega_k}+\frac{1}{\omega_i-\omega_j+\omega_k}+\frac{1}{-\omega_i+\omega_j+\omega_k}\right) \tag{2.32}$$

In the case of a type I resonance ($\omega_k \approx 2\omega_i$), the last term in Eq. 2.31 is removed. Similarly, for a type II Fermi resonance ($\omega_i \approx \omega_j + \omega_k$), the last term in Eq. 2.32 is removed. Note that type I resonances can also occur in $x_{i,j}$ since the summation over k is not restricted (Eq. 2.10).

Looking at the expanded terms in Eqs. 2.31-2.32, it becomes obvious that the near-degeneracy condition (Eq. 2.30)

$$\Delta_1(\text{type I}) = \left|\omega_k - 2\omega_i\right|, \tag{2.33}$$
$$\Delta_1(\text{type II}) = \left| -\omega_i + \omega_j + \omega_k \right|, \tag{2.34}$$

is only a *necessary criterion* as small denominators can be quenched by small cubic force constants. Deperturbation is an empiric procedure and criteria have been proposed to generalise the identification of strong resonances [176–178]. Most widely used is the criterion proposed by Martin *et al.* [176] who suggested to compare the resonance effect on the resultant fundamental term values by comparing the difference with and without inclusion of the resonance terms (Eqs. 2.33-2.34). The resultant expression involves a square root which is then expanded as a Taylor series (see Ref. [176]). In the so-called "Martin test", only the first term of this expansion

$$\Delta_2(\text{type I}) = \left|\frac{\phi_{i,i,k}^4}{256\Delta_1^3}\right|, \tag{2.35}$$
$$\Delta_2(\text{type II}) = \left|\frac{\phi_{i,j,k}^4}{64\Delta_1^3}\right|, \tag{2.36}$$

is consulted which serves as a *sufficient criterion*. Throughout this work, $\Delta_1 \leq 200\,\text{cm}^{-1}$ and $\Delta_2 \geq 1\,\text{cm}^{-1}$ are used.[54] In the literature, Δ_2, is also referred to as the "variational-perturbational" deviation [11].

After the removal of near-singularities, these missing couplings are explicitly reintroduced by quasi-degenerate perturbation theory in a variational-type framework. Effective Hamiltonians are set up where the deperturbed or "dressed" [77] term values are on the diagonal and the Fermi couplings are on the off-diagonals. The off-diagonal elements are proportional to the respective cubic force constants and take the following forms for type I ($\omega_k \approx 2\omega_i$) and II ($\omega_i \approx \omega_j + \omega_k$) Fermi resonances [72]:

$$\frac{\langle ..., n_i, n_j, n_k+1, ... | \tilde{H} | ..., n_i+2, n_j, n_k, ... \rangle}{hc} = \phi_{i,i,k}\sqrt{\frac{(n_i+1)(n_i+2)(n_k+1)}{2^5}} \tag{2.37}$$
$$\frac{\langle ..., n_i+1, n_j, n_k, ... | \tilde{H} | ..., n_i, n_j+1, n_k+1, ... \rangle}{hc} = \phi_{i,j,k}\sqrt{\frac{(n_i+1)(n_j+1)(n_k+1)}{2^3}} \tag{2.38}$$

This procedure shall be illustrated for the OH bend-torsion resonance in *trans*-HCOOH, a recurring theme in this work. The fingerprint vibrations of formic acid strongly mix and as a result of this mixing, the CH in-plane bend normal mode (ν_4) acquires slight OH in-plane bending character and vice versa. Thus, ν_4 must be included in resonance treatments of the OH

[54] These deperturbation thresholds are implemented as default in Gaussian 16 Rev. A.03 [168].

bend (ν_5) and the OH torsion overtone ($2\nu_9$). The lower-triangular part of the corresponding symmetric Hamilton matrix has the general form

$$\frac{\mathbf{H}^{\text{VPT2+F}}}{hc} = \begin{pmatrix} (\nu_4)^* & & \\ 0 & (\nu_5)^* & \\ \frac{1}{4}\phi_{4,9,9} & \frac{1}{4}\phi_{5,9,9} & (2\nu_9)^* \end{pmatrix}, \tag{2.39}$$

where the deperturbed term values are given by

$$(\nu_4)^* = \omega_4 + 2x_{4,4} + \frac{x^*_{4,9}}{2} + \frac{1}{2}\sum_{k\neq 4,9} x_{4,k}, \tag{2.40}$$

$$(\nu_5)^* = \omega_5 + 2x_{5,5} + \frac{x^*_{5,9}}{2} + \frac{1}{2}\sum_{k\neq 5,9} x_{5,k}, \tag{2.41}$$

$$(2\nu_9)^* = 2\omega_9 + 6x^*_{9,9} + x^*_{4,9} + x^*_{5,9} + \sum_{k\neq 4,5,9} x_{9,k}. \tag{2.42}$$

The VPT2+F term values are then obtained by diagonalisation of the above 3×3 matrix.

Fourth-rank resonances: VPT2+K

In analogy to the lower-rank Fermi resonances, fourth-rank resonances are mediated at lowest-order by quartic force constants. As the quartic contributions are diagonal in the transformed VPT2 Hamiltonian, fourth-rank resonances first appear in VPT4 [77]. Since the off-diagonal coupling element can be computed to lowest-order using the potential energy and rotational parameters that are routinely computed by many quantum chemistry programs in VPT2 calculations [11],[55] algebraic expressions have been determined in the past from the corresponding VPT4 expressions and incorporated into the framework of VPT2, yielding VPT2+K [72]; the "K" stands for the off-diagonal K constant.

An important difference to the VPT2 treatment of Fermi resonances, where the off-diagonal element is the scaled cubic force constant, is that to lowest-order the K constant is not just the scaled quartic force constant but there are additional cubic and Coriolis contributions that are scaled by the harmonic wavenumbers, much like in the x constants (Eqs. 2.9-2.10). It was realised long ago that these cubic contributions must be included for a balanced description as either contribution can dominate or, perhaps more importantly, they may cancel in the resultant off-diagonal coupling element [72, 77, 179, 180].

There are two general fourth-rank resonance scenarios where either two binary states ($\omega_i + \omega_j \approx \omega_k + \omega_l$) or a fundamental and ternary state ($\omega_i \approx \omega_j + \omega_k + \omega_l$) are coupled. These two general cases comprise six individual resonances that are mediated by

$$K_{i,j;k,l}, \quad K_{i,i;j,k}, \quad K_{i,i;j,j}, \quad K_{i;j,k,l}, \quad K_{i;j,j,k}, \quad K_{i;j,j,j}, \tag{2.43}$$

where a semicolon[56] in the K constants separates the indices of the two resonant components. The algebraic expressions for all K constants were most recently reported by Rosnik and Po-

[55] It is important to note that not the full quartic force field but only the diagonal ($\phi_{i,i,i,i}$, Eq. 2.9) and semi-diagonal ($\phi_{i,i,j,j}$, Eq. 2.10) quartic force constants enter into the energy expression at second-order of perturbation. The VPT2 displacement algorithms in many quantum chemistry programs provide enough information to also derive $\phi_{i,i,i,j}$ and $\phi_{i,i,j,k}$ [11]. However, in order to describe fourth-rank resonances with four distinct indices ($K_{i,j;k,l}$ and $K_{i;j,k,l}$, Eq. 2.43), a full quartic force field is necessary which would require many more displacements.

[56] Some authors use a comma to separate states on either side of the bra-ket (e.g. $K_{ij,kl}$ or $K_{i,jkl}$) but in this work, a comma is already designated to separate indices for two-digit mode labels ($i, j, k, l > 10$ for formic acid dimer). Thus, a semicolon is used instead ($K_{i,j;k,l}$ and $K_{i;j,k,l}$).

lik [72].[57] $K_{i,i;j,j}$ is the classical Darling-Dennison constant and, in analogy to the historical extension of the term "Fermi resonance" to include the general case $\omega_i \approx \omega_j + \omega_k$ where $k \neq j$, $K_{i,j;k,l}$ and $K_{i,i;j,k}$ can also be regarded as "Darling-Dennison" constants. Due to their algebraic similarity to the Darling-Dennison constants, $K_{i;j,k,l}$ and its two special cases shall be called "Darling-Dennison-like" constants.[58]

In this context, a seventh resonance is often mentioned where two fundamentals are coupled ($\omega_i \approx \omega_j$). The K constant[59] for this second-rank resonance is a special case of the fourth-rank resonance constant $K_{i,j;k,l}$ which is easily seen by the general form of the resonance constant

$$K_{i;j} = \frac{3}{2}(n_i + 1)K_{i,i;j,i} + \frac{3}{2}(n_j + 1)K_{i,j;j,j} + \sum_{l \neq i,j} \left(n_l + \frac{1}{2}\right) K_{i,l;j,l}. \tag{2.44}$$

By extending the above example of the OH bend-torsion resonance (Eq. 2.39) to VPT2+K, the

[57] See Ref. [11, p. 1315] where the authors pointed out typographical errors in Ref. [72].

[58] In the older vibration-rotation literature, e.g. Ref. [67], the terms "Fermi resonance" and "Darling-Dennison resonance" are predominantly used to refer to the eponymous resonances [175, 181] in CO_2 ($\omega_1 \approx 2\omega_2$) and H_2O ($2\omega_1 \approx 2\omega_3$). The definition of the term "Fermi resonance" was broadened in time and it has long been widely accepted that "Fermi resonance" is a synonym for *both* possible third-rank resonances, $\omega_i \approx 2\omega_j$ and $\omega_i \approx \omega_j + \omega_k$, see for example Refs. [180, 182] or [6, Fig. 24]. From a theoretical perspective, this generalisation makes sense since the same matrix element and same term in the vibration-rotation Hamiltonian is responsible for both resonances; the former is simply a special case of the latter, i.e. $j = k$. The term "Darling-Dennison resonance", on the other hand, has for a longer time been used more restrictively to only include the 'canonical' $2\omega_i \approx 2\omega_j$ case, the more general cases $2\omega_i \approx \omega_j + \omega_k$ and $\omega_i + \omega_j \approx \omega_k + \omega_l$ either being referred to as "generalised Darling-Dennison resonance" [180] or simply not referred to by a special name [6, 67]. In view of the transformation and generalisation of the term "Fermi resonance", there is no apparent reason not to extend the term "Darling-Dennison resonance" to include the latter two; in analogy to the Fermi resonance, $2\omega_i \approx 2\omega_j$ and $2\omega_i \approx \omega_j + \omega_k$ are just special cases of the general $\omega_i + \omega_j \approx \omega_k + \omega_l$ resonance. The related class of resonances involving a fundamental and a ternary state ($\omega_i \approx \omega_j + \omega_k + \omega_l$ and two specialised cases) was first discussed in the context of acetylene (C_2H_2). The general formulae were first published in the 1970s by Plíva [183] and subsequently by Martin and Taylor [180], Rosnik and Polik [72], and Franke *et al.* [11]. This class of resonances was not named and usually referred to as "1-3 resonance" [180]. In recent years, the definition "Darling-Dennison resonance" is increasingly being used synonymously for all seven possible resonances that are mediated to lowest-order by quartic force constants, including the aforementioned six fourth-rank resonances and the second-rank $\omega_i \approx \omega_j$ resonance. One of the earliest such generalisations can be found in Ref. [77]. This even broader definition of the term "Darling-Dennison" resonance is now used in the VPT2 routines and manuals of the quantum chemistry programs Gaussian (see https://gaussian.com/freq/; last accessed on November 18, 2021) and GUINEA (see http://slater.chemie.uni-mainz.de/cfour/index.php?n=Main.ManualForGUINEA; last accessed on November 18, 2021).

[59] The expression for $K_{i;j}$ in Eq. 2.44 is derived from Ref. [72, Eq. 118]. In analogy to the definition of K constants for third-rank [72, Eq. 85] and fourth-rank resonances [72, Eq. 98]

$$\langle ..., n_i + 1, n_j, n_k, ... | \tilde{H} | ..., n_i, n_j + 1, n_k + 1, ... \rangle = K_{i;j,k} \frac{\sqrt{(n_i + 1)(n_j + 1)(n_k + 1)}}{2^{3/2}},$$

$$\langle ..., n_i + 1, n_j + 1, n_k, n_l, ... | \tilde{H} | ..., n_i, n_j, n_k + 1, n_l + 1, ... \rangle = K_{i,j;k,l} \frac{\sqrt{(n_i + 1)(n_j + 1)(n_k + 1)(n_l + 1)}}{4},$$

where the indices have been adjusted to the nomenclature in this work, we can define $K_{i;j}$ for second-rank resonances as

$$\langle ..., n_i + 1, n_j, ... | \tilde{H} | ..., n_i, n_j + 1, ... \rangle = K_{i;j} \frac{\sqrt{(n_i + 1)(n_j + 1)}}{2},$$

where the denominator is the rth power of $\sqrt{2}$ (r is the rank, see Eq. 2.29).

effective Hamiltonian now additionally includes coupling between the two fundamental modes

$$\frac{\mathbf{H}^{\text{VPT2+K}}}{hc} = \begin{pmatrix} (\nu_4)^* & & \\ \frac{1}{2}K_{4;5} & (\nu_5)^* & \\ \frac{1}{4}\phi_{4,9,9} & \frac{1}{4}\phi_{5,9,9} & (2\nu_9)^* \end{pmatrix}. \tag{2.45}$$

2.1.3 Hybrid force fields

The motivation to use composite force fields, where the harmonic part is evaluated at a higher level of theory, is obvious and hybrid force fields have been used repeatedly in the past, see for example Refs. [184, 185]. Following the classification scheme by Franke *et al.* [11], there are four different hybrid force field approaches which can be summarised as follows:

1. *Additive approach*. The VPT2 equations are evaluated with a consistent lower-level quartic force field and the anharmonic corrections are added to the higher-level harmonic wavenumbers. This approach must be used with caution in effective Hamiltonian approaches.
2. *Substituted approach*. The lower-level harmonic force constants are replaced with corresponding higher-level values before the VPT2 equations are solved. This approach allows for a more natural effective Hamiltonian treatment and problems associated with the additive approach are overcome.
3. *Transformed approach*. The full quartic force field is evaluated at the lower-level and then transformed into the normal coordinates at the higher-level. Errors in the substituted approach that arise from different normal coordinate definitions at both levels of theory are completely overcome.[60] This approximation is the most expensive since the computation of a full quartic force field requires many more numerical displacements (see note 55, p. 22).
4. *Direct approach*. The cubic and quartic force constants are evaluated along the higher-level normal coordinates, using the lower-level to solve the electronic Schrödinger equation. The cubic and quartic force constants are evaluated at a non-stationary geometry which introduces errors that, according to Franke *et al.* [11], have so far not been well studied.

The substituted approach is recommended by Franke *et al.* as it does not involve additional computational cost and is generally more robust than the additive approach.

The file structure of GUINEA easily facilitates the use of this approach – the user simply has to replace the harmonic wavenumbers which are stored in a separate text file. Substituted hybrid force field calculations are also supported by newer versions of Gaussian (directive "DataAdd=Freq") but it is important to note that the results are not directly comparable to GUINEA or other 'manual' implementations based on the theory outlaid in the preceding sections because Gaussian scales the cubic and quartic force constants.[61] Illustrative results with either the exact or modified lower-level anharmonic force constants are shown in Section 8.1.

[60] The above-mentioned weakness of the substituted approach is discussed in the context of the cyclic formic acid dimer in Section 8.2.

[61] The force constants are internally stored in mass-weighted normal coordinates and converted into dimensionless normal coordinates immediately before the VPT2 calculation. The conversion into dimensionless normal coordinates involves the harmonic wavenumbers (Eqs. 2.4-2.5) and if new harmonic wavenumbers are supplied, Gaussian uses these *new* values to convert the force constants. This similarly affects hybrid force field calculations with PyVCI (see Section 2.1.4).

2.1.4 VCI+F: Perturbationally-corrected force field VCI

VPT2 in particular and perturbative vibrational models in general are inherently ill-suited to treat resonances and the identification of near-degeneracy situations still constitutes an obstacle in perturbative effective Hamiltonian calculations (see Section 2.1.2). Variational methods naturally treat resonances in an automated fashion but they usually require an analytical potential or a numerical grid representation of the potential and are thus very expensive. Focussing on methods that are applicable with a quartic force field expansion, the freely available PyPES/PyVCI [186, 187] program suite is a suitable method to guide effective VPT2 Hamiltonian calculations. Since PyVCI employs rectilinear normal coordinate sextic force field expansions of the potential energy, it fails for large-amplitude and pronounced curvilinear motions which is a well-known problem in variational calculations with force fields [188].

In instances where the large-amplitude motion is not strongly involved in the internal dynamics of the studied system, it is possible to converge eigenvalues with PyVCI in a lower-dimensional subspace by freezing the problematic large-amplitude coordinate(s) with only modest errors on the computed fundamental wavenumbers of the remaining modes [108]. The strong OH bend-torsion resonance in *trans*-HCOOH is an example where this procedure is ill-advised. The method to freeze large-amplitude motions in PyVCI as outlined in Ref. [108] is successful for formic acid insofar as the 8D variational calculation with PyVCI can be stabilised, yielding converged vibrational eigenvalues in the subspace of the remaining eight vibrational coordinates. To reintroduce couplings to the torsional coordinate, it is proposed to draw on the toolset provided by standard rectilinear normal mode VPT2+F since both methods use rectilinear coordinates and the harmonic oscillator as zeroth-order description. The method is described in the following using the example of formic acid.

Force field VCI

PyVCI [56, 189] utilises an approximate form of the $J = 0$ Watson Hamiltonian (Eq. 2.2) which is perturbatively expanded. The Hamiltonian[62] can be partitioned into four components

$$\hat{H}_{\mathrm{PyVCI}} = \hat{T}_{\mathrm{harm}} + \hat{T}_{\mathrm{anh}} + V_{\mathrm{harm}} + V_{\mathrm{anh}}, \tag{2.46}$$

where the harmonic part is the usual harmonic oscillator

$$\hat{H}_{\mathrm{harm}} = \hat{T}_{\mathrm{harm}} + V_{\mathrm{harm}} = \frac{hc}{2} \sum_i \omega_i \left(\hat{p}_i^2 + q_i^2 \right). \tag{2.47}$$

The anharmonic potential energy contains the cubic through sextic force constants

$$\begin{aligned} V_{\mathrm{anh}} = {} & \frac{hc}{6} \sum_{i,j,k} \phi_{i,j,k} q_i q_j q_k + \frac{hc}{24} \sum_{i,j,k,l} \phi_{i,j,k,l} q_i q_j q_k q_m \\ & + \frac{hc}{120} \sum_{i,j,k,l,m} \phi_{i,j,k,l,m} q_i q_j q_k q_l q_m + \frac{hc}{720} \sum_{i,j,k,l,m,n} \phi_{i,j,k,l,m,n} q_i q_j q_k q_l q_m q_n, \end{aligned} \tag{2.48}$$

and the anharmonic component of the kinetic energy operator contains the zeroth-order vibrational angular momentum without the Watson U term

$$\hat{T}_{\mathrm{anh}} = hc \sum_\alpha \tilde{B}_e^\alpha \sum_{i,j,k,l} \zeta_{i,j}^\alpha \zeta_{k,l}^\alpha \sqrt{\frac{\omega_j \omega_l}{\omega_i \omega_k}} q_i \hat{p}_j q_k \hat{p}_l. \tag{2.49}$$

[62] In PyVCI, the Hamiltonian is implemented in mass-weighted rectilinear normal mode coordinates Q_i and conjugated momenta $\hat{P}_i$. With the usual conversion factor (Eq. 2.5), this Hamiltonian can be converted into dimensionless normal coordinates q_i and conjugated momenta $\hat{p}_i$. For consistency, the PyVCI Hamiltonian here is expressed in dimensionless normal coordinates and conjugated momenta. These expressions are strictly equivalent to Ref. [56].

The VCI matrix is constructed from Hartree products of 1D harmonic oscillators

$$\Phi_{\mathbf{n}}(Q_1, ..., Q_{N_{\text{vib}}}) = \prod_{i=1}^{N_{\text{vib}}} \phi_{n_i}(Q_i), \tag{2.50}$$

where $\mathbf{n} = \{n_1, ..., N_{\text{vib}}\}$ is the vibrational excitation array that defines the harmonic oscillator basis function. A user-defined maximum excitation value determines which basis functions are included in the VCI matrix

$$\sum_{i}^{N_{\text{vib}}} n_i \leq n_{\text{max}}. \tag{2.51}$$

The eigenvalues of the VCI matrix are obtained with the Lanczos algorithm as implemented in the Fortran-based ARPACK function which is wrapped by a SciPy function.

Reintroducing frozen vibrational degrees of freedom

Building on the sum-of-fundamentals representation of the VPT2 term values (Eq. 2.15, p. 17), we have to first separate out the torsional mode of formic acid (ν_9)

$$\begin{aligned} G_0(n_1, ..., n_8, n_9) = \omega_9 n_9 + x_{9,9}(n_9^2 + n_9) + \sum_{i\neq 9} x_{i,9}\left(n_i n_9 + \frac{n_i + n_9}{2}\right) \\ + \underbrace{\sum_{i\neq 9}\left[\left(\omega_i n_i + x_{i,i}(n_i^2 + n_i) + \frac{n_i}{2}\sum_{k\neq i} x_{i,k}\right) + \sum_{j>i} x_{i,k} n_i n_j\right]}_{\Leftrightarrow \lambda_{\text{var}}(n_1,...,n_8)}. \end{aligned} \tag{2.52}$$

Freezing of the torsional coordinate as proposed in Ref. [108] corresponds to setting ω_9 and all $x_{i,9}$ to zero in VPT2. However, there are also cubic contributions of the torsion to

$$x_{i,i} \Leftarrow -\frac{\phi_{i,i,9}^2\left(8\omega_i^2 - 3\omega_9^2\right)}{16\omega_9\left(4\omega_i^2 - \omega_9^2\right)}, \tag{2.53}$$

$$x_{i,j} \Leftarrow -\frac{\phi_{i,i,9}\phi_{j,j,9}}{4\omega_9} - \frac{\phi_{i,j,9}^2\omega_9\left(\omega_i^2 + \omega_j^2 - \omega_9^2\right)}{2\Omega_{i,j,9}}, \tag{2.54}$$

where $i, j \neq 9$ (Eqs. 2.9-2.10, p. 15). For the current example, these contributions are fortuitously zero due to symmetry as the number of torsional indices is uneven (see note 51, p. 20). Next, we replace all terms in the second line of Eq. 2.52 with the corresponding variational 8D eigenvalue (λ_{var}) which has the largest overlap with the harmonic oscillator basis state $\mathbf{n} = \{n_1, ..., n_8\}$. By replacing the appropriate second-order terms with λ_{var}, we obtain a perturbatively-corrected variational analogue of VPT2. Consider the following three examples of ν_6+ν_7, ν_6+ν_9, and $2\nu_9$

$$G_0(n_6{=}1, n_7{=}1) = \lambda_{\text{var}}(n_6{=}1, n_7{=}1) + \frac{x_{6,9} + x_{7,9}}{2}, \tag{2.55}$$

$$G_0(n_6{=}1, n_9{=}1) = \lambda_{\text{var}}(n_6{=}1) + \omega_9 + 2x_{9,9} + 2x_{6,9} + \frac{1}{2}\sum_{i\neq 6,9} x_{9,i}, \tag{2.56}$$

$$G_0(n_9{=}2) = 2\omega_9 + 6x_{9,9} + \sum_{i\neq 9} x_{9,i}. \tag{2.57}$$

All accidental resonances are now accounted for by the variational calculation. The only drawback is that this does not extend to resonances that involve the torsion as it is reintroduced *post hoc*. As such, if strong Fermi resonances occur that involve the torsion, the anharmonicity constants in Eq. 2.52 must be deperturbed and effective Hamiltonians set up, quite similar to VPT2+F.[63] However, there is a central difference between VPT2+F and the proposed VCI+F method. Accidental resonances or resonance perturbations of states that are *involved* in resonances with torsionally-excited states but are not *directly* resonance-coupled to them are (approximately) accounted for by the preceding reduced-dimensional variational calculation. To lowest-order, only explicit Fermi resonances that involve the torsion must be accounted for. Some numerical results are provided in Section 5.4.

Proposed generalisation of VCI+F

There is room for future improvement of VCI+F. So far only the cubic part of the force field involving the frozen vibration is used. Additionally, the perturbative corrections are only applied in the harmonic oscillator basis whereas instead they should be transformed into the new VCI basis. This is especially important for resonance-perturbed states where it becomes challenging to assign a harmonic oscillator label. This can be remedied and the resonance treatment can further be automated without reliance on any *a priori* screenings of near-degeneracies that involve the removed coordinate. The general procedure is outlined in the following, again using the example of *trans*-formic acid.

The VCI matrix is set up to be block-diagonal

$$\mathbf{H}_{\mathrm{VCI}} = \begin{pmatrix} \mathbf{H}^{n_9=0} & & \\ & \mathbf{H}^{n_9=1} & \\ & & \ddots \end{pmatrix}, \tag{2.58}$$

where each block contains states that share a common n_9. The eigenvalues of the $n_9 = 0$ block are identical to the 8D eigenvalues which are obtained if the torsion is frozen as described in Ref. [108]. Basis functions in each block must satisfy the condition

$$\sum_{i\neq 9}^{N_{\mathrm{vib}}} n_i \leq (n_{\mathrm{max}} - n_9). \tag{2.59}$$

In each block, the matrix elements have the form

$$\mathbf{H}_{\mathbf{n},\mathbf{n}'} = \langle \Phi_{\mathbf{n}} | \, \hat{H}_{\mathrm{harm}} + \hat{H}_{\mathrm{anh}}^{\mathrm{active}} \, | \Phi_{\mathbf{n}'} \rangle \,, \tag{2.60}$$

where the anharmonic components of the Hamilton operator do not contain terms that involve indices of inactive modes. In a second step, the missing contributions from $\hat{H}_{\mathrm{anh}}^{\mathrm{inact}}$ are added to *all* matrix elements of the VCI matrix in the new eigenvector basis. The final results correspond to the eigenvalues of this new VCI matrix whose elements generally have the form

$$\mathbf{H}_{\mathbf{n},\mathbf{m}} = \left\langle \sum_{\mathbf{n}'} c_{\mathbf{n},\mathbf{n}'} \Phi_{\mathbf{n}'} \middle| \, \hat{H}_{\mathrm{anh}}^{\mathrm{inact}} \, \middle| \sum_{\mathbf{m}'} c_{\mathbf{m},\mathbf{m}'} \Phi_{\mathbf{m}'} \right\rangle = \sum_{\mathbf{n}',\mathbf{m}'} c_{\mathbf{n},\mathbf{n}'} c_{\mathbf{m},\mathbf{m}'} \langle \Phi_{\mathbf{n}'} | \, \hat{H}_{\mathrm{anh}}^{\mathrm{inact}} \, | \Phi_{\mathbf{m}'} \rangle \,. \tag{2.61}$$

63 The ideas of combining variational and perturbational vibrational methods have a long history and cannot exhaustively be covered here. Many approaches focus on making variational calculations more efficient by using perturbation theory to prune basis functions, e.g. see Refs. [53, 190–192]. The ideas presented here are similar to previous approaches that use perturbation theory to account for weak couplings to basis states that are not included in the pruned VCI Hamiltonian [189, 193, 194].

If, similar to the full-dimensional VCI calculation [108], couplings to higher-excited torsional states introduce instabilities in resultant VCI wavefunctions, one could restrict the terms in $\hat{H}^{\text{inact}}_{\text{anh}}$ to second-order and/or restrict the coupling between sub-blocks to those where Δn_9 is below a user-controlled value.

2.2 Linear Raman and FTIR jet spectroscopy

FTIR and Raman jet spectra of formic acid were obtained with well-established setups. FTIR spectra were recorded with the "filet-jet" (*fi*ne but *le*ng*th*y; a reference to the used slit nozzle and filet-shaped expansion zone) and Raman spectra with the "curry-jet" (*c*lassical *un*re*s*tricted *R*aman spectroscop*y*). In the following, both setups are briefly introduced[64] and key features highlighted.[65] Throughout this work, helium was used as carrier gas.

2.2.1 The curry-jet

The curry-jet was built by Zielke [195] and further developed and modified in subsequent years.[66] A graphical illustration of the curry-jet setup, as of 2019, can be found in Ref. [201]. In contrast to the FTIR jet expansions (filet-jet), the Raman jet expansions are continuous and the slit nozzle and helium feed-line can be heated which enables the use of thermal excitation as a means of population and size control which was used in this work to optimise the spectra for the study of formic acid monomer and its cyclic dimer, respectively.

Population and size control via thermal excitation. Thermal excitation followed by rapid jet-cooling was previously successful in detecting higher-energy conformers of carboxylic acid monomers [42, 86, 87, 89]. The measurement protocol developed by Meyer and Suhm [87, 89] is applied here towards the same goal, especially to systematically increase hot transitions from higher-excited vibrational states in the global minimum *trans* conformer that can be used to critically examine combination/overtone assignments. By intensity-scaling the spectra of a temperature series to a *trans* fundamental, isomeric *cis*-formic acid bands and non-isomeric *trans* hot bands can be easily distinguished from cold monomer and cluster bands as they increase in intensity with temperature whereas the cluster bands decrease. For the dimer measurements, moderate heating was applied which allows for the use of comparably high concentrations and, therefore, high signal intensity. For these measurements, the spectra are consequently intensity-scaled to known dimer bands, thus facilitating the distinction between monomeric bands which increase with temperature and signals due to larger clusters which decrease relative to dimers. However, odd-numbered formic acid clusters, e.g. the formic acid trimer, were shown to exhibit a more complex aggregation behaviour in supersonic expansions [125]. This results in deviations from the expected concentration behaviour which are addressed in Chapter 6.

[64] The filet- and curry-jet have been described in numerous publications. Particularly the following description of the curry-jet may exhibit similarities to previous publications [28, 41, 42, 91, 109] that are not explicitly marked as citations.

[65] For a comparison of similarities and differences of both jet spectroscopic setups, see for example Refs. [86, 125].

[66] For further details of the curry-jet, see for example Refs. [86, 119, 196–198]. See Refs. [199, 200] for a discussion of the most recent version of the setup. Two important technical innovations in comparison to previously published curry-jet spectra of formic acid [140, 141] include the possibility to heat the nozzle and feed-line before expansion and a more recent change from a pulsed to a continuous filling of the reservoir from which the gas is subsequently expanded [199]. For the resultant spectra, the main consequence is a much more stable concentration of the continuously expanded analyte-in-carrier gas beam over several succeeding measurement repetitions [199].

Data acquisition and measurement protocol. Formic acid was seeded in helium and expanded continuously through a vertical slit nozzle (0.15 mm width, 4 mm length) into an evacuated jet chamber. Both the nozzle and its feed-line are heatable and heating between 293 and 463 K was applied (20-190 °C). For monomer-optimised spectra, high temperatures between 373 and 463 K (100-190 °C) were used to enhance the formation of *cis*-formic acid and increase the intensity of hot *trans* bands while simultaneously suppressing cluster formation. As a compromise between a high dimer signal and moderate intensity of larger clusters, moderate heating of the nozzle between 293 and 333 K (20-60 °C) was utilised for dimer-optimised measurements. The expansion was probed at a 90° angle by a continuous-wave diode-pumped 532 nm solid-state laser (Spectra Physics Millennia eV) that was operated at 20-25 W. The distance between the nozzle and the laser was set to 1 mm. In the monomer measurements, a half-wave plate ($\lambda/2$) was installed into the optical path specifically for depolarisation measurements. In the dimer measurements, the waveplate was in place for all measurements. Note that without a waveplate, the default initial polarisation of the laser is perpendicular to the scattering plane ($\perp^{\mathrm{i}}$, see Section 2.3). Scattered light, perpendicular to both the flow direction and the laser, was collected by a camera lens and focussed onto a 1 m monochromator (McPherson). The scattered photons were dispersed onto a liquid nitrogen-cooled CCD camera (Princeton, PyLoN 400, 1340×400 pixel), binning over 400 vertical pixels. In each spectral window, several recordings with varying exposure times were measured and subsequently co-added. It should be noted that measurements were repeated for several central wavelength settings (λ_{Mon}). A central monochromator wavelength setting at λ_{Mon} roughly covers a spectral range from $\lambda_{\mathrm{Mon}}-10$ nm to $\lambda_{\mathrm{Mon}}+10$ nm. Near 600 cm^{-1}, this corresponds to a range of ~650 cm^{-1} but only ~450 cm^{-1} in the OH stretching region. The measurement details for each spectrum can be found in Appendix A.

Data post-processing and calibration. The Raman spectra were calibrated with neon[67] transition wavelengths [202] in vacuum[68] using a second-order polynomial[69] to convert from the pixel into the wavelength domain, without adjustment of the count rate. Note that the laser excitation wavenumber was subsequently subtracted from the scattering wavenumbers to obtain the Stokes shift, i.e. $\tilde{\nu} \equiv \tilde{\nu}_{\mathrm{Stokes}} = \tilde{\nu}_{\mathrm{Laser}} - \tilde{\nu}_{\mathrm{measured}}$. Spikes due to cosmic rays were eliminated by comparing multiple exposures for the same pixel column. All data post-processing was executed by a fully automated Python 3 program routine.[70] The combination of the resolving power of the monochromator and the spectral calibration results in a wavenumber uncertainty of about 1-2 cm^{-1}. Thus, a band position uncertainty of ± 2 cm^{-1} is ascribed throughout this work.

[67] For some spectral regions, additional krypton spectra were measured but not included in the calibration because they did not significantly improve the quality of the fit.

[68] Note that in previous Raman jet studies of the formic acid dimer [119, 141], neon transitions in air were used for spectral calibration. This does not significantly affect the low-frequency regions but can lead to band position deviations on the order of the spectral resolution for the spectral regions that are discussed in this work ($\geq$ 600 cm^{-1}).

[69] If only three reference points were available, a first-order polynomial was used.

[70] The first version of the script, described in Ref. [198], was developed by T. Forsting and later extended by N. Lüttschwager. In the course of this work, an automated calibration algorithm that directly determines and assigns the neon peak positions from a measured spectrum (Octave; written by M. Gawrilow, see Ref. [200]) was implemented into the Python 3 script. Previously separate steps in the post-processing of curry-jet spectra, necessitating the use of different computer programs, could be combined into one fully automated function call. The current and previous versions of the script are archived on GitLab. For internal reference: Version 20.06.4 of the script was used with the "madras.despike" method (based on a MatLab script by N. Lüttschwager).

2.2.2 The filet-jet

Since its first conceptualisation and construction by Borho [203], the filet-jet has seen many modifications and optimisations in the last two decades. A detailed and thorough description of the apparatus is given by Suhm and Kollipost in Ref. [204].[71] FTIR spectra are only consulted in this work in order to study the Raman-inactive vibrations of the cyclic formic acid dimer. Key differences between the utilised IR and Raman jet setups include that the filet-jet uses pulsed expansions; the nozzle and feed-line are not heatable; the distance between the centre of the IR beam and the nozzle is 10 mm, the sampled area of the jet expansion is thus generally colder compared to the curry-jet; the IR sampling cross-section is much larger. In order to distinguish between different cluster sizes, spectra with different reservoir pressures were recorded with the filet-jet, following the measurement protocol presented in Ref. [86]. The FTIR jet spectra for the main isotopologue have already been published in Ref. [109]. The newly shown FTIR jet spectra of deuterated formic acid (Figs. 6.1-6.2, pp. 116) were measured using the same experimental protocol (and conditions) and the reader is therefore referred to Refs. [86, 109] for further details. Newly recorded spectra have all been measured at a resolution of $2\,\mathrm{cm}^{-1}$. In addition to the new low-resolution spectra, previously published[72] filet-jet spectra with higher resolutions between 0.5 and $1\,\mathrm{cm}^{-1}$ are shown in Figs. 6.1-6.2 to facilitate an analysis of the band shape (see Section 2.4.3). The InSb/MCT sandwich detectors that are used for the detection of the mid-infrared radiation in this work and in Ref. [149] are different, resulting in different wavelength responses for the higher- and lower-resolution spectra. This is best seen near the filter gap of the detector $\sim 600\,\mathrm{cm}^{-1}$ (Fig. 6.2).

2.3 Raman intensities and depolarisation ratios

The Raman intensity $I(\theta; \mathcal{P}^{\mathrm{s}}, \mathcal{P}^{\mathrm{i}})$, depends on the scattering geometry and the polarisation $\mathcal{P}$ of the scattered and incident radiation, denoted "s" and "i", respectively. The opening angle between the unit vectors that define the propagation directions of the incident and scattered radiation is $\theta = \arccos(\mathbf{e}^{\mathrm{i}} \cdot \mathbf{e}^{\mathrm{s}})$ [206, Section 5.3]. The plane defined by these two vectors is the scattering plane. In the Raman measurements with the curry-jet (see Section 2.2.1), a 90° scattering geometry is used. Thus, we continue with $\theta = \pi/2$, focussing on pure vibrational Stokes[73] Raman scattering.[74]

Raman scattering corresponds to the fraction of light that is inelastically scattered by molecules. This is usually described in the oscillating electric dipole model. Very similar to IR spectroscopy, the vibrational Raman selection rules necessitate a *change* in the electric polarisability. The intensity of the scattered light is proportional to the scattering cross-section and the irradiance of the incident radiation. It is useful to express the intensity as

$$I = I_0 \sigma' b, \tag{2.62}$$

[71] For more recent discussions of the filet-jet, see also Refs. [86, 163, 205].

[72] The spectra were previously shown in Ref. [149] and have kindly been provided by F. Kollipost.

[73] For Stokes scattering, the incident wavenumber is greater than the scattered wavenumber, i.e. $\tilde{\nu}_{\mathrm{Laser}} > \tilde{\nu}_{\mathrm{s}}$.

[74] The general expressions for the transition polarisability are very involved. For a detailed discussion, see Refs. [206, 207]. A compact overview in the context of vibrational spectroscopy is given by Wilson, Decius, and Cross [153]. In analogy to the treatment of absorption and emission processes [153], it suffices to focus on the induced electric dipole approximation as Raman scattering from induced magnetic dipoles and electric quadrupoles rarely become important [206]. For pure vibrational Raman scattering, the following approximations are introduced [206, Chapter 5]: The Born-Oppenheimer approximation applies and the polarisability is a function of the vibrational coordinates only (adiabatic dynamic polarisability); there are no electronic transitions; the electronic ground state is non-degenerate; the excitation wavenumber of the incident radiation is much smaller than electronic but much larger than vibrational transitions in the molecule.

where b is a proportionality constant (including the number of particles), I_0 the intensity of the incident radiation,[75] and σ' the first differential scattering cross-section.[76] It follows from Eq. 2.62 that $\sigma' \equiv \sigma'(\theta; \mathcal{P}^{\mathrm{s}}, \mathcal{P}^{\mathrm{i}})$. Although σ' is strictly the "first differential cross-section", for brevity we shall simply refer to it as "cross-section" in the future.

2.3.1 Depolarisation ratios

To contrive recipes for computing σ', several approximations are necessary. Before we discuss the calculation of σ', it is instructive to first inspect its dependence on the scattering geometry and polarisation, which is the Raman activity $A(\theta; \mathcal{P}^{\mathrm{s}}, \mathcal{P}^{\mathrm{i}})$. There are four polarisation combinations for a 90° scattering geometry and linearly polarised incident radiation. The Raman activity[77] is a function of the so-called isotropic and anisotropic invariants of the transition polarisability tensor

$$A(\pi/2; \perp^{\mathrm{s}}, \perp^{\mathrm{i}}) = 45a^2 + 4\gamma^2, \tag{2.63}$$

$$A(\pi/2; \parallel^{\mathrm{s}}, \perp^{\mathrm{i}}) = A(\pi/2; \perp^{\mathrm{s}}, \parallel^{\mathrm{i}}) = A(\pi/2; \parallel^{\mathrm{s}}, \parallel^{\mathrm{i}}) = 3\gamma^2. \tag{2.64}$$

If we assume this tensor to be symmetric [206, p. 85], its Cartesian components are related to the invariants via

$$\langle (\alpha_{x,x})^2 \rangle = \langle (\alpha_{y,y})^2 \rangle = \langle (\alpha_{z,z})^2 \rangle = \frac{45a^2 + 4\gamma^2}{45}, \tag{2.65}$$

$$\langle (\alpha_{x,y})^2 \rangle = \langle (\alpha_{x,z})^2 \rangle = \langle (\alpha_{y,z})^2 \rangle = \frac{3\gamma^2}{45}. \tag{2.66}$$

Following Long's nomenclature, "$\langle \cdot \rangle$" indicates averaging over all spatial directions (since rotations have been separated out) and "$(\alpha_{i,j})$" is a component of the Cartesian transition polarisability moment which must be integrated over appropriate vibrational wavefunctions. As mentioned, there must be a change in the transition polarisability moment for Raman scattering to occur.[78]

From the above equations, we can deduce several things. For perpendicularly polarised incident radiation, which is the default setting throughout this work, the intensity depends on the polarisation of the scattered photons. This ratio is the *depolarisation ratio* which has the following form for linearly polarised incident radiation

$$\rho_l(\pi/2; \perp^{\mathrm{i}}) = \frac{I(\pi/2; \parallel^{\mathrm{s}}, \perp^{\mathrm{i}})}{I(\pi/2; \perp^{\mathrm{s}}, \perp^{\mathrm{i}})} = \frac{3\gamma^2}{45a^2 + 4\gamma^2} \leq \frac{3}{4}. \tag{2.67}$$

To measure ρ_l directly as defined in Eq. 2.67, one must use a polarisation filter to selectively collect either the perpendicularly or the parallelly polarised fraction of the scattered light whereas the incident polarisation remains unchanged. To minimise this loss of intensity in the curry-jet setup, instead the polarisation of the incident laser polarisation is modulated ($\perp^{\mathrm{i}} \rightarrow \parallel^{\mathrm{i}}$) with a retardation plate (half-wave plate; $\lambda/2$) while both polarisation components of the scattered light

[75] In Appendix A17 of Ref. [206], Long points out the inequality of the irradiance and intensity which are often used synonymously in this context. For the purposes here, it is easier to continue with I_0 and absorb the remaining terms from the irradiance into the proportionality constant b.

[76] The first differential scattering cross-section is related to the total cross-section, σ, via $\sigma = \int_0^{4\pi} \sigma' \mathrm{d}\Omega$, where $\mathrm{d}\Omega$ is an element of the solid angle [206, Eq. 5.4.6].

[77] Here the Raman activity is defined without the vibrational degeneracy. Some authors include the degeneracy, see also Ref. [208].

[78] The above considerations closely follow Long's detailed derivation in Chapter 5 [206]. The expressions are deliberately kept as general as possible for the discussion of the depolarisation ratio. It should be noted that Rayleigh scattering is implicitly included for the special case of no vibrational excitation.

are collected. This ratio of the different incident polarisations is given by

$$\delta = \frac{I(\pi/2; \|^{\mathrm{s}} + \perp^{\mathrm{s}}, \|^{\mathrm{i}})}{I(\pi/2; \|^{\mathrm{s}} + \perp^{\mathrm{s}}, \perp^{\mathrm{i}})} = \frac{6\gamma^2}{45a^2 + 7\gamma^2} \leq \frac{6}{7}. \tag{2.68}$$

Based on the above equation, the curry-jet spectra with parallelly polarised incident radiation ($\|^{\mathrm{i}}$) are scaled[79] by 7/6 to facilitate a comparison with $\perp^{\mathrm{i}}$ spectra.

There are some symmetry constraints on the possible values of ρ_l (and δ). The isotropic component a^2 becomes zero if the product of the irreducible representations of the initial and final vibrational state does not contain the totally symmetric representation. In other words, for all molecular systems considered in this work a^2 is zero for transitions from the vibrational ground state into non-totally symmetric vibrational states. In these cases, the vibrational band is completely depolarised and the depolarisation value is 0.75. These considerations generally extend to rotational $\Delta J \neq 0$ transitions. For the totally symmetric case, ρ_l can in principle take all values between 0 and 0.75.[80] In the limiting cases, the band is said to be completely polarised or completely depolarised. By comparison of $\perp^{\mathrm{i}}$ and $\|^{\mathrm{i}}$ ×7/6 spectra, we can conclude that all bands that persist are depolarised; they may or may not be totally symmetric. In these cases, an analysis of the band contour may yield further symmetry information (see Section 2.4.3). Bands that do not persist in the $\|^{\mathrm{i}}$ ×7/6 spectra but decrease in intensity relative to the $\perp^{\mathrm{i}}$ spectra, on the other hand, are totally symmetric.

2.3.2 Scattering cross-sections

Tractable expressions for σ' can be obtained in the double harmonic approximation for fundamental transitions.[81] Since the curry-jet does not measure energy but photon densities (Φ),[82] we first have to modify Eq. 2.62 by dividing by $hc\tilde{\nu}_{\mathrm{s}}$ [206, pp. 524]. In the harmonic approximation, the Stokes scattering wavenumber becomes $\tilde{\nu}_{\mathrm{s}} = \tilde{\nu}_{\mathrm{Laser}} - \omega_i$, where ω_i is the harmonic wavenumber of mode i. The (first differential) scattering cross-section for photon densities[83] is given by

$$\sigma'_{\Phi,i} = \frac{2\pi^2 h}{45c} \cdot \frac{\tilde{\nu}_{\mathrm{Laser}}(\tilde{\nu}_{\mathrm{Laser}} - \omega_i)^3}{\omega_i} \cdot \frac{g_i A_{i,\mathrm{harm}}}{1 - \exp\left(-\frac{hc\omega_i}{k_{\mathrm{B}} T_{\mathrm{vib}}}\right)}, \tag{2.69}$$

where the laser wavenumber is set to $\tilde{\nu}_{\mathrm{Laser}} = (532\,\mathrm{nm})^{-1}$, c the speed of light in vacuum, k_{B} the Boltzmann constant, T_{vib} the vibrational temperature (set to 100 K to roughly match the

[79] In experimental setups, the incident polarisation ratio may slightly deviate from the theoretical limit (Eq. 2.68). Indeed, the scattering efficiency of the curry-jet is polarisation-dependent. This was recently discussed by Gawrilow and Suhm in Ref. [199] (see also Refs. [196, 198, 200]). They proposed an empirically corrected value of 1.195 for $\delta_{\max}$ instead of $7/6 \approx 1.167$ (Eq. 2.68). The impact of correcting $\delta_{\max}$ was tested for selected spectra and differences were barely recognisable. Since depolarisation measurements are used only in a qualitative manner, this correction is neglected.

[80] This is true for the point groups considered in this work (C_s and C_{2h}). For high-symmetry point groups, see Ref. [207].

[81] A detailed derivation is given by Long [206, Section 5.7].

[82] See also Refs. [119, 195, 209] for a derivation of Raman scattering cross-sections tailored for the curry-jet.

[83] To convert the intensity from energy (I) to photon densities (Φ), we must divide Eq. 2.62 by the scattering wavenumber $hc\tilde{\nu}_{\mathrm{s}}$. To normalise I_0 in the same manner as I, ν_{s} must be replaced by $\tilde{\nu}_{\mathrm{Laser}}$:

$$\Phi = \frac{I}{hc\tilde{\nu}_{\mathrm{s}}} = \frac{I_0 \sigma' b}{hc\tilde{\nu}_{\mathrm{s}}} = b\left(\frac{I_0}{hc\tilde{\nu}_{\mathrm{Laser}}}\right) \cdot \left(\frac{hc\tilde{\nu}_{\mathrm{Laser}}}{hc\tilde{\nu}_{\mathrm{s}}}\right) \sigma' = b\Phi_0 \cdot \left(\frac{\tilde{\nu}_{\mathrm{Laser}}}{\tilde{\nu}_{\mathrm{s}}}\right) \sigma' = b\Phi_0 \sigma'_{\Phi}.$$

vibrational temperature in the expansion), and g_i the degeneracy of the vibration (= 1 for all vibrations investigated in this work).

The Raman activity requires some explanation. In Eq. 2.63-2.64, the activity is rather general whereas here $A_{i,\mathrm{harm}}$ is the Raman activity obtained in the double harmonic approximation. The invariants a^2 and γ^2 are calculated from the first derivates of the transition polarisability moment with respect to normal mode displacements. The *ab initio* computed Raman activity, as calculated by Gaussian, has the form

$$A_{i,\mathrm{harm}} = 45a_i^2 + 7\gamma_i^2. \tag{2.70}$$

Note that $A_{i,\mathrm{harm}}$, in particular in Eq. 2.69, has the units $\mathrm{m^4\,kg^{-1}}$ and must be multiplied by $(4\pi\varepsilon_0)^2$ to be converted into SI units [195]. Since Gaussian prints A_i in $\mathrm{Å^4\,amu^{-1}}$, the above form is more useful.

To account for the varying detection efficiency of differently polarised scattered light of the curry-jet, it was proposed [199] to modify the parallelly scattered part of the Raman activity

$$A_{i,\mathrm{harm}} = 45a_i^2 + 4\gamma_i^2 + \frac{3\gamma_i^2}{P(\omega_i)},$$

where $P(\omega_i)$ is a ninth-order polynomial depending on the harmonic wavenumber of mode i. The polynomial coefficients are tabulated in the supplementary material of Ref. [199]. The activity is not empirically corrected as the impact is negligible for all purposes in this work.

2.4 Theoretical treatment of vibrational transitions

2.4.1 Vibrational mode numbering

The vibrational nomenclature in this work is following established conventions. As suggested by Herzberg [172, pp. 271], vibrations are grouped by their symmetry and sorted by their frequency in descending order, i.e. {A′, A″} for C_s groups. For C_{2h}, however, instead of $\{\mathrm{A_g}, \mathrm{A_u}, \mathrm{B_g}, \mathrm{B_u}\}$, the ordering by Bertie and Michaelian [93] is adopted since it conveniently groups Raman- and IR-active modes $\{\mathrm{A_g}, \mathrm{B_g}, \mathrm{A_u}, \mathrm{B_u}\}$.

Each vibrational mode, labelled ν_i, is ascribed a cardinal number with $i = 1, ..., N_{\mathrm{vib}}$. The highest-frequency totally symmetric vibration is then ν_1. Since this system offers little information on the vibrational motion, these labels are augmented with the greek letters ν, δ, and γ that shall denote stretching, in-plane bending, and out-of-plane bending/torsional motions, respectively. The chemical groups that are mainly involved in the motion are indicated in parentheses, e.g ν(OH) denotes an OH stretching vibration. These local mode labels are only approximate and the true normal modes might be strongly mixed group vibrations.

Vibrations of monomeric formic acid, *t*F and *c*F, and the cyclic dimer, (FF), are fully characterised by these three information – symmetry, Herzberg label, and local mode label. The numbering used here for their (symmetrically) deuterated variants deviates from most of the experimental literature in that usually the ordering is adjusted if the energetic sequence within symmetry blocks changes whereas here the main isotopologue nomenclature is adopted as it greatly facilitates the comparison of deuteration effects. The conversion between different numbering systems is shown in Table 2.2. For asymmetrically substituted cyclic formic acid dimer, (FF′), only local mode and symmetry labels are used – (FF′) dimers are no longer C_{2h} but C_s symmetric and there is no benefit in retaining the Herzberg labels as their order would completely change.

Since the distinction between intermonomer vibrations based on the Herzberg label, local mode label, and symmetry is not possible anymore for the polar dimer, FF, and trimer, F(FF),

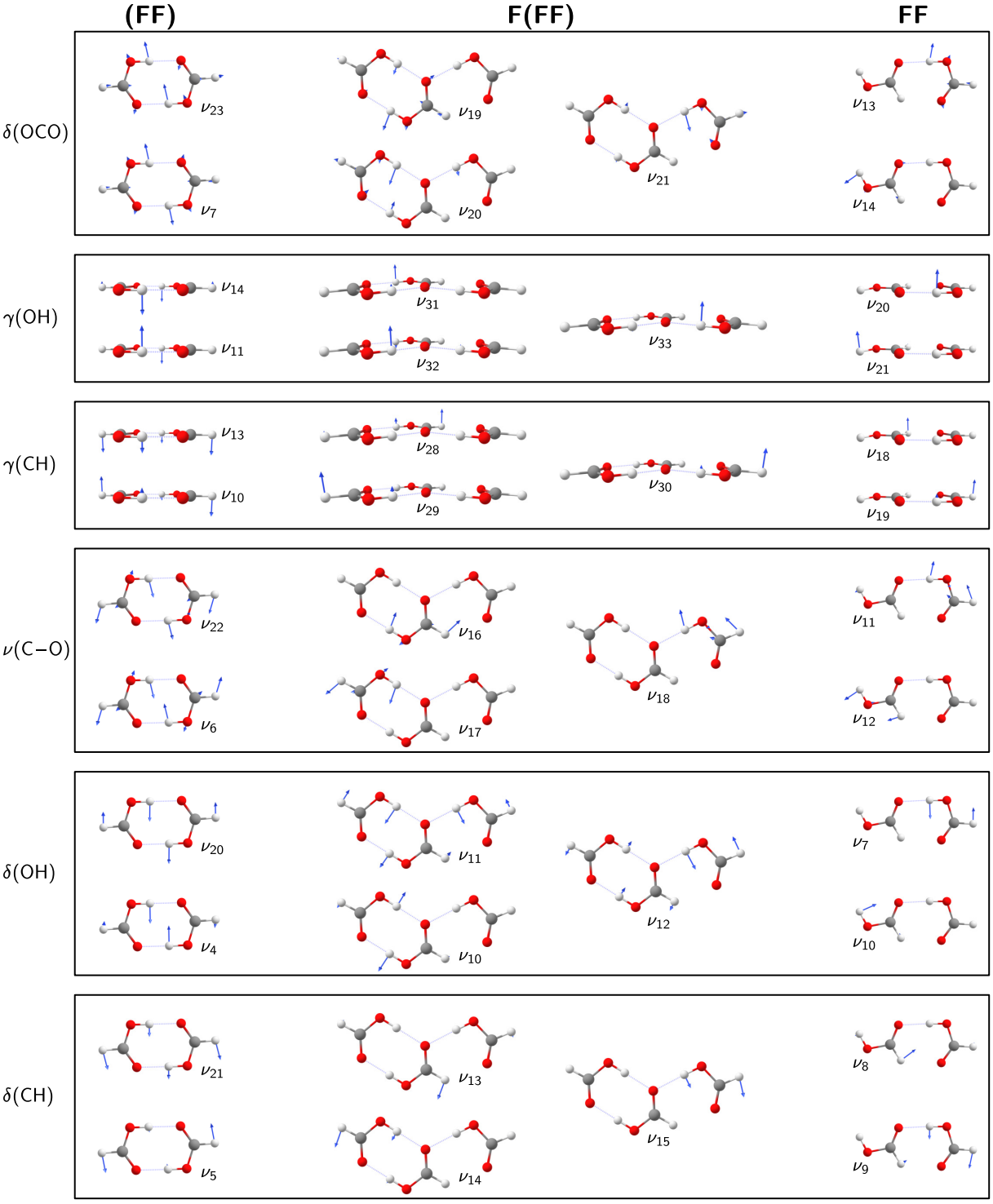

Figure 2.1 Fingerprint normal mode displacements (600-1500 cm^{-1}) of the cyclic formic acid dimer (FF), the polar trimer F(FF), and the polar dimer FF computed at the CCSD(T)-F12a/VDZ-F12 level. Reproduced from Ref. [109] (published under a Creative Commons Attribution license, CC BY 4.0).

the local mode labels are provided with additional subscripts. In FF, the subscript "a" indicates the hydrogen bond *a*ccepting unit. In F(FF), the monomer unit that *d*ocks onto the cyclic dimer is labelled "d". The intra-monomer fingerprint normal mode vibrations of (FF), FF, and F(FF) are visualised in Fig. 2.1 (p. 34).

Table 2.2 Conversion between different vibrational numbering conventions used for the formic acid monomer (both conformers) and the cyclic formic acid dimer. Deviations between the nomenclature employed in this work and that by Bertie *et al.* [93, 118], short "Bertie nomenclature", are marked with a dagger (†); deviations between the Herzberg nomenclature [172] and the latter are marked with a double dagger (‡). For the monomer, the Bertie and Herzberg nomenclature are identical.

Mode	Descr.	Γ	Bertie	Herzberg	Bertie	Herzberg	Bertie	Herzberg	Bertie	Herzberg
			HCOOH		DCOOH		HCOOD		DCOOD	
ν_1	ν(OH/D)	A′	ν_1		ν_1		† ν_2		ν_1	
ν_2	ν(CH/D)	A′	ν_2		ν_2		† ν_1		ν_2	
ν_3	ν(C=O)	A′	ν_3		ν_3		ν_3		ν_3	
ν_4	δ(CH/D)	A′	ν_4		† ν_6		ν_4		† ν_5	
ν_5	δ(OH/D)	A′	ν_5		† ν_4		† ν_6		† ν_6	
ν_6	ν(C−O)	A′	ν_6		† ν_5		† ν_5		† ν_4	
ν_7	δ(OCO)	A′	ν_7		ν_7		ν_7		ν_7	
ν_8	γ(CH/D)	A″	ν_8		ν_8		ν_8		ν_8	
ν_9	γ(OH/D)	A″	ν_9		ν_9		ν_9		ν_9	
			$(HCOOH)_2$		$(DCOOH)_2$		$(HCOOD)_2$		$(DCOOD)_2$	
ν_1	ν(OH/D)	A_g	ν_1	ν_1	ν_1	ν_1	† ν_2	ν_2	ν_1	ν_1
ν_2	ν(CH/D)	A_g	ν_2	ν_2	ν_2	ν_2	† ν_1	ν_1	ν_2	ν_2
ν_3	ν(C=O)	A_g	ν_3	ν_3	ν_3	ν_3	ν_3	ν_3	ν_3	ν_3
ν_4	δ(OH/D)	A_g	ν_4	ν_4	ν_4	ν_4	† ν_6	ν_6	† ν_5	ν_5
ν_5	δ(CH/D)	A_g	ν_5	ν_5	† ν_6	ν_6	† ν_4	ν_4	† ν_6	ν_6
ν_6	ν(C−O)	A_g	ν_6	ν_6	† ν_5	ν_5	† ν_5	ν_5	† ν_4	ν_4
ν_7	δ(OCO)	A_g	ν_7	ν_7	ν_7	ν_7	ν_7	ν_7	ν_7	ν_7
ν_8	ν(OH/D···O)	A_g	ν_8	ν_8	ν_8	ν_8	ν_8	ν_8	ν_8	ν_8
ν_9	δ(OH/D···O)	A_g	ν_9	ν_9	ν_9	ν_9	ν_9	ν_9	ν_9	ν_9
ν_{10}	γ(CH/D)	B_g	ν_{10}	‡ ν_{14}	† ν_{11}	‡ ν_{15}	ν_{10}	‡ ν_{14}	ν_{10}	‡ ν_{14}
ν_{11}	γ(OH/D)	B_g	ν_{11}	‡ ν_{15}	† ν_{10}	‡ ν_{14}	ν_{11}	‡ ν_{15}	ν_{11}	‡ ν_{15}
ν_{12}	γ(OH/D···O)	B_g	ν_{12}	‡ ν_{16}	ν_{12}	‡ ν_{16}	ν_{12}	‡ ν_{16}	ν_{12}	‡ ν_{16}
ν_{13}	γ(CH/D)	A_u	ν_{13}	‡ ν_{10}	† ν_{14}	‡ ν_{11}	ν_{13}	‡ ν_{10}	ν_{13}	‡ ν_{10}
ν_{14}	γ(OH/D)	A_u	ν_{14}	‡ ν_{11}	† ν_{13}	‡ ν_{10}	ν_{14}	‡ ν_{11}	ν_{14}	‡ ν_{11}
ν_{15}	γ(OH/D···O)	A_u	ν_{15}	‡ ν_{12}	ν_{15}	‡ ν_{12}	ν_{15}	‡ ν_{12}	ν_{15}	‡ ν_{12}
ν_{16}	Twist	A_u	ν_{16}	‡ ν_{13}	ν_{16}	‡ ν_{13}	ν_{16}	‡ ν_{13}	ν_{16}	‡ ν_{13}
ν_{17}	ν(OH/D)	B_u	ν_{17}	ν_{17}	ν_{17}	ν_{17}	† ν_{18}	ν_{18}	ν_{17}	ν_{17}
ν_{18}	ν(CH/D)	B_u	ν_{18}	ν_{18}	ν_{18}	ν_{18}	† ν_{17}	ν_{17}	ν_{18}	ν_{18}
ν_{19}	ν(C=O)	B_u	ν_{19}	ν_{19}	ν_{19}	ν_{19}	ν_{19}	ν_{19}	ν_{19}	ν_{19}
ν_{20}	δ(OH/D)	B_u	ν_{20}	ν_{20}	ν_{20}	ν_{20}	† ν_{22}	ν_{22}	† ν_{21}	ν_{21}
ν_{21}	δ(CH/D)	B_u	ν_{21}	ν_{21}	† ν_{22}	ν_{22}	† ν_{20}	ν_{20}	† ν_{22}	ν_{22}
ν_{22}	ν(C−O)	B_u	ν_{22}	ν_{22}	† ν_{21}	ν_{21}	† ν_{21}	ν_{21}	† ν_{20}	ν_{20}
ν_{23}	δ(OCO)	B_u	ν_{23}	ν_{23}	ν_{23}	ν_{23}	ν_{23}	ν_{23}	ν_{23}	ν_{23}
ν_{24}	δ(OH/D···O)	B_u	ν_{24}	ν_{24}	ν_{24}	ν_{24}	ν_{24}	ν_{24}	ν_{24}	ν_{24}

[a] Note that Bertie and Michaelian ascribed the Raman fundamentals at 1080.7 and 989.6 cm^{-1} to the CD and OD in-plane bends of $(DCOOD)_2$, respectively. Based on this assignment, the label mapping from this work to Ref. [93] would be $\{\nu_4, \nu_5, \nu_6\} \rightarrow \{\nu_6, \nu_5, \nu_4\}$. In agreement with Ref. [119], these two bands are inversely assigned here with the OD in-plane bend higher in wavenumber than the CD in-plane bend. Thus, $\{\nu_4, \nu_5, \nu_6\} \rightarrow \{\nu_5, \nu_6, \nu_4\}$.

2.4.2 Types of vibrational transitions

The classification of vibrational transitions into fundamentals, overtones, etc. mainly follows Herzberg [172, Section III.2]. This concept is extraordinarily useful but of course only approximate and builds on the assumption that we may ascribe harmonic oscillator quantum numbers to vibrational levels.

Fundamentals and overtones. If the lower state is the vibrational ground state and the change in vibrational quantum numbers involves only one mode i ($\Delta n_j = 0 \;\; \forall j \neq i$), we speak of fundamentals if $\Delta n_i = 1$ and first, second, third, etc. overtones for $\Delta n_i = 2, 3, 4,$ etc., respectively. The bands are labelled $n_i\nu_i$ where n_i is the vibrational quantum number in the final state whereas $n_i\tilde{\nu}_i$ is reserved for the wavenumber of that band.[84] One important symmetry consequence for (FF) is that its first overtones are all A_g symmetric and thus Raman-active. Since C_{2h} is a non-degenerate point group, we can generalise that for all $\Delta n_i = 3, 5, ...$ overtones have the same symmetry as the fundamental whereas for $\Delta n_i = 2, 4, ...$ they are A_g symmetric.

Combination bands. With "combination band" we shall collectively refer to all transitions from the vibrational ground state that involve a quantum number change in more than one vibrational mode. Herzberg aptly names this type of transition "summation band" [172, p. 265] as its wavenumber in a zeroth-order approximation is the sum of the involved fundamentals ($n_i = 1$) or overtones ($n_i > 1$), $\tilde{\nu}_{\text{comb}} \approx \sum_i n_i\tilde{\nu}_i$.[85] Combination bands for which $\sum_i \Delta n_i = 2$ are also called binary combinations; those for which $\sum_i \Delta n_i = 3$ ternary combinations etc. For C_{2h} symmetric (FF), it follows that binary combination bands of two IR-active or two Raman-active fundamentals are Raman-active.[86] Combination bands are labelled "$n_i\nu_i{+}n_j\nu_j{+}n_k\nu_k{+}...$". The nomenclature "$n_i\tilde{\nu}_i{+}n_j\tilde{\nu}_j{+}n_k\tilde{\nu}_k{+}...$" for the wavenumber of a combination band bears the danger that it cannot be distinguished from mathematical operations involving fundamental or overtone wavenumbers. Instead, the tilde extends over the entire label, e.g. $\widetilde{\nu_i{+}\nu_j}$.

Hot bands. Finally, all bands where the initial state is not the vibrational ground state but an excited vibrational state are called hot bands. The intensity of such bands is proportional to the Boltzmann factor of the initial state and increases with temperature, thus the name [210, p. 214]. Herzberg refers to these bands as "difference bands" [172, p. 266]. One central difference between hot and combination (or difference and summation) bands, say $\nu_k{-}\nu_l$ and $\nu_k{+}\nu_l$, is that the transition wavenumber from ν_l to ν_k *exactly* equals $\tilde{\nu}_k$ minus $\tilde{\nu}_l$. Thus, if we measure a hot band and know the experimental wavenumber of one involved vibrational level, we can calculate the *exact* wavenumber of the other level. Generally, one may expect that the intensity of $\nu_k{-}\nu_l$ is the same order of magnitude as that of $\nu_k{+}\nu_l$, weighted by the Boltzmann factor of the initial vibrational state [172, p. 267]. The above discussion also applies to cases where ν_k and/or ν_l are not fundamental but overtone/combination level.

An important special case is $\nu_k{+}\nu_l{-}\nu_l$ where the same vibration is excited in the lower and upper state, in addition to another vibration in the upper state. The initial state might be a fundamental level ($\nu_k{+}\nu_l{-}\nu_l$), an overtone/combination level (e.g. $\nu_k{+}2\nu_l{-}2\nu_l$), or l and k can be the same vibration ($2\nu_k{-}\nu_k$) as long as the total quantum number change is $\sum_i \Delta n_i = \Delta n_k = 1$. The intensity of such hot bands is expected to be similar to that of the fundamental ν_k times the

[84] Specifically, $n_i\tilde{\nu}_i$ is a set expression that may not be read as n_i *times* $\tilde{\nu}_i$ since the wavenumber of an overtone is only approximately the integral multiple of the fundamental wavenumber.

[85] Deviations arise from mechanical anharmonicity. This can be seen in Table 2.1 where the perturbative second-order expressions for combination bands have been rearranged into sum-of-fundamentals form.

[86] Generally, all binary combination or overtone bands are Raman-active, except for all four combinations between a Raman- and an IR-active mode, which are IR-active.

Boltzmann factor of the initial state [172, p. 267]. Thus, the intensity of such hot bands decreases rapidly with increasing wavenumber of the initial vibrational state. The above discussion can generally be extended to cases where ν_k is not a fundamental. Since then the intensity is expected to be the same order of magnitude as the corresponding overtone/combination band weighted by the appropriate Boltzmann factor, such hot bands are generally not expected to be visible in the spectra. Exceptions are overtone/combination bands that gain intensity through resonance with a bright fundamental.

In the mechanical harmonic limit, the wavenumber of $\nu_k+\nu_l-\nu_l$ would exactly coincide with that of ν_k. By rearranging the second-order perturbation theory expressions in Table 2.1, we can calculate the expected hot band wavenumbers for $k = l$ and $k \neq l$

$$2\tilde{\nu}_k - \tilde{\nu}_k = \tilde{\nu}_k + 2x_{k,k}, \tag{2.71}$$

$$\widetilde{\nu_k+\nu_l} - \tilde{\nu}_l = \tilde{\nu}_k + x_{k,l}. \tag{2.72}$$

In formic acid monomer, we might also need to consider binary combination/overtone levels as the lower state (see lowest-wavenumber levels in Tables D.4-D.7). The corresponding expressions are:

$$3\tilde{\nu}_k - 2\tilde{\nu}_k = \tilde{\nu}_k + 4x_{k,k}, \tag{2.73}$$

$$\widetilde{2\nu_k+\nu_l} - \widetilde{\nu_k+\nu_l} = \tilde{\nu}_k + 2x_{k,k} + x_{k,l}, \tag{2.74}$$

$$\widetilde{\nu_k+2\nu_l} - 2\tilde{\nu}_l = \tilde{\nu}_k + 2x_{k,l}, \tag{2.75}$$

$$\widetilde{\nu_k+\nu_l+\nu_m} - \widetilde{\nu_l+\nu_m} = \tilde{\nu}_k + x_{k,l} + x_{k,m}. \tag{2.76}$$

Usually, the anharmonicity constants are negative, resulting in small red-shifts relative to ν_k. If ν_k is perturbed by (Fermi) resonances, the above equations are only limitedly valid and larger red-shifts or even blue-shifts might be observed in some cases.[87]

2.4.3 Band contours and symmetry

A ro-vibrational transition of a non-linear molecule can be characterised by the change of at least one vibrational[88] and up to three rotational quantum numbers. The quantity we are interested to obtain from the IR and Raman spectra is the rotationless vibrational band centre $\tilde{\nu}_0$. While rotational excitations and consequently band widths are reduced by jet-cooling, vibrational bands of formic acid and its cyclic dimer exhibit a pronounced ro-vibrational contour even at the employed resolution of 0.5-2 cm^{-1}. For bands that exhibit a central Q branch, $\tilde{\nu}_0$ can usually be approximated as the centre of mass of the (unresolved) Q branch. Certain bands, however, do not exhibit a central Q branch and the resultant band contours can be very complex (*vide infra*). An analysis of the band contour is furthermore beneficial as it can provide valuable symmetry information to guide vibrational assignments. We will see that for the systems that are investigated in this work – F and (FF) –, it is possible to associate the observed band shape with the symmetry of the fundamental or overtone/combination transition without the need to explicitly model the ro-vibrational band contours (see for example Ref. [211]) or rely on quantum chemical predictions. The relevant theory is summarised in the following, tailored to the employed spectral resolutions and molecular systems.[89]

[87] See Section 4.4. In particular, the hot band structure near ν_5 of *trans*-HCOOD is very complex due to the OD bend-torsion resonance between ν_5 and $2\nu_9$ (pp. 81).

[88] For consistency, we shall continue to use $\mathbf{n} = \{n_1, ..., n_{\mathrm{vib}}\}$ for the vibrational excitation array.

[89] The following analysis primarily builds on Herzberg's book on the theory of IR and Raman spectroscopy [172] and also draws from the works of Hollas [210], Long [206], and Hills *et al.* [212]. Parts of this section have been published in an abridged version in Ref. [109].

Table 2.3 Rotor symmetry analysis of formic acid monomers and selected clusters at the CCSD(T)-F12a/VDZ-F12 level. The molecules and the principal axes of inertia are visualised in Fig. 2.2. 'eq.' indicates the global minimum configuration.

Molecule		Group	Rotor analysis						
			$\tilde{A}_e$	$\tilde{B}_e$	$\tilde{C}_e$	κ	$2\tilde{B}_e^{\text{eff}}$	$2(\tilde{A}_e - \tilde{B}_e^{\text{eff}})$	$4(\tilde{A}_e - \tilde{B}_e^{\text{eff}})$
F	*trans*-HCOOH (eq.)	C_s	2.59	0.40	0.35	−0.95	0.8	4.4	8.9
*c*F	*cis*-HCOOH	C_s	2.90	0.39	0.34	−0.96	0.7	5.1	10.1
(FF)	cyclic $(HCOOH)_2$ (eq.)	C_{2h}	0.20	0.08	0.06	−0.71	0.1	0.3	0.5
FF	polar $(HCOOH)_2$	C_s	0.28	0.05	0.04	−0.93	0.1	0.5	0.9
F(FF)	$(HCOOH)_3$ (eq.)	C_s	0.10	0.02	0.02	−0.92	0.04	0.2	0.3

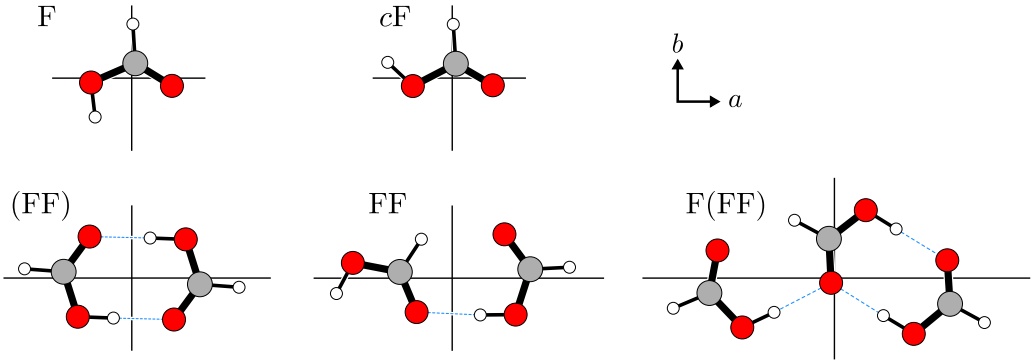

Figure 2.2 Formic acid and selected clusters that are investigated in this work. The geometries have been optimised at the CCSD(T)-F12a/VDZ-F12 level and are shown in the principal axis frame. The GLE scripts for the visualisation of the molecular structures were generated with PMIFST version 25a.VII.2017 [215].

(a) Rotor analysis

In addition to the formic acid monomer and its cyclic dimer, two different clusters of formic acid are explicitly taken into consideration in this work – FF and F(FF). The building block of all these clusters is the planar and C_s symmetric [80, 82] *trans*-formic acid molecule. The computed structures are all planar and asymmetric rotors ($\tilde{A} \neq \tilde{B} \neq \tilde{C}$), in agreement with previous explorations of the conformational hyperspaces of dimeric and trimeric formic acid [152, 213, 214] and available experimental IR and microwave data [120, 131, 151].

The cyclic dimer (FF) is C_{2h} symmetric if we neglect concerted proton exchange, whereas FF and F(FF) both belong to the C_s point group, as does F. For these two point groups, and generally for non-degenerate ground states, one can easily verify that the vibrational transition symmetry equals that of the vibration in the upper state (Γ') if the lower state is the vibrational ground state ($\Gamma'' =$ totally symmetric). The C_{2h} point group for (FF) has four irreducible representations but the inversion centre leads to either infrared (A_u, B_u) or Raman activity (A_g, B_g) in the electric dipole or polarisability approximation. The C_s point group has only two irreducible representations (A′, A″) which are in principle both infrared- and Raman-active.

The rotational selection rules and term formulae depend on the rotor symmetry. The rotational symmetry of formic acid and its clusters are analysed in Table 2.3; they are visualised in the principal axis frame in Fig. 2.2. Following the suggestion made by Ray [216], the asymmetry, i.e. the deviation from the symmetric top, can be expressed as

$$\kappa = \frac{2\tilde{B} - \tilde{A} - \tilde{C}}{\tilde{A} - \tilde{C}}, \tag{2.77}$$

where κ can range from −1 (near-prolate, $\tilde{C} \approx \tilde{B}$) up to +1 (near-oblate, $\tilde{A} \approx \tilde{B}$).

(b) Energy levels

All relevant C_s symmetric systems are coincidentally near-prolate tops with only the cyclic dimer exhibiting a more pronounced deviation from the prolate top. It is therefore instructive to start with the prolate top in the absence of external fields to then discuss deviations from this limiting case. In contrast to the well-known diatomic molecule [174] where rotational transitions[90] are only characterised by the change of the total angular momentum ΔJ, in symmetric top molecules there is a whole series of ΔJ lines for different values of K (projection of J onto the top axis). All lines for a given K value, which are collectively grouped in different branches according to their ΔJ value, are referred to as sub-band [172]. To distinguish between lines from different sub-bands, we designate each line the label ${}^{\Delta K}\Delta J_K(J)$ where $O, ..., S$ is substituted for ΔK and ΔJ [172, pp. 419].

At zeroth-order, the rotational energy levels can be represented by a rigid rotor and we shall neglect centrifugal distortion corrections as they are very small compared to the available resolution and manifest at larger J values. The ro-vibrational term value of a prolate top is given by [172, p. 400]

$$\frac{E_{\mathrm{rv}}}{hc} = S(\mathbf{n}, J, K) = G(\mathbf{n}) + F(J, K) = G(\mathbf{n}) + \tilde{B}J(J+1) + (\tilde{A} - \tilde{B})K^2. \tag{2.78}$$

If a molecule is near-prolate, we can replace $\tilde{B}$ in the above expression to a good approximation[91] with

$$\tilde{B}^{\mathrm{eff}} = \frac{\tilde{B} + \tilde{C}}{2}. \tag{2.79}$$

A ro-vibrational transition $\mathbf{n}'J'K' \leftarrow \mathbf{n}''J''K''$ is then given by

$$\tilde{\nu}_{\mathrm{rv}} = \tilde{\nu}_0 + F(J', K') - F(J'', K''), \tag{2.80}$$

where the pure vibrational band centre is condensed into $\tilde{\nu}_0$ and thus independent of the underlying parametrisation of the vibrational energy levels. As usual, $'$ and $''$ denote the upper and lower vibrational level, respectively.

When evaluating Eq. 2.80 in the following, it is very useful to define a variable m to unify the expressions for different rotational branches:

	O	P	Q	R	S
ΔJ	-2	-1	0	1	2
m	$-2J+1$	$-J$	0	$J+1$	$2J+3$

[90] We shall not consider the more complicated cases involving electronic angular momentum (or electron/nuclear spin).

[91] Following Townes and Schawlow [217, Chapters 3-4] (nomenclature adjusted to this work), the pure rotational levels of a prolate symmetric top are given by

$$F(J, K) = \tilde{B}J(J+1) + (\tilde{A} - \tilde{B})K^2$$

and that of a near-prolate top by

$$F(J, K) = \frac{\tilde{B} + \tilde{C}}{2}J(J+1) + \left(\tilde{A} - \frac{\tilde{B} + \tilde{C}}{2}\right)w$$

where w can be expanded as

$$w = K^2 + \sum_i c_i b_p^i = K^2 + \sum_i c_i \left(\frac{\kappa + 1}{\kappa - 3}\right).$$

The c_i parameters are tabulated [217, Appendix III]. We see that in the limit of a prolate top ($\kappa \to -1$) all terms in the sum become zero and $w \to K^2$. For slightly asymmetric tops, we may assume that the deviations of w from K^2 are very small and that $\frac{\tilde{B}+\tilde{C}}{2} \approx \tilde{B}$ is a good approximation.

(c) Selection rules

In the IR, symmetric top molecules give rise to bands where the transition dipole moment is parallel (∥) or perpendicular (⊥) with respect to the top axis [172]. The top axis is along the *a*-axis in prolate tops (*c* in oblate tops). The selection rules are [172]

$$\Delta K = 0, \qquad \Delta J = 0, \pm 1, \tag{2.81}$$

for parallel bands with the restriction $\Delta J = \pm 1$ for $K = 0$ and

$$\Delta K = \pm 1, \qquad \Delta J = 0, \pm 1, \tag{2.82}$$

for perpendicular bands. For Raman bands of symmetric tops, the distinction is made between totally symmetric and non-totally symmetric bands. The selection rules are [206]

$$\Delta K = 0, \qquad \Delta J = 0, \pm 1, \pm 2, \tag{2.83}$$

for totally symmetric bands with the restriction $J' + J'' \geq 2$ [172, 212] and

$$\Delta K = \pm 2, \qquad \Delta J = 0, \pm 1, \pm 2, \tag{2.84}$$

for non-totally symmetric bands, again with $J' + J'' \geq 2$. In all cases, we have the restriction $J \geq K$, i.e. more and more rotational lines are missing from sub-bands with increasing values of K [172, p. 418]. Already from the above selection rules, we can infer a certain similarity between parallel IR bands and totally symmetric prolate top Raman bands and also between perpendicular IR bands and non-totally symmetric prolate top Raman bands.

(d) IR spectrum

The IR spectra that arise from typical parallel and perpendicular bands are illustrated by Herzberg in Figs. 122 and 128 of Ref. [172]. The central difference is that parallel bands have an intensive, central *Q* branch whereas perpendicular bands tend to have a much broader intensity distribution.

Parallel bands. Inserting the above selection rules for parallel bands into Eq. 2.80 yields for each K sub-band

$$\begin{aligned} \tilde{\nu}^{\parallel} &= \tilde{\nu}_0 + 2m\tilde{B}' + (\tilde{B}' - \tilde{B}'')J(J+1) + [(\tilde{A}' - \tilde{A}'') - (\tilde{B}' - \tilde{B}'')]K^2 \\ &\approx \tilde{\nu}_0 + 2m\tilde{B}', \end{aligned} \tag{2.85}$$

where m can take values of $-J$, 0, and $J + 1$ for P, Q, and R branches. Within each sub-band, rotational lines are approximately separated by $2\tilde{B}'$, similar to IR bands of diatomic molecules, with the exception that also a Q branch with $\Delta J = 0$ is observed which approximately coincides with the vibrational band centre $\tilde{\nu}_0$. If the K fine structure is negligible and cannot be resolved, the rotational lines of each K sub-band coincide, the band contour resembling that of linear molecules. The K fine structure depends on the difference $(\tilde{A}' - \tilde{A}'') - (\tilde{B}' - \tilde{B}'')$ which is usually small compared to $2\tilde{B}'$, in particular for fundamentals [172, p. 419].[92] If only one central Q branch is resolved, we can infer that this difference is negligible at the employed resolution.

[92] The IR spectrum of a parallel band that results from non-negligible K contributions is illustrated by Herzberg in Fig. 122(c) of Ref. [172].

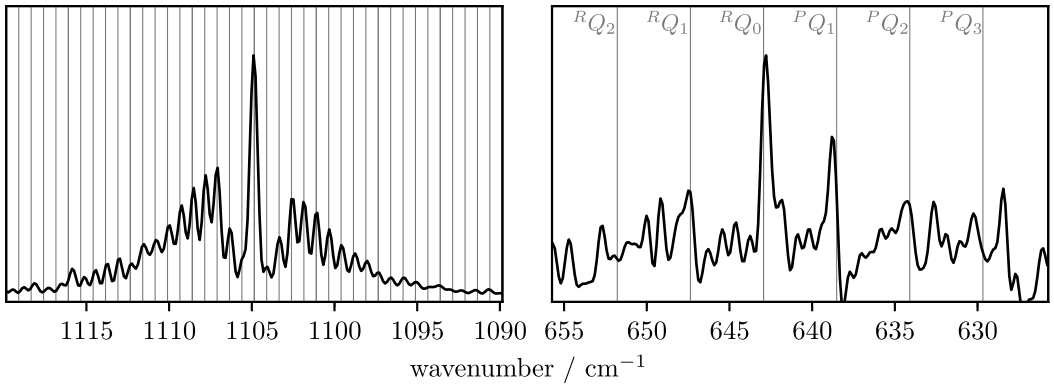

Figure 2.3 Excerpts of the FTIR jet spectrum of HCOOH at 0.5 cm^{-1} resolution from Figs. 6.1-6.2 (pp. 116). Grey lines correspond to ro-vibrational lines computed in the near-prolate limit, see text for details. (left) The ν_6 fundamental; ro-vibrational line simulations for a parallel band according to Eq. 2.85. (right) The ν_9 fundamental; ro-vibrational line simulations for the Q branches of a perpendicular band according to Eq. 2.86.

Perpendicular bands. We obtain the corresponding expressions for perpendicular K sub-bands by inserting the selection rules in Eq. 2.82 into Eq. 2.80

$$\begin{aligned}\tilde{\nu}^{\perp} &= \tilde{\nu}_0 + 2m\tilde{B}' + (\tilde{B}' - \tilde{B}'')J(J+1) + (1 \pm 2K) \times (\tilde{A}'-\tilde{B}') + [(\tilde{A}'-\tilde{A}'')-(\tilde{B}'-\tilde{B}'')]K^2 \\ &\approx \tilde{\nu}_0 + 2m\tilde{B}' + (1 \pm 2K) \times (\tilde{A}' - \tilde{B}') \end{aligned} \tag{2.86}$$

where m can take the same values as before. We can see that even for $\tilde{B}' \approx \tilde{B}''$ and $\tilde{A}' \approx \tilde{A}''$, different K sub-bands do not coincide and the approximate separation of the sub-band centres, i.e. the Q branches, is now $2(\tilde{A}' - \tilde{B}')$. The vibrational band centre $\tilde{\nu}_0$ can be determined if the $^RQ_0$ ($K = 0$, $\Delta K = +1$) and $^PQ_1$ ($K = 1$, $\Delta K = -1$) branches can be identified since $\tilde{\nu}_0$ is located approximately halfway in-between both. This depends on the structure of the P and R branches and the neglected effects due to $\tilde{B}' \neq \tilde{B}''$ and $\tilde{A}' \neq \tilde{A}''$ which can all distort the overall band shape so that individual peak maxima might not necessarily correspond to Q sub-branch.

Example – F. In *trans*-HCOOH, A′−A′ and A″−A′ bands correspond to hybrid ∥ + ⊥ and ⊥ bands in the (near-)prolate top limit, respectively. In Fig. 2.3 segments of the FTIR jet spectrum at 0.5 cm^{-1} resolution are shown in the vicinity of the ν_6 band (A′−A′, left) and ν_9 band (A″−A′, right). Using experimental band centres and ground state rotational constants from the literature, the rotational lines have been simulated in the near-prolate limit. The vibrational band centres $\tilde{\nu}_6 = 1104.85$ and $\tilde{\nu}_9 = 640.73$ cm^{-1} are taken from Refs. [218, 219]. From the ground state rotational constants in Ref. [95], $2\tilde{B}_0^{\text{eff}} = 0.75$ cm^{-1} and $2(\tilde{A}_0 - \tilde{B}_0^{\text{eff}}) = 4.42$ cm^{-1} are calculated.[93]

The ν_6 band seems to exhibit a typical PQR structure. Indeed, the simulated line positions (^QP, ^QQ, ^QR), which are separated by $2\tilde{B}_0^{\text{eff}}$, agree very well with the observed peaks. This approximate level satisfactorily explains all observed fine structure, even *quantitatively* for smaller J values near the central Q branch. The ν_6 band centre can reliably be estimated as the centre of mass of the central Q branch, 1104.9 cm^{-1}, which compares very well with the high-resolution value. Note that already at 1 cm^{-1} resolution, individual peaks in the R and P branches are no longer resolved and at 2 cm^{-1} resolution, the central Q branch no longer stands out and one observes a broad band contour with three peaks that correspond to the PQR maxima (see Fig. 6.1).

ν_9, on the other hand, exhibits a very complicated fine structure.[94] Only lines for the Q branches are simulated as these are expected to be the most intensive. The spacing of these lines

[93] Deviations in $2\tilde{B}^{\text{eff}}$ or $2(\tilde{A} - \tilde{B}^{\text{eff}})$ are below 0.02 cm^{-1} if instead of ground state rotational constants the experimental values for $n_6 = 1$ or $n_9 = 1$ are used.

[94] In the ν_9 spectrum, there are some additional weaker contributions from the nearby ν_7 fundamental

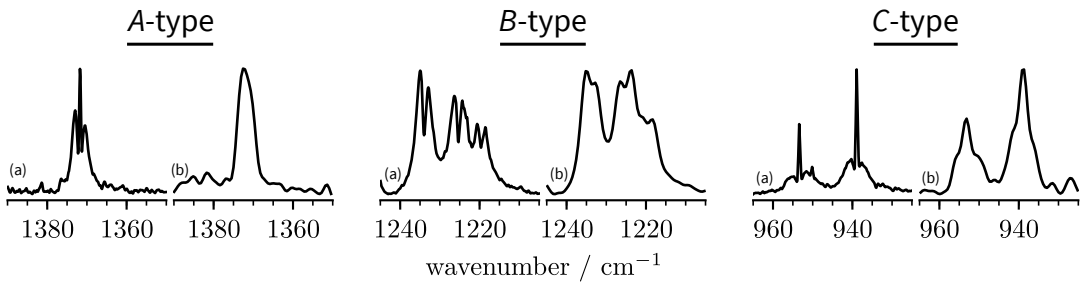

Figure 2.4 Excerpts of the FTIR jet spectrum of $(HCOOH)_2$ from Figs. 6.1-6.2 (pp. 116). (a) 0.5 cm^{-1} resolution. (b) 2 cm^{-1} resolution. The mainly *A*-type band is the ν_{21} fundamental, the mainly *B*-type band the ν_{22} resonance triad, and the *C*-type band the ν_{14} resonance dyad.

is $2(\tilde{A}_0 - \tilde{B}_0^{\text{eff}})$. The simulation indicates an assignment of the two most intensive bands to ${}^RQ_0$ and ${}^PQ_1$. Other *Q* sub-branches cannot be identified on intensity arguments alone. Many of the smaller peaks are separated by 0.8 cm^{-1} which roughly corresponds to $2\tilde{B}_0^{\text{eff}}$ and indicates that much of the fine structure is due to (partially resolved) *R* and *P* sub-branches. Nonetheless, with the two main *Q* branches identified, the vibrational band centre can be determined with satisfactory accuracy using the above-described method, $(642.8+638.8)/2 = 640.8\ cm^{-1}$, which compares very well with the high-resolution value.

Example – (FF). IR bands of an asymmetric rotor can be categorised as pure *A*, *B*, *C*, or hybrid bands, depending on the orientation of the transition dipole moment with respect to the principal axes. For the cyclic dimer (FF), only two types of transitions from the vibrational ground state are infrared-active, $B_u{-}A_g$ and $A_u{-}A_g$, which give rise to hybrid *A*+*B*- and *C*-type bands, respectively. In the limit of a near-prolate top, the following correlation applies: $A \rightarrow \parallel$, $B \rightarrow \perp$, and $C \rightarrow \perp$ [172, 210]. From this correlation, it immediately becomes obvious why *A*-type bands generally exhibit a *PQR* structure that is similar to parallel bands [172, 210]. *B*-type bands, on the other hand, lack a central *Q* branch.

For the cyclic formic acid dimer, the characteristic contours of *B*- and *C*-type bands are different (enough) to clearly distinguish between both. A central and sharp *Q* branch is found for *C*-type bands whereas the *B*-type bands are broader with two characteristic maxima that correspond to the unresolved *Q* branches where $\tilde{\nu}_0$ is approximately located in-between both. Examples of the three band types are shown in Fig. 2.4 at 0.5 and 2 cm^{-1} resolution.

While the polar dimer FF is a near-prolate top, its IR band contours are expected to resemble that of (FF) and not F at resolutions of 0.5-2 cm^{-1} due to the similarity of their rotational constants. For the trimer F(FF), one may hope for partial resolution of its band contours at best (see Table 2.3). Here the assignments have to rely more heavily on quantum chemical predictions.

(e) Raman spectrum.

For Raman bands of symmetric tops, the two band types are usually named after the transition symmetry, i.e. "totally symmetric" and "non-totally symmetric" [172, 206].

Totally symmetric prolate top bands. In analogy to the procedure for parallel IR bands, the term values for totally symmetric Raman sub-bands of a prolate top are approximately given by

$$\tilde{\nu}^{\text{t.s.}} \approx \tilde{\nu}_0 + 2m\tilde{B}', \tag{2.87}$$

(626.17 cm^{-1}, Ref. [218]). Also, some observed 'dips' in the intensity (e.g. slightly below ${}^PQ_1$) are artefacts that arise from a poorer signal-to-noise ratio at the band or filter gap of the detector. A comparison to ν_9 spectra recorded with a cooled bolometer (4 K, see Ref. [149]) shows that the main features in Fig. 2.3 still can safely be interpreted.

Instead of three, as in the IR, there are now five rotational branches. The key advantage of Raman spectroscopy is that the central Q branch is usually very dominant and can in most instances easily be distinguished from the rotational socket ($\Delta J \neq 0$), even if the latter is not resolved.

Non-totally symmetric prolate top bands. Lastly, non-totally symmetric sub-bands of a prolate top are approximately given by

$$\tilde{\nu}^{\text{non-t.s.}} \approx \tilde{\nu}_0 + 2m\tilde{B}' + (4 \pm 4K) \times (\tilde{A}' - \tilde{B}'). \tag{2.88}$$

One important difference to perpendicular IR bands is the presence of a zero-gap for non-totally symmetric prolate top Raman bands. The entire $K = 1$ sub-band for $\Delta K = -2$ is missing as it does not conserve the angular momentum.[95]

Asymmetric rotor. For the slightly asymmetric rotor, Hills *et al.*[96] distinguish between four different band types – A, B_a, B_b, and B_c. A-type Raman bands have no counterpart in the IR. In the near-prolate limit, the rotational selection rules for K are

	A	B_a	B_b	B_c
ΔK	$0, \pm 2$	± 2	± 1	± 1

For the most general case without any symmetry (C_1), all selection rules apply, i.e. $\Delta J = -2, ..., +2$ and $\Delta K = -2, ..., +2$, giving rise to overall 25 branches. For the C_s and C_{2h} point groups, there is a mixing of different band types but the characteristics of the above-discussed totally and non-totally symmetric bands survive. $\mathrm{A}'-\mathrm{A}'$ and $\mathrm{A_g}-\mathrm{A_g}$ transitions give rise to hybrid $A+B_c$-type bands whereas $\mathrm{A}''-\mathrm{A}'$ and $\mathrm{B_g}-\mathrm{A_g}$ transitions give rise to hybrid B_a+B_b-type bands. Relating these selection rules to the symmetric top limit, we see how $\Delta K \pm 1$ additionally becomes allowed due to symmetry lowering.[97] $A+B_c$-type bands are a mixture of totally symmetric and non-totally symmetric bands whereas B_a+B_b-type bands more resemble non-totally symmetric bands as they are missing the characteristic central Q branch – B_a- and B_b-type bands usually exhibit a lower intensity towards the band centre. The identification of the central Q branch or verification of its absence thus unambiguously allows an assignment of the observed band type for the C_s and C_{2h} point groups. These band contour information nicely complement the analysis of depolarised spectra where it is possible to distinguish between totally and non-totally symmetric scattering contributions. This synergy is illustrated in the following.

Impact of depolarisation ratio and examples. The usual dominance of the central Q branch in Raman spectroscopy has the distinct advantage that even weaker bands can be identified. Since the relative intensity of the central Q branch depends on the depolarisation ratio, it is instructive to look at some examples. For totally symmetric bands, the depolarisation ratio can range from completely polarised, $\rho_l = 0$, to completely depolarised, $\rho_l = 0.75$. Non-totally symmetric bands are always completely depolarised (see Section 2.3). In Fig. 2.5, jet-cooled

[95] Herzberg and Long both discuss Raman selection rules for the symmetric top molecule [172, 206]. The discussions in Refs. [172, 206] are equivalent for the resultant term formulae but differ with regard to the selection rules. For perpendicular bands, Long [206, p. 197] writes that "it should be noted that the first line ($K = 0$) in the series of Q branches with $\Delta K = +2$ occurs at $\tilde{\nu}_{\text{vib}} + 4(A - B)$, whereas the first line ($K = 1$) in the series of Q branches with $\Delta K = -2$ occurs at $\tilde{\nu}_{\text{vib}}$." Herzberg, on the other hand, stresses the existence of a zero-gap in the Raman spectrum because the sub-band $K = 1$ for $\Delta K = -2$ is missing due to the selection rule $J'' + J' \geq 2$ [172, pp. 442].

[96] The following discussion is completely based on Ref. [212].

[97] It is noted that Herzberg, who discusses the theory for Raman bands in less detail (due to the sparse number of well-resolved Raman spectra at that time), writes that for near-symmetric top molecules of the C_s point group, $\Delta K = \pm 1$ instead of ± 2 applies for $\mathrm{A}''-\mathrm{A}'$ transitions [172, p. 443].

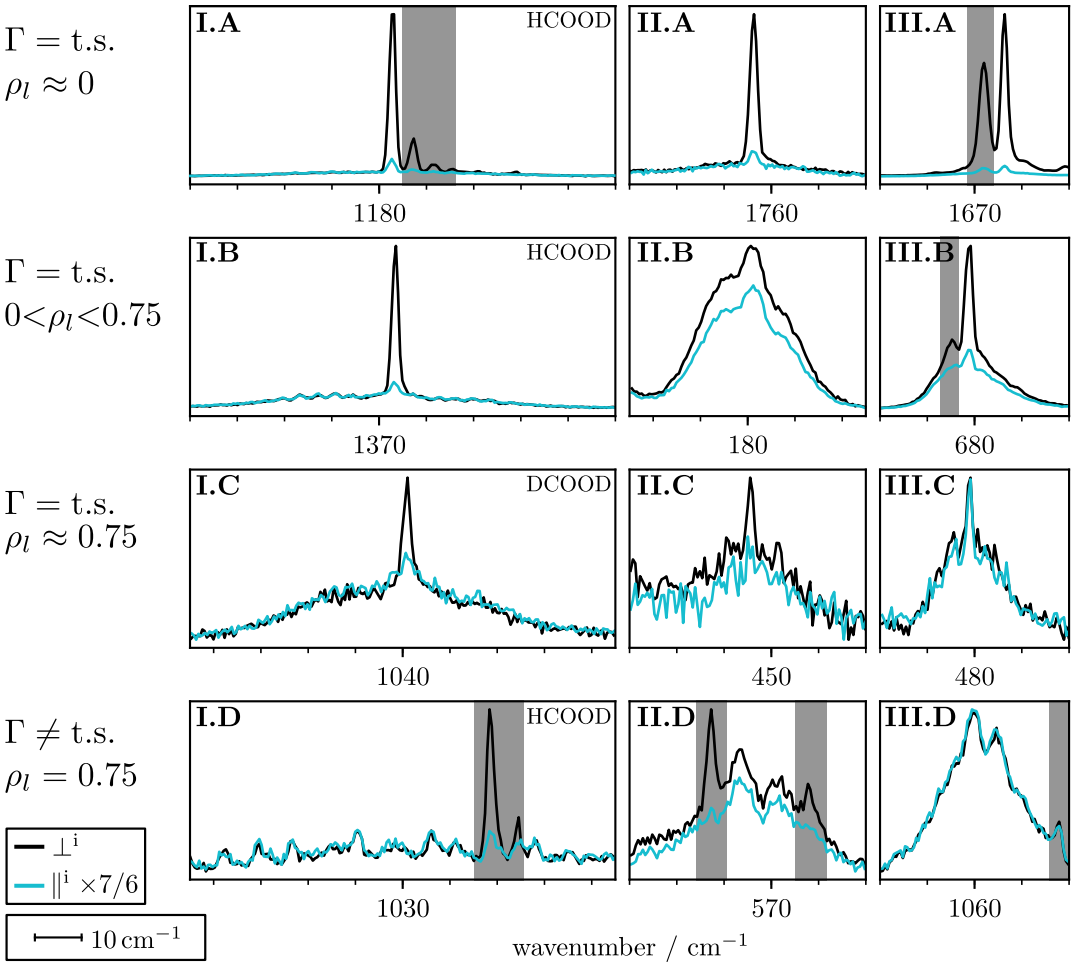

Figure 2.5 Jet-cooled Raman band profiles of selected totally (Γ = t.s.) and non-totally symmetric (Γ ≠ t.s.) bands with varying depolarisation ratios (ρ_l). Bands are shown for *trans*-formic acid (I), *trans*-propiolic acid (II, spectra from Ref. [42]), and the cyclic formic acid dimer (III). Overlapping contributions from other bands are greyed out.

Raman bands are shown for four limiting cases: A totally symmetric band that is near-completely polarised (A); a totally symmetric band with an intermediate depolarisation ratio (B); a near-completely depolarised totally symmetric band (C); a non-totally symmetric band (D). In the left panels, formic acid F is shown, which is a near-prolate top with comparably large $2\tilde{B}^{\text{eff}}$ and $4(\tilde{A} - \tilde{B}^{\text{eff}})$ values (see Table 2.3). In the right panels, (FF) is shown which exhibits a more pronounced asymmetry and has much smaller rotational constants. In the middle, *trans*-propiolic acid is shown – a "CC-stretched" [42] analogue of formic acid (H–C≡C–COOH) –, which has rotational characteristics that are similar to (FF).[98]

Row A illustrates the dominance of the central Q branch for near-completely polarised bands. While this greatly facilitates the determination of band centres, it complicates size assignments. When comparing IR bands of F and (FF), one can distinguish the two just by comparing the width of their band contours (see Figs. 2.3-2.4). Due to the additional O and S branches, where the spacing of lines is approximately $4\tilde{B}^{\text{eff}}$, the rotational $\Delta J \neq 0$ socket of Raman bands is generally much broader.

Row B shows totally symmetric bands with intermediate depolarisation ratios. In the absence of other overlapping contributions, one can already distinguish between F and (FF) based on the width of their rotational sockets. Since $\tilde{B}^{\text{eff}}$ is much larger in F, its vibrational bands extend over

[98] Due to the heavy acetylenic group, its computed equilibrium constants are much smaller than those of F: 0.40, 0.14, and 0.10 cm^{-1} (same level of theory as in Table 2.3). Similar to (FF), *trans*-propiolic acid exhibits a more pronounced asymmetry from the prolate top ($\kappa = -0.77$).

a much larger wavenumber region than in (FF) or *trans*-propiolic acid.

Rows C and D, on the other hand, illustrate the importance of depolarisation measurements ($\|^{\mathrm{i}}$ ×7/6) to safely assign non-totally symmetric bands. The propiolic acid spectrum (II.D) shows particularly well the complications that can arise if polarised bands (greyed out) overlap with non-totally symmetric bands.[99] If we imagine the A′ fundamental near 580 cm^{-1} to move just 10 cm^{-1} towards lower wavenumbers, it would coincide with the centre of the A″ symmetric band. Without depolarisation spectra, the resultant band contour could easily be confused with a depolarised, totally symmetric band (II.C). There can even be cases where the central Q branch is so weak that a symmetry assignment is not unambiguous if the signal-to-noise is too low.[100]

In summary, for totally symmetric Raman bands we only need to identify the central Q branch to obtain the vibrational band centre $\tilde{\nu}_0$. For non-totally Raman symmetric bands, usually a very broad structure with two characteristic peaks is observed. In these cases, the band centre can be approximated halfway between both. Care must be taken that the band contour is not distorted from other, overlapping bands. Depolarisation contributions may help in such situations but only if the additional scattering contributions are polarised. If the rotational constants, in particular the difference $\tilde{A} - \tilde{B}^{\mathrm{eff}}$, are rather large, more of the fine structure might be resolved. This is the case for the ν_8 band of *trans*-HCOOD (I.D) which is analysed in the following using the above-derived expressions for non-totally symmetric prolate tops.

Example – The CH out-of-plane bend of F. Out of the $4 \times 9 = 36$ fundamental vibrations of *trans*-formic acid and its deuterated isotopologues, ν_8 of *trans*-HCOOD – the CH out-of-plane bend – is the only fundamental that has so far not been observed in gas phase spectroscopic studies.[101]

The ν_8 Raman spectra of HCOOH and HCOOD are shown in Fig. 2.6.[102] As ν_8 overlaps with A′ symmetric bands, a comparison of the depolarised spectra (cyan) is much easier since other totally symmetric scattering contributions are minimised.[103]

We shall start with *trans*-HCOOH where a high-resolution band centre for ν_8 is available. Focussing on the $\|^{\mathrm{i}}$ ×7/6 spectrum, we see that the ν_8 band centre is about halfway in-between the two most intensive peaks of the whole ν_8 contour, quite reminiscent of the earlier analysis of the ν_9 IR band. Indeed, using the high-resolution band centre $\tilde{\nu}_8 = 1033.47\,\mathrm{cm}^{-1}$ and experimental ground state rotational constants from the literature,[104] we can model the Q sub-branches using Eq. 2.88. The sub-band centres are shown as grey lines in Fig. 2.6, suggesting that the

[99] For a more detailed discussion of this particular example, see Section III of Ref. [42].

[100] Such an example was discussed for *trans*-propiolic acid in Ref. [42]. The central Q is barely discernible for the two totally symmetric Raman bands at 1362 and 1302 cm^{-1}.

[101] ν_8 has been previously reported in a weakly perturbing neon matrix [117, 220]. However, in a neon matrix, ν_8 is slightly blue-shifted upon O–H deuteration whereas harmonic and anharmonic vibrational theories at various levels of electron correlation consistently predict a small red-shift. (See for example harmonic B3LYP-D3(BJ)/aVTZ [91], MCTDH on the RC-PES [22, 27], harmonic wavenumbers on both analytic formic acid potentials (Table D.3), and CVPT6 on both potentials in Ref. [28].) In Ref. [28], the experimental ν_8 gas phase band centre of *trans*-HCOOD was recently derived indirectly via its first overtone by assuming a second-order perturbation theory parametrisation of the energy levels. The determined deuteration shift of −2 cm^{-1} [28] is in agreement with (an)harmonic theory and shows that the neon blue-shift is caused by the matrix environment. The newly presented *purely experimental* analysis below also yields a deuteration shift of −2 cm^{-1}.

[102] The neon-calibrated spectra of HCOOH and HCOOD in Fig. 2.6 have both been linearly shifted along the abscissa to align the Q branch centroids of the ν_6 band of HCOOH with the high-resolution band centre at 1104.85 cm^{-1} [219].

[103] Note that the ν_8 band of HCOOH does not persist in Fig. 2.6 when the incident laser polarisation is changed ($\|^{\mathrm{i}}$ ×7/6) as would be expected. This is very likely an artefact (perhaps laser alignment drift) of that measurement as ν_8 exhibits the expected scaling behaviour in the dimer-optimised depolarisation spectra in Fig. 6.4 (p. 119).

[104] The ν_8 band centre and rotational constants are taken from Ref. [95]. From these ground state rotational constants, $4(\tilde{A}_0 - \tilde{B}_0^{\mathrm{eff}}) = 8.84\,\mathrm{cm}^{-1}$ is calculated.

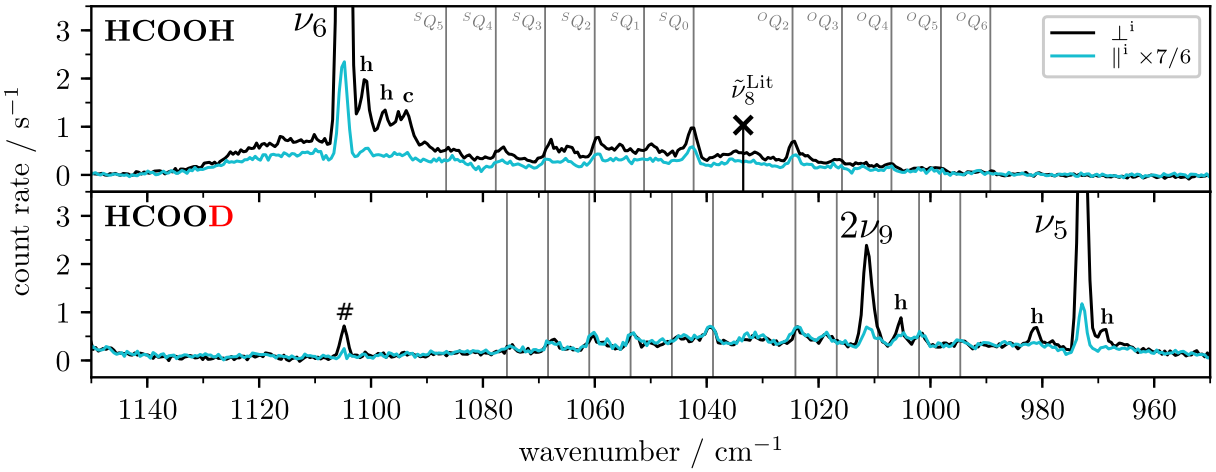

Figure 2.6 Raman jet spectra of HCOOH and HCOOD in the vicinity of the ν_8 band. The HCOOH impurity in the HCOOD spectrum is marked with a hash symbol (#) and hot bands are labelled as "h" (non-isomeric hot band) and "c" (*cis* fundamental). Grey lines are simulated Q branch sub-band centres (Eq. 2.88), see text for details.

two peaks can be interpreted as $^{S}Q_0$ and $^{O}Q_2$. The Raman band centre, which is approximated as halfway in-between both peaks, $(1042.5 + 1024.5)/2 = 1033.5\,\mathrm{cm}^{-1}$, excellently agrees with the high-resolution value.

As expected, O–H deuteration leaves the ν_8 band contour largely unaffected. Peaks in the ν_8 contour move closer together and the entire envelope shifts towards lower wavenumbers. Similarly for HCOOD, the simulated Q branches align very well with the observed maxima,[105] reinforcing the assignment of the two most intensive peaks to $^{S}Q_0$ and $^{O}Q_2$. With $^{S}Q_0$ and $^{O}Q_2$ as anchor points, we can also determine the band centre in HCOOD, $(1039.5 + 1023.5)/2 = 1031.5\,\mathrm{cm}^{-1}$. Since the high-resolution band centre of HCOOH must be rounded off to $1033\,\mathrm{cm}^{-1}$, we shall round the HCOOD band centre to $1031\,\mathrm{cm}^{-1}$.

[105] The ν_8 band centre is estimated by adding the shift of the band contour ($-2\,\mathrm{cm}^{-1}$) to the high-resolution band centre of HCOOH ($1033.47\,\mathrm{cm}^{-1}$). From the ground state rotational constants in Ref. [221], $4(\tilde{A}_0 - \tilde{B}_0^{\mathrm{eff}}) = 7.37\,\mathrm{cm}^{-1}$ is calculated.

Chapter 3

Formic acid monomer-optimised Raman jet spectra

The first environment-free, monomer-optimised Raman spectra of formic acid with little to no dimer contributions were published recently by Meyer [86, 87], paving the way to unearth a wealth of much weaker combination/overtone bands of formic acid that were previously hidden underneath cluster contributions. These measurements have been continued in this work to further minimise cluster contributions,[106] close spectral gaps, and extend them to partially and fully deuterated isotopologues.[107] In the following, a detailed description of the spectra is given. While the *trans* fundamentals can be assigned right away, many are visibly perturbed by resonances. Their mode assignments are addressed in the next chapter (Section 4.2) together with the assignments of cold (labelled "M"; Section 4.3) and hot monomer bands (labelled "H"; Section 4.4).[108]

The Raman jet spectra[109] of all four H/D isotopologues are shown in Figs. 3.1-3.7, covering the spectral region from 390 up to 3750 cm^{-1}. A legend is provided on p. 49. The raw data have been published in an online repository and made publicly available [222].[110] Details on the chemicals are listed in Table 3.1. Since the spectra of all four H/D isotopologues are analysed, we do not need to worry about bands that arise from isotopic impurities due to H/D exchange in the apparatus or manufacture-related isotopic H/D impurities as they can readily be identified. They are marked with a hash symbol (#).[111] The spectra are a patchwork of several individual

[106] The difference can perhaps best be seen by comparing the intensity of cluster bands in the Raman spectrum of HCOOH near the $2\nu_9$ band (cf. p. 56 and Ref. [86, p. 47]).

[107] The HCOOD and DCOOD Raman jet spectra presented in Ref. [86] only cover selected spectral regions.

[108] The distinction between "hot" and "cold" is made based on the initial vibrational state of a vibrational transition (for details, see Section 2.4.2). All transitions that originate from the vibrational ground state, i.e. the vibrational ground state of *trans*-formic, are called "cold bands". "Hot band" is used here as a collective term, referring to all transitions that originate from excited vibrational states. This includes transitions from the vibrational *cis* ground state which may be seen as a torsionally excited state.

[109] The Raman jet band centres reported in this work generally agree, apart from a few assignments [119], with previously reported values obtained from curry-jet spectra within the resolution uncertainty of 2 cm^{-1} [86].

[110] These spectra have already been shown in the supplementary material of Ref. [28] and segments in the supplementary material of Ref. [91]. However, in Ref. [28], the spectra only cover the region from 3750 down to 870 cm^{-1}, whereas now also the lower-frequency OCO bending fundamental ν_7 is included (Fig. 3.7). The depolarised HCOOD and DCOOD spectra near ν_1 were measured after the publication of Ref. [28] and are shown for the first time. The figures have been newly created for this work using a similar visualisation template as in Ref. [28]. The perhaps greatest difference to that work is the (slight) adjustment of the baseline correction, intensity scaling, and displayed wavenumber range for individual measurements (see Appendix A).

[111] In the HCOOD and DCOOD spectra, there are about 2-3% impurities due to the usual OD → OH isotopic exchange. However, it should be noted that there is an estimated DCOOD impurity of 4-6% in the DCOOH spectra (see supplementary material of Ref. [91]).

Table 3.1 Details about chemicals used in the monomer-optimised Raman measurements. The lot numbers are included for deuterated compounds.

Chemical	CAS number	Manufacturer	Purity	Lot number
HCOOH	64-18-6	Acros Organics	98+%	
DCOOH	917-71-5	ABCR	95%; 98% D	1401769, 1429695
HCOOD	925-94-0	ABCR, Cambridge Isotope Laboratories	95%; 98% D	1424534, PR-19516/07238FA1
DCOOD	920-42-3	ABCR	95%; 98% D	1414704

measurements at different monochromator settings with slightly varying acid-in-helium concentrations and laser powers that all influence the count rate. Measurement details are reported in Appendix A.

It is worth noting that even at the highest temperature (190 °C or 463 K), formic acid does not seem to decompose as indicated by the absence of detectable amounts of its decomposition products, H_2 and CO_2 or H_2O and CO.[112] The apparent thermal stability of formic acid under the applied conditions must be contrasted with recent Raman measurements of propiolic acid (H–C≡C–COOH) under similar conditions where substantial decomposition into CO_2 and C_2H_2 was observed above 433 K [42]. There are weak scattering signals in the spectra that correspond to O_2 and N_2, which are likely introduced through small leaks along the gas line. There are also traces of water in the jet expansions. The overall concentration is very small and significant amounts of formic acid hydrates can safely be ruled out. The air[113] and water[114] impurities are labelled accordingly in the Raman spectra.

In each spectral region, up to four spectra in a temperature series are shown that have been intensity-scaled (≤ 1.0) to a monomer fundamental with the lowest intensity in each series (trace A). The scaling not only enables the discrimination of monomer and cluster bands – the latter decrease with temperature and are marked with an asterisk (∗) – but also the distinction of cold and hot monomer bands as the latter increase with temperature. Auxiliary symmetry information comes from depolarisation measurements which are shown in selected spectral regions (trace B). In addition, they are very useful to identify weak combination/overtone bands hidden underneath the A″ symmetric rotational socket of fundamental bands (see Fig. 3.2).

For the main fundamentals ν_1-ν_6, four spectra have been recorded whereas spectral gaps in-between and above these fundamentals have been filled with at most two spectra in each temperature series. In these instances, measurements at each temperature were started from a known fundamental to determine appropriate scaling factors. Since these measurements were conducted at an intermediate acid-in-helium concentration, spectra from differently concentrated formic acid measurements that include the same band are allowed to slightly overlap to highlight the relative intensity change.[115] Below the ν_4-ν_6 group vibrations, the vibrational Raman

[112] Signals corresponding to CO_2 and CO are good indicators for decomposition since small amounts of water are always found in the jet spectra. The expected band position for the CO stretch can be calculated using diatomic constants from Ref. [174, Table 39], $2170.21-2\times13.461 = 2143\,\mathrm{cm}^{-1}$. The Raman-active symmetric stretching vibration of CO_2 is split into a Fermi resonance doublet [181] located at 1285 and 1388 cm^{-1} [223].

[113] Using diatomic constants from Ref. [174, Table 39], the expected band positions can be calculated for O_2, $1580.361 - 2 \times 12.0730 = 1556\,\mathrm{cm}^{-1}$, and N_2, $2359.61 - 2 \times 14.456 = 2331\,\mathrm{cm}^{-1}$. The observed Raman band centres are at 1555-1556 and 2329-2330 cm^{-1}, respectively. Note that M_H in the DCOOD spectrum ($2330\,\mathrm{cm}^{-1}$) does not primarily correspond to N_2 but is ascribed to *trans*-DCOOD. This was verified through a control measurement under the same expansion conditions with pure helium (not shown).

[114] The vibrational band centres are taken from Ref. [223]: 1595, 3657, 3756 (H_2O); 1402, 2727, 3707 (HDO); 1178, 2671, 2788 cm^{-1} (D_2O). The symmetric stretching vibration of H_2O and D_2O has a comparably high Raman activity and is observed in the Raman spectra. In the case of partially deuterated water, only the higher-frequency OH stretch is observed.

[115] See for example the M_N band in the HCOOH spectrum (Fig. 3.3).

Table 3.2 Raman jet band fundamentals (in cm^{-1}) of C_s symmetric *trans*-formic acid and its deuterated isotopologues in comparison to gas phase literature values. Fermi resonance doublets are indicated by braces and their mode assignments are discussed in Section 4.2. ν_1-ν_7 are in-plane (A′) and ν_8 and ν_9 out-of-plane vibrations (A″). Note that vibrational levels are labelled according to Table 2.2 (p. 35).

	trans-HCOOH			*trans*-DCOOH			*trans*-HCOOD			*trans*-DCOOD		
	Ra. jet[a]	Lit.		Ra. jet	Lit.		Ra. jet[a]	Lit.		Ra. jet[b]	Lit.	
ν_1	3570	3570.5	[94]	3569	3566	[118]	2631	2631.64	[224]	2632	2631.87	[225]
	3567											
ν_2	2942	2942.06	[94]	2219	2219.69	[226]	2954			2231	2232	[93]
							2938	2938	[118]	2194	2195	[93]
ν_3	1776	1776.83	[96]	1762	1762.9	[227]	1772	1772.12	[228]	1761	1760	[93]
				1725	1725.87	[227]				1725	1725.12	[229]
ν_4	1379	1379.05	[230]	971	970.89	[231]	1365	1366.48	[230]	1039	1042	[93]
ν_5	1306	1306.14	[95]	1299	1297	[118]	972	972.85	[232]	945	945	[93]
$2\nu_9$	1220	1220.83	[110]	1206			1010	1011.68	[232]	965		
ν_6	1104	1104.85	[219]	1142	1142.31	[233]	1176	1177.09	[234]	1170	1170.80	[235]
ν_7	626	626.17	[218]	620	620.57	[236]	558	558.27	[221]	554	554.44	[221]
ν_8	1033	1033.47	[219]		873.38	[237]	1031				873.2	[238]
ν_9		640.73	[218]		631.54	[236]		508.13	[221]		492.23	[221]

[a] See pp. 45 for the determination of the ν_8 band centre of *trans*-HCOOH and *trans*-HCOOD.
[b] See pp. 68 for the determination of the $2\nu_9$ band centre of *trans*-DCOOD.

spectra provide no 'new' information as they only include the OCO bend ν_7 and the very weakly Raman-active OD and OH/OD out-of-plane vibrations ν_8 and ν_9, respectively, that have all been measured before at higher resolution for all four H/D isotopologues (see Table 3.2). Nonetheless, the Raman spectra below 870 cm^{-1} are included for convenience and sake of completeness (Fig. 3.7).[116] To allow for a comparison of the relative intensities – ν_7 has a comparably high Raman activity –, the ν_7 spectra have been scaled based on one nearby group vibration (ν_4, ν_5 or ν_6), occasionally using – contrary to usual practice – a scaling factor >1 (see Appendix A).[117]

The assignment of the seven A′ symmetric *trans*-formic acid fundamentals (ν_1-ν_7) is straightforward based on their intensity alone. Out of the A″ symmetric fundamentals of all H/D isotopologues, just the band structure of the CH out-of-plane bend ν_8 of HCOOH and HCOOD can clearly be seen and analysed (see pp. 45). As already mentioned, many *trans* fundamentals are visibly perturbed by resonances. The band centres are listed together with available (high-resolution) literature gas phase values in Table 3.2. Their assignments are discussed in the next chapter (Section 4.2).

Legend

A note on scaling factors: All scaling factors that are additionally shown in Figs. 3.1-3.7 are not included in the scaling factors reported in Appendix A. This includes the grey spectra (433 K, trace A) which are just the orange spectra multiplied by 0.05. The depolarised spectra

[116] The ν_9 band of DCOOD is partially cut-off – the band centre is located at 492 cm^{-1} [221] but the spectrum in Fig. 3.7 does not extend below 490 cm^{-1}.

[117] For the deuterated compounds, at least one fundamental out of the three group vibrations (ν_4, ν_5 or ν_6) is also present in the same spectrum as ν_7, greatly facilitating the determination of appropriate scaling factors by simply comparing the integrated band intensities of this fundamental in the ν_7 spectrum and the spectrum included in Fig. 3.6. For the HCOOH measurement, the ν_7 spectrum ends shortly before the ν_6 fundamental. The scaling factor had instead to be determined using another measurement in the ν_6 region that was conducted under the same conditions as the ν_7 spectrum.

with parallelly polarised incident radiation (cyan, trace B) are additionally multiplied by 7/6 (see Section 2.2.1 for an explanation of the 7/6 factor).

M Bands that scale like cold *trans* monomer bands of the parent isotopologue. Band centres are listed in Table 4.3 (p. 71). The scaling alone does not permit a distinction between different isotopologues. By comparing the spectra of different H/D isotopologues, isotopic H/D variants can be identified which are labelled "#" instead of "M". The analysis in Section 4.3 reveals that some M bands turn out to be fundamentals of carbon-13 variants of the parent isotopologue, e.g. D^{13}COOH in the DCOOH spectrum.

H Bands that scale like isomeric hot bands of formic acid, i.e. *cis*-formic acid, or non-isomeric hot bands from vibrationally excited *trans* states. Band centres are listed in Table 4.4 (p. 80).

$*$ Bands that scale like clusters of formic acid, including dimers.

\# H/D variants of the parent *trans* isotopologue, e.g. DCOOD and HCOOH in the DCOOH spectrum.

The labels "M" and "H" are provided with subscripts (A, B, ...) for bookkeeping purposes; these are not correlated across spectra of different isotopologues.

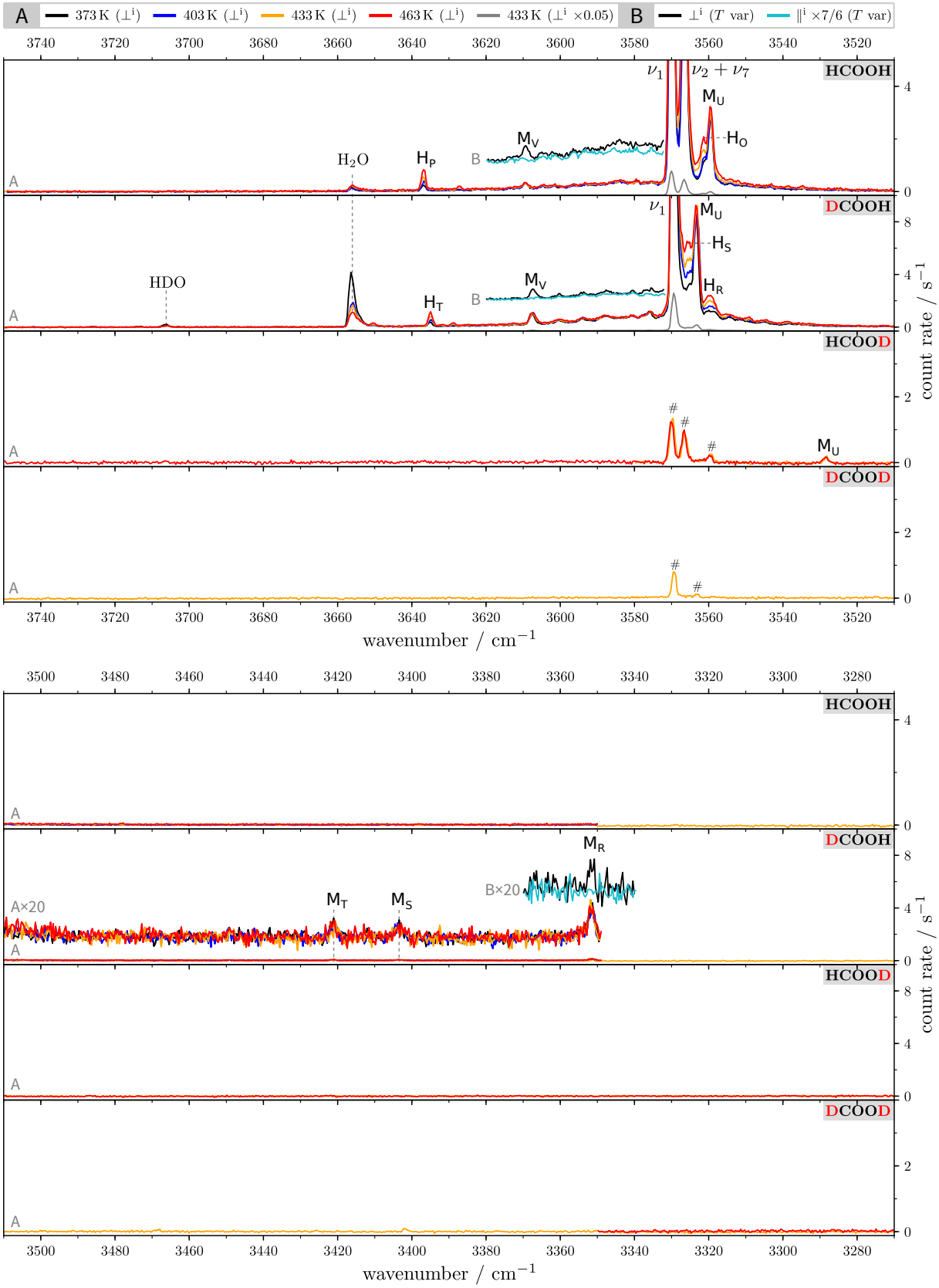

Figure 3.1 Raman jet spectra of HCOOH and its deuterated isotopologues between 3270 and 3750 cm^{-1} using helium as carrier gas. See text for details. The spectra are publicly available [222].

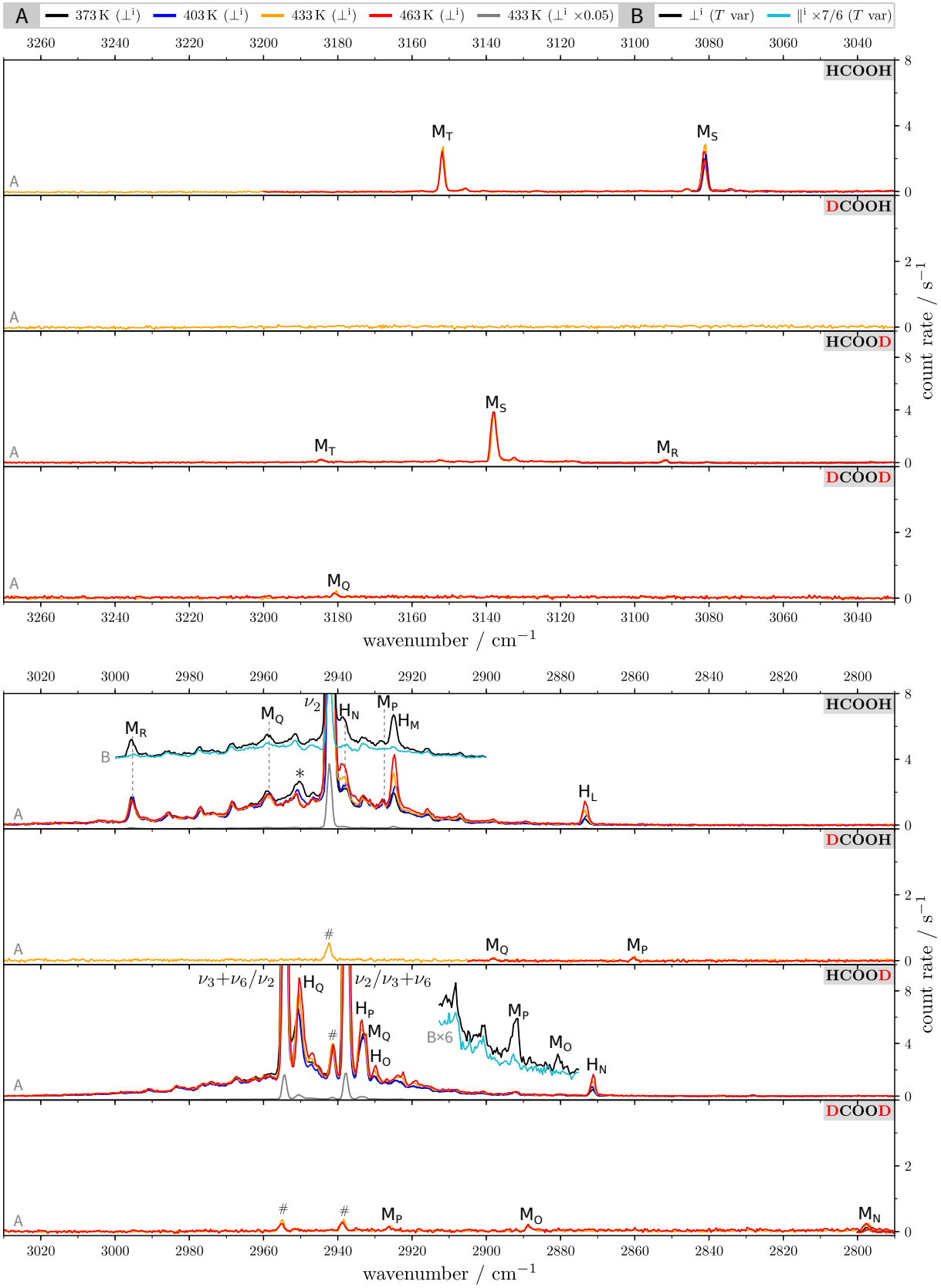

Figure 3.2 Raman jet spectra of HCOOH and its deuterated isotopologues between 2790 and 3270 cm^{-1} using helium as carrier gas. See text for details. The spectra are publicly available [222].

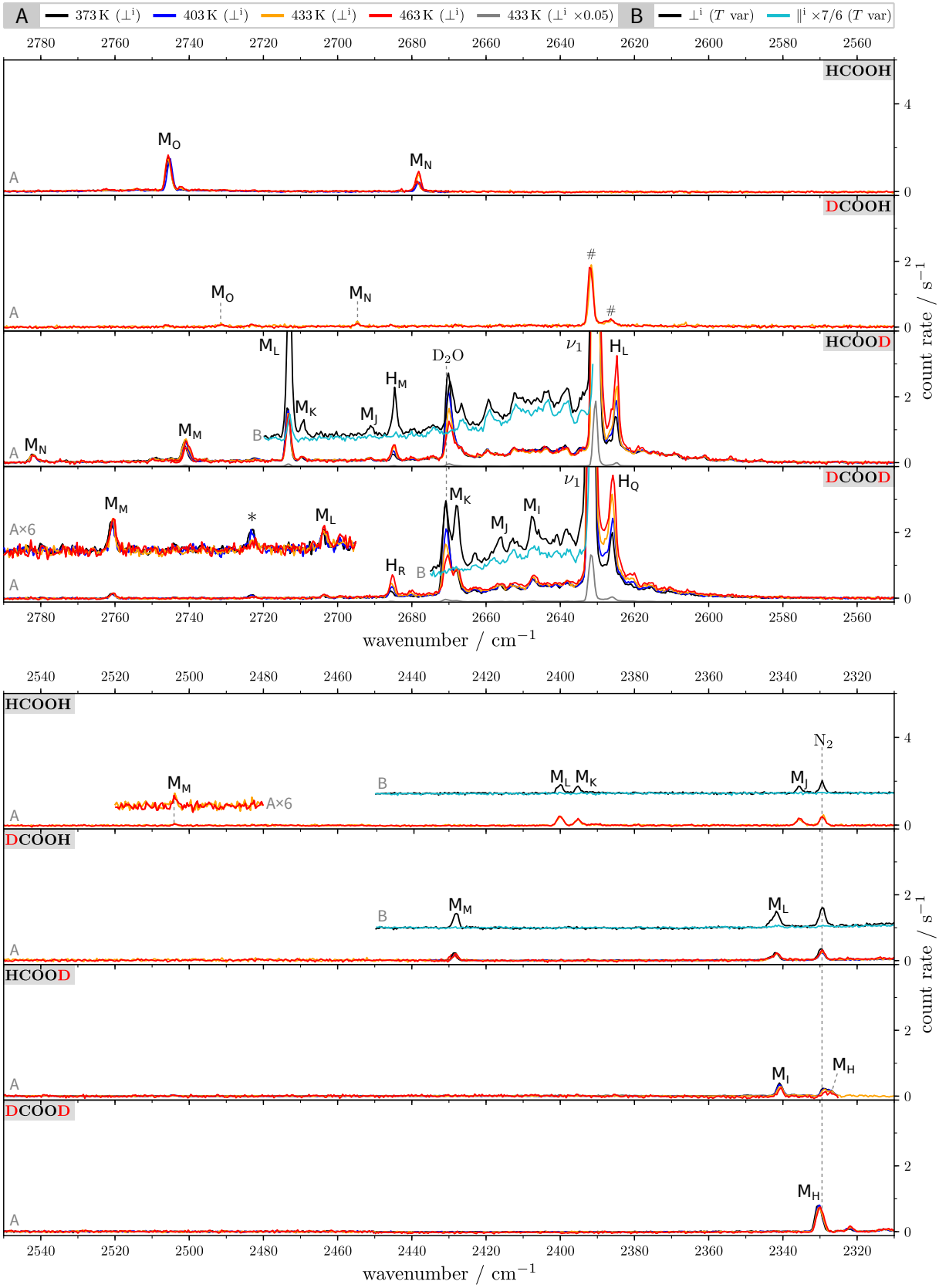

Figure 3.3 Raman jet spectra of HCOOH and its deuterated isotopologues between 2310 and 2790 cm^{-1} using helium as carrier gas. See text for details. The spectra are publicly available [222].

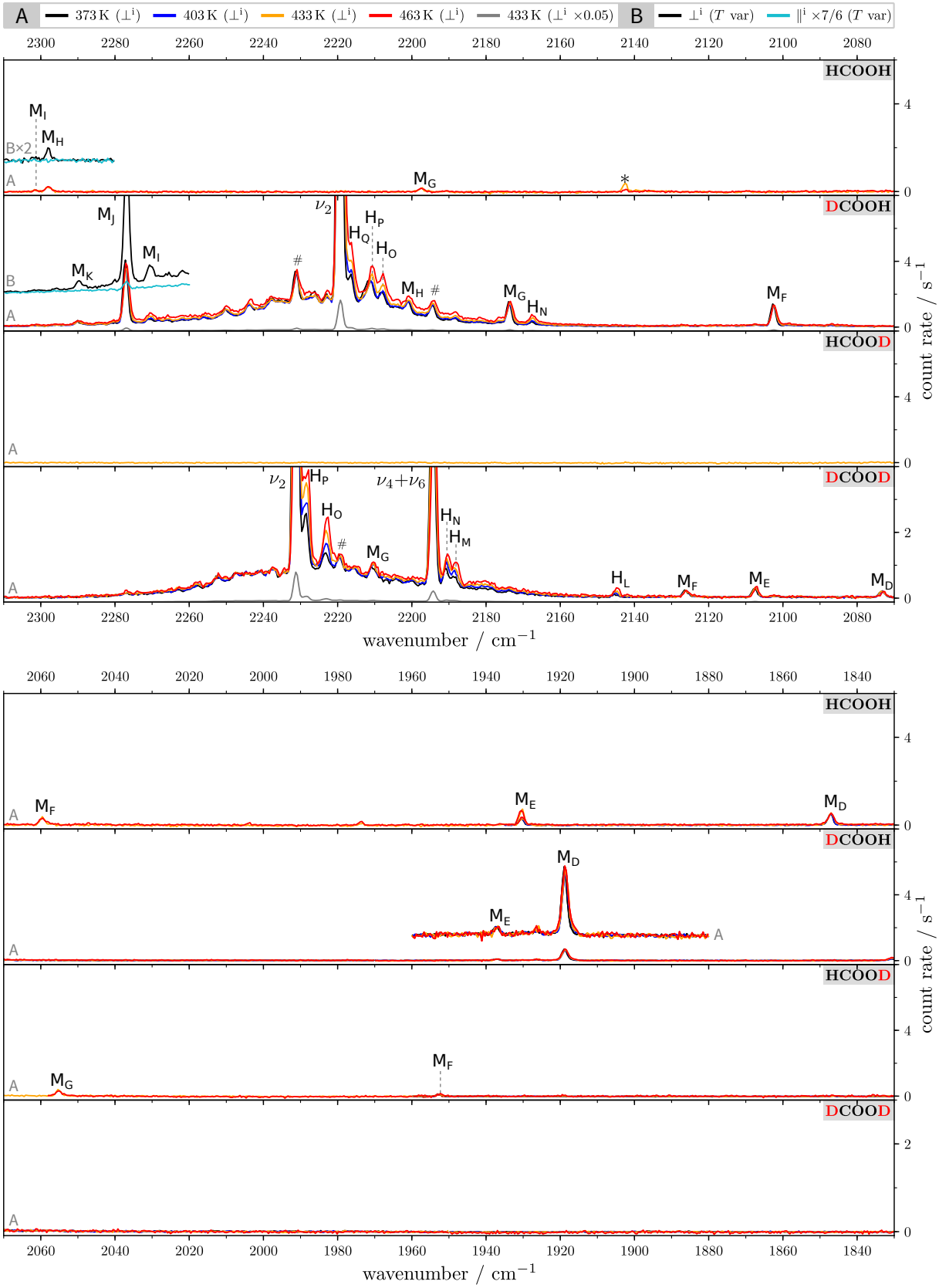

Figure 3.4 Raman jet spectra of HCOOH and its deuterated isotopologues between 1830 and 2310 cm^{-1} using helium as carrier gas. See text for details. The spectra are publicly available [222].

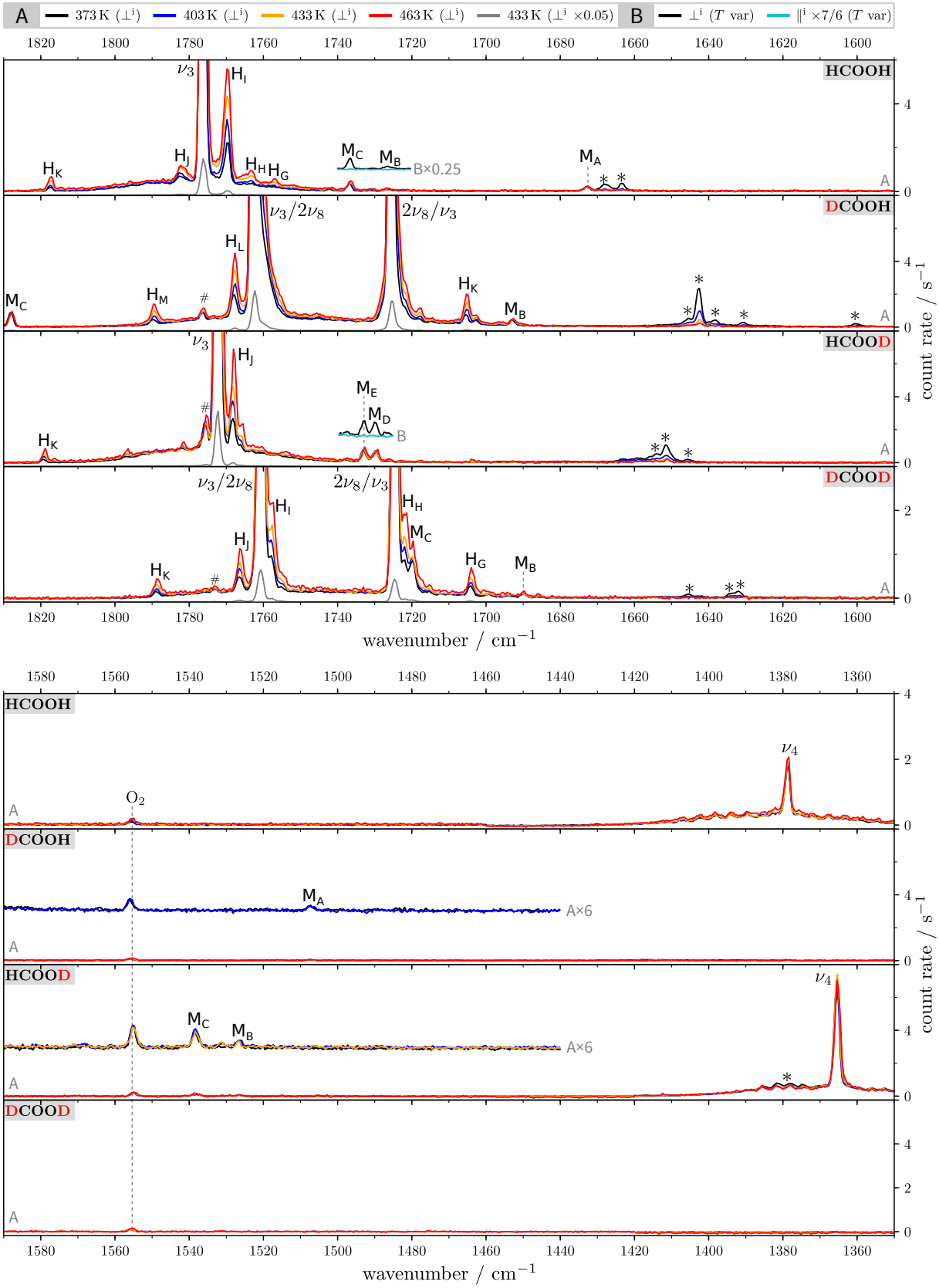

Figure 3.5 Raman jet spectra of HCOOH and its deuterated isotopologues between 1350 and 1830 cm^{-1} using helium as carrier gas. See text for details. The spectra are publicly available [222].

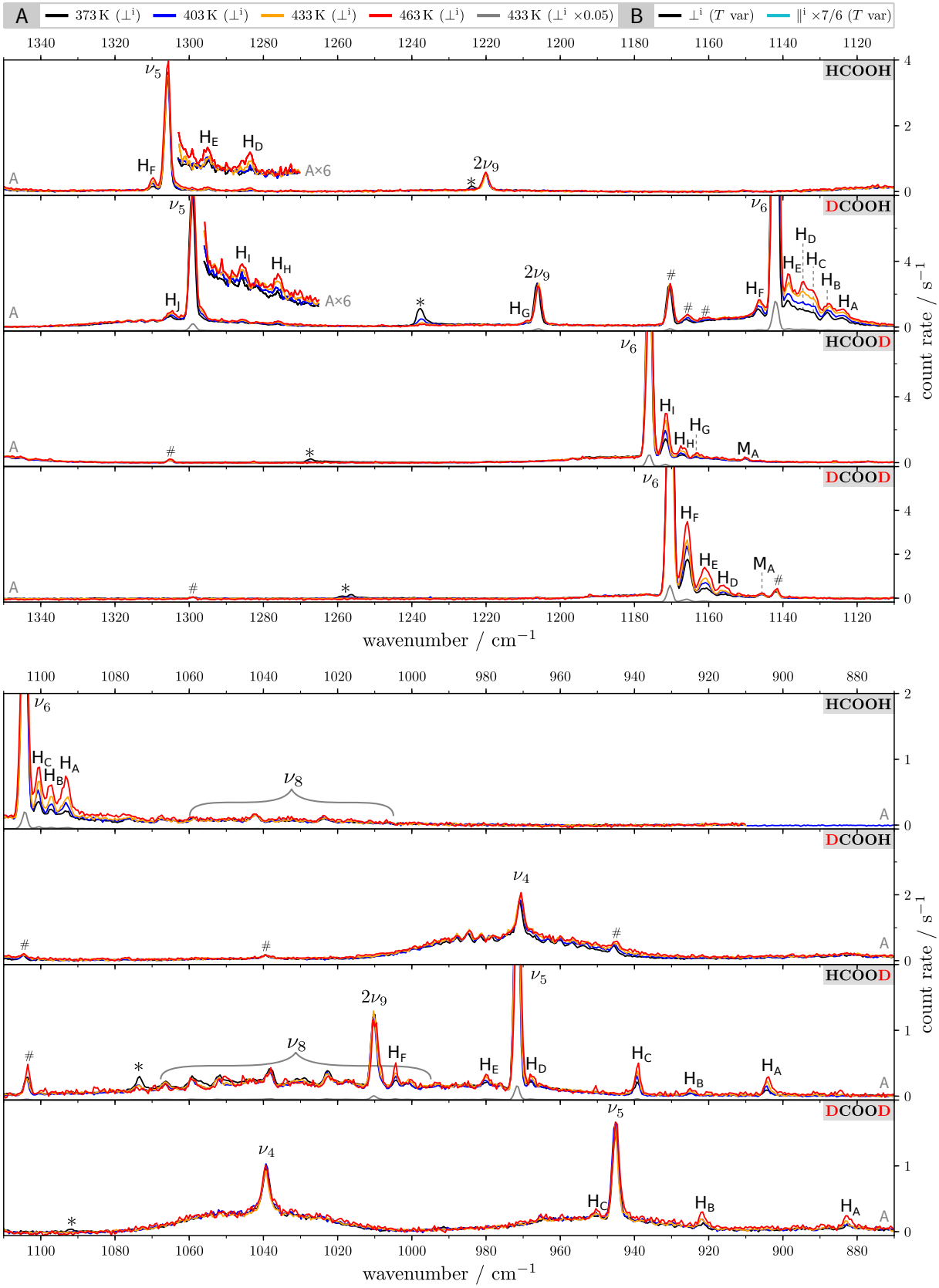

Figure 3.6 Raman jet spectra of HCOOH and its deuterated isotopologues between 870 and 1350 cm^{-1} using helium as carrier gas. See text for details. The spectra are publicly available [222].

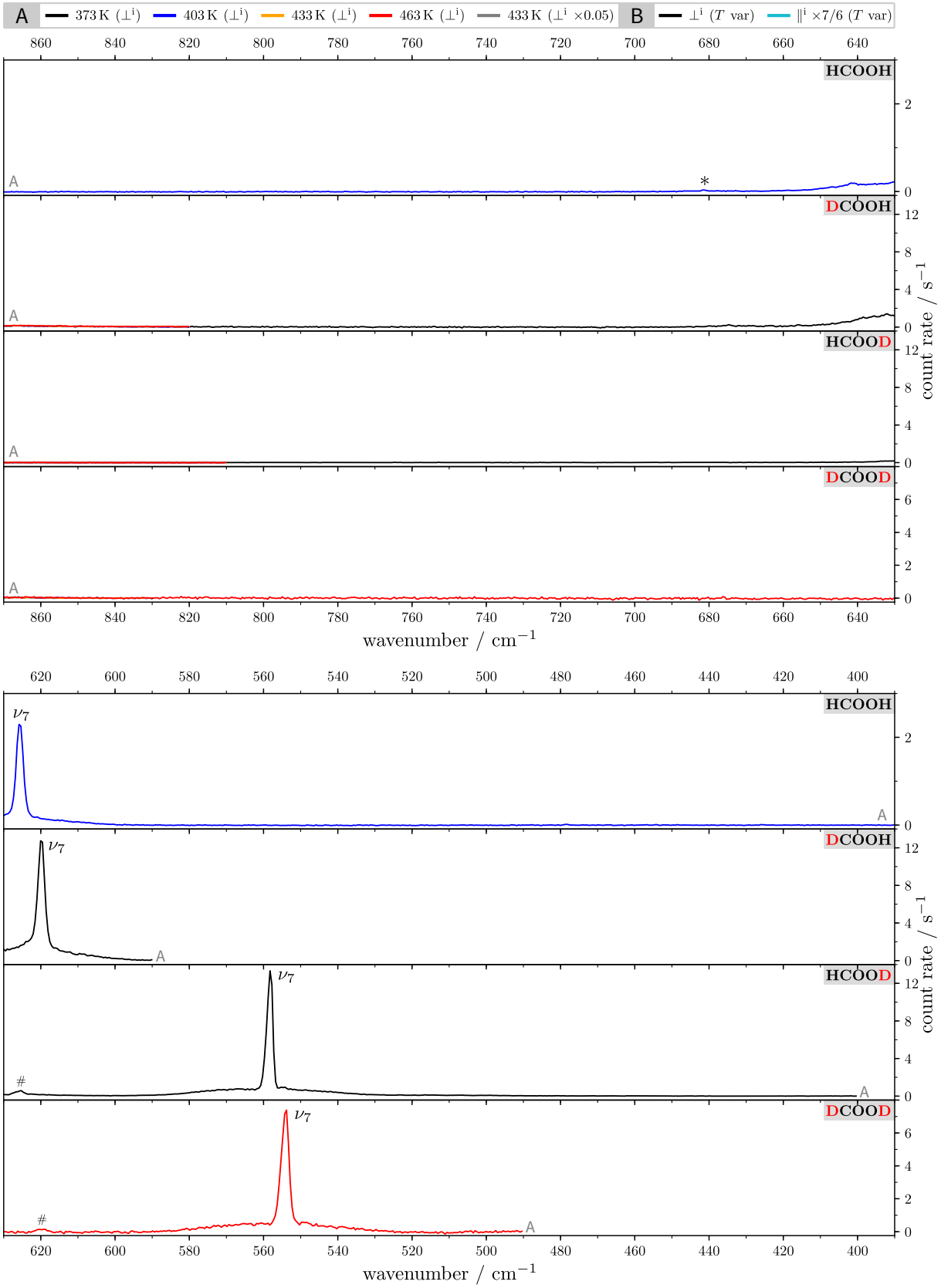

Figure 3.7 Raman jet spectra of HCOOH and its deuterated isotopologues between 390 and 870 cm^{-1} using helium as carrier gas. See text for details. The spectra are publicly available [222].

Chapter 4

Assignment of vibrational formic acid monomer bands

This chapter is dedicated to the extension and update of the experimental vibrational database of formic acid. Many overtone/combination band assignments and especially the analysis of hot bands rely on some guidance from theory. For this purpose, computed[118] canonical Van Vleck perturbation theory (CVPT) energy levels on the CCSD(T)-F12-quality formic acid potentials by Tew and Mizukami [21], TM-PES, and Richter and Carbonnière [22], RC-PES, are consulted throughout this chapter. The accuracy of the vibrational method and the potential energy functions is benchmarked first using the available experimental data for the fundamental vibrations of *trans*-HCOOH and *cis*-HCOOH (Section 4.1).[119] Many *trans* fundamentals are perturbed by strong resonances and knowledge of these resonance polyads greatly facilitates the assignment of observed "M" and "H" Raman bands. The fundamentals of all H/D isotopologues of *trans*-formic acid are, therefore, examined in Section 4.2.[120] Building on the analysis of important resonance polyads,[121] it will be attempted to assign all observed monomeric Raman bands down to the noise level. In Section 4.3 the assignment of cold bands ("M") is discussed,[122] followed by an analysis of hot bands ("H") in Section 4.4.[123] Once the interpretation of the Raman spectrum of formic acid monomer is completed in the fundamental region up to 3750 cm^{-1}, previous IR assignments and band centres are reviewed in Section 4.5.[124] The updated and extended

[118] The CVPT*n* calculations have been performed by E. L. Sibert III and published in Ref. [28] under a Creative Commons Attribution license (CC BY 4.0). Since the computed energy levels are extensively used in this chapter, they are reproduced for the convenience of the reader in Appendix D.

[119] The analysis in Section 4.1 closely follows Sections III.B and V of Ref. [28].

[120] The resonance analysis of *trans*-formic acid fundamentals in Section 4.2 closely follows Ref. [91]. The investigation of the OH bend-torsion resonance in Section 4.2 partially builds on published spectra [86] and analyses [91] but contains unpublished, novel interpretations regarding the $2\nu_9$ band of *trans*-DCOOD.

[121] In Section 4.3.2, the OH bend-torsion polyad quantum number, as defined for the bending fundamental in Section 4.2, is adjusted for higher-excited combination/overtone levels in this polyad. The analysis in that section closely follows the discussion in Section IV.C of Ref. [28]

[122] Many assignments have been previously published in Refs. [28, 91]. While the proposed assignments of cold monomer bands in Ref. [28] remain valid, some M bands are newly reported and assigned in this work: M_A, M_E, M_H (DCOOH); M_J, M_K, M_O, M_P, M_Q (HCOOD); M_C, M_G, M_I, M_J (DCOOD).

[123] Many isomeric *cis* hot band assignments have been published by Meyer [86, 87]. As a part of this work, additional *cis* assignments have been previously published in Ref. [91] and non-isomeric *trans* hot band assignments in Ref. [28]. Some H bands are newly assigned in this work: H_A, H_E, H_O, H_P, H_Q (DCOOD); H_H (HCOOD); H_E, H_H, H_I, H_M, H_N, H_P (DCOOD). The assignment of H_N has been proposed by Meyer [86] and can be confirmed in this work whereas the tentative assignments of H_B (DCOOH), H_G (HCOOD), and H_D (DCOOD) have already been suggested in Ref. [28]. In some cases, the H band centres have been adjusted compared to Ref. [28]. The changes are ± 1 cm^{-1} and, therefore, within the resolution and calibration uncertainty of ± 2 cm^{-1}.

[124] The IR reassignments in Section 4.5 have been published in advance in Ref. [28]. In some cases, the reassignments proposed here deviate from those already published in Ref. [28]: 2600 and 3106.5 cm^{-1} (HCOOH);

benchmark-quality vibrational database of monomeric formic acid is summarised in Section 4.6 (Table 4.8).[125]

4.1 Assessing errors in computed vibrational levels

Computed anharmonic fundamentals of HCOOH are listed together with experimental reference data in Table 4.1; deviations between experiment and anharmonic calculations are visualised in Fig. 4.1, including data for the three deuterated isotopologues of formic acid.

Inspection of Table 4.1 shows that the CVPT6 results for *trans*-HCOOH compare favourably with ICPH-VCI and MCTDH reference data. Deviations on the same potential are within 2 cm^{-1}.

Comparison for *cis*-HCOOH indicates that the ICPH-VCI eigenvalues are not fully converged[126] which was already suspected based on VPT2 comparisons [22].[127] The largest discrepancy between theory and experiment is found for CVPT6 on the TM-PES which overestimates ν_1 of *cis*-HCOOH by 16 cm^{-1}. Given that CVPT4 and CVPT6 fundamentals agree to within 4 cm^{-1} for *cis*-HCOOH on that potential, this discrepancy is likely due to the potential energy surface. ν_1 of the *cis* conformer was not reported in Ref. [21] and is, therefore, missing in Fig. 4.1.

MCTDH and CVPT6 results for *cis*-HCOOH compare favourably with deviations within 3 cm^{-1}. Deviations for ν_1 are slightly larger and it is noteworthy that upon C–H deuteration, the ν_1 deviations on the RC-PES increase between MCTDH (3625 cm^{-1}, Ref. [27]) and CVPT6 (3637 cm^{-1}). Moreover, the deuteration shifts for both (−6 cm^{-1} MCTDH, +1 cm^{-1} CVPT6), are outside the experimental error bars (−2(2) cm^{-1}). While the absolute band position deviations of ν_1 are large on the TM-PES, CVPT6 correctly reproduces the experimental C–H deuteration shift (−1 cm^{-1}).

In essence, the benchmark in Fig. 4.1 shows that both potential energy functions perform well for all fundamentals and their resonance perturbers whilst the TM-PES tends to overestimate experiment and the RC-PES tends to underestimate experiment.

Error estimation for higher-excited states

Naturally, the theory-experiment discrepancies and the theory-theory deviations between different potentials will only increase for higher-excited vibration states, especially the trend of the potentials to either over- or underestimate experiment. Knowledge of the theory-experiment deviation for each fundamental can be used to estimate the expected error for higher-excited vibrational states. To lowest-order, the error can be assumed to be a linear combination of the individual errors per vibrational mode, scaled by the respective quanta of excitation

$$\delta(\mathbf{n}) = \sum_{i=1}^{N_{\text{vib}}} n_i \left(\tilde{\nu}_i - \tilde{\nu}_{i,\text{exp}}\right), \tag{4.1}$$

2601.13 cm^{-1} (HCOOD).

[125] The benchmark database published in Ref. [28] is partly outdated. In addition to new Raman band assignments or Raman band centre adjustments (see notes 120, 122, 123), new *trans*-formic acid-^{13}C bands that are hidden underneath H bands could be assigned based on dimer-optimised spectra at a lower temperature (Fig. 6.3, p. 118). Changes from the IR side include: Addition of the newly measured ν_1 *cis*-HCOOH band [90]; addition of DCOOD fundamentals previously not measured at high-resolution (cf. Table 3.2, p. 49) which have been determined from FTIR jet spectra at 1 cm^{-1} resolution (published in Ref. [149]) that are partly shown in Figs. 6.1-6.2 (pp. 116); new determination of the $2\nu_3$ band centre of HCOOH and HCOOD from spectra published in Ref. [126].

[126] See Ref. [29] and Section 5.3.1 where the convergence of ICPH-VCI eigenvalues is examined.

[127] The VPT2 data on both potentials as published in Ref. [22] are incorrect. For details, see Section 5.2.

Table 4.1 Computed fundamentals of *trans*- and *cis*-HCOOH together with experimental reference values (from Table 4.8, pp. 91). The CVPT6, ICPH-VCI, and MCTDH values are from Refs. [21, 22, 28].

			trans-HCOOH					*cis*-HCOOH				
			TM-PES		RC-PES			TM-PES		RC-PES		
	Descr.	Γ	ICPH-VCI	CVPT6	CVPT6	MCTDH	Exp.	ICPH-VCI	CVPT6	CVPT6	MCTDH	Exp.
ν_1	ν(OH)	A′	3575	3576	3568	3567	3570.5		3653	3636	3631	3637.16
ν_2	ν(CH)	A′	2938	2940	2939	2937	2942.06	2880	2878	2874	2871	2873
ν_3	ν(C=O)	A′	1783	1783	1773	1774	1776.83	1824	1821	1810	1810	1818
ν_4	δ(CH)	A′	1379	1380	1374	1375	1379.05	1394	1389	1384	1383	
ν_5	δ(OH)	A′	1305	1305	1300	1301	1306.14	1255	1246	1247	1246	
ν_6	ν(C−O)	A′	1108	1108	1106	1106	1104.85	1103	1096	1097	1097	1093
ν_7	δ(OCO)	A′	627	627	623	623	626.17	668	657	652	652	
ν_8	γ(CH)	A″	1034	1035	1032	1032	1033.47	1038	1020	1014	1011	
ν_9	γ(OH)	A″	638	640	637	637	640.73	492	491	491	491	493.42

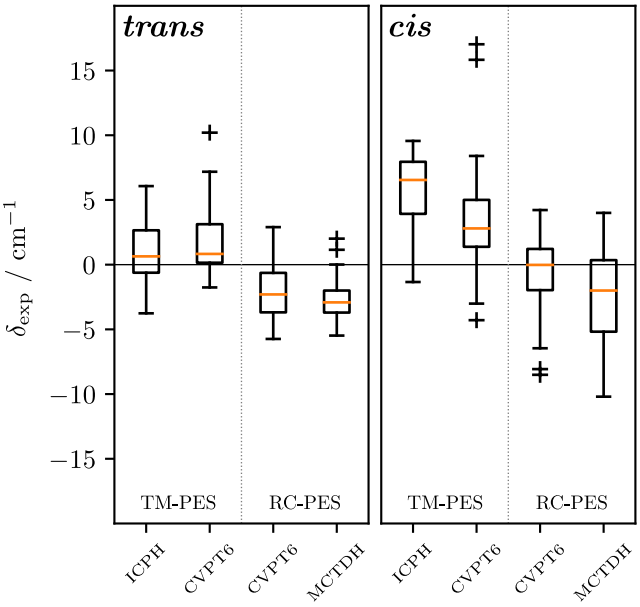

Figure 4.1 Deviation between experimental and computed formic acid fundamental wavenumbers ($\delta_{exp} = \tilde{\nu}_{calc} - \tilde{\nu}_{exp}$). Experimental data are from Table 4.8, pp. 91 (preferably IR) and computational data from Refs. [21, 22, 27, 28]. Data for all four H/D isotopologues are aggregated for *trans*- and *cis*-formic acid with 43 and 19 data points, respectively (Table 4.8). These 43 points comprise all *trans* fundamentals and their strong resonance partners including $2\nu_9$ (HCOOH), $2\nu_8$ and $2\nu_9$ (DCOOH), $\nu_3+\nu_6$ and $2\nu_9$ (HCOOD), and $\nu_4+\nu_6$ and $2\nu_8$ (DCOOD). For the ICPH-VCI model, 10 and 8 data points are used, respectively, as ν_1 of *cis* is not reported in Ref. [21] and deuterated data are not available. Each box extends from the lower quartile to the upper quartile of the data, and whiskers extend out to twice the interquartile range. Outliers are marked as crosses (+) and each box is bisected by a line indicating the median.

where $\mathbf{n} = \{n_1, ..., N_{vib}\}$ is the vibrational excitation array that defines the combination/overtone level. Remaining errors would arise from vibrational anharmonicity. If a state is strongly perturbed by resonances, the true error may deviate more than expected based on Eq. 4.1.

Impact of anharmonic effects

To highlight the role of anharmonic effects, we shall focus on the anharmonicity constants from second-order perturbation theory, expanded in curvilinear normal mode coordinates. It is instructive to compare $x_{i,j}$ values as they allow a global comparison of anharmonic effects with only $N_{vib}(N_{vib}+1)/2 = 45$ parameters – the CVPT6 Hamiltonian has over 4000 terms, in contrast. Let us consider the two CO stretching vibrations ν_3 and ν_6. For *trans*- and *cis*-HCOOH, the CVPT6 data in Table 4.1 indicate a similar performance of the two potentials across both conformers with pronounced deviations for ν_3 (10-11 cm^{-1}) and much smaller absolute differences for ν_6 (1-2 cm^{-1}). The comparison to experiment further attests to a high accuracy for ν_6 in all four cases with deviations within 4 cm^{-1} whereas for ν_3 absolute deviations range from −8 up to +6 cm^{-1}. How does this affect predictions for excited vibrational states involving mode 3? Fig. 4.2 provides some insights.

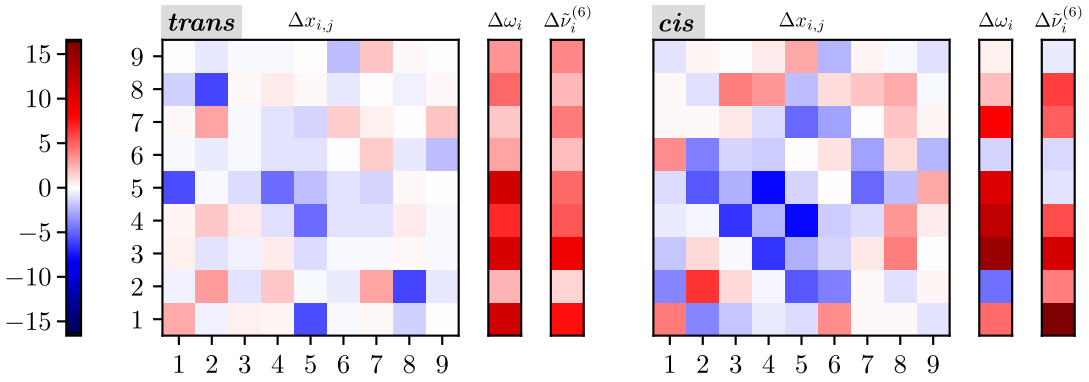

Figure 4.2 Comparison of differences in vibrational constants of HCOOH (left *trans*, right *cis*) between the TM-PES and RC-PES (in cm^{-1}), e.g. $\Delta x_{i,j} \equiv x_{i,j}(\text{TM-PES}) - x_{i,j}(\text{RC-PES})$. The vibrational constants have been computed with canonical Van Vleck perturbation theory, expanded in curvilinear normal mode coordinates. ω and x are the usual harmonic wavenumbers and second-order anharmonicity constants (from Table D.3) and $\tilde{\nu}^{(6)}$ the eigenvalues of the CVPT6 Hamiltonian.

Deviations between both potentials are disentangled in Fig. 4.2 into harmonic ($\Delta\omega_i$) and individual second-order anharmonic contributions ($\Delta x_{i,j}$) which are contrasted to the total CVPT6 deviations ($\Delta\tilde{\nu}_i^{(6)}$). Starting with ν_6, based on similar errors in the harmonic (2.9, $-1.3\,\mathrm{cm}^{-1}$) and CVPT6 (2.1, $-1.3\,\mathrm{cm}^{-1}$) wavenumbers for *trans*- and *cis*-HCOOH, respectively, we can infer similar net anharmonicities between both potentials. Comparison of $\Delta x_{6,j}$ values in Fig. 4.2 illustrates that in the case of *cis*-HCOOH the similar performance of both potentials is largely a result of error cancellation. The same applies to ν_3 where again individual anharmonicity constants are much more similar for *trans* – deviations are within $\pm 1\,\mathrm{cm}^{-1}$ – whereas for *cis* the individual differences range from -6.5 up to $4.1\,\mathrm{cm}^{-1}$. Thus, the anharmonic corrections for *trans*-formic acid are more similar on the two potentials and the resulting deviations in computed energy levels can primarily be ascribed to deviations in the underlying harmonic force field. This argument holds when comparisons are made to experiment for $x_{1,j}$ where the full set of x constants is available for *trans*-HCOOH.[128] Returning to the task of estimating errors, this means we can obtain reliable estimates for combination/overtone levels using Eq. 4.1. For *cis*-formic acid, on the other hand, the difference between the surfaces in both harmonic and anharmonic contributions is more pronounced.

Let us conclude by considering numerical examples for the respective overtones, $2\nu_3$ and $2\nu_6$, of *trans*-HCOOH, where we can compare predictions to accurate gas phase band centres (see Table 4.8, p. 91). Starting with $2\nu_3$, the *ab initio* CVPT6 predictions are 3545 and $3529\,\mathrm{cm}^{-1}$ on the TM-PES and RC-PES, respectively – the gas phase band centre is located in-between both at $3534\,\mathrm{cm}^{-1}$. Subtracting the expected error yields much more accurate predictions with 3534 and $3536\,\mathrm{cm}^{-1}$, respectively. Similarly for $2\nu_6$, the *ab initio* predictions 2199-2204 cm^{-1} can be narrowed down to 2198-2199 cm^{-1} which compare very well with the experimental band centre at $2196.3\,\mathrm{cm}^{-1}$.

4.2 Resonance analysis of *trans*-formic acid fundamentals

Segments of the Raman jet spectra of formic acid and its three deuterated isotopologues are shown in Fig. 4.3. Looking at the fundamental bands of the *trans* conformer, we see that several fundamentals are perturbed by resonances (doublets connected by brackets), in some cases

[128] In Ref. [126] the authors compiled experimental $x_{1,j}$ values for *trans*-HCOOH from experimentally known overtone and combination bands. In light of the $\nu_5 \leftrightarrow 2\nu_9$ label switch, $x_{1,5}$ value must be updated to $x_{1,5} = 4857 - 3570.5 - 1306.2 = -20\,\mathrm{cm}^{-1}$.

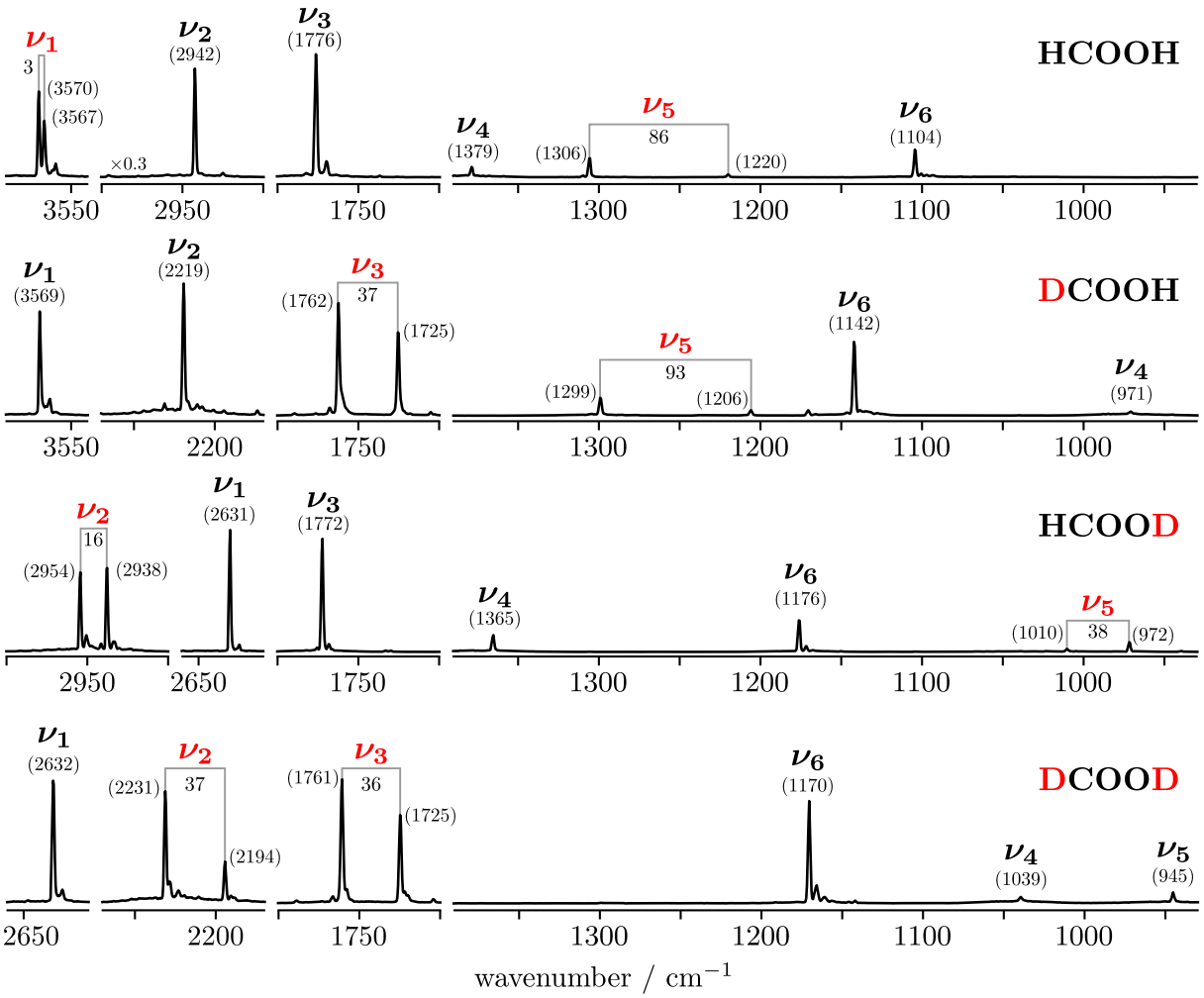

Figure 4.3 Overview of the Raman jet spectra of formic acid and its three deuterated isotopologues in the spectral range of the six fundamentals ν_1-ν_6 (nozzle temperature at 433 K; mind concentration variations, cf. Table A.1). Fundamentals, which are visibly perturbed by resonance, are highlighted in red. In these cases, also the band centre of the perturber and the band centre splitting is shown. Adapted from Ref. [91] (published under a Creative Commons Attribution license, CC BY 3.0).

leading to a near 1:1 intensity distribution, such as is the case for the C–H stretch (ν_2) of *trans*-HCOOD. In the following, these resonances are analysed.

The resonance analysis follows the theory as laid out by Herzberg [172, pp. 215] where two central assumptions are made. The resonance comprises only two interacting levels and only one transition carries intensity at zeroth-order. From the experimentally determined band centres ($\tilde{\nu}$) and integrated band intensities (I), the magnitude of the coupling element can be determined [239] in this approximation to

$$|W_{\text{exp}}| = \frac{|\Delta\tilde{\nu}|\sqrt{R}}{1+R}, \tag{4.2}$$

where $R = I_{\text{high}}/I_{\text{low}}$ ($R \geq 1$). The deperturbed band centre then corresponds to the centre of gravity of the two bands. The observed intensity ratio, I_{low}:I_{high}, equals the ratio of the square of the mixing coefficients of the zeroth-order wavefunctions, b^2:a^2.

The results of the two-level resonance analysis are summarised in Table 4.2 together with *ab initio* predictions of the coupling constant $|W|$ from a cubic force field expansion of the TM-PES. The three high-frequency stretching vibrations ν_1-ν_3 and the OH/D in-plane bend (ν_5) are involved in accidental degeneracies for at least one H/D isotopologue of formic acid but the

Table 4.2 Resonance analysis for Fermi resonance-perturbed *trans*-formic acid fundamentals. Band centres and coupling constants are in cm^{-1}. "high" and "low" refer to the relative intensities, not the wavenumbers of the respective bands. Error bars, given in parentheses, have been calculated using the Gaussian error propagation with generous band centre uncertainties of $\pm 2\,cm^{-1}$ and integrated band intensity errors of ±20%.

			Band centre (Raman)			Intensity (Raman)	$\lvert W \rvert$	
	Iso.	Perturber	Low	High	Fund. (dep.)	$I_{low} : I_{high}$	Raman[a]	Calc.[b]
ν_1	HCOOH	$\nu_2+\nu_7$	3567	3570	3569	2:3(0.5)	2(2)	0.3
ν_2	HCOOD	$\nu_3+\nu_6$	2954	2938	2946	1:1(0.5)	8(2)	8.7
ν_2	DCOOD	$\nu_3+\nu_4$	2194	2231	2219	1:2(1)	17(2)	18.9
ν_3	DCOOH	$2\nu_8$	1725	1762	1747	2:3(0.5)	18(2)	18.3
ν_3	DCOOD	$2\nu_8$	1725	1761	1747	2:3(0.5)	18(2)	18.1
ν_5	HCOOH	$2\nu_9$	1220	1306	1296	1:7(2)	28(4)	39.6
ν_5	DCOOH	$2\nu_9$	1206	1299	1286	1:7(2)	31(4)	42.7
ν_5	HCOOD	$2\nu_9$	1010	972	981	3(1):1	17(2)	16.8

[a] For ν_2 of HCOOD, only the Q branches are integrated to determine $\lvert W \rvert$. Similarly for ν_5 of HCOOD, the bands are integrated after subtraction of the depolarised components ($\perp^i - 7/6\ \parallel^i$), since ν_8 overlaps with ν_5 and $2\nu_9$.
[b] Calculated from a cubic force field expansion of the TM-PES (see Eqs. 2.37-2.38, p. 21).

coupling strengths vary which is reflected in the observed intensity transfers and band centre splittings.

Resonance perturbations of ν_1. As expected from the small spectral splitting of $3\,cm^{-1}$, the resonance of the O–H stretch (ν_1) of *trans*-HCOOH has the overall weakest coupling strength. An assignment of the perturber to $\nu_2+\nu_7$ is consistent with its absence in the DCOOH spectrum and the small experimental coupling constant of $2(2)\,cm^{-1}$ is in agreement with the vanishingly small *ab initio* value. The very high intensity of $\nu_2+\nu_7$, despite the small coupling constant, and its absence in the Raman spectra of the deuterated isotopologues clearly point at a dark state gaining intensity from ν_1 due to a 'true' near-degeneracy.[129] CVPT6 on either analytic formic acid potential, however, predicts an essentially pure $\nu_2+\nu_7$ state without significant wavefunction contribution from the zeroth-order O–H stretch. Given that the coupling is very weak, this is not surprising, as the CVPT6 energy separation of both states is 7-8 cm^{-1}, thus 2-3 times larger than the experimental splitting of $3\,cm^{-1}$. Only slight modifications of the harmonic O–H stretching force constant by a few cm^{-1} in order to reproduce the experimental fundamental band centre yield mixing ratios of about 1:1 and a splitting of $2\,cm^{-1}$ on the harmonically-modified TM-PES.

Resonance perturbations of ν_2. Bertie *et al.* reported a resonance between the C–H stretch (ν_2) and a combination vibration of the two CO stretches ($\nu_3+\nu_6$) in the Raman gas phase spectrum of HCOOD [118]. The higher-wavenumber band they reported ($2941.8\,cm^{-1}$, Ref. [118]), however, corresponds to HCOOH impurities. Fig. 4.3 shows that ν_2 of *trans*-HCOOD, coincidentally, is indeed involved in a strong resonance where the higher-wavenumber band is located at $2954\,cm^{-1}$. This second band was probably not identified by Bertie *et al.* due to additional contributions from the C–H stretch of the cyclic dimer which is nearby [118, 119]. Nonetheless, the

[129] Using the relationship [239] $\delta = \Delta\tilde{\nu}(R-1)/(R+1)$, where δ is the deperturbed, zeroth-order separation of the two interacting levels, we obtain $\delta = 3(3/2-1)/(3/2+1) = 0.6\,cm^{-1}$. Thus, the significant intensity transfer to $\nu_2+\nu_7$ can be ascribed to an accidental near-degeneracy which leads to a pronounced mixing between zeroth-order wavefunctions in spite of a vanishingly small coupling element.

initially proposed assignment to $\nu_3+\nu_6$ is correct and can be confirmed by CVPT6. Whilst the lower-wavenumber band is slightly more intensive, indicative of a higher fundamental character, a much more appropriate description of this resonance is provided by the polyad representation

$$N_2^{\mathrm{OD}} = n_2 + \frac{n_3 + n_6}{2}. \tag{4.3}$$

Similarly in fully deuterated formic acid, ν_2 is involved in strong resonances. This was already recognised by Bertie and Michaelian who reported band centres for both [93]. Their assignment of the lower-wavenumber band to $\nu_4+\nu_6$, a combination vibration of the CD in-plane bend and C−O stretch, also remains valid. Whereas in DCOOD the fundamental can be assigned unambiguously, we can define a polyad quantum number in analogy to HCOOD

$$N_2^{\mathrm{d2}} = n_2 + \frac{n_4 + n_6}{2}. \tag{4.4}$$

The experimentally determined coupling strengths for both ν_2 resonances are in good agreement with cubic Fermi constants on the TM-PES (Table 4.2).

Resonance perturbations of ν_3. Upon C−H deuteration, the out-of-plane bend of this moiety (ν_8) is shifted down by about 160 cm^{-1} and its first overtone becomes resonant with the C=O stretch (ν_3). This very strong resonance has been recognised early on and observed in gas phase [93, 118, 227], jet-cooled [141, 149], and matrix isolation studies [117, 240]. A survey of the existing (predominantly IR) literature shows that usually the lower-wavenumber band is identified as the fundamental.[130] While both bands are of similar intensity in the Raman spectra of DCOOH and DCOOD, the higher-wavenumber band is distinctly higher in intensity for both isotopologues.[131]

The inverse intensity pattern between IR and Raman could be an indication for a breakdown of the bright state picture, i.e. $2\nu_8$ carrying some intrinsic IR or Raman intensity. In the Raman spectra of the two C−H isotopologues, HCOOH and HCOOD, $2\nu_8$ is observed between 2055 and 2060 cm^{-1}. It is well separated from ν_3 (∼300 cm^{-1}) and any other fundamental vibration (>400 cm^{-1}). Its exceedingly small intensity confirms that $2\nu_8$ is essentially a dark state. Does $2\nu_8$ perhaps have some intrinsic IR intensity? In Fig. 4.4, the Raman jet spectra of the $\nu_3/2\nu_8$ doublet are contrasted to highly diluted formic acid FTIR jet spectra using helium as carrier gas.[132] Across both isotopologues, the higher-wavenumber IR band is slightly but distinctly more intensive, in agreement with the much clearer Raman intensity pattern. Whereas the Raman spectrum is free of clusters in this spectral region, the lower-wavenumber band of the $\nu_3/2\nu_8$ doublet overlaps with the IR-active C=O stretch of the cyclic formic acid dimer which is centred [147, 149] at 1719.3 (DCOOH) and 1717.5 cm^{-1} (DCOOD). Indeed, small dimer contributions slightly distort the contours of the lower-wavenumber band in Fig. 4.4, providing a plausible explanation for why it was identified as fundamental in previous IR studies.

The deperturbed separation of ν_3 and $2\nu_8$ is very small and amounts to a few cm^{-1}. Particularly for anharmonic vibrational methods, the energetic order of fundamental and overtone is

[130] In the IR spectra of Millikan and Pitzer [92], the resonance-split bands were not resolved due to thermal broadening of ν_3 and $2\nu_8$. By embedding formic acid in a neon matrix [117], Redington was able to resolve both bands and obtain deperturbed band centres following a two-level analysis [172]. Interestingly, the lower-wavenumber band in Redington's spectra is higher in intensity, as is the case in the high-resolution gas phase infrared spectrum of DCOOH that was reported by Goh *et al.* [227]. Madeja and Havenith did not show the spectrum of the higher-wavenumber resonance partner in their rotational analysis of the DCOOD ν_3 band [229] but a similar scenario to DCOOH appears plausible.

[131] The gas phase Raman spectra of DCOOH and DCOOD published by Bertie *et al.* show the same intensity pattern for ν_3 and $2\nu_8$ [93, 118], as do the Raman jet spectra reported by Xue [119]. Note that for DCOOD, Bertie and Michaelian assigned the perturber to $2\nu_8$ [93] whereas for DCOOH, the perturber was ascribed to

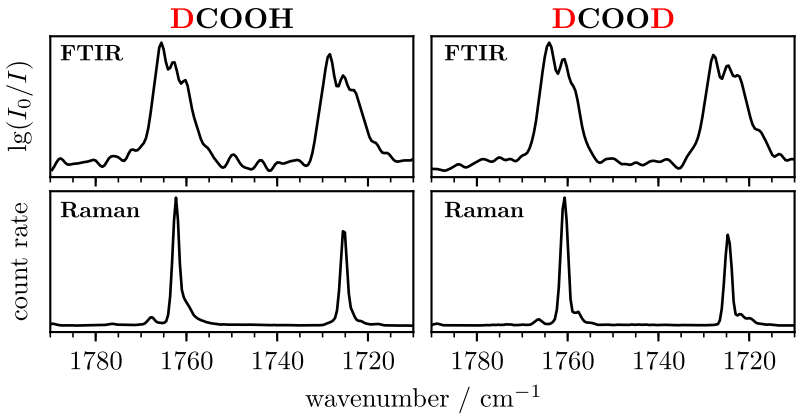

Figure 4.4 FTIR and Raman jet spectra the $\nu_3/2\nu_8$ resonance doublet in DCOOH and DCOOD. The Raman spectra are an excerpt from Fig. 4.3. See text for details on the FTIR spectra.

very susceptible to slight deviations in the nuclear vibrational treatment and underlying potential.[133] Thus, it is questionable how meaningful it is to localise the fundamental and assign it to either the lower- or higher-wavenumber band or simply withdraw into the polyad representation

$$N_3 = n_3 + \frac{n_8}{2}, \tag{4.5}$$

which is the most ideal pathway from the perspective of anharmonic vibrational calculations.

Resonance perturbations of ν_5. The last resonance perturbations in Table 4.2 involve the OH/D in-plane bend (ν_5). As mentioned in the introduction, it undergoes a very strong resonance with the overtone of its respective torsion vibration ($2\nu_9$). Recently, Hull experimentally confirmed [107] the proposed reassignment [21, 22] of the overtone to the lower-wavenumber band. By providing the complementary Raman picture, Meyer could show by detailed comparison of the respective IR and Raman jet spectra of HCOOH that the intensity pattern of this resonance is inverse between IR and Raman. In the Raman spectrum, the usual scenario of a dark state stealing intensity from a bright fundamental is found, whereas in the IR, the overtone is more intensive [86].[134]

$\nu_6+\nu_7$ [118].

[132] The FTIR spectra have kindly been provided by K. A. E. Meyer. Each FTIR spectrum has been averaged over 1000 individual scans. For internal reference, the DCOOH spectra were measured on 15.01.2020 (scans d-h) and the DCOOD spectra on 07.01.2020 (scans b-h).

[133] The sensitivity of the $\nu_3/2\nu_8$ resonance to the vibrational treatment (and PES parametrisation) is perhaps best illustrated by comparing CVPT6 to MCTDH. Utilising the RC-PES, Aerts *et al.* reported $J = 0$ MCTDH energy levels for both conformers of all three deuterated formic acid isotopologues [27]. The CVPT6 energy levels for ν_3 and $2\nu_8$ of *trans*-DCOOD on this potential (1723.0 and 1760.5 cm^{-1}) agree within 1.5 cm^{-1} with the variational MCTDH predictions (1759.0 and 1721.5 cm^{-1}), however, CVPT6 identifies the lower-wavenumber component as the fundamental, whereas MCTDH predicts more fundamental character for the higher-wavenumber level.

[134] See Fig. 4.4 of Ref. [86]. The broad IR feature contains additional contributions from the cyclic dimer, more specifically the ν_{22} resonance triad (see Section 7.2). Comparing the intensity of this dimeric resonance triad (Fig. 6.1, p. 116), which decreases with decreasing wavenumber, with the spectrum reported in Fig. 4.4 of Ref. [86], one immediately sees that the monomeric contribution (centred at 1220.83 cm^{-1}, Ref. [110]) is the main contributor to the overall absorption feature in Fig. 4.4 of Ref. [86]. The higher-wavenumber IR band of the $\nu_5/2\nu_9$ resonance doublet, however, is not discernible in the reported FTIR jet spectrum. This is consistent with prior findings that the higher-wavenumber band of the bend-torsion doublet is less visible in the IR spectrum of HCOOH [94, 95] which probably triggered the misassignment in the first place.

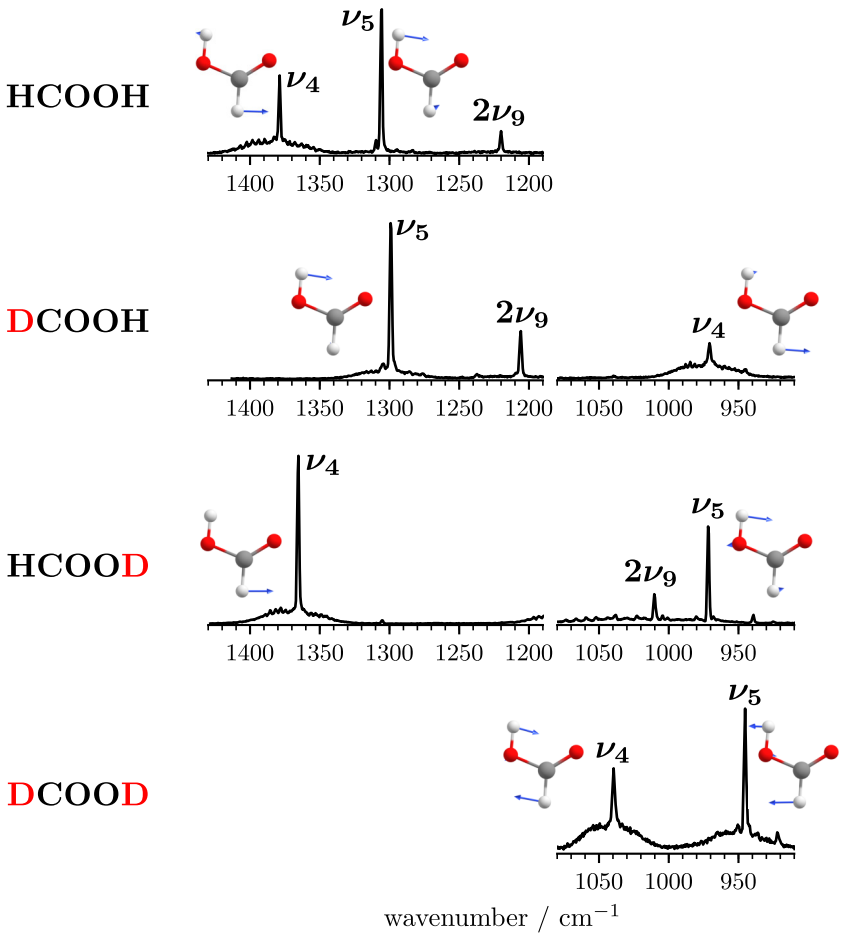

Figure 4.5 Excerpt of the formic acid Raman jet spectra shown in Fig. 4.3. Note that intensities can quantitatively be compared within each row but not across different rows, i.e. isotopologues. Adapted from Ref. [91] (published under a Creative Commons Attribution license, CC BY 3.0).

Since $3\tilde{\nu}_5 \approx \tilde{\nu}_1$, there is a significant number of multi-quantum states in the fundamental range that are coupled through this bend-torsion resonance. Particularly for bookkeeping purporses, it is very useful to define a resonance polyad quantum number

$$N_5 = n_5 + \frac{n_9}{2}. \tag{4.6}$$

Note that for larger values of N_5, the polyad definition needs to be adjusted (see Section 4.3.2).

It is worth noting that the two-level analysis of the Raman resonance pair yields a distinctly smaller coupling strength than predicted by a cubic force field (Table 4.2). In the two-level picture, the Raman intensity ratio of the $2\nu_9$ and ν_5 bands would need to be 1:2 in order to yield a coupling constant that quantitatively agrees with the cubic force field estimate. These discrepancies could be indicative of additional electrical anharmonic effects that influence the $2\nu_9$:ν_5 Raman intensity ratio in favour of the fundamental or mechanical couplings to additional states that are not included in the two-level bright state analysis, possibly ν_4. It is also conceivable that the cubic Fermi constant is missing important higher-order contributions [6, Section 3.4]. The value reported by Baskakov *et al.* (42 cm^{-1}, Ref. [95]), on the other hand, excellently agrees with the cubic Fermi coupling element on the TM-PES (40 cm^{-1}). That value was obtained by fitting ro-vibrational IR lines using a semi-global effective Hamiltonian.

Deuteration data for this important resonance are partly missing and/or outdated.[135] In Fig. 4.5, we see how this resonance evolves in the Raman spectra upon deuteration. In *trans*-

[135] See for example Refs. [93, 118, 232], references cited in Ref. [95], and also Ref. [117] (matrix isolation).

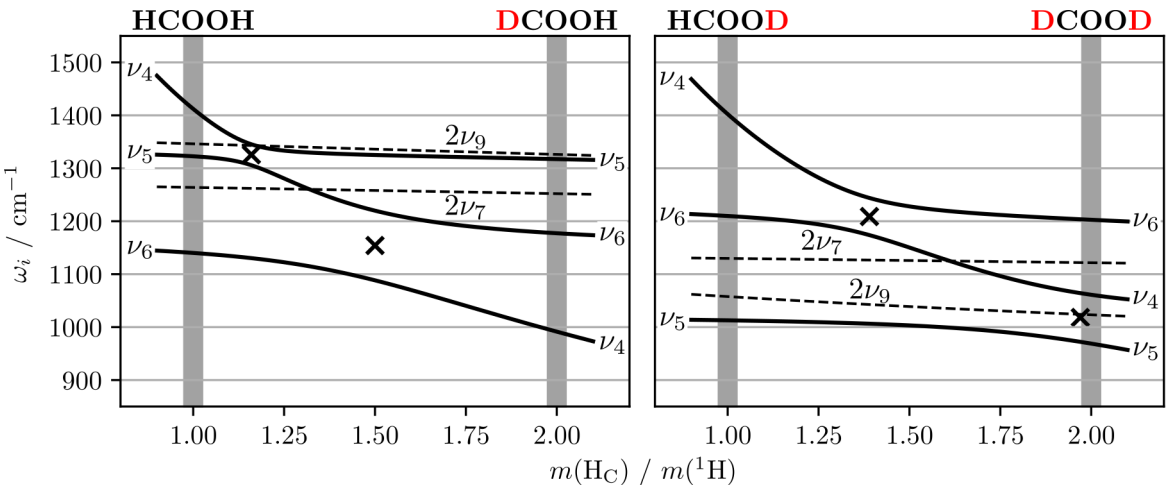

Figure 4.6 Harmonic wavenumbers (in cm^{-1}, TM-PES) of A′ symmetric *trans*-formic acid fundamentals and overtones between 850 and 1550 cm^{-1} as a function of the C–H proton mass. A cross marks the point where the curves would cross in the limit of no interaction.

DCOOH,[136] the resonance pattern remains qualitatively unchanged but the experimental two-level coupling strength $|W|$ slightly increases from 28(4) to 31(4) cm^{-1}. The increase by 3 cm^{-1} quantitatively agrees with the increase of the computed cubic coupling constant but consequently the absolute experimental coupling strength is still much smaller than predicted with a cubic force field (see Table 4.2). Since C–H deuteration minimises the involvement of ν_4 in the bend-torsion resonance, the necessity to include ν_4 in the bright state analysis appears less likely as the major source of this discrepancy. In *trans*-HCOOD, the fundamental moves below the overtone which gains in relative intensity. The bright state Raman coupling strength decreases to 17(2) cm^{-1} as expected for the smaller OD amplitudes (Table 4.2). For *trans*-HCOOD, the experimental and calculated coupling constants agree within the generous experimental error bars. A look into the corresponding FTIR jet spectrum of HCOOD (see Fig. 6.2, p. 117) shows that both bands have a near 1:1 intensity ratio, providing further evidence that $2\nu_9$ has intrinsic IR intensity.[137]

The OD bend-torsion resonance in DCOOD. In fully deuterated *trans*-formic acid, the resonance between ν_5 and $2\nu_9$ is seemingly detuned and $2\nu_9$ is not observed in the Raman spectrum (Fig. 4.5). It was recognised early on that the two in-plane bending vibrations, ν_4 and ν_5, must strongly interact in *trans*-DCOOD based on their wavenumber shifts relative to that of both singly deuterated *trans*-formic acid isotopologues [92, 241]. Indeed, Fig. 4.5 shows that the two *trans*-DCOOD bands at 945 and 1039 cm^{-1} are either above or below their respective counterparts in singly-deuterated formic acid which are near-isoenergetic (971-972 cm^{-1}). This mode mixing is further reflected in the band shapes of ν_4 and ν_5. In the other three isotopologues, ν_5 has a much smaller depolarisation ratio than ν_4, resulting in a large polarised component to the Q branch and, therefore, high intensity ratio of its Q branch relative to the $\Delta J \neq 0$ rotational contour. In *trans*-DCOOD, however, ν_5 is strongly depolarised, as indicated by the low intensity of its Q branch.

Analysis of the harmonic wavenumbers of the three normal vibrations ν_4, ν_5, and ν_6 as a function of the C–H proton mass from $1m(^1\mathrm{H})$ up to $2m(^1\mathrm{H})$ allows us to inspect the magnitude of the avoided crossings. Fig. 4.6 shows that the avoided crossings are very large (40-130 cm^{-1})

[136] Note that only the higher-wavenumber band was observed by Bertie *et al.* in the gas phase Raman spectrum of DCOOH [118].

[137] In this context, results from a two-state IR bright state analysis [107] must be viewed with caution.

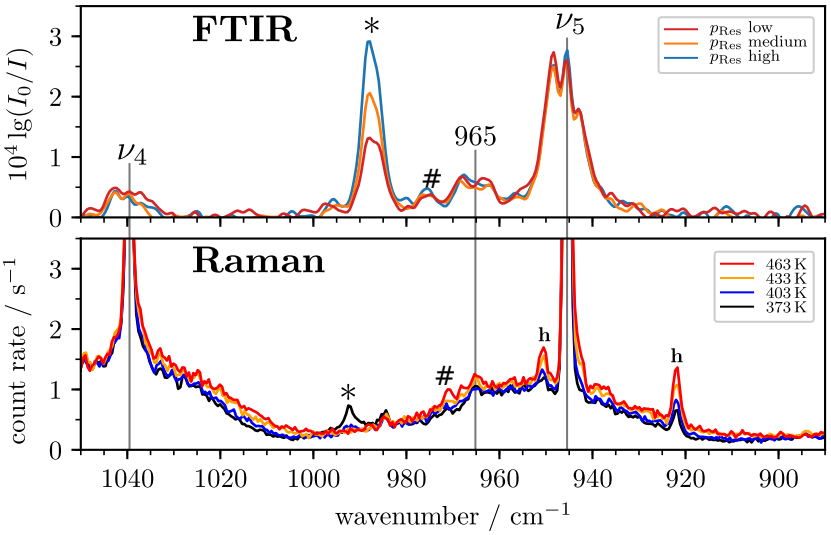

Figure 4.7 FTIR and Raman jet spectra of DCOOD intensity-scaled to the C–O stretching fundamental of the monomer (not shown) with the lowest intensity in a reservoir pressure series (IR) or temperature series (Raman). Isotopic H/D impurities are marked with a hash symbol (#) and clusters with an asterisk (∗) and hot bands are labelled as "h". The Raman spectra were published in Ref. [86, p. 222] and are kindly provided by the author. The FTIR jet spectra are shown in Fig. 6.2 (p. 117; scaled instead to a cyclic dimer band).

which is indicative of a strong interaction between ν_4, ν_5, and ν_6 [99]. The delocalisation of the two bending vibrations is only very small in hydrogenated and singly deuterated *trans*-formic acid since the avoided crossings appear near half-integer masses of $1.5m(^1\mathrm{H})$. Indeed, the bending normal modes shown in Fig. 4.5 mostly correspond to local bending vibrations of the OH/D or CH/D moieties for these isotopologues. One avoided crossing of ν_4 and ν_5, however, accidentally coincides with an integer value that corresponds to *trans*-DCOOD. The normal modes in Fig. 4.5 show that the two respective normal modes can alternatively be classified as in-phase (ν_4) and out-of-phase (ν_5) linear combinations of the local mode CD and OD in-plane bends.

Correcting the two CVPT6 predictions of $2\nu_9$ for the expected error (Eq. 4.1), the gas phase band centre is expected at $(966 \pm 1)\,\mathrm{cm}^{-1}$. Indeed, Meyer observed a band at $965\,\mathrm{cm}^{-1}$ in the Raman jet spectrum of DCOOD at slightly higher acid concentrations than employed in this work which seems to scale like a cold monomer band [86]. The spectra are kindly provided by the author and are reproduced in Fig. 4.7. Since the bending fundamentals of singly deuterated formic acid are both centred slightly above $970\,\mathrm{cm}^{-1}$, an alternative assignment to isotopic impurities (including carbon-13) can safely be ruled out, leaving $2\nu_9$ as the only possible *trans*-DCOOD assignment (Table D.7). Since $2\nu_9$ seems to carry intrinsic IR activity for the other isotopologues, a comparison with the corresponding IR spectrum can provide further confirmation. Monomer-scaled FTIR jet spectra of DCOOD at different reservoir pressures are shown in the top panel of Fig. 4.7. Centred at $965\,\mathrm{cm}^{-1}$, there is an absorption feature that scales like a monomer and the $5\text{-}6\,\mathrm{cm}^{-1}$ separation of the maxima matches the separation of the *P* and *R* branch maxima of the nearby ν_5 fundamental, further strengthening an assignment to *trans*-DCOOD, i.e. $2\nu_9$. In the gas phase, the band centre is shifted by $+2\,\mathrm{cm}^{-1}$ relative to a weakly perturbing neon matrix where it was observed at $962.8\,\mathrm{cm}^{-1}$ by Redington [117].

4.3 Assignment of overtone and combination bands

All M bands are A′ symmetric, as indicated by their band contours and confirmed by depolarisation measurements in critical cases where an A″ assignment seems equally possible (see spectra in Chapter 3). Therefore, we will only consider A′ symmetric energy levels in the following

discussion which greatly simplifies the assignments. The band centres and vibrational mode assignments are compactly listed in Table 4.3.

4.3.1 M bands below 2600 cm^{-1}

Based on a sum-of-fundamentals estimate of the expected positions of binary A′ states, it should be expected that some observed M bands correspond to multi-quantum vibrational excitations ($\Delta n \geq 3$). In Ref. [28], the mode assignments were based on CVPT6 energy levels computed on the TM-PES and RC-PES. Such a comfortable situation is rather the exception and for other increasingly larger systems, *ab initio* VPT2 at the MP2 or DFT level is often the most (or even only) affordable method when also factoring in the availability of computing facilities and overall computation time. It is more instructive to try assigning the M bands based on semi-experimental SOF+x. The vibrational energy levels are calculated using the second-order expression in Eq. 2.17 (p. 17). To enhance the accuracy, experimental fundamentals (see Table 3.2, p. 49) are combined with MP2/aVTZ x constants.

The majority of M bands is located between 1500 and 3200 cm^{-1}. They are shown in Fig. 4.8 for all four H/D isotopologues in the top panels together with all fundamentals in this spectral region. In the respective bottom panels, semi-experimental SOF+x predictions are included for all A′ symmetric two-quantum energy levels except for those that are already assigned (see Table 4.2, p. 64). Building on the preceding analysis of resonance polyads in formic acid, it is quite obvious that we need to additionally consider those ternary and quaternary states that are in resonance with binary states, e.g. ν_3+2ν_9 which is coupled to ν_3+ν_5 or ν_5+2ν_9 and 4ν_9 which are coupled to 2ν_5 in *trans*-HCOOH. The polyad representation comes in handy, as it provides a recipe which ternary and quaternary states to include. The excitation array $\mathbf{n} = \{n_1, ..., n_9\}$ is modified for each isotopologue based on Eqs. 4.3-4.6:

$$\begin{aligned}
\mathbf{n}(\text{HCOOH}) &= \{n_1, n_2, n_3, n_4, N_5, n_6, n_7, n_8\} \\
\mathbf{n}(\text{DCOOH}) &= \{n_1, n_2, N_3, n_4, N_5, n_6, n_7\} \\
\mathbf{n}(\text{HCOOD}) &= \{n_1, N_2^{\text{OD}}, n_3, n_4, N_5, n_6, n_7, n_8\} \\
\mathbf{n}(\text{DCOOD}) &= \{n_1, N_2^{\text{d2}}, N_3, n_4, n_5, n_6, n_7, n_9\}
\end{aligned}$$

In Fig. 4.8, different values of N_i are reflected in the colour. States are green if all $N_i = 0$. Red and blue are reserved for cases where at least one N_i is 1 or 2, respectively. Note that 'disconnected' polyads, e.g. $\{N_3, N_5\} = \{1, 1\}$, are red and not blue. For red and blue states, the SOF+x expressions must be adjusted to incorporate resonance effects.[138] For third overtones, e.g. $4\nu_i$ ($N_i = 2$), there is a certain indeterminacy since different second-order formulations exist[139] that are only strictly equivalent in the absence of resonances. In these cases, appropriate error bars[140] are provided in Fig. 4.8. Note that for HCOOD, the error bars are narrower than the

[138] To incorporate Fermi resonance effects, the appropriate SOF+x expressions (Table 2.1, p. 17) are modified by replacing $2\times(\tilde{\nu}_i) + 2x_{i,i}$ with $2\tilde{\nu}_i$ for resonance-perturbed first overtones and $\tilde{\nu}_i + x_{i,j} + \tilde{\nu}_j$ with $\widetilde{\nu_i+\nu_j}$ for binary combination levels.

[139] $4\tilde{\nu}_i$ can either be computed from the fundamental $4\times(\tilde{\nu}_i) + 12x_{i,i}$, the fundamental and first overtone $2\times(\tilde{\nu}_i) + 2\tilde{\nu}_i + 10x_{i,i}$, the fundamental and second overtone $\tilde{\nu}_i + 3\tilde{\nu}_i + 6x_{i,i}$, and just the first overtone $2\times(2\tilde{\nu}_i) + 8x_{i,i}$.

[140] With $\tilde{\nu}_9$, $2\tilde{\nu}_9$, and $3\tilde{\nu}_9$ available for HCOOH, $4\tilde{\nu}_9$ can be estimated in four different ways (see note 139):

$$\begin{aligned}
4\times(\tilde{\nu}_9) + 12x^*_{9,9} &= 4\times 640.73 - 12\times 10.8 = 2433\,\text{cm}^{-1}, \\
2\times(\tilde{\nu}_9) + 2\tilde{\nu}_9 + 10x^*_{9,9} &= 2\times 640.73 + 1220.83 - 10\times 10.8 = 2394\,\text{cm}^{-1}, \\
\tilde{\nu}_9 + 3\tilde{\nu}_9 + 6x^*_{9,9} &= 640.73 + 1931.1 - 6\times 10.8 = 2507\,\text{cm}^{-1}, \\
2\times(2\tilde{\nu}_9) + 8x^*_{9,9} &= 2\times 1220.83 - 8\times 10.8 = 2355\,\text{cm}^{-1},
\end{aligned}$$

Table 4.3 Band list ($\tilde{\nu}_0$, in cm^{-1}) of cold *trans*-formic acid bands in the monomer-optimised Raman jet spectra (Chapter 3). All bands are polarised and, therefore, A′ symmetric. Fundamentals and their strong Fermi resonance partners were discussed previously and are not included here (see Table 3.2, p. 49). Energy levels are computed with CVPT6 on the TM-PES and RC-PES. Note that vibrational levels are labelled according to Table 2.2 (p. 35).

		CVPT6		Assignment	
	$\tilde{\nu}_0$	TM-PES	RC-PES	Label	Γ
trans-HCOOH					
M_A	1673	1675	1668	$\nu_8+\nu_9$	A′
M_B	1726	1732	1725	$\nu_6+\nu_7$	A′
M_C	1737	1743		$\nu_3(^{13}C)$	A′
M_D	1847	1850	1839	$\nu_7+2\nu_9$	A′
M_E	1931	1932	1921	$\nu_5+\nu_7$	A′
M_F	2060	2066	2060	$2\nu_8$	A′
M_G	2197	2204	2199	$2\nu_6$	A′
M_H	2298	2305	2295	$4\nu_9/\nu_6+2\nu_9$	A′
M_I	2301	2304	2292	$\nu_7+\nu_8+\nu_9$	A′
M_J	2336	2338	2331	$\nu_6+2\nu_9/4\nu_9$	A′
M_K	2395	2402	2389	$\nu_3+\nu_7$	A′
M_L	2400	2405	2396	$\nu_5+\nu_6$	A′
M_M	2504	2507	2499	$\nu_5+2\nu_9/2\nu_5$	A′
M_N	2678	2678	2669	$\nu_4+\nu_5$	A′
M_O	2746	2747	2736	$2\nu_4$	A′
M_P	2928	2928		$\nu_2(^{13}C)$	A′
M_Q	2960	2964	2952	$\nu_7+4\nu_9$	A′
M_R	2995	3002	2987	$\nu_3+2\nu_9$	A′
M_S	3081	3087	3073	$\nu_3+\nu_5$	A′
M_T	3153	3160	3145	$\nu_3+\nu_4$	A′
M_U	3559			[a]	A′
M_V	3609			[a]	A′
trans-DCOOH					
M_A	1508	1509	1503	$\nu_8+\nu_9$	A′
M_B	1693	1699		$2\nu_8(^{13}C)/\nu_3(^{13}C)$	A′
M_C	1828	1830	1820	$\nu_7+2\nu_9$	A′
M_D	1919	1921	1910	$\nu_5+\nu_7$	A′
M_E	1937	1936	1937	$2\nu_4$	A′
M_F	2103	2106	2101	$\nu_4+\nu_6$	A′
M_G	2174	2175	2170	$\nu_4+2\nu_9$	A′
M_H	2200	2200		$\nu_2(^{13}C)$	A′
M_I	2271	2269	2263	$\nu_4+\nu_5$	A′
M_J	2277	2282	2272	$2\nu_6$	A′
M_K	2290	2293	2283	$4\nu_9$	A′
M_L	2342	2344	2337	$\nu_6+2\nu_9$	A′
M_M	2428	2431	2421	$\nu_5+\nu_6$	A′
M_N	2695	2701	2695	$\nu_4+2\nu_8/\nu_3+\nu_4$	A′
M_O	2731	2736	2733	$\nu_3+\nu_4/\nu_4+2\nu_8$	A′
M_P	2860	2870	2858	$\nu_6+2\nu_8/\nu_3+\nu_6$	A′
M_Q	2898	2906	2896	$\nu_3+\nu_6/\nu_6+2\nu_8$	A′
M_R	3352	3352	3347	$\nu_2+\nu_6$	A′
M_S	3404	3408	3398	$\nu_6+4\nu_9$	A′
M_T	3421	3424	3409	$3\nu_6$	A′
trans-DCOOH (continued)					
M_U	3563			[a]	A′
M_V	3607			[a]	A′
trans-HCOOD					
M_A	1150	1154		$\nu_6(^{13}C)$	A′
M_B	1527	1529	1522	$\nu_5+\nu_7$	A′
M_C	1539	1542	1536	$\nu_8+\nu_9$	A′
M_D	1730	1734	1730	$\nu_6+\nu_7$	A′
M_E	1733	1740		$\nu_3(^{13}C)$	A′
M_F	1953	1955	1946	$2\nu_5$	A′
M_G	2055	2061	2057	$2\nu_8$	A′
M_H	2327	2334	2323	$\nu_3+\nu_7$	A′
M_I	2341	2348	2345	$2\nu_6$	A′
M_J	2692	2697	2689	$\nu_5+\nu_6+\nu_7$	A′
M_K	2710	2713	2709	$\nu_6+\nu_8+\nu_9$	A′
M_L	2713	2712	2707	$2\nu_4$	A′
M_M	2741	2749	2737	$\nu_3+\nu_5$	A′
M_N	2782	2788	2775	$\nu_3+2\nu_9$	A′
M_O	2880			[b]	A′
M_P	2892			[c]	A′
M_Q	2933	2935	2922	$\nu_4+\nu_7+2\nu_9$	A′
M_R	3092	3096	3089	$\nu_4+\nu_6+\nu_7$	A′
M_S	3137	3145	3132	$\nu_3+\nu_4$	A′
M_T	3184	3191	3182	$\nu_1+\nu_7$	A′
M_U	3529	3540	3525	$2\nu_3$	A′
trans-DCOOD					
M_A	1146	1149		$\nu_6(^{13}C)$	A′
M_B	1690	1698		$2\nu_8(^{13}C)/\nu_3(^{13}C)$	A′
M_C	1720	1723	1717	$\nu_6+\nu_7$	A′
M_D	2073	2074	2065	$2\nu_4$	A′
M_E	2108	2110	2106	$\nu_5+\nu_6$	A′
M_F	2126	2129	2123	$\nu_6+2\nu_9$	A′
M_G	2210	2211		$\nu_2(^{13}C)$	A′
M_H	2330	2338	2329	$2\nu_6$	A′
M_I	2647			[d]	A′
M_J	2656	2660	2652	$\nu_5+\nu_6+\nu_7$	A′
M_K	2668	2673	2665	$\nu_5+2\nu_8/\nu_3+\nu_5$	A′
M_L	2704	2707	2702	$\nu_3+\nu_5/\nu_5+2\nu_8$	A′
M_M	2761	2768	2757	$\nu_4+2\nu_8/\nu_3+\nu_4$	A′
M_N	2797	2803	2795	$\nu_3+\nu_4/\nu_4+2\nu_8$	A′
M_O	2888	2898	2888	$\nu_6+2\nu_8/\nu_3+\nu_6$	A′
M_P	2926	2934	2926	$\nu_3+\nu_6/\nu_6+2\nu_8$	A′
M_Q	3181	3188	3178	$\nu_1+\nu_7$	A′

[a] Likely a member of a highly-excited bend-torsion polyad (see pp. 78).
[b] Assignment ambiguous, either $\nu_3+2\nu_7$ of *trans*-HCOOD or ν_2 of *trans*-H^{13}COOD (see pp. 77).
[c] Assignment ambiguous, either $2\nu_6+\nu_7$ or $\nu_4+\nu_5+\nu_7$ (see pp. 77).
[d] Possibly a *trans*-D^{13}COOD band (see p. 77).

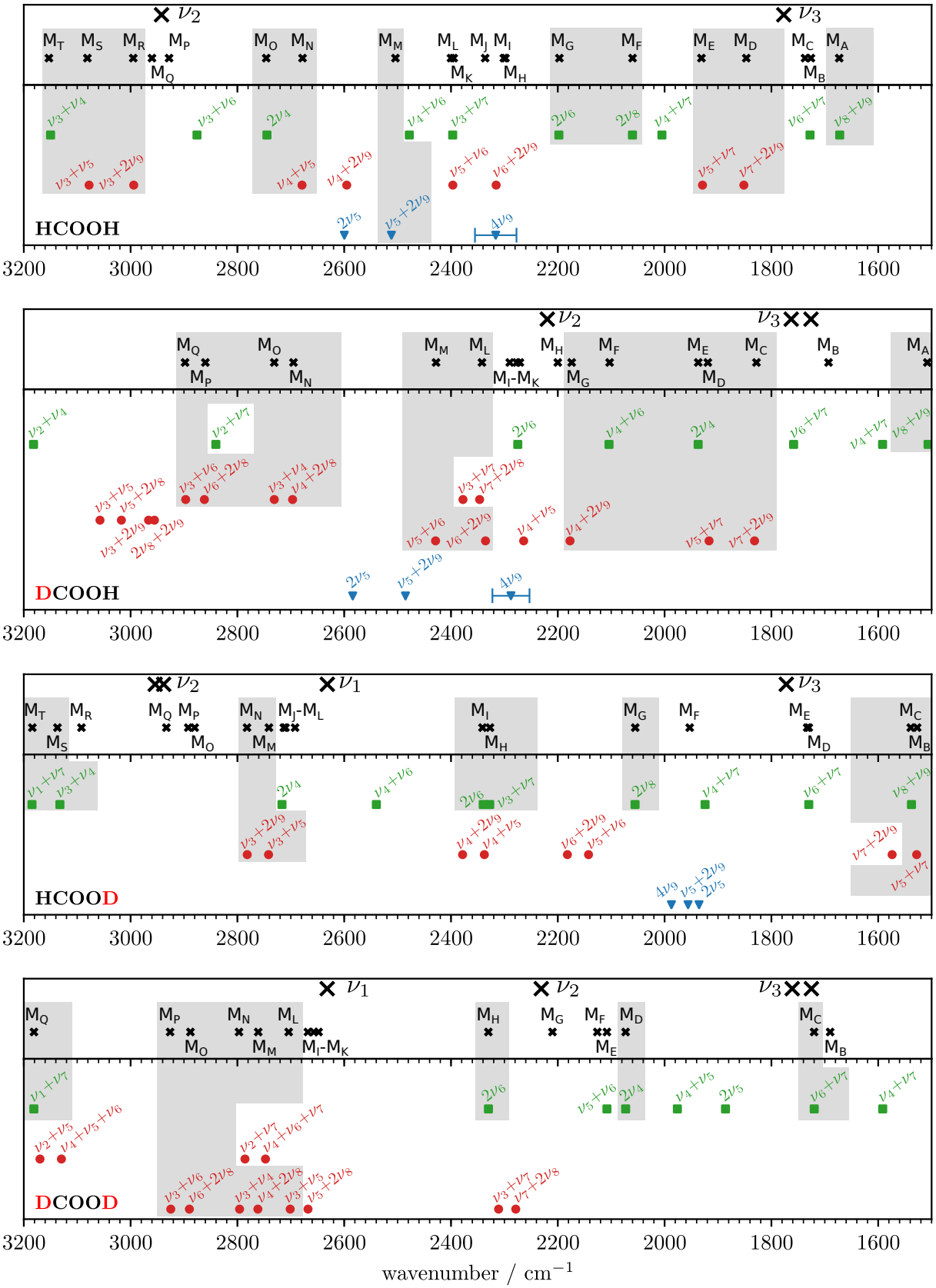

Figure 4.8 Observed M bands in the Raman jet spectra of formic acid and predicted semi-experimental SOF+x band centres for all A′ symmetric two-quantum *trans*-formic acid states and their Fermi resonance partners. Different excitations of resonance polyads (N_i) are reflected in the colour (0 = green, 1 = red, 2 = blue). Straightforward assignments, which are in agreement with CVPT6 results, are greyed out. See text for details.

width of the symbol and thus not shown. Moreover, based on the close proximity of the three $N_5 = 2$ states, these particular SOF+x predictions must be used with caution.[141]

Several M bands in Fig. 4.8 can be assigned right away on the basis of the SOF+x predictions and/or by comparison to other isotopologues. These assignments are highlighted in grey and agree with the previous CVPT6-guided assignments [28]. The remaining M bands are discussed in the following.

M bands below 1500 cm^{-1}. In the HCOOD (M_A) and DCOOD (M_A) spectra (Fig. 3.6, p. 56), a band is observed near the C−O stretch (ν_6) which is shifted from it by −26 and −24 cm^{-1}, respectively. The isotope pattern, i.e. the similar shift, and absence of this band in the HCOOH and DCOOH spectra indicate an assignment to ν_6 of the respective *trans*-formic acid-^{13}C isotopologues. The relative intensities match the natural abundance of carbon-13 and the isotope shift for HCOOD is in excellent agreement with previous observations in a weakly perturbing neon matrix [117].

By comparing the monomer-optimised spectra (Fig. 3.6, p. 56) with the Raman jet spectra at a higher acid concentration (Fig. 6.3, p. 118), it is possible to identify carbon-13 bands of HCOOH and DCOOH that are otherwise hidden underneath hot bands. Monomeric hot and carbon-13 bands are labelled "M_h" and "M_{13}" in the latter, respectively. Since the dimer-optimised spectra have been recorded at much lower nozzle temperatures and are intensity-scaled to dimer bands, monomeric hot and monomeric carbon-13 bands can be distinguished by their scaling behaviour with temperature – faster increasing monomer bands correspond to cold bands.[142]

M bands between 1500 and 1800 cm^{-1}. To the lower-wavenumber side of the C=O stretching fundamentals (ν_3), there is one additional band in the spectrum of each isotopologue which does not correspond to any binary vibrational energy level or higher-excited Fermi resonance partner (Fig. 4.8). Moreover, there are no other higher-excited A′ symmetric energy levels in this spectral region for any H/D isotopologue of *trans*-formic acid. In analogy to the surplus bands

where the former equation incorporates no resonance effects (even x is deperturbed). The bend-torsion resonance effectively pushes $4\tilde{\nu}_9$ towards lower wavenumbers, thus 2355 cm^{-1} can be regarded as an upper-bound limit whereas the lower-bound is estimated from the difference without and with resonance effects, 2355 − (2433 − 2355) = 2277 cm^{-1}. The SOF+x prediction shown in Fig. 4.8 and Table 4.3 is the average of these limits with error bars extending from 2277 to 2355 cm^{-1}. The same procedure is carried out for $4\nu_9$ of *trans*-DCOOH and *trans*-HCOOD.

141 With increasing quantum numbers in the bend-torsion polyad, the off-diagonal coupling elements increase (Eq. 2.37, p. 21). Defining $W = \phi_{5,9,9}/4$, the lower-triangular parts of the VPT2+F Hamiltonians take the following forms:

$$\frac{\mathbf{H}_{N_5=1}}{hc} = \begin{pmatrix} (\nu_5)^* & \\ W & (2\nu_9)^* \end{pmatrix} \qquad \frac{\mathbf{H}_{N_5=2}}{hc} = \begin{pmatrix} (2\nu_5)^* & & \\ \sqrt{2}W & (\nu_5+2\nu_9)^* & \\ 0 & \sqrt{6}W & (4\nu_9)^* \end{pmatrix}$$

As long as bend-torsion states are not perturbed by other accidental resonances, we would expect the maximum separation of states to increase from $N_5 = 1$ to $N_5 = 2$. The SOF+x predictions in Fig. 4.8 become suspiciously close in HCOOD. This could be indicative of a sequence change from $N_5 = 1$ to $N_5 = 2$, i.e. $4\tilde{\nu}_9$ moving below $2\tilde{\nu}_5$, which cannot be described in this simple model.

142 Below 1500 cm^{-1}, two such *trans*-formic bands are observed in the HCOOH spectrum (1095 and 1295 cm^{-1}) and one in the DCOOH spectrum (1128 cm^{-1}). The two bands at 1095 and 1128 cm^{-1} are easily identified as ν_6 of *trans*-H^{13}COOH and *trans*-D^{13}COOH, respectively. The H^{13}COOH band centre is in excellent agreement with the available high-resolution band centre (1095.40 cm^{-1}, Refs. [242, 243]). In analogy, the band at 1295 cm^{-1} can be identified as the OH in-plane bend (ν_5) of *trans*-H^{13}COOH. The previously reported gas phase band centre (1206.7 cm^{-1}, Ref. [244]) must be reassigned to $2\nu_9$ of *trans*-H^{13}COOH in light of the $\nu_5 \leftrightarrow 2\nu_9$ label switch.

near ν_6, the additional band for each isotopologue can be assigned to the respective carbon-13 species. In the HCOOH and HCOOD spectra, the carbon-13 ν_3 band is close to $\nu_6+\nu_7$ of the carbon-12 isotopologue. By comparison of the observed hot bands near ν_6 and experimentally available carbon-13 shifts, $\nu_6+\nu_7$ can be assigned to the respective lower-wavenumber band in the HCOOH (M_B) and HCOOD spectrum (M_D).[143] The assignments of the carbon-13 bands in the DCOOH and DCOOD spectra (both M_B), on the other hand, are clear. The substantial isotope shifts indicate that the $\nu_3/2\nu_8$ resonance persists in *trans*-D^{13}COOH and *trans*-D^{13}COOD and the observed carbon-13 bands correspond to the lower-wavenumber pair of this resonance doublet whereas the higher-wavenumber band is most likely hidden underneath the carbon-12 doublet.[144]

M bands between 1800 and 2600 cm^{-1}. Moving beyond the ν_3 fundamental and climbing the spectral ladder up to 2600 cm^{-1}, the onset of the O–D stretching band (ν_1), there are clusters of bands in the HCOOH (M_H-M_L), DCOOH (M_H-M_K), and DCOOD spectra (M_E-M_G) and one single band in the HCOOD spectrum (M_F) that require a detailed discussion. The following discussion is sorted backwards, starting with HCOOD.

On the basis of the visualised SOF+x predictions (Fig. 4.8), one could ascribe M_F of HCOOD to a transition into a state in the $N_5 = 2$ polyad. The CVPT6 energy levels in Table D.6 confirm this and indicate an assignment of M_F to the OD bending overtone $2\nu_5$, as opposed to $\nu_5+2\nu_9$ as indicated by SOF+x. It should be noted that SOF+x fails in reproducing the correct sequence $\tilde{\nu}_5+2\tilde{\nu}_9 > 2\tilde{\nu}_5 > 4\tilde{\nu}_9$ because the relative position of the two overtones, $2\nu_5$ and $4\nu_9$, is inverse to the energetic order of ν_5 and $2\nu_9$ (see note 141, p. 73).

For DCOOD, SOF+x suggests the assignment of M_E to $\nu_5+\nu_6$ which is confirmed by CVPT6. Moreover, inspection of the CVPT6 list of A′ symmetric energy levels in this region shows that M_F (2126 cm^{-1}) corresponds to $\nu_6+2\nu_9$ (Table D.7). Note that $\nu_6+2\nu_9$ was not included in Fig. 4.8 because of the weakening of the OD bend-torsion resonance in *trans*-DCOOD (pp. 68). Indeed, the 3:2 intensity ratio of M_E and M_F rather indicates direct intensity gain from the nearby ν_2 fundamental than resonance-mediated intensity transfer due to a strengthening of the bend-torsion resonance which remains similarly weak between $\nu_5+\nu_6$ and $\nu_6+2\nu_9$. The last unassigned DCOOD band in this spectral region (M_G) does not correspond to any *trans*-DCOOD energy level of A′ symmetry which similarly applies to the DCOOH band M_H (cf. Tables D.5 and D.7). Considering that both these bands are red-shifted relative to the respective C–D fundamental (ν_2), a carbon-13 assignment appears very plausible for this particularly Raman-active mode. Indeed, the harmonic carbon-13 red-shift of ν_2 is 19-20 cm^{-1} for both isotopologues on the TM-

[143] For HCOOH, the assignment of $\nu_6+\nu_7$ to M_B is clear in view of computed CVPT6 energy levels (Table D.4) and the ν_6 hot bands where $\nu_6+\nu_7-\nu_7$ can unambiguously be assigned (pp. 83). With M_B assigned to $\nu_6+\nu_7$, M_C can be ascribed to ν_3 of *trans*-H^{13}COOH. Note that an alternative assignment of M_C to $\nu_6+\nu_9$ (A″) can be ruled out since all M bands are polarised, thus totally symmetric. The resultant carbon-13 shift of −39 cm^{-1} is in excellent agreement with the observed −40 cm^{-1} in the thermal gas phase and in a neon matrix [117, 244]. In analogy to HCOOH, M_D (1730 cm^{-1}) is ascribed to $\nu_6+\nu_7$ of *trans*-HCOOD and M_E (1733 cm^{-1}) to ν_3 of *trans*-H^{13}COOD. These assignments are commensurable with respect to the carbon-13 shift which is −39 cm^{-1} for HCOOH and HCOOD and the assignment of $\nu_6+\nu_7-\nu_7$ in the HCOOD spectrum (pp. 83). The rotational fine structure of the $\nu_6+\nu_7$ band has been investigated in the past and three band centres (different effective fit Hamiltonians) have been published, 1735.27 [245], 1735.81 [246], and 1732.08 cm^{-1} [228]. The Raman jet band centre agrees within the error bars of ±2 with the most recent value [228].

[144] A harmonic estimate using the TM-PES shows that the ω_3 red-shift (37-38 cm^{-1}) is quantitatively matched by the $2\omega_8$ red-shift (36 cm^{-1}) for both C–D isotopologues of *trans*-formic acid when replacing carbon-12 with carbon-13. By transferring the experimental resonance splitting from the carbon-12 to the carbon-13 isotopologues, we can estimate the approximate positions of the unobserved higher-wavenumber bands: 1762 + (1693 − 1725) = 1730 cm^{-1} (*trans*-D^{13}COOH) and 1761 + (1690 − 1725) = 1726 cm^{-1} (*trans*-D^{13}COOD). For comparison, the lower-wavenumber band of the resonance doublet is located at 1725 cm^{-1} in the carbon-12 isotopologues.

PES in excellent agreement with the observed red-shifts for M_H (DCOOH, 19 cm^{-1}) and M_G (DCOOD, 21 cm^{-1}). Remembering that ν_2 of *trans*-DCOOD is resonance-perturbed (pp. 64), the similarity of the carbon-13 shift across both C – D isotopologues indicates that the resonance between ν_2 and $\nu_4+\nu_6$ persists in *trans*-D^{13}COOD which is confirmed by CVPT6.

With M_H in the DCOOH spectrum assigned, we can turn to the assignments of the remaining DCOOH bands (M_I-M_K). SOF+x indicates plausible assignments to $\nu_4+\nu_5$, $2\nu_6$, and $4\nu_9$, respectively, which are confirmed by CVPT6. It is noteworthy that even the relative sequence of the three bands is correctly predicted by SOF+x. Most crucial is the assignment[145] of M_J to $2\nu_6$ as the assignments of M_I and M_K are then trivial based on their large wavenumber separation (19 cm^{-1}). Note that $4\nu_9$ and $\nu_6+2\nu_9$ are predicted to be in resonance.

The assignments in this spectral region for DCOOH and HCOOD facilitate the assignment of the remaining HCOOH bands M_H-M_L. M_K (2395 cm^{-1}) and M_L (2400 cm^{-1}) can unambiguously be ascribed to $\nu_3+\nu_7$ and $\nu_5+\nu_6$, respectively – an inverse assignment is not compatible with the observed hot band structure near ν_3 and ν_5 (see Section 4.4). The list of candidates for the remaining three HCOOH bands (M_H-M_J) is clear in light of the additional symmetry information. After exclusion of A″ symmetric states, which are not compatible with the observed polarisation of the bands, this leaves only four possible vibrational states in this spectral region: $\nu_7+\nu_8+\nu_9$, $4\nu_9$, $\nu_6+2\nu_9$, and $\nu_6+2\nu_7$ – the next higher and lower A′ symmetric levels are $2\nu_6$ (2197 cm^{-1}, M_G) and $\nu_3+\nu_7$ (2395 cm^{-1}, M_K). SOF+x correctly rules out $\nu_6+2\nu_7$ which is expected above 2350 cm^{-1} but for the individual assignments of M_H-M_J, the CVPT6 results must be consulted. The SOF+x estimates of $\nu_6+2\nu_9$ and $4\nu_9$ are near-isoenergetic and located halfway in-between the observed band centres, indicative of an accidental near-degeneracy. Indeed, CVPT6 predicts a near 1:1 resonance between $\nu_6+2\nu_9$ and $4\nu_9$ (states 30 and 31, Table D.4). In light of this, M_I is assigned to $\nu_7+\nu_8+\nu_9$ which is the lowest-intensity band out of the three. The CVPT6 eigenvector coefficients of $\nu_7+\nu_8+\nu_9$ indicate an accidental and weak resonance with the $4\nu_9$ and $\nu_6+2\nu_9$ doublet which might explain the absence of $\nu_7+\nu_8+\nu_9$ from the Raman spectra of deuterated formic acid. In analogy to DCOOH, where $4\nu_9$ is below $\nu_6+2\nu_9$ (M_K and M_L), M_H of HCOOH is primarily ascribed to $4\nu_9$ but it must be stressed that $4\nu_9$ and $\nu_6+2\nu_9$ should rather be treated as a quantum doublet in HCOOH.

4.3.2 Excursus: The OH bend-torsion polyad at $N_5 = 2$ – involvement of the C – O stretch

The preceding analysis showed that many HCOOH combination/overtone bands are observed in the Raman spectra between 2200 and 2600 cm^{-1} (Table 4.3). This is quite remarkable given that for deuterated isotopologues – which have a higher density of vibrational states – clusters of bands are usually found in the vicinity of fundamentals. For most observed bands, we can rationalise their visibility in the bright state picture through wavefunction overlap from the bright fundamentals [28]. Fig. 4.8 shows that in this particular spectral region, there is the interesting situation of different N_5 polyads intersecting in HCOOH, more specifically $\{n_4, n_6, N_5\} = \{1, 0, 1\}$, $\{0, 1, 1\}$, and $\{0, 0, 2\}$. Before continuing with the assignment of M bands above 2600 cm^{-1}, it is instructive to have a closer look at these polyads, especially with regard to the strong mixing of $4\nu_9$ and $\nu_6+2\nu_9$ – members of $\{0, 0, 2\}$, and $\{0, 1, 1\}$, respectively – and its implications for higher excitations in the bend-torsion polyad.[146]

[145] A previous high-resolution IR study locates the $2\nu_6$ band centre of *trans*-DCOOH at 2254.24 cm^{-1} [226] which is more than 20 cm^{-1} below the Raman jet assignment and CVPT6 predictions. The analysis of the experimental data for the three other H/D isotopologues and CVPT6 results for *trans*-DCOOH in Section 4.5 independently lead to the conclusion that the $2\nu_6$ band centre of *trans*-DCOOH is between 2270 and 2280 cm^{-1}.

[146] The following analysis closely follows the discussion in Section IV.C of Ref. [28]

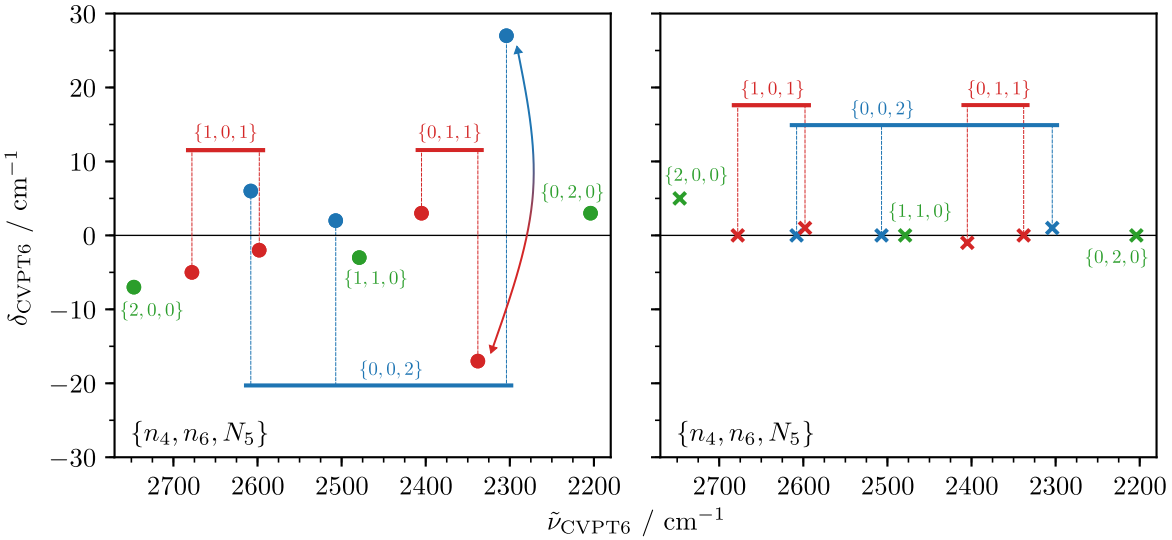

Figure 4.9 Eigenvalue differences between the full CVPT6 Hamiltonian and either (left) the CVPT6 OH bend-torsion polyad Hamiltonian or (right) the fully coupled CVPT6 10-state Hamiltonian plotted against the full CVPT6 wavenumbers for *trans*-HCOOH.

The presence of significant mixing between states that share the polyad quantum number N_5 makes it challenging to identify additional resonance interactions between zeroth-order states. One way to circumvent this issue is to examine the couplings in the polyad eigenstate representation where all the couplings between states sharing common $\{n_1, ..., n_4, N_5, n_6, ..., n_8\}$ quantum numbers are subsumed into the zeroth-order CVPT6 effective Hamiltonian. The 10×10 Hamiltonian matrix in this representation is visualised in Fig. 4.9 for states that satisfy the condition $2 = n_4 + n_6 + N_5$.[147] Note that the diagonal values of this 10-state Hamiltonian are simply the eigenvalues of the polyad eigenstate representation. The ordinate represents the wavenumber difference between the eigenvalues of the full CVPT6 Hamilton matrix and either the polyad eigenvalues (left, disks) or those of the 10×10 effective Hamilton matrix (right, crosses). The blue points in Fig. 4.9 correspond to $N_5 = 2$, the red points correspond to $N_5 = 1$, and the green states have $N_5 = 0$. The smaller the vertical distance to zero in Fig. 4.9, the better the polyad or 10-state effective Hamilton representation.

There are two important results of the N_5 polyad representation. First, the similarities between CVPT6 eigenvalues of the full and effective 10×10 Hamiltonian ($\pm 1\,\mathrm{cm}^{-1}$) indicate that there is only minor coupling between the states shown in Fig. 4.9 and all other states of the full CVPT6 Hamilton matrix, with one exception; the C–H bending overtone $2\nu_4$ ($\{2, 0, 0\}$) is missing contributions from the C–H stretch (ν_2). Upon inclusion of ν_2 into the effective Hamiltonian, the $\{2, 0, 0\}$ eigenvalue agrees to within $1\,\mathrm{cm}^{-1}$ with the CVPT6 value. Finally, the diagonal elements, i.e. polyad eigenvalues, match reasonably well with the eigenvalues of the 10×10 matrix or the full CVPT6 Hamiltonian, with only two exceptions. The exceptions are indicated by the double-headed arrow which result from an isolated resonance between the lowest energy states of the $\{0, 0, 2\}$ and $\{0, 1, 1\}$ polyads. The cubic term that mediates this interaction is the same that couples ν_6 and $2\nu_9$ in the original normal mode representation. The current representation is an excellent basis for describing the coupling.

Inspection of CVPT6 eigenvectors at higher excitation wavenumbers indicates that the C–O stretch (ν_6) remains an integral part of the OH bend-torsion polyad for $N_5 \geq 2$. Thus, Eq. 4.6

[147] The effective 10×10 CVPT6 Hamiltonian matrix is shown in the supplementary material of Ref. [28]

(p. 67) should be modified to include the C–O stretch starting with[148] $N_5 = 2$:

$$N_{56} = n_5 + n_6 + \frac{n_9}{2}. \tag{4.7}$$

4.3.3 M bands above 2600 cm^{-1}

M bands between 2600 and 2800 cm^{-1}. Fig. 4.8 shows that the majority of the observed DCOOD bands above 2600 cm^{-1} correspond to different $N_3 = 1$ polyads. By comparing the splittings for different $\{N_3, n_i\} = \{1, 1\}$ pairs, e.g. ν_3+ν_6 and ν_6+2ν_8, we can safely assign M_K to $\{N_3, n_5\} = \{1, 1\}$. The two weaker bands at 2647 cm^{-1} (M_I) and 2656 cm^{-1} (M_J) are hidden underneath the rotational contour of the OD stretch (ν_1) and are unveiled by depolarisation measurements (Fig. 3.3, p. 53). Inspection of SOF+x predictions for other ternary and quaternary energy levels (not shown) reveals a possible assignment of M_J to ν_5+ν_6+ν_7. CVPT6 confirms this assignment and further indicates that M_I most likely does not correspond to a vibrational transition in *trans*-DCOOD (cf. Table D.7). An assignment to ν_1 of *trans*-D^{13}COOD would be surprising in light of the pronounced blue-shift (+16 cm^{-1}). However, it is noted that CVPT6 does predict an unusual sensitivity of this mode towards carbon-13 exchange (cf. Tables D.2 and D.7) and very strong resonance perturbations which are most likely the cause. Indeed such perturbations in the carbon-13 analogue are to be expected based on the available carbon-12 data in this spectral region.[149]

Lastly, there are three HCOOD bands (M_J-M_L) whose assignments deserve a few comments. The most intensive band at 2713 cm^{-1} (M_L) corresponds to 2ν_4. The band centre compares well with the previously reported Raman band centre at 2714 cm^{-1} [118]. Out of all possible A′ symmetric ternary states, ν_5+ν_6+ν_7 and ν_6+ν_8+ν_9 are the most plausible assignments for the two weaker bands (M_J and M_K) given that also ν_5+ν_7 and ν_8+ν_9 are observed at lower wavenumbers (M_B and M_C). SOF+x band positions (2692 and 2708 cm^{-1}) are in excellent agreement with the experimental band centres (2692 and 2710 cm^{-1}). These assignments are supported by CVPT6 energy levels which show that the only other A′ symmetric state in this spectral region, 3ν_7+2ν_9, is expected halfway between M_J and M_K when including the expected error (Eq. 4.1).

M bands between 2800 and 3200 cm^{-1}. The remaining M bands below 3200 cm^{-1} are located near the C–H stretching fundamentals (ν_2) of HCOOH and HCOOD. Meyer was able to unearth two peaks at 2928 cm^{-1} (M_P) and 2960 cm^{-1} (M_Q) that are hidden underneath the pronounced rotational contour of ν_2 in the Raman spectrum of HCOOH [86, p. 54]. The lower-wavenumber band (M_P) corresponds to the C–H stretching fundamental of *trans*-H^{13}COOH.[150] A survey of the SOF+x predictions for all three- and four-quantum energy levels indicates that there is no possible *trans*-HCOOH assignment for M_Q. CVPT6 on the TM-PES predicts only one A′ symmetric energy level between 2940 and 2980 cm^{-1}, ν_7+4ν_9. This assignment is further corroborated by the bright state model since ν_7+4ν_9 has a squared wavefunction contribution from

[148] The hot band analysis for ν_6 reveals substantial involvement of the C–O stretch already starting with $N_5 = 1.5$ in *trans*-DCOOH (pp. 83).

[149] In *trans*-D^{13}COOD, the CVPT6 eigenvectors indicate strong mixing between ν_1 and ν_5+2ν_8 which, in turn, belongs to a polyad that includes ν_3+ν_5 and ν_5+ν_6+ν_7. All three combination states are observed in the Raman jet spectrum of DCOOD (M_J-M_L). Neglecting the sensitivity of ν_5 to carbon-13 isotopic exchange, we can approximate the isotope shift of M_J (2668 cm^{-1}, ν_5+2ν_8) by transferring the carbon-13 shift of 2ν_8 which is experimentally known. This yields 2668+(1690−1725) = 2633 cm^{-1} for ν_5+2ν_8 for *trans*-D^{13}COOD which is just slightly above the ν_1 fundamental of *trans*-DCOOD at 2632 cm^{-1}. A near-degeneracy in *trans*-D^{13}COOD thus appears very plausible.

[150] The carbon-13 red-shift in the Raman spectrum (14 cm^{-1}) agrees with IR values in a weakly perturbing neon matrix (14.5 cm^{-1}, Ref. [117]) and high-resolution thermal gas phase (11.3 cm^{-1}, Ref. [244]). The absolute band position deviation for ν_2 of *trans*-H^{13}COOH between IR gas phase [244] and Raman jet amounts to 1 cm^{-1}.

the C–H stretch that is higher than that of $\nu_4+\nu_5$ which is also observed in the Raman spectrum (M_N).[151]

The three HCOOD bands M_O-M_Q cannot be assigned based on the energy levels included in Fig. 4.8. Again, we turn to CVPT6 energy levels which show that this spectral region is dominated by different N_5 polyads. Overall, there are six A′ symmetric energy levels in this region (states 92-97, Table D.6). When correcting the expected error using Eq. 4.1, $\nu_4+\nu_7+2\nu_9$ is the best match for M_Q (2933 cm^{-1}) which is further corroborated by a large bright state coefficient on the TM-PES (8.4%). M_O cannot safely be assigned to $\nu_3+2\nu_7$ of *trans*-HCOOD as the possibility of an alternative carbon-13 assignment cannot be ruled out.[152] For M_P, there are two equally plausible candidates, $2\nu_6+\nu_7$ and $\nu_4+\nu_5+\nu_7$. The former is preferred based on the bright state model[153] but the latter could plausibly gain intensity indirectly through its resonance with $\nu_4+\nu_7+2\nu_9$ (M_Q). The assignments of M_O and M_P are thus left open in Table 4.3.

M bands above 3200 cm^{-1}. All remaining M bands above 3200 cm^{-1} are observed in the O–H stretching (ν_1) spectra of HCOOH and DCOOH, except for one band in the HCOOD spectrum (M_U). M_U most likely corresponds to $2\nu_3$ but its high intensity, despite no nearby bright fundamental, and its simultaneous absence in the HCOOH spectrum, in spite of a nearby fundamental to gain intensity from, is puzzling.[154] While chemical impurity as the source of M_U cannot be ruled out entirely, it appears to be very unlikely – a similar band is neither observed in the HCOOH spectrum nor that of the deuterated isotopologues.

In the HCOOH spectrum (Fig. 3.1, p. 51), ν_1 and $\nu_2+\nu_7$ are framed by two much weaker bands, labelled M_U and M_V. Except for the anticipated disappearance of $\nu_2+\nu_7$, the corresponding DCOOH spectrum is very similar to that of HCOOH. The two M bands are incidentally also labelled M_U and M_V. Three additional, much weaker bands well below ν_1 (M_R-M_T) are found in the DCOOH spectrum between 3352 and 3421 cm^{-1}.

Starting with M_U and M_V, the combined isotope information rules out any involvement of the C–H/D stretching and bending modes (ν_2, ν_4, ν_8). The strong resonance between ν_3 and $2\nu_8$ in DCOOH also makes ν_3 an unlikely candidate, leaving ν_5, ν_6, ν_7, and ν_9. From the A′ symmetry constraint we can further conclude that $\frac{n_9}{2} \in \mathbb{N}$. With $2\tilde{\nu}_9 \approx 2\tilde{\nu}_7 \approx \tilde{\nu}_6 \approx \tilde{\nu}_5$ and $3\tilde{\nu}_5 \approx \tilde{\nu}_1$, the two perturber states very likely satisfy the condition

$$3 = n_5 + n_6 + \frac{n_7}{2} + \frac{n_9}{2}. \tag{4.8}$$

The involvement of the OCO bend (ν_7) appears questionable based on its weak involvement with $N_5 = 1$ and $N_{56} = 2$ polyads while the detection of $\nu_7+4\nu_9$ certainly begs the question if starting

[151] This model predicts that two additional bands near M_P (2928 cm^{-1}), $\nu_6+\nu_7+2\nu_9$ and $2\nu_7+\nu_8+\nu_9$, should have sufficient intensity to be observed. They are coupled to $\nu_7+4\nu_9$ and one can easily see the similarity to a similar polyad near 2300 cm^{-1} that was discussed above. $\nu_6+\nu_7+2\nu_9$ and $2\nu_7+\nu_8+\nu_9$ are not observed and are probably hidden underneath the hot bands.

[152] CVPT6 predicts that the Fermi resonance between ν_2 and $\nu_3+\nu_6$ is weakened but persists in *trans*-H^{13}COOD. As a result of carbon-13 exchange, the ν_2 band centre of *trans*-H^{13}COOD is expected to approximately coincide with that of *trans*-HCOOD at 2938 cm^{-1}, which, therefore, cannot be separated from the main isotopologue at the present low resolution. With *trans*-H^{13}COOD Raman jet band centres of ν_6 and ν_3 available (M_A and M_E), it is possible to estimate an upper-limit for $\nu_3+\nu_6$ in *trans*-HCOOD, 1733 + 1150 = 2883 cm^{-1}, which is near the error-corrected CVPT6 prediction for $\nu_3+2\nu_7$ of *trans*-HCOOD (2881 cm^{-1}, both potentials).

[153] The squared wavefunction overlap from the zeroth-order C–H stretch is 0.1% for $\nu_4+\nu_5+\nu_7$ and 0.5% for $2\nu_6+\nu_7$ (CVPT6 on the TM-PES).

[154] Oswald *et al.* observed $2\nu_3$ in the FTIR jet spectra of HCOOH and HCOOD which is consistent with their interpretation of only weak resonance interaction between ν_1 and $2\nu_3$ in *trans*-HCOOH [126]. The Raman band centre of M_U (3529 cm^{-1}) agrees with the IR band centre of $2\nu_3$ within 1 cm^{-1} when interpreting the reported [126] maxima of the *trans*-HCOOD band as *P* and *R* branch maxima, $2\tilde{\nu}_3 = (3531 + 3526)/2 = 3529\ cm^{-1}$.

with $N_{56} = 3$, ν_7 perhaps becomes involved in the extended OH bend-torsion polyad. The currently available experimental and computational data do not permit either conclusion. If ν_7 is not involved, the above condition reduces to the extended OH bend-torsion polyad ($N_{56} = 3$).

The assignments of the three other DCOOH bands (M_R-M_T) certainly support the hypothesis of an involvement of the extended OH bend-torsion polyad. Starting with the most intensive band (M_R, 3352 cm^{-1}), the computed CVPT6 eigenvalues in Table D.5 indicate only two A′ symmetric energy levels, ν_2+ν_6 and ν_3+ν_4+ν_7, as possible assignments. Bearing in mind that all transitions that involve ν_3 energy levels are resonance-doubled in DCOOH, the latter can be ruled out since the second band, which is expected near 3320 cm^{-1}, is missing. The assignment of M_S to ν_6+4ν_9 is clear with no other A′ symmetric candidate nearby (Table D.5). Lastly, M_T can either be assigned to 3ν_6 or ν_4+2ν_7+2ν_9. 3ν_6 appears much more plausible in light of a predicted resonance between ν_6+4ν_9, 3ν_6, and ν_2+ν_6. Note that ν_6+4ν_9 and 3ν_6 are both members of the extended OH bend-torsion polyad $N_{56} = 3$.

Returning to the assignment of M_U and M_V, inspection of the CVPT6 term values and squared leading eigenvector coefficients in Tables D.4 and D.5 shows that we can at best narrow down the list of suspects. Several states in this spectral region are strongly coupled – especially through the ν_5/2ν_9 resonance – as evidenced by comparably small leading eigenvector coefficients (cf. Tables D.4-D.5). It appears more promising to subsume into the N_5 or N_{56} polyad representation. Currently, the strong OH bend-torsion resonance does not allow the identification of other important couplings which are ‘smeared out’.

It is worth pointing out similarities to the O–H stretching Raman spectrum of *trans*-propiolic acid [42], a related carboxylic acid where the carbon-bound H atom is replaced by an acetylenic –C≡C–H group. The O–H stretching fundamental of *trans*-propiolic acid is also accompanied by an intensive, lower-wavenumber satellite that corresponds to a non-binary combination/overtone band and two weaker bands that are located at the higher-wavenumber side of the O–H stretching *Q* branch [42, Fig. 3A]. Interestingly, there is evidence for the OH torsion resonance to persist in propiolic acid but change its resonance partner from the OH in-plane bend (ν_5 in formic acid) to the C–O stretch (ν_6 in formic acid).[155] The OH bend, in turn, becomes near-degenerate with a combination band that has one quantum each in the out-of-plane bending vibration of the OCO group and the OH torsion. While the vibrational characterisation of the *trans*-propiolic acid fundamentals has only recently been completed and the combination/overtone manifold only begun to be explored (see Ref. [42] and references cited therein), the initial data in Ref. [42] point at a similarly complex involvement of the OH torsion in the internal dynamics of *trans*-propiolic acid.

4.4 Assignment of hot bands

In this section, the assignment of observed hot bands, labelled “H” (see Chapter 3), is discussed. The band centres and assignments of well-resolved hot bands are listed in Table 4.4. These hot bands either correspond to isomeric *cis* fundamentals or non-isomeric hot band transitions from thermally populated vibrational *trans* states. Based on considerations outlined in Section 2.4.2 (see paragraph on hot bands), the assignments here are guided by simulated hot band shifts using CVPT6 energy levels in Tables D.4-D.7. In addition, CVPT2 anharmonicity constants from Table D.3 are consulted since at second-order of perturbation theory, the hot band shift can directly be related to the anharmonicity constants (Eqs. 2.71-2.76, p. 37).

[155] The assignment of the *trans*-propiolic band at 1118 cm^{-1} that is in resonance with the C–O stretch (1154 cm^{-1}) could not be finally clarified in Ref. [42]. VPT2 calculations presented in Ref. [42] indicate an assignment of 1118 cm^{-1} either to the OH torsion overtone or a CCO bending combination level.

Table 4.4 Band list ($\tilde{\nu}_0$, in cm^{-1}) of formic acid monomer hot bands in the monomer-optimised Raman jet spectra (Chapter 3). The hot band shift is referenced to the nearest *trans*-formic acid fundamental and measured directly from the separation of the experimental band centroids. $\tilde{\nu}_f$ is the experimentally-derived term value of the upper vibrational level that is obtained by adding the wavenumber of the lower level ($\tilde{\nu}_i$). Experimental values for $\tilde{\nu}_i$ are taken from Table 3.2 (p. 49). Note that vibrational levels are labelled according to Table 2.2 (p. 35).

		Raman jet			Hot band shift			Exp.	
		$\tilde{\nu}_0$	Rotamer	Assignment ($\nu_f-\nu_i$)	Obs.	TM-PES	RC-PES	$\tilde{\nu}_f$	$\tilde{\nu}_i$
HCOOH	H_A	1093	*cis*	ν_6	−11	−12	−9	1093	
	H_B	1097	*trans*	$\nu_6+\nu_9-\nu_9$	−7	−7	−7	1738	640.73
	H_C	1101	*trans*	$\nu_6+\nu_7-\nu_7$	−4	−2	−4	1727	626.17
	H_D	1284	*trans*	$2\nu_5-2\nu_9/\nu_5+2\nu_9-2\nu_9$	−22	−20	−18	2505	1220.83
	H_E	1295	*trans*	$\nu_5+\nu_6-\nu_6$	−11	−8	−10	2400	1104.85
	H_F	1310	*trans*	$\nu_5+\nu_9-\nu_9$	4	5	5	1951	640.73
	H_G	1757	*trans*	$2\nu_3-\nu_3$	−19	−20	−18	3534	1776.83
	H_H	1763							
	H_I	1770	*trans*	$\nu_3+\nu_7-\nu_7$	−6	−7	−7	2396	626.17
	H_J	1782	*trans*	$\nu_3+\nu_9-\nu_9/\nu_7+3\nu_9-\nu_9$	6	5	4	2423	640.73
	H_K	1818	*cis*	ν_3	41	39	37	1818	
	H_L	2873	*cis*	ν_2	−69	−62	−65	2873	
	H_M	2925	*trans*	$\nu_2+\nu_8-\nu_8$	−17	−21	−17	3958	1033.47
	H_N	2938	*trans*	$\nu_2+\nu_9-\nu_9$	−4	1	−1	3579	640.73
	H_O	3562							
	H_P	3638	*cis*	ν_1	68	77	68	3638	
DCOOH	H_A	1124	*trans*	$3\nu_9-\nu_9$	−18	−18	−17	1756	631.54
	H_B	1128	*cis*	ν_6	−14	−14	−9	1128	
	H_C	1132							
	H_D	1135							
	H_E	1139	*trans*	$\nu_6+\nu_7-\nu_7$	−4	−4	−4	1760	620.57
	H_F	1147	*trans*	$\nu_6+\nu_9-\nu_9$	5	4	6	1779	631.54
	H_G	1209	*trans*	$\nu_7+2\nu_9-\nu_7$	3	2	1	1830	620.57
	H_H	1276	*trans*	$2\nu_5-2\nu_9/\nu_5+2\nu_9-2\nu_9$	−23	−20	−19	2482	1206
	H_I	1286	*trans*	$\nu_5+\nu_6-\nu_6$	−13	−13	−12	2428	1142.31
	H_J	1305	*trans*	$\nu_5+\nu_9-\nu_9$	6	7	6	1937	631.54
	H_K	1705	*trans*	$3\nu_8-\nu_8$	−56	−53	−56	2578	873.38
	H_L	1768	*trans*	$\nu_3+\nu_8-\nu_8$	6	6	8	2641	873.38
	H_M	1790	*cis*	ν_3	28	26	20	1790	
	H_N	2167	*cis*	ν_2	−52	−48	−50	2167	
	H_O	2208	*trans*	$\nu_2+\nu_4-\nu_4$	−11	−13	−12	3179	970.89
	H_P	2211	*trans*	$\nu_2+\nu_8-\nu_8$	−8	−10	−8	3084	873.38
	H_Q	2217	*trans*	$\nu_2+\nu_9-\nu_9$	−3	−3	−3	2849	631.54
	H_R	3560							
	H_S	3566							
	H_T	3635	*cis*	ν_1	66	73	65	3635	
HCOOD	H_A	904	*cis*	ν_5	−67	−73	−64	904	
	H_B	925	*trans*	$4\nu_9-\nu_5$	−47	−48	−48	1898	972.85
	H_C	939	*trans*	$3\nu_9-\nu_9$	−32	−33	−33	1447	508.13
	H_D	968	*trans*	$\nu_5+\nu_7-\nu_7$	−4	−3	−3	1526	558.27
	H_E	980	*trans*	$2\nu_5-\nu_5$	8	9	9	1953	972.85
	H_F	1005	*trans*	$\nu_5+\nu_9-\nu_9$	33	32	32	1513	508.13
	H_G[a]	1163	*cis*	ν_6	−13	−16	−17	1163	
	H_H[a]	1167	*trans*	$2\nu_6-\nu_6$	−9	−11	−14	2344	1177.09
	H_I	1172	*trans*	$\nu_6+\nu_9-\nu_9$	−4	−4	−3	1680	508.13
	H_I	1172	*trans*	$\nu_6+\nu_7-\nu_7$	−4	−5	−5	1730	558.27
	H_J	1768	*trans*	$\nu_3+\nu_7-\nu_7$	−4	−4	−4	2326	558.27
	H_K	1819	*cis*	ν_3	47	43	44	1819	

continued

Table 4.6 (continued)

		Raman jet			Hot band shift			Exp.	
		$\tilde{\nu}_0$	Rotamer	Assignment ($\nu_f - \nu_i$)	Obs.	TM-PES	RC-PES	$\tilde{\nu}_f$	$\tilde{\nu}_i$
HCOOD	H_L	2625	*trans*	$\nu_1+\nu_7-\nu_7$	−5	−6	−5	3183	558.27
	H_M	2685	*cis*	ν_1	55	53	54	2685	
	H_N	2871	*cis*	ν_2	−66	−65	−64	2871	
	H_O	2930							
	H_P	2934							
	H_Q	2951							
DCOOD	H_A	883	*cis*	ν_5	−62	−66	−60	883	
	H_B	922	*trans*	$3\nu_9-\nu_9$	−23	−24	−26	1414	492.23
	H_C	950	*trans*	$\nu_5+\nu_9-\nu_9$	5	5	6	1442	492.23
	H_D[a]	1156	*cis*	ν_6	−14	−13	−11	1156	
	H_E[a]	1161	*trans*	$2\nu_6-\nu_6$	−10	−9	−11	2332	1170.80
	H_F	1166	*trans*	$\nu_6+\nu_9-\nu_9$	−5	−4	−3	1658	492.23
	H_F	1166	*trans*	$\nu_6+\nu_7-\nu_7$	−5	−5	−5	1720	554.44
	H_G	1704	*trans*	$3\nu_8-\nu_8$	−56	−53	−56	2577	873.2
	H_H	1722	*trans*	$2\nu_8+\nu_7-\nu_7$	−39	−37	−40	2276	554.44
	H_I	1758	*trans*	$\nu_3+\nu_7-\nu_7$	−3	−2	−2	2312	554.44
	H_J	1766	*trans*	$\nu_3+\nu_8-\nu_8$	6	6	8	2639	873.2
	H_K	1789	*cis*	ν_3	28	26	23	1789	
	H_L	2145	*cis*	ν_2	−86	−90	−86	2145	
	H_M	2188	*trans*	$\nu_4+\nu_6+\nu_8-\nu_8$	−43	−44	−42	3061	873.2
	H_N	2191	*trans*	$\nu_4+\nu_6+\nu_9-\nu_9$	−41	−40	−40	2683	492.23
	H_O	2223	*trans*	$\nu_2+\nu_8-\nu_8$	−8	−8	−7	3096	873.2
	H_P	2229	*trans*	$\nu_2+\nu_9-\nu_9$	−3	−3	−2	2721	492.23
	H_Q	2626	*trans*	$\nu_1+\nu_7-\nu_7$	−6	−6	−5	3180	554.44
	H_R	2685	*cis*	ν_1	54	55	54	2685	

[a] These assignments are rather tentative.

Hot bands near the OH/D in-plane bend (ν_5). In the vicinity of the OH bending fundamental of HCOOH (ν_5), there are three hot bands (H_D-H_F).[156] Since all $x_{5,j}$ constants are negative for *trans*-HCOOH (Table D.3), the blue-shift of the most intensive hot band (H_F) is an indication that the upper level might be resonance-perturbed. The N_5 polyad is an obvious candidate and with the aid of the CVPT6 eigenvalues, we can assign H_F to $\nu_5+\nu_9-\nu_9$. H_E can readily be assigned to $\nu_5+\nu_6-\nu_6$ since other $\nu_5+\nu_i-\nu_i$ type hot bands are predicted to be much less shifted from the ν_5 fundamental.[157] H_D (1284 cm^{-1}), on the other hand, might also correspond to a transition between N_5 states because the size of the red-shift exceeds the predicted shifts based on CVPT2 anharmonicity constants by far. An assignment to ν_5 of *cis*-HCOOH can be ruled out which is expected around 1250 cm^{-1}. Comparison of several CVPT6 energy levels that correspond to the $N_5 = 1$ and $N_5 = 2$ polyads, as lower and upper levels, respectively, yields a suitable transition from $2\nu_9$ into the lower-wavenumber level of the strongly coupled pair $2\nu_5/\nu_5+2\nu_9$.

The three hot bands in the ν_5 spectrum of DCOOH (H_H-H_J) are readily assigned by analogy to HCOOH. The fourth DCOOH band near $2\nu_9$ (H_G) can be assigned to $2\nu_9+\nu_7-\nu_7$ since the $3\nu_9-\nu_9$ hot band would be shifted several tens of cm^{-1} away from $2\nu_9$.

The (perhaps most interesting) hot band structure is observed in the vicinity of the OD

[156] H_E might have additional contributions from the ν_5 fundamental of *trans*-$H^{13}COOH$ (p. 73).

[157] In light of a possible accidental near-degeneracy between $\nu_5+\nu_6$ and $\nu_3+\nu_7$ (pp. 74), it should be noted that neither is a hot band observed near ν_5 that could be assigned to $\nu_3+\nu_7-\nu_6$, nor near ν_3 that corresponds to $\nu_5+\nu_6-\nu_7$.

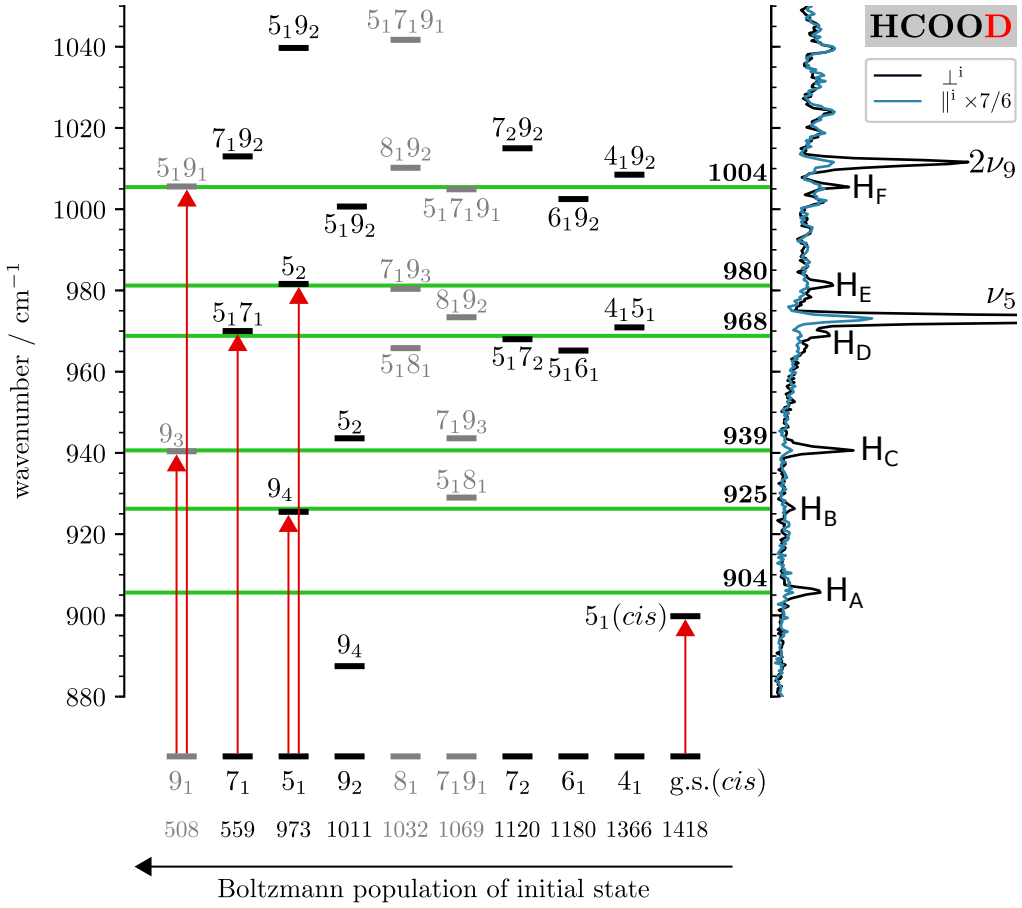

Figure 4.10 Comparison between computed hot band transitions of HCOOD (CVPT6, TM-PES) and observed hot bands in the Raman jet spectrum. The energy levels are labelled "k_m" where the vibrational mode k is indexed by the quanta of excitation m. Note that an isolated resonance that is predicted between 5_18_1 and 7_19_3 couples four states that belong to two different $\nu_5/2\nu_9$ polyads. See text for details.

in-plane bending fundamental of *trans*-HCOOD which spans 100 cm^{-1} with overall six well-resolved, non-overlapping hot bands (H$_A$-H$_F$). Most hot band shifts are in sign and magnitude incompatible with the anharmonicity constants which again indicates the involvement of N_5 polyads. Since ν_5 is the only A′ symmetric bright fundamental in this spectral region, we only need to consider transitions of the type $\nu_5+\nu_i-\nu_i$ and $2\nu_9+\nu_i-\nu_i$ due to the bend-torsion resonance. If the lower level is ν_5 or $2\nu_9$, then all three possible transitions between $N_5 = 1$ and $N_5 = 2$ states have to be considered.

The resultant final energy levels are visualised in Fig. 4.10 for the ten lowest initial vibrational energy levels where the tenth corresponds to the *cis* ground state which can alternatively be seen as a torsionally-excited state. The term values are normalised column-wise by subtracting the term value of the initial energy level at the bottom. Thus, the ordinate axis reflects the transition wavenumbers which can directly be compared to experiment (Fig. 4.10). The symmetry of vibrational states is reflected in the colour (A′ black, A″ grey), however, only A′−A′ and A″−A″ transitions are possible since the observed hot bands are all polarised and thus totally symmetric. The experimental band centres are depicted as green lines. Since the intensities are proportional to the Boltzmann population of the lower level, the transition intensities should decrease from left to right. Consequently, the first match (from left to right) is assigned as the major contributor to a hot band, indicated by a red arrow, while additional contributions cannot be ruled out. Note that the previously discussed weakening of the bend-torsion resonance from *trans*-HCOOD to *trans*-DCOOD (pp. 68) is also reflected in the ν_5 hot band structure of both (cf. Fig. 3.6, p. 56).

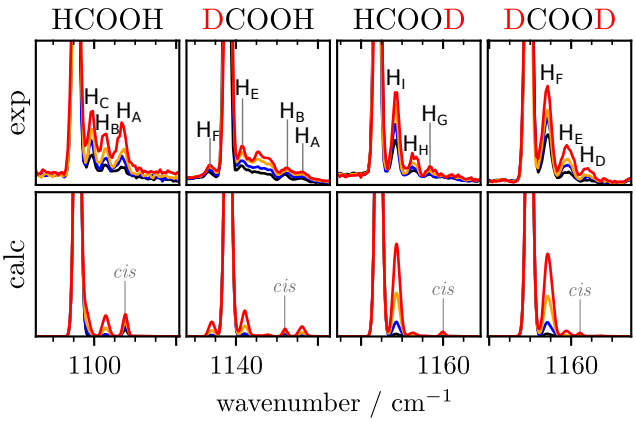

Figure 4.11 Experimental Raman jet and calculated hot band progressions in the vicinity of the C–O stretch (ν_6). To enable comparability of the relative hot band intensities, the limits on the ordinate are set to 1/3 of the maximum intensity of ν_6 for each isotopologue. Wavenumber ticks are separated by 5 cm^{-1}. Adapted from Ref. [28] (published under a Creative Commons Attribution license, CC BY 4.0). (exp) The spectra in a temperature series (373-463 K in uniform steps) are intensity-scaled to the ν_6 fundamental with the lowest intensity. (calc) The ν_6 Raman spectrum is simulated by assigning a linear transition term to the C–O stretch and using CVPT6 energies on the TM-PES. The wavenumber axis is shifted to match the experimental ν_6 band centre. The *trans* fundamental is scaled with 3/20 to reproduce the relative experimental intensities. For the *cis* fundamental, the scaled transition oscillator strength of the *trans* fundamental is multiplied by the appropriate Boltzmann factor and the relative *cis-trans* Raman intensity factor (taken from Table S3 of Ref. [91]). The width of the Gaussian functions is set to $\sigma = \sqrt{0.5\,\mathrm{cm}^{-1}}$ to roughly match experiment.

In contrast to the wealth of hot bands in the HCOOD spectrum that are far apart, only two *trans* hot bands are observed in the DCOOD spectrum (H_B and H_C) that correspond to $3\nu_9-\nu_9$ and $\nu_5+\nu_9-\nu_9$. Contrary to expectations, the former has a much higher intensity than the latter. This could either be an indication of additional hot band contributions or a higher intensity of the $3\nu_9-\nu_9$ transition due to electric anharmonicity. One could point out the same for the HCOOD hot band at 939 cm^{-1} (H_C) but from the data shown in Fig. 4.10, the high intensity of H_C could plausibly be interpreted as $2\nu_5-2\nu_9$ additionally contributing to the observed intensity.

Hot bands near the C–O stretch (ν_6). In the HCOOH spectrum, there are three distinct hot bands near the C–O stretching fundamental (ν_6), which are shifted from it by −11, −7, and −4 (H_A-H_C). Meyer and Suhm ascribed the latter two to $\nu_6+\nu_7-\nu_7$ and $\nu_6+\nu_9-\nu_9$, respectively, and the former to ν_6 of *cis*-HCOOH which profits from an increased Raman scattering cross section relative to ν_6 of *trans*-HCOOH [87].[158] Meyer noted [86] that the assignments in Ref. [96], which put the $\nu_6+\nu_7$ level above $\nu_6+\nu_9$, are not compatible with the hot bands in the Raman spectra. An assignment of $\nu_6+\nu_7$ and $\nu_6+\nu_9$ inverse to Ref. [96], on the other hand, yields hot band shifts that are in excellent agreement with the observed hot band structure. Already in 2018, Richter and Carbonnière proposed such a reassignment, based on an improved root mean square deviation to experiment for their MCTDH results [22] and the ICPH-VCI calculations by Tew and Mizukami [21].

Fig. 4.11 combines the experimental and computational perspectives, displaying the ν_6 hot

[158] In Ref. [91], this assignment was reviewed in light of an error made in Ref. [87] where the shift of $2\nu_6-\nu_6$ relative to ν_6 was assumed to be $x_{6,6}$ rather than $2x_{6,6}$. By considering the missing factor of two (using $x_{i,j}$ values provided in Table 1 of Ref. [87]), the predicted shift of this non-isomeric hot band becomes similar to the expected *cis-trans* shift of ν_6. As such, $2\nu_6-\nu_6$ of *trans*-HCOOH could contribute to the hot band at 1093 cm^{-1} (H_C) which was ascribed primarily to ν_6 of *cis*-HCOOH; indeed the hot band is expected at 2196.3 − 1104.85 = 1091.5 cm^{-1} using high-resolution values from Ref. [94]. The expected intensity of the $2\nu_6-\nu_6$ hot band, however, is distinctly too small for it to be the sole contributor to H_C. The *cis*-HCOOH assignment, therefore, remains unaffected.

bands for all four isotopologues. For the hot band simulations, CVPT6 energy levels on the TM-PES are used. In the absence of anharmonic Raman intensities, a simple model is used to simulate the Raman intensities. Essentially only anharmonic terms in the polarisability are neglected and the fundamental-to-hot band intensity ratio is adjusted by one scaling parameter for all four isotopologues to match experiment. Considering the crudeness of the intensity model, the experimental hot band structure of HCOOH is surprisingly well reproduced. Note that the choice of width for the Gaussian functions and the underestimated shift (simulation −2, experiment −4 cm^{-1}) cause $\nu_6+\nu_7-\nu_7$ to overlap with the ν_6 fundamental in *trans*-HCOOH.

Moving towards HCOOD and DCOOD, the simulations show that an overlap of the two hot bands $\nu_6+\nu_7-\nu_7$ and $\nu_6+\nu_9-\nu_9$ results in the comparably high intensity of H_I (HCOOD) and H_F (DCOOD). The interpretation of the two weaker ν_6 hot bands in the HCOOD (H_G, H_H) and DCOOD (H_D, H_E) spectra is not as straightforward. In light of the comparably large red-shifts (cf. Table D.3), $2\nu_6-\nu_6$ of *trans*-formic acid or ν_6 of *cis*-formic acid are the most plausible assignments. CVPT6 on both potentials consistently predicts ν_6 of *cis*-formic acid below $2\nu_6-\nu_6$ across both OD isotopologues. The bands are (very cautiously) assigned accordingly in Table 4.4.

In the DCOOH spectrum, the hot band structure around ν_6 is distinctly more complex. Most striking is H_F which is blue-shifted from the *trans* fundamental. By analogy to the previous discussion of ν_5 hot bands, the upper level is most likely resonance-perturbed. H_F can be assigned to $\nu_6+\nu_9-\nu_9$ which, due to a strong resonance between $\nu_6+\nu_9$ and $3\nu_9$, is shifted above the ν_6 fundamental (cf. Table D.5). $3\nu_9-\nu_9$, in turn, can be located at the lower-wavenumber end of the hot band structure and is assigned to H_A. By analogy to the other deuterated isotopologues, H_B can cautiously be ascribed to ν_6 of the *cis* conformer. The remaining ν_6 hot bands, H_C and H_D, cannot be assigned with the presently available data.

Hot bands near the C=O stretch (ν_3). We start with HCOOD where the hot band structure is the simplest. By analogy to *cis*-HCOOH where ν_3 was located at 1818 cm^{-1} [87, 89], H_K (1819 cm^{-1}) can be assigned to the ν_3 band of *cis*-HCOOD. For the assignment of H_J, $\nu_3+\nu_9-\nu_9$ and $\nu_3+\nu_7-\nu_7$ are obvious choices. On the basis of the CVPT6 energy levels, H_J is assigned to the latter, since $\nu_3+\nu_9-\nu_9$ is predicted to overlap with the ν_3 fundamental.

Moving to HCOOH, the previous assignment of H_I to $\nu_3+\nu_7-\nu_7$ by Meyer and Suhm [87] can be confirmed by the CVPT6 results and by analogy to HCOOD. The weak intensity and large red-shift of H_G (cf. Table D.3) are consistent with an assignment to $2\nu_3-\nu_3$.[159] H_H cannot safely be assigned which leaves the interesting case of H_J which is shifted by +6 cm^{-1} from ν_3. The incompatibility of the blue-shift with second-order anharmonicity constants again points to resonance perturbations of at least one involved vibrational level. Inspection of the CVPT6 eigenvectors of all binary $\nu_3+\nu_i$ states reveals a near 1:1 mixing between $\nu_3+\nu_9$ and $\nu_7+3\nu_9$ across both potentials. The assignment of H_J to $\nu_3+\nu_9-\nu_9$ or $\nu_7+3\nu_9-\nu_9$ is furthermore consistent with the absence of a blue-shifted hot band in the HCOOD spectrum.

In the DCOOH ν_3 spectrum, three hot bands are identified (H_K-H_M) whereas five can be resolved in the DCOOD spectrum at 1704, 1722, 1758, 1766, and 1789 cm^{-1} (H_G-H_K). The DCOOD assignments are discussed in the following, the DCOOH assignments are analogous. The shift of the H_K relative to the $\nu_3/2\nu_8$ centre of mass amounts to +42 cm^{-1}, similar to the *cis*-*trans* shift observed in HCOOH and HCOOD (42-47 cm^{-1}). Note that the similarity of the *cis*-*trans* shifts across different H/D isotopologues, when referenced to the unperturbed *trans* ν_3 band centre, indicates that the resonance to $2\nu_8$ is weakened or completely quenched in the *cis* isomer. This is consistent with the CVPT6 results. H_G and H_J clearly correspond to transitions from ν_8

[159] The resulting term value for $2\nu_3$, 1776.83 + 1757 = 3534 cm^{-1}, is furthermore in good agreement with the helium nanodroplet value at 3533 cm^{-1} [115, 121] and low-resolution FTIR jet band centre 3534 cm^{-1}. (Note that the FTIR band centre has newly been determined in this work from the spectra published in Ref. [126].)

into the $\nu_3+\nu_8/3\nu_8$ doublet as they exhibit very unusual shifts and mirror the intensity ratio of ν_3 and $2\nu_8$. H_H and H_I are both red-shifted by $-3\,cm^{-1}$ when referenced to the nearest member of the $\nu_3/2\nu_8$ doublet. Transitions originating from ν_9 or ν_7 appear plausible. As for HCOOH and HCOOD, CVPT2 anharmonicity constants ($x_{3,i}$, Table D.3) indicate that hot bands originating from ν_9 will overlap with ν_3 and $2\nu_8$ (shift between 0 and $-1\,cm^{-1}$) whereas the predicted shift of ν_7 hot bands is in agreement with experiment ($-4\,cm^{-1}$). When computing the red-shift directly from the resonance-perturbed CVPT6 energy levels, similar results are obtained.

Hot bands near the C–H/D stretch (ν_2). In the C–H stretching spectrum of HCOOH, there are three distinct hot bands at 2873, 2925, and 2938 cm^{-1} (H_L-H_N). Meyer and Suhm observed the former two and assigned them to ν_2 of *cis*-HCOOH and $\nu_2+\nu_8-\nu_8$ of *trans*-HCOOH, respectively, on the basis of deperturbed anharmonicity constants at the B3LYP-D3 level [87]. H_N overlaps with the C–H stretching fundamental of the cyclic formic acid dimer [87, 119] and was later observed in jet spectra at a lower acid concentration [86]. Meyer proposed an assignment to $\nu_2+\nu_9-\nu_9$, possibly with additional contributions from $\nu_2+\nu_6-\nu_6$ [86]. The assignments for H_L-H_N are all confirmed from the perspective of CVPT6 energy levels and CVPT2 anharmonicity constants (Table D.3). These calculations indicate a negligible hot band shift of $\nu_2+\nu_7-\nu_7$ which can further be confirmed with $\widetilde{\nu_2+\nu_7}$ experimentally available (Table 3.2, p. 49). The resultant hot band shift is $-1\,cm^{-1}$.

By analogy to HCOOH, the HCOOD hot band at 2871 cm^{-1} (H_N) is assigned to ν_2 of *cis*-HCOOD. The other three non-isomeric HCOOD hot bands (H_O-H_Q) cannot safely be assigned due to the near 1:1 resonance between ν_2 and $\nu_3 + \nu_6$, rendering second-order anharmonicity constants unusable. For an assignment of these hot bands, reliable and converged energy levels up to 4500 cm^{-1} are necessary.

Moving down the spectral ladder into the C–D stretching manifold, the large hot band shifts of H_N (2167 cm^{-1}, DCOOH) and H_L (2145 cm^{-1}, DCOOD) unveil them as *cis*-formic acid bands (ν_2). In Ref. [91], H_N was rather tentatively ascribed to *cis*-DCOOH due to the unexpectedly large isotope shift of 22 cm^{-1} relative to *cis*-DCOOD (H_L). The assignment is secured by CVPT6 (Table D.1). Indeed, this deuteration shift is not predicted in the harmonic approximation and is almost zero on both potentials. For both isotopologues, *cis*-DCOOH and *cis*-DCOOD, a Fermi resonance to $\nu_4+\nu_6$ is predicted. ν_2 of DCOOD appears to be the only fundamental across all H/D isotopologues that is involved in a resonance that is shared by both rotamers whereas all other strong resonance perturbations in *trans*-formic acid (Section 4.2) are either weakened or completely quenched in the *cis* conformer (and vice versa).

H_O in the DCOOH spectrum corresponds to $\nu_2+\nu_4-\nu_4$ and its absence (predicted shift near zero) in the DCOOD spectrum can be ascribed to the resonance between ν_2 and $\nu_4+\nu_6$. The remaining non-isomeric hot band assignments for DCOOH (H_P-H_Q) and DCOOD (H_M-M_P) in Table 4.4 are analogous to HCOOH. It should be noted that the consistently higher intensity of $\nu_2+\nu_8-\nu_8$ hot bands in comparison to other ν_2 hot bands, e.g. $\nu_2+\nu_7-\nu_7$, indicates either additional contributions to the overall intensity from other hot bands or intensity gain via mechanical or electrical anharmonicity. (Recall that $\tilde{\nu}_7$ is always lower than $\tilde{\nu}_8$ and, therefore, has a more favourable Boltzmann factor.) Overall, the isomeric and non-isomeric hot band assignments for all four isotopologues reflect the geometric coupling between the C–H/D stretch (ν_2) and its two bending vibrations (ν_4 and ν_8) but also to the OH/D torsion (ν_9). The latter coupling is mediated by the C–O bond [98] and is also responsible for the large *cis-trans* shifts of ν_2 (50-90 cm^{-1}).

Hot bands near the O–H/D stretch (ν_1). The ν_1 band of *cis*-formic acid can readily be assigned for all four isotopologues due to its large spectral shift from the respective *trans* fundamental [87, 91]. Similar to ν_2 hot bands of HCOOD, the remaining hot bands in the HCOOH

(H_O) and DCOOH (H_R and H_S) spectra cannot be assigned purely on the basis of second-order anharmonicity constants and converged energy levels up to 5000 cm^{-1} are necessary.

The remaining hot bands in the HCOOD (H_L) and DCOOD (H_Q) spectra both correspond to $\nu_1+\nu_7-\nu_7$. The assignment is straightforward in light of the anharmonicity constants (Table D.3) and the derived term values for $\nu_1+\nu_7$ agree within 1 cm^{-1} with the observed cold band centres (M_T and M_Q, Table 4.3). Note that the intensity of these hot bands relative to the ν_1 fundamental is distinctly higher in the DCOOD spectrum. One possible source of this higher intensity could be additional, cold transitions that overlap with H_Q.[160] Since the O–D stretching fundamentals of the cyclic formic acid dimers, $(HCOOD)_2$ and $(DCOOD)_2$, are shifted towards 2200 cm^{-1} upon dimerisation [93, 118, 119, 140], a measurement without heating of the nozzle is expected to reveal possible cold monomeric contributions that are hidden underneath H_Q.

4.5 Review of previous IR assignments

Building on the HCOOH reassignments proposed by Tew and Mizukami [21] and Richter and Carbonnière [22], previous IR assignments for all formic acid H/D isotopologues will be reviewed in this section in light of new Raman jet data. HCOOH bands where the present analysis is in agreement with the proposed reassignments in Refs. [21, 22] are not included in Table 4.7. This especially concerns the $\nu_5 \leftrightarrow 2\nu_9$ label switch. Tentative assignments by Tew and Mizukami that remain tentative from the perspective of this work are also not further discussed. All proposed revisions are compactly summarised in Table 4.7 and are discussed in the following. Since all reassignments concern *trans*-formic acid, the prefix "*trans*" is dropped in the following. Let us start, however, with the $2\nu_6$ band of DCOOH which is not included in Table 4.7 because the following discussion rather concerns the accuracy of the band centre than the vibrational assignment *per se*.

DCOOH. 2254.24 cm^{-1}. Tan *et al.* analysed the rotationally-resolved room temperature gas phase IR spectrum of DCOOH between 2130 and 2300 cm^{-1} and obtained ro-vibrational parameters for the ν_2 fundamental and $2\nu_6$ by fitting observed lines [226] (note differing nomenclature; Table 2.2, p. 35). In light of the new assignment of $2\nu_6$ in the Raman spectrum of DCOOH (2277 cm^{-1}, Table 4.3), the accuracy of the previously reported IR band centre at 2254.24 cm^{-1} appears questionable. The assignment of the Raman band can be secured independently based on anharmonic vibrational energy levels and experimental isotope data. On the basis of Eq. 4.1 (p. 60), the error-corrected CVPT6 term value of $2\nu_6$ on the TM-PES amounts to $2282.2 - 2.4 \times 2 = 2277.4\,cm^{-1}$. The similarly calculated value on the RC-PES is $2272.3 + 2.4 \times 2 = 2278.5\,cm^{-1}$. These values are in excellent agreement with the observed Raman jet band centre. On the basis of experimental data in Tables 3.2 (p. 49) and 4.3 and the assumption $x_{6,6}(\text{iso 1}) \approx 0.5 \times 2\tilde{\nu}_6(\text{iso 2}) - \tilde{\nu}_6(\text{iso 2})$, the DCOOH $2\nu_6$ band centre can be estimated in three ways using Eq. 2.1 (p. 17):

$$\text{via HCOOH: } 2\tilde{\nu}_6(\text{DCOOH}) \approx 2 \times 1142.31 + 2197 - 2 \times 1104.85 = 2272\,cm^{-1}$$
$$\text{via HCOOD: } 2\tilde{\nu}_6(\text{DCOOH}) \approx 2 \times 1142.31 + 2341 - 2 \times 1177.09 = 2271\,cm^{-1}$$
$$\text{via DCOOD: } 2\tilde{\nu}_6(\text{DCOOH}) \approx 2 \times 1142.31 + 2330 - 2 \times 1170.80 = 2273\,cm^{-1}.$$

The 4-6 cm^{-1} underestimation to the observed Raman band centre at 2277 cm^{-1} is in agreement with the (comparably weak) resonance between ν_2 and $2\nu_6$ in DCOOH, as indicated by the CVPT6 eigenvectors. Diagonalisation of the corresponding 2×2 effective VPT2+F Hamiltonian on the TM-PES shows that $2\nu_6$ is shifted by 2.5 cm^{-1} relative to the deperturbed band centre. The

[160] See previous discussion on possible resonance perturbations of ν_1 in *trans*-D^{13}COOD (pp. 77).

Table 4.7 Summary of proposed (re)assignments for *trans*-formic acid IR bands. "n.a." and "n.d." refer to bands that have initially not been assigned and mode assignments that are not discussed, respectively. Note that Refs. [21, 22] only cover HCOOH, whereas Ref. [27] only treats the three deuterated isotopologues. Tentative assignments are set in parentheses. Note that vibrational levels are labelled according to Table 2.2 (p. 35).

	IR		Assignment				
Isotop.	$\tilde{\nu}_0$	Ref.	Initial	Ref. [21]	Ref. [22]	Ref. [27]	This work
HCOOH	1726.40	[96]	$\nu_6+\nu_9$	n.d.	$\nu_6+\nu_7$		$\nu_6+\nu_7$
	1736.96	[96]	$\nu_6+\nu_7$	n.d.	$\nu_6+\nu_9$		$\nu_6+\nu_9$
	2298.6	[94]	$(\nu_5+\nu_6)$	$\nu_7+\nu_8+\nu_9$	$(\nu_6+2\nu_9)$		$(4\nu_9)$
	2338	[94]	n.a.	$\nu_5+\nu_8$	$(\nu_5+\nu_8)$		$(\nu_6+2\nu_9)$
	2376	[94]	$\nu_3+\nu_7$	$(\nu_6+\nu_7+\nu_9)$	$\nu_6+\nu_7+\nu_9$		see text
	2400.2	[94]	$2\nu_5$	$(\nu_3+\nu_7)$	$\nu_5+\nu_6$		$\nu_5+\nu_6$
	2600	[94]	$\nu_4+\nu_5$	$(\nu_4+2\nu_9)$	n.d		$(2\nu_5/\nu_5+2\nu_9)$
	3106.5	[94]	$(\nu_4+\nu_6+\nu_7)$	$(\nu_4+\nu_6+\nu_7)$	n.d.		$(3\nu_7+2\nu_9)$
	3826	[94]	$(2\nu_4+\nu_6)$	$(2\nu_4+\nu_6)$	n.d.		$\nu_3+2\nu_8$
	3963.6	[94]	$\nu_2+\nu_8$	$(\nu_2+\nu_8)$	n.d.		$(\nu_3+2\nu_6)$
HCOOD	2142.4	[238]	n.a.			n.d.	$\nu_5+\nu_6$
	2178.8	[238]	n.a.			n.d.	$\nu_6+2\nu_9$
	2601.13	[224]	$3\nu_7+\nu_8$			n.d.	$(\nu_7+\nu_8+2\nu_9)$

size and direction of the VPT2+F prediction are in good agreement with the above experimental isotopologue analysis. Thus, the most likely source of the IR-Raman discrepancy might be the missing Fermi interaction between ν_2 and $2\nu_6$ in the effective Hamiltonian that was employed in Ref. [226].

HCOOH. 1726.40 and 1736.96 cm^{-1}. Building on previous high-resolution studies in this spectral region [94, 247], Perrin *et al.* presented a thorough and the so far most detailed analysis of the rotationally-resolved HCOOH spectrum in the vicinity of ν_3 [96]. They included couplings to and between four nearby combination states in the effective fit Hamiltonian and obtained ro-vibrational parameters and band centres at 1726.40, 1736.96, 1792.63, and 1843.48 cm^{-1}. The reassignments concerning the former two to $\nu_6+\nu_7$ and $\nu_6+\nu_9$, respectively, have been discussed in a previous section (pp. 83). In light of the $\nu_5 \leftrightarrow 2\nu_9$ label switch [107], also the latter two must be reassigned to $3\nu_9$ and $\nu_7+2\nu_9$, respectively. Note that the $\nu_5+\nu_7/\nu_7+2\nu_9$ Fermi pair was observed before by Freytes *et al.* [94] with IR spectroscopy who determined their band centres via their central Q branches (1847.8 and 1931.1 cm^{-1}). The similarly estimated low-resolution Raman jet band centres agree well with the band centres by Freytes *et al.* within the Raman resolution and calibration uncertainty of ± 2 cm^{-1} but both are incompatible with the $\nu_7+2\nu_9$ band centre reported by Perrin *et al.* [96]. The 4 cm^{-1} discrepancy might be resolved by inclusion of lines that correspond to $\nu_5+\nu_7$ in the effective fit Hamiltonian that was employed in Ref. [96]. Similarly, the sub-cm^{-1} accuracy of the $3\nu_9$ band centre [96] appears questionable without inclusion of the Fermi partner $\nu_5+\nu_9$ which is centred at 1951 cm^{-1}. In all these contexts, a reinvestigation of the high-resolution ν_3 spectrum appears compelling. Similarly, the $\nu_5 \leftrightarrow 2\nu_9$ label switch calls for an update of the global fit of vibrational energy levels up to 1500 cm^{-1} [95], possibly together with ro-vibrational lines from Ref. [96].[161]

HCOOH. 2298.6 and 2338 cm^{-1}. Regarding the assignment of the IR bands at 2298.6 and 2338 cm^{-1} that were reported for the first time by Freytes *et al.* in 2002 [94], Richter and Carbonnière summarised [22] that the

[161] See also Ref. [248] for the most recent additions of HCOOH ro-vibrational lines to the HITRAN database.

> "observed level at 2298.6 cm^{-1} labeled as $\nu_5+\nu_6$ matches perfectly the calculated one at 2294 cm^{-1} labeled as $(2\nu_9+\nu_6)$ after the usual ν_5 to $2\nu_9$ switch, also when the expected error progression is taken into account. Tew attributed this one rather to the lower 3 mode combination $\nu_7+\nu_8+\nu_9$ which is equally possible in view of our data while Tew's $(2\nu_9+\nu_6)$ value would be about 13 cm^{-1} higher than the observed one. The experimentally unassigned level at 2338 cm^{-1} – tentatively assigned as $\nu_8+\nu_5$ by us – can either be $\nu_8+\nu_5$ or $4\nu_9$ given our error progressions, but it can only be $\nu_8+\nu_5$ in view of Tew's data."

The CVPT6 calculations on both formic acid potentials resolve the discrepancy between the ICPH-VCI and MCTDH results and show that the ICPH-VCI values are consistently *above* the CVPT6 values which is indicative of convergence errors.[162] In view of the near 1:1 resonance between $\nu_6+2\nu_9$ and $4\nu_9$ (pp. 74), the two IR assignments are linked and an assignment of either band should clarify the assignment of the other. An assignment to the $\nu_6+2\nu_9/4\nu_9$ doublet is more favourable since ν_6 has a very high infrared visibility [249] and many of the combination/overtone bands observed by Freytes *et al.* [94] do involve[163] ν_6 whereas both ν_5 and ν_8 have weak infrared intensities and it is questionable whether the combined excitation would generate a large transition dipole moment.

HCOOH. 2376 cm^{-1}. The HCOOH band at 2376 cm^{-1} was initially assigned by Freytes *et al.* to $\nu_3+\nu_7$ [94]. $\nu_3+\nu_7$ is observed in the Raman jet spectra at 2395 cm^{-1} (pp. 74) and the assignment is confirmed by comparison to hot bands involving $\nu_3+\nu_7$ (pp. 84). Tew and Mizukami tentatively reassigned [21] the 2376 cm^{-1} band to $\nu_6+\nu_7+\nu_9$ "which is considered the more likely match than the neighbouring bands at 2361 $(\nu_6+2\nu_7)$ or 2402 $(\nu_3+\nu_7)$" This argument holds in view of CVPT6 results on both surfaces and MCTDH data by Richter and Carbonnière [22]. However, it is worth pointing out that for all four calculations the anharmonic predictions are still 9-14 cm^{-1} below experiment when the expected error progressions are taken into account. Given the remarkable agreement with experiment for states involving three and four quanta when the expected error is considered, an assignment of this band to a cold *trans*-HCOOH transition, i.e. from the vibrational ground state, appears questionable.

HCOOH. 2400.2 cm^{-1}. Refs. [21, 22] are in disagreement regarding the assignment of the 2400.2 cm^{-1} IR band [94] for which an assignment to $\nu_5+\nu_6$ and $\nu_3+\nu_7$ was proposed. Richter and Carbonnière pointed out that taking into account the expected error progressions, $\nu_3+\nu_7$ is expected at lower wavenumbers across both variational calculations [22]. The reassignment to $\nu_5+\nu_6$ is consistent in view of the assignment of the HCOOH Raman bands at 2395 and 2400 cm^{-1} (Section 4.3) and also the assignment of the $\nu_3+\nu_7-\nu_7$ and $\nu_5+\nu_6-\nu_6$ hot bands (Section 4.4). Lastly, an inverse assignment of $\nu_3+\nu_7$ and $\nu_5+\nu_6$ (the latter below the former) is not compatible with the observed hot bands.

HCOOH. 2600 cm^{-1}. In view of the available computed vibrational data in Table D.4, the IR band at 2600 cm^{-1} [94] could plausibly be assigned to two different polyads, $\{n_4, N_5\} = \{1,1\}$ or $\{0,2\}$. The couplings between these polyads were discussed in detail in Section 4.3.2. Note that the two higher-energy states in the $\{0,2\}$ polyad are strongly coupled in the normal mode representation ($\nu_5+2\nu_9$ and $2\nu_5$). Tew and Mizukami tentatively ascribed the IR band to $\nu_4+2\nu_9$ [21] which corresponds to $\{1,1\}$ in the polyad representation. The second state in this polyad, however, is not observed in the IR spectrum of HCOOH [94]. The possible (and more plausible) assignment of the IR band at 2298.6 cm^{-1} to $4\nu_9$ – the lowest-energy member of the

[162] See Ref. [29] and Section 5.3.1 where the convergence of ICPH-VCI eigenvalues is examined.

[163] Many of the IR assignments originally proposed in Ref. [94] have been reassigned, see for example updated assignments in Ref. [21] and proposed here (Table 4.8).

$\{0, 2\}$ polyad – was discussed above. The second state in the $\{0, 2\}$ polyad was also observed in Ref. [94]. In these contexts, an assignment of the IR band at 2600 cm^{-1} to the last member of the $\{0, 2\}$ polyad is more convincing but still, the assignment needs further confirmation and is, therefore, marked as tentative in Table 4.7.

HCOOH. 3106.5 cm^{-1}. Regarding the assignment of the IR band at 3106.5 cm^{-1} [94], the CVPT6 energy levels in Table D.4 indicate overall three possible assignments: $3\nu_7+2\nu_9$ (A′), $\nu_4+\nu_6+\nu_7$ (A′), and $\nu_4+\nu_6+\nu_9$ (A″). In Refs. [21, 94], it was tentatively ascribed to $\nu_4+\nu_6+\nu_7$. In view of the error-corrected performance of computed vibrational energy levels in comparison to experiment, however, an assignment of the IR band at 3106.5 cm^{-1} to $\nu_4+\nu_6+\nu_7$ can be ruled out: $\nu_4+\nu_6+\nu_7$ is not observed in the Raman spectrum of HCOOH but that of HCOOD at 3092 cm^{-1} (Table 4.3). Using Eq. 4.1, the error-corrected CVPT6 predictions for HCOOD on both potentials are 3093-3094 cm^{-1} and agree with experiment within the resolution and calibration uncertainty of ± 2 cm^{-1}. The similarly corrected predictions for HCOOH are 3099-3100 cm^{-1}. Note that this energy level is not predicted to be involved in strong resonances, neither in HCOOH nor HCOOD. An alternative assignment to $\nu_4+\nu_6+\nu_9$ of HCOOH appears equally doubtful with error-corrected predictions of 3113-3115 cm^{-1} from either CVPT6 (both potentials) or MCTDH [22]. Lacking more plausible assignments, the IR band at 3106.5 cm^{-1} is very cautiously ascribed to $3\nu_7+2\nu_9$ but marked as (highly) tentative in Table 4.7.

HCOOH. 3826 cm^{-1}. From the perspective of the published computed anharmonic term values [21, 22, 28], there are only two assignments that seem plausible for the HCOOH band at 3826 cm^{-1} [94]: $2\nu_4+\nu_6$ and $\nu_3+2\nu_8$. On the basis of the expected error progression (Eq. 4.1), an assignment to $\nu_3+2\nu_8$ is more convincing as $2\nu_4+\nu_6$ is expected at 3831-3835 cm^{-1} whereas $\nu_3+2\nu_8$ is uniformly located at 3826-3827 cm^{-1}.

HCOOH. 3963.6 cm^{-1}. Meyer noted that a previous IR assignment of $\nu_2+\nu_8$ [94] is incompatible with the extracted term value from hot band assignments [86]. The anharmonic calculations further support the Raman jet assignment which was discussed above (pp. 85), thus the IR assignment at 3963.6 cm^{-1} [94] must be revised. From the vibrational term values shown in Table D.4, there are only two plausible assignments for the IR band at 3963.6 cm^{-1}: $\nu_3+2\nu_6$ or $2\nu_4+\nu_5$. The other assignments correspond to highly excited ($n \geq 5$) states and appear less likely. Since a second band, corresponding to $2\nu_4+2\nu_9$, was not reported by Freytes *et al.*, an assignment to $\nu_3+2\nu_6$ is more favourable. However, given the overall weak intensity of the 3963.6 cm^{-1} band, the corresponding $2\nu_4+2\nu_9$ band might be too weak to be observed, thus the assignment is marked as tentative in Table 4.7.

HCOOD. 2142.4 and 2178.8 cm^{-1}. Williams reported two parallel bands in the IR gas phase spectrum of HCOOD that nearly seven decades later remain unassigned [238]. With the additional symmetry information from the band contour, an assignment of both bands is straightforward with CVPT6 term values from Table D.6. The bands at 2142.4 and 2178.8 cm^{-1} can be assigned to the Fermi pair[164] $\nu_5+\nu_6$ and $\nu_6+2\nu_9$, respectively. Note that even when considering A″ symmetric states in this region, the proposed assignment is the best energy match.

[164] Marushkevich *et al.* observed $\nu_5+\nu_6$ at similar wavenumbers and reported vibrational band centres at 2139.8 and 2176.8 cm^{-1} in a neon and 2144.1 and 2181.0 cm^{-1} in an argon matrix [84]. While the doublet was interpreted as matrix site splitting, the similarity to the unperturbed gas phase band centres indicates an alternative interpretation as a Fermi resonance doublet.

HCOOD. 2601.13 cm^{-1}. A'dawiah *et al.* analysed the rotationally-resolved thermal gas phase infrared spectrum of the O–D stretching fundamental (ν_1) of HCOOD [224] and H^{13}COOD [250]. The authors included additional Coriolis couplings to a nearby A″ state in the fit Hamiltonian and reported vibrational band centres at 2601.13 (HCOOD) and 2596.31 cm^{-1} (H^{13}COOD) for the perturber which was assigned to $3\nu_7+\nu_8$ in both cases [224, 250]. A simple sum-of-fundamentals estimate for HCOOD, however, clearly shows that the $3\nu_7+\nu_8$ band centre is expected at much higher wavenumbers ($3\times558+1031=2705$ cm^{-1}) which is near the computed anharmonic prediction (2712 cm^{-1}, Table D.6). Moreover, the carbon-13 shift of -5 cm^{-1} appears much too small for the C–H out-of-plane bend ν_8. For the carbon-12 isotopologue, $\nu_7+\nu_8+2\nu_9$ (2604 cm^{-1}) is the best energy match for the band centre at 2601.13 cm^{-1}. While $\nu_7+\nu_8+2\nu_9$ (2585 cm^{-1}) is also the best match for the band at 2596.31 cm^{-1} based on CVPT6 energy levels for the carbon-13 isotopologue (not shown), it should be noted that the theory-experiment agreement is much poorer. In view of similar discrepancies discussed above for the DCOOH band at 2254.24 cm^{-1}, the question arises whether additional couplings and/or vibrational states must be included in the fit Hamiltonian that was employed in Refs. [224, 250].

4.6 Vibrational benchmark database of monomeric formic acid

The discussion of Raman and IR band (re)assignments in the preceding sections is condensed in Table 4.8 which comprises benchmark-quality vibrational band centres of different formic acid isotopologues and conformers. Bands whose assignments are not secured yet or that await a mode assignment[165] and available band centres in the overtone manifold above 4000 cm^{-1} are not included.

The following labelling system is used in Table 4.8:

- Q — Vibrational band centres are approximated from the position of the central *Q* branch. Band centre uncertainties of ±2 and ±1 cm^{-1} are ascribed to Raman and FTIR[166] jet band centres from this work, respectively.
- rv — Vibrational band centres are obtained by fitting rotationally-resolved lines using effective fit Hamiltonians. The value of the band centre depends on the form of the effective Hamilton matrix (included states and included operators). For these bands, two decimal places are shown even if more significant digits are reported in the original publication.
- h — Vibrational band centres ($\tilde{\nu}_f$) are determined from difference bands in the Raman spectra ($\nu_f-\nu_i$). The assignments were discussed in Section 4.4 (see Table 4.4, p. 80). The observed difference band ($\tilde{\nu}_f-\tilde{\nu}_i$) is ascribed an uncertainty of ±2 cm^{-1}. Since $\tilde{\nu}_i$ is available from high-resolution spectroscopy in almost all cases, $\tilde{\nu}_f$ is ascribed an uncertainty of ±2 cm^{-1}. Larger uncertainties are annotated in Table 4.8.
- c — Vibrational band centres are obtained from the analysis of the unresolved rovibrational band contour. This only applies to the ν_8 Raman band centres of *trans*-HCOOH and *trans*-HCOOD (see pp. 45). The Raman band centres are ascribed a smaller uncertainty of ±1 cm^{-1} (see pp. 45).

[165] The assignments of a few IR bands that were reported by Freytes *et al.* [94] remain tentative (see Table 4.7, p. 87). These band centres are not included in Table 4.8 and require further investigation. Combination states reported in Refs. [90, 224, 250] are also not included as they are still awaiting a mode assignment. Similarly, some Raman bands in Tables 4.3 (p. 71) and 4.4 (pp. 80) remain unassigned.

[166] The FTIR band centres are determined from dimer-optimised spectra shown in Figs. 6.1-6.2 (pp. 116).

If the method of determining the band centre is not explicitly reported in the reference, the corresponding cell is left empty in Table 4.8.

Table 4.8 Experimental term values ($\tilde{\nu}_0$, in cm^{-1}) referenced to the respective ground state for different isotopologues and rotamers of formic acid below 4000 cm^{-1}. Note that vibrational levels (the vibrational mode is indexed by the quanta of excitation) are labelled according to Table 2.2 (p. 35). See text for details.

				Raman		IR		
Iso.	Conf.	Label	Γ	$\tilde{\nu}_0$	Comment	$\tilde{\nu}_0$	Reference	Comment
HCOOH	*trans*	7_1	A′	626	*Q*	626.17	[218]	rv
HCOOH	*trans*	9_1	A″			640.73	[218]	rv
HCOOH	*trans*	8_1	A″	1033	c	1033.47	[219]	rv
HCOOH	*trans*	6_1	A′	1104	*Q*	1104.85	[219]	rv
HCOOH	*trans*	9_2	A′	1220	*Q*	1220.83	[110]	rv
HCOOH	*trans*	7_2	A′			1253.44	[95]	rv
HCOOH	*trans*	7_19_1	A″			1268.69	[95]	rv
HCOOH	*trans*	5_1	A′	1306	*Q*	1306.14	[95]	rv
HCOOH	*trans*	4_1	A′	1379	*Q*	1379.05	[230]	rv
HCOOH	*trans*	8_19_1	A′	1673	*Q*			
HCOOH	*trans*	6_17_1	A′	1726	*Q*	1726.40	[96]	rv
HCOOH	*trans*	6_19_1	A″	1738	h	1737.96	[96]	rv
HCOOH	*trans*	3_1	A′	1776	*Q*	1776.83	[96]	rv
HCOOH	*trans*	9_3	A″			1792.63	[96]	rv
HCOOH	*trans*	7_19_2	A′	1847	*Q*	1847.8	[94]	*Q*
HCOOH	*trans*	5_17_1	A′	1931	*Q*	1931.1	[94]	*Q*
HCOOH	*trans*	5_19_1	A″	1951	h			
HCOOH	*trans*	8_2	A′	2060	*Q*			
HCOOH	*trans*	6_18_1	A″			2132	[94]	
HCOOH	*trans*	6_2	A′	2197	*Q*	2196.3	[94]	*Q*
HCOOH	*trans*	$9_4/6_19_2$	A′	2298	*Q*			
HCOOH	*trans*	$7_18_19_1$	A′	2301	*Q*			
HCOOH	*trans*	$6_19_2/9_4$	A′	2336	*Q*			
HCOOH	*trans*	3_17_1	A′	2395	*Q*			
HCOOH	*trans*	5_16_1	A′	2400	*Q*	2400.2	[94]	*Q*
HCOOH	*trans*	$3_19_1/7_19_3$	A″	2423	h			
HCOOH	*trans*	$5_19_2/5_2$	A′	2504	*Q*	2504	[94]	
HCOOH	*trans*	4_15_1	A′	2678	*Q*			
HCOOH	*trans*	4_2	A′	2746	*Q*	2745	[94]	
HCOOH	*trans*	3_18_1	A″			2803	[94]	
HCOOH	*trans*	3_16_1	A′			2876.6	[94]	*Q*
HCOOH	*trans*	2_1	A′	2942	*Q*	2942.06	[94]	rv
HCOOH	*trans*	7_19_4	A′	2960	*Q*			
HCOOH	*trans*	3_19_2	A′	2995	*Q*			
HCOOH	*trans*	3_15_1	A′	3081	*Q*			
HCOOH	*trans*	3_14_1	A′	3153	*Q*	3152.3	[94]	*Q*
HCOOH	*trans*	3_2	A′	3534	h	3534	[126]	*Q*, [a]
HCOOH	*trans*	2_17_1	A′	3567	*Q*			
HCOOH	*trans*	1_1	A′	3570	*Q*	3570.5	[94]	
HCOOH	*trans*	2_19_1	A″	3579	h			
HCOOH	*trans*	3_18_2	A′			3826	[94]	
HCOOH	*trans*	2_18_1	A″	3958	h			
$H^{13}COOH$	*trans*	7_1	A′			621.60	[251]	rv
$H^{13}COOH$	*trans*	9_1	A″			639.08	[251]	rv
$H^{13}COOH$	*trans*	8_1	A″			1019.61	[243]	rv
$H^{13}COOH$	*trans*	6_1	A′	1095	*Q*	1095.40	[243]	rv
$H^{13}COOH$	*trans*	9_2	A′			1206.7	[244]	

continued

Table 4.8 (continued)

				Raman		IR		
Iso.	Conf.	Label	Γ	$\tilde{\nu}_0$	Comment	$\tilde{\nu}_0$	Reference	Comment
$H^{13}COOH$	*trans*	5_1	A′	1295	*Q*			
$H^{13}COOH$	*trans*	4_1	A′			1386.2	[244]	
$H^{13}COOH$	*trans*	3_1	A′	1737	*Q*	1735.7	[244]	
$H^{13}COOH$	*trans*	2_1	A′	2928	*Q*	2927.4	[244]	
$H^{13}COOH$	*trans*	1_1	A′			3572.0	[244]	
HCOOH	*cis*	9_1	A″			493.42	[88]	rv
HCOOH	*cis*	6_1	A′	1093	*Q*			
HCOOH	*cis*	3_1	A′	1818	*Q*			
HCOOH	*cis*	2_1	A′	2873	*Q*			
HCOOH	*cis*	1_1	A′	3637	*Q*	3637.16	[90]	rv
DCOOH	*trans*	7_1	A′	620	*Q*	620.57	[236]	rv
DCOOH	*trans*	9_1	A″			631.54	[236]	rv
DCOOH	*trans*	8_1	A″			873.38	[237]	rv
DCOOH	*trans*	4_1	A′	971	*Q*	970.89	[231]	rv
DCOOH	*trans*	6_1	A′	1142	*Q*	1142.31	[233]	rv
DCOOH	*trans*	9_2	A′	1206	*Q*			
DCOOH	*trans*	5_1	A′	1299	*Q*			
DCOOH	*trans*	$8_1 9_1$	A′	1508	*Q*			
DCOOH	*trans*	$8_2/3_1$	A′	1725	*Q*	1725.87	[227]	rv
DCOOH	*trans*	9_3	A″	1756	h			
DCOOH	*trans*	$6_1 7_1$	A′	1760	h			
DCOOH	*trans*	$3_1/8_2$	A′	1762	*Q*	1762.9	[227]	
DCOOH	*trans*	$6_1 9_1$	A″	1779	h			
DCOOH	*trans*	$7_1 9_2$	A′	1828	*Q*			
DCOOH	*trans*	$5_1 7_1$	A′	1919	*Q*			
DCOOH	*trans*	4_2	A′	1937	*Q*			
DCOOH	*trans*	$5_1 9_1$	A″	1937	h			
DCOOH	*trans*	$4_1 6_1$	A′	2103	*Q*			
DCOOH	*trans*	$4_1 9_2$	A′	2174	*Q*			
DCOOH	*trans*	2_1	A′	2219	*Q*	2219.69	[226]	rv
DCOOH	*trans*	$4_1 5_1$	A′	2271	*Q*			
DCOOH	*trans*	6_2	A′	2277	*Q*			
DCOOH	*trans*	9_4	A′	2290	*Q*			
DCOOH	*trans*	$6_1 9_2$	A′	2342	*Q*			
DCOOH	*trans*	$5_1 6_1$	A′	2428	*Q*			
DCOOH	*trans*	$5_1 9_2/5_2$	A′	2482	h, [b]			
DCOOH	*trans*	$8_3/3_1 8_1$	A″	2578	h			
DCOOH	*trans*	$3_1 8_1/8_3$	A″	2641	h			
DCOOH	*trans*	$4_1 8_2/3_1 4_1$	A′	2695	*Q*			
DCOOH	*trans*	$3_1 4_1/4_1 8_2$	A′	2731	*Q*			
DCOOH	*trans*	$2_1 9_1$	A″	2849	h			
DCOOH	*trans*	$6_1 8_2/3_1 6_1$	A′	2860	*Q*			
DCOOH	*trans*	$3_1 6_1/6_1 8_2$	A′	2898	*Q*			
DCOOH	*trans*	$2_1 8_1$	A″	3084	h			
DCOOH	*trans*	$2_1 4_1$	A′	3179	h			
DCOOH	*trans*	$2_1 6_1$	A′	3352	*Q*			
DCOOH	*trans*	$6_1 9_4$	A′	3404	*Q*			
DCOOH	*trans*	6_3	A′	3421	*Q*			
DCOOH	*trans*	1_1	A′	3569	*Q*			
$D^{13}COOH$	*trans*	6_1	A′	1128	*Q*			
$D^{13}COOH$	*trans*	$8_2/3_1$	A′	1693	*Q*			

continued

Table 4.8 (continued)

				Raman		IR		
Iso.	Conf.	Label	Γ	$\tilde{\nu}_0$	Comment	$\tilde{\nu}_0$	Reference	Comment
D^{13}COOH	*trans*	2_1	A′	2200	*Q*			
DCOOH	*cis*	3_1	A′	1790	*Q*			
DCOOH	*cis*	2_1	A′	2167	*Q*			
DCOOH	*cis*	1_1	A′	3635	*Q*			
HCOOD	*trans*	9_1	A″			508.13	[221]	rv
HCOOD	*trans*	7_1	A′	558	*Q*	558.27	[221]	rv
HCOOD	*trans*	5_1	A′	972	*Q*	972.85	[232]	rv
HCOOD	*trans*	9_2	A′	1010	*Q*	1011.68	[232]	rv
HCOOD	*trans*	8_1	A″	1031	c			
HCOOD	*trans*	6_1	A′	1176	*Q*	1177.09	[234]	rv
HCOOD	*trans*	4_1	A′	1365	*Q*	1366.48	[230]	rv
HCOOD	*trans*	9_3	A″	1447	h			
HCOOD	*trans*	$5_1 9_1$	A″	1512	h			
HCOOD	*trans*	$5_1 7_1$	A′	1527	*Q*			
HCOOD	*trans*	$8_1 9_1$	A′	1539	*Q*			
HCOOD	*trans*	$6_1 9_1$	A″	1679	h	1680.96	[228]	rv
HCOOD	*trans*	$6_1 7_1$	A′	1730	*Q*	1732.08	[228]	rv
HCOOD	*trans*	3_1	A′	1772	*Q*	1772.12	[228]	rv
HCOOD	*trans*	9_4	A′	1898	h			
HCOOD	*trans*	5_2	A′	1953	*Q*			
HCOOD	*trans*	8_2	A′	2055	*Q*			
HCOOD	*trans*	$5_1 6_1$	A′			2142.4	[238]	*Q*
HCOOD	*trans*	$6_1 9_2$	A′			2178.8	[238]	*Q*
HCOOD	*trans*	$3_1 7_1$	A′	2327	*Q*			
HCOOD	*trans*	6_2	A′	2341	*Q*			
HCOOD	*trans*	1_1	A′	2631	*Q*	2631.64	[224]	rv
HCOOD	*trans*	$5_1 6_1 7_1$	A′	2692	*Q*			
HCOOD	*trans*	$6_1 8_1 9_1$	A′	2710	*Q*			
HCOOD	*trans*	4_2	A′	2713	*Q*			
HCOOD	*trans*	$3_1 5_1$	A′	2741	*Q*			
HCOOD	*trans*	$3_1 9_2$	A′	2782	*Q*			
HCOOD	*trans*	$4_1 7_1 9_2$	A′	2933	*Q*			
HCOOD	*trans*	$2_1/3_1 6_1$	A′	2938	*Q*			
HCOOD	*trans*	$3_1 6_1/2_1$	A′	2954	*Q*			
HCOOD	*trans*	$4_1 6_1 7_1$	A′	3092	*Q*			
HCOOD	*trans*	$3_1 4_1$	A′	3137	*Q*			
HCOOD	*trans*	$1_1 7_1$	A′	3184	*Q*			
HCOOD	*trans*	3_2	A′	3529	*Q*	3529	[126]	*Q*, [a]
H^{13}COOD	*trans*	6_1	A′	1150	*Q*			
H^{13}COOD	*trans*	3_1	A′	1733	*Q*			
H^{13}COOD	*trans*	1_1	A′			2631.13	[250]	rv
HCOOD	*cis*	5_1	A′	904	*Q*			
HCOOD	*cis*	3_1	A′	1819	*Q*			
HCOOD	*cis*	2_1	A′	2871	*Q*			
HCOOD	*cis*	1_1	A′	2685	*Q*			
DCOOD	*trans*	9_1	A″			492.23	[221]	rv
DCOOD	*trans*	7_1	A′	554	*Q*	554.44	[221]	rv
DCOOD	*trans*	8_1	A″			873.2	[238]	*Q*, [c]
DCOOD	*trans*	5_1	A′	945	*Q*	946		*Q*
DCOOD	*trans*	9_2	A′	965	*Q*	965		*Q*
DCOOD	*trans*	4_1	A′	1039	*Q*	1040		*Q*

continued

Table 4.8 (continued)

				Raman		IR		
Iso.	Conf.	Label	Γ	$\tilde{\nu}_0$	Comment	$\tilde{\nu}_0$	Reference	Comment
DCOOD	*trans*	6_1	A′	1170	*Q*	1170.80	[235]	rv
DCOOD	*trans*	9_3	A″	1414	h			
DCOOD	*trans*	$5_1 9_1$	A″	1442	h			
DCOOD	*trans*	$6_1 9_1$	A″	1658	h			
DCOOD	*trans*	$6_1 7_1$	A′	1720	*Q*			
DCOOD	*trans*	$8_2/3_1$	A′	1725	*Q*	1725.12	[229]	rv
DCOOD	*trans*	$3_1/8_2$	A′	1761	*Q*	1761		*Q*
DCOOD	*trans*	4_2	A′	2073	*Q*			
DCOOD	*trans*	$5_1 6_1$	A′	2108	*Q*			
DCOOD	*trans*	$6_1 9_2$	A′	2126	*Q*			
DCOOD	*trans*	$4_1 6_1$	A′	2194	*Q*			
DCOOD	*trans*	2_1	A′	2231	*Q*			
DCOOD	*trans*	$7_1 8_2/3_1 7_1$	A′	2276	h			
DCOOD	*trans*	$3_1 7_1/7_1 8_2$	A′	2312	h			
DCOOD	*trans*	6_2	A′	2330	*Q*			
DCOOD	*trans*	$8_3/3_1 8_1$	A″	2577	h, [d]			
DCOOD	*trans*	1_1	A′	2632	*Q*	2631.87	[225]	rv
DCOOD	*trans*	$3_1 8_1/8_3$	A″	2639	h, [d]			
DCOOD	*trans*	$5_1 6_1 7_1$	A′	2656	*Q*			
DCOOD	*trans*	$5_1 8_2/3_1 5_1$	A′	2668	*Q*			
DCOOD	*trans*	$4_1 6_1 9_1$	A″	2683	h			
DCOOD	*trans*	$3_1 5_1/5_1 8_2$	A′	2704	*Q*			
DCOOD	*trans*	$2_1 9_1$	A″	2721	h			
DCOOD	*trans*	$4_1 8_2/3_1 4_1$	A′	2761	*Q*			
DCOOD	*trans*	$3_1 4_1/4_1 8_2$	A′	2797	*Q*			
DCOOD	*trans*	$6_1 8_2/3_1 6_1$	A′	2888	*Q*			
DCOOD	*trans*	$3_1 6_1/6_1 8_2$	A′	2926	*Q*			
DCOOD	*trans*	$4_1 6_1 8_1$	A″	3061	h, [d]			
DCOOD	*trans*	$2_1 8_1$	A″	3096	h, [d]			
DCOOD	*trans*	$1_1 7_1$	A′	3181	*Q*			
D^{13}COOD	*trans*	6_1	A′	1146	*Q*			
D^{13}COOD	*trans*	$8_2/3_1$	A′	1690	*Q*			
D^{13}COOD	*trans*	2_1	A′	2210	*Q*			
DCOOD	*cis*	5_1	A′	883	*Q*			
DCOOD	*cis*	3_1	A′	1789	*Q*			
DCOOD	*cis*	2_1	A′	2145	*Q*			
DCOOD	*cis*	1_1	A′	2685	*Q*			

[a] The band centre has newly been determined in this work on the basis of the published spectra which were kindly provided by the authors of Ref. [126].

[b] Uncertainty of $\pm 3\,\mathrm{cm}^{-1}$ since $\tilde{\nu}_i$ is only available from low-resolution Raman spectroscopy.

[c] The band centre has a single-sided error bar of $-1\,\mathrm{cm}^{-1}$ since two band centres are reported in Ref. [238] due to a typographical error ($873.2\,\mathrm{cm}^{-1}$ in Table I and $872.2\,\mathrm{cm}^{-1}$ on p. 248).

[d] The band centre uncertainty is $+2$ and $-3\,\mathrm{cm}^{-1}$ since the term value was determined with $\tilde{\nu}_8 = 873.2\,\mathrm{cm}^{-1}$ which has a single-sided error bar of $-1\,\mathrm{cm}^{-1}$ (see note d).

Chapter 5

Theoretical description of formic acid vibrations

Previous *ab initio* studies of HCOOH have been primarily concerned with the *trans* rotamer. These have either focussed on the fundamental region below 4000 cm^{-1} or the C–H and O–H stretching overtone manifolds, have either used effective perturbative Hamiltonians or variational methods, and have either accounted for the full vibrational dimensionality or employed reduced-dimensional models.[167] With a plethora of new experimental reference data for *trans*-HCOOH that fill important gaps in the spectral region up to 4000 cm^{-1} (Table 4.8, pp. 91) the vibrational dynamics of *trans*-HCOOH in the fundamental region will be systematically investigated in this chapter in order to link, merge, and extend insights from previous investigations. The primary focus is to benchmark nuclear vibrational models and explore the applicability of low-order perturbative vibrational models, such as rectilinear normal mode VPT2, to complement recent variational and curvilinear perturbative perspectives [21, 22, 29, 109].

5.1 Definition of effective Hamiltonians for *trans*-HCOOH

The vibrational benchmarking database of *trans*-H^{12}COOH in Table 4.8 (pp. 91) comprises overall 42 term values between 600 and 4000 cm^{-1}. Less than 50% of these energy levels can be computed with 'pure' VPT2 whereas all others are somehow involved in resonance interactions with one or several N_5 polyads (Eq. 4.6, p. 67). The accuracy of perturbative predictions depends on the appropriate treatment of such resonances. As such, before we can continue to investigate the performance of VPT2 in the following, we need to define appropriate resonance Hamiltonians. In Table 5.1, resonance polyads are proposed for all experimentally available term values of *trans*-HCOOH up to 4000 cm^{-1}. The division into three sets I-III reflects excitations in the OH bend-torsion polyad, i.e. $N_5 = 0, 1, 2$, respectively. States that are coupling to states from a higher-excited N_5 polyad are included in the same set at the latter.

The definition of resonance polyads is informed by the Martin test and the experimental analysis provided in the preceding chapter. With default thresholds (Section 2.1.2), the Martin test detects the following three resonances: $\omega_2 \approx \omega_3 + \omega_5$, $\omega_4 \approx 2\omega_9$, and $\omega_5 \approx 2\omega_9$. The involvement of ν_4 (CH in-plane bend) in the OH bend-torsion resonance can be understood from a geometrical perspective as ν_4 exhibits partial OH bending character and ν_5, in turn, partial CH bending character. Indeed, a recurring motif in Table 5.1 is the $\nu_4/\nu_5/2\nu_9$ triplet. The effective Hamiltonians have been defined to be as small as possible while retaining all relevant couplings. The accuracy of these minimum effective Hamiltonians was validated by comparison to the

[167] See for example Refs. [98, 101, 114] where the OH overtone manifold is investigated or Refs. [21, 22, 24, 29, 99, 109] where the fundamental region is discussed.

Table 5.1 Vibrational benchmarking set of *trans*-HCOOH. Effective Hamiltonians are proposed in order to model the experimentally available term values with perturbation theory. States that are grouped together (braces) belong to the same effective Hamiltonian. The experimental term values are compiled in Table 4.8 (pp. 91).

Set	Data points	Experimentally available	Effective Hamiltonian
I	18	ν_7, ν_9, ν_8, ν_6, $2\nu_7$, $\nu_7{+}\nu_9$, $\nu_8{+}\nu_9$, $\nu_6{+}\nu_7$, $\nu_6{+}\nu_9$, ν_3, $2\nu_8$, $\nu_6{+}\nu_8$, $2\nu_6$, $\nu_3{+}\nu_8$, $\nu_3{+}\nu_6$, $2\nu_3$, ν_1, $\nu_3{+}2\nu_8$	
II	16	$2\nu_9$, ν_5, ν_4, $3\nu_9$, $\nu_5{+}\nu_9$, $\nu_7{+}2\nu_9$, $\nu_5{+}\nu_7$, $2\nu_4$, ν_2, $\nu_3{+}2\nu_9$, $\nu_3{+}\nu_5$, $\nu_3{+}\nu_4$, $\nu_2{+}\nu_7$, $\nu_2{+}\nu_9$, $\nu_2{+}\nu_8$, $[\nu_3{+}\nu_9/\nu_7{+}3\nu_9]^a$	$\{2\nu_9, \nu_5, \nu_4\}$, $\{3\nu_9, \nu_5{+}\nu_9, \nu_4{+}\nu_9\}$, $\{\nu_7{+}2\nu_9, \nu_5{+}\nu_7, \nu_4{+}\nu_7\}$, $\{2\nu_4, \nu_2, \nu_3{+}2\nu_9, \nu_3{+}\nu_5, \nu_3{+}\nu_4\}$, $\{\nu_2{+}\nu_7, \nu_3{+}\nu_7{+}2\nu_9, \nu_3{+}\nu_5{+}\nu_7, \nu_3{+}\nu_4{+}\nu_7\}$, $\{\nu_2{+}\nu_9, \nu_3{+}3\nu_9, \nu_3{+}\nu_5{+}\nu_9, \nu_3{+}\nu_4{+}\nu_9\}$, $\{\nu_2{+}\nu_8, \nu_3{+}\nu_8{+}2\nu_9, \nu_3{+}\nu_5{+}\nu_8, \nu_3{+}\nu_4{+}\nu_8\}$, $\{\nu_3{+}\nu_9, \nu_7{+}3\nu_9, \nu_5{+}\nu_7{+}\nu_9, \nu_4{+}\nu_7{+}\nu_9\}$
III	8	$\nu_7{+}\nu_8{+}\nu_9$, $\nu_3{+}\nu_7$, $4\nu_9$, $\nu_6{+}2\nu_9$, $\nu_5{+}\nu_6$, $\nu_4{+}\nu_5$, $\nu_7{+}4\nu_9$, $[\nu_5{+}2\nu_9/2\nu_5]^a$	$\{\nu_7{+}\nu_8{+}\nu_9, \nu_3{+}\nu_7, 4\nu_9, \nu_6{+}2\nu_9, \nu_5{+}\nu_6, \nu_5{+}2\nu_9, 2\nu_5, \nu_4{+}2\nu_9, \nu_4{+}\nu_5\}$, $\{\nu_7{+}4\nu_9, \nu_6{+}\nu_7{+}2\nu_9, \nu_5{+}\nu_6{+}\nu_7, \nu_5{+}\nu_7{+}2\nu_9, 2\nu_5{+}\nu_7, \nu_4{+}\nu_7{+}2\nu_9, \nu_4{+}\nu_5{+}\nu_7\}$

[a] Resonance doublets; only the respective higher-wavenumber band has experimentally been observed.

eigenvalues of the full CVPT6 matrix using the same potential [28]. Despite the significant intensity transfer between ν_1 and $\nu_2{+}\nu_7$, the analysis in Section 4.2 showed that the coupling between them is so weak that it can be treated perturbatively. Both states are therefore sorted into Set I.

The C–H stretching region (ν_2) deserves a few comments (see also Appendix C.3). The C–H stretch is very sensitive to the form of the effective Hamiltonian treatment – 2938 without and 2944 cm^{-1} with $2\nu_4$ included in the effective ν_2 VPT2 Hamiltonian (TM-PES). Based on the effective Hamiltonian results from Section 4.3.2, $2\nu_4$ is grouped together with ν_2 (Set II, Table 5.1). Due to its simultaneous connection to the $N_5 = 2$ polyad, one could in principle treat all observed states between 2300 up to 3200 cm^{-1} in the same effective Hamiltonian. Since the proposed disconnected Hamiltonians in Table 5.1 are able to reproduce the reference values of the full CVPT6 Hamilton matrix with sufficient accuracy, smaller effective Hamiltonians are preferred. However, they may need some adjustment if additional members of the $\{n_7, N_5\} = \{1, 2\}$ polyad are observed since some of them are predicted to be near ν_2.

5.2 Fundamentals of *trans*- and *cis*-HCOOH

The *trans* conformer

Differently calculated term values of the nine *trans*-HCOOH fundamentals are compared in Table 5.2. The TM-PES is used throughout all calculations to remove additional error sources that could fortuitously cancel. Furthermore, the Watson Hamiltonian is employed to focus on differences between variational and perturbative vibrational methods. Strictly speaking, not the pure Watsonian but its ICPH modification is used in the 9D VCI calculations (column L) but in the absence of pure Watsonian VCI data, ICPH-VCI serves as a computational reference whose accuracy for the nine *trans* fundamentals was validated in Section 4.1 against experiment. The numerical deviations between both have so far not been quantified for formic acid but at least for the fundamental vibrations the deviations between both models are expected to be negligible.[168]

[168] See for example comparisons of Watsonian VCI and ICPH-VCI calculations for the tetra-atomic HOPO and its deuterated isotopologue [252].

Table 5.2 Assessment of variational and perturbational models for the fundamentals of *trans*-HCOOH (in cm^{-1}) on the TM-PES. Results in parentheses are obtained with lower-order force fields and are referenced to the 'exact' results (D to C; F and G to E).

				1D						9D (dep.)		9D (pert.)		
			Harm	VPT2	VPT4		VCI[a]			VPT2[b]	VPT4[b]	VPT2[b]	VPT4[b]	VCI[c]
			Full	QFF[d]	SFF[d]	QFF[d]	Full[d]	QFF[d]	SFF[d]	QFF[e]	SFF[f]	QFF[e]	SFF[f]	5-B
	Descr.	Γ	A	B	C	D	E	F	G	H	I	J	K	L
ν_1	ν(OH)	A′	3767	3604	3599	(+64.0)	3601	(+65.0)	(−6.9)			3576	3577	3575
ν_2	ν(CH)	A′	3092	2975	2972	(+41.7)	2973	(+42.5)	(−6.2)	2933	2935	2944	2946	2938
ν_3	ν(C=O)	A′	1818	1805	1805	(+1.5)	1805	(+1.4)	(−0.1)			1783	1783	1783
ν_4	δ(CH)	A′	1412	1418	1416	(+1.7)	1416	(+1.4)	(−0.3)	1373	1373	1380	1377	1379
ν_5	δ(OH)	A′	1323	1320	1321	(−1.0)	1320	(−0.7)	(+0.1)	1273	1272	1302	1289	1305
ν_6	ν(C−O)	A′	1140	1149	1148	(+1.6)	1148	(+1.5)	(−0.1)			1107	1107	1108
ν_7	δ(OCO)	A′	632	640	639	(+0.4)	639	(+0.4)	(−0.0)			627	627	627
ν_8	γ(CH)	A″	1056	1096	1085	(+8.1)	1087	(+5.9)	–[g]			1034	1035	1034
ν_9	γ(OH)	A″	673	967	617	(+93.2)	834	(+26.3)	–[g]			640	637	638

[a] Eigenvalues are computed with QVib (see Appendix B.4).
[b] The effective Hamiltonians are defined in Table 5.1. Deperturbed and perturbed term values correspond to the diagonal values and eigenvalues of the effective Hamiltonians, respectively
[c] From Ref. [21]; full VCI using a 5-body expansion of the potential and the ICPH modification of the Watsonian. Note that the previous discussion of convergence errors (Section 5.3.1) does not affect the *trans* fundamentals.
[d] Force constants are obtained with QFit (see Appendix B.4).
[e] The numerical quartic force field is computed from analytic second derivatives (see Appendix B.2).
[f] As item *e* but the quintic and sextic force constants are not exact (see Appendix B.2).
[g] Eigenvalues are not converged due to a negative leading coefficient in the polynomial expansion of the potential.

Details of the individual computations can be found in Appendix B and the footnotes of Table 5.2. VPT*n* calculations in reduced and full dimensionality have been performed with GUINEA. Numerical sensitivities of force constants are overall negligible and effects on computed fundamentals are within 1 cm^{-1}.[169]

We can divide the following discussion of the nine vibrational modes into three groups: The high-frequency X−H stretching vibrations (ν_1-ν_2, A′), the in-plane fingerprint vibrations (ν_3-ν_7, A′), and the out-of-plane bending vibrations (ν_8-ν_9, A″).

The two stretching vibrations are energetically and geometrically cleanly separated from other vibrational modes and the rectilinear normal mode displacements are mostly localised along the X−H bonds. As such, the excellent performance of VPT2 is not surprising. The perturbational 1D predictions agree with 1D VCI to within 3 cm^{-1} (B, C versus E), despite very large potential energy contributions beyond a quartic force field (D, F, G). The cancellation of higher-order vibrational corrections beyond VPT2 can be ascribed to the local mode character of these stretching vibrations or, in other words, the Morse-likeness of the C−H and O−H stretches as VPT2 is exact for the vibrational term values of the Morse potential [77, 173]. Nonetheless, vibrational coupling is essential to correctly model the X−H stretching levels as previously pointed out [101]. The size of these couplings is reflected in the deviations between 1D and 9D VPT2 (H, J versus B). The slightly larger deviations for ν_2 in the full-dimensional treatment (J, K versus L) were discussed above (Section 5.1) and are mostly due to the effective Hamiltonian treatment.

At the other wavenumber end, the predictions for the two A″ symmetric out-of-plane modes

[169] Absolute deviations of 9D VPT2 fundamentals are within 1 cm^{-1} when instead the QFF is obtained from single-point energies. Similarly, deviations for 1D VPT2 or VPT4 are well below 1 cm^{-1} when they are instead computed with force constants obtained via numerical differentiation.

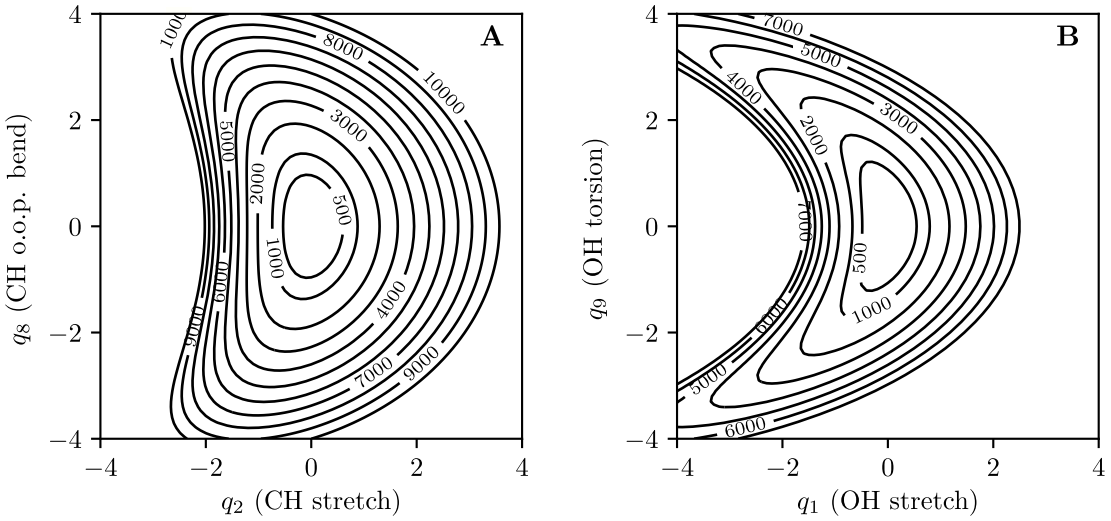

Figure 5.1 Potential energy scans (TM-PES, in cm^{-1}) of *trans*-HCOOH along the XH stretches and XH out-of-plane bending or torsion vibrations in dimensionless normal coordinates.

significantly differ between different vibrational models in one dimension (B, C, E). This is especially pronounced for the OH torsion (ν_9). The diagonal 1D anharmonicity of ν_9 is small and negative for VPT4 but several hundreds of cm^{-1} and positive for VPT2 and VCI – yet the net anharmonicity constitutes only 5% of the zero-point-corrected term value (A versus J, K, L). The discrepancies between 1D VPT2 and VPT4 can be understood by inspection of the individual contributions to the anharmonic 1D correction (Eq. 2.27, p. 19). Note that all terms in Eq. 2.27 that are set in brackets are zero since ν_8 and ν_9 are both non-totally symmetric. In view of a very large and positive quartic force constant ($\phi_{9,9,9,9} \approx 2350\,cm^{-1}$), we can easily rationalise why the anharmonic 1D correction is positive and very large for ν_9 at second-order of perturbation – the 1D VPT2 correction is $+\phi_{9,9,9,9}/8$. This is almost completely offset by the inclusion of fourth-order corrections due to additional negative contributions in 1D VPT4 (Eqs. 2.21-2.22, pp. 18). The 1D VPT4 term value of ν_9 is very close to the full-dimensional value (C, K), however, the incompatibility of 1D VPT4 and VCI (C, E) indicates that this near-quantitative agreement is most likely accidental.

In view of these large discrepancies between different vibrational models and the pronounced sensitivity of the 1D results to the force field completeness, it must be asked whether the quantitative agreement for ν_9 to within $2\,cm^{-1}$ in the full-dimensional treatments (J, K, L) is partly fortuitous and perhaps facilitated by the cancellation of higher-dimensional anharmonic corrections. This is not the case and we can rationalise the deviations between different 1D models as the inadequateness of rectilinear coordinates to describe an essentially curvilinear motion. One-dimensional cuts along the rectilinear torsional coordinate are not physically meaningful.[170] In order to describe the inherently curvilinear torsional path, the O–H stretching coordinate (q_1) must be included to counteract the simultaneous stretching of the O–H bond in rectilinear coordinate space (the q_9 normal coordinate is perpendicular to the molecular plane). The banana shape of the two-dimensional contour plot along q_1 and q_9 in Fig. 5.1B nicely illustrates the curvilinear nature of the torsion as the minimum energy path is not a vertical line – effective elongation of the OH bond – but is bent to the left as negative displacements along q_1 correspond to a simultaneous shortening of the OH bond length. In principle, the same applies to the CH out-of-plane bend (ν_8), however, the curvature in Fig. 5.1A is much less pronounced and

[170] The 2D pendulum or stretch-bend coupling in carbon dioxide are textbook examples of the relationship between rectilinear and curvilinear descriptions of bending motions. For further reading, see for example Ref. [253] or Refs. [3, 46].

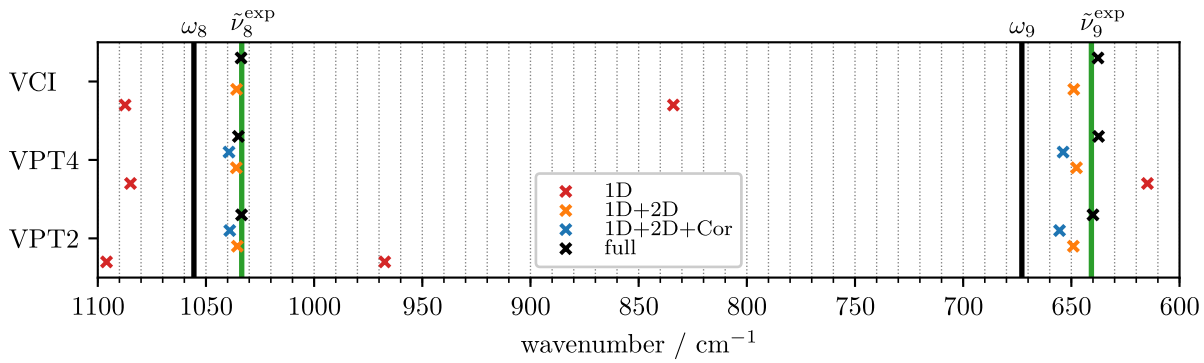

Figure 5.2 Differently calculated term values of the ν_8 and ν_9 fundamentals of *trans*-HCOOH from Table 5.2 compared to experiment (Table 4.8, p. 91). The additional 2D term values are computed according to Eq. 2.28 (p. 19) and include essential coupling to the respective XH stretch. Note that "1D+2D+Cor" is not available VCI (see Appendix B.4).

low-order expansions in rectilinear coordinates, therefore, remain a valid approximation towards much higher excitation energies.

Returning to the sensitivity of different 1D models for ν_9, it should be realised that in these calculations only the $q_1 = 0$ region of the potential is sampled which corresponds to vertical displacements in the contour plot at $q_1 = 0$ where the potential energy increases rapidly beyond $|q_9| = 0.5$ (Fig. 5.2B). This explains the sensitivity of 1D rectilinear VCI with respect to the order of the force field expansion (E, F, G). When additional relaxation of the O–H stretch is included by extension to 2D, much lower regions of the potential are probed for even larger displacements of q_9. In the bottom panel of Fig. 5.2, the discrepancies between the 1D and 9D rectilinear perspectives are bridged by 2D term values that include additional out-of-plane bend-stretch coupling. The perturbative 2D calculations are computed according to Eq. 2.28 (p. 19) and include additional contributions from the OH stretch ($j = 1$) for ν_9 and correspondingly from the CH stretch ($j = 2$) for ν_8. The 2D VCI term values are computed from the eigenvalues of the potentials shown in Fig. 5.2. Indeed, VPT2, VPT4, and VCI can all be reconciled in the 2D approach and the resultant term values are in-between the harmonic and anharmonic 9D values. Moreover, in this 2D sub-space perturbation theory once again agrees with VCI to within 1-2 cm^{-1}.

Lastly, we turn to the mid-frequency group vibrations. The 1D analysis in Table 5.2 indicates that the diagonal anharmonicity is very small (D, F, G). For such vibrations, it is not uncommon that the off-diagonal anharmonicity outweighs the diagonal anharmonicity. Overall, it is not surprising that VPT2 and VPT4 both reproduce the VCI term values of ν_3, ν_6, and ν_7 to within 1 cm^{-1} in the 9D treatment (J, K, L). For these modes, rectilinear normal mode VPT2 is a suitable method and is expected to yield quantitatively correct predictions for higher excitations along these modes. For the in-plane CH (ν_4) and OH (ν_5) bends, the previous arguments for ν_8 and ν_9 apply. A 2D VPT2 treatment with additional XH in-plane bend-stretch coupling (Eq. 2.28) yields 1387 and 1292 cm^{-1} for ν_4 and ν_5, respectively. Already two-thirds of their total deperturbed anharmonicities are recovered by simply accounting for the curvilinearity of the bending vibrations. The deperturbed 9D term values of ν_4 and ν_5 seem to be converged with respect to the order of perturbation theory (H, I) and larger discrepancies in the perturbed calculations (J, K, L) can be ascribed to their resonance interaction with the OH torsion overtone ($2\nu_9$). The perturbed term values in Table 5.2 are obtained by diagonalisation of an appropriate

effective Hamiltonian which takes the following form at second-order (see Eq. 2.39, p. 22)

$$\frac{\mathbf{H}_{\text{eff}}^{\text{VPT2}}}{hc} = \begin{pmatrix} 1373.1 & & \\ 0 & 1273.5 & \\ -26.9 & 39.6 & 1256.8 \end{pmatrix}, \tag{5.1}$$

and fourth-order (see Eq. 2.45, p. 24)

$$\frac{\mathbf{H}_{\text{eff}}^{\text{VPT4}}}{hc} = \begin{pmatrix} 1373.3 & & \\ 4.8 & 1272.2 & \\ -21.1 & 27.8 & 1245.6 \end{pmatrix}. \tag{5.2}$$

The Fermi coupling strengths ($W_{i,9,9}$) decrease and the deperturbed wavenumber difference between ν_5 and $2\nu_9$ simultaneously increases to effectively weaken the resonance coupling from second- to fourth-order. It is worth noting that when comparing to experimentally deperturbed values, $(2\nu_9)^* = 1249\,\text{cm}^{-1}$, $W_{5,9,9} = 42\,\text{cm}^{-1}$ [95] (mind $\nu_5 \leftrightarrow 2\nu_9$ label switch), VPT4 is nearer experiment for $(2\nu_9)^*$ whereas the VPT2 value is 'better' for $W_{5,9,9}$. This illustrates that one must tread carefully when comparing experimental effective Hamiltonians to low-order perturbative calculations [6]. Focussing instead on the perturbed 9D term values (J, K, L), it is noticeable that the full-dimensional VPT4 eigenvalues of the above effective Hamiltonian are inferior compared to VCI (Table 5.2). Whether this result is a genuine failure of VPT4 or due to errors in the approximated[171] quintic and sextic force constants is worth investigating in the future.

In summary, the success of VPT2 for the fundamentals of *trans*-formic acid is by no means fortuitous. In view of the pronounced curvilinearity of the torsion, rather the question arises up to how many torsional excitations VPT2 is still able to provide accurate results. The benchmarks in the following sections shed further light on this issue.

The *cis* conformer

Considering the above-discussed excellent performance of VPT2 for *trans*-HCOOH fundamentals, the VPT2 term values for the fundamentals of *cis*-HCOOH as published in Ref. [22] are in need of clarification. Differently computed *cis*-HCOOH fundamentals on both analytic potentials are compiled from the literature and listed in Table 5.3. The VPT2 wavenumbers from Ref. [22] are contrasted to differently computed VPT2 wavenumbers from this work (A-C). In A, the term values are calculated using sum-of-states VPT2. However, the Hamiltonian is not the exact VPT2 Hamiltonian but missing Coriolis contributions. In B, these missing contributions are included. Thus, the results in B represent exact sum-of-states VPT2. In C, the correct Hamiltonian is used and near-degeneracies are treated the usual way by deperturbation and subsequent diagonalisation of appropriate effective Hamiltonians (VPT2+F). Informed by the Martin test, a 2×2 effective Hamiltonian is set up with ν_2 and $2\nu_4$.

Comparison of the four different VPT2 calculations across both potentials suggests that the wavenumbers in Ref. [22] were computed following method A, i.e. without Coriolis contributions and no resonance treatment. Particularly for the XH stretching (ν_1-ν_2) and out-of-plane bending vibrations (ν_8-ν_9), these Coriolis contributions are very important for accurate band positions. ν_8 seems to exhibit a more pronounced numerical sensitivity on the RC-PES than on the TM-PES. Numerical sensitivities of the VPT2 wavenumbers, however, are negligible. The VPT2 values shown in Table 5.3 (A-C) were calculated with a numerical quartic force field that was obtained from single-point energies as described in Appendix B.2. When instead analytic second derivatives are used (only available for TM-PES), the maximum absolute deviations are

[171] On the transformation of force constants between different coordinate systems, see for example the works by Mills and Császár [3, 188, 254, 255].

Table 5.3 Assessment of differently computed fundamentals of *cis*-HCOOH (in cm^{-1}). CVPT6 values are from Ref. [28] and variational GENIUSH-Smolyak and MCTDH results, which serve as a reference, from Refs. [22, 29]. VPT2 results from Ref. [22] are contrasted to differently computed VPT2 values from this work (A-C). See text for details.

			TM-PES						RC-PES					
			VPT2				CVPT6	GENIUSH	VPT2				CVPT6	MCTDH
	Descr.	Γ	[22]	A	B	C			[22]	A	B	C		
ν_1	ν(OH)	A′	3633	3634	3640	3640	3653	n.r.	3623	3623	3629	3629	3636	3631
ν_2	ν(CH)	A′	2860	2860	2865	2873	2878	2873	2860	2857	2861	2880	2874	2871
ν_3	ν(C=O)	A′	1819	1819	1820	1820	1821	1821	1808	1809	1809	1809	1810	1810
ν_4	δ(CH)	A′	1384	1385	1386	1386	1389	1389	1383	1383	1384	1384	1384	1383
ν_5	δ(OH)	A′	1242	1242	1244	1244	1246	1247	1245	1245	1247	1247	1247	1246
ν_6	ν(C−O)	A′	1096	1096	1097	1097	1096	1096	1096	1098	1099	1099	1097	1097
ν_7	δ(OCO)	A′	657	657	658	658	657	657	651	651	652	652	652	652
ν_8	γ(CH)	A″	1014	1015	1020	1020	1020	1021	1002	1003	1008	1008	1014	1011
ν_9	γ(OH)	A″	482	482	489	489	491	490	483	483	491	491	491	491

well within 1 cm^{-1} for the fundamentals. The larger deviations for ν_1 between VPT2, CVPT6, and the variational references are presumably due to strong resonances to highly excited states $n > 4$, as indicated by the CVPT6 eigenvectors. This similarly affects ν_2 which is unanimously predicted to be in resonance with $2\nu_4$ [21, 22, 28]. Otherwise, the newly computed VPT2 fundamentals of *cis*-HCOOH in columns C compare very favourably with CVPT6 and the respective variational reference values.

5.3 A curvilinear perspective

5.3.1 The internal coordinate path ansatz

Across Refs. [22, 28, 29], evidence was produced that points to convergence errors in the published ICPH-VCI eigenvalues of HCOOH [21], particularly with respect to highly excited torsional states. In the following, these convergence issues are investigated in detail by repeating the calculations presented in Ref. [21] with systematically increased coverage of vibrational basis functions in the torsional coordinate.[172]

The path coordinate is defined numerically by a fixed number of points along the internal coordinate path. At each point along the path, $3N_{\mathrm{vib}} - 7$ adiabatic perpendicular bath coordinates are defined, i.e. the vibrational coordinate system changes for each point along the path. For implementation details, see Ref. [21]. There are three parameters in Dynamol that control the size of the vibrational basis. N is the number of VSCF modals which in turn are expanded in terms of trigonometric (path mode) and harmonic oscillator (perpendicular bath modes) functions. This contraction of the VSCF modals is controlled by M which must be defined in the preceding VSCF calculation and cannot be changed in the subsequent VCI calculation. The configurations included in the VCI matrix are restricted by Q. Only configurations with a total sum of vibrational quanta equal to or less than Q are included in the VCI basis. Note that Q and N are not completely independent since the highest possible excitation in each vibrational coordinate i is controlled by N_i. We shall adopt the nomenclature from Ref. [21] and use the index "s" for the torsional path mode and "k" for the eight bath modes. In the final calculations shown in Table 6 of Ref. [21], (M_k, M_s), (N_k, N_s), and Q were set to $(11, 31)$, $(7, 9)$, and 10, re-

[172] The calculations were executed with a copy of the Dynamol program which has kindly been provided by D. P. Tew.

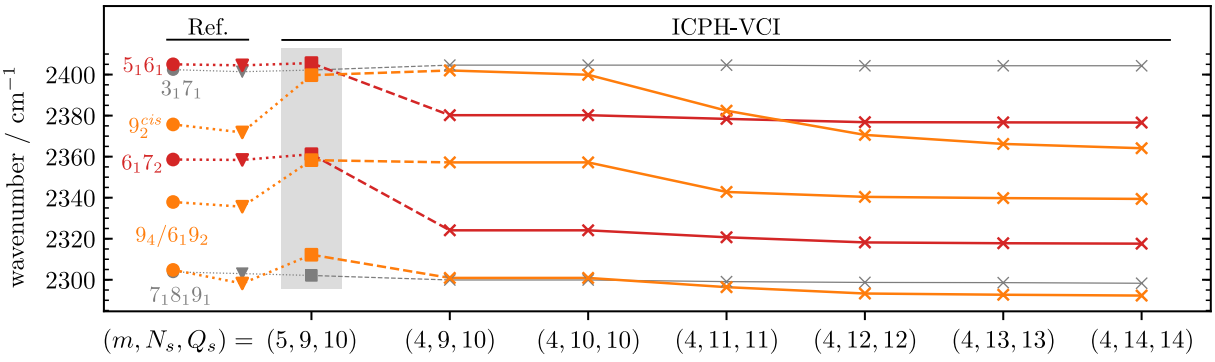

Figure 5.3 All computed A′ symmetric vibrational states of *cis*- and *trans*-HCOOH between 2280 and 2420 cm^{-1} (relative to the *trans* ground state) on the TM-PES. The 5-body ICPH-VCI results underlaid in grey are taken from the supplementary material of Ref. [21]; 4-body calculations are newly computed. ICPH-VCI results are contrasted to CVPT6 (disks) and GENIUSH-Smolyak (triangles) reference values on that potential [28, 29]. Grey-coloured ICPH-VCI states are converged with respect to the potential energy expansion (m) and vibrational basis size (N_s, Q_s) and orange-coloured states exhibit the expected convergence behaviour whereas the behaviour of red states calls for an explanation.

spectively. In all new VCI calculations, the results from the same underlying VSCF calculation are used to allow for comparability but instead a 4-body[173] expansion of the potential is used. In order to check the convergence of excited torsional states, N_s and Q must be increased. However, increasing Q also leads to the inclusion of higher-excited states that are exclusively excited along the bath modes which does not (significantly) improve the eigenvalues but unnecessarily increases the computational cost. To circumvent this issue, (a development version of) the Dynamol program has been slightly modified to separate Q into two independent parameters: Q_k controls the maximum allowed excitation of basis functions that are not excited in the path mode and Q_s controls the inclusion of basis functions where the path mode, i.e. the torsion, is excited. ICPH-VCI eigenvalues obtained with a 4-body expansion of the potential and different basis sizes are compared to the published 5-body results in Fig. 5.3. All other parameters are fixed, i.e. $(M_k, M_s) = (11, 31)$, $N_k = 7$, and $Q_k = 10$. These energy levels are contrasted to CVPT6 and near-completely converged GENIUSH-Smolyak ($b = 9$) reference values on the same potential.

As expected, all three torsional states (orange) systematically decrease in wavenumber and the $4\nu_9$ and $\nu_6{+}2\nu_9$ term values move towards the reference values. The lower-wavenumber band of this resonance doublet even moves below $\nu_7{+}\nu_8{+}\nu_9$, in agreement with experiment and converged GENIUSH-Smolyak reference values. The first torsional overtone of *cis*-HCOOH decreases by about 40 cm^{-1} and also moves towards the reference values. Repeating the 5-body calculations with increased N_s and Q_s values is expected to minimise the deviations of ICPH-VCI eigenvalues to other vibrational models but due to the joint treatment of both rotamers, the calculations are very expensive. As an example, the 4-body calculations in Fig. 5.3 were executed in parallel on an 18-core computer with an Intel Xeon Gold 6240 CPU. The calculations took between 3 and 18 days of computing time. Thus, in order to converge $2\nu_9^{cis}$ with a 5-body potential, several weeks (possibly a few months) of computing time are expected.

The convergence of the red states ($\nu_6{+}2\nu_7$ and $\nu_5{+}\nu_6$), on the other hand, is unexpected and calls for an explanation. From the data presented in Fig. 5.3, one might gain the impression that for $\nu_6{+}2\nu_7$, additional 5-body[174] potential coupling is essential which is doubtful in view of the

[173] For VSCF and VMP2 calculations, Dynamol is currently limited to a 4-body expansion of the potential [21]. Thus, all 5-body VCI calculations already use VSCF modals that were optimised with a 4-body expansion of the potential.

[174] Note that in the ICPH formalism, as implemented in Dynamol, the path mode is included in every term of the m-

convergence of $\nu_7+\nu_8+\nu_9$. On the basis of its eigenvectors, $\nu_6+2\nu_7$ is found to be an essentially pure state. The 4-body error, i.e. the resultant vibrational wavenumber deviation between a 4-body and 5-body expansion of the potential, is within 6 cm^{-1} for fundamental modes of *trans*-HCOOH [21]. For other non-resonant multi-quantum states, it is found that the 4-body error is approximately the sum of the 4-body error per vibrational mode times vibrational quanta of excitation. Based on this, the 4-body error for $\nu_5+\nu_6$ and $\nu_6+2\nu_7$ are each expected to be about 10 cm^{-1} – the observed 4-body errors amount to 25 and 37 cm^{-1}, respectively. This clearly points to error sources of a less physical nature, perhaps due to numerical instabilities.

It is striking that these problems are found for states that are energetically close to highly excited path states but surprisingly, $\nu_3+\nu_7$ and $\nu_7+\nu_8+\nu_9$ seem to be unaffected. In both problematic cases, however, the C–O stretch (ν_6) is involved. Without more detailed investigations, one can only speculate but inspection of the eigenvectors of the two problematic states indicates that these deviations are most likely due to numerical instabilities which are not present in the 5-body calculations where the numerical grids are generally larger. While $\nu_6+2\nu_7$ is not expected to interact strongly with the states from the extended OH bend-torsion polyad $N_{56} = 2$, which is the case with CVPT6 and GENIUSH-Smolyak, the 4-body calculation (with $N_s, Q_s = 14, 14$) yields a state that is only 60% pure and the two next larger contributions, each about 7-8%, are from the $\nu_6+2\nu_9$ and $4\nu_9$ basis functions. For $\nu_5+\nu_6$, the situation is quite similar. The two eigenstates that have the highest $\nu_5+\nu_6$ character in the 4-body calculation are located at 2292 cm^{-1} and 2377 cm^{-1}. These states each have only 19-30% $\nu_5+\nu_6$ character and the leading basis function is $\nu_6+2\nu_9$ in each case with 29-38%. These couplings are not reflected by the CVPT6 and GENIUSH-Smolyak eigenvectors. Richter and Carbonnière reported strong mixing between the ν_5 and ν_6 eigenstates of *cis*-HCOOH which in their MCTDH calculation are mixtures of the corresponding zeroth-order states [22]. This coupling is also found with GENIUSH-Smolyak on the TM-PES [29], indicating a genuine mixing of the OH in-plane bend (ν_5) and C–O stretch (ν_6) in *cis*-formic acid. Environment-free gas phase data is so far only available for ν_6 [87]. Given that in the respective energy region two torsional states become close in energy that correspond to different conformers ($2\nu_9^{cis}$ and $4\nu_9$), it is possible that rapid changes in the definitions of the ν_5 and ν_6 (from *trans* to *cis* and vice versa) bath modes cause the observed discrepancies in Fig. 5.3.

5.3.2 The OH torsion

The true torsional potential of formic acid is periodic with two asymmetric minima. Defining the torsional coordinate τ as the dihedral angle along H–O–C=O, the *trans* isomer corresponds to $\tau = 2n\pi$ and *cis* to $\tau = (2n+1)\pi$, $\forall n \in \mathbb{N}$. To account for the periodicity, which is a prerequisite to model wavefunction delocalisation effects, torsional potentials are usually expressed as Fourier series expansions [210]. This periodicity is utilised in the internal coordinate path Hamiltonian method and related methods or a full internal coordinate ansatz. Whereas single-well methods in general and perturbational methods, such as VPT and CVPT, in particular cannot account for this periodicity, the CVPT implementation of Sibert III [68, 69] correctly accounts for the curvilinear nature of the torsional coordinate by expanding the Hamiltonian in curvilinear normal mode coordinates. Delocalisation effects between both wells do not play an important role in low-lying vibrational states [21, 29]. To quantify the impact of the coordinate system on the torsional term values, we shall examine the anharmonicity of successive torsional eigenstates in the following.

mode decomposition of the potential energy. Thus, for a given m-body expansion, the vibrational Hamiltonian mediates coupling between bath modes up to order $m-1$. For example, the 4-body Hamiltonian only couples up to three bath modes. For further details see Ref. [21] and references therein.

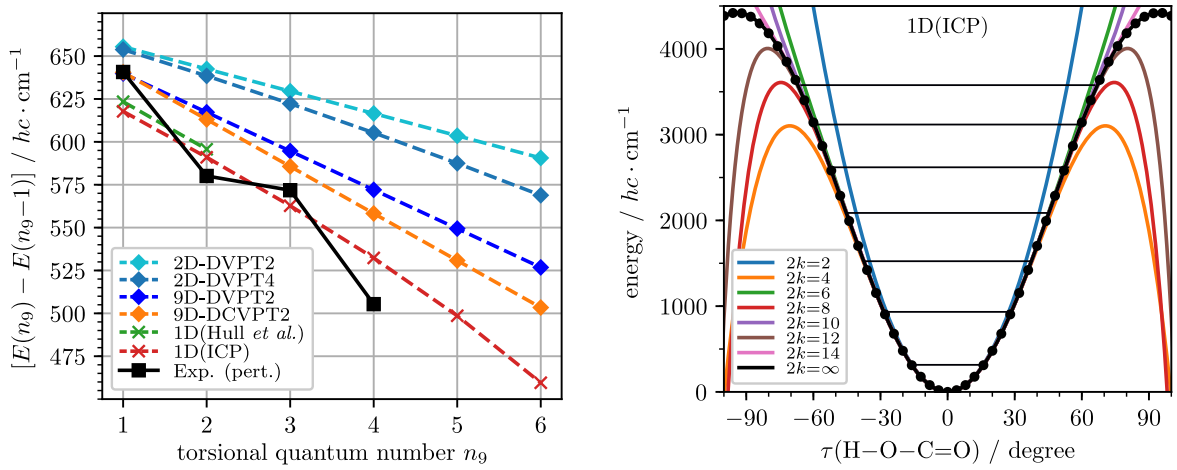

Figure 5.4 (left) Intervals between neighbouring deperturbed torsional energy levels of *trans*-HCOOH computed on the TM-PES and additional values reported by Hull *et al.* [107]. Note that the deperturbed computational results cannot directly be compared to the resonance-perturbed experimental band centres. (right) Energy scan along the internal coordinate path on the TM-PES about the *trans* equilibrium at $\tau = 0$. The Fourier fit (black line; Eq. 5.3) accurately represents the *ab initio* single-point energies (disks). The truncated force field approximations are calculated according to Eq. 5.4. The first seven eigenvalues are shown which correspond to eigenfunctions that are localised in the *trans* well.

In the left panel of Fig. 5.4, the intervals for successive torsional energy levels are shown using single- (diamonds) and double-well vibrational models (crosses) in conjunction with rectilinear (blue shades) and curvilinear (red shades) coordinate systems that all employ the TM-PES [21].[175] The values reported by Hull *et al.* (green) were obtained with a potential at the CCSD(T) level which was extrapolated to the complete basis set limit [107]. All computational models are deperturbed and do not account for the OH bend-torsion resonance which starts with $n_9 = 2$. This facilitates a comparison between full-dimensional and reduced-dimensional models. Since the torsion is perturbed by resonances, (deperturbed) rectilinear and curvilinear perturbative representations yield different results. Resonance-perturbed experimental data are shown as black squares but only serve as an orientation.

Starting with the deperturbed perturbative methods, it should be noted that the slope of the curves equals $2x^*_{9,9}$ at second-order. Informed by the results from Section 5.2, the reduced-dimensional models include coupling to the O−H stretch. The difference between the full-dimensional deperturbed VPT2 and CVPT2 in Fig. 5.4 reflects the deviations between a rectilinear (VPT2) and curvilinear (CVPT2) normal mode description at lowest-order of approximation. As expected, the curvilinear model is steeper, i.e. accounting for more torsional anharmonicity. Generally, it is difficult to separate diagonal anharmonicity from resonance effects in the experimental data. However, CVPT2 seems to come closest to the general trend of the experimental values up to $n_9 = 4$. The full-dimensional VPT2 model, on the other hand, is steeper than the 2D VPT2 treatment. This reflects vibrational coupling effects on the diagonal anharmonicity constant (cf. Eq. 2.9, p. 15). And lastly, in the 2D treatment, VPT4 accounts for more torsional anharmonicity than VPT2. This nicely illustrates that the inadequateness of rectilinear coordinates is somewhat remedied by going to higher orders of perturbation theory, thus also accounting for effects that are associated with the non-linear transformation between curvilinear and rectilinear coordinates.[176]

[175] In Fig. 5.4 torsional states up to $n_9 = 6$ in the *trans* well are included. Based on recent calculations [29], *trans-cis* delocalisation effects are expected to start with $n_9 = 7$.

[176] See also Fig. 1 of Ref. [73], where Gong *et al.* compare VPT2 and VPT4 for bending intervals in the Si_2C molecule. The performance of both models is qualitatively similar to the 1D results for the torsion of *trans*-HCOOH in Fig. 5.4.

These results are not surprising and they show that the predictive power of perturbative methods deteriorates much faster for inherently curvilinear motions when expanded in rectilinear rather than curvilinear normal mode coordinates. For variational Watson models, this means that higher energy regimes along the torsional coordinate must be sampled in order to accurately describe excited torsional states. In perturbative Watson models, the potential expansion is usually tied to the order of perturbation theory, thus necessitating going to higher orders. Depending on the accuracy one is aiming for, however, low-order rectilinear normal mode perturbation theory may still be an option to study excited torsional states. This will be quantified in the next section by comparing computed term values of excited torsional states to experiment by including resonance effects (Section 5.4).

Before doing so, however, it is insightful to compare the perturbative results to reduced-dimensional but fully variational models that take the torsional periodicity into account and employ the exact torsional potential. The internal coordinate path in formic acid corresponds to rotation about the C–O bond. When setting up the internal coordinate path for formic acid, DYNAMOL [21, 55] defines configurations in a predefined interval along τ while the other degrees of freedom are subject to a constrained optimisation. The Fourier expansion

$$V(\tau) = \frac{1}{2}\sum_{m=1}^{7} V_m \left[1 - \cos\left(m\tau\right)\right], \tag{5.3}$$

was recently used by Hull *et al.* for the formic acid torsion [107] and is also used here to obtain an analytic representation of the potential energy scan along the internal coordinate path (4° steps; disks in Fig. 5.4). With an analytic representation available, truncated force field expansions can readily be obtained by expanding the cosine as a Taylor series [256]

$$V(\tau) = \frac{1}{2}\sum_{m=1}^{7} V_m \sum_{k=1}^{\infty} \frac{(-1)^{k+1}(m\tau)^{2k}}{(2k)!} = \frac{1}{2}\sum_{m=1}^{7} V_m \left(\frac{m^2}{2}\tau^2 - \frac{m^4}{24}\tau^4 + \frac{m^6}{720}\tau^6 + \ldots\right). \tag{5.4}$$

The 1D eigenvalues in the exact[177] potential are visualised Fig. 5.4, labelled "1D(ICP)". They were obtained with a recent computer implementation of the Chung-Phillips ansatz [257] that was published by Medel *et al.* [258]. Note that there are deviations[178] to recently published values by Hull *et al.* [107]. Since the effective anharmonicity, i.e. the slope of the curves, is the primary interest here, this does not impair the current discussion as the slopes of the green and red curves are very similar in Fig. 5.4 (left).

As is well known [107, 259, 260], the pronounced diagonal anharmonicity of the OH torsion complicates low-order perturbative treatments. Rewardingly, full-dimensional deperturbed CVPT2 is very close to the exact 1D anharmonicity, especially up to $n_9 = 4$. In Table 5.4, the eigenvalues for the exact potential and several truncated[179] force field expansions are com-

[177] The deviations between eigenvalues in the exact and fitted potential are below 0.1 cm^{-1}.

[178] The Chung-Phillips method as implemented by Medel *et al.* [258] yields 617 and 1205 cm^{-1} relative to the ground state for the first and second excited torsional states when using the Fourier series potential reported by Hull *et al.* [107]. These values compare favourably with corresponding values on the TM-PES (Table 5.4). Hull *et al.* used another method to solve the 1D Schrödinger equation of the torsional potential and reported 623 and 1219 cm^{-1} [107]. The deviations presumably arise from different treatments of the inertia tensor along the curvilinear path. In absence of an equilibrium geometry for the published potential [107], the equilibrium geometry on the TM-PES is used for both potentials. Deviations when instead the equilibrium geometries at the CCSD(T)/aVTZ or CCSD(T)/aVQZ levels are used are negligible (1-2 cm^{-1}).

[179] Since truncation of the cosine at $2k$ for even values of k leads to a negative leading coefficient (Eq. 5.4), the potential energy is set to 10^{10} Hartree for points beyond the maxima in order to converge the eigenvalues. Note that for the truncated force field expansions where the leading coefficient is negative ($2k = 4, 8, 12, \ldots$), the gradient becomes small near the maxima just before the potential is artificially increased thus affecting the convergence of eigenvalues near that threshold. At $2k = 4$, for example, this leads to a seeming near-convergence of the $n_9 = 6$ eigenvalue (Table 5.4).

Table 5.4 Fourier fit coefficients for the torsional internal coordinate path on the TM-PES (Eq. 5.3). The potentials are visualised in Fig. 5.4. The eigenvalues are computed with the Chung-Phillips algorithm [257] as implemented by Medel *et al.* [258] and compared to truncated force field approximations (Eq. 5.4) for the first six excited torsional states in the *trans* well. The exact results are referenced to the ground state at 315 cm^{-1}. All reported values are in units of cm^{-1}.

Fourier fit		Eigenvalues (for $2k$ = ...)									
m	V_m	n_9^{ICP}	∞	n_9^{trans}	14	12	10	8	6	4	2
1	1391.0734	1	618	1	0	0	0	0	0	−2	32
2	3652.2301	2	1209	2	0	0	0	0	1	−8	84
3	89.3554	3	1772	3	0	0	0	−1	5	−22	164
4	−48.0136	5	2304	4	0	0	2	−3	14	−42	274
5	7.6843	7	2803	5	1	3	6	1	32	−52	417
6	3.9156	9	3262	6	3	21	21	32	70	−8	599
7	0.0571										

pared. The eigenvalues of the exact potential ("∞") are labelled with quantum numbers in the internal coordinate path ansatz where $n_9^{\mathrm{ICP}} = 4, 6, 8$ correspond to states localised in the *cis* well. The mapping between n_9^{ICP} and n_9^{trans} is shown in Table 5.4. Eigenvalue differences to the exact solution are shown for truncated force field expansions up to $2k = 14$. The data show that in order to fully converge the nth excited state, a force field expansion ($\equiv 2k$) up to ($2n$+4)th order is necessary. Negligible errors of a few cm^{-1} are obtained when the potential is truncated at ($2n$+2)th order and acceptable errors well within 10 cm^{-1} for truncation at ($2n$)th order. These results indicate that in order to fully converge states in the OH bend-torsion polyad for $N_5 = 3$, the CVPT treatment must be carried out to at least eighth-order. Fig. 1 of Ref. [21] indicates that *trans-cis* delocalisation effects for *trans* eigenvalues are to be expected starting with $n_9^{trans} = 6$. The 1D wavefunctions computed according to Ref. [258] predict significant mixing to start with $n_9^{trans} = 7$ which is in agreement with more recent full-dimensional variational results by Martín Santa Daría *et al.* [29].

5.4 Multi-quantum vibrational states of *trans*-HCOOH

In the following, vibrational term value differences are compared, either against experiment or a computational reference. All 42 experimentally available vibrational *trans*-H^{12}COOH levels below 4000 cm^{-1} are selected which comprise 9, 25, 6, 1, and 1 one- through five-quantum states. Note that almost all included $n > 2$ states are either highly-excited torsional states or in resonance with such states (see Table 5.1). For convenience and comparability across experiment-theory and theory-theory benchmarks, the experimental term values are used throughout as abscissa. Potential experimental misassignments bear no impact on the theory-theory benchmarks, e.g. in cases where computed levels are strongly perturbed by resonances and assignments are ambiguous. For example, the assignments in the ν_6+2ν_9/4ν_9 doublet vary across different calculations. For consistency, in the experiment-theory and theory-theory benchmarks, the respective lower levels are compared against each other and similarly the upper levels. In such cases, the normal mode labels, based on the experimental analysis presented in Chapter 4, are only shown for convenience in Figs. 5.5-5.6.

All VPT2 calculations have been done with GUINEA using effective Hamiltonians as defined in Table 5.1. For comparability, the numerical quartic force field expansions of the TM-PES and RC-PES are both computed using only single-point energies, as detailed in Appendix B.2, but deviations are very small if instead the quartic force field on the TM-PES is computed from analytic second derivatives. Mean and maximum absolute deviations for the investigated states

are well below 1 and 2 cm^{-1}, respectively. Other values are taken from the literature [21, 22, 28, 29].[180] Note that for GENIUSH-Smolyak, values from the $b = 9$ calculation are used [29].

Experimental benchmark

Starting with the experiment-theory benchmark, Fig. 5.5 does not convey new insights but nicely illustrates several well-known points.

The comparison of the two analytic potentials (blue and red) overall shows that the TM-PES tends to overestimate experiment whereas the RC-PES tends to underestimate experiment. These findings are in agreement with the observations in Section 4.1 and Ref. [28]. CVPT6, which is expanded in curvilinear normal coordinates, overall performs very similarly to the variational reference results on both potentials. Their error profiles are very similar and absolute errors to experiment are within 10 cm^{-1}. Some MCTDH data points are absent from Fig. 5.5 as $\nu_3+2\nu_8$, $\nu_2+\nu_9$, and $\nu_2+\nu_8$ are not reported in Ref. [22]. Note the $\nu_3+\nu_4$ MCTDH eigenvalue, which deviates by -66 cm^{-1}, was marked as not converged in Ref. [22].

Lastly, VPT2+K on the two analytic potentials overall compares well with experiment. The error profiles of VPT2+K and CVPT6 are relatively similar and absolute deviations to experiment are mostly within 10 cm^{-1}. The deviations for $\nu_2+\nu_8$, $\nu_2+\nu_7$, and $2\nu_3$ appear to be partly due to the underlying potentials. The larger deviations for $\nu_7+4\nu_9$ and $4\nu_9$, however, highlight the true shortcomings of a second-order perturbative treatment in rectilinear normal coordinates. In view of the findings in Section 5.3.2, this is not surprising and it is remarkable that the absolute deviations to experiment are still within 15 cm^{-1}, even for $\nu_7+4\nu_9$. When instead of the CCSD(T)-F12-quality quartic force fields a semi-diagonal *ab initio* MP2/aVTZ quartic force field is used, the absolute errors drastically increase up to 30 cm^{-1}, also for states that do not belong to the bend-torsion polyad (crosses). The violet data points bridge the gap between pure MP2 and CCSD(T)-F12 where the MP2 force field is enhanced by replacing the harmonic part with corresponding values at the CCSD(T)-F12a/VDZ-F12 level. These hybrid force field data points illustrate the importance of the harmonic and anharmonic force field for quantitative success. Nearly all absolute errors reduce to well within 10 cm^{-1}. For moderately excited states with up to three vibrational quanta of excitation, the MP2-quality anharmonicities are found to be fully sufficient.

Computational benchmark

To focus in more detail on the differences between vibrational models, energy levels computed on the TM-PES are compared against the near-completely converged GENIUSH-Smolyak reference values. The results are visualised in Fig. 5.6.

Starting with ICPH-VCI, the pictorial representation of the data shows that the largest errors are associated with torsionally-excited states. This is in line with findings from Section 5.3.1 and Refs. [28, 29]. For $\nu_7+4\nu_9$, the deviation is even above 100 cm^{-1}. The performance of CVPT6 further improves in comparison to Fig. 5.5. Based on the data shown in Fig. 5.6, an overall excellent performance can be attested, especially for complicated states such as $4\nu_9$ and $\nu_7+4\nu_9$.

The data in Fig. 5.6 allow for an unambiguous assessment of the performance of VPT2. On the whole, the error profile of VPT2+K is mostly similar to that of CVPT6.

While it is unsurprising that the largest errors correspond to highly-excited torsional states, $\nu_7+4\nu_9$ and $4\nu_9$, the analysis of the errors for successive torsional states ($n_9\nu_9$) provides very valuable insights. Since $4\nu_9$ is a resonance doublet, the value for $\nu_6+2\nu_9$ is included as the assignments switch. On the semi-diagonal hybrid force field, the error to GENIUSH-Smolyak increases from 0.2, 4.7, 14.2, to 12.2/23.1 cm^{-1}. These errors reflect the accumulated effect of

[180] For CVPT6, only selected values on the RC-PES are reported in Ref. [28].

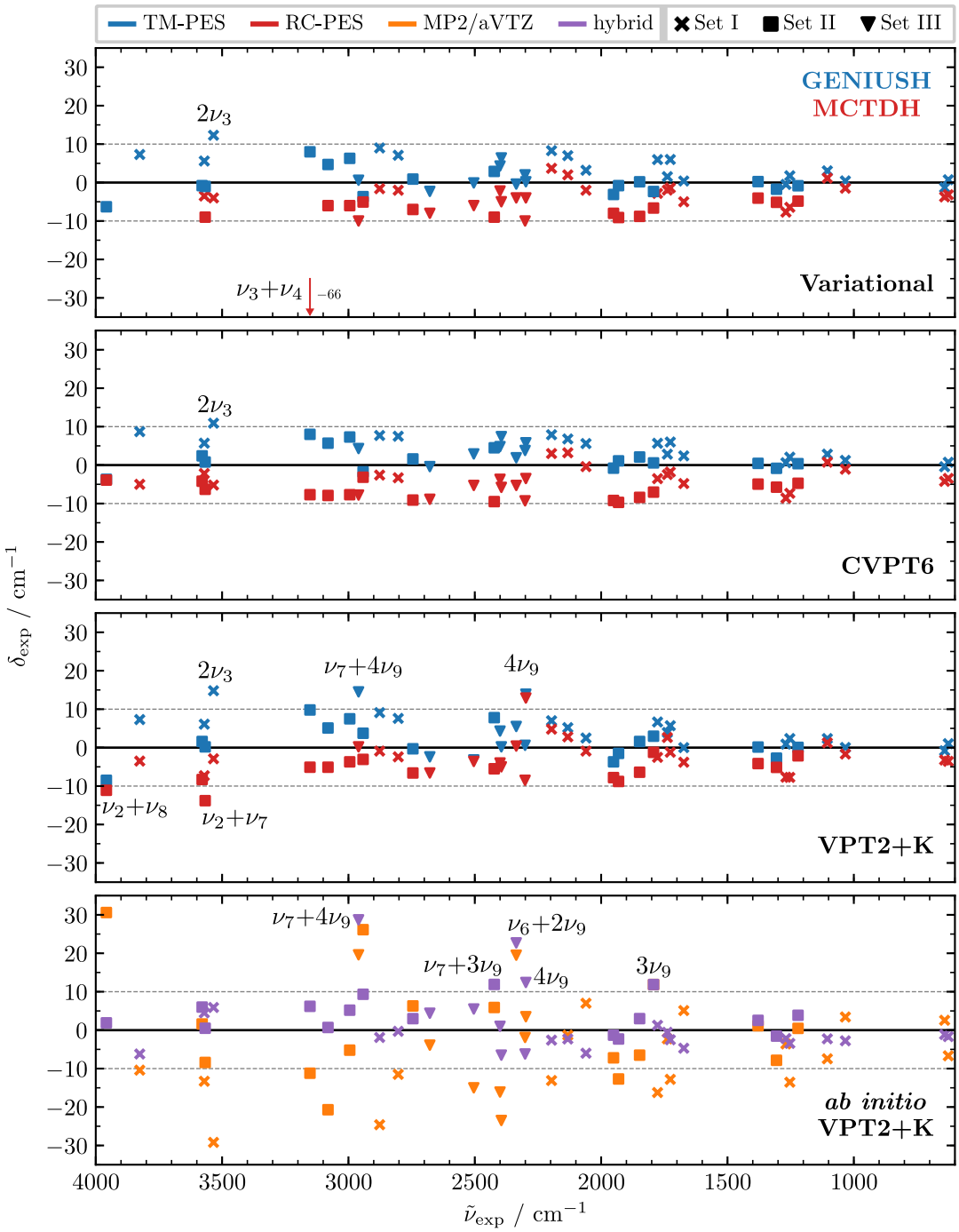

Figure 5.5 Comparison of *trans*-HCOOH vibrational term values against experiment ($\delta_{\text{exp}} = \tilde{\nu}_{\text{calc}} - \tilde{\nu}_{\text{exp}}$). The *ab initio* MP2/aVTZ quartic force field is further enhanced with CCSD(T)-F12a/VDZ-F12 harmonic wavenumbers (hybrid force field). The variational GENIUSH-Smolyak ($b = 9$) and MCTDH values are from Refs. [22, 29] and the CVPT6 data from Ref. [28]. Absolute deviations greater than $10\,\text{cm}^{-1}$ are labelled, except for pure MP2. The sets are defined in Table 5.1.

electronic structure errors, rectilinear VPT2 errors, and possible errors that arise from the (comparably small) effective Hamiltonian treatment. Removing the electronic structure error source, the error on the TM-PES increases from 0.4, 1.0, 5.2, to $5.9/13.7\,\text{cm}^{-1}$. Beyond $n_9 = 2$, the electronic structure errors thus already outweigh the inherent VPT2 errors. Since the torsion is heavily perturbed by resonances, these errors may further include possible shortcomings that arise from the small effective Hamiltonian treatment. It would be desirable to quantify this impact, as $4\nu_9$ in particular is in an energetic region where several different N_5 polyads overlap (see

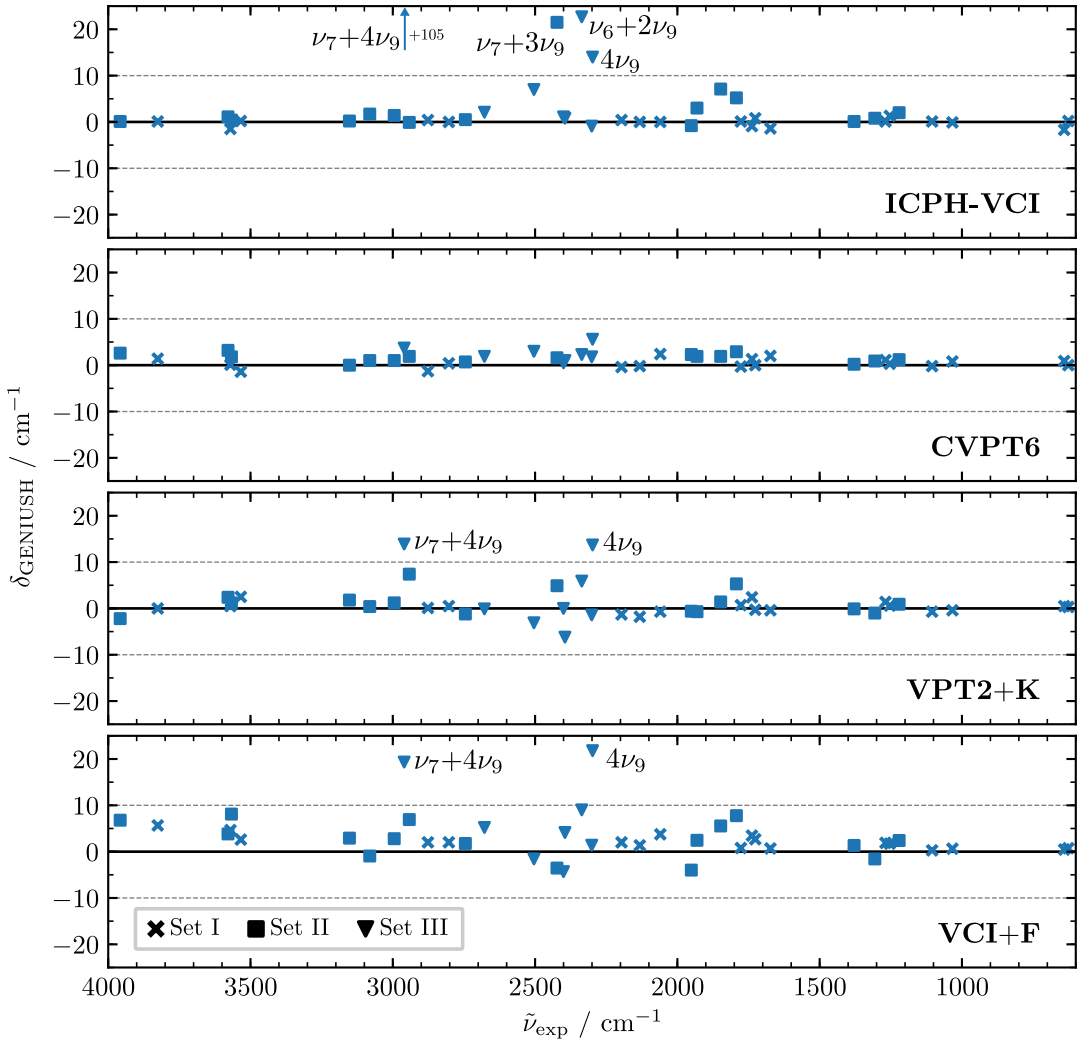

Figure 5.6 Comparison of *trans*-HCOOH vibrational term values against GENIUSH-Smolyak reference values ($\delta_{\mathrm{GENIUSH}} = \tilde{\nu}_{\mathrm{calc}} - \tilde{\nu}_{\mathrm{GENIUSH}}$). The GENIUSH-Smolyak values from the $b = 9$ calculation are used [29]. The ICPH-VCI and CVPT6 data are from Refs. [21, 28]. The TM-PES is used in all four calculations. Absolute deviations greater than 10 cm^{-1} are labelled. The sets are defined in Table 5.1.

Section 4.3.2). The CPVT*n* effective Hamiltonians, which are expanded in curvilinear normal coordinates, are compact but much larger in comparison. For example, the CVPT2 errors for $n_9 = 1, ..., 4$ relative to GENIUSH-Smolyak are 1.2, 0.8, 6.5, 2.1/10.3 cm^{-1}. To fully disentangle the effective Hamiltonian error from the rectilinear coordinate representation, rectilinear normal mode CVPT2 is necessary. To conclude the discussion of VPT2+K, two comments are in order. If a quartic force field is computed *ab initio*, four-mode quartic force constants with four distinct are usually not available (see note 55, p. 22). The impact of four-mode quartic force constants is limited to $\nu_3+\nu_7$ and $\nu_5+\nu_6$ which change by ± 3 cm^{-1}. The resultant splitting is overestimated without $\phi_{3,7,5,6}$ because cubic and quartic contributions to the Darling-Dennison constant $K_{3,7;5,6}$ would otherwise mostly cancel. The mean (maximum) absolute deviations of VPT2+F to VPT2+K with a full quartic force field in units of cm^{-1} are 0.9 (3.1) and 2.3 (5.3) for states in Sets II and III, respectively.

Lastly, the error profile of VCI+F is, unsurprisingly, rather similar to that of VPT2+K – naturally, VCI+F inherits the weakness of VPT2 to describe highly excited torsional states. Due to the currently rudimentary treatment of the bend-torsion resonance in VCI+F, VPT2+K is quantitatively slightly better than VCI+F but the errors are acceptable given that the VCI+F calculation is fully automated and can further be improved as outlined in Section 2.1.4.

Table 5.5 Statistical analysis (in cm^{-1}) of the vibrational benchmarks of *trans*-HCOOH shown in Figs. 5.5-5.6. The benchmarks include 42 vibrational energy levels up to 4000 cm^{-1}, comprising 9, 25, 6, 1, and 1 one- through five-quantum states (see Table 5.1). In the hybrid MP2/aVTZ quartic force field, the harmonic force field is replaced with CCSD(T)-F12a/VDZ-F12 harmonic force constants. Note that "GENIUSH" is just an abbreviation for "GENIUSH-Smolyak".

	Hybrid	TM-PES					RC-PES		
	VPT2+K	VCI+F	VPT2+K	CVPT6	ICPH-VCI[a]	GENIUSH	VPT2+K	CVPT6	MCTDH[b]
MAD(Exp.)	5.0	6.0	4.4	3.8	7.8	3.4	4.8	5.3	6.6
MAX(Exp.)	28.7	22.0	14.8	10.9	106.1	12.3	13.8	9.7	66.3
MAD(GENIUSH)		4.0	2.2	1.4	5.0				
MAX(GENIUSH)		21.8	13.9	5.6	105.5				

[a] When excluding $\nu_7+4\nu_9$, the MAD and MAX reduce to 5.4 and 24.4 cm^{-1}, respectively, against experiment; 2.5 and 22.7 cm^{-1}, respectively, against GENIUSH-Smolyak.

[b] Note that $\nu_3+2\nu_8$, $\nu_2+\nu_9$, and $\nu_2+\nu_8$ are not reported in Ref. [22] and therefore not included in the analysis. When excluding $\nu_3+\nu_4$, the MAD and MAX reduce to 5.0 and 10.0 cm^{-1}, respectively.

5.5 An interim conclusion

The preceding benchmarks are condensed in Table 5.5 into mean and maximum absolute deviations, both to experiment and near-completely converged GENIUSH-Smolyak reference values.

Overall, the wealth of experimental data and the OH bend-torsion polyad make formic acid the ideal litmus test to examine approximate solutions of the electronic Schrödinger equation and different nuclear vibrational structure methodologies.

The outliers for MCTDH ($\nu_3+\nu_4$) and ICPH-VCI ($\nu_7+4\nu_9$) are intentionally included to reflect the importance of convergence with respect to the vibrational basis in the context of variational calculations. Otherwise, higher-order curvilinear normal coordinate CVPT and the variational models (ICPH-VCI, GENIUSH-Smolyak, MCTDH) yield very accurate results. The deviations between GENIUSH-Smolyak and experiment are almost entirely due to the underlying potential, allowing the quantification of amalgamated fitting errors and electronic structure deficiencies (basis set incompleteness, higher-order correlation, core-valence correlation, scalar relativity, non-Born Oppenheimer corrections, etc.).

Particularly the several VPT2 benchmarks illustrate that when using *ab initio* MP2 (semi-diagonal) quartic force fields – while not shown, this similarly concerns DFT – the underlying electronic structure is the main bottleneck with regard to accuracy. This underscores the importance to test and validate VPT2 using high-level electronic structure potentials or force fields. Hybrid force field VPT2, which combines cheap MP2 anharmonicities with CCSD(T)-F12-quality harmonics, is particularly well suited as an efficient method to guide experimental assignments.

Chapter 6

Formic acid dimer-optimised FTIR and Raman jet spectra

In the preceding chapters, the vibrational spectrum of formic acid monomer was studied relying almost exclusively on Raman spectroscopy. The global minimum arrangement of two C_s symmetric formic acid molecules exhibits inversion symmetry and no longer permits a Raman-exclusive (or IR-exclusive) approach but rather necessitates the combination of Raman and IR spectroscopy. To study this cyclic dimer, FTIR and new, dimer-optimised Raman jet spectra of formic acid and its three deuterated isotopologues have been measured. Details about the used chemicals are listed in Table 6.1. Relative isotopic impurities[181] have been determined via the C–O stretch band of monomeric formic acid (see Table 6.2). The dimer-optimised FTIR spectra cover a spectral range between 600 and 1950 cm^{-1}; the dimer-optimised Raman spectra were measured at three different monochromator settings, overall covering a spectral range from 180 up to 1960 cm^{-1}. The spectra are shown up to 1500 cm^{-1} in this chapter and described in the following.[182] The spectra have been published in this wavenumber region in an online repository and made publicly available [261, 262].[183] Details about the spectra such as spectral resolution, scaling factors, etc. can be found in Appendix A. The vibrational band centres are reported in the next chapter, alongside the discussion of vibrational mode assignments.

The focus of this work is the analysis of the (FF) spectral region above 600 cm^{-1}, but since the measured Raman spectra extend well into the lower-wavenumber intermolecular vibrational manifold, the spectra are shown for sake of completeness in Fig. 6.5. The analysis of the jet-cooled Raman spectrum of formic acid in the intermolecular region has largely been completed one decade ago for all four H/D isotopologues [140, 141]. This permits a straightforward mode assignment of all observed bands below 600 cm^{-1}, all of which correspond to (monomers, marked "M", and) fundamentals and overtone/combination bands of (FF). The mode labels are directly used to mark (FF) bands in Fig. 6.5; the band centres are compared to literature values in the next chapter.

[181] For the new measurements, deuterated compounds were purchased from ABCR and used without further purification (see Table 6.1). As observed with other batches of DCOOH purchased from ABCR (see Chapter 3), larger amounts of DCOOD impurities are found in the DCOOH spectra (see Table 6.2). The FTIR and Raman spectra of DCOOH were measured before that of HCOOD or DCOOD, ruling out isotopic H/D exchange in the apparatus (metal walls, tubing, etc.) as the main cause.

[182] The spectral analysis is confined to the spectral region between 600 and 1500 cm^{-1} in this work. Above 1500 cm^{-1}, the spectra become increasingly complicated. For their analysis, reliable anharmonic vibrational modelling is necessary which at the moment is not available.

[183] The Raman and FTIR spectra of the hydrogenated isotopologue, $(HCOOH)_2$, have been published and analysed in advance in Ref. [109]. The method of assigning bands presented in this chapter naturally closely follows the method already outlined in Ref. [109], thus there might be overlapping content in this chapter that is not explicitly marked as a citation.

Table 6.1 Details about chemicals used in the dimer-optimised FTIR and Raman measurements. The lot numbers are included for deuterated compounds and their isotopic purities are analysed in Table 6.2 (new measurements). Details about the chemicals in the higher-resolution FTIR measurements (mid panels in Figs. 6.1-6.2) are reproduced from Ref. [149].

		FTIR & Raman (this work)			FTIR from Ref. [149]	
Chemical	CAS number	Manufacturer	Purity	Lot number	Manufacturer	Purity
HCOOH	64-18-6	Acros Organics	98+%		Sigma-Aldrich	>98%
DCOOH	917-71-5	ABCR	95%; 98% D	1429695, 1443405	Sigma-Aldrich	95%; 98% D
HCOOD	925-94-0	ABCR	95%; 98% D	1424534	Sigma-Aldrich	95%; 98% D
DCOOD	920-42-3	ABCR	95%; 98% D	1414704	Sigma-Aldrich	95%; 98% D

Table 6.2 Quantification of isotopic formic acid impurities (see Table 6.1) based on their measured Raman spectra. The relative concentrations are estimated based on the monomeric C – O stretching bands (Fig. 6.3) using computed Raman scattering cross-sections at the MP2/aVTZ level and experimental band integrals.[a] Whether or not the Raman scattering cross-section is modified as described in Section 2.3.2 has a negligible impact on the determined relative concentrations.

	HCOOH spectrum		DCOOH spectrum		HCOOD spectrum		DCOOD spectrum	
Label	Isotopologue	conc.	Isotopologue	conc.	Isotopologue	conc.	Isotopologue	conc.
M	HCOOH		DCOOH		HCOOD		DCOOD	
M_{13}	$H^{13}COOH$	1%	$D^{13}COOH$	1%	$H^{13}COOD$	1%	$D^{13}COOD$	1%
$M_{\#}$			HCOOH	1%	HCOOH	3%	DCOOH	1%
$M_{\#}$			DCOOD	4%			HCOOD	2%

[a] Relative concentrations c_1/c_2 are calculated according to $\int I_i(\tilde{\nu})\mathrm{d}\tilde{\nu} \propto \sigma_i c_i'$; $\int I(\tilde{\nu})\mathrm{d}\tilde{\nu}$ is the experimental band integral and σ' the computed (first differential) Raman scattering cross-section (see Eq. 2.69, p. 32).

The spectral analysis of the intramolecular fingerprint region, on the other hand, remains incomplete. The FTIR and Raman spectra in the range from 600 to 1500 cm^{-1} are shown in Figs. 6.1-6.4. Formic acid monomer bands are marked "M", bands that are ascribed to IR- and Raman-active (FF) bands "I" and "R", respectively, and all other cluster bands "X". A detailed legend is provided on pp. 114. When ascribing bands to the cyclic formic acid dimer (FF), possible contributions from isolated formic acid molecules or other formic acid clusters must be carefully evaluated, i.e. monomeric formic acid F, the higher-energy polar dimer FF, asymmetrically substituted (FF′) dimers where F′ is a carbon-13 and H/D variant, the trimer F(FF), and larger clusters ($n > 3$). One central advantage in the assignment of (FF) bands is that due to the inversion symmetry, they are either IR- or Raman-active, whereas all other clusters that are explicitly considered – FF, F(FF), and asymmetrically substituted (FF′) – are C_s symmetric and their vibrations are in principle simultaneously IR- and Raman-active.

The assignments are guided by VPT2 predictions (only for fundamentals, bottom panels; details on pp. 114), symmetry information from depolarisation measurements (Raman, mid panels) and band contours (IR and Raman, mid panels), and size information from the scaling with reservoir pressure (IR, top panels) and nozzle temperature (Raman, top panels). The individual points are explained in more detail below.

Pressure and temperature series: FTIR jet spectra in a reservoir pressure series are intensity-scaled to a known cyclic dimer band for each H/D isotopologue. These spectra have newly been measured as part of this work. By intensity-scaling spectra in a pressure series to a known (FF) band, larger cluster contributions can be discriminated as they increase with pressure. Monomer

bands decrease with pressure and the assignments are easily verified by comparing their band centres to the experimental term values in Table 4.8.

In the Raman jet spectra, gentle heating of the nozzle and helium feed-line is employed to control the formation of clusters. Spectra in a temperature series are intensity-scaled to a known (FF) band for each H/D isotopologue and monochromator setting. Monomer bands increase with temperature due to suppressed aggregation of clusters and can again easily be identified. For the discrimination between dimers and trimers, on the other hand, the temperature series is not as straightforward as the pressure series due to a more complex aggregation behaviour of odd-numbered formic acid clusters, e.g. the formic acid trimer [125]. This is best seen by comparing the scaling behaviour of two HCOOH bands X_I and X_M in Figs. 6.1 and 6.3 – the pressure series clearly shows that both correspond to $n > 2$ clusters, whereas in the temperature series, they exhibit an intensity maximum at the intermediate temperature. IR and Raman scaling factors can be found in Appendix A.

Depolarisation and band contour analysis: The newly measured FTIR spectra are at a resolution of 2 cm^{-1}. At this resolution, it is difficult to distinguish between *C*-type and *A*+*B*-type (FF) bands. For this purpose, FTIR spectra at a higher resolution[184] (0.5-1 cm^{-1}) are shown in the mid panels. As described in Section 2.4.3, this information facilitates the discrimination between A_u and B_u symmetric (FF) transitions.

In the Raman spectra, further symmetry information comes from depolarisation measurements which have been conducted at the intermediate temperature (see Section 2.3.1). Bands that vanish in the weighted difference spectra ($\perp^i - \parallel^i \times 7/6$) are totally symmetric and correspond to A′ (C_s) or A_g (C_{2h}) symmetric transitions.

VPT2 calculations: Lastly, VPT2 predictions for fundamentals of several formic acid clusters are shown as a guide. The next-higher energy dimer conformer is the polar dimer FF which is therefore included in the formal analysis. However, it is noted that to this date – except for a very questionable assignment in Ref. [127] (see Ref. [109]) –, FF has not been detected in jet expansions or gas phase spectroscopic measurements. Much more relevant, on the other hand, is the formic acid trimer F(FF) which has been detected by gas phase microwave spectroscopy [151] and more recently using vibrational spectroscopy in supersonic jet expansions [125, 126]. In the FTIR spectra (Figs. 6.1-6.2), only M and $M_\#$ bands are observed at the available signal-to-noise ratio. This restriction does not apply to the Raman spectra where in addition to $M_\#$ also M_{13} bands are observed that correspond to carbon-13 isotopologues (Figs. 6.3-6.4). Indeed, Xue and Suhm observed several Raman bands in the OCO bending range 600-750 cm^{-1} which they ascribed to partially deuterated (FF′) [141]. Based on the isotopic impurities listed in Table 6.2, overall eight asymmetrically substituted (FF′) isotopologues are therefore included in the VPT2 analysis of the Raman jet spectra (Figs. 6.3-6.4).

The VPT2 predictions are shown in the bottom panels of Figs. 6.1-6.4. The symmetry of the vibrations is colour-coded and the intensity is hue-coded. The edges of very pale symbols are slightly darkened for better visibility. In the FTIR spectra, VPT2[185] intensities (in km mol^{-1}) are shown whereas harmonic scattering cross-sections (in 10^{-36} m^2 sr^{-1}) are used for the Raman

[184] These higher-resolved spectra have been recorded with a previous version of the same FTIR jet setup (the filet-jet) and published in Ref. [149]. The spectra have kindly been provided by F. Kollipost with permission for reproduction.

[185] Note that the very high VPT2 intensity of a trimeric DCOOH band at 860 cm^{-1} should be treated with caution; the harmonic value is similar to that of other trimeric isotopologues (17 km mol^{-1}) and the resultant VPT2 intensity might be numerically unstable or sensitive to the resonance treatment: Several A″ symmetric fundamentals are close by which might necessitate a second-rank resonance treatment.

spectra. These Raman scattering cross-sections are modified as described in Section 2.3.2 to account for the polarisation-dependent scattering efficiency of the setup.

To profit from error compensation effects, the same electronic structure level was used for all clusters. To obtain the highest-possible accuracy up to the trimer, an MP2/aVTZ semi-diagonal quartic force field was combined with CCSD(T)-F12a/VDZ-F12-quality harmonic wavenumbers to yield a substituted hybrid force field. For convenience, the hybrid force field VPT2+F calculations were performed with Gaussian, as described in Appendix B.3 with default deperturbation thresholds (see Section 2.1.2).

Legend

To unify the nomenclature for all four isotopologues, (FF), FF, and F(FF) refer to the cyclic dimer, polar dimer, and trimer of the respective *parent isotopologue* – the "F" must be replaced with HCOOH in the HCOOH spectrum, DCOOH in the DCOOH spectrum, etc.

Cluster nomenclature

(FF) Cyclic formic acid dimer of the parent isotopologue.

FF Polar formic acid dimer of the parent isotopologue.

F(FF) Formic acid trimer of the parent isotopologue.

(FF_{13}) Cyclic dimer between the parent isotopologue and its carbon-13 variant, e.g. ($H^{13}COOD-HCOOD$) in the HCOOD spectrum.

($F_{OD}F_{d2}$) Cyclic (HCOOD – DCOOD) dimer.

($F_{CD}F_{d2}$) Cyclic (DCOOH – DCOOD) dimer.

($F_{h2}F_{CD}$) Cyclic (HCOOH – DCOOH) dimer.

($F_{h2}F_{OD}$) Cyclic (HCOOH – HCOOD) dimer.

Experimental band labels

M Formic acid monomer band which is overlaid in grey. The band centres are not listed separately; they can all be found in Table 4.8. To avoid a back-and-forth, subscripts are provided in Figs. 6.1-6.5 that further distinguish between different types of transitions and isotopologues.

- M Cold band, i.e. a transition from the vibrational ground state (only *trans*), of the parent isotopologue, e.g. a *trans*-HCOOD fundamental in the HCOOD spectrum.
- $M_{\#}$ Cold band corresponding to an H/D variant of the parent isotopologue, e.g. *trans*-DCOOH in the HCOOD spectrum (see Table 6.2).
- M_{13} Cold band corresponding to a carbon-13 variant of the parent isotopologue, e.g. a *trans*-$H^{13}COOD$ fundamental in the HCOOD spectrum (see Table 6.2).
- M_h Isomeric (*cis*) or non-isomeric (*trans*) hot band of the parent isotopologue, i.e. a transition that does not originate from the vibrational ground state (otherwise M band).

W Band that seemingly scales like a monomer (W = inverted M) but very likely corresponds to a chemical impurity. The two W bands (1118 cm^{-1} HCOOD spectrum, 1110 cm^{-1} DCOOD spectrum) are also present in the monomer-optimised Raman spectra but cannot be seen in Fig. 3.6 (p. 56) where the formic acid concentration is much smaller and the signal-to-noise ratio thus poorer than in Fig. 6.3.

I Band that is ascribed to an IR-active (A_u, B_u) vibration of the cyclic dimer (FF). The band centres and mode assignments are listed in Table 7.2 (p. 124).

R Band that is ascribed to a Raman-active (A_u, B_u) vibration of the cyclic dimer (FF). The band centres and mode assignments are listed in Table 7.2 (p. 124).

X All other cluster bands which are listed separately in Table 7.3 (p. 125), comprising four different types:

(a) Band that cannot be assigned to the cyclic dimer (FF) of the parent isotopologue due to simultaneous IR and Raman activity.
(b) Band that is suspected to correspond to F(FF) or FF of the parent isotopologue.
(c) Band that is suspected to correspond to an asymmetrically substituted (FF′) isotopologue where F is the parent isotopologue and F′ an H/D or carbon-13 variant of it, e.g. (HCOOH – H^{13}COOH) in the HCOOH spectrum or (DCOOH – DCOOD) in the DCOOH spectrum.
(d) Band that is suspected to be overtone/combination bands of (FF) of the parent isotopologue but cannot be assigned safely, yet.

The labels “I”, “R”, and “X” are provided with subscripts (A, B, ...) for bookkeeping purposes; these are not correlated across spectra of different isotopologues.

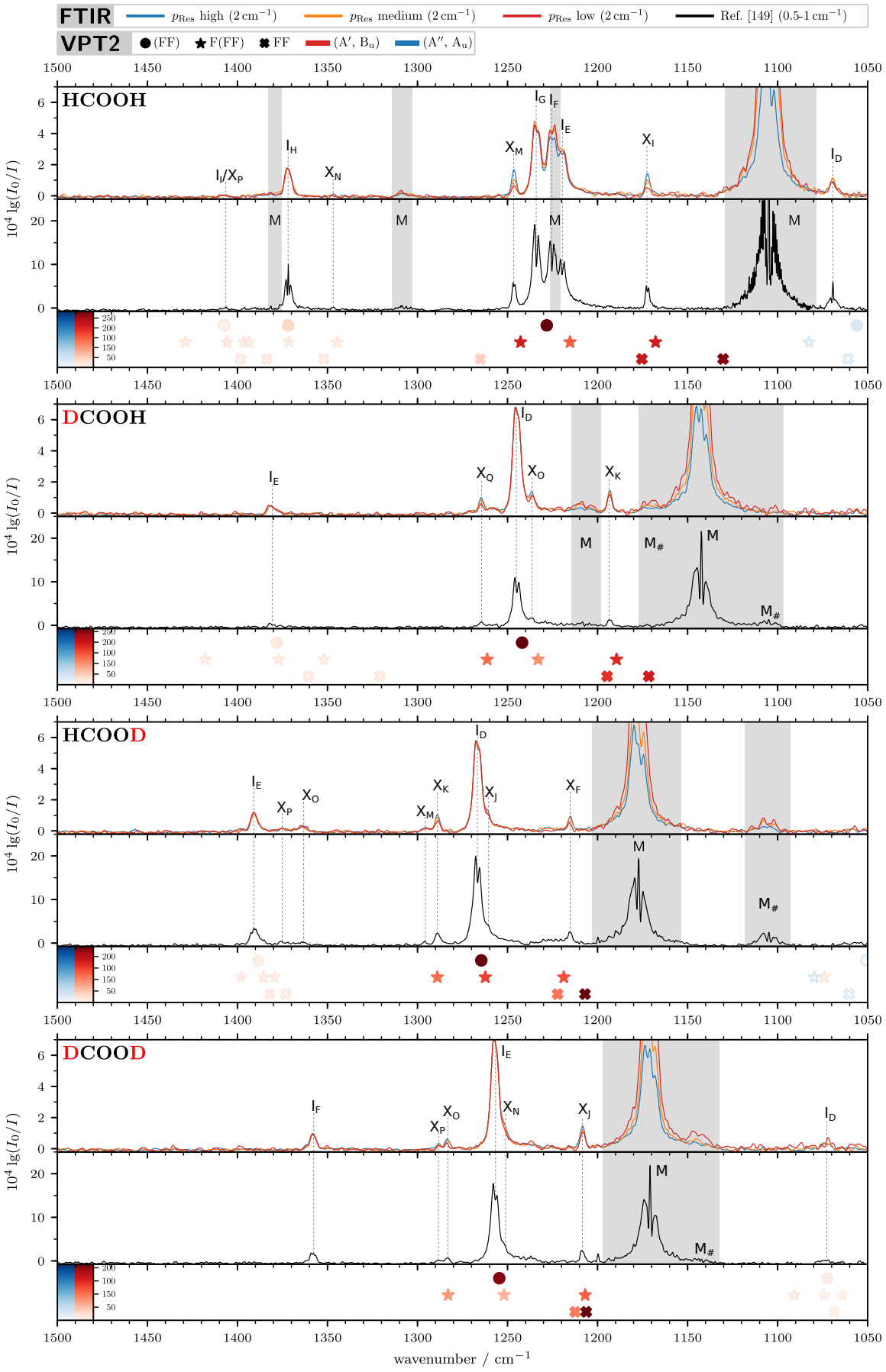

Figure 6.1 FTIR jet spectra optimised for formic acid dimer signal between 1050 and 1500 cm^{-1} using helium as carrier gas. See text for details. The pressure series spectra are publicly available [262].

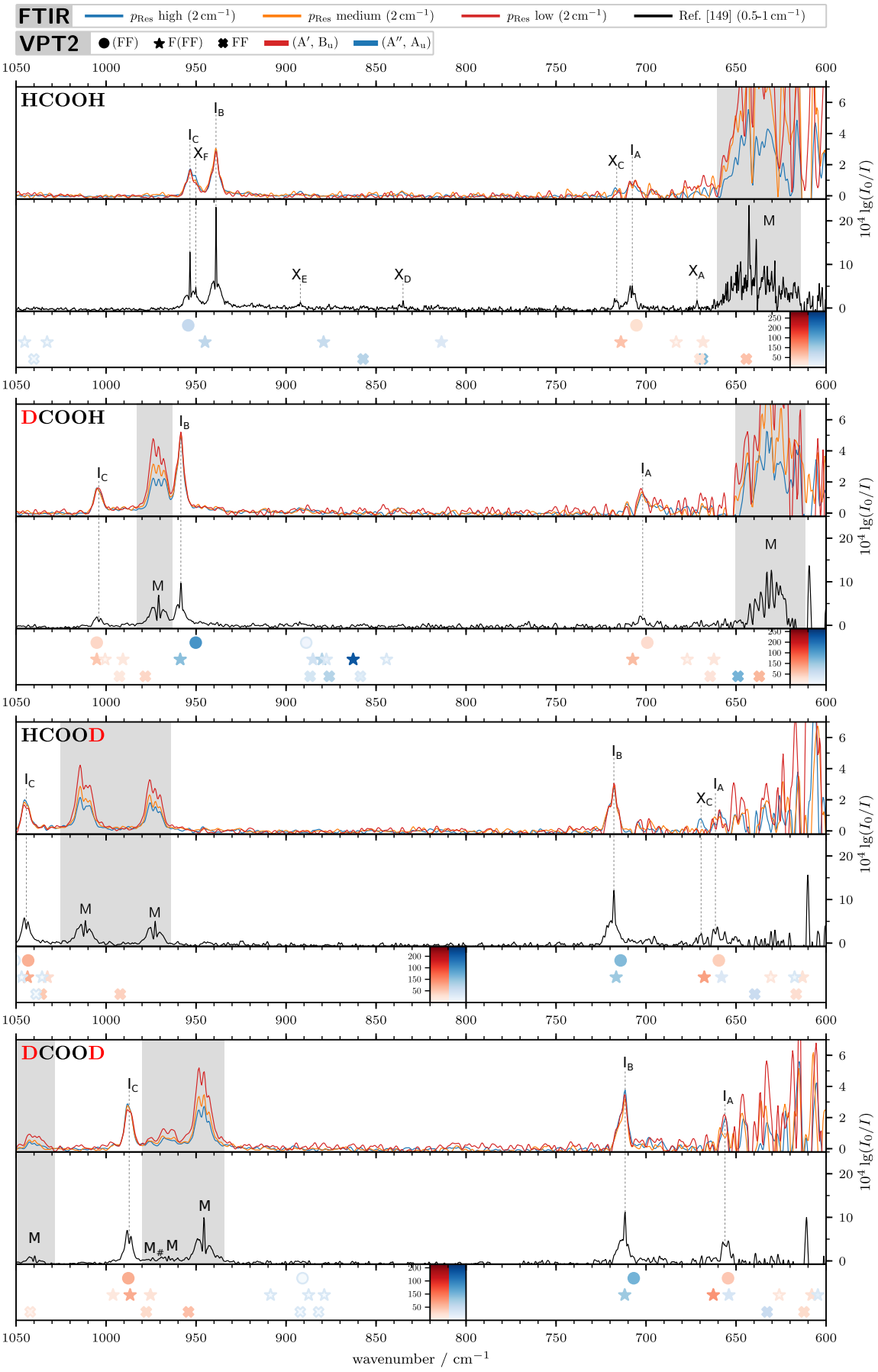

Figure 6.2 FTIR jet spectra optimised for formic acid dimer signal between 600 and 1050 cm^{-1} using helium as carrier gas. See text for details. The pressure series spectra are publicly available [262].

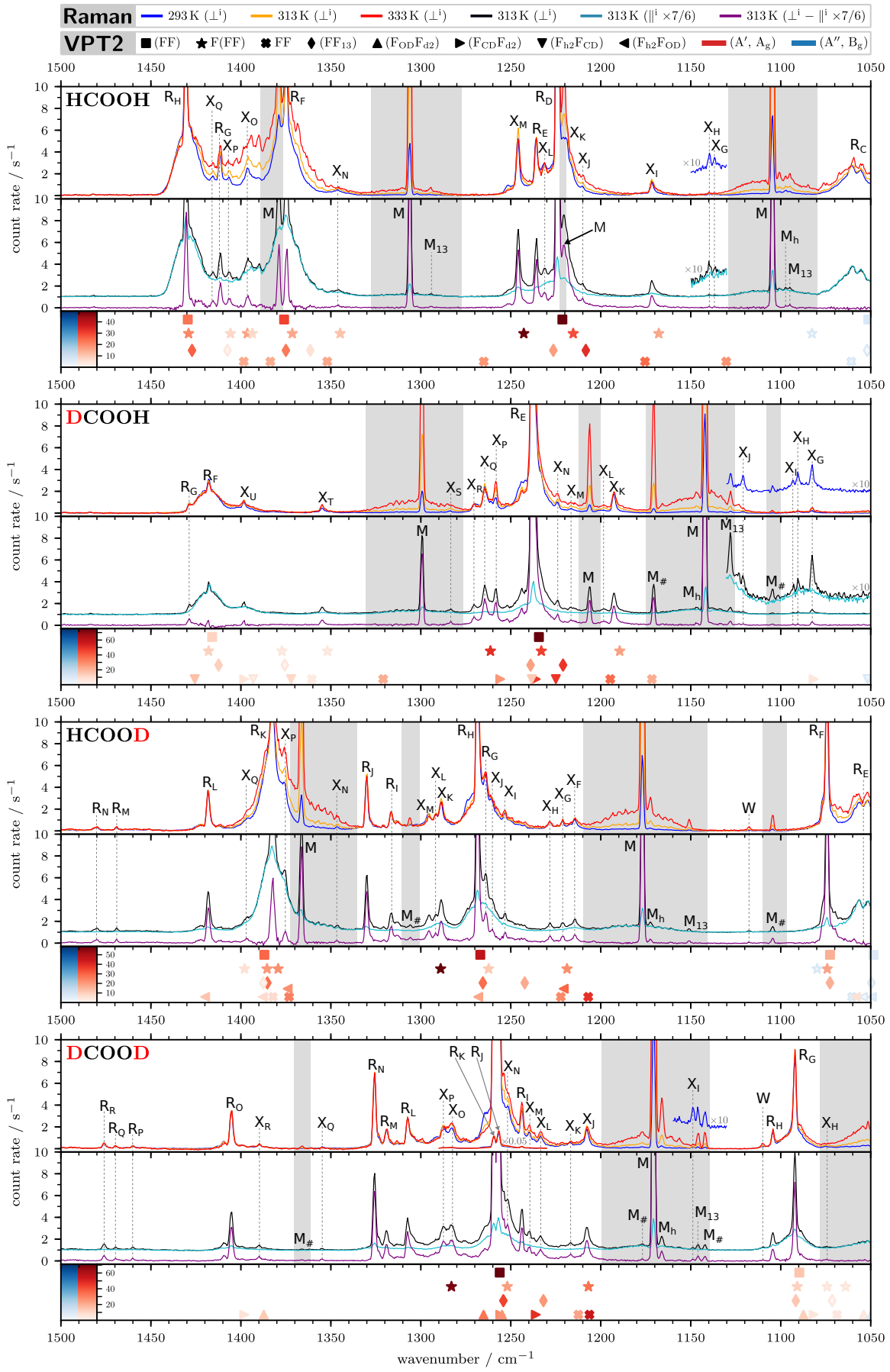

Figure 6.3 Raman jet spectra optimised for formic acid dimer signal between 1050 and 1500 cm^{-1} using helium as carrier gas. See text for details. The spectra are publicly available [261].

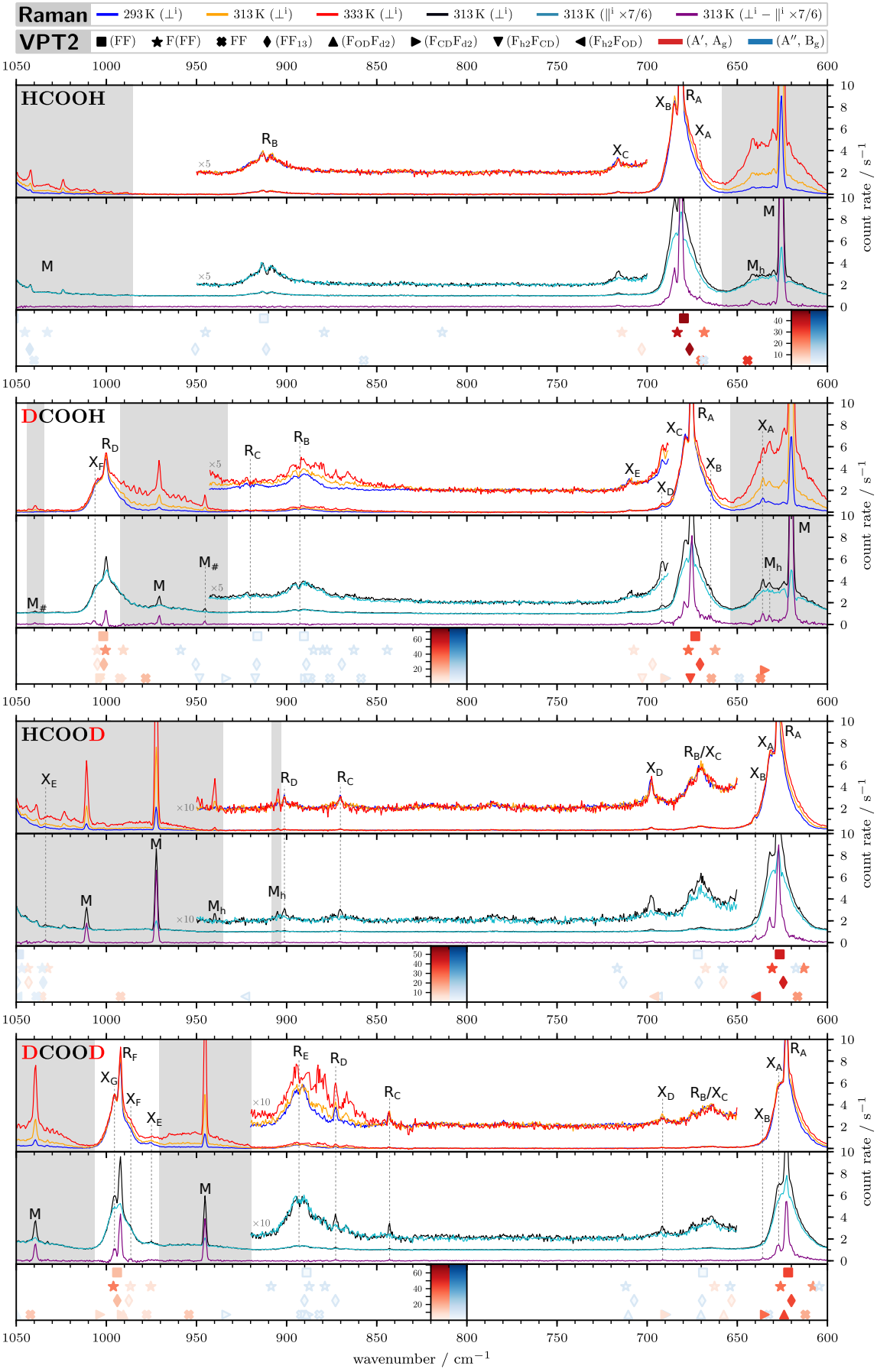

Figure 6.4 Raman jet spectra optimised for formic acid dimer signal between 600 and 1050 cm^{-1} using helium as carrier gas. See text for details. The spectra are publicly available [261].

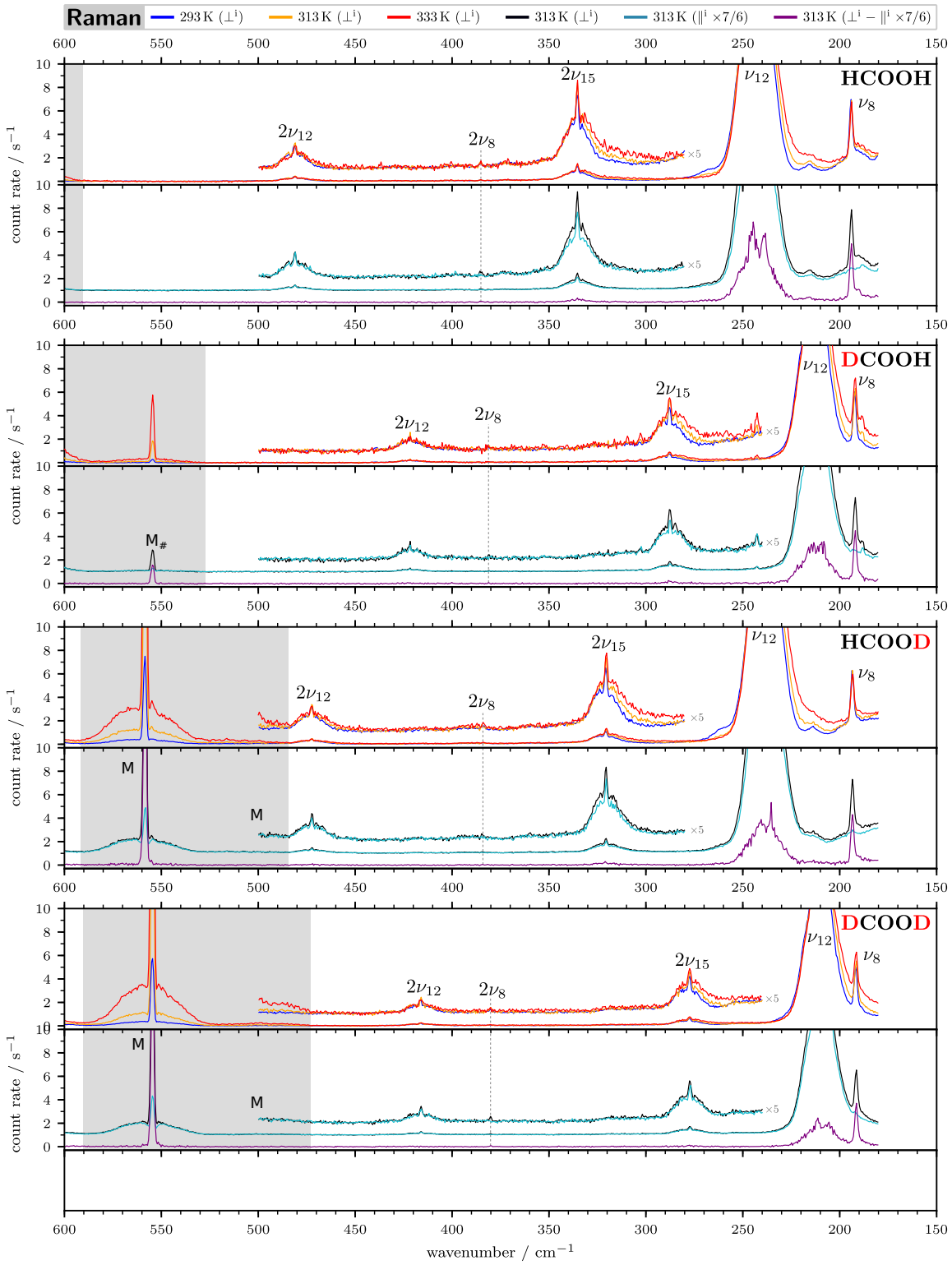

Figure 6.5 Raman jet spectra optimised for formic acid dimer signal between 180 and 600 cm^{-1} using helium as carrier gas. Mode labels are shown for (FF) bands. See text for details. The spectra are publicly available [261].

Chapter 7

Assignment of vibrational formic acid cluster bands

In this chapter, the assignment of formic acid cluster bands is discussed. First, previous assignments [119, 140, 141] in the intermolecular Raman spectrum below 600 cm^{-1} are reviewed in light of the new jet-cooled spectra (Section 7.1), followed by a reanalysis [119, 149] of the intramolecular fingerprint region between 600 and 1500 cm^{-1} (Section 7.2).[186]

7.1 Reanalysis of the intermolecular region below 600 cm^{-1}

Previously reported [140, 141] jet-cooled band (FF) centres in this spectral region are compared in Table 7.1 to values determined from Fig. 6.5 (p. 120).

All $(HCOOH)_2$ band centres agree to within 1 cm^{-1} with previously reported values. The three bands at 319, 400, and 435 cm^{-1}, two of which were assigned rather tentatively in Ref. [141], are not observed in Fig. 6.5. This similarly applies to the 518 cm^{-1} Raman band which was assigned to $2\nu_{24}$ [148]. The HCOOH bands at 336, 385, and 482 cm^{-1} have been suggested to be (FF) overtone bands. In light of several trimer assignments in the fingerprint region (*vide infra*), the possibility of alternative F(FF) assignments should be discussed. Harmonic and VPT2 predictions consistently locate all F(FF) intermolecular fundamentals below 300 cm^{-1} and all intramolecular fundamentals above 600 cm^{-1} – similar to (FF). Thus, (FF) assignments for the bands at 336, 385, and 482 cm^{-1} are preferred.

For the three symmetrically deuterated isotopologues, all previously observed overtone bands ($2\nu_{12}$ and $2\nu_{15}$) are reproduced with the addition of the rather weak dimer stretch overtone ($2\nu_8$) which was only available for $(HCOOH)_2$ before [141].

The proposed [141] mode assignments for the three observed overtone bands can be confirmed across all four isotopologues (Table 7.1). With semi-experimental SOF+x estimates (not shown) of binary through quaternary A_g symmetric vibrational states – the band shapes rule out B_g –, we can rule out alternative assignments based on the observed isotope pattern. Only for the highest-wavenumber overtone band at 482 cm^{-1} (previous assignment $2\nu_{12}$), the isotope pattern would fit an alternative assignment to $2\nu_{15}+2\nu_{16}$. First, the binary assignment to $2\nu_{12}$ appears much more plausible. Second, the absolute SOF+x band positions for $2\nu_{12}$ agree much better with experiment.

In the spirit of reanalysing the intermolecular region, an assignment is proposed for pre-

[186] The assignments in the fingerprint region of $(HCOOH)_2$ have been previously published in Ref. [109]. The assignments here are the same with the exception of X_J which was left unassigned in Ref. [109] and is ascribed to the C – O stretching fundamental of (HCOOH – H^{13}COOH) in this work. As such, the discussion for $(HCOOH)_2$ is kept brief in Section 7.2 and the interested reader is referred to Ref. [109], which is open access.

Table 7.1 Comparison of jet-cooled Raman band centres of the cyclic formic acid dimer (in cm^{-1}) in the intermolecular vibrational range. Previously determined band centres are from Refs. [140, 141], as compiled in Ref. [141]. Band centres from this work are determined from Fig. 6.5 (p. 120; the spectra only reach down to 180 cm^{-1}). Note that vibrational levels are labelled according to Table 2.2 (p. 35).

		$(HCOOH)_2$			$(DCOOH)_2$			$(HCOOD)_2$			$(DCOOD)_2$		
Mode	Γ	T.W.	[141]	[140]	T.W.	[141]	[140]	T.W.	[141]	[140]	T.W.	[141]	[140]
$2\nu_{16}$	A_g	n.a.	139		n.a.	139		n.a.	139		n.a.	139	
ν_9	A_g	n.a.	161	165	n.a.	159	162	n.a.	157	160	n.a.	157	158
ν_8	A_g	194	194	194	192	193	192	194	194	194	192	192	192
ν_{12}	A_g	242	242	242	212	212	212	238	238	237	210	210	209
$2\nu_9$	A_g		319?										
$2\nu_{15}$	A_g	336	336		288	289		321	321		278	278	
$2\nu_8$	A_g	385	386		382			384			380		
$\nu_9+\nu_{12}$	B_g		400										
$\nu_8+\nu_{12}$	B_g		435?										
$2\nu_{12}$	A_g	482	482		422	423		473	473		416	417	

viously observed cluster bands in the far-infrared spectrum of formic acid. In search for the highest-frequency intermolecular (FF) vibration, ν_{24}, Kollipost *et al.* marked a band, which appears at 270 cm^{-1} as a shoulder on the higher-frequency wing of the ν_{24} band at 264 cm^{-1}, as a cluster, i.e. trimer or larger [148]. In the far-infrared spectra of all three deuterated isotopologues, ν_{24} is similarly found to be accompanied by such a blue-shifted satellite [149, p. 123]. From the raw data of the spectra published in Ref. [149], band centres at 270, 264, 262, and 257 cm^{-1} are determined in this work for the sequence $(HCOOH)_3$, $(DCOOH)_3$, $(HCOOD)_3$, and $(DCOOD)_3$. It can be shown that this band corresponds to the highest-frequency intermolecular vibration of the formic acid trimer (ν_{22}). Shown below are the normal mode displacements calculated for the main isotopologue at the CCSD(T)-F12a/VDZ-F12 level.

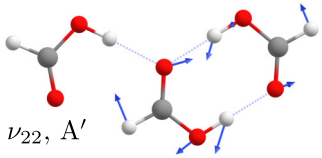

F(FF), ν_{22}, A′

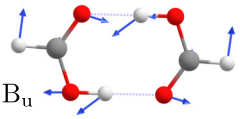

(FF), ν_{24}, B_u

Indeed, the normal mode displacements of ν_{22} are almost exclusively localised on the cyclic formic acid dimer sub-unit and correspond to ν_{24} of the cyclic dimer. Note that symmetric deuteration leaves the normal modes qualitatively unchanged. The experimental blue-shift to ν_{24} across all four isotopologues (6-7 cm^{-1}) compares very well with the harmonic (8-9 cm^{-1}) and hybrid MP2/aVTZ VPT2 predictions (4-5 cm^{-1}). Blue-shifted satellites accompanying (FF) fundamentals are frequently observed in the fingerprint region and the trimer assignment proposed here is consistent with the analysis in the fingerprint region where these features are similarly ascribed to trimer fundamentals (see Section 7.2 and Ref. [109]).

7.2 Reanalysis of the fingerprint region 600-1500 cm^{-1}

Bands in the dimer-optimised jet spectra that are ascribed to (FF) are listed in Table 7.2; all other cluster bands, including tentative (FF) assignments, are listed separately in Table 7.3. The proposed band assignments to F(FF) or asymmetrically substituted cyclic dimers (FF′) are based on calculated VPT2 band positions and intensities which are visualised together with the jet spectra in Figs. 6.1-6.4. To guide the assignment of (FF) combination/overtone bands, semi-experimental SOF+x band centres of binary states are consulted (Table D.9). I and R bands that

correspond to (FF) fundamentals are in most cases easily identified based on VPT2 predictions and previous investigations [119, 149]. Some assignments are self-evident whereas others are in need of a few comments. In the following, the discussion is sorted thematically (a-j).

(a) Fundamentals of (FF)

The tentative assignment of I_I to ν_{20} of $(HCOOH)_2$ has already been addressed previously [109, 149]. In essence, the VPT2 data shown in Fig. 6.1 (p. 116) indicate an alternative assignment of I_I, which is partially labelled X_P, to the trimer F(FF). In Ref. [109], it was argued that the corresponding trimer vibration – ν_{11} (A′) –, which is indeed observed in the Raman jet spectrum of HCOOH (X_P), is qualitatively the same as ν_{20} of the cyclic dimer (cf. Fig. 2.1, p. 34). As such, we can assume that profiting from error cancellation effects, the calculations should correctly predict the energetic order of both fundamentals and their relative intensities. Given that the trimer vibration in question only has a two times higher computed IR band strength, an assignment of (FF) as the main contributor to I_I is plausible in light of the roughly one order of magnitude higher (FF) concentration [109].

Discounting low-resolution thermal gas phase spectroscopy, the CH/D out-of-plane mode (ν_{13}) of deuterated (FF) is the only missing fundamental in this spectral range. Indeed, its detection is expected to be difficult since already in the monomer, the CH/D out-of-plane bend has a weak IR activity. In fact, the detection of ν_{13} in the HCOOH spectrum is rather a coincidence and ν_{13} gains IR intensity through substantial mixing with the nearby intramolecular OH torsion (see Fig. 8.5, p. 138).[187]

Lastly, the VPT2 band centres in Fig. 6.4 (p. 119) indicate a possible overlap around 700 cm^{-1} between the Raman-active OD torsion of the cyclic dimer and an OCO bending fundamental of the trimer for HCOOD and DCOOD. The depolarised spectra in Fig. 6.4 show that the spectral features are largely depolarised. The depolarised fraction is labelled R_B in both cases and ascribed to the OD torsion of (FF), in agreement with earlier assignments [119, 141]. However, there are additional polarised contributions in the HCOOD and DCOOD spectra which are partially labelled X_C and ascribed to the OCO bending fundamental of the F(FF).

(b) Assignments to F(FF)

The trimer assignments in the HCOOH spectra, which have been published in advance, are mainly theory-driven in Ref. [109]. In light of additional deuteration data presented here, these assignments are further confirmed and additional trimer bands can be assigned in the spectra of deuterated isotopologues. As discussed in (a), the X_C bands in the HCOOD and DCOOD spectra partially overlap with depolarised (FF) fundamentals and only the polarised fraction corresponds to F(FF).

The shifts relative to (FF) fundamentals reveal important information about the Davydov couplings. Many (FF) fundamentals are accompanied by blue-shifted satellites on the higher-wavenumber wings of their ro-vibrational band contours. In such cases, we can infer that the

[187] A quantitative comparison of *trans*-HCOOH and *trans*-DCOOH shows that this mixing can already be described in the double (mechanical and electrical) harmonic approximation. As one would expect, the CH/D out-of-plane vibration, γ(CH/D), does not generate a significant transition dipole moment and is therefore only weakly IR-active in both monomeric isotopologues (1-4 km mol^{-1}). The OH torsion, γ(OH), on the other hand, is much more IR-active (131-134 km mol^{-1}). In DCOOH, γ(OH) overall gains intensity upon dimerisation which is in line with expectations. In HCOOH, on the other hand, the IR activities significantly change upon dimerisation where the IR-active component of γ(CH), ν_{13}, gains in intensity whereas the IR-active component of γ(OH), ν_{14}, loses IR intensity in comparison to the free monomer. Comparison to $(DCOOH)_2$ indicates that the dimerisation-induced intensity change in $(HCOOH)_2$ is mainly the result of a redistribution of the zeroth-order γ(OH) intensity as the sum of both dimeric out-of-plane bending modes, ν_{13} and ν_{14}, is about the same in $(HCOOH)_2$ ($66 + 114 = 180$ km mol^{-1}) and $(DCOOH)_2$ ($9 + 165 = 174$ km mol^{-1}).

Table 7.2 Band list (in cm^{-1}) of observed IR- and Raman-active cyclic formic acid dimer bands between 600 and 1500 cm^{-1} (see Chapter 6). Tentative mode assignments are set in brackets. Note that vibrational levels are labelled according to Table 2.2 (p. 35). The I/R labels are provided with subscripts (A, B, ...) for bookkeeping purposes which are not correlated across different isotopologues.

	IR						Raman					
		$\tilde{\nu}_0$	Band	Descr.	Mode	Γ		$\tilde{\nu}_0$	Band	Descr.	Mode	Γ
$(HCOOH)_2$	I_A	707.6	$A+B$	δ(OCO)	ν_{23}	B_u	R_A	681	$A+B_c$	δ(OCO)	ν_7	A_g
	I_B	938.9	C	γ(OH)	ν_{14}	A_u	R_B	911	B_a+B_b	γ(OH)	ν_{11}	B_g
	I_C	953.4	C		$\nu_{12}+\nu_{23}$	A_u	R_C	1058	B_a+B_b	γ(CH)	ν_{10}	B_g
	I_D	1069.3	C	γ(CH)	ν_{13}	A_u	R_D	1224	$A+B_c$	ν(C−O)	ν_6	A_g
	I_E	1219.7	$A+B$		$\nu_{10}+\nu_{15}$	B_u	R_E	1236	$A+B_c$		$[\nu_{13}+\nu_{15}]$	A_g
	I_F	1225.3	$A+B$		$\nu_9+\nu_{11}+\nu_{15}$	B_u	R_F	1375	$A+B_c$	δ(CH)	ν_5	A_g
	I_G	1234.0	$A+B$	ν(C−O)	ν_{22}	B_u	R_G	1412	$A+B_c$		$[\nu_6+\nu_8]$	A_g
	I_H	1371.7	A	δ(CH)	ν_{21}	B_u	R_H	1430	$A+B_c$	δ(OH)	ν_4	A_g
	I_I	1407		δ(OH)	ν_{20}	B_u						
$(DCOOH)_2$	I_A	702	$A+B$	δ(OCO)	ν_{23}	B_u	R_A	675	$A+B_c$	δ(OCO)	ν_7	A_g
	I_B	958.5	C	γ(OH)	ν_{14}	A_u	R_B	893	B_a+B_b	γ(CD)	ν_{10}	B_g
	I_C	1004.0	$A+B$	δ(CD)	ν_{21}	B_u	R_C	920	B_a+B_b	γ(OH)	ν_{11}	B_g
	I_D	1244.8	$A+B$	ν(C−O)	ν_{22}	B_u	R_D	1000	$A+B_c$	δ(CD)	ν_5	A_g
	I_E	1381	$A+B$	δ(OH)	ν_{20}	B_u	R_E	1238	$A+B_c$	ν(C−O)	ν_6	A_g
							R_F	1418	$A+B_c$	δ(OH)	ν_4	A_g
							R_G	1429	$A+B_c$		$\nu_6+\nu_8$	A_g
$(HCOOD)_2$	I_A	661	$A+B$	δ(OCO)	ν_{23}	B_u	R_A	627	$A+B_c$	δ(OCO)	ν_7	A_g
	I_B	717.9	C	γ(OD)	ν_{14}	A_u	R_B	672	B_a+B_b	γ(OD)	ν_{11}	B_g
	I_C	1044.3	$A+B$	δ(OD)	ν_{20}	B_u	R_C	870	$A+B_c$		$\nu_{14}+\nu_{15}$	A_g
	I_D	1266.5	$A+B$	ν(C−O)	ν_{22}	B_u	R_D	901	$A+B_c$		$\nu_{11}+\nu_{12}$	A_g
	I_E	1391.0	$A+B$	δ(CH)	ν_{21}	B_u	R_E	1054	B_a+B_b	γ(CH)	ν_{10}	B_g
							R_F	1074	$A+B_c$	δ(OD)	ν_4	A_g
							R_G	1264	$A+B_c$		$\nu_4+\nu_8$	A_g
							R_H	1269	$A+B_c$	ν(C−O)	ν_6	A_g
							R_I	1317	$A+B_c$		$2\nu_{23}$	A_g
							R_J	1330	$A+B_c$		$2\nu_{11}$	A_g
							R_K	1382	$A+B_c$	δ(CH)	ν_5	A_g
							R_L	1418	$A+B_c$		$2\nu_{14}$	A_g
							R_M	1469	$A+B_c$		$\nu_9+2\nu_{23}$	A_g
							R_N	1480	$A+B_c$		$\nu_9+2\nu_{11}$	A_g
$(DCOOD)_2$	I_A	656	$A+B$	δ(OCO)	ν_{23}	B_u	R_A	623	$A+B_c$	δ(OCO)	ν_7	A_g
	I_B	711.7	C	γ(OD)	ν_{14}	A_u	R_B	669	B_a+B_b	γ(OD)	ν_{11}	B_g
	I_C	987.1	$A+B$	δ(CD)	ν_{21}	B_u	R_C	843	$A+B_c$		$\nu_{14}+\nu_{15}$	A_g
	I_D	1072	$A+B$	δ(OD)	ν_{20}	B_u	R_D	873	$A+B_c$		$\nu_{11}+\nu_{12}$	A_g
	I_E	1256.6	$A+B$	ν(C−O)	ν_{22}	B_u	R_E	893	B_a+B_b	γ(CD)	ν_{10}	B_g
	I_F	1357.9	$A+B$		$\nu_{11}+\nu_{14}$	B_u	R_F	992	$A+B_c$	δ(CD)	ν_5	A_g
							R_G	1092	$A+B_c$	δ(OD)	ν_4	A_g
							R_H	1104	$A+B_c$		$\nu_{10}+\nu_{12}$	A_g
							R_I	1244	$A+B_c$		$\nu_4+\nu_9$	A_g
							R_J	1257	$A+B_c$	ν(C−O)	ν_6	A_g
							R_K	1260	$A+B_c$		$\nu_9+\nu_{10}+\nu_{12}$	A_g
							R_L	1307	$A+B_c$		$2\nu_{23}$	A_g
							R_M	1319	$A+B_c$		$\nu_{20}+\nu_{24}$	A_g
							R_N	1326	$A+B_c$		$2\nu_{11}$	A_g
							R_O	1405	$A+B_c$		$2\nu_{14}$	A_g
							R_P	1460	$A+B_c$		$\nu_9+2\nu_{23}$	A_g
							R_Q	1470	$A+B_c$		$\nu_9+\nu_{20}+\nu_{24}$	A_g
							R_R	1476	$A+B_c$		$\nu_9+2\nu_{11}$	A_g

Table 7.3 Observed non-monomeric formic acid band maxima (in cm^{-1}) in the IR and Raman jet spectra of formic acid (see Chapter 6) that a) cannot be assigned to the cyclic (FF) dimer due to simultaneous IR and Raman activity, b+c) are suspected to correspond to FF, F(FF), or asymmetrically substituted (FF′) fundamentals, or d) cannot be assigned safely to (FF), yet. Bands that are very tentatively assigned to a species are marked with a question mark. Note that vibrational levels are labelled as detailed in Section 2.4.1. The X labels are provided with subscripts (A, B, ...) for bookkeeping purposes which are not correlated across different isotopologues.

	$\tilde{\nu}_0$		Assignment					$\tilde{\nu}_0$		Assignment			
	IR	Ra	Species	Descr.	Mode	Γ		IR	Ra	Species	Descr.	Mode	Γ
HCOOH spectrum							HCOOD spectrum						
X_A	672	671	F(FF)	δ_d(OCO)	ν_{21}	A′	X_A		632	F(FF)	δ(OCO)	ν_{20}	A′
X_B		685	F(FF)	δ(OCO)	ν_{20}	A′	X_B		640	($F_{h2}F_{OD}$)	δ(OCO)		A′
X_C	717	716	F(FF)	δ(OCO)	ν_{19}	A′	X_C	670	671	F(FF)	δ(OCO)	ν_{19}	A′
X_D	835		F(FF)?	γ(OH)?		A″?	X_D		698	($F_{h2}F_{OD}$)	δ(OCO)		A′
X_E	892		F(FF)?	γ(OH)?		A″?	X_E	1035	1034	F(FF)	δ_d(OD)	ν_{12}	A′
X_F	950		F(FF)?	γ(OH)?		A″?	X_F	1215	1215	F(FF)	ν_d(C−O)	ν_{18}	A′
X_G		1137					X_G		1221	($F_{h2}F_{OD}$)	ν(C−O)		A′
X_H		1140					X_H		1229	(FF)?		$\nu_4+\nu_9$?	A_g?
X_I	1172	1172	F(FF)	ν_d(C−O)	ν_{18}	A′	X_I		1254	(FF)?		$2\nu_7$?	A_g?
X_J		1210	(FF_{13})	ν(C−O)		A′	X_J	1261	1261	F(FF)	ν(C−O)	ν_{17}	A′
X_K		1219	F(FF)	ν(C−O)	ν_{17}	A′	X_K	1288	1289	F(FF)	ν(C−O)	ν_{16}	A′
X_L		1231					X_L		1292	(FF)?			A_g?
X_M	1246	1246	F(FF)	ν(C−O)	ν_{16}	A′	X_M	1296	1296	F(FF)		$\nu_{19}+\nu_{20}$	A′
X_N	1347	1346	F(FF)	δ_d(CH)	ν_{15}	A′	X_N		1347				
X_O		1397	F(FF)	δ(CH)	ν_{13}	A′	X_O	1363		(FF)?		$\nu_{11}+\nu_{14}$	B_u?
X_P	1407	1406	F(FF)	δ(OH)	ν_{11}	A′	X_P	1376	1376	F(FF)	δ_d(CH)	ν_{15}	A′
X_Q		1416					X_Q		1397	F(FF)	δ(CH)	ν_{13}	A′
DCOOH spectrum							DCOOD spectrum						
X_A		636	($F_{CD}F_{d2}$)	δ(OCO)		A′	X_A		627	F(FF)	δ(OCO)	ν_{20}	A′
X_B		665	F(FF)	δ_d(OCO)	ν_{21}	A′	X_B		636	($F_{CD}F_{d2}$)	δ(OCO)		A′
X_C		679	F(FF)	δ(OCO)	ν_{20}	A′	X_C		664	F(FF)	δ(OCO)	ν_{19}	A′
X_D		692	($F_{CD}F_{d2}$)	δ(OCO)		A′	X_D		692	($F_{CD}F_{d2}$)	δ(OCO)		A′
X_E		710	F(FF)	δ(OCO)	ν_{19}	A′	X_E		975	F(FF)	δ_d(CD)	ν_{15}	A′
X_F		1007	F(FF)	δ(CD)	ν_{13}	A′	X_F	988	987	F(FF)	δ(CD)	ν_{14}	A′
X_G		1083					X_G		996	F(FF)	δ(CD)	ν_{13}	A′
X_H		1091					X_H		1076	F(FF)	δ(OD)	ν_{11}	A′
X_I		1093					X_I		1149				
X_J		1121					X_J	1208	1208	F(FF)	ν_d(C−O)	ν_{18}	A′
X_K	1194	1193	F(FF)	ν_d(C−O)	ν_{18}	A′	X_K		1217				
X_L		1199					X_L		1234				
X_M		1217					X_M		1240				
X_N		1224	(FF_{13})	ν(C−O)		A′	X_N	1252	1252	F(FF)	ν(C−O)	ν_{17}	A′
X_O	1237		F(FF)	ν(C−O)	ν_{17}	A′	X_O	1284	1283	F(FF)	ν(C−O)	ν_{16}	A′
X_P		1258					X_P	1289	1288	F(FF)		$\nu_{19}+\nu_{20}$	A′
X_Q	1265	1265	F(FF)	ν(C−O)	ν_{16}	A′	X_Q		1355				
X_R		1271					X_R		1390	(FF)?		$\nu_9+\nu_{21}+\nu_{24}$?	A_g?
X_S		1284											
X_T		1355											
X_U		1399											

Davydov splitting of the (FF) sub-unit into a symmetric (in-phase) and antisymmetric (out-of-phase) linear combination largely survives. The wavenumber pattern of the C−O stretching fundamentals in (FF) and F(FF), on the other hand, clearly shows that the couplings between the individual oscillators significantly change. Indeed, harmonic normal mode displacements shown in Fig. 2.1 (p. 34) indicate three rather isolated, i.e. localised, C−O stretching vibrations

in F(FF).

In the C–O stretching spectra of HCOOD (X_K, X_M) and DCOOD (X_O, X_P), the highest-wavenumber C–O stretching fundamental of F(FF) appears as a doublet, both in the IR and Raman. The similar band positions and intensity patterns across IR and Raman point at potential wavefunction overlap between the bright fundamental and a nearby dark state. Indeed, hybrid force field VPT2 results support this hypothesis. With default thresholds, Gaussian detects a Fermi resonance to a combination level involving two OCO bending fundamentals in $(DCOOD)_3$. The computed band centres (1283 cm^{-1} and 1287 cm^{-1}) agree with the experimental band centres within 2 cm^{-1}. For $(HCOOD)_3$, this resonance is not detected but the computed band centres again agree excellently with experiment (1289 and 1297 cm^{-1}). The perturbing level exhibits an increased VPT2 IR intensity (6 km mol^{-1}) which is consistent with a weakening but persistence of the resonance as found experimentally (see Fig. 6.1, p. 116).

(c) Assignments to (FF′)

In the OCO bending range of each deuterated isotopologue, two X bands are ascribed to the OCO bending fundamentals of asymmetrically deuterated (FF′). The assignments and band centres agree (to within 1 cm^{-1}) with the previous analysis by Xue and Suhm [141]. It is worth noting that for X_A (637 cm^{-1} in Ref. [141]), which is an OCO bending fundamental of (DCOOH–DCOOD), Xue and Suhm noted an unusually high intensity, suspecting additional dimeric contributions underneath it. Also in the new Raman jet spectra (Fig. 6.4, p. 119) this band exhibits an unusually high intensity, compared to the same band in the DCOOD spectrum. The depolarised spectra reveal that the majority of the intensity in the DCOOH spectrum is depolarised, supporting the hypothesis of additional contributions that do not correspond to the OCO bend of (DCOOH–DCOOD). The polarised fraction is ascribed to (DCOOH–DCOOD) whereas the more dominant depolarised socket calls for a non-totally symmetric assignment. Given that the OH torsion of *trans*-DCOOH, which is completely depolarised and expected to exhibit a broad band contour, is nearby (631.54 cm^{-1}, Ref. [236]), a monomeric assignment to the OH torsion appears more plausible than a dimeric assignment.

Based on the explicit consideration of asymmetrically substituted (FF′) dimers between a carbon-12 isotopologue and its carbon-13 variant in Fig. 6.3 (p. 118), it is possible to assign weak scattering signals in the C–O stretching spectra of HCOOH (X_J) and DCOOH (X_N). The experimental carbon-13 red-shift (14 cm^{-1}) is in excellent agreement with harmonic CCSD(T)-F12a/VDZ-F12 (12-15 cm^{-1}) and hybrid MP2/aVTZ VPT2 predictions (13 cm^{-1}). On similar grounds, X_G in the HCOOD spectrum is ascribed to the C–O stretch of (HCOOH–HCOOD).

(d) Possible assignments to FF

There are indications for small concentrations of the polar dimer FF. The possibility of a FF assignment was discussed for weak signals in the Raman jet spectrum of HCOOH (X_G, X_H) in Ref. [109]. It is worth noting that also in the DCOOH Raman spectrum very weak scattering signals are observed that might correspond to FF (X_L). Overall, from a jet-spectroscopic perspective, the C–O stretching region appears very promising for future spectroscopic searches for the polar dimer, given the high Raman visibility of the C–O stretching vibrations and the larger spectral separation from monomer and cyclic dimer bands [109].

(e) (FF) combination/overtone bands of O–H isotopologues – IR bands

As mentioned in the introduction and clearly seen in Fig. 6.1 (p. 116), ν_{22} is split into a triplet with perturbed band centres located between 1220 and 1234 cm^{-1}. Despite several (experiment-focussed) investigations [110, 145, 146, 149], there is no consensus regarding the assignment of

both perturbers. Briefly, it is accepted that one perturber is $\nu_{10}+\nu_{15}$ whereas the other must be at least a ternary B_u state. Goroya *et al.* proposed to assign the second perturber to $\nu_{23}+2\nu_{24}$ [110]. Employing a heuristic effective Hamiltonian MP2 VPT2 approach, $\nu_9+\nu_{11}+\nu_{15}$ was put forward as an alternative assignment in Ref. [28]. Two central assumptions were made in that work: Only binary and ternary states were considered which, due to symmetry constraints, must be B_u symmetric. Furthermore, the harmonic force constants were empirically corrected in order to reproduce the deperturbed experimental fundamentals of $(HCOOH)_2$ with DVPT2. To illustrate the robustness of the newly proposed assignment with respect to the underlying electronic structure level, the effective Hamiltonian calculations are repeated here without empirical modification of the force constants using instead the CCSD(T)-F12-quality QB-PES [23]. The experimental SOF and semi-experimental SOF+x term values for all binary and ternary vibrational states of B_u symmetry between 1200 and 1300 cm^{-1} are reproduced from Ref. [109] and listed in Table 7.4. Due to the strong Fermi resonance between ν_{14} and $\nu_{12}+\nu_{23}$ (see Ref. [109]), $\nu_{12}+\nu_{16}+\nu_{23}+\nu_{24}$ is additionally included. Adopting the nomenclature from Ref. [109], the three effective VPT2 Hamiltonians are labelled **I**-**III** and their eigenvalues are listed in Table 7.4 together with the squared eigenvector coefficient from the zeroth-order ν_{22} fundamental. **I** includes all eight states shown in Table 7.4 and allows for all possible resonance interactions between them that can be mediated by a full quartic force field (VPT2+K). Similar to the results with the empirically-corrected MP2/aVTZ force field [109], $\nu_{23}+2\nu_{24}$ does not strongly interact with ν_{22} on the QB-PES. **II** only retains the essential couplings to $\nu_{10}+\nu_{15}$ and $\nu_9+\nu_{11}+\nu_{15}$ and has the following lower-triangular form

$$\frac{\mathbf{H}^{\mathrm{II}}}{hc} = \begin{pmatrix} (\nu_{10}+\nu_{15})^* & & \\ \frac{1}{2\sqrt{2}}\phi_{10,9,11} & (\nu_9+\nu_{11}+\nu_{15})^* & \\ \frac{1}{2\sqrt{2}}\phi_{22,10,15} & \frac{1}{4}K_{22;9,11,15} & (\nu_{22})^* \end{pmatrix} = \begin{pmatrix} 1228.8 & & \\ 5.5 & 1228.5 & \\ -4.0 & 1.1 & 1228.7 \end{pmatrix}, \tag{7.1}$$

where the couplings to the removed five states are absorbed into the deperturbed VPT2 term values (∗) on the diagonal. In **III**, the Darling-Dennison-like resonance between ν_{22} and $\nu_9+\nu_{11}+\nu_{15}$ is turned off (VPT2+F). The eigenvalues of the three effective Hamiltonians are compared to the previously published empirically-corrected MP2/aVTZ force field values in Table 7.4. The results from Ref. [109] can qualitatively be confirmed. The fundamental and ternary level appear to be coupled through their simultaneous Fermi resonance with $\nu_{10}+\nu_{15}$. Since deuteration experiments confirm that the perturbers are dark states that gain intensity via resonance (see Refs. [145, 149] and Fig. 6.1, p. 116), the highest-wavenumber band in this triad can be identified as ν_{22}. For convenience, the assignment order of $\nu_{10}+\nu_{15}$ and $\nu_9+\nu_{11}+\nu_{15}$ in Table 7.2 is adopted from Ref. [109] but it is noted that the harmonic oscillator labels of the two lower-wavenumber bands are not very meaningful in this context and an inverse assignment is equally conceivable.

Rasheeda *et al.* very recently reinvestigated this resonance triad also using VPT2 [25]. They can qualitatively reproduce the above-discussed effective Hamiltonian results but note that the prerequisite resonance perturbation of ν_{10} is not indicated by their most accurate *ab initio* VPT2 calculation. The resonance between ν_1 and $\nu_2+\nu_7$ in *trans*-HCOOH (see Section 4.2) is an excellent example where theory must be accurate to within 1 cm^{-1} in order to correctly model the remarkable mixing that is observed experimentally since the coupling matrix element is vanishingly small and the coupling almost entirely driven by the near-degeneracy. The current situation appears to be similar and it should be realised that from an experimental side, the low-resolution Raman jet spectra neither allow to confirm nor entirely reject a resonance between ν_{10} and $\nu_9+\nu_{11}$. This is due to the complicated and broad band shape of ν_{10}. The SOF+x prediction for $\nu_9+\nu_{11}$ (1069 cm^{-1}, Table D.9) indicates that it would partially overlap with the higher-wavenumber wing of the ν_{10} contour (R_B; Fig. 6.4, p. 119). The more cleanly separated ν_{11} fundamental in

Table 7.4 Term values (in cm^{-1}) of B_u symmetric binary, ternary, and selected quaternary vibrational states of $(HCOOH)_2$ between 1200 and 1300 cm^{-1}. The squared eigenvector coefficient of the zeroth-order ν_{22} fundamental is shown in parentheses. The SOF and SOF+x values are taken from Ref. [109].

				QB-PES						Ref. [109]	
State	Γ	SOF	SOF+x	**I**		**II**		**III**		**III**	
ν_{22}	B_u			1229.6	(0.68)	1229.6	(0.65)	1228.6	(0.65)	1235.0	(0.51)
$\nu_{23}+2\nu_{24}$	B_u	1236	1217	1206.8	(0.00)						
$\nu_{10}+\nu_{15}$	B_u	1226	1224	1234.9	(0.13)	1234.9	(0.14)	1235.4	(0.18)	1218.6	(0.17)
$\nu_9+\nu_{11}+\nu_{15}$	B_u	1240	1227	1221.2	(0.19)	1221.3	(0.21)	1221.9	(0.17)	1228.1	(0.32)
$\nu_8+\nu_{11}+\nu_{15}$	B_u	1273	1256	1258.2	(0.00)						
$\nu_{14}+\nu_{16}+\nu_{24}$	B_u	1272	1263	1250.7	(0.00)						
$\nu_{12}+\nu_{16}+\nu_{23}+\nu_{24}$	B_u	1287	1277	1272.0	(0.00)						
$\nu_9+\nu_{10}+\nu_{16}$	B_u	1288	1289	1285.9	(0.00)						

Fig. 6.4 (p. 119, R_B) exhibits an almost symmetric band shape. ν_{10}, on the other hand, overlaps with the monomeric ν_8 band which overall distorts the ν_{10} contour (cf. Figs. 2.5.III.D and 2.6, pp. 44). As such, a weak resonance between $\nu_9+\nu_{11}$ and ν_{10} should not be dismissed before resolving the complicated ν_{10} contour.

(f) (FF) combination/overtone bands of O–H isotopologues – Raman bands

Two $(HCOOH)_2$ mode assignments of R_E and R_G are marked as tentative in Table 7.2. The assignment of R_E is still (slightly) tentative [109], given its only partially resolved band structure and proximity to a F(FF) fundamental. While $\nu_6+\nu_8$ can unambiguously be assigned in the DCOOH spectrum (R_G), the similar assignment in the HCOOH spectrum (also R_G) remains tentative [109]. Based on SOF+x predictions, R_G of $(HCOOH)_2$ could alternatively be assigned to $2\nu_{23}$. Ideally, only one of the bands would be present in the DCOOH Raman spectrum, facilitating the HCOOH assignment. However, there is the possibility that X_U in the DCOOH spectrum corresponds to $2\nu_{23}$ of the cyclic dimer, see (i) below.

(g) (FF) combination/overtone bands of O–D isotopologues – IR bands

It is quite interesting to note that the combination of both torsional modes ($\nu_{11}+\nu_{14}$) has substantial IR intensity in $(HCOOH)_2$, $(DCOOH)_2$, and $(DCOOD)_2$ (see Ref. [149]) but not in $(HCOOD)_2$. In fact, this combination band is suspected to be present in the IR spectra of several cyclic carboxylic acid dimers [42], even mixed carboxylic acid dimers [86], and it was recently proposed that they carry intrinsic oscillator strength [42]. In light of this, its presence in the DCOOD spectrum (I_F) and simultaneous absence in the HCOOD spectrum is unexpected. A very weak absorption feature at 1363 cm^{-1} (X_O) could possibly correspond to this combination band. An assignment to F(FF) appears less likely because no F(FF) fundamental is expected nearby and no corresponding Raman band is observed. If X_O is ascribed to this combination band, the C–H deuteration shift would amount to only -5 cm^{-1} (I_F, DCOOD) whereas CCSD(T)-F12a/VDZ-F12 harmonic, MP2/aVTZ hybrid force field VPT2, and semi-experimental SOF+x predictions indicate a two-digit shift (see Table D.9). Thus, the assignment is marked as tentative in Table 7.3 and requires further investigations.

(h) (FF) combination/overtone bands of O–D isotopologues – Raman bands

Upon inspection of Tables 7.2 and 7.3 or the Raman spectra in Figs. 6.3-6.4 (pp. 118), one notices a distinct similarity across O–X isotopologues. The plethora of observed combination and overtone bands in the Raman jet spectra of O–H deuterated formic acid reflects the hydrogen

bond-mediated resonance couplings between the C – O stretch (ν_6) and several vibrational states involving the OD in-plane (ν_4, ν_{20}) and out-of-plane bends (ν_{11}, ν_{14}). At higher wavenumbers, one can even see certain spectral patterns repeating themselves. The shifts, e.g. between R_L-R_N and R_P-R_R (DCOOD), roughly correspond to the fundamental excitation wavenumber of the dimer in-plane bend (ν_9). The experimental band centres agree to within a few cm^{-1} with semi-experimental SOF+x band centres for these ternary states (data now shown). Similarly, X_H, X_I, X_L (HCOOD) and X_R (DCOOD) are suspected to correspond to (FF) combination/overtone bands but their assignments are rather tentative due to their proximity to observed or expected F(FF) or (FF′) fundamentals.

The ν_6 fundamental of $(DCOOD)_2$ deserves a few comments as it is split into a near 1:1 doublet located at 1257 and 1260 cm^{-1} (R_J, R_K). The small splitting of 3 cm^{-1} is indicative of a rather weak coupling and we have to assume that the significant intensity transfer to R_K (1260 cm^{-1}) is largely driven by an accidental near-degeneracy with a nearby A_g symmetric state. The data in Table D.9 show that the perturber is not a binary state. Considering only ternary states, semi-experimental SOF+x provides three possible assignments: ν_9+ν_{10}+ν_{12} (1259 cm^{-1}), ν_5+2ν_{15} (1264 cm^{-1}), and ν_{12}+ν_{16}+ν_{21} (1266 cm^{-1}). The by far best agreement to experiment is found for ν_9+ν_{10}+ν_{12}. The nearby band R_I (1244 cm^{-1}) can either be assigned to ν_4+ν_9 or 2ν_7 which are expected at 1246 and 1245 cm^{-1}, respectively. Considering that the Martin test predicts a resonance between ν_{10}+ν_{12} and ν_4, in agreement with the unusually high intensity of R_H (Fig. 6.3, p. 118), an assignment of the ν_6 perturber R_K to ν_9+ν_{10}+ν_{12} and R_I to ν_4+ν_9 is preferred.

(i) Note on unassigned DCOOH X bands

In contrast to the HCOOD and DCOOD Raman jet spectra, the interpretation of the DCOOH Raman spectrum is more complicated. Only one combination band can safely be ascribed to (FF) and many X bands in Table 7.3 are left unassigned. It is striking that, similar to the Raman spectrum of HCOOH, most X bands are located near (FF) fundamentals, especially near the C – O stretching band which is the most visible fingerprint fundamental of formic acid and its clusters. In all these contexts, an interpretation of these X bands as other formic acid clusters or asymmetrically substituted isotopologues (FF′) appears more plausible than the alternative explanation of several (FF) combination/overtone bands. At least four of these X bands (X_G, X_P, X_T, and X_U) exhibit an unexpected scaling behaviour as they increase with temperature. Since this behaviour is not observed in the Raman spectra of the other isotopologues, it is questionable whether this seeming temperature effect is genuinely due to (non-monomeric) hot bands. In view of the persistently large DCOOD impurity in the DCOOH spectra (see Table 6.2), an assignment to (DCOOH – DCOOD) appears plausible. Indeed, many of the unassigned X bands of DCOOH coincide with predicted fundamentals of (DCOOH – DCOOD) (see Figs. 6.3-6.4, pp. 118). The seeming temperature dependence would thus reflect an increase of the (DCOOH – DCOOD) concentration over the course of the measurement as dimer spectra in a temperature series were measured over the course of a day (see Table A.3). This hypothesis could easily be verified in the future by spectroscopically characterising the mixed jet expansion of DCOOH and DCOOD.

(j) Comparison to previous analyses

In light of the presented reanalysis, the analysis of the jet-cooled IR fingerprint spectra by Kollipost [149] can fully be confirmed. The only change to Ref. [149] is that several unassigned bands that were suspected to correspond to larger (>dimeric) formic acid clusters are ascribed to the formic acid trimer F(FF) and provided mode assignments (see Table 7.3). The IR band centres of the fingerprint modes are newly determined from the spectra published in Ref. [149].

Table 7.5 Fundamental wavenumbers (in cm^{-1}) of the C_{2h} symmetric cyclic formic acid dimer from gas phase or jet-cooled high-resolution and jet-cooled low-resolution spectroscopy up to 1500 cm^{-1}. "$(XY)_2$" indicates the isotope patterns of the C–X and O–Y groups. Experimentally deperturbed band centres are bolded.

		Raman[a]					IR[b]			
Description	Mode	$(HH)_2$	$(DH)_2$	$(HD)_2$	$(DD)_2$	Mode	$(HH)_2$	$(DH)_2$	$(HD)_2$	$(DD)_2$
	A_g					B_u				
	⋮					⋮				
δ(OH/D)	ν_4	1430	1418	1074	1092	ν_{20}	1407	1381	1044.3	1072
δ(CH/D)	ν_5	1375	1000	1382	992	ν_{21}	1371.78	1004.0	1391.08	987.1
ν(C–O)	ν_6	1224	1238	1269	**1258**	ν_{22}	**1230**	1244.85	1266.5	1256.6
δ(OCO)	ν_7	681	675	627	623	ν_{23}	707.6	702	661	656
ν(OH/D···O)	ν_8	194	193	194	192					
δ(OH/D···O)	ν_9	161	159	157	157	ν_{24}	264	258	255	250
	B_g					A_u				
γ(CH/D)	ν_{10}	1058	893	1054	893	ν_{13}	1069.3			
γ(OH/D)	ν_{11}	911	920	672	669	ν_{14}	**944**	958.5	717.9	711.7
γ(OH/D···O)	ν_{12}	242	212	238	210	ν_{15}	168.47			
Twist						ν_{16}	69.2			

[a] ν_8, ν_9, and ν_{12} are from Ref. [141]; other Raman band centres from this work; ν_6 of $(DCOOD)_2$ is a resonance doublet at 1257 and 1260 cm^{-1}, the latter peak being less intensive.

[b] ν_{15} and ν_{16} are from Ref. [129]; ν_{24} is from Ref. [148]; ν_{22} of $(HCOOH)_2$ is from Ref. [110] with resonance-perturbed averaged band centres at 1219.72, 1225.35, and 1233.96 cm^{-1}, the latter being most intensive; ν_{22} of $(DCOOH)_2$ (averaged) is from Ref. [144]; ν_{21} of $(HCOOH)_2$ and $(HCOOD)_2$ is from Ref. [150]; other IR band centres are newly determined in this work from spectra published in Ref. [149]; ν_{14} is a resonance doublet at 938.9 and 953.4 cm^{-1}, the latter peak being less intensive.

Deviating from the analysis in Ref. [149], the ν_{23} band centre of $(HCOOH)_2$ is slightly relocated to 707.6 cm^{-1}.[188]

The analysis of the jet-cooled Raman fingerprint spectra, on the other hand, significantly deviates from Ref. [119]. Overall, the current jet measurements have been conducted at slightly less concentrated conditions and the number of observed bands or rather peaks is less compared to Ref. [119]. Many bands that are ascribed to trimers in Table 7.3 were either left unassigned in Ref. [119] or (tentatively) ascribed to (FF) combination/overtone bands. For the fundamentals of (FF), the new values agree to within 1-2 cm^{-1} with previously reported band centres [119, 140, 141].

7.3 Summary of cyclic formic acid dimer fundamentals

The available high-resolution jet-cooled or gas phase and low-resolution jet-cooled fundamental wavenumbers of the cyclic formic acid dimer are summarised in Table 7.5, focussing on all vibrational modes below 1500 cm^{-1}.

Due to their strong resonances, deperturbed band centres are shown for ν_{22} and ν_{14}. Several Raman-active fundamentals are involved in weaker resonances but the deperturbation shifts are within the spectral resolution of ± 2 cm^{-1} and therefore neglected. Despite a deperturbation shift of only 1 cm^{-1}, the ν_6 fundamental of $(DCOOD)_2$, which is resonance-split in two near-equally intensive bands, is deperturbed and bolded in Table 7.5 for mnemotechnical reasons.

[188] In Table 6.2 of Ref. [149], two maxima are listed for ν_{23} at 707.6 and 708.8 cm^{-1}. By closely comparing the band shape of ν_{23} to that of better resolved A or $A+B$ type bands (1810.6 and 1371.7 cm^{-1}), the Q branch of ν_{23} can be ascribed to the peak at 707.6 cm^{-1} and the peak at 708.8 cm^{-1} to the maximum of its R branch.

Chapter 8

Theoretical description of cyclic formic acid dimer vibrations

Other than with the monomer (Chapter 5), where the availability of essentially exact nuclear vibrational reference data allowed detachment from experiment and the underlying electronic structure to focus entirely on the vibrational treatment, this is not the case with the dimer. Building on the experimental characterisation of the cyclic formic acid dimer fingerprint vibrations in the previous chapter, we have to carefully and systematically evaluate electronic structure and nuclear vibrational structure errors against experiment. The following analysis is divided into three parts – the six intermolecular pair vibrations of the dimer (Section 8.1), the intramolecular fingerprint vibrations below 1500 cm^{-1} (Section 8.2), and the zero-point vibrational and dissociation energy[189] of the cyclic dimer (Section 8.3). In light of the findings in Appendix C.2, previously published anharmonic benchmarks of the pair [130] and fingerprint modes [109] of the cyclic formic acid dimer are revisited.[190]

8.1 The six pair modes

The pair modes are all located below 300 cm^{-1} and are energetically well separated from the intra-monomer vibrations (see Fig. 1.3, p. 9).[191] The six normal mode displacements are visualised in Fig. 8.1. The two B symmetric librations (ν_{12} and ν_{24}) are relatively stiff, because both act on the two hydrogen bonds in opposing directions, but these two modes do not mix due to their different symmetry even if they are close in energy. The two A_u modes (ν_{15} and ν_{16}) may mix but since the energy required for twisting the two monomer planes is much lower than bending them, this is less pronounced. The two A_g modes (ν_8 and ν_9) are very close in energy and may mix more intensely (*vide infra*).

The harmonic approximation

In the mechanical harmonic approximation, the restoring force is assumed to increase linearly along each normal mode. For the pair modes, an overestimation rather than underestimation is expected since the force should soften with increasing separation of the monomers and move towards zero in the limit of two non-interacting molecules. We start with Hartree-Fock theory

[189] Parts of Section 8.3 have been published in an abridged version in Ref. [109] and its supplementary material.

[190] The previously published [109, 130] harmonic benchmarks are also included in Sections 8.1 and 8.2 for completeness. The analyses closely follow Refs. [109, 130] and there might be overlapping content that is not explicitly marked as a citation.

[191] See Ref. [130] for a detailed review of the van der Waals vibrations of $(HCOOH)_2$.

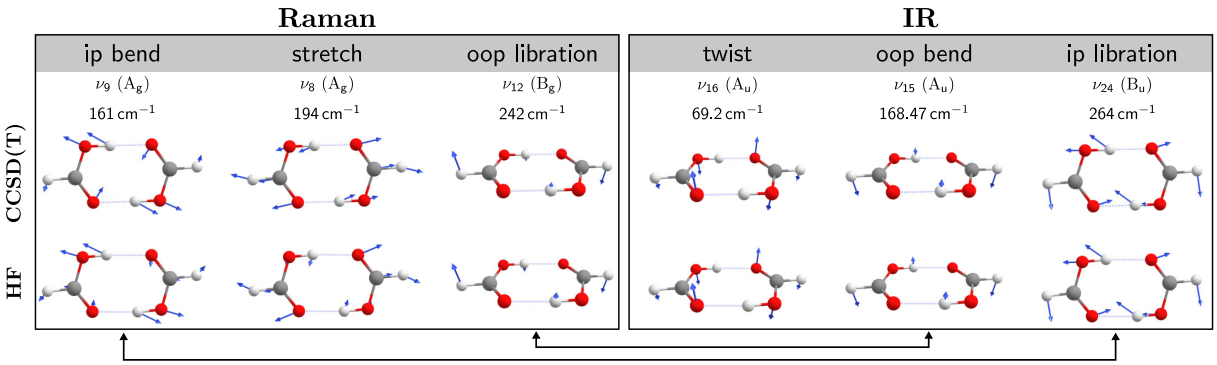

Figure 8.1 Normal modes of all six pair vibrations of the cyclic formic acid dimer $(HCOOH)_2$ calculated at the CCSD(T)/aVTZ and HF/aVTZ level. Davydov pairs are connected by arrows. The experimental fundamental wavenumbers are from Table 7.5 (p. 130). Note that normal mode arrows on hydrogen atoms in the background appear smaller and out-of-plane arrows may appear non-orthogonal to the molecular plane due to perspective distortion. Adapted from Ref. [130] (published under a Creative Commons Attribution license, CC BY 4.0).

Table 8.1 Experimental anharmonic and calculated harmonic (ω) values for the six intermolecular fundamentals of $(HCOOH)_2$ for increasingly improved coverage of electron correlation and basis set completeness (in cm^{-1}). The CCSD(T)/aVQZ values are taken from Ref. [102] and the experimental values are from Table 7.5 (p. 130).

			ω(HF)			ω(MP2)			ω(CCSD(T))			
	Descr.	Γ	aVDZ	aVTZ	aVQZ	aVDZ	aVTZ	aVQZ	aVDZ	aVTZ	aVQZ	$\tilde{\nu}_{exp}$
ν_9	δ(OH···O)	A_g	161	159	159	169	169	169	168	168	167	161
ν_8	ν(OH···O)	A_g	180	179	178	209	213	212	206	211	209	194
ν_{12}	γ(OH···O)	B_g	241	239	238	258	258	259	251	253	255	242
ν_{16}	Twist	A_u	75	75	75	69	69	71	68	69	72	69.2
ν_{15}	γ(OH···O)	A_u	167	169	167	175	179	178	171	176	177	168.47
ν_{24}	δ(OH···O)	B_u	220	218	217	275	283	281	269	277	275	264

and then systematically increase electron correlation effects from MP2 through to the CCSD(T) level. The basis sets are systematically increased to converge the six pair modes.

In Table 8.1, the harmonic predictions are compared to (anharmonic) experiment for all six pair modes. The best MP2 wavenumbers are larger than corresponding values at the CCSD(T) level which is expected from the usually shorter MP2 bond lengths in comparison to CCSD(T), and, therefore stiffer inter-monomer force constants [75, pp. 821]. The exception is the dimer twist where deviations due to change in the one-electron basis are of the same magnitude as deviations between N-electron models due to correlation effects. Rewardingly, the highest electron correlation level yields harmonic wavenumbers which are higher than experiment in all cases, by up to 8%. Overall, electron correlation effects are found to be much more important than basis set incompleteness errors for the six pair modes.

The shapes of the normal modes are very similar at the MP2 and CCSD(T) levels and comparison to HF in Fig. 8.1 reveals that the A_u, B_u, and B_g modes are qualitatively unaffected by the inclusion of electron correlation. This is not the case for two A_g modes, the dimer stretch (ν_8) and in-plane bend (ν_9). At the Hartree-Fock level, ν_8 mixes with ν_9 and acquires significant bending character whereas MP2 and CCSD(T) predict a better separation between stretching and bending character. This decoupling is caused by an increase in the energetic separation of the two normal modes which nearly doubles when including post-Hartree-Fock electron correlation (Table 8.1). It is known from depolarised Raman measurements that the two modes are indeed rather cleanly separated in character [141]. Another, more subtle deficiency of the HF calculations is the relative order of the two B symmetric librations. Experiment and correlated

Table 8.2 Experimental and calculated anharmonic ($\tilde{\nu}$, VPT2) values for the six intermolecular fundamentals of $(HCOOH)_2$ for increasingly improved coverage of electron correlation and basis set completeness (in cm^{-1}). The anharmonic correction ($\tilde{\nu} - \omega$) is shown in parentheses. Experimental values are from Table 7.5 (p. 130).

			$\tilde{\nu}$(HF)				$\tilde{\nu}$(MP2)				$\tilde{\nu}$(B3LYP-D3(BJ))				
	Descr.	Γ	aVDZ		aVTZ		aVDZ		aVTZ		aVDZ		aVTZ		$\tilde{\nu}_{exp}$
ν_9	δ(OH···O)	A_g	150	(−11)	148	(−11)	160	(−9)	161	(−7)	174	(−7)	169	(−9)	161
ν_8	ν(OH···O)	A_g	166	(−14)	164	(−14)	194	(−15)	199	(−14)	211	(−12)	209	(−12)	194
ν_{12}	γ(OH···O)	B_g	221	(−20)	220	(−19)	245	(−13)	246	(−12)	255	(−11)	247	(−14)	242
ν_{16}	Twist	A_u	67	(−8)	69	(−6)	65	(−4)	73	(+4)	75	(−1)	56	(−19)	69.2
ν_{15}	γ(OH···O)	A_u	162	(−5)	163	(−6)	169	(−7)	169	(−10)	184	(−3)	182	(−3)	168.47
ν_{24}	δ(OH···O)	B_u	202	(−18)	199	(−20)	263	(−12)	273	(−10)	292	(−5)	288	(−6)	264

calculations (already at the harmonic level) agree in locating the *ungerade* mode (ν_{24}) above the *gerade* mode (ν_{12}) whereas the HF sequence is inverted. This does not affect the mode pattern because there is no harmonic mixing due to symmetry. However, it leads to a coincidental agreement with experiment for the harmonic ν_{12} prediction and to deviations of more than 40 cm^{-1} for the highest-wavenumber intermolecular mode ν_{24}.

The key remaining question is whether the deviation between the best harmonic calculation, i.e. CCSD(T) with large basis, and experiment of still up to 8% is due to residual deficiencies of the electronic structure calculation or due to anharmonic motion in the rather moderately floppy formic acid dimer.

Beyond the harmonic approximation

Moving beyond the harmonic approximation, we first include anharmonic corrections using second-order vibrational perturbation theory expanded in rectilinear normal mode coordinates. By numerical differentiation of *ab initio* computed analytic Hessians, anharmonic corrections can efficiently be computed for this deca-atomic system with Gaussian 16 at the HF and MP2 levels using double- or triple-zeta basis sets (details in Appendix B). DFT methods are very popular in anharmonic frequency calculations because they are relatively cheap [263]. Thus B3LYP-D3(BJ) is also included as an intermediary between HF and MP2 since it combines the inexpensiveness of the former with the increased accuracy of the latter.

The anharmonic VPT2 fundamentals ($\tilde{\nu}$) and anharmonic corrections ($\delta_{anh} = \tilde{\nu} - \omega$) are listed in Table 8.2. Other than in Ref. [130], no error bars are ascribed because nine slightly different start geometries yield anharmonic corrections that agree within a few tenths of cm^{-1} (see Appendix C.2). Several trends are evident from the data in Table 8.2. Whereas the two A_g modes are more sensitive to the harmonic N-electron treatment but rather insensitive to the one-electron basis set, the opposite is the case for the anharmonic corrections of the two A_u modes, ν_{15} and ν_{16}. At the MP2 level, the aVDZ and aVTZ predictions differ in the sign of the anharmonic correction of ν_{16}. At the B3LYP-D3(BJ) level, the anharmonic correction of ν_{16} is negative but clearly too large with an aVTZ basis. Generally, δ_{anh} tends to be less negative at the MP2 level than at the HF level and $\tilde{\nu}$ is nearer experiment at the MP2 level than B3LYP-D3(BJ) level.

A detailed comparison of the remaining deviation between anharmonic MP2 and experiment (Table 8.2), on the one hand, and the missing N-electron correlation effects between harmonic MP2 and CCSD(T) (Table 8.1), on the other hand, suggests a composite method which combines harmonic CCSD(T) wavenumbers with MP2 anharmonicities to be essentially exact for the pair modes. The substituted hybrid force field approach is used in the following but it is noted that also the additive approach can be used for the pair modes as they are not perturbed by resonances.

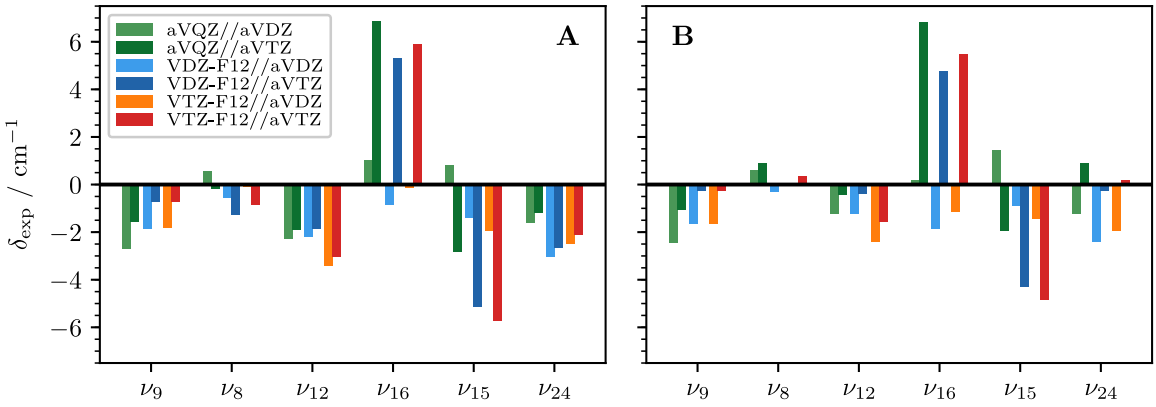

Figure 8.2 Deviations between calculated anharmonic (VPT2) and experimental fundamentals of the six $(HCOOH)_2$ pair modes ($\delta_{exp} = \tilde{\nu} - \tilde{\nu}_{exp}$). Composite force fields are used with coupled-cluster-quality harmonic (CCSD(T)/aVQZ, CCSD(T)-F12a/VXZ-F12) and MP2-quality anharmonic force constants for systematically increasing basis sets. A and B differ in the method of inserting the new harmonic force constants (see text).

As discussed earlier (Section 2.1.3), Gaussian 16 automatically scales the cubic and quartic force constants by the ratio of the original and new harmonic wavenumbers. In the left panel of Fig. 8.2 the Gaussian-computed fundamental wavenumbers are shown (A) whereas in the right panel the pure MP2 cubic and quartic force constants are used (B). For consistency, both hybrid force field VPT2 calculations are performed with GUINEA. Overall, Fig. 8.2 shows that differently combined MP2 anharmonicity and CCSD(T) harmonicity yield very accurate predictions for the six pairs modes. The predictions for the Raman-active modes are mostly within the experimental error bars of $\pm 2\,\mathrm{cm}^{-1}$ and method B yields essentially exact results for these modes with an anharmonic MP2/aVTZ force field. The two A_u symmetric modes, ν_{15} and ν_{16}, on the other hand, are outliers in opposite directions with approximately similar magnitudes. Without additional data at hand (MP2 with a larger basis and/or coupled-cluster), it is difficult to assess to what extent the deviations for ν_{15} and ν_{16} are correlated or just coincidental. We will return to this discussion later (pp. 135).

The Qu and Bowman formic acid dimer potential

On the whole, Fig. 8.2 provides quite compelling evidence that CCSD(T) harmonic wavenumbers are very close to the true harmonic wavenumbers if the VPT2 calculations can be trusted in this case. The quantitative success of the composite hybrid force field ansatz for the pair modes (Fig. 8.2) can further be confirmed by VPT2 on a quartic force field expansion of the QB-PES (details in Appendix B.2) which reproduces the six experimental fundamental pair excitation wavenumbers to within $3\,\mathrm{cm}^{-1}$. The success of VPT2 with high-level (hybrid) force fields must be contrasted with recent full-dimensional rectilinear normal mode VCI results [32] on this analytic potential. The VCI predictions are shown together with VSCF results in Fig. 8.3A. While inclusion of vibrational correlation (VSCF→VCI) significantly improves the worst results, absolute errors are still between 17-41 cm^{-1} or equivalently 8-39%. In view of the performance of reduced-dimensional (pair modes and both intramolecular OH torsions) internal coordinate variational results [33] and full-dimensional rectilinear normal mode VPT2 which are shown alongside the VSCF and VCI results in Fig. 8.2A, this should not (entirely) be blamed on the underlying potential but rather on the approximations required for a high-dimensional variational calculation, such as a limited number of modes which are coupled together and a limited vibrational basis set.

Martín Santa Daría *et al.* suggested [33] that theory-experiment discrepancies for the intermolecular modes are not entirely due to the choice of coordinates but also due to problems

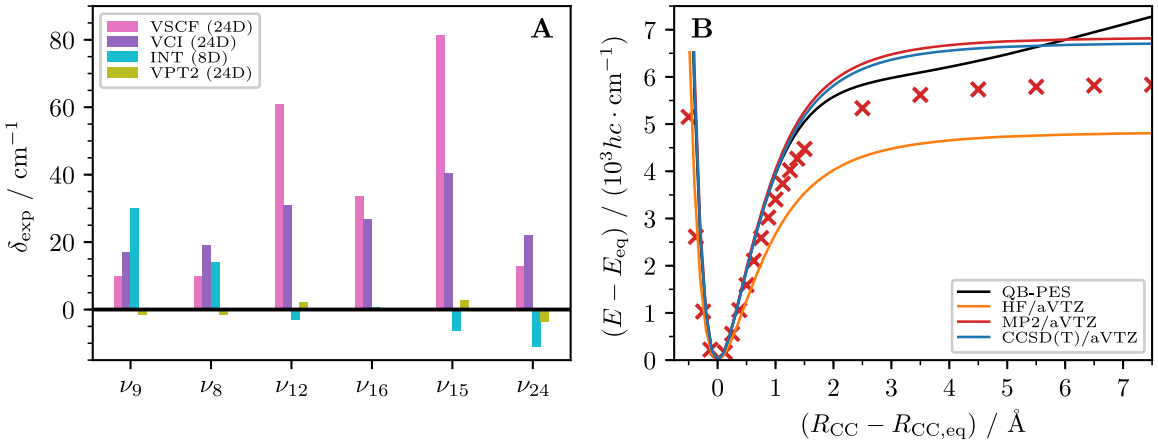

Figure 8.3 (A) Vibrational benchmark of the $(HCOOH)_2$ pair vibrations ($\delta_{exp} = \tilde{\nu} - \tilde{\nu}_{exp}$) computed on the QB-PES using various anharmonic nuclear vibrational models (from Refs. [32, 33]; VPT2 from this work). (B) Potential energy scan of $(HCOOH)_2$ along the CC distance with (crosses) and without relaxation of the other degrees of freedom (lines). At each level of theory, the respective equilibrium structure is used.

arising from the QB-PES. They observed problems in their calculations for the two A_g symmetric pair modes ν_8 and ν_9 which are evident from Fig. 8.3A. If these deviations are truly due to shortcomings in the analytic potential, they probably manifest at larger distances from the equilibrium since they do not seem to impair force field-based approaches that expand the potential in a Taylor series around the minimum.

Fig. 8.3B provides two important insights. The potential energy of the dimer is shown as a function of the separation of the two monomers (ΔR_{CC}). Keeping in mind that ν_8 corresponds to the dissociation of the cyclic dimer into two monomers (see Fig. 8.1), an unrelaxed scan (lines) reflects diagonal 1D anharmonicity, whereas a constrained optimisation with R_{CC} kept fixed (crosses) illustrates the impact of mode coupling to all other 23 vibrations. Focussing first on the blue and red lines, we see that the CCSD(T)-F12-quality QB-PES and *ab initio* CCSD(T)/aVTZ agree well up to $4000\,cm^{-1} \cdot hc$. Above that energy, however, the curvature significantly changes. The QB-PES is not able to correctly describe dissociation of the cyclic dimer into two monomers and the energy monotonically increases with larger separation of the two monomers, even beyond the shown range. Whether this unphysical behaviour is related to the reported problems [33] with ν_8 and ν_9 cannot be ascertained but it should be addressed in future improvements of the potential. To illuminate the importance of vibrational mode coupling for the ν_8 fundamental ($194\,cm^{-1}$), it suffices to concentrate on the energy region below $4000\,cm^{-1} \cdot hc$. MP2/aVTZ is able to reproduce the coupled-cluster potential very well and seems to recover most of the electron correlation that is absent at the HF/aVTZ level. Comparison of the red line and crosses in Fig. 8.3B shows that the effects of relaxation are very large. While not visible, even at small displacements, e.g. $\Delta R_{CC} = 0.125$ Å, the deviations have a sizeable impact on the ν_8 fundamental. At this point, the unrelaxed energy is $223\,cm^{-1} \cdot hc$ but reduces to $162\,cm^{-1} \cdot hc$ when the other degrees of freedom are subject to a constrained optimisation. In all these contexts, missing vibrational mode couplings as the cause for the ν_8/ν_9 discrepancies [33] appear very plausible, particularly in light of similar findings on a different full-dimensional potential [25].

Beyond fundamental excitations

After the preceding analyses showed that the systematic increase of electron correlation and introduction of small anharmonic corrections via second-order vibrational perturbation theory provides a satisfactory description of the fundamental excitation of the pair modes, it must lastly

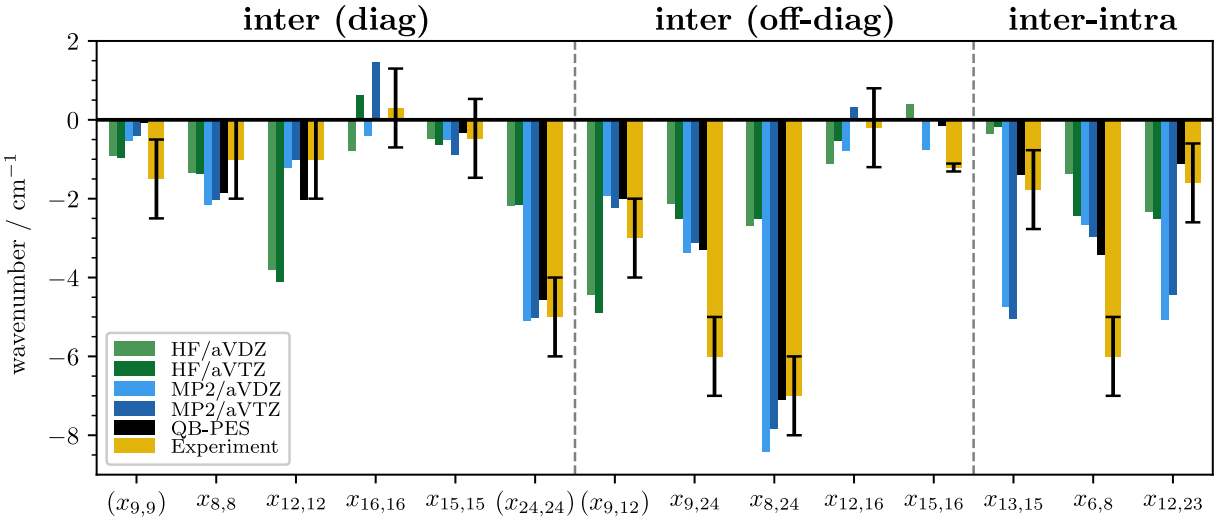

Figure 8.4 Selected diagonal and off-diagonal second-order anharmonicity constants for the six intermolecular modes of $(HCOOH)_2$. Experimental values are calculated according to expressions in Table 2.1 using experimentally observed transition wavenumbers from Table 7.2 and Ref. [130]. The experimental values are provided with error bars that have been estimated in Ref. [130].

be addressed whether this is to some extent fortuitous. For this purpose, it is worth to dissect the total anharmonic contribution further via Eq. 2.16 (p. 17), in order to check for potential coincidental error compensation. Even if the net anharmonicity is small, it may still be the result of mutually cancelling anharmonic contributions [264]. Through measurement of binary combination and overtone bands, we can extract individual $x_{i,i}$ and $x_{i,j}$ constants (see Table 2.1, p. 17).

The computed anharmonicity constants are compared to experimental values in Fig. 8.2, as compiled in Ref. [130]. For very tentative experimental reference values (see Section 7.1), $x_{i,i}/x_{i,j}$ are set in parentheses. Again, no error bars are ascribed to the *ab initio* computed anharmonicity constants as deviations are negligible if slightly different reference geometries are used (see Appendix C.2). For the QB-PES, numerical sensitivities of the computed x constants have not been explored.

Agreement between theory and experiment is very satisfactory within the experimental error bars. The close correlation between theory and experiment suggests that error compensation amongst the $x_{i,i}/x_{i,j}$ values is not a major issue. Two things are noteworthy in this context. A pronounced tendency for negative anharmonic corrections is perhaps not so surprising if one remembers that these are pair modes which correlate with translations and rotations in the limit of high vibrational excitation. However, it strongly indicates that there can be little error compensation for the anharmonicity in the fundamentals, because that would require both negative and positive contributions. Furthermore, electron correlation effects are mostly accounted for at the MP2 level except for the couplings between intra- and intermolecular modes. Here, the CCSD(T)-F12-quality QB-PES performs noticeably better. The basis set dependence effects are very modest except for the diagonal anharmonicity of the lowest-wavenumber dimer twist $(x_{16,16})$.

Returning to the previous discussion regarding a potential deterioration from MP2/aVDZ to MP2/aVTZ in an anharmonic treatment of the two A_u modes ν_{15} and ν_{16} (see Fig. 8.2), the present analysis sheds some further light on this matter. Comparison of each individual term in $\delta_{15,\mathrm{anh}}$ and $\delta_{16,\mathrm{anh}}$ (not shown) reveals that for both, the largest deviations between both basis sets correspond to the respective diagonal anharmonicity constants, i.e. $2x_{15,15}$ and $2x_{16,16}$, respectively. Rewardingly, both are experimentally available. While it should be taken into consideration that

the QB-PES is affected by fitting errors and the experimental error bars for $x_{15,15}$ encompass all predicted values, Fig. 8.4 overall indicates that MP2/aVDZ seems to profit from error cancellation effects for these two particular values (missing N-electron correlation and one-electron basis incompleteness).

Lastly, remembering that the Hartree-Fock sequence of ν_{12} and ν_{24} is inverted (Tables 8.1-8.2), it is an interesting coincidence that the HF anharmonicity constants in Fig. 8.2 match experiment and correlated anharmonic theory much better if the ν_{12} and ν_{24} labels are switched. Note that in Fig. 7 of Ref. [130], these labels are accidentally switched. The HF values for $x_{12,12}$ and $x_{24,24}$ must be interchanged [130, Fig. 7] which similarly applies to $x_{9,12}$ and $x_{9,24}$. $x_{8,24}$ and $x_{12,16}$ are unaffected by this label switch as the correct values are within the previously reported (large) error bars. The main conclusions from Section 5 of Ref. [130] remain unaffected and can be confirmed in view of the new and numerically more stable anharmonicity constants.

On the whole, the analysis presented throughout this section validates popular composite VPT2 approaches for fundamental excitations of the pair modes of formic acid dimer where the harmonic predictions are carried to the highest affordable electronic structure level, whereas the anharmonic corrections can be dealt with at a lower level of theory [11, 102].

8.2 The intramolecular fingerprint vibrations

In the same spirit as for the monomer (Section 5.4), we could proceed and directly compare absolute transition wavenumbers ($\tilde{\nu}$) of the dimeric fingerprint vibrations to judge how well different combinations of electronic structure and nuclear vibrational methods predict the observed band centres. In this benchmark, little systematic error cancellation is expected. As a consequence, harmonic approaches are bound to fail in most instances. When the shift from the monomer to the dimer vibrations is analysed, there is chance for some anharmonic error cancellation. This also allows focussing on hydrogen bonding effects and may introduce some tolerance towards a poorer description of the monomer. Moreover, the smaller size of these dimerisation shifts compared to absolute wavenumbers highlights imperfections in the hydrogen bond description on a relative scale. Since much of the monomer anharmonicity survives in the cyclic dimer, it cancels in the difference. Therefore, even harmonic models may succeed to some extent. Since the separation of monomer modes is cleaner in the Raman-active fundamentals (Fig. 8.5), we shall focus on the dimerisation shifts in the Raman spectra

$$\Delta_{\mathrm{s}} = \tilde{\nu}_{\mathrm{Dim}}(\mathrm{Raman}) - \tilde{\nu}_{\mathrm{Mon}}, \tag{8.1}$$

rather than the analogous IR shifts

$$\Delta_{\mathrm{a}} = \tilde{\nu}_{\mathrm{Dim}}(\mathrm{IR}) - \tilde{\nu}_{\mathrm{Mon}}. \tag{8.2}$$

One way to judge harmonic and anharmonic predictions on a similar footing is to analyse the Davydov splittings that arise from the complementarity of IR and Raman modes with respect to the inversion symmetry of the cyclic dimer

$$\Delta_{\mathrm{as}} = \tilde{\nu}_{\mathrm{Dim}}(\mathrm{IR}) - \tilde{\nu}_{\mathrm{Dim}}(\mathrm{Raman}). \tag{8.3}$$

The hydrogen bond-induced coupling of the modes into symmetric and antisymmetric counterparts can be very subtle such that theory or experiment may even fail to match these splittings with respect to their sign.[192] Building on the analysis of the six intermolecular vibrations, we

[192] Despite the publication of jet-cooled Raman and FTIR band centres in the fingerprint regions several years ago [119, 149], outdated thermal gas phase band centres are still regularly used in theoretical benchmarks. The

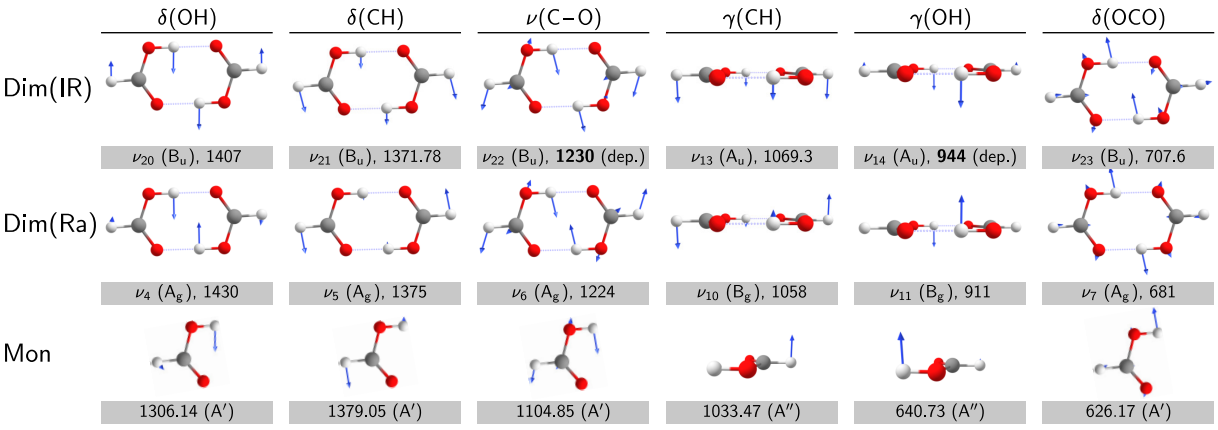

Figure 8.5 Davydov pairs of $(HCOOH)_2$ fundamental vibrations in the fingerprint region between 600 and 1500 cm^{-1}. The normal mode displacements are computed at the CCSD(T)-F12a/VDZ-F12 level and shown with experimental fundamental wavenumbers (Table 7.5; monomer from Table 4.8, p. 91). Note that normal mode arrows on hydrogen atoms in the background appear smaller and out-of-plane arrows may appear non-orthogonal to the molecular plane due to perspective distortion. Adapted from Ref. [109] (published under a Creative Commons Attribution license, CC BY 4.0).

shall continue in the following with the analysis of the computational data in terms of these three quantities $\tilde{\nu}$, Δ_s, Δ_{as}.

For *trans*-HCOOH, the band positions from Table 4.8 (p. 91) are used and for $(HCOOH)_2$ the band positions from Table 7.5; for resonance perturbed dimer modes, the experimentally-deperturbed values are taken, i.e. $\tilde{\nu}_{22} = 1230\,cm^{-1}$ and $\tilde{\nu}_{14} = 944\,cm^{-1}$. In analogy to experiment, deperturbed VPT2 is used for the dimer vibrations. For the monomer, however, VPT2+F term values are used exclusively since the OH bend-torsion resonance is much more complex and deperturbation of the experimental term values would introduce additional, unwanted sources of error. The dimeric Raman band centres have an uncertainty of $\pm 2\,cm^{-1}$ but the six IR band centres are in principle more accurate. To account for the deperturbation procedure of ν_{14} and ν_{22} and the higher band centre uncertainty of ν_{20}, however, we shall ascribe an uncertainty of $\pm 2\,cm^{-1}$ to all six IR band centres. The experimental band centre uncertainties of the monomer modes are negligible.

The harmonic approximation

The deficiencies of the Hartree-Fock method are too severe for the intramolecular modes that we do not include them in the following analysis. The performance of harmonic B3LYP-D3(BJ), MP2, and CCSD(T) for the three quantities $\tilde{\nu}$, Δ_s, Δ_{as} is compactly summarised in Fig. 8.6. Agreement with experiment is achieved when the disks fall within the green stripes and the extent of filling in symbols represents increasing basis set completeness along the guiding lines.

Focussing on CCSD(T) with the largest basis set, one can immediately see that none of the harmonic predictions for the absolute band positions match experiment. Only two predictions match the experimental dimerisation shift but 4 out of 6 Davydov splittings fall in the experimental error margin. This may be taken as first evidence for increasingly cancelling anharmonicities in these observables. Note that smaller basis sets yield partially better agreement with experiment for any of the three observables. Especially for the absolute band positions, this is

importance of using appropriate experimental reference data was emphasised in Ref. [109, Section V.A]. Using the example of the fingerprint modes of $(HCOOH)_2$, it was shown that in many cases the sign of the Davydov splittings, i.e. the energetic order of complementary IR- and Raman-active modes, is inverse to high-resolution or jet-cooled low-resolution values. Also, the thermal shift on the absolute band centres can be quite severe and the possibility of misassignments in the low-resolution thermal gas phase spectra was pointed out.

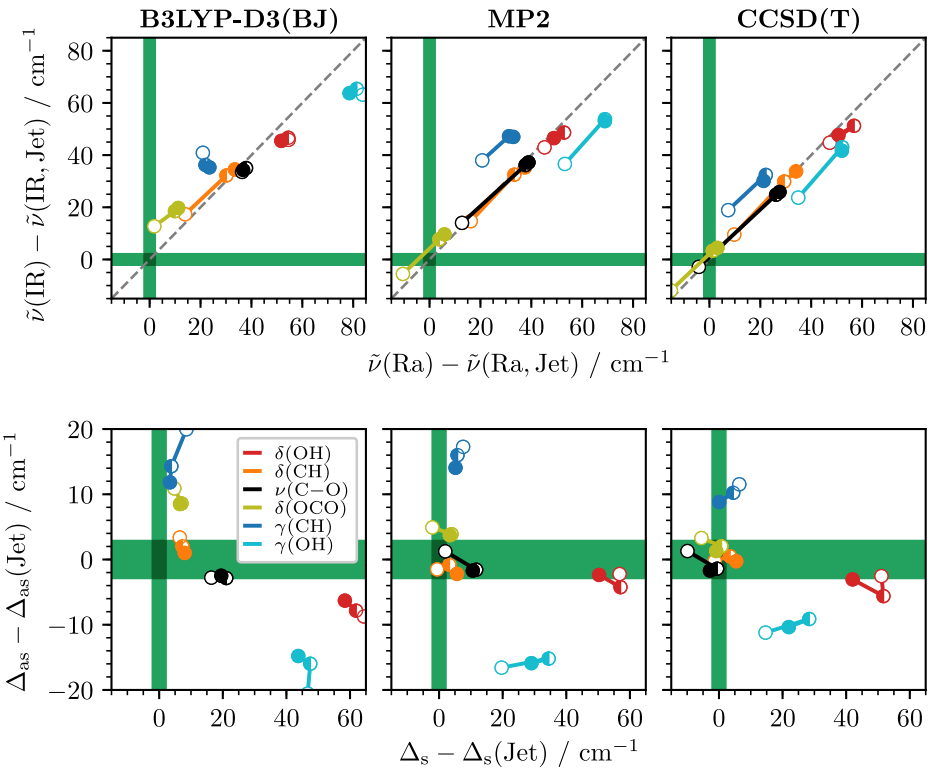

Figure 8.6 Davydov analysis of computed harmonic (disks) fundamentals of $(HCOOH)_2$ compared to jet-cooled values with increasing basis set completeness (aVDZ ○; aVTZ ◐; aVQZ ●). The CCSD(T)/aVQZ values are from Ref. [102]. Green areas represent the experimental error bars.

most likely a result of cancelling basis set incompleteness errors and missing vibrational anharmonicity. The two neighbouring out-of-plane modes γ(CH) and γ(OH) are outliers in opposite directions, indicating electronic structure deficiencies or important anharmonic contributions to the mixing between these normal modes (see normal modes in Fig. 8.5). δ(OCO) looks surprisingly harmonic for both dimer modes and like for the free monomer, theory only overshoots experiment by about 4 cm^{-1}. As δ(OCO) modulates the hydrogen bond O−H···O angle, this apparent harmonicity is likely a result of mutually cancelling anharmonic corrections. The two modes with the largest dimerisation shift Δ_s involve in-plane and out-of-plane OH bending. These motions are facilitated by the zero-point motion of the hydrogen bond modes which is of course missing in the harmonic approximation where all modes are exactly separable and do not couple. Therefore, the harmonic shifts overshoot, less so for γ(OH) than for δ(OH). Part of that is due to the missing Fermi resonance treatment at the harmonic level because the experimental monomer values are not deperturbed. This effect is also responsible for most of the discrepancy in δ(CH) which has a partial OH bending character (see Section 5.1).

For the lower-level electron correlation methods, it is noticeable that MP2 is generally very similar to CCSD(T). B3LYP-D3(BJ) performs very differently – one striking difference is the basis set insensitivity of B3LYP-D3(BJ) for ν(C−O). Similar to CCSD(T), the harmonic MP2 and B3LYP-D3(BJ) predictions for the absolute wavenumbers do not match experiment with the exception of occasional fortuitous success for δ(OCO) which indeed looks rather harmonic. While this overall performance is to be expected at the harmonic level, the error profile of MP2 suggests a very balanced description of complementary modes as most points lie on the diagonal. Especially rewarding is that also the basis set progression is parallel to the main diagonal, indicating a systematic improvement with increased coverage of the one-particle space. Overall, the predictions of MP2 for the relative quantities Δ_{as} and Δ_s are very similar to CCSD(T) and overall superior to B3LYP-D3(BJ). With the exception of the two out-of-plane modes, all

Davydov splittings are either near or fall within the experimental error margin at the MP2 level. The performance of B3LYP-D3(BJ), on the other hand, is suspected to reflect the empirical nature of the exchange-correlation functional. The description of complementary modes is less balanced, resulting in a poorer description of the Davydov splittings and dimerisation shifts. Overall, Fig. 8.6 suggests that the improvements of CCSD(T) over MP2 are not significant if one stops at the harmonic approximation and harmonic MP2/aVDZ is a particularly attractive cost-efficient approximation that yields reliable predictions for Davydov splittings and dimerisation shifts. For the particular example of the $(HCOOH)_2$ fingerprint vibrations, MP2/aVDZ seems to outperform B3LYP-D3(BJ) even in the harmonic approximation but it was shown in previous benchmarks of carboxylic acid monomers and dimers that harmonic B3LYP-D3(BJ) can yield quite accurate predictions due to fortuitous error cancellation [41, 89, 126].

Beyond the harmonic approximation

Moving beyond the harmonic approximation, anharmonic DVPT2 corrections are added to the dimer vibrations and VPT2+F is used for the monomer vibrations. Since the energetic order of the monomeric OH bend and torsion overtone is very sensitive to the underlying electronic structure method, see for example Ref. [24], the higher-wavenumber band is used throughout. Higher-level harmonic force constants at the CCSD(T)-F12a/VDZ-F12 level are used to enhance the *ab initio* force fields. For the cyclic formic acid dimer, the double-zeta F12 basis set is a satisfying trade-off in accuracy and cost.[193] In order to simulate standard black-box calculation scenarios, the substituted hybrid force field method as employed by Gaussian 16 is used, which scales the cubic and quartic force constants (see Section 2.1.3).

In Fig. 8.7, the performance of VPT2 with pure and CCSD(T)-edited MP2 and B3LYP-D3(BJ) quartic force fields is compared to experiment with increasing basis set completeness. Focussing first on the pure force fields, we see that the trends from the harmonic benchmark continue. It is particularly insightful to take a closer look at the absolute anharmonic predictions for δ(OCO) and γ(OH). At the MP2 level, an improvement for δ(OCO) and simultaneous deterioration for γ(OH) is observed from aVDZ to aVTZ. The former systematically improves for the right reason while the latter initially profits from fortuitous success due to the systematic cancellation of higher-order electron correlation and basis set incompleteness errors (see Section 5.4). This systematic improvement – or the systematic cancellation – is not provided at the B3LYP-D3(BJ) level. In line with previous findings [41], B3LYP-D3(BJ) does not significantly improve upon inclusion of vibrational anharmonicity and the difficulties in describing the rather harmonic OCO bending modes are particularly striking. The differences between MP2 and B3LYP-D3(BJ) are even more pronounced for the Davydov splittings and dimerisation shifts. Already with an aVDZ basis, MP2 reproduces experiment for most modes and the theory-experiment agreement systematically improves with the larger aVTZ basis set in most cases. For these quantities, the B3LYP-D3(BJ) prediction even deteriorates upon inclusion of anharmonicity, for example for ν(C–O), and only the Davydov splitting of γ(OH) is in agreement with experiment.

The central question that remains is to what extent the observed deficiencies, particularly for B3LYP-D3(BJ), can be remedied by replacing the harmonic force constants with higher-level values. Indeed, the hybrid force field results in Fig. 8.7 show that most deficiencies of B3LYP-D3(BJ) and MP2 are remedied but still MP2 is found to outperform B3LYP-D3(BJ). Combined with CCSD(T)-F12a/VDZ-F12 harmonic wavenumbers, MP2/aVTZ yields predictions for all three target parameters that are either within or near the experimental error bars. The only notable deviation is found for $\tilde{\nu}$ and Δ_{as} of γ(CH). A closer inspection of $\tilde{\nu}$ locates the source of

[193] The maximum absolute deviation of fundamental wavenumbers is below 3.8 cm^{-1} relative to VTZ-F12 and for the fingerprint modes between 600 and 1500 cm^{-1} even below 2.3 cm^{-1}.

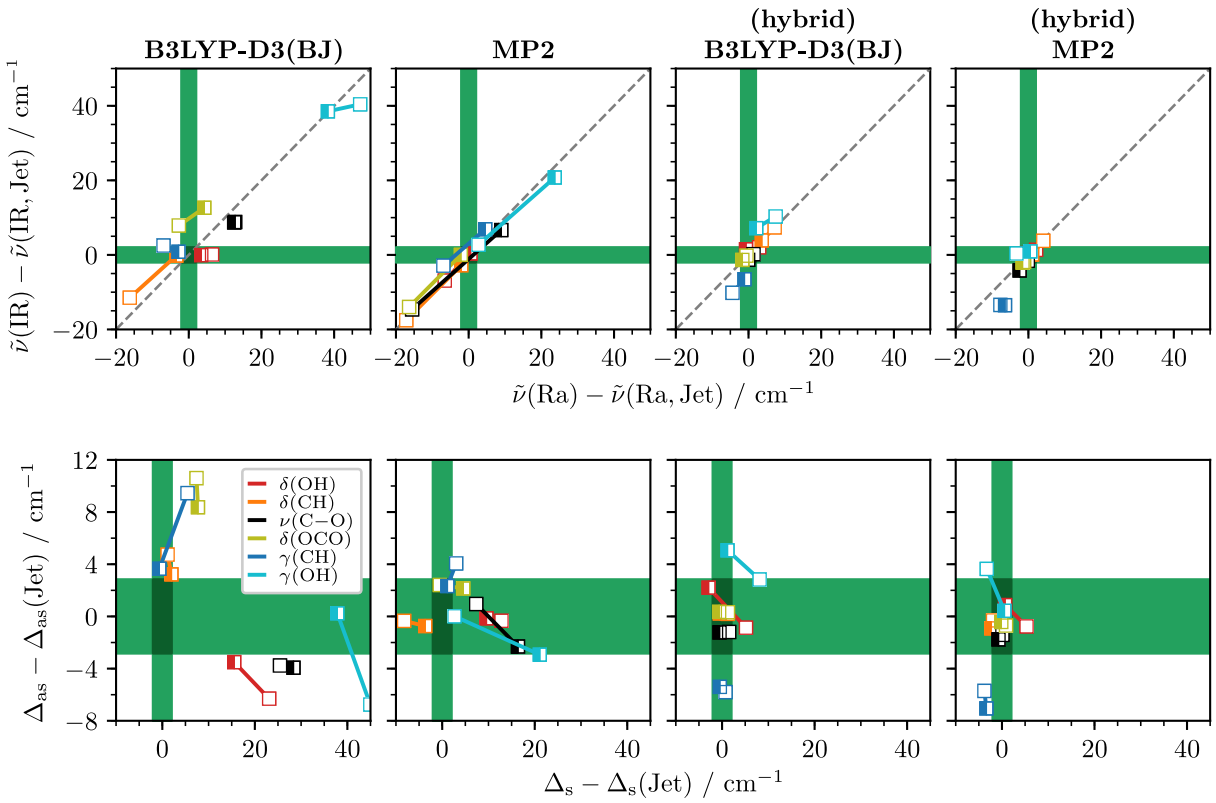

Figure 8.7 Davydov analysis of computed anharmonic (VPT2, squares) fundamentals of $(HCOOH)_2$ compared to jet-cooled values with increasing basis set completeness (aVDZ □; aVTZ ◧). Green areas represent the experimental error bars. In the hybrid force field calculations, the harmonic force field is replaced with corresponding values at the CCSD(T)-F12a/VDZ-F12 level.

this discrepancy in the IR-active component ν_{13} – the mode which exhibits significant γ(OH) character (see Fig. 8.5). For this particular mode, the pure MP2 or B3LYP-D3(BJ) predictions are better than the respective hybrid force field predictions and the larger error of ν_{13} can be ascribed to a failure of the substituted hybrid force field approach, necessitating the more expensive "transformed approach".[194] By inspecting the lower- and higher-level normal modes, one can readily identify possible pitfalls of a hybrid ansatz for particular modes. Otherwise, the hybrid force field approach significantly improves the predictive power of VPT2 with lower-level force fields and the gain in accuracy in Fig. 8.7 shows that an MP2/aVDZ quartic force field combined with high-level harmonic wavenumbers is a particularly attractive trade-off in accuracy and computational cost.

The Qu and Bowman formic acid dimer potential

Finally, let us compare variational and perturbative predictions on the QB-PES for the fingerprint modes of $(HCOOH)_2$. In contrast to the (comparably rather stiff but) more floppy pair modes (see Section 8.1), one might expect a better agreement between VCI and experiment for the intramolecular modes.

Predictions on the QB-PES with various nuclear vibrational models (harmonic, VSCF, VCI, VPT2) are compactly summarised in Table 8.3. Since resonance effects on $\tilde{\nu}_{14}$ and $\tilde{\nu}_{22}$ are not captured by the VSCF (by design) or VCI calculations (due to convergence errors), VPT2 and experiment are deperturbed. As previously seen for the pair modes, VCI improves upon the worst VSCF results but absolute errors remain very large. VPT2 on a quartic force field expansion of

[194] Similar problems of changing normal mode definitions were encountered by Franke *et al.* for the ethylperoxy radical [265] which they circumvented by applying the transformed hybrid force field (see Section 2.1.3).

Table 8.3 Differently computed fundamental excitations (in cm^{-1}) of $(HCOOH)_2$ fingerprint vibrations compared to deperturbed experiment (Table 7.5, p. 130). Experiment and VPT2 are deperturbed and VCI effectively as well, as ν_{14} and ν_{22} are essentially pure states. VSCF and VCI data are taken from Ref. [32].

			Hybrid force field			QB-PES				
	Descr.	Γ	Harm.[a]	PyVCI+VPT2[a,b]	VCI+F[c]	Harm.	DVPT2	VSCF	VCI	Exp. (dep.)
ν_7	δ(OCO)	A_g	684	682	687	693	680	688	700	681
ν_{11}	γ(OH)	B_g	953	930	914	956	909	981	945	911
ν_{10}	γ(CH)	B_g	1080	1058	1059	1084	1058	1095	1079	1058
ν_6	ν(C−O)	A_g	1248	1229	1228	1255	1228	1246	1252	1224
ν_5	δ(CH)	A_g	1410	1381	1379	1408	1374	1384	1391	1375
ν_4	δ(OH)	A_g	1478	1436	1426	1481	1430	1458	1457	1430
ν_{23}	δ(OCO)	B_u	711	709	707	716	705	713	726	707.6
ν_{14}	γ(OH)	A_u	977	959	934	970	937	1007	975	944
ν_{13}	γ(CH)	A_u	1099	1073	1068	1100	1065	1112	1091	1069.3
ν_{22}	ν(C−O)	B_u	1253	1233	1232	1258	1229	1248	1252	1230
ν_{21}	δ(CH)	B_u	1405	1378	1377	1406	1369	1381	1388	1371.78
ν_{20}	δ(OH)	B_u	1453	1415	1404	1448	1400	1421	1424	1407
MAD(Exp.)					4		3	27	23	
MAX(Exp.)					10		7	70	34	

[a] From an unpublished master thesis (see note 195). The hybrid force field is a rectilinear normal mode SFF at the MP2/aVDZ level (no frozen core), obtained as described in Ref. [189] from an 18D intra-monomer 3MR curvilinear normal mode QFF, where the harmonic wavenumbers are replaced *post hoc* by corresponding values at the LCCSD(T)-F12a/VDZ-F12 level. The six intermolecular degrees of freedom are frozen as described in Ref. [108].

[b] 18D PyVCI+VPT2 calculation as described in Ref. [189] with $n_{max} = 6$ and MR = 6.

[c] The 18D PyVCI+VPT2 eigenvalues are corrected by replacing the LCCSD(T)-F12a harmonic wavenumbers with corresponding values on the QB-PES (see note 196). Coupling to the missing six intermolecular vibrations is reintroduced using x constants on the QB-PES as outlined in Section 2.1.4. Note that ν_{14} and ν_{22} are deperturbed (see text).

the QB-PES, on the other hand, yet again provides very accurate fundamentals. The performance for the rather well-behaved OCO bend (ν_7, ν_{23}) is very telling. Already at the harmonic level, the absolute band positions are near experiment. The deviations correspond to a moderate anharmonicity of only 1-2 %, as one would expect of this heavy-atom motion. The fundamental wavenumbers systematically decrease in the order harmonic→VSCF→VPT2 towards experiment. The VPT2 errors are within $\pm 2\,cm^{-1}$. With VCI, however, the absolute wavenumbers increase relative to VSCF and absolute errors to experiment are $\sim 20\,cm^{-1}$.

In light of all presented analyses throughout this and Chapter 5, there is little doubt that the overall success of VPT2 in Table 8.3 is genuine, indicating that the VCI eigenvalues [32] are not converged. It would be desirable to interface the QB-PES with PyPES in the future, facilitating complementary force field VCI calculations with PyVCI, to bridge the gap between VPT2 and grid-based VCI. In the meantime, initial results with a hybrid force field from an unpublished master thesis[195] help to (partly) bridge this gap. In that work, a composite LCCSD(T)-F12a/MP2 hybrid sextic force field was employed. The *ab initio* sextic force field was obtained as described in Ref. [186] and the harmonic wavenumbers were replaced *post hoc*. The six intermolecular degrees of freedom were frozen following the method outlined in Ref. [108]. To reduce the size of the VCI matrix, VPT2 screening was employed as described in Ref. [189].

The resultant 24D harmonic and 18D PyVCI+VPT2 fundamentals are included in Table 8.3. A direct comparison to results on the QB-PES or experiment is not very meaningful. To 'level

[195] Nejad, A., "Anharmonic vibrational analysis of formic acid and its complexes", Göttingen, **2018**.

the playing-field', the LCCSD(T)-F12a harmonic wavenumbers are replaced with corresponding values on the QB-PES.[196] Second, most of the missing couplings to the six intermolecular modes are reintroduced following the method outlined in Section 2.1.4, using x constants on the QB-PES. Since ν_{14} and ν_{22} are perturbed by Fermi resonances that involve intermolecular vibrations, the resultant predictions are effectively deperturbed. The resultant 24D VCI+F fundamental wavenumbers not only compare very well with experiment but also 24D DVPT2 on the QB-PES, providing final confirmation that the success of VPT2 on the QB-PES is genuine and not largely affected by error compensation.

8.3 Dissociation energy of the cyclic dimer

The energy required to dissociate one cyclic formic acid dimer into two monomers was determined experimentally in 2012 by Kollipost *et al.* [148]. In the usual Born-Oppenheimer separation of electronic and vibrational degrees of freedom, the dissociation energy (defined here as a positive quantity) can formally be separated into the sum of a purely electronic

$$D_e = 2 \times E_{\text{Mon}} - E_{\text{Dim}} \tag{8.4}$$

and a zero-point vibrational energy contribution

$$\Delta\text{ZPVE} = 2 \times \text{ZPVE}_{\text{Mon}} - \text{ZPVE}_{\text{Dim}}. \tag{8.5}$$

In 2015, Miliordos and Xantheas discussed errors in the approach of Kalescky *et al.* [266] and were able to compute the dissociation energy to within the experimental uncertainty, using a composite approach. The electronic component was computed at the CCSD(T) level, extrapolated to the basis set limit and augmented by the zero-point correction at the MP2/aVDZ VPT2 level. In 2016, Qu and Bowman published the dimeric ZPVE on their analytical potential using DMC and very recently Käser and Meuwly reported VPT2 and DMC values for *trans*-HCOOH and its cyclic dimer on their transfer-learned potential [24]. There are several points worth pointing out.

Differently computed zero-point vibrational energies of *trans*-HCOOH and its cyclic dimer are compiled in Table 8.4. Reminding ourselves that the VPT2 ZPVE is resonance-free (pp. 16), the sole error source in VPT2 is the numerical sensitivity of the cubic and quartic force constants. First, the variational (ICPH-VCI, GENIUSH-Smolyak, MCTDH) values for the monomer attest VPT2 a remarkably high accuracy. The VPT2 prediction on the TM-PES even slightly outperforms ICPH-VCI and the deviation to GENIUSH-Smolyak and MCTDH is just $1\,\text{cm}^{-1}$.[197] As the ZPVE is an extensive property, the absolute VPT2 error will necessarily increase for larger systems. Still, the deviation to DMC on the QB-PES is just $6\,\text{cm}^{-1}$ outside the DMC simulation uncertainty – equivalently $0.07\,\text{kJ mol}^{-1}$ or $0.02\,\text{kcal mol}^{-1}$ –, which is quite remarkable. Second, the comparison of *ab initio* MP2 and CCSD(T)-F12-quality VPT2 predictions shows

[196] As with hybrid force field VPT2 (see Section 2.1.3), one could replace the harmonic wavenumbers before (substituted) or after (additive) the PyVCI+VPT2 calculation. Here, the inexpensive additive approach is employed by simply adding the difference of the two harmonic force fields to the PyVCI+VPT2 eigenvalues, shown in Table 8.3

[197] The VPT2 value on the TM-PES shown in Table 8.4 is actually $7351.5\,\text{cm}^{-1}$ and has been obtained on a quartic force field computed from single-point energies, as described in Appendix B.2. If instead analytic Hessians are used (see Appendix B.2), the VPT2 ZPVE changes only by $-0.2\,\text{cm}^{-1}$, indicating that numerical errors are negligible. The GENIUSH-Smolyak ZPVE, as reported in the supplementary material of Ref. [29], is $7350.8\,\text{cm}^{-1}$ (rounded to one digit) and is converged well within $0.1\,\text{cm}^{-1}$. For comparison, the ICPH-VCI value, as reported in the supplementary material of Ref. [21], is $7354.49...\,\text{cm}^{-1}$ and thus rounded off to 7354 in Table 8.4.

Table 8.4 Comparison of computed zero-point vibrational energies ($\tilde{\nu}$, in cm^{-1}) of *trans*-HCOOH and its cyclic dimer. Reported DMC simulation uncertainties are indicated in parentheses. The VPT2 values are further decomposed into harmonic (ω) and anharmonic (δ_{anh}) contributions. The harmonic zero-point vibrational energies on the transfer-learned potential are calculated from values reported in the supplementary material of Ref. [24].

			trans-HCOOH			$(HCOOH)_2$		
Electronic structure	Nuclear vib. structure	Ref.	ω	$\tilde{\nu}$	δ_{anh}	ω	$\tilde{\nu}$	δ_{anh}
MP2/aVDZ	VPT2	This work	7390	7286	−104	15490	15238	−252
MP2/aVTZ	VPT2	This work	7431	7331	−100	15556	15307	−249
QB-PES	VPT2	This work				15584	15324	−260
QB-PES	DMC	Ref. [23]					15337(7)	
TM-PES	VPT2	This work	7456	7352	−104			
TM-PES	GENIUSH-Smolyak	Ref. [29]		7351				
TM-PES	ICPH-VCI	Ref. [21]		7354				
RC-PES	VPT2	This work	7427	7326	−101			
RC-PES	MCTDH	Ref. [22]		7327				
Transfer-learned	VPT2	Ref. [24]	7411	7311	−100	15545	15349	−196
Transfer-learned	DMC	Ref. [24]		7321(12)			15299(5)	

that the main errors stem from the harmonic MP2 force field. Hybrid CCSD(T)-F12/MP2 VPT2 is thus optimally equipped to provide highly accurate zero-point energies with comparably little computational cost. Third, a comparison to the transfer-learned VPT2 and DMC values clearly indicates 'problems' with the VPT2 values as published in Ref. [24]. For the monomer, VPT2 and DMC on the transfer-learned potential agree within the comparably large DMC simulation error. Moreover, the VPT2 anharmonicity δ_{anh} compares very well with values on the TM-PES, RC-PES, and MP2. For the dimer, however, VPT2 deviates much more from DMC than anticipated based on corresponding values on the QB-PES. Dissecting the transfer-learned VPT2 value into harmonic and anharmonic contributions clearly shows that the anharmonic correction is erroneous. By comparison to VPT2 on the QB-PES or at the MP2 level, the absolute anharmonic VPT2 component is estimated to be 50-60 cm^{-1} too small which perfectly matches in size and direction the VPT2-DMC deviation on the transfer-learned dimer potential.[198]

Turning to the zero-point-corrected dissociation energy, we can take the experimental value of $D_0 = 59.5(5)\,kJ\,mol^{-1}$ [148] and add the 'best' available – hybrid CCSD(T)-F12a/VDZ-F12//MP2/aVTZ – *ab initio* VPT2 zero-point energy difference to derive $D_e = 67.4(5)\,kJ\,mol^{-1}$. Miliordos and Xantheas showed that such an experimentally-derived well depth is matched by CCSD(T) at the complete basis set limit with $67.4(5)\,kJ\,mol^{-1}$ [102]. Explicitly correlated methods provide an alternative route to such extrapolation techniques. Rewardingly, CCSD(T)-F12a yields 67.8 with a VDZ-F12 basis set, reproducing the basis set limit CCSD(T) value within the extrapolation uncertainty.

[198] It is unclear why the size of the anharmonic contribution to the transfer-learned VPT2 ZPVE is roughly 20% too small. For comparison, the contributions to the VPT2 ZPVE that arise from anharmonic components of the kinetic energy operator (Coriolis and Watson U) are both well below $5\,cm^{-1}$.

Chapter 9

Summary and outlook

Taking a multi-spectroscopic approach of a different kind – experimental[199] (IR and Raman) and computational (perturbative and variational) vibrational spectroscopy –, the spectroscopic record of formic acid and its cyclic dimer was reviewed, corrected, and extended. As a side product of the dimer-focussed analysis, the number of assigned formic acid trimer fundamentals could be drastically increased. The vibrational database of the monomer (Table 4.8, pp. 91) has been digitised (https://qmbench.net) with the dimer and trimer databases to follow soon (Tables 7.2-7.3, pp. 124). In contrast to the formic acid trimer, the higher-energy polar dimer still eludes detection in jet expansions. Since it is a fragment of the trimer (Fig. 1.4, p. 11), the validated theoretical description of the trimer promises to provide reliable spectral predictions for future searches of the metastable pairing of two formic acid molecules.

The result of the analysis of the formic acid spectra in Chapter 4 is a revised, significantly extended, and thoroughly validated vibrational database of the monomer below 4000 cm^{-1} with overall 186 environment-free band centres, including both rotational conformers, several hydrogen and carbon isotopologues, and a plethora of highly-excited vibrational states up to five-quantum vibrational levels. Essentially, the experimental and computational vibrational spectroscopic characterisation of *trans*-formic acid up to 3500 cm^{-1} can now be regarded completed with a few minor exceptions.[200] It was found that the impact of the OH bend-torsion resonance polyad ($N_5 = n_5+n_9/2$) on the entire vibrational dynamics of *trans*-HCOOH is more far-reaching than previously believed. A new key insight is that starting with $N_5 = 2$, the C–O stretch (ν_6) becomes heavily involved in this polyad ($N_{56} = n_5+n_6+n_9/2$), which is strongly suspected to perturb the OH stretching fundamental ($N_{56} = 3$). Starting with $N_{56} = 3.5$, *trans-cis* delocalisation effects are expected to manifest [29]. Considering that high-level computational studies unanimously predict ν_5 and ν_6 to be strongly coupled in the *cis* conformer [22, 29], particularly fruitful future research directions include revisiting the postponed analysis of the rotationally-resolved, environment-free OH stretch [114] and spectroscopically characterising states in the $N_{56} \geq 3$ polyad towards increasing *trans-cis* delocalisation.

Building on pioneering jet-cooled studies [119, 149], the reanalysis of the formic acid dimer fingerprint region 600-1500 cm^{-1} closes previous gaps between the intermolecular manifold [129, 130, 141, 148] and the intramolecular carbonyl stretching region [89], producing a large number of benchmark-quality combination and overtone bands. O–H deuteration was found to have a profound impact on the vibrational spectrum of the cyclic dimer with an increased number of Raman-active dimer combination and overtone bands beyond 1200 cm^{-1}. Other than the rather isolated resonances of IR-active fingerprint modes in $(HCOOH)_2$, e.g. ν_{14} and ν_{22}, the

[199] The experimental IR and Raman spectra have been made publicly available [222, 261, 262].

[200] A few *trans*- (Table 4.3, p. 71; Table 4.4, pp. 80; Table 4.7, p. 87) and *cis*-formic acid bands (see supplementary material of Ref. [90]) remain unassigned.

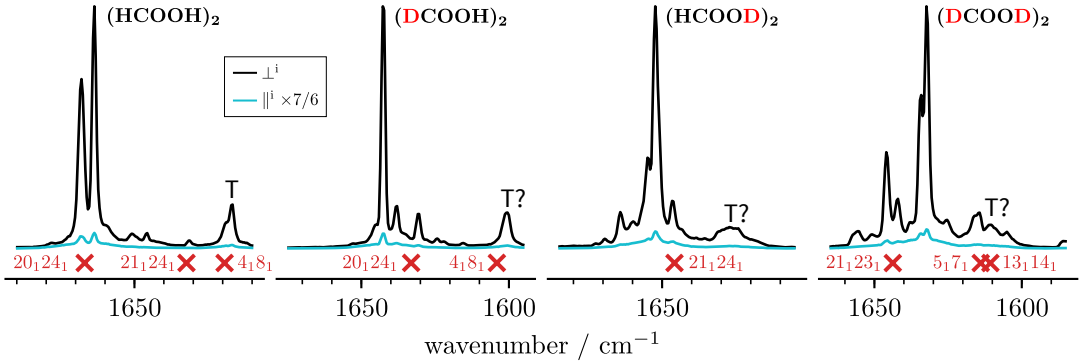

Figure 9.1 Raman jet spectra of formic acid in the C=O stretching region at high acid concentration. The formic acid trimer (T) has been assigned by Meyer and Suhm for the main isotopologue [125].

assignment of the Raman-active perturbers in $(HCOOD)_2$ and $(DCOOD)_2$ demonstrates a systematic and strong hydrogen bond-mediated vibrational coupling between the C–O stretching fundamental and other carboxylic acid group vibrations. This includes the OCO bending ($2\nu_{23}$) and OD torsion overtones ($2\nu_{11}$, $2\nu_{14}$) and several weaker binary and ternary bands that involve excitations of the intermolecular in- (ν_9, ν_{24}) or out-of-plane (ν_{12}, ν_{15}) bending/libration modes. Despite the measured jet spectra extending up to 1950 cm^{-1}, an analysis beyond 1500 cm^{-1} was not attempted as the increasing complexity of the spectra makes high-level computational guidance indispensable. This is illustrated in Fig. 9.1 using the example of the Raman-active C=O stretch for which resonance perturbations consistently increase from left to right. The following should be considered: There are no monomer bands and, based on the analysis of the fingerprint region, overall negligible $n \geq 4$ cluster contributions, leaving the cyclic dimer and trimer as main contributors with an estimated [109] concentration ratio of 10:1. Both have only one Raman-active fundamental in this spectral region. These two are predicted to have similar intensities. The expected binary A_g band positions are shown in red, indicating that the main perturbers correspond to $n \geq 3$ multi-quantum vibrational states. Moreover, Fig. 9.1 indicates that the resonance perturbations in the dimer may survive in the trimer. In all these contexts, the complexity of the dimeric OH/D stretching spectra appears to be the logical consequence of a built-in mechanical coupling of the carboxylic group vibrations [132, 267, 268].

Lastly, the rigorous nuclear structure benchmarks revealed two important insights. In the formic acid monomer,[201] the OH torsion is well-known to be the Achilles' heel of rectilinear normal coordinate VPT2. Its further involvement in the OH bend-torsion polyad makes vibrational benchmarks of the torsion the ideal litmus test. In Section 5.4, torsional term values up to $n_9 = 4$ computed with VPT2 on the TM-PES [21] and a high-level hybrid CCSD(T)-F12a/VDZ-F12//MP2/aVTZ force field were compared against fully converged variational reference values [29] on the TM-PES. The benchmark clearly showed that the inherent VPT2 error is outweighed by the underlying electronic structure errors, conclusively demonstrating that in order to assess the quality and performance of VPT2, large basis set coupled-cluster potentials of high quality are necessary. Second, hybrid CCSD(T)-F12-edited MP2/aVDZ hybrid force field VPT2 was found to be a compelling trade-off between accuracy and cost[202] that provides reliable and surprisingly accurate predictions for fundamentals and medium vibrational excitations of the formic acid dimer and trimer in the examined energy regions up to 1500 cm^{-1}.

[201] The performance of several nuclear vibrational models is summarised in Table 5.5 (p. 110) for the monomer.

[202] As an example, with an Intel Xeon Gold 6240 CPU, the total CPU time necessary to compute a quartic force field of the formic acid dimer with Gaussian 16 increases from 26 h (B3LYP-D3/aVDZ), 29 h (MP2/aVDZ), 155 h (B3LYP-D3/aVTZ), up to 1034 h (for MP2/aVTZ). The total CPU time on the same machine required to compute the Hessian at the CCSD(T)-F12a/VDZ-F12 level with Molpro 2018.1 amounts to only 26 h.

Appendices and references

Appendix A

Details on measured spectra

This appendix contains details on all measured formic acid spectra that are shown throughout this work. The spectra have been published in an online repository and made publicly available [222, 261, 262].

Formic acid monomer-optimised spectra:

Table A.1 Details on Raman spectra (temperature series) shown in Figs. 3.1-3.7. The data can be downloaded from Ref. [222] (mind "_des_avg_cal.dat" filename extension).

Table A.2 Details on depolarised Raman spectra shown in Figs. 3.1-3.7.

Formic acid dimer-optimised spectra:

Table A.3 Details on Raman spectra (temperature series, top) shown in Figs. 6.3-6.5. The data can be downloaded from Ref. [261] (mind "_des_avg_cal.dat" filename extension).

Table A.4 Details on depolarised Raman spectra (middle) shown in Figs. 6.3-6.5. The data can be downloaded from Ref. [261] (mind "_des_avg_cal.dat" filename extension).

Table A.5 Details on FTIR spectra (pressure series, top) shown in Figs. 6.1-6.2. The data can be downloaded from Ref. [262].

Table A.6 Details on FTIR spectra (higher resolution, middle) shown in Figs. 6.1-6.2. These spectra have been published in Ref. [149].

A.1 Legend

FTIR spectra

Spectra that are listed under the same colour have been averaged, each weighted by the number of scans (N_{Scan}). The deviations in the experimental conditions (cf. p_{Res}) illustrate the experimental uncertainty of the employed formic acid concentration.

Trace	Colour of the spectrum, as shown in the figures.
T_{s}	Saturator temperature.
p_{Res}	Reservoir pressure.
$\Delta\tilde{\nu}$	Spectral resolution.
Apt	Aperture.
MCT detector	Name of the detector (internal reference).
Filter	Spectral bandpass filter. The "F15" filter (internal reference) is transparent between 600 and 2000 cm^{-1}.
N_{Scan}	Number of averaged sampled scans (gas pulses).
Scal	Intensity scaling factor.

Raman spectra

The measured Raman intensity (counts) is converted into a count rate (s^{-1}) via

$$\frac{\text{count rate}}{\mathrm{s}^{-1}} = \mathrm{Scal} \cdot \frac{\mathrm{s}}{t_{\mathrm{e}}} \cdot (\text{counts} - \mathrm{BL}) \,. \tag{A.1}$$

Trace	Colour of the spectrum, as shown in the figures.
λ_{Mon}	Central wavelength setting of the monochromator, roughly covering a spectral range from $\lambda_{\mathrm{Mon}}-10\,\mathrm{nm}$ to $\lambda_{\mathrm{Mon}}+10\,\mathrm{nm}$.
T_{s}	Saturator temperature.
T_{n}	Temperature of the helium feed-line and nozzle.
F in He:He	Ratio of additional helium dilution to the formic acid-in-helium mixture (F in He). This number is an internal reference for the flow meters and does not apply to spectra measured with a previous version of the setup.
p_{Res}	Reservoir pressure.
$\mathcal{P}^{\mathrm{i}}$	Incident laser polarisation with respect to the scattering plane.
P	Incident laser power.
t_{e}	Exposure time for a single scan.
N_{Scan}	Number of averaged scans.
BL	Intensity baseline correction.
Scal	Intensity scaling factor.

A.2 Formic acid monomer-optimised jet spectra

Table A.1 Measurement details on formic acid monomer-optimised Raman spectra (temperature series) shown in Figs. 3.1-3.7. See legend in Appendix A.1 for further explanations. The data can be downloaded from Ref. [222] (mind "_des_avg_cal.dat" filename extension).

Iso	Trace	Range / cm^{-1}		λ_{Mon}	T_s		T_n		F in He:He	p_{Res}	$\mathcal{P}^i$	P	t_e	N_{Scan}	BL	Scal	Date	Filename
		min	max	nm	°C	K	°C	K		mbar		W	s				DD.MM	
HCOOH	black	910	1460	569.0	10	283	100	373	15:100	500	$\perp^i$	25	300	7	662	0.3859	08.01.2020	200108_f_F_[...]_7x300s
HCOOH	black	1460	1935	584.5	10	283	100	373	15:100	500	$\perp^i$	25	300	6	650	0.5198	08.01.2020	200108_e_F_[...]_6x300s
HCOOH	black	2670	3085	629.0	10	283	100	373	15:100	500	$\perp^i$	25	300	6	654	0.6175	09.01.2020	200109_a_F_[...]_6x300s
HCOOH	black	3350	3750	657.0	10	283	100	373	15:100	500	$\perp^i$	25	300	6	638	0.5349	09.01.2020	200109_b_F_[...]_6x300s
HCOOH	blue	390	910	550.0	−10	263	130	403	–	1000	$\perp^i$	25	300	6	691	0.1752	15.11.2018	181115_e_F_[...]_6x300s
HCOOH	blue	910	1460	569.0	10	283	130	403	15:100	500	$\perp^i$	25	300	6	662	0.4367	08.01.2020	200108_i_F_[...]_6x300s
HCOOH	blue	1460	1935	584.6	10	283	130	403	15:100	500	$\perp^i$	25	300	6	650	0.5951	08.01.2020	200108_h_F_[...]_6x300s
HCOOH	blue	2670	3085	629.0	10	283	130	403	15:100	500	$\perp^i$	25	300	6	654	0.7254	09.01.2020	200109_c_F_[...]_6x300s
HCOOH	blue	3350	3750	657.0	10	283	130	403	15:100	500	$\perp^i$	25	300	6	638	0.6416	09.01.2020	200109_d_F_[...]_6x300s
HCOOH	orange	910	1460	569.0	10	283	160	433	15:100	500	$\perp^i$	25	300	7	662	0.6167	08.01.2020	200108_k_F_[...]_7x300s
HCOOH	orange	1460	1935	584.5	10	283	160	433	15:100	500	$\perp^i$	25	300	6	650	0.8995	08.01.2020	200108_j_F_[...]_6x300s
HCOOH	orange	1925	2190	593.0	10	283	160	433	30:100	500	$\perp^i$	20	240	5	649	1.0000	28.09.2020	200928_c_F_[...]_5x240
HCOOH	orange	2190	2450	606.0	10	283	160	433	30:100	500	$\perp^i$	20	240	5	649	1.0000	28.09.2020	200928_d_F_[...]_5x240
HCOOH	orange	2450	2680	616.0	10	283	160	433	30:100	500	$\perp^i$	20	240	5	649	1.0000	28.09.2020	200928_e_F_[...]_5x240
HCOOH	orange	2670	3085	629.0	10	283	160	433	15:100	500	$\perp^i$	25	300	6	654	0.7255	09.01.2020	200109_e_F_[...]_6x300s
HCOOH	orange	3075	3200	632.0	10	283	160	433	30:100	500	$\perp^i$	20	240	5	649	1.0000	28.09.2020	200928_f_F_[...]_5x240
HCOOH	orange	3200	3350	648.0	10	283	160	433	30:100	500	$\perp^i$	20	240	5	649	1.0000	28.09.2020	200928_g_F_[...]_5x240
HCOOH	orange	3350	3750	657.0	10	283	160	433	15:100	500	$\perp^i$	25	300	6	638	0.7176	09.01.2020	200109_f_F_[...]_6x300s
HCOOH	red	910	1460	569.0	10	283	190	463	15:100	500	$\perp^i$	25	300	12	662	1.0000	08.01.2020	200108_m_F_[...]_12x300s
HCOOH	red	1460	1935	584.5	10	283	190	463	15:100	500	$\perp^i$	25	300	6	650	1.0000	08.01.2020	200108_l_F_[...]_6x300s
HCOOH	red	1925	2190	593.0	10	283	190	463	30:100	500	$\perp^i$	20	240	5	649	0.8459	28.09.2020	200928_i_F_[...]_5x240
HCOOH	red	2190	2450	606.0	10	283	190	463	30:100	500	$\perp^i$	20	240	5	649	0.8459	28.09.2020	200928_j_F_[...]_5x240
HCOOH	red	2450	2680	616.0	10	283	190	463	30:100	500	$\perp^i$	20	240	5	649	0.8459	28.09.2020	200928_k_F_[...]_5x240
HCOOH	red	2670	3085	629.0	10	283	190	463	15:100	500	$\perp^i$	25	300	6	654	1.0000	09.01.2020	200109_g_F_[...]_6x300s
HCOOH	red	3075	3200	632.0	10	283	190	463	30:100	500	$\perp^i$	20	240	5	649	0.6129	28.09.2020	200928_l_F_[...]_5x240

continued

Table A.1 (continued)

Iso	Trace	Range / cm^{-1}		λ_{Mon}	T_s		T_n		F in He:He	p_{Res}	$\mathcal{P}^i$	P	t_e	N_{Scan}	BL	Scal	Date	Filename
		min	max	nm	°C	K	°C	K		mbar		W	s				DD.MM	
HCOOH	red	3350	3750	657.0	10	283	190	463	15:100	500	$\perp^i$	25	300	6	638	1.0000	09.01.2020	200109_h_F_[...]_6x300s
DCOOH	black	590	820	559.0	10	283	100	373	20:100	500	$\perp^i$	25	300	12	680	1.9193	22.01.2020	200122_d_FCD_[...]_12x300s
DCOOH	black	820	1410	565.0	10	283	100	373	40:100	500	$\perp^i$	25	300	6	660	0.5171	17.01.2020	200117_i_FCD_[...]_6x300s
DCOOH	black	1410	1970	584.5	10	283	100	373	40:100	500	$\perp^i$	25	300	6	654	0.4271	17.01.2020	200117_j_FCD_[...]_6x300s
DCOOH	black	1970	2435	602.5	10	283	100	373	40:100	500	$\perp^i$	25	300	6	649	0.4677	18.01.2020	200118_h_FCD_[...]_6x300s
DCOOH	black	3349	3750	657.0	10	283	100	373	40:100	500	$\perp^i$	25	300	6	645	0.7036	18.01.2020	200118_g_FCD_[...]_6x300s
DCOOH	blue	820	1410	565.0	10	283	130	403	40:100	500	$\perp^i$	25	300	6	660	0.6118	17.01.2020	200117_g_FCD_[...]_6x300s
DCOOH	blue	1410	1970	584.5	10	283	130	403	40:100	500	$\perp^i$	25	300	6	654	0.5268	17.01.2020	200117_h_FCD_[...]_6x300s
DCOOH	blue	1970	2435	602.5	10	283	130	403	40:100	500	$\perp^i$	25	300	6	649	0.3622	18.01.2020	200118_f_FCD_[...]_6x300s
DCOOH	blue	3349	3750	657.0	10	283	130	403	40:100	500	$\perp^i$	25	300	6	645	0.7470	18.01.2020	200118_e_FCD_[...]_6x300s
DCOOH	orange	820	1410	565.0	10	283	160	433	40:100	500	$\perp^i$	25	300	6	660	0.8179	17.01.2020	200117_e_FCD_[...]_6x300s
DCOOH	orange	1410	1970	584.5	10	283	160	433	40:100	500	$\perp^i$	25	300	6	654	0.7267	17.01.2020	200117_f_FCD_[...]_6x300s
DCOOH	orange	1970	2435	602.5	10	283	160	433	40:100	500	$\perp^i$	25	300	6	649	0.4750	18.01.2020	200118_d_FCD_[...]_6x300s
DCOOH	orange	2425	2905	620.5	10	283	160	433	30:100	500	$\perp^i$	20	240	4	640	1.0000	27.10.2020	201027_g_FCD_[...]_4x240s
DCOOH	orange	2905	3355	639.0	10	283	160	433	30:100	500	$\perp^i$	20	240	4	640	1.0000	27.10.2020	201027_f_FCD_[...]_4x240s
DCOOH	orange	3349	3750	657.0	10	283	160	433	40:100	500	$\perp^i$	25	300	6	645	0.9243	18.01.2020	200118_c_FCD_[...]_6x300s
DCOOH	red	820	1410	565.0	10	283	190	463	40:100	500	$\perp^i$	25	300	6	660	1.0000	17.01.2020	200117_c_FCD_[...]_6x300s
DCOOH	red	1410	1970	584.5	10	283	190	463	40:100	500	$\perp^i$	25	300	6	654	1.0000	17.01.2020	200117_d_FCD_[...]_6x300s
DCOOH	red	1970	2435	602.5	10	283	190	463	40:100	500	$\perp^i$	25	300	6	649	1.0000	18.01.2020	200118_b_FCD_[...]_6x300s
DCOOH	red	2425	2905	620.5	10	283	190	463	30:100	500	$\perp^i$	20	240	4	650	0.7137	27.10.2020	201027_i_FCD_[...]_4x240s
DCOOH	red	3349	3750	657.0	10	283	190	463	40:100	500	$\perp^i$	25	300	6	645	1.0000	18.01.2020	200118_a_FCD_[...]_6x300s
HCOOD	black	400	810	554.0	15	288	100	373	50:100	500	$\perp^i$	25	300	6	665	0.3523	17.06.2020	200617_d_FOD_[...]_6x300s
HCOOD	black	810	1420	566.0	10	283	100	373	40:100	500	$\perp^i$	24	300	6	645	0.3009	20.06.2020	200620_i_FOD_[...]_6x300s
HCOOD	black	1420	1960	584.6	10	283	100	373	40:100	500	$\perp^i$	25	200	9	652	0.3797	18.06.2020	200618_h_FOD_[...]_9x200s
HCOOD	black	2325	2745	617.4	10	283	100	373	40:100	500	$\perp^i$	25	200	9	645	0.2622	18.06.2020	200618_i_FOD_[...]_9x200s
HCOOD	black	2735	3115	629.1	10	283	100	373	40:100	500	$\perp^i$	24	200	8	646	0.3839	20.06.2020	200620_j_FOD_[...]_8x200s
HCOOD	blue	810	1420	566.0	10	283	130	403	40:100	500	$\perp^i$	25	300	6	659	0.3289	20.06.2020	200620_h_FOD_[...]_6x300s
HCOOD	blue	1420	1960	584.6	10	283	130	403	40:100	500	$\perp^i$	25	300	6	652	0.4273	18.06.2020	200618_f_FOD_[...]_6x300s
HCOOD	blue	2325	2745	617.4	10	283	130	403	40:100	500	$\perp^i$	25	200	9	645	0.2768	18.06.2020	200618_g_FOD_[...]_9x200s

continued

Table A.1 (continued)

Iso	Trace	Range / cm^{-1}		λ_{Mon}	T_s		T_n		F in He:He	p_{Res}	$\mathcal{P}^i$	P	t_e	N_{Scan}	BL	Scal	Date	Filename
		min	max	nm	°C	K	°C	K		mbar		W	s				DD.MM	
HCOOD	blue	2735	3115	629.0	10	283	130	403	40:100	500	$\perp^i$	25	200	7	646	0.3250	20.06.2020	200620_g_FOD_[...]_7x200s
HCOOD	orange	810	1420	566.1	10	283	160	433	40:100	500	$\perp^i$	25	300	6	659	0.3377	20.06.2020	200620_f_FOD_[...]_6x300s
HCOOD	orange	1420	1960	584.6	10	283	160	433	40:100	500	$\perp^i$	25	300	6	665	0.4539	18.06.2020	200618_d_FOD_[...]_6x300s
HCOOD	orange	1950	2150	593.0	10	283	160	433	30:100	500	$\perp^i$	20	240	4	649	0.8068	29.09.2020	200929_a_FOD_[...]_4x240
HCOOD	orange	2150	2325	611.0	10	283	160	433	30:100	500	$\perp^i$	20	240	4	649	0.5945	29.09.2020	200929_b_FOD_[...]_4x240
HCOOD	orange	2325	2745	617.4	10	283	160	433	40:100	500	$\perp^i$	25	300	6	653	0.2492	18.06.2020	200618_e_FOD_[...]_6x300s
HCOOD	orange	2735	3115	629.0	10	283	160	433	40:100	500	$\perp^i$	25	300	5	662	0.3710	20.06.2020	200620_e_FOD_[...]_5x300s
HCOOD	orange	3115	3580	648.0	10	283	160	433	30:100	500	$\perp^i$	20	240	4	640	0.8849	27.10.2020	201027_c_FOD_[...]_4x240s
HCOOD	orange	3580	3750	663.0	10	283	160	433	30:100	500	$\perp^i$	20	240	4	640	1.0000	27.10.2020	201027_d_FOD_[...]_4x240s
HCOOD	red	810	1420	566.0	10	283	190	463	40:100	500	$\perp^i$	24	300	6	689	1.0000	22.06.2020	200622_b_FOD_[...]_20x300
HCOOD	red	1420	1960	584.6	10	283	190	463	40:100	500	$\perp^i$	25	300	7	745	1.0000	20.06.2020	200620_b_FOD_[...]_7x300s
HCOOD	red	1950	2058	588.0	10	283	190	463	30:100	500	$\perp^i$	20	240	4	649	1.0000	29.09.2020	200929_g_FOD_[...]_4x240
HCOOD	red	2325	2745	617.4	10	283	190	463	40:100	500	$\perp^i$	25	300	6	701	1.0000	18.06.2020	200618_c_FOD_[...]_6x300s
HCOOD	red	2735	3115	629.0	10	283	190	463	40:100	500	$\perp^i$	25	300	6	685	1.0000	20.06.2020	200620_c2_FOD_[...]_6x300s
HCOOD	red	3115	3580	648.0	10	283	190	463	30:100	500	$\perp^i$	20	240	4	652	1.0000	27.10.2020	201027_h_FOD_[...]_4x240s
DCOOD	black	830	1420	566.0	10	283	100	373	25:100	500	$\perp^i$	25	300	6	673	0.4216	16.01.2020	200116_a_Fd2_[...]_6x300s
DCOOD	black	1420	1950	584.5	10	283	100	373	15:100	500	$\perp^i$	25	300	6	655	0.3038	14.01.2020	200114_j_Fd2_[...]_6x300s
DCOOD	black	1950	2450	602.5	10	283	100	373	15:100	500	$\perp^i$	25	300	6	652	0.4810	15.01.2020	200115_l_Fd2_[...]_6x300s
DCOOD	black	2450	2800	617.4	10	283	100	373	15:100	500	$\perp^i$	25	300	6	651	0.6234	15.01.2020	200115_k_Fd2_[...]_6x300s
DCOOD	blue	830	1420	566.0	10	283	130	403	25:100	500	$\perp^i$	25	300	5	673	0.5030	16.01.2020	200116_c_Fd2_[...]_5x300s
DCOOD	blue	1420	1950	584.5	10	283	130	403	15:100	500	$\perp^i$	25	300	6	655	0.3545	14.01.2020	200114_g_Fd2_[...]_6x300s
DCOOD	blue	1950	2450	602.5	10	283	130	403	15:100	500	$\perp^i$	25	300	6	652	0.5205	15.01.2020	200115_i_Fd2_[...]_6x300s
DCOOD	blue	2450	2800	617.4	10	283	130	403	15:100	500	$\perp^i$	25	300	6	651	0.6824	15.01.2020	200115_h_Fd2_[...]_6x300s
DCOOD	orange	830	1420	566.0	10	283	160	433	25:100	500	$\perp^i$	25	300	6	673	0.4955	16.01.2020	200116_e_Fd2_[...]_6x300s
DCOOD	orange	1420	1950	584.5	10	283	160	433	15:100	500	$\perp^i$	25	300	6	655	0.3932	14.01.2020	200114_d_Fd2_[...]_6x300s
DCOOD	orange	1950	2450	602.5	10	283	160	433	15:100	500	$\perp^i$	25	300	6	652	0.5392	15.01.2020	200115_f_Fd2_[...]_6x300s
DCOOD	orange	2450	2800	617.4	10	283	160	433	15:100	500	$\perp^i$	25	300	6	651	0.7766	15.01.2020	200115_e_Fd2_[...]_6x300s
DCOOD	orange	2790	3050	627.0	10	283	160	433	30:100	500	$\perp^i$	20	240	5	639	0.7003	28.10.2020	201028_a_Fd2_[...]_5x240s
DCOOD	orange	3050	3350	639.0	10	283	160	433	30:100	500	$\perp^i$	20	240	4	639	0.7003	28.10.2020	201028_b_Fd2_[...]_4x240s

continued

Table A.1 (continued)

Iso	Trace	Range / cm^{-1}		λ_{Mon}	T_s		T_n		F in He:He	p_{Res}	$\mathcal{P}^i$	P	t_e	N_{Scan}	BL	Scal	Date	Filename
		min	max	nm	°C	K	°C	K		mbar		W	s				DD.MM	
DCOOD	orange	3350	3750	657.0	10	283	160	433	30:100	500	$\perp^i$	20	240	5	639	0.7003	28.10.2020	201028_c_Fd2_[...]_5x240s
DCOOD	red	490	830	556.0	10	283	190	463	25:100	500	$\perp^i$	25	300	10	675	2.2746	16.01.2020	200116_i_Fd2_[...]_10x300s
DCOOD	red	830	1420	566.0	10	283	190	463	25:100	500	$\perp^i$	25	300	6	673	1.0000	16.01.2020	200116_g_Fd2_[...]_6x300s
DCOOD	red	1420	1950	584.5	10	283	190	463	15:100	500	$\perp^i$	25	300	7	655	1.0000	14.01.2020	200114_a_Fd2_[...]_7x300s
DCOOD	red	1950	2450	602.5	10	283	190	463	15:100	500	$\perp^i$	25	300	6	652	1.0000	15.01.2020	200115_c_Fd2_[...]_6x300s
DCOOD	red	2450	2800	617.4	10	283	190	463	15:100	500	$\perp^i$	25	300	6	651	1.0000	15.01.2020	200115_a_Fd2_[...]_6x300s
DCOOD	red	2790	3050	627.0	10	283	190	463	30:100	500	$\perp^i$	20	240	4	639	1.0000	28.10.2020	201028_f_Fd2_[...]_4x240s
DCOOD	red	3050	3350	645.0	10	283	190	463	30:100	500	$\perp^i$	20	240	4	639	1.0000	28.10.2020	201028_g_Fd2_[...]_5x240s

Table A.2 Measurement details on formic acid monomer-optimised Raman spectra (depolarised) that are partly shown in Figs. 3.1-3.7. See legend in Appendix A.1 for further explanations.

Iso	Trace	Range / cm^{-1}		λ_{Mon}	T_s		T_n		F in He:He	p_{Res}	$\mathcal{P}^i$	P	t_e	N_{Scan}	BL	Scal	Date	Filename
		min	max	nm	°C	K	°C	K		mbar		W	s				DD.MM	
HCOOH	black	390	900	550.0	−10	263	130	403	–	1000	$\perp^i$	25	300	6	685	1.0000	15.11.2018	181115_e_F_[...]_6x300s
HCOOH	cyan	390	900	550.0	−10	263	130	403	–	1000	$\parallel^i$	25	300	6	671	1.0000	15.11.2018	181115_d_F_[...]_6x300s
HCOOH	black	900	1480	567.0	−10	263	130	403	–	1000	$\perp^i$	25	300	7	685	1.0000	12.11.2018	181112_a_F_[...]_7x300s
HCOOH	cyan	900	1480	567.0	−10	263	130	403	–	1000	$\parallel^i$	25	300	7	671	1.0000	12.11.2018	181112_b_F_[...]_7x300s
HCOOH	black	1480	1980	584.6	−10	263	130	403	–	1000	$\perp^i$	25	180	10	660	1.0000	15.11.2018	181115_b_F_[...]_10x180s
HCOOH	cyan	1480	1980	584.6	−10	263	130	403	–	1000	$\parallel^i$	25	180	10	651	1.0000	15.11.2018	181115_c_F_[...]_10x180s
HCOOH	black	1980	2507	604.5	10	283	190	463	30:100	500	$\perp^i$	20	240	4	649	1.0000	29.09.2020	200929_o_F_[...]_4x240
HCOOH	cyan	1980	2507	604.5	10	283	190	463	30:100	500	$\parallel^i$	20	240	4	649	1.0000	29.09.2020	200929_n_F_[...]_4x240
HCOOH	black	2665	3150	629.0	−20	253	190	463	–	500	$\perp^i$	25	300	7	666	1.0000	09.11.2018	181109_g_F_[...]_7x300
HCOOH	cyan	2665	3150	629.0	−20	253	190	463	–	500	$\parallel^i$	25	300	8	661	1.0000	09.11.2018	181109_h_F_[...]_8x300
HCOOH	black	3525	3750	665.0	10	283	190	463	30:100	500	$\perp^i$	20	240	4	649	1.0000	29.09.2020	200929_m_F_[...]_4x240
HCOOH	cyan	3525	3750	665.0	10	283	190	463	30:100	500	$\parallel^i$	20	240	4	649	1.0000	29.09.2020	200929_l_F_[...]_4x240
DCOOH	black	1910	2450	602.5	10	283	190	463	40:100	500	$\perp^i$	20	300	6	645	1.0000	03.09.2020	20200903_a_FCD_[...]_6x300s
DCOOH	cyan	1910	2450	602.5	10	283	190	463	40:100	500	$\parallel^i$	20	300	7	634	1.0000	03.09.2020	20200903_b_FCD_[...]_7x300s

continued

Table A.2 (continued)

Iso	Trace	Range / cm^{-1}		λ_{Mon}	T_s		T_n		F in He:He	p_{Res}	$\mathcal{P}^i$	P	t_e	N_{Scan}	BL	Scal	Date	Filename
		min	max	nm	°C	K	°C	K		mbar		W	s				DD.MM	
DCOOH	black	3220	3670	652.0	10	283	190	463	30:100	500	$\perp^i$	20	240	4	640	1.0000	27.10.2020	201027_k_FCD_[...]_4x240s
DCOOH	cyan	3220	3670	652.0	10	283	190	463	30:100	500	$\parallel^i$	20	240	4	640	1.0000	27.10.2020	201027_j_FCD_[...]_4x240s
HCOOD	black	2510	3005	624.0	10	283	160	433	30:100	500	$\perp^i$	25	240	6	641	1.0000	10.05.2021	20210510_f_FOD_[...]_6x240s
HCOOD	cyan	2510	3005	624.0	10	283	160	433	30:100	500	$\parallel^i$	25	240	6	641	1.0000	10.05.2021	20210510_g_FOD_[...]_6x240s
HCOOD	black	830	1450	567.0	10	283	190	463	30:100	500	$\perp^i$	20	240	5	651	1.0000	29.09.2020	200929_e_FOD_[...]_5x240
HCOOD	cyan	830	1450	567.0	10	283	190	463	30:100	500	$\parallel^i$	20	240	5	651	1.0000	29.09.2020	200929_d_FOD_[...]_5x240
HCOOD	black	1490	2058	588.0	10	283	190	463	30:100	500	$\perp^i$	20	240	4	642	1.0000	29.09.2020	200929_g_FOD_[...]_4x240
HCOOD	cyan	1490	2058	588.0	10	283	190	463	30:100	500	$\parallel^i$	20	240	4	642	1.0000	29.09.2020	200929_f_FOD_[...]_4x240
DCOOD	black	800	1400	566.0	10	283	160	433	40:100	500	$\perp^i$	20	300	5	636	1.0000	02.09.2020	20200902_f_FD2_[...]_5x300s
DCOOD	cyan	800	1400	566.0	10	283	160	433	40:100	500	$\parallel^i$	20	300	5	634	1.0000	02.09.2020	20200902_e_FD2_[...]_5x300s
DCOOD	black	1400	1950	584.5	10	283	160	433	40:100	500	$\perp^i$	20	120	3	632	1.0000	02.09.2020	20200902_j_FD2_[...]_6x120s
DCOOD	cyan	1400	1950	584.5	10	283	160	433	40:100	500	$\parallel^i$	20	120	3	632	1.0000	02.09.2020	20200902_i_FD2_[...]_3x120s
DCOOD	black	1950	2400	602.5	10	283	160	433	40:100	500	$\perp^i$	20	180	4	630	1.0000	02.09.2020	20200902_h_FD2_[...]_4x180s
DCOOD	cyan	1950	2400	602.5	10	283	160	433	40:100	500	$\parallel^i$	20	180	4	630	1.0000	02.09.2020	20200902_g_FD2_[...]_4x180s
DCOOD	black	2400	2677	611.0	10	283	160	433	30:100	500	$\perp^i$	25	240	6	644	1.0000	10.05.2021	20210510_d_Fd2_[...]_6x240s
DCOOD	cyan	2400	2677	611.0	10	283	160	433	30:100	500	$\parallel^i$	25	240	6	644	1.0000	10.05.2021	20210510_e_Fd2_[...]_6x240s

A.3 Formic acid dimer-optimised jet spectra

Table A.3 Measurement details on formic acid dimer-optimised Raman spectra (temperature series) shown in Figs. 6.3-6.5. See legend in Appendix A.1 for further explanations. The data can be downloaded from Ref. [261] (mind "_des_avg_cal.dat" filename extension).

Iso	Trace	Range / cm^{-1}		λ_{Mon}	T_s		T_n		F in He:He	p_{Res}	$\mathcal{P}^i$	P	t_e	N_{Scan}	BL	Scal	Date	Filename
		min	max	nm	°C	K	°C	K		mbar		W	s				DD.MM	
HCOOH	blue	180	830	547.5	18	291	22	295	40:100	700	$\perp^i$	25	300	5	674	0.3582	23.02.2021	20210223_c_F_[...]_5x300s
HCOOH	blue	830	1450	567.0	18	291	20	293	40:100	700	$\perp^i$	25	300	5	686	0.3736	23.02.2021	20210223_b_F_[...]_5x300s
HCOOH	blue	1450	1500	584.6	18	291	20	293	40:100	700	$\perp^i$	25	240	5	660	0.3880	23.02.2021	20210223_a_F_[...]_5x240s
HCOOH	orange	180	830	547.5	18	291	40	313	40:100	700	$\perp^i$	25	300	4	674	0.6626	23.02.2021	20210223_f_F_[...]_4x300s
HCOOH	orange	830	1450	567.0	18	291	40	313	40:100	700	$\perp^i$	25	300	4	673	0.6764	23.02.2021	20210223_e2_F_[...]_4x300s
HCOOH	orange	1450	1500	584.6	18	291	40	313	40:100	700	$\perp^i$	25	240	5	660	0.5633	23.02.2021	20210223_d_F_[...]_5x240s
HCOOH	red	180	830	547.5	18	291	60	333	40:100	700	$\perp^i$	25	300	4	674	1.0000	23.02.2021	20210223_i_F_[...]_4x300s
HCOOH	red	830	1450	567.0	18	291	60	333	40:100	700	$\perp^i$	25	300	4	673	1.0000	23.02.2021	20210223_h_F_[...]_4x300s
HCOOH	red	1450	1500	584.6	18	291	60	333	40:100	700	$\perp^i$	25	240	5	660	1.0000	23.02.2021	20210223_g_F_[...]_5x240s
DCOOH	blue	180	830	547.5	18	291	23	296	40:100	700	$\perp^i$	25	300	4	680	0.3752	25.02.2021	20210225_c_FCD_[...]_4x300s
DCOOH	blue	830	1450	567.0	18	291	22	295	40:100	700	$\perp^i$	25	300	4	691	0.2702	25.02.2021	20210225_b_FCD_[...]_4x300s
DCOOH	blue	1450	1500	584.6	18	291	21	294	40:100	700	$\perp^i$	25	140	8	654	0.3158	25.02.2021	20210225_a_FCD_[...]_8x140s
DCOOH	orange	180	830	547.5	18	291	40	313	40:100	700	$\perp^i$	25	300	4	675	0.7059	25.02.2021	20210225_f_FCD_[...]_4x300s
DCOOH	orange	830	1450	567.0	18	291	40	313	40:100	700	$\perp^i$	25	300	4	655	0.5214	25.02.2021	20210225_e2_FCD_[...]_4x300s
DCOOH	orange	1450	1500	584.6	18	291	40	313	40:100	700	$\perp^i$	25	140	8	652	0.4877	25.02.2021	20210225_d_FCD_[...]_8x140s
DCOOH	red	180	830	547.5	18	291	60	333	40:100	700	$\perp^i$	25	300	4	678	1.0000	25.02.2021	20210225_g_FCD_[...]_4x300s
DCOOH	red	830	1450	567.0	18	291	60	333	40:100	700	$\perp^i$	25	300	5	668	1.0000	25.02.2021	20210225_i_FCD_[...]_5x300s
DCOOH	red	1450	1500	584.6	18	291	60	333	40:100	700	$\perp^i$	25	300	4	672	1.0000	25.02.2021	20210225_h_FCD_[...]_4x300s
HCOOD	blue	180	830	547.5	18	291	23	296	40:100	700	$\perp^i$	25	300	4	669	0.3948	01.03.2021	20210301_c_FOD_[...]_4x300s
HCOOD	blue	830	1450	567.0	18	291	22	295	40:100	700	$\perp^i$	25	300	4	672	0.3503	01.03.2021	20210301_b_FOD_[...]_4x300s
HCOOD	blue	1450	1500	584.6	18	291	21	294	40:100	700	$\perp^i$	25	240	5	667	0.3813	01.03.2021	20210301_a_FOD_[...]_5x240s
HCOOD	orange	180	830	547.5	18	291	40	313	40:100	700	$\perp^i$	25	300	4	669	0.6198	01.03.2021	20210301_f_FOD_[...]_4x300s
HCOOD	orange	830	1450	567.0	18	291	40	313	40:100	700	$\perp^i$	25	300	4	672	0.5673	01.03.2021	20210301_e2_FOD_[...]_4x300s
HCOOD	orange	1450	1500	584.6	18	291	40	313	40:100	700	$\perp^i$	25	240	6	660	0.5168	01.03.2021	20210301_d_FOD_[...]_6x240s

continued

Table A.3 (continued)

Iso	Trace	Range / cm^{-1}		λ_{Mon}	T_s		T_n		F in He:He	p_{Res}	$\mathcal{P}^i$	P	t_e	N_{Scan}	BL	Scal	Date	Filename
		min	max	nm	°C	K	°C	K		mbar		W	s				DD.MM	
HCOOD	red	180	830	547.5	18	291	60	333	40:100	700	$\perp^i$	25	300	7	669	1.0000	02.03.2021	20210302_b_FOD_[...]_7x300s
HCOOD	red	830	1450	567.0	18	291	60	333	40:100	700	$\perp^i$	25	300	4	672	1.0000	01.03.2021	20210301_h_FOD_[...]_4x300s
HCOOD	red	1450	1500	584.6	18	291	60	333	40:100	700	$\perp^i$	25	240	5	655	1.0000	01.03.2021	20210301_g_FOD_[...]_5x240s
DCOOD	blue	180	830	547.5	18	291	23	296	40:100	700	$\perp^i$	25	300	4	670	0.3250	03.03.2021	20210303_c_FD2_[...]_4x300s
DCOOD	blue	830	1450	567.0	18	291	22	295	40:100	700	$\perp^i$	25	300	4	688	0.3475	03.03.2021	20210303_b_FD2_[...]_4x300s
DCOOD	blue	1450	1500	584.6	18	291	21	294	40:100	700	$\perp^i$	25	240	5	664	0.4101	03.03.2021	20210303_a_FD2_[...]_5x240s
DCOOD	orange	180	830	547.5	18	291	40	313	40:100	700	$\perp^i$	25	300	4	670	0.5284	03.03.2021	20210303_f_FD2_[...]_4x300s
DCOOD	orange	830	1450	567.0	18	291	40	313	40:100	700	$\perp^i$	25	300	4	688	0.5662	03.03.2021	20210303_e2_FD2_[...]_4x300s
DCOOD	orange	1450	1500	584.6	18	291	40	313	40:100	700	$\perp^i$	25	240	5	664	0.5462	03.03.2021	20210303_d_FD2_[...]_5x240s
DCOOD	red	180	830	547.5	18	291	60	333	40:100	700	$\perp^i$	25	300	9	670	1.0000	03.03.2021	20210303_i_FD2_[...]_9x300s
DCOOD	red	830	1450	567.0	18	291	60	333	40:100	700	$\perp^i$	25	300	5	688	1.0000	03.03.2021	20210303_h_FD2_[...]_5x300s
DCOOD	red	1450	1500	584.6	18	291	60	333	40:100	700	$\perp^i$	25	240	6	664	1.0000	03.03.2021	20210303_g_FD2_[...]_6x240s

Table A.4 Measurement details on formic acid dimer-optimised Raman spectra (depolarised) shown in Figs. 6.3-6.5. See legend in Appendix A.1 for further explanations. The data can be downloaded from Ref. [261] (mind "_des_avg_cal.dat" filename extension).

Iso	Trace	Range / cm^{-1}		λ_{Mon}	T_s		T_n		F in He:He	p_{Res}	$\mathcal{P}^i$	P	t_e	N_{Scan}	BL	Scal	Date	Filename
		min	max	nm	°C	K	°C	K		mbar		W	s				DD.MM	
HCOOH	black	180	830	547.5	18	291	40	313	40:100	700	$\perp^i$	25	300	4	674	0.6626	23.02.2021	20210223_f_F_[...]_4x300s
HCOOH	cyan	180	830	547.5	18	291	40	313	40:100	700	$\parallel^i$	25	300	5	650	0.6626	23.02.2021	20210223_f2_F_[...]_5x300s
HCOOH	black	830	1450	567.0	18	291	40	313	40:100	700	$\perp^i$	25	300	4	673	0.6764	23.02.2021	20210223_e2_F_[...]_4x300s
HCOOH	cyan	830	1450	567.0	18	291	40	313	40:100	700	$\parallel^i$	25	300	5	656	0.6764	23.02.2021	20210223_e_F_[...]_5x300s
HCOOH	black	1450	1500	584.6	18	291	40	313	40:100	700	$\perp^i$	25	240	5	660	0.5633	23.02.2021	20210223_d_F_[...]_5x240s
HCOOH	cyan	1450	1500	584.6	18	291	40	313	40:100	700	$\parallel^i$	25	240	6	640	0.5633	23.02.2021	20210223_d2_F_[...]_6x240s
DCOOH	black	180	830	547.5	18	291	40	313	40:100	700	$\perp^i$	25	300	4	675	0.7059	25.02.2021	20210225_f_FCD_[...]_4x300s
DCOOH	cyan	180	830	547.5	18	291	40	313	40:100	700	$\parallel^i$	25	300	5	650	0.7059	25.02.2021	20210225_f2_FCD_[...]_5x300s
DCOOH	black	830	1450	567.0	18	291	40	313	40:100	700	$\perp^i$	25	300	4	655	0.5214	25.02.2021	20210225_e2_FCD_[...]_4x300s

continued

Table A.4 (continued)

Iso	Trace	Range / cm^{-1}		λ_{Mon}	T_s		T_n		F in He:He	p_{Res}	$\mathcal{P}^i$	P	t_e	N_{Scan}	BL	Scal	Date	Filename
		min	max	nm	°C	K	°C	K		mbar		W	s				DD.MM	
DCOOH	cyan	830	1450	567.0	18	291	40	313	40:100	700	$\parallel^i$	25	300	5	655	0.5214	25.02.2021	20210225_e_FCD_[...]_5x300s
DCOOH	black	1450	1500	584.6	18	291	40	313	40:100	700	$\perp^i$	25	140	8	652	0.4877	25.02.2021	20210225_d_FCD_[...]_8x140s
DCOOH	cyan	1450	1500	584.6	18	291	40	313	40:100	700	$\parallel^i$	25	140	10	641	0.4877	25.02.2021	20210225_d2_FCD_[...]_10x140s
HCOOD	black	180	830	547.5	18	291	40	313	40:100	700	$\perp^i$	25	300	4	669	0.6198	01.03.2021	20210301_f_FOD_[...]_4x300s
HCOOD	cyan	180	830	547.5	18	291	40	313	40:100	700	$\parallel^i$	25	300	5	650	0.6198	01.03.2021	20210301_f2_FOD_[...]_5x300s
HCOOD	black	830	1450	567.0	18	291	40	313	40:100	700	$\perp^i$	25	300	4	672	0.5673	01.03.2021	20210301_e2_FOD_[...]_4x300s
HCOOD	cyan	830	1450	567.0	18	291	40	313	40:100	700	$\parallel^i$	25	300	5	654	0.5673	01.03.2021	20210301_e_FOD_[...]_5x300s
HCOOD	black	1450	1500	584.6	18	291	40	313	40:100	700	$\perp^i$	25	240	6	660	0.5168	01.03.2021	20210301_d_FOD_[...]_6x240s
HCOOD	cyan	1450	1500	584.6	18	291	40	313	40:100	700	$\parallel^i$	25	240	6	644	0.5168	01.03.2021	20210301_d2_FOD_[...]_6x240s
DCOOD	black	180	830	547.5	18	291	40	313	40:100	700	$\perp^i$	25	300	4	670	0.5284	03.03.2021	20210303_f_FD2_[...]_4x300s
DCOOD	cyan	180	830	547.5	18	291	40	313	40:100	700	$\parallel^i$	25	300	5	650	0.5284	03.03.2021	20210303_f2_FD2_[...]_5x300s
DCOOD	black	830	1450	567.0	18	291	40	313	40:100	700	$\perp^i$	25	300	4	688	0.5662	03.03.2021	20210303_e2_FD2_[...]_4x300s
DCOOD	cyan	830	1450	567.0	18	291	40	313	40:100	700	$\parallel^i$	25	300	5	665	0.5662	03.03.2021	20210303_e_FD2_[...]_5x300s
DCOOD	black	1450	1500	584.6	18	291	40	313	40:100	700	$\perp^i$	25	240	5	664	0.5462	03.03.2021	20210303_d_FD2_[...]_5x240s
DCOOD	cyan	1450	1500	584.6	18	291	40	313	40:100	700	$\parallel^i$	25	240	6	645	0.5462	03.03.2021	20210303_d2_FD2_[...]_6x240s

Table A.5 Measurement details on formic acid dimer-optimised FTIR spectra (pressure series) shown in Figs. 6.1-6.2. See legend in Appendix A.1 for further explanations. The data can be downloaded from Ref. [262].

Iso	Range / cm^{-1}		Trace	T_s		p_{Res}	$\Delta\tilde{\nu}$	Apt	MCT detector	Filter	N_{Scan}	Scal	Date	Filename
	min	max		°C	K	mbar	cm^{-1}	mm					DD.MM	
HCOOH	600	1500	blue	0	273	500	2.0	3	sandwich_neu	F15	50	0.3792	20.01.2021	20210120_F_[...]_fpm.50
HCOOH	600	1500	blue	0	273	500	2.0	3	sandwich_neu	F15	100	0.3792	20.01.2021	20210120_F_[...]_gpm.100
HCOOH	600	1500	blue	0	273	600	2.0	3	sandwich_neu	F15	50	0.3792	20.01.2021	20210120_F_[...]_ppm.50
HCOOH	600	1500	blue	0	273	600	2.0	3	sandwich_neu	F15	50	0.3792	20.01.2021	20210120_F_[...]_qpm.50
HCOOH	600	1500	blue	0	273	700	2.0	3	sandwich_neu	F15	50	0.3792	20.01.2021	20210120_F_[...]_ipm.50
HCOOH	600	1500	blue	0	273	700	2.0	3	sandwich_neu	F15	50	0.3792	20.01.2021	20210120_F_[...]_jpm.50
HCOOH	600	1500	orange	0	273	400	2.0	3	sandwich_neu	F15	50	0.8251	20.01.2021	20210120_F_[...]_lpm.50

continued

Table A.5 (continued)

Iso	Range / cm^{-1}		Trace	T_s		p_{Res}	$\Delta\tilde{\nu}$	Apt	MCT detector	Filter	N_{Scan}	Scal	Date	Filename
	min	max		°C	K	mbar	cm^{-1}	mm					DD.MM	
HCOOH	600	1500	orange	0	273	400	2.0	3	sandwich_neu	F15	100	0.8251	20.01.2021	20210120_F_[...]_mpm.100
HCOOH	600	1500	orange	0	273	400	2.0	3	sandwich_neu	F15	50	0.8251	20.01.2021	20210120_F_[...]_npm.50
HCOOH	600	1500	red	0	273	300	2.0	3	sandwich_neu	F15	20	1.0000	19.01.2021	20210119_F_[...]_ppm.20
HCOOH	600	1500	red	0	273	300	2.0	3	sandwich_neu	F15	30	1.0000	19.01.2021	20210119_F_[...]_qpm.30
HCOOH	600	1500	red	0	273	300	2.0	3	sandwich_neu	F15	50	1.0000	20.01.2021	20210120_F_[...]_bpm.50
HCOOH	600	1500	red	0	273	300	2.0	3	sandwich_neu	F15	100	1.0000	20.01.2021	20210120_F_[...]_cpm.100
HCOOH	600	1500	red	0	273	300	2.0	3	sandwich_neu	F15	50	1.0000	20.01.2021	20210120_F_[...]_dpm.50
DCOOH	600	1500	blue	5	278	700	2.0	3	sandwich_neu	F15	50	0.3622	29.01.2021	20210129_DCOOH_[...]_cpm.50
DCOOH	600	1500	blue	5	278	700	2.0	3	sandwich_neu	F15	50	0.3622	29.01.2021	20210129_DCOOH_[...]_dpm.50
DCOOH	600	1500	blue	5	278	500	2.0	3	sandwich_neu	F15	50	0.3622	29.01.2021	20210129_DCOOH_[...]_hpm.50
DCOOH	600	1500	orange	0	273	500	2.0	3	sandwich_neu	F15	50	0.5724	28.01.2021	20210128_DCOOH_[...]_fpm.50
DCOOH	600	1500	orange	0	273	600	2.0	3	sandwich_neu	F15	50	0.5724	28.01.2021	20210128_DCOOH_[...]_ipm.50
DCOOH	600	1500	orange	0	273	600	2.0	3	sandwich_neu	F15	50	0.5724	28.01.2021	20210128_DCOOH_[...]_jpm.50
DCOOH	600	1500	orange	5	278	500	2.0	3	sandwich_neu	F15	50	0.5724	29.01.2021	20210129_DCOOH_[...]_bpm.50
DCOOH	600	1500	red	0	273	500	2.0	3	sandwich_neu	F15	50	1.0000	28.01.2021	20210128_DCOOH_[...]_dpm.50
DCOOH	600	1500	red	0	273	450	2.0	3	sandwich_neu	F15	50	1.0000	28.01.2021	20210128_DCOOH_[...]_mpm.50
DCOOH	600	1500	red	0	273	450	2.0	3	sandwich_neu	F15	50	1.0000	28.01.2021	20210128_DCOOH_[...]_npm.50
HCOOD	600	1500	blue	0	273	600	2.0	3	sandwich_neu	F15	50	0.3913	01.02.2021	20210201_HCOOD_[...]_kpm.50
HCOOD	600	1500	blue	0	273	600	2.0	3	sandwich_neu	F15	50	0.3913	01.02.2021	20210201_HCOOD_[...]_lpm.50
HCOOD	600	1500	orange	0	273	500	2.0	3	sandwich_neu	F15	50	0.5431	01.02.2021	20210201_HCOOD_[...]_dpm.50
HCOOD	600	1500	orange	0	273	500	2.0	3	sandwich_neu	F15	50	0.5431	01.02.2021	20210201_HCOOD_[...]_epm.50
HCOOD	600	1500	orange	0	273	500	2.0	3	sandwich_neu	F15	50	0.5431	01.02.2021	20210201_HCOOD_[...]_fpm.50
HCOOD	600	1500	orange	0	273	500	2.0	3	sandwich_neu	F15	50	0.5431	01.02.2021	20210201_HCOOD_[...]_opm.50
HCOOD	600	1500	orange	0	273	500	2.0	3	sandwich_neu	F15	50	0.5431	01.02.2021	20210201_HCOOD_[...]_ppm.50
HCOOD	600	1500	red	0	273	400	2.0	3	sandwich_neu	F15	50	1.0000	01.02.2021	20210201_HCOOD_[...]_ipm.50
HCOOD	600	1500	red	0	273	400	2.0	3	sandwich_neu	F15	100	1.0000	01.02.2021	20210201_HCOOD_[...]_jpm.100
HCOOD	600	1500	red	0	273	400	2.0	3	sandwich_neu	F15	50	1.0000	01.02.2021	20210201_HCOOD_[...]_mpm.50
HCOOD	600	1500	red	0	273	400	2.0	3	sandwich_neu	F15	50	1.0000	01.02.2021	20210201_HCOOD_[...]_npm.50

continued

Table A.5 (continued)

Iso	Range / cm^{-1}		Trace	T_s		p_{Res}	$\Delta\tilde{\nu}$	Apt	MCT detector	Filter	N_{Scan}	Scal	Date	Filename
	min	max		°C	K	mbar	cm^{-1}	mm					DD.MM	
DCOOD	600	1500	blue	0	273	700	2.0	3	sandwich_neu	F15	50	0.3975	03.02.2021	20210203_DCOOD_[...]_jpm.50
DCOOD	600	1500	blue	0	273	700	2.0	3	sandwich_neu	F15	50	0.3975	03.02.2021	20210203_DCOOD_[...]_kpm.50
DCOOD	600	1500	blue	0	273	700	2.0	3	sandwich_neu	F15	50	0.3975	03.02.2021	20210203_DCOOD_[...]_lpm.50
DCOOD	600	1500	orange	0	273	600	2.0	3	sandwich_neu	F15	50	0.5941	02.02.2021	20210202_DCOOD_[...]_gpm.50
DCOOD	600	1500	orange	0	273	600	2.0	3	sandwich_neu	F15	50	0.5941	03.02.2021	20210203_DCOOD_[...]_npm.50
DCOOD	600	1500	orange	0	273	600	2.0	3	sandwich_neu	F15	50	0.5941	03.02.2021	20210203_DCOOD_[...]_opm.50
DCOOD	600	1500	orange	0	273	600	2.0	3	sandwich_neu	F15	50	0.5941	03.02.2021	20210203_DCOOD_[...]_ppm.50
DCOOD	600	1500	red	0	273	500	2.0	3	sandwich_neu	F15	50	1.0000	04.02.2021	20210204_DCOOD_[...]_bpm.50
DCOOD	600	1500	red	0	273	450	2.0	3	sandwich_neu	F15	50	1.0000	04.02.2021	20210204_DCOOD_[...]_dpm.50
DCOOD	600	1500	red	0	273	450	2.0	3	sandwich_neu	F15	50	1.0000	04.02.2021	20210204_DCOOD_[...]_epm.50
DCOOD	600	1500	red	0	273	450	2.0	3	sandwich_neu	F15	50	1.0000	04.02.2021	20210204_DCOOD_[...]_fpm.50

Table A.6 Measurement details on formic acid dimer-optimised FTIR spectra (higher resolution) shown in Figs. 6.1-6.2. See legend in Appendix A.1 for further explanations.

Iso	Range / cm^{-1}		Trace	T_s		p_{Res}	$\Delta\tilde{\nu}$	Apt	MCT detector	Filter	N_{Scan}	Scal	Date	Filename
	min	max		°C	K	mbar	cm^{-1}	mm					DD.MM	
HCOOH	600	1500	black	10	283	400	0.5	5	sandwich_alt	–	50	1.0000	19.10.2011	04_FA_10C_10p_05cm_apm.50
HCOOH	600	1500	black	10	283	400	0.5	5	sandwich_alt	–	50	1.0000	19.10.2011	04_FA_10C_10p_05cm_bpm.50
HCOOH	600	1500	black	10	283	400	0.5	5	sandwich_alt	–	50	1.0000	19.10.2011	04_FA_10C_10p_05cm_cpm.50
HCOOH	600	1500	black	10	283	400	0.5	5	sandwich_alt	–	50	1.0000	24.10.2011	04_FA_10C_10p_05cm_dpm.50
DCOOH	600	1500	black	10	283	300	1.0	5	sandwich_alt	–	50	1.0000	28.11.2011	03_FA_Cd_10C_10p_1cm_apm.50
HCOOD	600	1500	black	10	283	300	1.0	5	sandwich_alt	–	50	1.0000	28.11.2011	03_FA_Od_10C_10p_1cm_apm.50
DCOOD	600	1500	black	10	283	300	1.0	5	sandwich_alt	–	50	1.0000	30.11.2011	03_FA_d2_10C_10p_1cm_apm.50

Appendix B

Details on quantum chemical calculations

B.1 Electronic structure calculations

Three quantum chemistry programs are used in this work to obtain approximate solutions of the electronic Schrödinger equation. Gaussian 16 Rev. A.03 [168] is used for HF, MP2 [269], and B3LYP-D3(BJ) [270–273], CFOUR version 2.1 [170, 171] for canonical CCSD(T) [274], and Molpro version 2018.1 [54, 275, 276] for explicitly correlated CCSD(T)-F12a [277]. In all calculations, symmetry is enabled and the frozen core approximation is used. Dunning's augmented correlation consistent aug-cc-pVXZ (aVXZ) basis sets are used to expand the one-particle atomic orbitals [278]. In the explicitly correlated F12 calculations, the corresponding cc-pVXZ-F12 (VXZ-F12) basis sets by Peterson *et al.* are used [279]. Details of the calculations and specified keywords are summarised in Table B.1.

B.2 Force field expansions

Ab initio quartic force fields

Semi-diagonal *ab initio* quartic force fields at the HF, MP2, or B3LYP level are computed with Gaussian 16 Rev. A.03. By default, two displaced (in opposing direction) Hessians are computed per normal mode. The input keywords are listed in Table B.1. Note that the geometry optimisation and quartic force field calculation are executed separately as this would otherwise lead to increased numerical errors in the computed cubic and quartic force constants (see Appendix C.2).

Quartic force fields of analytic potentials

Three published Fortran-based potential energy functions of the formic acid monomer and dimer are extensively used in this work. The RC-PES [22] and QB-PES [23] only evaluate the energy for a given geometry whereas the TM-PES [21] additionally computes analytic first and second derivatives. The utilised equilibrium geometries are reported in Table B.2.

Full quartic force field expansions in rectilinear normal coordinates are computed on all three analytic potentials using a Fortran program that utilises symmetry and only requires single-point energies.[203] Its uses fourth-order central differences to compute first and second derivatives of the energy; for the third and fourth derivatives, second-order central difference formulae are used.

The TM-PES was additionally interfaced with the PyPES program [186, 187] which requires analytic second derivatives in order to compute full quartic force field expansions. PyPES does

[203] The program has been written by B. Schröder who kindly provided a copy.

Table B.1 Details of *ab initio* calculations. The conversion from *ab initio* Raman activities into cross-sections is described in Section 2.3.2.

Program	Calculation	Geometry	Calculation-specific keywords
Gaussian	B3LYP		`Empiricaldispersion=GD3BJ DenFit Integral(Grid=SuperFineGrid)`
Gaussian	Opt	XYZ	`Opt=VeryTight`
Gaussian	Hessian		`Freq`
Gaussian	Raman		`Freq=Raman`
Gaussian	QFF	via `%OldChk`	`Freq=Anharm`
Molpro	Opt	Z-matrix/XYZ	`{GOPT, GAUSSIAN, GRMS=1.d-5, SRMS=1.d-5} {GTHRESH, OPTSTEP=6.d-5, OPTGRAD=1.d-6, ENERGY=1.d-10, ZERO=1.d-16}`
Molpro	Hessian		`{MASS,ISO} {FREQUENCIES} {GTHRESH, ENERGY=1.d-10, ZERO=1.d-16}`
CFOUR	CCSD(T)		`SCF_CONV=9, CC_CONV=9, CC_PROGRAM=ECC, ABCDTYPE=AOBASIS, LINEQ_CONV=9, FROZEN_CORE=ON`
CFOUR	Opt	Z-matrix	`GEO_CONV=9, OPT_MAXCYC=100, GEO_METHOD=NR`
CFOUR	Hessian		`VIB=EXACT`

Table B.2 Cartesian equilibrium geometries (in Å) of F, *c*F, and (FF). The geometries on the respective potentials were optimised using the Python function "scipy.optimize.minimize" (SciPy version 1.2.1).

trans monomer RC-PES			cis monomer RC-PES		
C	-0.0989970197	-0.4140062948	0.0	C	-0.1011305054	-0.4005213503	0.0
O	1.1330284674	0.1218768993	0.0	O	1.0967234627	0.2219906283	0.0
O	-1.1209384000	0.2153780019	0.0	O	-1.1323214974	0.2004916486	0.0
H	-0.0321707233	-1.5059225401	0.0	H	-0.0287608757	-1.4987952366	0.0
H	1.0190331330	1.0829445454	0.0	H	1.7978711226	-0.4373659837	0.0

trans monomer TM-PES			cis monomer TM-PES		
C	0.0989714491	0.4134816626	0.0	C	0.1014798017	0.4002201075	0.0
H	0.0330960279	1.5051907751	0.0	H	0.0304190855	1.4979861613	0.0
O	1.1197017093	-0.2152170387	0.0	O	1.1312167170	-0.2005097515	0.0
O	-1.1318640659	-0.1216631983	0.0	O	-1.0961139700	-0.2217464964	0.0
H	-1.0185066928	-1.0819122665	0.0	H	-1.7958277670	0.4381746606	0.0

Cyclic dimer QB-PES			
H	-2.9856234050	-0.2613706684	0.0
H	2.9856234050	0.2613706684	0.0
H	-0.5128796068	1.1163775605	0.0
H	0.5128796068	-1.1163775605	0.0
O	-1.1718824645	-1.1552335280	0.0
O	1.1718824645	1.1552335280	0.0
O	-1.5047716183	1.0752800226	0.0
O	1.5047716183	-1.0752800226	0.0
C	-1.8960260665	-0.1765662375	0.0
C	1.8960260665	0.1765662375	0.0

not exploit symmetry and default settings are used. By comparing VPT2 wavenumbers on the differently obtained quartic force fields, it could be verified that cumulative deviations in the cubic and (diagonal and semi-diagonal) quartic force constants are relatively small – deviations are within 1 cm^{-1} for resultant VPT2 fundamentals.

Sextic force fields of analytic potentials

Sextic force field expansions on the TM-PES are computed with PyPES as detailed in Ref. [187]. The computation of the SFF involves an intermediate step via curvilinear normal modes. When defining the connectivity in formic acid as

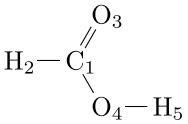

then PyPES by default sets up four bond (r_{12}, r_{13}, r_{14}, r_{45}), four bend (θ_{213}, θ_{214}, θ_{314}, θ_{145}), and two dihedral angle (τ_{2145}, τ_{3145}) extension coordinates. Explicit definitions of these coordinates with respect to Cartesian coordinates are given in the supplementary material of Ref. [186]. The curvilinear normal modes are expanded as linear combinations of these internal coordinates, where the bond extension coordinates are replaced by Simons-Parr-Finlan coordinates [280] to improve the convergence properties. In Section 5.4, a reduced-dimensional SFF of *trans*-HCOOH is used where the OH torsional coordinate is removed before defining the curvilinear normal modes. This method has been described in [108]. Similar to the procedure for CH_2NH [108], the two dihedral angles (τ_{2145}, τ_{3145}) are replaced by the sine of an appropriate out-of-plane bending coordinate (ω_{1243}).

B.3 VPT*n* (Gaussian and GUINEA)

Gaussian

In Gaussian 16 Rev. A.03 [70, 159, 168, 169], the force field data can be loaded from a previous VPT2 calculation and new harmonic wavenumbers are optionally provided via "DataAdd=Freq"[204] using the following template:

```
%OldChk=<checkpoint file with force field data>
# <el. struct. method> CheckBasis Geom=AllCheck
# Freq=(ReadFC,Anharmonic,ReadAnharm)

DataAdd=Freq
Resonances=(NoDarDen)

<new wavenumbers in cm-1>
```

GUINEA

GUINEA version 3.0 is a stand-alone module of CFOUR version 2.1 [170, 171] which reads all necessary parameters from text files. As such, it is not limited to force fields that are generated by CFOUR. In the supplementary material of Ref. [109], it has been described in detail how the information from a Gaussian-generated output file can be parsed and converted into the GUINEA data structure. Effective Hamiltonian calculations with GUINEA have been described in Ref. [171].

B.4 Reduced-dimensional VCI (QVib)

QVib is a Fortran-based program which facilitates the computation of anharmonic wavenumbers and wavefunctions in reduced-dimensionality using rectilinear normal coordinates utilising the

[204] This procedure yields the same results as the procedure described in the manual, see https://gaussian.com/freq/ (last accessed on November 18, 2021) under "ReadAnharm Input", where the force field data is written to a text file and later retrieved via "DataSrc=(InQMWX,NMOrder=Desc)".

variational principle. An analytic representation of the potential must first be obtained with QFit which fits polynomials of the desired order to potential energy scans in dimensionless normal coordinates.[205] The form of the fit polynomials is tailored to be as physical as possible:

- The geometries are rigorously optimised and the gradient, i.e. the first derivative of the potential, along each normal coordinate is thus assumed to be zero.
- If the respective normal coordinate is not totally symmetric, all polynomial coefficients of uneven order $(1, 3, 5, 7, ...)$ are set to zero (see note 51, p. 20) and energies for the same absolute displacements are averaged in order to minimise numerical noise.

The general form of the fit polynomials is given by

$$V_{\mathrm{fit}}(q_i) = \sum_{n_i}^{m_i} a_i^{(n_i)} q_i^{n_i} = a_i^{(0)} + a_i^{(2)} q_i^2 + ... + a_i^{(m_i)} q_i^{m_i}, \tag{B.1}$$

$$V_{\mathrm{fit}}(q_i, q_j) = \sum_{n_i}^{m_i} \sum_{n_j}^{m_j} a_{i,j}^{(n_i,n_j)} q_i^{n_i} q_j^{n_j} = a_{i,j}^{(0,0)} + a_{i,j}^{(2,0)} q_i^2 + a_{i,j}^{(0,2)} q_j^2 + a_{i,j}^{(2,1)} q_i^2 q_j + ... \tag{B.2}$$

The standard deviation of the fitted potentials is between 10^{-3} and $10^{-4}\,\mathrm{cm}^{-1}$ for 1D fits and between 10^{-1} and $10^{-2}\,\mathrm{cm}^{-1}$ for 2D fits. The fitted polynomial coefficients can be related[206] to the higher-order derivatives of the potential with respect to dimensionless normal coordinates (Eq. 2.7, p. 15). A comparison of the coefficients yields

$$\left.\frac{\partial^{n_i} V}{\partial q_i^{n_i}}\right|_{\mathrm{eq}} = n_i! \times a_i^{(n_i)}, \tag{B.3}$$

$$\left.\frac{\partial^{n_i+n_j} V}{\partial q_i^{n_i} \partial q_j^{n_j}}\right|_{\mathrm{eq}} = n_i! \times n_j! \times a_{i,j}^{(n_i,n_j)}. \tag{B.4}$$

The vibrational eigenvalues are obtained numerically via Hermite-Gauss quadrature by diagonalisation of the matrix representation of the vibrational Hamiltonian

$$\hat{H}_{\mathrm{QVib}} = V_{\mathrm{fit}} + \frac{hc}{2} \sum_i \omega_i \hat{p}_i^2 \tag{B.5}$$

in a harmonic oscillator basis. In this work, the basis is increased until the ground and first excited state are converged to within $10^{-1}\,\mathrm{cm}^{-1}$. QVib utilises an approximate form of the $J = 0$ Watsonian where anharmonic contributions to the kinetic energy operator are neglected (cf. Eq. 2.2).

[205] The QVib and QFit programs were written by P. Botschwina and further developed by B. Schröder. Copies of the programs have kindly been provided by B. Schröder. For applications, see Refs. [281, 282].

[206] See also Ref. [79], where Ramakrishnan and Rauhut discuss a method for obtaining approximate semi-quartic force field expansions from n-mode representations of the potential energy hypersurface.

Appendix C

Numerical sensitivities and errors in Gaussian-VPT2

C.1 Erroneous Coriolis coupling constants in Gaussian 09

In the course of the numerical sensitivity benchmark discussed below, it was found that the VPT2 results, if computed instead with Gaussian 09 Rev. E.01 [283], depend on the *orientation* of the reference geometry due to an erroneous evaluation of the Coriolis constants ($\zeta^{\alpha}_{i,j}$, see Ref. [66, Eq. 4.1.7]) which has been fixed as of version 16 Rev. A.03 [168].[207]

There are established conventions for the six possible mappings between laboratory (XYZ) and molecule-fixed Eckart axes (abc), e.g. III^r where $X = a$, $Y = b$, and $Z = c$. In Gaussian 09 Rev. E.01, the Coriolis coupling constants are not evaluated in the Eckart frame (as should be) but in the laboratory frame that is specified in the input file. These findings are consistent with observations by Heger *et al.* [162, 163] who reported numerical deviations if the same geometry is either specified by the user in the input file or read automatically from a checkpoint file. Presumably, Gaussian uses a default representation for the Cartesian geometry when writing the checkpoint file.

To confirm this result, the total anharmonic energies of vibrational states and individual contributions to the second-order anharmonicity constants were computed with different programs and compared: Gaussian 09 Rev. E.01, Gaussian 16 Rev. A.03, GUINEA version 3.0, and a self-written Python program based on Eqs. 2.8-2.11 (pp. 15). The same quartic force field was used to separate out numerical sensitivities due to deviations in the cubic and quartic force constants.

C.2 Numerical sensitivities of cubic and quartic force constants in Gaussian 16

In numerical quartic force field calculations, Gaussian generates two displaced geometries in opposing directions along each normal coordinate in order to compute analytic second derivatives of the molecular energy. The VPT2 routine was first implemented in Gaussian 03 [70] and since Gaussian 16 [168], the "FourPoint" option has been available. As the name implies, four instead of two displacements per normal coordinate are included in the numerical differentiation step. The default option is "TwoPoint".

In the following, four different calculations are repeated with Gaussian 16 Rev. A.03 for nine differently obtained, independent reference geometries of the cyclic formic acid dimer

[207] In VPT2, the Coriolis coupling constants contribute to the off-diagonal second-order anharmonicity constants and the zero-point vibrational correction (see Eqs. 2.10-2.11, p. 15).

$(HCOOH)_2$ to quantify the numerical sensitivities of the different numerical approaches.

A. Geometry optimisation and VPT2 calculation ("TwoPoint") are requested in the same calculation. For reproducibility, nine independent equilibrium structures (combination of HF, MP2, and CCSD(T) with aVDZ, aVTZ, and aVQZ basis sets) that were previously employed in Ref. [130], are used here as initial start structures. The following template is employed:

```
%chk=<filename>
# <Method> <basis set>
# Opt=VeryTight
# Freq=(Anharm,ReadAnharm,TwoPoint)

Comment

0 1
<xyz; 10 decimal places>
```

B. For each optimised geometry from A, a new VPT2 and force field calculation is requested. As reference geometry, the optimised geometry from step A is loaded from the checkpoint file and a "FourPoint" VPT2 calculation is requested without re-optimisation. The following template is used:

```
%OldChk=<chk file from A>
%Chk=<filename>
# <Method> <basis set>
# Geom=AllCheck
# Freq=(Anharm,ReadAnharm,FourPoint)
```

C. As B, but a "TwoPoint" VPT2 calculation is requested and the pre-optimised geometry from D is used.

D. As A, but a "FourPoint" VPT2 calculation is requested.

The resultant anharmonicity constants and total anharmonic corrections[208] are analysed at the MP2/aVDZ level in terms of the mean (MAD) and maximum (MAX) absolute deviation. Generally, one would expect similar error profiles for the pairs A+C and B+D, the common denominator being the order of the finite difference equations. Surprisingly, however, the error profiles of the pairs A+D and B+C are very similar (Figs. C.1-C.2). These results clearly demonstrate that the common denominator is whether the geometry optimisation and numerical quartic force field computation are separated into two separate calculations or not. It is noted that these findings are independent of differently combining "*n*Point" (which in any case should not have an effect on the geometry optimisation) and similar results are obtained if method B is combined with geometries from method D and similarly method C with A. Moreover, it suffices if the Cartesian geometry is supplied manually via the input file in methods B and C. This was tested by using the geometry in the Eckart frame which is written to the Gaussian-produced output file with 13 decimal places. The numerical deviations in computed anharmonicity constants are negligible if 10 decimal places are specified for the Cartesian reference geometry. The sensitivity of the results with respect to less than 10 decimal places was not tested.

Illustrative results for other methods and basis sets are shown in Table C.1. Especially impressive are the improvements with the larger aVTZ basis set, where the numerical noise dramatically increases from C to D. By separating the optimisation and numerical differentiation

[208] $\delta_{i,\mathrm{anh}}$ might profit from some error compensation if numerical errors in individual anharmonicity constants fortuitously cancel. As such, $\delta_{i,\mathrm{anh}}$ is first computed for each set of independently computed second-order anharmonicity matrices and then analysed in terms of mean or maximum absolute deviation.

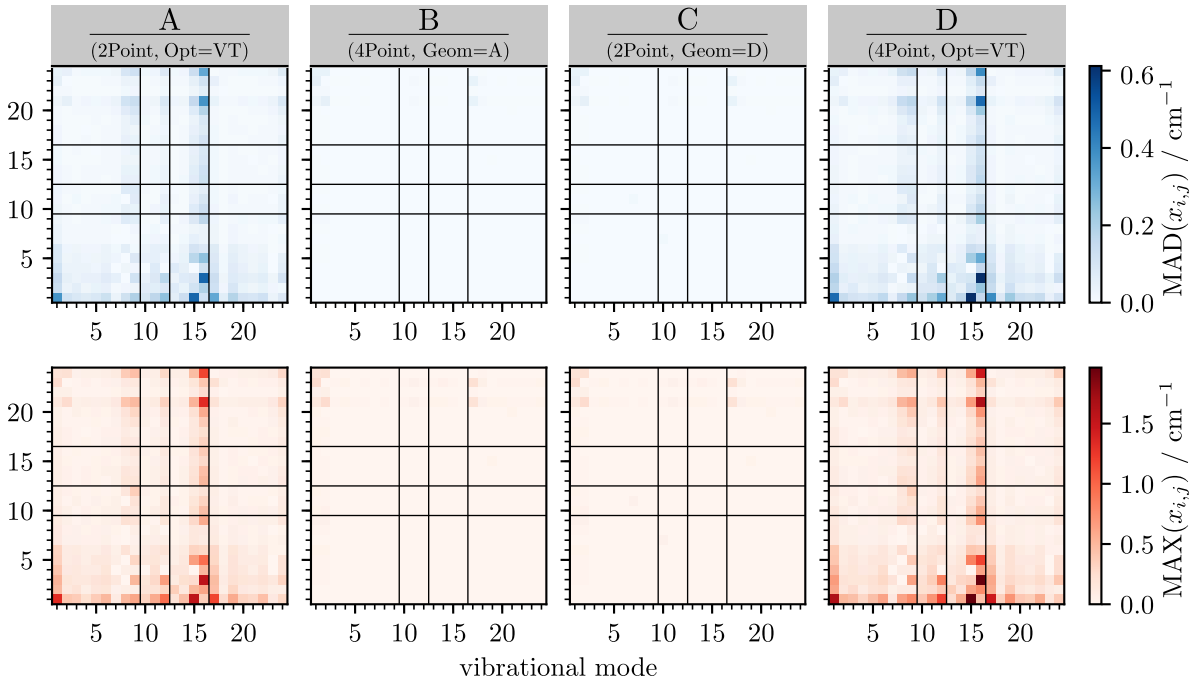

Figure C.1 Mean and maximum absolute deviation of second-order anharmonicity constants (Eqs. 2.9-2.10, p. 15) for the cyclic formic acid dimer $(HCOOH)_2$ computed at the MP2/aVDZ level. Different symmetry blocks are separated by black lines (1-9 A_g, 10-12 B_g, 13-16 A_u, 17-24 B_u).

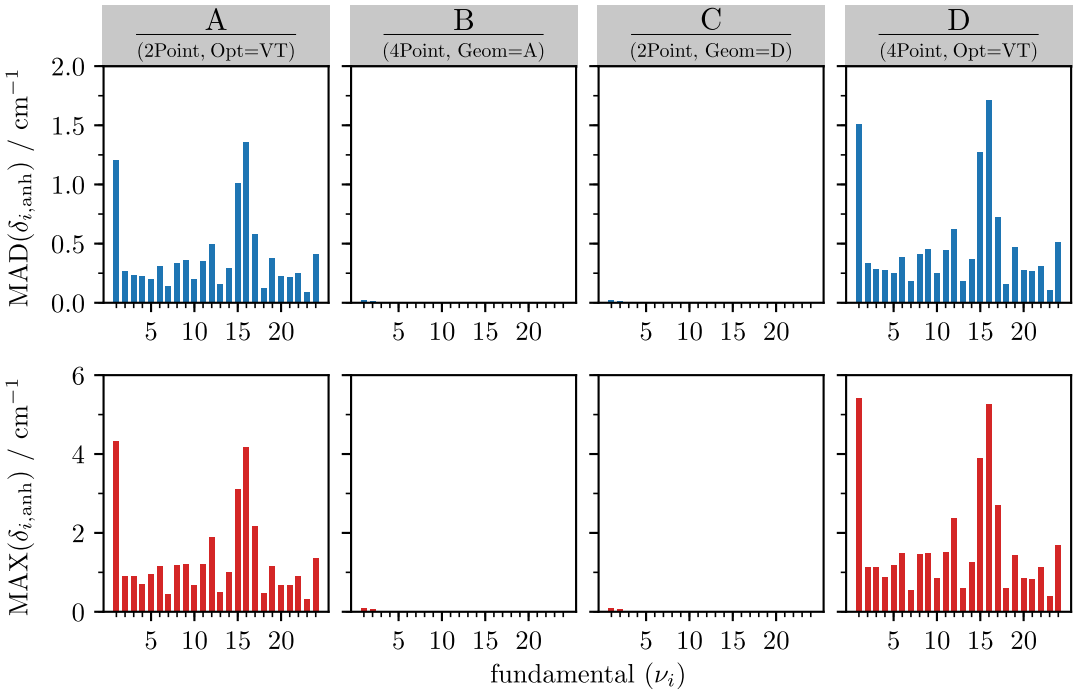

Figure C.2 Mean and maximum absolute deviation of second-order anharmonic corrections (Eq. 2.16, p. 17) to the fundamentals of the cyclic formic acid dimer $(HCOOH)_2$, computed at the MP2/aVDZ level.

calculations, numerical errors in the anharmonicity constants can in all cases be minimised below 0.3 cm^{-1}. Similarly, errors in anharmonic fundamental wavenumbers are minimised below 0.3 cm^{-1}.

The presented benchmarks do not indicate a significant improvement of “FourPoint” over “TwoPoint”. On the contrary, the data in Fig. C.2 even show that the numerical noise increases when “FourPoint” is used together with a geometry optimisation (A versus D). Future investig-

Table C.1 Numerical errors (in cm^{-1}) of computed second-order anharmonicity constants and anharmonic corrections for fundamentals of $(HCOOH)_2$. For the B3LYP calculations, additionally "# Empiricaldispersion=GD3BJ DenFit Integral(Grid=SuperFineGrid)" was specified in the input.

	B3LYP-D3(BJ)				MP2			
	aVDZ		aVTZ		aVDZ		aVTZ	
	C	D	C	D	C	D	C	D
MAD($x_{i,j}$)	0.0004	0.0531	0.0005	0.3590	0.0012	0.0441	0.0026	0.1497
MAX($x_{i,j}$)	0.0780	3.7049	0.0634	32.8929	0.2660	1.9646	0.2774	7.3261
MAD($\delta_{i,\mathrm{anh}}$)	0.0008	0.4732	0.0010	3.9564	0.0028	0.4892	0.0210	1.1741
MAX($\delta_{i,\mathrm{anh}}$)	0.0276	8.7955	0.0264	75.7921	0.0984	5.4036	0.2119	15.0333

ations have to show whether this is due to implementational errors.[209] These benchmarks show how VPT2 results obtained with Gaussian can be reproduced to within spectroscopic accuracy. This *internal* consistency must be contrasted in the future with *external* validations by comparing numerical quartic force fields from different quantum chemistry programs and numerical differentiation routines where the electronic energies (or derivatives) are obtained externally.

C.3 Erroneous VPT2 resonance Hamiltonians in Gaussian

The strong Fermi resonance between ν_5 and $2\nu_9$ in *trans*-HCOOH leads to effective VPT2 Hamiltonians where fundamentals and ternary states are strongly coupled not directly through a Darling-Dennison-like resonance but through a binary state that undergoes a Fermi resonance with the fundamental *and* the ternary state. In such instances, it was found that the black-box "GVPT2" [263] implementation in Gaussian 16 (A.03 and C.01) does not set up correct VPT2 resonance Hamiltonians,[210] leading to substantial errors in the energy levels of fundamentals and binary states. In the following, this is illustrated using the example of the C–H stretching fundamental ν_2 of *trans*-HCOOH. The form of the effective Hamiltonian is based on considerations outlined in Section 5.1 (Set II, Table 5.1).

Term values of ν_2 and its resonance partners are computed with VPT2[211] in five different ways using the same force field:

A. Gaussian with default settings:

```
%OldChk=<checkpoint file with force field data>
# MP2 CheckBasis Geom=AllCheck
# Freq=(ReadFC,Anharmonic,ReadAnharm)

PT2Model=GVPT2
Spectro=(MaxQuanta=2)
DataAdd=Freq

<new wavenumbers in cm-1>
```

[209] A non-exhaustive google scholar search of the recent literature indicates that the (expected) numerical improvements of "FourPoint" have not systematically been addressed so far.

[210] This limitation in the resonance treatment seems to be known amongst experts and workers in the field [11, 284].

[211] The calculations were performed with Gaussian 16 Rev. A.03 and GUINEA version 3.0. For reproducibility, the utilised Gaussian input lines are shown. GUINEA prints the effective Hamiltonian upon request and is thus fully transparent. Instead, the general form of the effective Hamiltonians is reported.

The following resonances are detected: $\omega_2 \approx \omega_3 + \omega_5$, $\omega_4 \approx 2\omega_9$, and $\omega_5 \approx 2\omega_9$ (no second-rank or fourth-rank resonances).

B. As A, but with additional ternary states:

```
%OldChk=<checkpoint file with force field data>
# MP2 CheckBasis Geom=AllCheck
# Freq=(ReadFC,Anharmonic,ReadAnharm)

PT2Model=GVPT2
Spectro=(MaxQuanta=3)
DataAdd=Freq

<new wavenumbers in cm-1>
```

The following new resonances are detected (in addition to item A): $\omega_1 \approx 2\omega_5 + \omega_6$, $\omega_1 \approx \omega_3 + \omega_5 + \omega_7$, $\omega_2 \approx \omega_5 + \omega_8 + \omega_9$, $\omega_2 \approx \omega_4 + \omega_6 + \omega_7$, and $\omega_2 \approx \omega_3 + 2\omega_9$.

C. As B, but with manual inclusion of the Fermi resonance $\omega_2 \approx 2\omega_4$:

```
%OldChk=<checkpoint file with force field data>
# MP2 CheckBasis Geom=AllCheck
# Freq=(ReadFC,Anharmonic,ReadAnharm)

PT2Model=GVPT2
Spectro=(MaxQuanta=3)
DataAdd=Freq
Resonances=Add

<new wavenumbers in cm-1>

1-2 2 4 4
```

D. GUINEA using a 4×4 effective VPT2+F Hamiltonian that is constructed from ν_2, ν_3+$2\nu_9$, ν_3+ν_5, and ν_3+ν_4:

$$\frac{\mathbf{H}^{\mathrm{D}}}{hc} = \begin{pmatrix} (\nu_2)^* & & & \\ 0 & (\nu_3{+}2\nu_9)^* & & \\ \frac{1}{2\sqrt{2}}\phi_{2,3,5} & \frac{1}{4}\phi_{5,9,9} & (\nu_3{+}\nu_5)^* & \\ \frac{1}{2\sqrt{2}}\phi_{2,3,4} & \frac{1}{4}\phi_{4,9,9} & 0 & (\nu_3{+}\nu_4)^* \end{pmatrix}. \tag{C.1}$$

E. As D, but the effective VPT2+F Hamiltonian additionally includes $2\nu_4$:

$$\frac{\mathbf{H}^{\mathrm{E}}}{hc} = \begin{pmatrix} (2\nu_4)^* & & & & \\ \frac{1}{4}\phi_{2,4,4} & (\nu_2)^* & & & \\ 0 & 0 & (\nu_3{+}2\nu_9)^* & & \\ 0 & \frac{1}{2\sqrt{2}}\phi_{2,3,5} & \frac{1}{4}\phi_{5,9,9} & (\nu_3{+}\nu_5)^* & \\ 0 & \frac{1}{2\sqrt{2}}\phi_{2,3,4} & \frac{1}{4}\phi_{4,9,9} & 0 & (\nu_3{+}\nu_4)^* \end{pmatrix}. \tag{C.2}$$

The results from A-E are summarised in Table C.2 and compared to theoretical reference calculations on the TM-PES [21] and experiment.

Table C.2 Assessment of differently calculated GVPT2 (Gaussian implementation) and VPT2+F term values of the ν_2 polyad in *trans*-HCOOH (A-E, see text). These predictions are compared to high-level computational reference values from Refs. [28, 29] and experiment (compiled from Table 4.8, p. 91). Note that "GENIUSH" is an abbreviation for "GENIUSH-Smolyak". The *ab initio* MP2/aVTZ force field is enhanced with CCSD(T)-F12a/VDZ-F12 harmonic force constants. All values are in units of cm^{-1}.

	hybrid *ab initio* force field					TM-PES				
	GVPT2			VPT2+F		VPT2+F		CVPT6	GENIUSH	
	A	B	C	D	E	D	E			Exp.
$2\nu_4$	2735	2735	2729		2747		2745	2747	2746	2745
ν_2	2936	2932	2942	2938	2946	2938	2944	2940	2938	2942.06
$\nu_3+2\nu_9$		3038	3038	3003	3003	3003	3003	3002	3001	2995
$\nu_3+\nu_5$	3054	3054	3054	3083	3083	3085	3085	3087	3086	3081
$\nu_3+\nu_4$	3157	3157	3157	3159	3159	3162	3162	3160	3160	3152.3

To bridge the differences in the electronic structure calculations and PES parametrisation, the effective Hamiltonian calculations (D, E) are repeated with a quartic force field expansion of the TM-PES. The numerical quartic force field is computed using analytic second derivatives of the energy (see Appendix B.2). Comparison of eigenvalues of $\mathbf{H}^{\mathrm{E}}$ across different force fields shows that the electronic structure deviations are within 3 cm^{-1} and thus negligible. Furthermore, VPT2+F calculations on the TM-PES (D, E) compare very favourably with the theoretical references and it is noted that deviations to VPT2+K are within 1 cm^{-1}. The deviations between GENIUSH-Smolyak and experiment illustrate errors that arise from the underlying potential (fit error and electronic structure deficiencies). It can be seen that the ν_2 term value is very sensitive to the inclusion of $2\nu_4$ in the effective Hamiltonian treatment with deviations of 6-8 cm^{-1} for D and E. Rewardingly, these values are lower- and upper-limits that enclose the reference values (CVPT6, GENIUSH-Smolyak), indicating the indeficiencies are not primarily due to the low-order perturbative rectilinear normal coordinate treatment but rather due to the small effective Hamiltonian (see also Section 5.1).

Focussing now on the VPT2 term values as computed by Gaussian (A-C), it is not surprising that the deviations are very large for A since Gaussian by default does not include ternary states. Due to the strong OH bend-torsion resonance, however, the inclusion of $\nu_3+2\nu_9$ is crucial. Thus, one would expect that the deviations between B and D (or B and E) on the *ab initio* force field are significantly reduced since ternary states are included. This is not the case and the ν_2 term value even moves in the 'wrong' direction towards lower wavenumbers. On the basis of the matrix elements that are written to the output file by Gaussian,

$$\frac{\mathbf{H}^{\mathrm{B}}}{hc} = \begin{pmatrix} (\nu_5+\nu_8+\nu_9)^* & & & & \\ \frac{1}{4}K_{2;5,8,9} & (\nu_2)^* & & & \\ 0 & \frac{1}{2\sqrt{2}}K_{2;3,9,9} & (\nu_3+2\nu_9)^* & & \\ 0 & \frac{1}{2\sqrt{2}}\phi_{2,3,5} & 0 & (\nu_3+\nu_5)^* & \\ 0 & \frac{1}{4}K_{2;4,6,7} & 0 & 0 & (\nu_4+\nu_6+\nu_7)^* \end{pmatrix} \tag{C.3}$$

$$= \begin{pmatrix} 2934.8 & & & & \\ -3.0 & 2939.9 & & & \\ 0 & -9.8 & 3037.5 & & \\ 0 & -22.2 & 0 & 3049.7 & \\ 0 & -4.6 & 0 & 0 & 3093.9 \end{pmatrix}, \tag{C.4}$$

can be reverse-engineered. Diagonalisation of the above matrix yields eigenvalues that are identical to the values computed by Gaussian (partly shown in Table C.2, column B). This Hamilton matrix only includes direct resonance couplings to the fundamental, whereas couplings between $n > 1$ states are completely missing. Interestingly, the theory-experiment deviation for ν_2 is smallest upon inclusion of the Fermi resonance interaction between ν_2 and $2\nu_4$ (Table C.2, column C). The fortuitous success of this – highly erroneous – calculation is only unveiled upon further inspection of the other combination states.

In summary, Gaussian does not account for Fermi couplings between $n > 1$ states, such as $\nu_3+\nu_5$ and $\nu_3+2\nu_9$ or similarly (but less important here) $\nu_3+\nu_4$ and $\nu_3+2\nu_9$, but only treats direct Fermi or Darling-Dennison-like resonances to fundamental states. As such, only the Darling-Dennison-like resonance between ν_2 and $\nu_3+2\nu_9$ is additionally treated. Evidently, the direct 1-3 resonance is insignificant whereas the Fermi resonances between $n = 2$ and $n = 3$ states in the OH bend-torsion polyad have a sizeable impact on the ν_2 fundamental.

Appendix D

Auxiliary data supporting vibrational assignments

This appendix contains information supporting the assignment of vibrational formic acid monomer (Chapter 4) and dimer bands (Chapter 7).

Formic acid monomer[212]:

Table D.1 CVPT6 fundamental wavenumbers of *cis*-formic acid computed on the TM-PES and RC-PES.

Table D.2 CVPT6 fundamental wavenumbers of *trans*-formic acid-^{13}C computed on the TM-PES.

Table D.3 Deperturbed CVPT2 anharmonicity constants of *cis*-HCOOH and all four H/D isotopologues of *trans*-formic acid computed on the TM-PES and RC-PES.

Table D.4 Vibrational *trans*-HCOOH term values below 4000 cm^{-1} computed on the TM-PES.

Table D.5 Vibrational *trans*-DCOOH term values below 3700 cm^{-1} computed on the TM-PES.

Table D.6 Vibrational *trans*-HCOOD term values below 3600 cm^{-1} computed on the TM-PES.

Table D.7 Vibrational *trans*-DCOOD term values below 3300 cm^{-1} computed on the TM-PES.

Formic acid dimer:

Table D.8 Estimation of the vibrational band centres ($\tilde{\nu}_0$) of the missing A_u modes of symmetrically deuterated isotopologues of (FF).

Table D.9 Binary combination/overtone band centres of (FF) and its symmetrically deuterated isotopologues, estimated using semi-experimental SOF+x.

[212] The CVPTn data of the formic acid monomer have been computed by E. L. Sibert III, see Ref. [28] for details. Most of the data have been published in the supplementary material of Ref. [28] and are reproduced in the following for the convenience of the reader. The second-order anharmonicity constants of deuterated *trans*-formic acid in Table D.3 were not previously published.

CVPT6 fundamentals of *cis*-formic acid

Table D.1 Fundamentals of *cis*-formic acid computed with CVPT6 on the TM-PES [21] and RC-PES [22]. For details of the calculations see Ref. [28] and references therein.

			cis-HCOOH		*cis*-DCOOH		*cis*-HCOOD		*cis*-DCOOD	
Mode	Descr.	Γ	TM-PES	RC-PES	TM-PES	RC-PES	TM-PES	RC-PES	TM-PES	RC-PES
ν_1	ν(OH)	A′	3653	3636	3652	3637	2691	2685	2693	2685
ν_2	ν(CH)	A′	2878	2874	2170	2167	2876	2872	2143	2143
ν_3	ν(C=O)	A′	1821	1810	1792	1782	1822	1815	1791	1783
ν_4	δ(CH)	A′	1389	1384	989	986	1388	1383	1037	1030
ν_5	δ(OH)	A′	1246	1247	1238	1235	900	905	880	884
ν_6	ν(C−O)	A′	1096	1097	1131	1130	1164	1162	1161	1159
ν_7	δ(OCO)	A′	657	652	651	646	630	623	622	615
ν_8	γ(CH)	A″	1020	1014	868	862	1022	1015	867	861
ν_9	γ(OH)	A″	491	491	486	486	375	375	369	370

CVPT6 fundamentals of *trans*-formic acid-^{13}C

Table D.2 Fundamentals of *trans*-formic acid-^{13}C computed with CVPT6 on the TM-PES [21]. For details of the calculations see Ref. [28] and references therein.

			trans-H^{13}COOH	*trans*-D^{13}COOH	*trans*-H^{13}COOD	*trans*-D^{13}COOD
Mode	Descr.	Γ	TM-PES	TM-PES	TM-PES	TM-PES
ν_1	ν(OH)	A′	3581	3577	2638	2645
ν_2	ν(CH)	A′	2928	2200	2937	2211
ν_3[a]	ν(C=O)	A′	1743	1730	1740	1728
ν_4	δ(CH)	A′	1380	971	1364	1039
ν_5	δ(OH)	A′	1293	1293	971	946
ν_6	ν(C−O)	A′	1099	1131	1154	1149
ν_7	δ(OCO)	A′	622	617	556	552
ν_8	γ(CH)	A″	1021	857	1018	857
ν_9	γ(OH)	A″	639	630	506	491

[a] ν_3 is involved in a strong Fermi resonance with $2\nu_8$. In the table, the higher-wavenumber levels are shown. The lower-wavenumber levels are at 1699 (D^{13}COOH) and 1698 cm^{-1} (D^{13}COOD).

CVPT2 anharmonicity constants

Table D.3 Second-order anharmonicity constants, expanded in curvilinear normal mode coordinates, and harmonic wavenumbers (all in cm^{-1}) computed with CVPT2 on the TM-PES [21] and RC-PES [22]. For details of the calculations and deperturbation criteria, see Ref. [28] and references therein.

		$x_{i,j}$ (TM-PES)										$x_{i,j}$ (RC-PES)								
i	ω_i	1	2	3	4	5	6	7	8	9	ω_i	1	2	3	4	5	6	7	8	9
cis-HCOOH																				
1	3829	−83									3824	−88								
2	3007	−3	−63								3011	1	−69							
3	1861	−6	5	−10							1846	−4	4	−9						
4	1428	−3	−30	−13	−7						1416	−2	−29	−7	−4					
5	1299	−16	−3	−7	−9	−12					1289	−15	2	−5	−1	−11				
6	1124	−4	−4	−7	−7	−12	−5				1125	−8	0	−6	−5	−12	−5			
7	664	−1	−1	−5	0	−3	−5	0			656	−1	−1	−6	1	2	−2	0		
8	1038	1	−19	−5	6	−1	−4	1	−4		1036	0	−18	−9	3	1	−6	−1	−6	
9	522	−12	0	−3	−2	−4	−3	2	0	−10	521	−11	0	−3	−3	−7	0	2	0	−9
trans-HCOOH																				
1	3766	−84									3755	−86								
2	3092	−3	−59								3090	−3	−62							
3	1818	−1	0	−9							1807	−1	1	−9						
4	1412	−5	−28	−7	−5						1405	−5	−30	−8	−4					
5	1323	−23	−1	−5	−9	−8					1311	−17	−1	−3	−4	−6				
6	1140	−4	−2	−5	−7	−14	−6				1137	−4	−2	−5	−6	−13	−6			
7	632	−4	2	−6	0	−5	−2	1			630	−4	−1	−5	1	−4	−3	0		
8	1056	−3	−24	−5	3	−2	−4	0	−3		1051	−1	−18	−5	3	−2	−3	0	−2	
9	673	−3	−3	−1	−1	−1	−4	3	0	−14	670	−3	−2	−1	−1	−1	−1	1	0	−14
trans-DCOOH																				
1	3766	−84									3755	−86								
2	2300	−2	−30								2298	−2	−32							
3	1786	−1	−7	−9							1776	−1	−5	−8						
4	992	−2	−18	−2	−3						992	−3	−18	−2	−3					
5	1317	−28	−2	−4	−2	−9					1306	−21	0	−3	−2	−7				
6	1177	−2	−4	−7	−6	−13	−5				1168	−1	−3	−7	−6	−12	−4			
7	626	−3	1	−5	1	−4	−4	1			624	−4	−1	−5	1	−3	−5	0		
8	888	−1	−12	−4	0	−1	−2	0	−2		883	−1	−9	−4	0	−1	−2	0	−1	
9	663	−4	−3	0	0	1	−6	3	1	−14	660	−3	−2	−1	0	0	−4	1	0	−14
trans-HCOOD																				
1	2738	−45									2730	−46								
2	3092	−2	−59								3090	−2	−62							
3	1811	−1	1	−9							1800	−1	1	−9						
4	1402	−1	−33	−8	−7						1395	−2	−32	−8	−5					
5	1013	−7	0	−5	−3	−5					1004	−4	0	−4	−2	−5				
6	1209	−4	−4	−4	−3	−8	−7				1207	−3	−2	−3	−4	−7	−7			
7	565	−5	2	−5	0	−3	−5	1			563	−5	−1	−5	1	−3	−5	0		
8	1053	−2	−24	−5	4	−3	−3	0	−3		1048	−1	−18	−5	3	−2	−3	0	−2	
9	529	−1	−3	−1	−1	−2	−6	2	0	−8	526	−1	−2	−1	−1	−2	−5	0	0	−8
trans-DCOOD																				
1	2739	−45									2730	−46								
2	2299	−2	−30								2297	−2	−32							
3	1782	−1	−6	−9							1771	−1	−5	−9						
4	1061	−7	−9	−3	−3						1053	−5	−9	−3	−2					
5	969	−2	−11	−3	−8	−2					966	−2	−9	−3	−8	−2				
6	1202	−2	−4	−7	−6	−7	−6				1197	−1	−3	−5	−4	−6	−6			
7	561	−5	1	−4	−2	−1	−5	1			559	−5	−1	−4	−1	−1	−5	0		
8	888	0	−12	−4	0	−2	−1	0	−2		883	0	−9	−4	1	−1	−2	0	−1	
9	512	−2	−3	0	−2	0	−5	2	0	−8	510	−1	−2	−1	−3	0	−4	1	0	−8

CVPT6 eigenvalues of *trans*-HCOOH

Table D.4 Zero-point corrected vibrational term values (in cm^{-1}) of *trans*-HCOOH up to 4000 cm^{-1}. The vibrational states are computed with CVPT*n* on the TM-PES [21]. For details of the calculations, see Ref. [28]. The two leading squared coefficients (P, sixth-order) are shown together with deviations to lower orders of perturbation theory ($\Delta(n) = E(n) - E(6)$; $n = 2, 4$). Squared coefficients printed as "0.00" are below 0.5%.

					state 1		state 2							state 1		state 2	
No.	Γ	$E(6)$	Δ(4)	Δ(2)	P	Label	P	Label	No.	Γ	$E(6)$	Δ(4)	Δ(2)	P	Label	P	Label
2	A′	627.0	−0.1	0.6	1.00	7_1			56	A′	2772.8	−0.6	−4.7	0.93	$6_1 8_1 9_1$	0.06	$8_1 9_3$
3	A″	640.3	0.0	0.3	1.00	9_1			57	A″	2810.5	−0.3	−0.7	0.98	$3_1 8_1$	0.01	8_3
4	A″	1034.7	−0.4	−1.3	1.00	8_1	0.00	$7_1 9_1$	58	A″	2817.6	−4.2	−3.2	0.55	9_5	0.18	$6_2 9_1$
5	A′	1107.7	−0.2	−0.9	0.99	6_1	0.01	9_2	59	A′	2826.4	−1.0	−0.2	0.98	$6_2 7_1$	0.01	$6_1 7_1 9_2$
6	A′	1221.2	−0.4	−0.4	0.67	9_2	0.30	5_1	60	A′	2830.3	−1.0	−1.2	0.70	$8_1 9_3$	0.20	$5_1 8_1 9_1$
7	A′	1255.5	−0.4	1.3	1.00	7_2	0.00	9_2	61	A″	2835.5	−0.8	2.5	0.70	$6_2 9_1$	0.20	9_5
8	A″	1269.3	0.0	1.7	1.00	$7_1 9_1$	0.00	8_1	62	A′	2884.3	0.0	0.4	0.97	$3_1 6_1$	0.01	$5_1 6_1 7_1$
9	A′	1305.3	0.4	−0.8	0.69	5_1	0.28	9_2	63	A″	2884.6	−1.3	−2.0	0.62	$7_1 8_1 9_2$	0.34	$5_1 7_1 8_1$
10	A′	1379.5	0.1	0.4	0.95	4_1	0.04	9_2	64	A″	2894.0	1.2	15.1	0.62	$6_1 9_3$	0.20	$5_1 6_1 9_1$
11	A″	1661.4	−0.5	−0.4	1.00	$7_1 8_1$	0.00	$7_2 9_1$	65	A″	2919.4	−1.1	1.9	0.99	$7_3 8_1$	0.00	$7_1 8_1 9_2$
12	A′	1675.4	−0.3	−1.7	1.00	$8_1 9_1$	0.00	3_1	66	A′	2933.5	−0.2	2.6	0.85	$7_2 8_1 9_1$	0.05	$6_1 7_1 9_2$
13	A′	1732.5	−0.4	0.0	0.99	$6_1 7_1$	0.01	$7_1 9_2$	67	A′	2934.3	−3.1	−3.0	0.31	$6_1 7_1 9_2$	0.26	$7_1 9_4$
14	A″	1740.8	−0.3	−2.5	0.91	$6_1 9_1$	0.08	9_3	68	A′	2940.3	−0.1	0.5	0.90	2_1	0.03	$3_1 5_1$
15	A′	1782.6	0.0	0.5	0.98	3_1	0.01	$5_1 7_1$	69	A′	2964.3	0.8	11.5	0.45	$7_1 9_4$	0.23	$6_1 7_1 9_2$
16	A″	1793.2	−0.3	3.6	0.70	9_3	0.19	$5_1 9_1$	70	A″	2964.9	0.2	−1.3	0.64	$5_1 7_1 8_1$	0.32	$7_1 8_1 9_2$
17	A′	1849.9	−0.6	0.1	0.64	$7_1 9_2$	0.32	$5_1 7_1$	71	A′	2983.2	2.1	0.6	0.76	$5_1 8_1 9_1$	0.18	$8_1 9_3$
18	A′	1885.6	−0.9	2.2	0.99	7_3	0.00	$7_1 9_2$	72	A′	2986.1	−1.6	3.4	0.98	$6_1 7_3$	0.00	$7_3 9_2$
19	A″	1899.6	−0.1	3.3	1.00	$7_2 9_1$	0.00	$7_1 8_1$	73	A″	2996.2	−0.9	1.7	0.94	$6_1 7_2 9_1$	0.05	$7_2 9_3$
20	A′	1932.2	0.0	−1.0	0.66	$5_1 7_1$	0.30	$7_1 9_2$	74	A′	3002.3	−0.1	0.2	0.64	$3_1 9_2$	0.28	$3_1 5_1$
21	A″	1950.2	1.6	1.3	0.77	$5_1 9_1$	0.16	9_3	75	A′	3025.1	−0.2	−0.3	0.84	$3_1 7_2$	0.07	$5_1 6_1 7_1$
22	A′	2006.1	0.0	1.6	0.94	$4_1 7_1$	0.05	$7_1 9_2$	76	A′	3029.6	0.3	0.1	0.54	$5_1 6_1 7_1$	0.29	$6_1 7_1 9_2$
23	A″	2023.8	0.2	3.4	0.91	$4_1 9_1$	0.06	9_3	77	A″	3038.1	1.7	−1.9	0.50	$5_1 6_1 9_1$	0.14	$6_1 9_3$
24	A′	2065.7	−1.6	−3.1	1.00	8_2	0.00	3_1	78	A″	3040.4	1.0	2.1	0.44	$3_1 7_1 9_1$	0.19	$4_1 7_1 8_1$
25	A″	2138.8	−0.5	−2.3	0.99	$6_1 8_1$	0.01	$8_1 9_2$	79	A″	3044.3	−0.1	2.0	0.75	$4_1 7_1 8_1$	0.13	$3_1 7_1 9_1$
26	A′	2204.2	−0.5	−1.9	0.98	6_2	0.02	$6_1 9_2$	80	A″	3057.3	0.2	9.0	0.54	$7_2 9_3$	0.28	$3_1 7_1 9_1$
27	A″	2256.6	−1.1	−3.2	0.65	$8_1 9_2$	0.32	$5_1 8_1$	81	A′	3061.1	−0.5	1.8	0.92	$4_1 8_1 9_1$	0.06	$8_1 9_3$
28	A″	2289.7	−0.7	0.6	1.00	$7_2 8_1$	0.00	$8_1 9_2$	82	A″	3079.5	6.2	11.1	0.33	$5_1 9_3$	0.31	$5_2 9_1$
29	A′	2303.8	−0.2	0.3	0.92	$7_1 8_1 9_1$	0.03	9_4	83	A′	3086.7	0.4	0.1	0.65	$3_1 5_1$	0.29	$3_1 9_2$
30	A′	2304.8	−2.5	−4.5	0.34	9_4	0.32	$6_1 9_2$	84	A″	3093.6	−4.4	−6.3	0.99	8_3	0.01	$3_1 8_1$
31	A′	2337.9	0.0	8.0	0.41	9_4	0.28	$6_1 9_2$	85	A′	3103.2	0.0	1.6	0.93	$4_1 6_1 7_1$	0.04	$6_1 7_1 9_2$
32	A″	2338.4	0.5	−1.4	0.67	$5_1 8_1$	0.30	$8_1 9_2$	86	A′	3111.7	−2.2	−2.5	0.62	$7_3 9_2$	0.33	$5_1 7_3$
33	A′	2358.6	−0.9	1.4	0.99	$6_1 7_2$	0.01	$7_2 9_2$	87	A″	3116.7	0.2	0.9	0.71	$4_1 6_1 9_1$	0.11	$4_1 9_3$
34	A″	2368.0	−0.5	−0.6	0.93	$6_1 7_1 9_1$	0.06	$7_1 9_3$	88	A′	3135.1	−1.0	−4.9	0.51	$5_2 7_1$	0.30	$5_1 7_1 9_2$
35	A′	2402.4	0.1	−2.1	0.65	$3_1 7_1$	0.20	$5_1 6_1$	89	A′	3149.4	−2.4	5.8	0.98	7_5	0.01	$5_1 7_3$
36	A′	2405.0	0.4	0.2	0.43	$5_1 6_1$	0.32	$3_1 7_1$	90	A′	3160.4	0.5	1.0	0.91	$3_1 4_1$	0.04	$3_1 9_2$
37	A″	2415.6	−0.2	0.0	0.52	$4_1 8_1$	0.26	$3_1 9_1$	91	A″	3163.7	−0.8	7.9	0.99	$7_4 9_1$	0.01	$5_1 7_2 9_1$
38	A″	2418.4	0.0	2.1	0.43	$4_1 8_1$	0.23	$3_1 9_1$	92	A′	3166.2	−1.6	−4.2	0.98	$6_1 8_2$	0.01	$3_1 4_1$
39	A″	2427.5	0.1	5.0	0.50	$3_1 9_1$	0.38	$7_1 9_3$	93	A″	3170.6	−1.5	6.7	0.60	$4_1 9_3$	0.18	$4_1 5_1 9_1$
40	A′	2478.8	0.5	0.0	0.92	$4_1 6_1$	0.03	$6_1 9_2$	94	A′	3192.1	−1.4	−1.3	0.62	$5_1 7_3$	0.31	$7_3 9_2$
41	A′	2480.1	−1.4	−0.1	0.62	$7_2 9_2$	0.32	$5_1 7_2$	95	A″	3208.6	1.2	1.0	0.75	$5_1 7_2 9_1$	0.17	$7_2 9_3$
42	A′	2506.9	0.3	−2.0	0.52	5_2	0.31	$5_1 9_2$	96	A′	3225.7	−0.5	−0.6	0.56	$4_1 7_1 9_2$	0.34	$4_1 5_1 7_1$
43	A′	2516.9	−1.6	3.6	0.99	7_4	0.01	$5_1 7_2$	97	A″	3231.8	−0.8	−3.5	0.98	$6_2 8_1$	0.02	$6_1 8_1 9_2$
44	A″	2531.2	−0.4	5.3	1.00	$7_3 9_1$	0.00	$5_1 7_1 9_1$	98	A′	3235.3	1.6	−2.8	0.41	$5_1 7_1 9_2$	0.41	$5_2 7_1$
45	A′	2561.2	−0.5	−1.3	0.64	$5_1 7_2$	0.31	$7_2 9_2$	99	A″	3254.6	3.3	−1.9	0.57	$5_2 9_1$	0.24	$5_1 9_3$
46	A″	2578.5	1.5	1.2	0.76	$5_1 7_1 9_1$	0.17	$7_1 9_3$	100	A′	3264.1	−1.1	4.4	0.93	$4_1 7_3$	0.05	$7_3 9_2$
47	A′	2597.8	−0.5	−1.4	0.60	$4_1 9_2$	0.30	$4_1 5_1$	101	A″	3282.9	−0.1	7.3	0.90	$4_1 7_2 9_1$	0.07	$7_2 9_3$
48	A′	2607.5	2.4	−0.6	0.42	5_2	0.41	$5_1 9_2$	102	A′	3288.5	−3.2	−6.7	0.58	$8_2 9_2$	0.31	$5_1 8_2$
49	A′	2634.4	−0.4	2.9	0.94	$4_1 7_2$	0.05	$7_2 9_2$	103	A′	3289.5	−2.3	−2.9	0.87	6_3	0.04	$8_2 9_2$
50	A″	2652.7	0.2	5.2	0.91	$4_1 7_1 9_1$	0.07	$7_1 9_3$	104	A′	3295.1	−5.2	10.7	0.75	9_6	0.14	$5_1 9_4$
51	A′	2677.6	0.8	5.2	0.57	$4_1 5_1$	0.22	$4_1 9_2$	105	A′	3304.7	0.1	5.6	0.54	$4_1 5_1 7_1$	0.23	$4_1 7_1 9_2$
52	A′	2692.0	−1.7	−1.8	1.00	$7_1 8_2$	0.00	$3_1 7_1$	106	A′	3319.7	−2.0	−0.3	0.99	$7_2 8_2$	0.00	$8_2 9_2$
53	A″	2706.8	−1.6	−4.3	0.99	$8_2 9_1$	0.00	$3_1 8_1$	107	A″	3321.9	2.4	10.4	0.63	$4_1 5_1 9_1$	0.11	$4_2 9_1$
54	A′	2746.6	0.6	−2.3	0.84	4_2	0.11	$4_1 9_2$	108	A″	3334.5	−1.7	−1.2	0.98	$7_1 8_2 9_1$	0.00	$3_1 7_1 8_1$
55	A″	2763.2	−0.7	−1.0	0.99	$6_1 7_1 8_1$	0.01	$7_1 8_1 9_2$	109	A″	3340.0	−2.8	−9.9	0.40	$6_1 8_1 9_2$	0.26	$8_1 9_4$

continued

Table D.4 (continued)

					state 1		state 2							state 1		state 2	
No.	Γ	$E(6)$	Δ(4)	Δ(2)	P	Label	P	Label	No.	Γ	$E(6)$	Δ(4)	Δ(2)	P	Label	P	Label
110	A′	3367.6	−0.3	−2.6	0.65	$5_1 8_2$	0.31	$8_2 9_2$	164	A″	3712.7	1.3	6.2	0.55	$4_1 5_1 8_1$	0.24	$4_1 8_1 9_2$
111	A′	3373.0	0.7	−0.4	0.83	$4_2 7_1$	0.12	$4_1 7_1 9_2$	165	A″	3719.4	−4.4	−4.4	0.99	$7_1 8_3$	0.01	$3_1 7_1 8_1$
112	A″	3373.8	−1.1	2.9	0.49	$8_1 9_4$	0.19	$6_1 8_1 9_2$	166	A′	3729.1	−0.5	3.3	0.91	$4_1 6_1 7_2$	0.04	$6_1 7_2 9_2$
113	A′	3386.2	−1.9	2.5	0.36	$6_1 9_4$	0.31	$6_2 9_2$	167	A″	3732.1	2.3	4.3	0.74	$3_1 5_1 9_1$	0.15	$3_1 9_3$
114	A″	3389.0	−1.1	0.8	0.98	$6_1 7_2 8_1$	0.01	$7_2 8_1 9_2$	168	A″	3733.0	−7.4	29.3	0.82	9_7	0.13	$5_1 9_5$
115	A″	3396.2	0.9	2.9	0.76	$4_2 9_1$	0.14	$4_1 9_3$	169	A′	3735.1	−4.5	−8.1	0.98	$8_3 9_1$	0.01	$3_1 8_1 9_1$
116	A′	3399.2	−0.7	−2.0	0.94	$6_1 7_1 8_1 9_1$	0.05	$7_1 8_1 9_3$	170	A″	3743.8	0.0	3.3	0.71	$4_1 6_1 7_1 9_1$	0.10	$4_1 7_1 9_3$
117	A″	3430.6	−0.2	−2.0	0.84	$3_1 7_1 8_1$	0.07	$5_1 6_1 8_1$	171	A′	3744.4	−3.2	−6.4	0.61	$7_4 9_2$	0.31	$5_1 7_4$
118	A′	3433.3	0.7	14.9	0.39	$6_1 9_4$	0.26	$6_2 9_2$	172	A′	3765.9	−3.0	−9.4	0.47	$5_2 7_2$	0.28	$5_1 7_2 9_2$
119	A″	3433.8	0.8	−1.3	0.54	$5_1 6_1 8_1$	0.29	$6_1 8_1 9_2$	173	A′	3769.6	−0.4	−2.0	0.47	$4_1 5_1 6_1$	0.25	$4_1 6_1 9_2$
120	A′	3446.7	−0.8	−1.7	0.63	$3_1 8_1 9_1$	0.21	$4_1 8_2$	174	A′	3780.7	0.5	2.8	0.87	$3_1 4_1 7_1$	0.04	$3_1 7_1 9_2$
121	A″	3447.7	−4.4	−1.3	0.43	$7_1 9_5$	0.31	$6_2 7_1 9_1$	175	A′	3782.7	−3.5	8.8	0.96	7_6	0.03	$5_1 7_4$
122	A′	3449.7	−1.7	3.0	0.97	$6_2 7_2$	0.01	$6_1 7_2 9_2$	176	A″	3784.7	0.0	−3.0	0.82	$4_2 8_1$	0.09	$4_1 8_1 9_2$
123	A′	3452.2	−1.5	−1.9	0.74	$4_1 8_2$	0.16	$3_1 8_1 9_1$	177	A′	3785.4	−1.1	−8.6	0.62	5_3	0.14	$5_1 9_4$
124	A′	3460.9	−0.6	2.8	0.59	$7_1 8_1 9_3$	0.18	$3_1 8_1 9_1$	178	A′	3790.0	−1.8	−2.4	0.98	$6_1 7_1 8_2$	0.01	$7_1 8_2 9_2$
125	A″	3461.1	−0.9	9.1	0.58	$6_2 7_1 9_1$	0.31	$7_1 9_5$	179	A″	3796.5	−0.3	6.6	0.41	$4_1 7_1 9_3$	0.21	$3_1 4_1 9_1$
126	A′	3491.3	1.2	−3.3	0.56	$5_1 6_2$	0.35	$6_2 9_2$	180	A″	3797.1	−1.3	11.2	0.97	$7_5 9_1$	0.02	$5_1 7_3 9_1$
127	A′	3502.9	−0.2	1.5	0.94	$3_1 6_1 7_1$	0.02	$5_1 6_1 7_2$	181	A″	3800.9	−1.6	−7.4	0.92	$6_1 8_2 9_1$	0.04	$8_2 9_3$
128	A″	3511.3	0.3	−0.4	0.54	$4_1 6_1 8_1$	0.23	$3_1 6_1 9_1$	182	A″	3806.9	0.4	7.1	0.67	$3_1 4_1 9_1$	0.18	$4_1 7_1 9_3$
129	A″	3513.8	1.2	2.3	0.23	$4_1 6_1 8_1$	0.23	$7_2 8_1 9_2$	183	A′	3824.6	−2.5	−0.9	0.60	$5_1 7_4$	0.30	$7_4 9_2$
130	A″	3514.1	−2.0	−1.9	0.38	$7_2 8_1 9_2$	0.21	$5_1 7_2 8_1$	184	A′	3834.7	−1.6	−2.8	0.84	$3_1 8_2$	0.10	$4_2 6_1$
131	A″	3522.6	1.5	18.4	0.39	$3_1 6_1 9_1$	0.39	$6_1 7_1 9_3$	185	A′	3834.8	2.0	1.3	0.72	$4_2 6_1$	0.12	$3_1 8_2$
132	A″	3538.5	0.1	−2.5	0.54	$5_2 8_1$	0.29	$5_1 8_1 9_2$	186	A″	3840.5	0.7	0.9	0.73	$5_1 7_3 9_1$	0.16	$7_3 9_3$
133	A′	3544.9	0.1	2.7	0.94	3_2	0.02	$3_1 5_1 7_1$	187	A″	3853.5	−1.2	−1.3	0.98	$6_2 7_1 8_1$	0.01	$6_1 7_1 8_1 9_2$
134	A″	3550.3	−1.8	3.8	0.98	$7_4 8_1$	0.01	$5_1 7_2 8_1$	188	A′	3854.3	−3.4	−10.5	0.51	$6_2 8_1 9_1$	0.24	$8_1 9_5$
135	A′	3564.0	−3.8	−2.6	0.31	$6_1 7_2 9_2$	0.18	$7_2 9_4$	189	A′	3855.1	−1.1	−0.8	0.51	$4_1 7_2 9_2$	0.37	$4_1 5_1 7_2$
136	A′	3564.5	−0.7	5.2	0.85	$7_3 8_1 9_1$	0.05	$6_1 7_2 9_2$	190	A″	3864.0	−3.1	−6.8	0.70	$8_2 9_3$	0.21	$5_1 8_2 9_1$
137	A′	3565.2	1.6	1.6	0.66	$4_1 6_2$	0.09	$5_2 6_1$	191	A′	3866.0	0.1	−5.9	0.40	$5_2 7_2$	0.40	$5_1 7_2 9_2$
138	A′	3567.8	0.0	1.6	0.83	$2_1 7_1$	0.03	$3_1 5_1 7_1$	192	A′	3868.0	−1.7	−1.5	0.31	$8_1 9_5$	0.27	$6_2 8_1 9_1$
139	A″	3570.2	0.0	2.5	0.52	$3_1 9_3$	0.20	$3_1 5_1 9_1$	193	A′	3872.8	0.7	−1.6	0.36	$4_1 5_2$	0.16	$8_1 9_5$
140	A′	3576.2	−0.5	−2.8	0.54	1_1	0.13	$4_1 6_2$	194	A″	3883.9	2.5	−4.9	0.56	$5_2 7_1 9_1$	0.23	$5_1 7_1 9_3$
141	A″	3581.4	0.1	1.2	0.74	$2_1 9_1$	0.16	$3_1 9_3$	195	A″	3890.2	−3.6	3.1	0.49	$6_1 9_5$	0.18	$6_3 9_1$
142	A′	3581.8	1.2	1.3	0.43	1_1	0.14	$5_1 9_4$	196	A′	3895.2	−2.1	6.4	0.91	$4_1 7_4$	0.06	$7_4 9_2$
143	A′	3591.7	1.7	14.2	0.47	$7_2 9_4$	0.20	$6_1 7_2 9_2$	197	A″	3908.7	−0.2	−1.1	0.96	$3_1 6_1 8_1$	0.01	$5_1 6_1 7_1 8_1$
144	A″	3593.4	−0.3	−1.0	0.62	$5_1 7_2 8_1$	0.33	$7_2 8_1 9_2$	198	A′	3908.8	−1.9	−0.1	0.50	$6_3 7_1$	0.19	$5_2 9_2$
145	A′	3610.9	2.0	1.0	0.75	$5_1 7_1 8_1 9_1$	0.18	$7_1 8_1 9_3$	199	A′	3908.9	2.4	−8.4	0.46	$6_3 7_1$	0.21	$5_2 9_2$
146	A′	3614.5	−2.6	5.8	0.88	$6_1 7_4$	0.03	$5_2 6_1$	200	A″	3914.4	−0.7	9.6	0.89	$4_1 7_3 9_1$	0.07	$7_3 9_3$
147	A′	3615.0	6.1	10.2	0.30	$5_2 6_1$	0.20	$5_1 9_4$	201	A′	3915.5	−3.5	−4.7	0.60	$7_1 8_2 9_2$	0.35	$5_1 7_1 8_2$
148	A″	3625.2	−1.5	4.5	0.94	$6_1 7_3 9_1$	0.03	$7_3 9_3$	202	A″	3918.8	−0.8	9.5	0.67	$6_3 9_1$	0.21	$6_1 9_5$
149	A′	3626.0	−0.3	3.7	0.59	$3_1 7_1 9_2$	0.29	$3_1 5_1 7_1$	203	A′	3924.7	−4.8	21.9	0.50	$7_1 9_6$	0.24	$6_1 8_1 9_3$
150	A″	3635.5	−1.2	−4.2	0.58	$4_1 8_1 9_2$	0.33	$4_1 5_1 8_1$	204	A′	3928.5	−0.7	9.6	0.37	$6_1 8_1 9_3$	0.27	$7_1 9_6$
151	A″	3637.9	4.2	1.3	0.43	$5_1 8_1 9_2$	0.41	$5_2 8_1$	205	A′	3934.1	−1.0	5.7	0.50	$4_1 5_1 7_2$	0.23	$4_1 7_2 9_2$
152	A′	3649.3	−0.5	1.7	0.89	$3_1 7_3$	0.03	$5_1 6_1 7_2$	206	A′	3948.8	−2.5	1.7	0.98	$7_3 8_2$	0.01	$7_1 8_2 9_2$
153	A′	3656.0	−0.2	0.8	0.57	$5_1 6_1 7_2$	0.31	$6_1 7_2 9_2$	207	A″	3950.7	1.6	9.2	0.61	$4_1 5_1 7_1 9_1$	0.12	$4_2 7_1 9_1$
154	A″	3664.3	0.7	−1.8	0.54	$3_1 7_2 9_1$	0.20	$5_1 6_1 7_1 9_1$	208	A″	3954.3	−0.7	−1.7	0.92	$2_1 8_1$	0.03	$4_2 8_1$
155	A″	3666.6	1.8	3.5	0.41	$5_1 6_1 7_1 9_1$	0.19	$3_1 7_2 9_1$	209	A″	3963.4	−1.9	1.8	0.97	$7_2 8_2 9_1$	0.01	$7_3 8_1 9_2$
156	A′	3670.1	2.2	3.0	0.33	$4_1 6_1 9_2$	0.32	$4_1 9_4$	210	A′	3965.3	3.0	−3.0	0.53	$4_2 5_1$	0.16	$4_2 9_2$
157	A″	3672.0	−0.4	2.7	0.86	$4_1 7_2 8_1$	0.06	$3_1 7_2 9_1$	211	A″	3967.8	−3.4	−6.1	0.42	$6_1 7_1 8_1 9_2$	0.24	$5_1 6_1 7_1 8_1$
158	A″	3688.4	0.3	12.2	0.61	$7_3 9_3$	0.19	$3_1 7_2 9_1$	212	A′	3974.5	−0.2	0.6	0.94	$3_1 6_2$	0.02	$5_1 6_2 7_1$
159	A′	3689.5	−0.5	3.9	0.91	$4_1 7_1 8_1 9_1$	0.06	$7_1 8_1 9_3$	213	A′	3977.3	−0.8	6.5	0.31	$4_2 9_2$	0.24	$4_1 5_2$
160	A′	3698.0	3.2	−5.8	0.40	$5_1 6_1 9_2$	0.32	$5_2 6_1$	214	A″	3983.6	1.9	25.0	0.57	$6_2 9_3$	0.21	$5_1 6_2 9_1$
161	A″	3706.7	5.6	10.1	0.32	$5_1 7_1 9_3$	0.31	$5_2 7_1 9_1$	215	A′	3993.5	−0.6	−1.9	0.63	$5_1 7_1 8_2$	0.33	$7_1 8_2 9_2$
162	A′	3707.7	0.2	−0.3	0.59	$3_1 5_1 7_1$	0.30	$3_1 7_1 9_2$	216	A″	3999.5	−0.4	6.4	0.50	$7_1 8_1 9_4$	0.15	$6_1 7_1 8_1 9_2$
163	A′	3712.0	−2.6	8.2	0.36	$4_1 9_4$	0.24	$4_1 5_1 6_1$									

CVPT6 eigenvalues of *trans*-DCOOH

Table D.5 Zero-point corrected vibrational term values (in cm^{-1}) of *trans*-DCOOH up to 3700 cm^{-1}. The vibrational states are computed with CVPT*n* on the TM-PES [21]. For details of the calculations, see Ref. [28]. The two leading squared coefficients (P, sixth-order) are shown together with deviations to lower orders of perturbation theory ($\Delta(n) = E(n) - E(6)$; $n = 2, 4$). Squared coefficients printed as "0.00" are below 0.5%.

					state 1		state 2							state 1		state 2	
No.	Γ	$E(6)$	Δ(4)	Δ(2)	P	Label	P	Label	No.	Γ	$E(6)$	Δ(4)	Δ(2)	P	Label	P	Label
2	A′	621.1	−0.1	0.4	1.00	7_1			57	A″	2560.6	0.8	2.5	0.74	$5_1 7_1 9_1$	0.22	$7_1 9_3$
3	A″	630.7	0.1	0.2	1.00	9_1			58	A″	2567.1	0.3	−0.9	0.99	$4_2 9_1$	0.00	$4_1 9_3$
4	A″	874.8	−0.1	−0.7	1.00	8_1			59	A″	2588.3	−1.3	−3.7	0.57	8_3	0.42	$3_1 8_1$
5	A′	971.4	0.0	−0.5	1.00	4_1	0.00	9_2	60	A′	2593.5	0.7	−0.8	0.48	5_2	0.36	$5_1 9_2$
6	A′	1144.7	0.0	−0.5	0.99	6_1	0.01	9_2	61	A″	2634.6	−0.4	0.0	0.99	$6_1 7_1 8_1$	0.00	$7_1 8_1 9_2$
7	A′	1206.3	−0.1	−0.3	0.71	9_2	0.28	5_1	62	A′	2640.8	−0.2	−0.3	0.67	$6_1 8_1 9_1$	0.20	$8_1 9_3$
8	A′	1243.8	−0.4	0.8	1.00	7_2	0.00	9_2	63	A″	2647.1	−0.9	0.4	0.57	$3_1 8_1$	0.43	8_3
9	A″	1254.2	0.0	1.3	1.00	$7_1 9_1$			64	A′	2661.9	0.6	−0.5	0.44	$8_1 9_3$	0.31	$6_1 8_1 9_1$
10	A′	1299.3	−0.1	−0.6	0.71	5_1	0.28	9_2	65	A′	2700.8	−0.5	−1.3	0.56	$4_1 8_2$	0.43	$3_1 4_1$
11	A″	1495.7	−0.2	0.0	1.00	$7_1 8_1$	0.00	$4_1 9_1$	66	A″	2709.5	−0.3	−0.7	0.60	$7_1 8_1 9_2$	0.35	$5_1 7_1 8_1$
12	A′	1509.4	−0.1	−0.7	0.99	$8_1 9_1$	0.01	5_1	67	A′	2723.5	−0.2	−0.5	0.95	$4_1 6_1 7_1$	0.03	$2_1 7_1$
13	A′	1592.9	0.0	0.3	1.00	$4_1 7_1$	0.00	$8_1 9_1$	68	A″	2724.2	0.6	−0.8	0.54	$4_1 6_1 9_1$	0.34	$4_1 9_3$
14	A″	1602.1	0.1	−0.4	1.00	$4_1 9_1$	0.00	9_3	69	A′	2735.8	−0.1	0.0	0.56	$3_1 4_1$	0.43	$4_1 8_2$
15	A′	1731.3	−0.4	−1.4	0.59	8_2	0.41	3_1	70	A″	2740.8	−0.5	1.6	0.42	$4_1 6_1 9_1$	0.39	$4_1 9_3$
16	A″	1757.4	0.5	1.1	0.48	9_3	0.40	$6_1 9_1$	71	A″	2741.8	−0.8	2.0	0.99	$7_3 8_1$	0.00	$7_1 8_1 9_2$
17	A′	1761.7	−0.3	0.1	0.97	$6_1 7_1$	0.02	8_2	72	A′	2756.7	−0.2	2.7	0.98	$7_2 8_1 9_1$	0.01	$5_1 7_2$
18	A′	1766.3	−0.2	0.3	0.58	3_1	0.40	8_2	73	A″	2790.5	2.4	9.5	0.72	9_5	0.16	$5_1 9_3$
19	A″	1779.4	−0.4	−0.3	0.60	$6_1 9_1$	0.30	9_3	74	A″	2794.7	−0.7	−1.0	0.61	$5_1 7_1 8_1$	0.35	$7_1 8_1 9_2$
20	A′	1829.7	−0.3	0.5	0.69	$7_1 9_2$	0.30	$5_1 7_1$	75	A′	2798.8	−0.2	0.5	0.65	$4_1 7_1 9_2$	0.30	$4_1 5_1 7_1$
21	A″	1845.7	−0.1	−1.0	1.00	$4_1 8_1$	0.00	$8_1 9_2$	76	A″	2810.4	0.2	−1.7	1.00	$4_2 8_1$	0.00	$2_1 8_1$
22	A′	1867.9	−0.9	1.4	1.00	7_3	0.00	$7_1 9_2$	77	A′	2811.5	0.3	2.5	0.66	$5_1 8_1 9_1$	0.22	$8_1 9_3$
23	A″	1879.0	−0.1	2.6	1.00	$7_2 9_1$	0.00	9_3	78	A′	2839.0	−0.2	1.5	0.66	$2_1 7_1$	0.24	$4_1 7_3$
24	A′	1921.3	−0.5	−1.5	0.68	$5_1 7_1$	0.30	$7_1 9_2$	79	A′	2840.7	−0.6	2.5	0.75	$4_1 7_3$	0.21	$2_1 7_1$
25	A′	1936.4	0.2	−1.1	1.00	4_2	0.00	2_1	80	A″	2845.7	0.3	0.4	0.87	$2_1 9_1$	0.06	$6_2 9_1$
26	A″	1936.5	0.8	3.2	0.75	$5_1 9_1$	0.21	9_3	81	A″	2851.0	0.1	3.1	0.99	$4_1 7_2 9_1$	0.01	$2_1 9_1$
27	A″	2017.7	−0.2	−0.9	0.99	$6_1 8_1$	0.01	$8_1 9_2$	82	A′	2870.1	−0.5	−1.0	0.53	$6_1 8_2$	0.45	$3_1 6_1$
28	A″	2086.9	0.0	−1.7	0.62	$8_1 9_2$	0.33	$5_1 8_1$	83	A″	2885.0	−0.1	1.4	0.49	$6_1 9_3$	0.32	$6_2 9_1$
29	A′	2106.4	0.0	−2.1	0.96	$4_1 6_1$	0.03	2_1	84	A′	2891.2	−0.5	−1.7	0.61	$4_1 5_1 7_1$	0.26	$4_1 7_1 9_2$
30	A″	2118.1	−0.4	0.9	1.00	$7_2 8_1$	0.00	$8_1 9_2$	85	A′	2895.3	0.4	−1.8	0.97	4_3	0.01	$4_1 5_1 7_1$
31	A′	2132.5	−0.1	0.8	0.99	$7_1 8_1 9_1$	0.01	$5_1 7_1$	86	A′	2896.6	−0.4	−0.1	0.82	$6_2 7_1$	0.06	$2_1 7_1$
32	A″	2172.7	−0.3	−0.9	0.64	$5_1 8_1$	0.33	$8_1 9_2$	87	A′	2905.8	−0.3	−0.8	0.51	$3_1 6_1$	0.44	$6_1 8_2$
33	A′	2175.0	−0.1	−0.5	0.67	$4_1 9_2$	0.29	$4_1 5_1$	88	A″	2907.8	0.7	1.3	0.72	$4_1 5_1 9_1$	0.21	$4_1 9_3$
34	A′	2215.8	−0.3	1.1	0.96	$4_1 7_2$	0.03	2_1	89	A′	2917.1	0.7	6.7	0.64	$7_1 9_4$	0.17	$5_1 7_1 9_2$
35	A′	2218.4	0.2	1.0	0.84	2_1	0.04	6_2	90	A″	2917.4	−1.7	−3.4	0.61	$6_2 9_1$	0.25	$6_1 9_3$
36	A″	2225.9	0.2	1.2	1.00	$4_1 7_1 9_1$	0.00	$7_1 9_3$	91	A′	2942.4	−0.2	−0.3	0.37	$3_1 9_2$	0.22	$8_2 9_2$
37	A′	2269.2	−0.2	−1.0	0.68	$4_1 5_1$	0.25	$4_1 9_2$	92	A′	2962.5	−1.1	0.9	0.59	$6_1 7_1 9_2$	0.28	$5_1 6_1 7_1$
38	A′	2282.2	0.4	−0.5	0.76	6_2	0.10	9_4	93	A′	2969.4	−0.8	0.6	0.51	$3_1 7_2$	0.43	$7_2 8_2$
39	A′	2292.6	0.5	2.6	0.58	9_4	0.16	6_2	94	A′	2977.3	−0.3	−1.6	0.29	$3_1 9_2$	0.29	$8_2 9_2$
40	A′	2344.5	−1.1	−1.5	0.60	$6_1 9_2$	0.27	$5_1 6_1$	95	A″	2977.8	−0.1	−1.8	0.95	$4_1 6_1 8_1$	0.04	$2_1 8_1$
41	A′	2349.9	−0.6	−0.5	0.50	$7_1 8_2$	0.45	$3_1 7_1$	96	A″	2985.1	−0.3	1.1	0.57	$3_1 7_1 9_1$	0.36	$7_1 8_2 9_1$
42	A″	2365.3	−0.2	−0.5	0.51	$3_1 9_1$	0.42	$8_2 9_1$	97	A′	2999.9	−1.5	1.9	0.97	$6_1 7_3$	0.02	$7_2 8_2$
43	A′	2380.1	−0.7	0.9	0.96	$6_1 7_2$	0.03	$7_1 8_2$	98	A′	3003.5	−0.4	1.9	0.53	$7_2 8_2$	0.45	$3_1 7_2$
44	A″	2381.5	0.2	1.5	0.51	$6_1 7_1 9_1$	0.34	$7_1 9_3$	99	A″	3005.5	−0.2	2.1	0.67	$6_1 7_2 9_1$	0.21	$7_2 9_3$
45	A′	2384.0	−0.3	1.0	0.51	$3_1 7_1$	0.46	$7_1 8_2$	100	A″	3018.1	0.0	2.5	0.34	$7_1 8_2 9_1$	0.20	$3_1 7_1 9_1$
46	A″	2397.8	−0.1	0.9	0.34	$6_1 7_1 9_1$	0.21	$8_2 9_1$	101	A″	3026.3	0.0	6.5	0.37	$7_2 9_3$	0.21	$3_1 7_1 9_1$
47	A″	2403.2	−0.2	2.4	0.30	$3_1 9_1$	0.28	$8_2 9_1$	102	A′	3027.8	−0.3	−1.1	0.30	$3_1 5_1$	0.30	$5_1 8_2$
48	A′	2431.1	0.1	−1.2	0.67	$5_1 6_1$	0.28	$6_1 9_2$	103	A″	3030.6	3.8	13.9	0.36	$5_1 9_3$	0.23	$5_2 9_1$
49	A′	2454.7	−0.8	0.4	0.67	$7_2 9_2$	0.31	$5_1 7_2$	104	A′	3049.4	−0.4	−2.0	0.64	$5_1 6_1 7_1$	0.30	$6_1 7_1 9_2$
50	A″	2467.1	−0.1	0.0	1.00	$4_1 7_1 8_1$	0.00	$8_2 9_1$	105	A″	3054.0	0.1	−1.2	0.55	$4_1 8_1 9_2$	0.33	$4_1 5_1 8_1$
51	A′	2480.0	−0.1	−1.0	0.94	$4_1 8_1 9_1$	0.02	5_2	106	A′	3062.8	−0.1	−4.8	0.92	$4_2 6_1$	0.07	$2_1 4_1$
52	A′	2485.1	0.0	−0.4	0.46	5_2	0.29	$5_1 9_2$	107	A′	3063.2	−0.3	−0.6	0.38	$3_1 5_1$	0.24	$5_1 8_2$
53	A′	2493.3	−1.5	2.2	0.99	7_4	0.00	$5_1 7_2$	108	A″	3071.9	0.7	−0.2	0.61	$5_1 6_1 9_1$	0.18	$6_1 9_3$
54	A″	2505.0	−0.3	4.2	1.00	$7_3 9_1$	0.00	$5_1 7_1 9_1$	109	A′	3081.1	−1.6	−0.7	0.66	$7_3 9_2$	0.31	$5_1 7_3$
55	A′	2545.6	−1.2	−2.6	0.67	$5_1 7_2$	0.32	$7_2 9_2$	110	A″	3082.8	0.0	0.1	0.84	$2_1 8_1$	0.06	$4_1 8_1 9_2$
56	A′	2558.5	0.2	0.1	0.99	$4_2 7_1$	0.00	$2_1 7_1$	111	A″	3090.0	−0.3	1.3	0.99	$4_1 7_2 8_1$	0.00	$2_1 8_1$

continued

Table D.5 (continued)

					state 1		state 2							state 1		state 2	
No.	Γ	$E(6)$	Δ(4)	Δ(2)	P	Label	P	Label	No.	Γ	$E(6)$	Δ(4)	Δ(2)	P	Label	P	Label
112	A′	3103.5	−0.1	0.5	0.94	$4_1 7_1 8_1 9_1$	0.02	$5_2 7_1$	166	A″	3462.4	0.3	−0.6	0.42	$5_2 8_1$	0.31	$5_1 8_1 9_2$
113	A′	3108.7	−1.0	−3.1	0.46	$5_2 7_1$	0.28	$5_1 7_1 9_2$	167	A′	3466.2	−1.8	3.8	0.95	$4_1 7_4$	0.02	$2_1 7_2$
114	A′	3119.9	−2.5	3.6	0.99	7_5	0.00	$5_1 7_3$	168	A″	3469.0	0.4	1.7	0.85	$2_1 7_1 9_1$	0.08	$6_2 7_1 9_1$
115	A″	3132.1	−0.7	6.3	1.00	$7_4 9_1$	0.00	$5_1 7_2 9_1$	169	A″	3477.3	−0.3	5.3	0.98	$4_1 7_3 9_1$	0.01	$2_1 7_1 9_1$
116	A′	3137.8	0.2	−0.9	0.64	$4_2 9_2$	0.29	$4_2 5_1$	170	A′	3479.1	−2.7	−5.5	0.45	$6_2 9_2$	0.26	$5_1 6_2$
117	A″	3142.1	−0.3	−1.2	0.62	$4_1 5_1 8_1$	0.32	$4_1 8_1 9_2$	171	A′	3484.1	−1.3	−0.7	0.73	3_2	0.25	8_4
118	A″	3154.1	−0.2	−1.6	0.91	$6_2 8_1$	0.04	$2_1 8_1$	172	A′	3485.0	−0.9	−0.1	0.46	$3_1 6_1 7_1$	0.44	$6_1 7_1 8_2$
119	A′	3171.9	−2.2	−3.6	0.65	$5_1 7_3$	0.32	$7_3 9_2$	173	A″	3492.1	0.0	1.5	0.40	$3_1 6_1 9_1$	0.22	$6_1 8_2 9_1$
120	A′	3177.2	0.6	1.9	0.79	$2_1 4_1$	0.07	$4_2 6_1$	174	A″	3505.4	−0.2	2.7	0.39	$6_1 7_1 9_3$	0.34	$6_2 7_1 9_1$
121	A′	3181.9	−0.1	1.5	0.97	$4_2 7_2$	0.01	$2_1 4_1$	175	A′	3510.6	−1.5	−0.2	0.83	$6_2 7_2$	0.05	$2_1 7_2$
122	A″	3182.2	0.9	2.2	0.59	$8_1 9_4$	0.12	$5_1 8_1 9_2$	176	A″	3514.0	0.0	1.4	0.38	$3_1 9_3$	0.26	$6_1 8_2 9_1$
123	A″	3186.7	0.5	1.8	0.71	$5_1 7_2 9_1$	0.21	$7_2 9_3$	177	A′	3516.0	−0.7	−0.8	0.53	$4_1 5_1 7_2$	0.23	$4_1 7_2 9_2$
124	A″	3191.4	0.5	1.2	0.98	$4_2 7_1 9_1$	0.01	$5_1 7_2 9_1$	178	A′	3519.3	0.0	0.7	0.63	$4_3 7_1$	0.12	$6_1 7_1 8_2$
125	A″	3206.3	−1.5	−2.3	0.53	$7_1 8_3$	0.45	$3_1 7_1 8_1$	179	A′	3520.3	0.0	0.1	0.36	$6_1 7_1 8_2$	0.33	$3_1 6_1 7_1$
126	A′	3217.9	−0.2	−3.2	0.46	$5_2 7_1$	0.36	$5_1 7_1 9_2$	180	A″	3527.0	0.6	−0.7	0.90	$4_3 9_1$	0.03	$4_1 5_1 7_1 9_1$
127	A″	3223.8	−1.3	−3.3	0.51	$6_1 8_1 9_2$	0.32	$5_1 6_1 8_1$	181	A″	3529.6	−0.6	−0.7	0.22	$6_2 7_1 9_1$	0.21	$3_1 6_1 9_1$
128	A′	3226.6	−1.0	−2.7	0.47	$3_1 8_1 9_1$	0.47	$8_3 9_1$	182	A′	3531.0	−1.6	1.9	0.53	$3_1 8_2$	0.31	8_4
129	A′	3231.6	−0.1	−2.3	0.52	$4_2 5_1$	0.16	$4_2 9_2$	183	A″	3532.3	1.1	1.4	0.62	$4_1 5_1 7_1 9_1$	0.19	$4_1 7_1 9_3$
130	A′	3235.4	0.4	−0.7	0.71	$4_1 6_2$	0.08	9_6	184	A″	3533.6	−1.3	1.6	0.31	$6_2 7_1 9_1$	0.21	$6_1 7_1 9_3$
131	A″	3236.0	4.1	6.3	0.48	$5_2 9_1$	0.34	$5_1 9_3$	185	A′	3541.1	6.8	37.8	0.28	$5_1 9_4$	0.14	$5_2 9_2$
132	A′	3242.2	1.4	15.5	0.35	9_6	0.17	$4_2 5_1$	186	A′	3542.6	0.6	8.4	0.59	$7_2 9_4$	0.17	$5_1 7_2 9_2$
133	A″	3252.8	−0.8	1.1	0.98	$6_1 7_2 8_1$	0.00	$3_1 7_1 8_1$	187	A″	3553.6	0.2	−1.8	0.31	$8_2 9_3$	0.15	$5_1 8_2 9_1$
134	A′	3262.2	−0.5	0.6	0.78	$6_1 7_1 8_1 9_1$	0.12	$7_1 8_1 9_3$	188	A″	3557.1	−1.5	−3.2	0.55	$4_1 8_3$	0.43	$3_1 4_1 8_1$
135	A″	3264.4	−1.0	1.7	0.52	$3_1 7_1 8_1$	0.46	$7_1 8_3$	189	A′	3557.9	0.2	−6.3	0.42	$5_1 6_2$	0.20	$6_2 9_2$
136	A′	3277.0	3.6	5.4	0.39	$4_1 9_4$	0.28	9_6	190	A′	3563.0	−0.4	2.0	0.34	$3_1 7_1 9_2$	0.18	$3_1 5_1 7_1$
137	A′	3280.8	0.1	0.9	0.30	$7_1 8_1 9_3$	0.18	$8_3 9_1$	191	A′	3566.4	2.4	−7.7	0.24	$4_1 5_2$	0.23	$4_1 5_1 9_2$
138	A′	3288.2	−0.2	1.9	0.33	$3_1 8_1 9_1$	0.29	$8_3 9_1$	192	A′	3569.9	0.1	−2.0	0.86	1_1	0.05	$4_1 5_2$
139	A″	3303.6	−0.7	−1.8	0.61	$5_1 6_1 8_1$	0.33	$6_1 8_1 9_2$	193	A′	3582.1	−1.6	2.7	0.58	$6_1 7_2 9_2$	0.28	$5_1 6_1 7_2$
140	A′	3304.3	−0.9	−0.8	0.58	$4_1 6_1 9_2$	0.25	$4_1 5_1 6_1$	194	A′	3589.9	−1.2	1.9	0.56	$3_1 7_3$	0.37	$7_3 8_2$
141	A′	3319.6	−0.6	−0.2	0.49	$3_1 4_1 7_1$	0.49	$4_1 7_1 8_2$	195	A′	3597.8	−0.6	−0.1	0.30	$7_1 8_2 9_2$	0.27	$5_1 7_1 8_2$
142	A″	3333.6	−0.9	−0.7	0.57	$7_2 8_1 9_2$	0.36	$5_1 7_2 8_1$	196	A″	3598.9	0.0	0.8	0.99	$4_1 6_1 7_1 8_1$	0.00	$4_1 7_1 8_1 9_2$
143	A″	3334.5	−0.2	−0.6	0.51	$3_1 4_1 9_1$	0.40	$4_1 8_2 9_1$	197	A″	3605.9	−0.5	2.8	0.61	$3_1 7_2 9_1$	0.31	$7_2 8_2 9_1$
144	A′	3341.8	−0.7	1.2	0.95	$4_1 6_1 7_2$	0.03	$2_1 7_2$	198	A′	3607.1	0.0	−1.3	0.76	$4_1 6_1 8_1 9_1$	0.13	$4_1 8_1 9_3$
145	A″	3347.3	0.3	0.2	0.70	$4_1 6_1 7_1 9_1$	0.17	$4_1 7_1 9_3$	199	A′	3615.1	−1.5	−3.7	0.45	$5_2 6_1$	0.22	$5_1 6_1 9_2$
146	A′	3352.3	0.6	1.4	0.64	$2_1 6_1$	0.14	6_3	200	A″	3616.3	−1.0	0.0	0.56	$3_1 4_1 8_1$	0.44	$4_1 8_3$
147	A′	3354.4	0.1	1.1	0.44	$3_1 4_1 7_1$	0.44	$4_1 7_1 8_2$	201	A′	3620.9	−2.6	3.2	0.97	$6_1 7_4$	0.02	$7_3 8_2$
148	A″	3360.3	0.2	−2.0	0.49	$5_2 8_1$	0.19	$5_1 8_1 9_2$	202	A′	3624.6	−0.6	3.6	0.60	$7_3 8_2$	0.38	$3_1 7_3$
149	A″	3362.0	0.0	4.3	0.45	$4_1 7_1 9_3$	0.22	$4_1 6_1 7_1 9_1$	203	A′	3627.7	1.5	1.8	0.48	$4_1 8_1 9_3$	0.22	$4_1 6_1 8_1 9_1$
150	A″	3366.8	−1.3	3.7	0.99	$7_4 8_1$	0.00	$5_1 7_2 8_1$	204	A″	3629.3	−0.8	3.5	0.82	$6_1 7_3 9_1$	0.10	$7_3 9_3$
151	A″	3371.6	−0.1	1.5	0.45	$4_1 8_2 9_1$	0.42	$3_1 4_1 9_1$	205	A″	3640.0	0.1	4.5	0.47	$7_2 8_2 9_1$	0.20	$3_1 7_2 9_1$
152	A′	3382.0	−0.3	5.0	0.98	$7_3 8_1 9_1$	0.01	$5_1 7_3$	206	A′	3647.1	−0.7	−0.9	0.33	$3_1 5_1 7_1$	0.24	$5_1 7_1 8_2$
153	A′	3392.4	−0.1	−2.5	0.64	$4_1 5_1 6_1$	0.19	$4_1 6_1 9_2$	207	A″	3651.0	0.4	10.2	0.44	$7_3 9_3$	0.15	$3_1 7_2 9_1$
154	A′	3407.6	0.3	4.2	0.48	$6_1 9_4$	0.13	6_3	208	A″	3655.2	3.4	10.5	0.27	$5_1 7_1 9_3$	0.19	$5_2 7_1 9_1$
155	A″	3417.1	2.2	15.7	0.70	$7_1 9_5$	0.16	$5_1 7_1 9_3$	209	A′	3664.7	−0.4	−1.3	0.54	$4_2 8_2$	0.45	$3_1 4_2$
156	A″	3418.7	−1.3	−1.2	0.59	$5_1 7_2 8_1$	0.36	$7_2 8_1 9_2$	210	A″	3668.3	0.7	4.8	0.31	$3_1 5_1 9_1$	0.29	$5_1 8_2 9_1$
157	A′	3423.7	−1.5	−5.5	0.61	6_3	0.14	$6_1 9_4$	211	A′	3669.8	−1.3	−2.8	0.63	$5_1 6_1 7_2$	0.31	$6_1 7_2 9_2$
158	A′	3424.1	−0.7	0.7	0.61	$4_1 7_2 9_2$	0.29	$4_1 5_1 7_2$	212	A″	3679.1	0.0	0.0	0.58	$4_1 7_1 8_1 9_2$	0.36	$4_1 5_1 7_1 8_1$
159	A″	3433.0	0.3	0.1	0.99	$4_2 7_1 8_1$	0.00	$4_1 8_2 9_1$	213	A″	3680.6	4.4	52.4	0.55	9_7	0.14	$4_2 9_3$
160	A′	3434.9	0.5	2.8	0.62	$5_1 7_1 8_1 9_1$	0.22	$7_1 8_1 9_3$	214	A′	3682.0	−0.5	−0.8	0.31	$3_1 5_1 7_1$	0.27	$5_1 7_1 8_2$
161	A′	3437.3	−3.0	−7.0	0.44	$3_1 8_2$	0.42	8_4	215	A′	3687.6	0.2	−0.4	0.99	$4_2 6_1 7_1$	0.00	$4_2 8_2$
162	A′	3445.1	0.1	−1.2	0.73	$4_2 8_1 9_1$	0.20	$2_1 9_2$	216	A″	3690.8	4.2	−4.8	0.54	$4_2 6_1 9_1$	0.19	9_7
163	A′	3445.3	0.1	2.1	0.57	$2_1 9_2$	0.21	$4_2 8_1 9_1$	217	A″	3691.3	1.0	1.1	0.58	$5_1 6_1 7_1 9_1$	0.17	$6_1 7_1 9_3$
164	A′	3453.5	0.0	−1.4	0.47	$4_1 5_2$	0.27	$4_1 5_1 9_2$	218	A′	3696.2	3.6	11.7	0.62	$8_1 9_5$	0.10	$5_1 8_1 9_3$
165	A′	3461.4	−0.2	2.6	0.83	$2_1 7_2$	0.07	$6_2 7_2$	219	A′	3699.6	0.4	−0.3	0.53	$3_1 4_2$	0.46	$4_2 8_2$

CVPT6 eigenvalues of *trans*-HCOOD

Table D.6 Zero-point corrected vibrational term values (in cm^{-1}) of *trans*-HCOOD up to 3600 cm^{-1}. The vibrational states are computed with CVPT*n* on the TM-PES [21]. For details of the calculations, see Ref. [28]. The two leading squared coefficients (P, sixth-order) are shown together with deviations to lower orders of perturbation theory ($\Delta(n) = E(n) - E(6)$; $n = 2, 4$). Squared coefficients printed as "0.00" are below 0.5%.

					state 1		state 2							state 1		state 2	
No.	Γ	$E(6)$	Δ(4)	Δ(2)	P	Label	P	Label	No.	Γ	$E(6)$	Δ(4)	Δ(2)	P	Label	P	Label
2	A″	507.7	0.0	−0.1	1.00	9_1			54	A′	2485.0	−0.1	−2.6	0.47	$8_1 9_3$	0.28	$5_1 8_1 9_1$
3	A′	559.1	−0.1	0.5	1.00	7_1			55	A′	2509.5	0.2	1.9	0.74	$5_2 7_1$	0.16	$7_1 9_4$
4	A′	973.1	−0.1	−0.9	0.64	5_1	0.36	9_2	56	A″	2510.5	1.4	5.7	0.47	$5_2 9_1$	0.45	$5_1 9_3$
5	A′	1011.1	0.2	0.9	0.63	9_2	0.36	5_1	57	A′	2542.0	0.2	−0.8	0.96	$4_1 6_1$	0.01	$5_1 8_1 9_1$
6	A″	1032.2	−0.4	−1.0	0.97	8_1	0.03	$7_1 9_1$	58	A′	2543.0	0.0	1.4	0.56	$5_1 8_1 9_1$	0.32	$8_1 9_3$
7	A″	1069.0	0.0	1.2	0.97	$7_1 9_1$	0.03	8_1	59	A″	2551.7	−0.2	2.8	0.32	$5_1 7_1 8_1$	0.26	$7_1 8_1 9_2$
8	A′	1119.7	−0.3	0.8	1.00	7_2	0.00	6_1	60	A″	2569.4	−1.2	−2.0	0.71	$8_2 9_1$	0.16	$7_2 9_3$
9	A′	1179.8	−0.2	−1.0	0.99	6_1	0.01	9_2	61	A′	2572.5	2.1	7.4	0.62	$5_1 7_1 9_2$	0.15	$5_2 7_1$
10	A′	1366.0	0.3	−0.4	1.00	4_1	0.00	$5_1 7_1$	62	A″	2574.6	−0.1	3.4	0.51	$5_1 7_1 8_1$	0.28	$7_2 9_3$
11	A″	1448.1	−0.1	−0.7	0.67	9_3	0.32	$5_1 9_1$	63	A″	2604.4	−0.1	1.2	0.63	$7_1 8_1 9_2$	0.14	$5_1 7_1 8_1$
12	A″	1513.3	0.4	2.5	0.67	$5_1 9_1$	0.32	9_3	64	A″	2614.1	0.1	−1.1	0.67	$6_1 9_3$	0.29	$5_1 6_1 9_1$
13	A′	1529.1	−0.2	0.6	0.53	$5_1 7_1$	0.33	$7_1 9_2$	65	A′	2618.3	−1.6	−0.9	0.91	$7_1 8_2$	0.08	$7_2 8_1 9_1$
14	A′	1541.7	−0.4	−1.6	0.82	$8_1 9_1$	0.18	$5_1 7_1$	66	A″	2636.1	1.9	7.3	0.55	$5_1 7_2 9_1$	0.33	$7_2 9_3$
15	A′	1572.1	0.5	2.7	0.66	$7_1 9_2$	0.29	$5_1 7_1$	67	A′	2637.8	−0.1	−0.5	0.99	1_1	0.01	$3_1 5_1$
16	A″	1590.7	−0.4	−0.1	0.96	$7_1 8_1$	0.04	$7_2 9_1$	68	A′	2648.5	−1.3	1.1	0.51	$5_1 7_3$	0.30	$7_3 9_2$
17	A″	1631.6	0.0	2.2	0.95	$7_2 9_1$	0.04	$7_1 8_1$	69	A′	2665.5	−1.0	−0.1	0.65	$7_2 8_1 9_1$	0.29	$5_1 7_3$
18	A′	1681.9	−1.0	0.5	0.99	7_3	0.01	$6_1 7_1$	70	A″	2680.6	0.1	1.8	0.69	$5_1 6_1 9_1$	0.27	$6_1 9_3$
19	A″	1683.3	−0.1	−0.8	0.98	$6_1 9_1$	0.01	9_3	71	A′	2697.1	−0.5	−1.0	0.53	$5_1 6_1 7_1$	0.35	$6_1 7_1 9_2$
20	A′	1734.1	−0.3	−0.4	0.96	$6_1 7_1$	0.02	3_1	72	A′	2699.0	0.9	6.2	0.66	$7_3 9_2$	0.18	$5_1 7_3$
21	A′	1779.3	0.0	0.1	0.97	3_1	0.02	$6_1 7_1$	73	A′	2711.6	1.0	−4.0	0.95	4_2	0.03	2_1
22	A″	1873.2	0.2	−0.6	0.99	$4_1 9_1$	0.00	$8_1 9_2$	74	A″	2712.1	−1.1	0.8	0.92	$7_3 8_1$	0.06	$7_4 9_1$
23	A′	1898.6	0.0	0.1	0.69	9_4	0.25	$5_1 9_2$	75	A′	2713.4	−0.6	−2.2	0.83	$6_1 8_1 9_1$	0.14	$5_1 6_1 7_1$
24	A′	1924.4	0.2	0.3	0.99	$4_1 7_1$	0.00	$5_1 7_2$	76	A′	2738.6	0.3	2.6	0.59	$6_1 7_1 9_2$	0.29	$5_1 6_1 7_1$
25	A′	1954.7	0.0	0.3	0.76	5_2	0.15	9_4	77	A′	2748.9	−0.2	−0.2	0.64	$3_1 5_1$	0.32	$3_1 9_2$
26	A″	1998.0	−0.2	0.4	0.34	$5_1 8_1$	0.28	$7_1 9_3$	78	A′	2749.8	0.9	5.1	0.77	9_6	0.18	$5_1 9_4$
27	A″	2012.6	0.1	1.2	0.38	$5_1 8_1$	0.37	$7_1 9_3$	79	A″	2761.4	−1.3	2.2	0.71	$7_4 9_1$	0.25	$6_1 7_1 8_1$
28	A′	2012.8	0.8	4.0	0.65	$5_1 9_2$	0.19	5_2	80	A″	2762.3	−0.7	−0.9	0.66	$6_1 7_1 8_1$	0.21	$7_4 9_1$
29	A″	2042.4	−0.2	−0.4	0.67	$8_1 9_2$	0.26	$5_1 8_1$	81	A′	2788.3	0.2	0.8	0.65	$3_1 9_2$	0.32	$3_1 5_1$
30	A′	2060.7	−1.6	−2.6	0.95	8_2	0.05	$7_1 8_1 9_1$	82	A″	2798.2	−0.3	2.0	0.87	$6_1 7_2 9_1$	0.05	$6_1 7_1 8_1$
31	A″	2073.9	1.1	4.8	0.61	$5_1 7_1 9_1$	0.33	$7_1 9_3$	83	A″	2804.3	−0.4	−0.9	0.94	$3_1 8_1$	0.03	$6_1 7_1 8_1$
32	A′	2087.7	−0.5	1.4	0.52	$5_1 7_2$	0.31	$7_2 9_2$	84	A′	2812.0	−4.4	−3.5	0.97	7_5	0.02	$6_1 7_3$
33	A′	2103.2	−0.6	−0.8	0.72	$7_1 8_1 9_1$	0.25	$5_1 7_2$	85	A″	2812.3	0.0	−2.3	0.65	$4_1 9_3$	0.33	$4_1 5_1 9_1$
34	A′	2134.7	0.8	4.5	0.67	$7_2 9_2$	0.23	$5_1 7_2$	86	A″	2842.5	−0.7	−1.9	0.66	$3_1 7_1 9_1$	0.29	$6_2 9_1$
35	A′	2145.0	−0.4	−2.5	0.60	$5_1 6_1$	0.38	$6_1 9_2$	87	A′	2848.4	−1.2	−0.3	0.88	$6_1 7_3$	0.07	$3_1 7_2$
36	A″	2150.6	−0.6	0.6	0.94	$7_2 8_1$	0.06	$7_3 9_1$	88	A″	2849.1	−0.2	−0.9	0.67	$6_2 9_1$	0.27	$3_1 7_1 9_1$
37	A′	2182.3	0.0	0.4	0.58	$6_1 9_2$	0.39	$5_1 6_1$	89	A′	2873.0	0.4	6.6	0.38	$5_2 9_2$	0.32	$5_1 9_4$
38	A″	2195.7	−0.5	2.6	0.93	$7_3 9_1$	0.06	$7_2 8_1$	90	A″	2875.0	0.5	2.8	0.66	$4_1 5_1 9_1$	0.31	$4_1 9_3$
39	A″	2208.5	−0.5	−1.8	0.96	$6_1 8_1$	0.03	$6_1 7_1 9_1$	91	A″	2885.2	1.9	13.9	0.70	$7_1 9_5$	0.20	$5_1 7_1 9_3$
40	A″	2240.0	−0.2	0.7	0.92	$6_1 7_1 9_1$	0.03	$6_1 8_1$	92	A′	2889.8	−1.3	−2.0	0.67	$3_1 7_2$	0.27	$6_2 7_1$
41	A′	2245.9	−2.3	−0.8	0.98	7_4	0.02	$6_1 7_2$	93	A′	2892.9	0.0	−0.7	0.60	$4_1 5_1 7_1$	0.29	$4_1 7_1 9_2$
42	A″	2286.4	0.0	0.0	0.97	$3_1 9_1$	0.02	$6_1 7_1 9_1$	94	A′	2899.8	−0.6	−0.9	0.64	$6_2 7_1$	0.24	$3_1 7_2$
43	A′	2290.3	−0.6	−0.1	0.92	$6_1 7_2$	0.05	$3_1 7_1$	95	A′	2909.5	−0.3	−1.5	0.86	$4_1 8_1 9_1$	0.12	$4_1 5_1 7_1$
44	A″	2333.1	0.3	2.0	0.75	9_5	0.21	$5_1 9_3$	96	A′	2928.0	0.6	2.4	0.72	5_3	0.20	$5_1 9_4$
45	A′	2334.3	−0.4	−0.4	0.88	$3_1 7_1$	0.06	6_2	97	A′	2934.9	0.5	2.2	0.59	$4_1 7_1 9_2$	0.21	$4_1 5_1 7_1$
46	A′	2336.9	0.1	−1.9	0.65	$4_1 5_1$	0.32	$4_1 9_2$	98	A″	2935.2	0.3	−1.7	0.61	$8_1 9_4$	0.26	$5_1 8_1 9_2$
47	A′	2348.3	−0.7	−3.6	0.91	6_2	0.06	$3_1 7_1$	99	A′	2940.7	−0.1	0.4	0.65	2_1	0.17	$3_1 6_1$
48	A′	2374.5	0.3	1.0	0.66	$4_1 9_2$	0.33	$4_1 5_1$	100	A″	2959.5	−0.1	−0.2	0.94	$4_1 7_1 8_1$	0.05	$4_1 7_2 9_1$
49	A″	2401.5	−0.1	−0.9	0.97	$4_1 8_1$	0.03	$4_1 7_1 9_1$	101	A′	2961.1	−0.2	−1.2	0.76	$3_1 6_1$	0.19	2_1
50	A″	2430.2	0.4	3.7	0.45	$5_2 9_1$	0.28	$5_1 9_3$	102	A″	2976.9	0.1	1.8	0.44	$5_2 8_1$	0.20	$5_2 7_1 9_1$
51	A″	2434.4	0.2	1.0	0.87	$4_1 7_1 9_1$	0.05	$5_2 9_1$	103	A″	2990.6	1.2	5.9	0.32	$5_2 8_1$	0.26	$5_2 7_1 9_1$
52	A′	2452.2	0.7	7.1	0.61	$7_1 9_4$	0.23	$5_1 7_1 9_2$	104	A″	2996.4	0.2	2.2	0.86	$4_1 7_2 9_1$	0.05	$4_1 7_1 8_1$
53	A′	2483.9	−0.1	1.1	0.84	$4_1 7_2$	0.09	$8_1 9_3$	105	A′	3005.7	2.4	7.7	0.53	$5_2 9_2$	0.23	$5_1 9_4$

continued

Table D.6 (continued)

					state 1		state 2							state 1		state 2	
No.	Γ	$E(6)$	Δ(4)	Δ(2)	P	Label	P	Label	No.	Γ	$E(6)$	Δ(4)	Δ(2)	P	Label	P	Label
106	A′	3006.6	1.4	11.5	0.47	$7_2 9_4$	0.17	$5_1 7_2 9_2$	158	A′	3347.4	0.7	2.4	0.53	$3_1 7_1 9_2$	0.20	$3_1 5_1 7_1$
107	A′	3027.7	−1.2	0.0	0.52	$5_1 8_2$	0.23	$8_2 9_2$	159	A″	3358.3	−0.8	2.9	0.81	$6_1 7_3 9_1$	0.07	$3_1 7_1 8_1$
108	A″	3040.5	0.5	3.4	0.61	$5_1 8_1 9_2$	0.15	$8_1 9_4$	160	A″	3358.9	−0.6	−0.9	0.78	$3_1 7_1 8_1$	0.06	$6_1 7_2 8_1$
109	A′	3045.1	−0.7	1.0	0.94	$4_1 7_3$	0.02	$5_2 7_2$	161	A″	3363.6	0.1	−0.2	0.34	$4_1 7_1 9_3$	0.28	$4_1 5_1 8_1$
110	A″	3045.1	0.1	−0.7	0.97	$4_1 6_1 9_1$	0.02	$4_1 9_3$	162	A′	3370.1	1.1	0.2	0.69	$8_1 9_5$	0.20	$5_1 8_1 9_3$
111	A′	3049.4	−0.4	−0.1	0.40	$7_1 8_1 9_3$	0.27	$5_1 8_2$	163	A′	3372.6	1.0	4.8	0.63	$4_1 5_1 9_2$	0.18	$4_1 5_2$
112	A′	3058.6	0.6	0.4	0.69	$6_1 9_4$	0.22	$5_1 6_1 9_2$	164	A″	3373.3	−1.0	−3.9	0.86	$6_2 8_1$	0.05	$3_1 7_1 8_1$
113	A′	3066.4	0.2	3.6	0.64	$5_2 7_2$	0.17	$7_2 9_4$	165	A″	3377.5	0.1	−0.6	0.46	$4_1 5_1 8_1$	0.28	$4_1 7_1 9_3$
114	A″	3069.1	3.4	10.1	0.43	$5_1 7_1 9_3$	0.41	$5_2 7_1 9_1$	166	A′	3380.5	−7.8	−8.6	0.96	7_6	0.02	$6_1 7_4$
115	A′	3071.2	−1.5	−2.6	0.65	$8_2 9_2$	0.15	$5_1 8_2$	167	A″	3396.9	−1.6	−2.2	0.67	$6_2 7_1 9_1$	0.24	$3_1 7_2 9_1$
116	A″	3086.3	−4.3	−5.3	0.91	8_3	0.07	$7_1 8_2 9_1$	168	A″	3404.1	1.5	8.7	0.58	$5_3 9_1$	0.25	$5_1 9_5$
117	A′	3096.1	0.1	0.0	0.96	$4_1 6_1 7_1$	0.01	$3_1 4_1$	169	A″	3406.2	0.0	2.1	0.65	$3_1 7_2 9_1$	0.20	$6_2 7_1 9_1$
118	A′	3103.8	0.7	3.7	0.42	$5_1 7_1 8_1 9_1$	0.32	$7_1 8_1 9_3$	170	A′	3408.6	−2.3	−1.3	0.84	$6_1 7_4$	0.10	$3_1 7_3$
119	A″	3108.6	−0.1	4.9	0.31	$5_1 7_2 8_1$	0.26	$7_2 8_1 9_2$	171	A″	3409.0	−0.2	0.0	0.65	$4_1 8_1 9_2$	0.22	$4_1 5_1 8_1$
120	A′	3119.4	−0.6	−2.4	0.74	$5_2 6_1$	0.12	$6_1 9_4$	172	A′	3423.7	2.1	13.1	0.35	$5_2 7_1 9_2$	0.30	$5_1 7_1 9_4$
121	A″	3130.9	−1.6	−1.2	0.66	$7_1 8_2 9_1$	0.10	$7_3 9_3$	173	A′	3433.7	−2.1	−2.4	0.93	$4_1 8_2$	0.06	$4_1 7_1 8_1 9_1$
122	A′	3133.9	3.6	10.8	0.57	$5_1 7_2 9_2$	0.14	$7_2 9_4$	174	A″	3434.5	1.2	4.8	0.52	$4_1 5_1 7_1 9_1$	0.26	$4_1 7_1 9_3$
123	A″	3136.0	−0.1	6.1	0.52	$5_1 7_2 8_1$	0.34	$7_3 9_3$	175	A″	3438.0	4.1	25.0	0.60	$7_2 9_5$	0.17	$5_1 7_2 9_3$
124	A′	3144.5	0.4	0.7	0.94	$3_1 4_1$	0.03	2_1	176	A′	3445.0	−2.5	−3.8	0.58	$6_2 7_2$	0.36	$3_1 7_3$
125	A″	3145.0	−0.1	−0.9	0.98	$1_1 9_1$	0.01	$3_1 5_1 9_1$	177	A″	3445.7	−0.1	−0.1	0.64	$2_1 9_1$	0.23	$3_1 6_1 9_1$
126	A″	3148.6	1.8	10.0	0.80	9_7	0.16	$5_1 9_5$	178	A′	3450.8	−0.4	0.1	0.60	$4_1 5_1 7_2$	0.26	$4_1 7_2 9_2$
127	A″	3162.7	0.0	1.3	0.43	$6_1 7_1 9_3$	0.19	$5_1 6_1 7_1 9_1$	179	A′	3455.7	−0.9	0.8	0.52	$3_1 7_3$	0.27	$6_2 7_2$
128	A″	3168.1	−0.2	2.3	0.57	$7_2 8_1 9_2$	0.19	$5_1 7_3 9_1$	180	A′	3461.4	0.3	1.9	0.47	$5_2 8_1 9_1$	0.25	$5_1 8_1 9_3$
129	A′	3175.9	0.5	3.3	0.62	$5_1 6_1 9_2$	0.21	$5_2 6_1$	181	A″	3464.9	0.0	−1.0	0.71	$3_1 6_1 9_1$	0.24	$2_1 9_1$
130	A′	3177.2	−1.7	0.6	0.87	$7_2 8_2$	0.10	$7_3 8_1 9_1$	182	A′	3470.3	−0.4	−0.5	0.72	$4_1 7_1 8_1 9_1$	0.16	$4_1 5_1 7_2$
131	A″	3178.0	−0.3	−0.9	0.51	$5_1 6_1 8_1$	0.22	$6_1 7_1 9_3$	183	A′	3480.4	1.7	6.2	0.68	$5_3 7_1$	0.21	$5_1 7_1 9_4$
132	A′	3191.1	−0.2	0.8	0.98	$1_1 7_1$	0.01	$3_1 5_1 7_1$	184	A″	3485.4	1.4	7.6	0.45	$6_1 9_5$	0.16	$7_1 8_1 9_4$
133	A″	3199.9	2.5	9.4	0.50	$5_1 7_3 9_1$	0.32	$7_3 9_3$	185	A″	3487.9	0.7	1.9	0.28	$6_1 9_5$	0.26	$7_1 8_1 9_4$
134	A″	3209.8	−0.3	−0.4	0.61	$6_1 8_1 9_2$	0.28	$5_1 6_1 8_1$	186	A′	3494.4	−0.7	−4.8	0.32	$2_1 7_1$	0.25	$3_1 6_1 7_1$
135	A′	3211.3	−2.8	−0.7	0.49	$5_1 7_4$	0.30	$7_4 9_2$	187	A′	3498.6	0.2	4.9	0.46	$4_1 7_2 9_2$	0.15	$4_1 5_1 7_2$
136	A″	3217.9	0.7	−3.8	0.93	$4_2 9_1$	0.03	$2_1 9_1$	188	A″	3499.1	3.5	9.5	0.50	$5_2 9_3$	0.34	$5_3 9_1$
137	A″	3224.3	0.2	0.1	0.61	$3_1 9_3$	0.32	$3_1 5_1 9_1$	189	A′	3504.2	−1.1	−5.2	0.35	6_3	0.30	$4_1 5_1 6_1$
138	A′	3229.2	−1.8	−0.1	0.58	$7_3 8_1 9_1$	0.33	$5_1 7_4$	190	A′	3505.9	−0.3	−3.5	0.33	$4_1 5_1 6_1$	0.30	6_3
139	A′	3233.9	−1.8	−3.3	0.91	$6_1 8_2$	0.06	$6_1 7_1 8_1 9_1$	191	A′	3515.2	−0.1	−0.4	0.44	$3_1 6_1 7_1$	0.31	$2_1 7_1$
140	A″	3236.7	0.8	4.7	0.61	$5_1 6_1 7_1 9_1$	0.26	$6_1 7_1 9_3$	192	A″	3517.8	−0.7	−3.9	0.38	$4_1 7_2 8_1$	0.24	$8_2 9_3$
141	A′	3251.8	−0.9	−0.3	0.50	$5_1 6_1 7_2$	0.32	$6_1 7_2 9_2$	193	A″	3519.4	−0.5	0.0	0.52	$4_1 7_2 8_1$	0.18	$8_2 9_3$
142	A′	3262.0	−0.1	−2.1	0.66	$4_1 9_4$	0.25	$4_1 5_1 9_2$	194	A″	3530.0	0.6	4.6	0.35	$5_2 7_1 8_1$	0.19	$5_2 7_2 9_1$
143	A′	3265.1	0.6	6.8	0.64	$7_4 9_2$	0.15	$5_1 7_4$	195	A′	3531.6	3.4	18.1	0.82	9_8	0.15	$5_1 9_6$
144	A′	3269.8	1.2	−3.4	0.73	$4_2 7_1$	0.16	$6_1 7_1 8_1 9_1$	196	A′	3536.2	1.3	5.6	0.44	$5_1 8_1 9_3$	0.38	$5_2 8_1 9_1$
145	A′	3270.4	−1.0	−1.2	0.51	$6_1 7_1 8_1 9_1$	0.22	$4_2 7_1$	197	A′	3539.7	−0.2	1.0	0.86	3_2	0.10	$3_1 6_1 7_1$
146	A″	3275.4	−2.3	0.0	0.91	$7_4 8_1$	0.07	$7_5 9_1$	198	A′	3541.9	0.2	1.1	0.59	$4_1 6_1 9_2$	0.35	$4_1 5_1 6_1$
147	A″	3289.2	0.5	2.1	0.63	$3_1 5_1 9_1$	0.33	$3_1 9_3$	199	A″	3549.4	2.0	9.8	0.31	$5_2 7_1 8_1$	0.27	$5_2 7_2 9_1$
148	A′	3296.9	0.6	5.0	0.58	$6_1 7_2 9_2$	0.21	$5_1 6_1 7_2$	200	A″	3559.7	−0.3	2.7	0.87	$4_1 7_3 9_1$	0.06	$4_1 7_2 8_1$
149	A′	3298.9	3.6	23.0	0.74	$7_1 9_6$	0.17	$5_1 7_1 9_4$	201	A′	3561.5	2.3	13.5	0.40	$7_3 9_4$	0.18	$7_2 8_1 9_3$
150	A′	3300.3	−1.1	−4.0	0.40	$3_1 5_1 7_1$	0.25	$3_1 7_1 9_2$	202	A′	3563.1	5.1	13.1	0.50	$5_2 7_1 9_2$	0.23	$5_1 7_1 9_4$
151	A″	3303.8	0.8	12.5	0.43	$5_1 9_5$	0.34	$5_2 9_3$	203	A″	3569.1	−1.2	0.0	0.48	$5_1 8_2 9_1$	0.34	$8_2 9_3$
152	A′	3306.5	−0.7	−2.1	0.43	$5_1 6_2$	0.31	$6_2 9_2$	204	A″	3572.6	0.1	0.3	0.94	$4_1 6_1 8_1$	0.04	$4_1 6_1 7_1 9_1$
153	A′	3313.2	−0.4	−1.3	0.69	$3_1 8_1 9_1$	0.18	$3_1 5_1 7_1$	205	A′	3581.2	−1.2	6.0	0.33	$5_1 7_1 8_2$	0.22	$7_1 8_2 9_2$
154	A′	3315.2	0.3	−1.2	0.69	$4_1 5_2$	0.13	$4_1 9_4$	206	A″	3589.2	0.2	2.8	0.46	$5_2 6_1 9_1$	0.35	$5_1 6_1 9_3$
155	A″	3317.4	−0.6	0.2	0.85	$6_1 7_2 8_1$	0.06	$6_1 7_3 9_1$	207	A′	3597.2	−3.8	−4.9	0.69	$8_3 9_1$	0.24	$5_1 7_1 8_2$
156	A″	3329.7	−3.4	−0.3	0.89	$7_5 9_1$	0.07	$7_4 8_1$	208	A″	3600.7	1.8	6.6	0.47	$5_1 7_1 8_1 9_2$	0.14	$7_1 8_1 9_4$
157	A′	3340.9	−1.2	−3.0	0.42	$6_2 9_2$	0.35	$5_1 6_2$									

CVPT6 eigenvalues of *trans*-DCOOD

Table D.7 Zero-point corrected vibrational term values (in cm^{-1}) of *trans*-DCOOD up to 3300 cm^{-1}. The vibrational states are computed with CVPT*n* on the TM-PES [21]. For details of the calculations, see Ref. [28]. The two leading squared coefficients (P, sixth-order) are shown together with deviations to lower orders of perturbation theory ($\Delta(n) = E(n) - E(6)$; $n = 2, 4$). Squared coefficients printed as "0.00" are below 0.5%.

					state 1		state 2							state 1		state 2	
No.	Γ	$E(6)$	$\Delta(4)$	$\Delta(2)$	P	Label	P	Label	No.	Γ	$E(6)$	$\Delta(4)$	$\Delta(2)$	P	Label	P	Label
2	A″	491.6	0.0	0.0	1.00	9_1			53	A′	2274.7	−0.5	−0.5	0.91	$6_1 7_2$	0.06	$3_1 7_1$
3	A′	555.0	−0.1	0.4	1.00	7_1			54	A′	2283.2	−0.6	−0.9	0.50	$7_1 8_2$	0.41	$3_1 7_1$
4	A″	874.4	−0.2	−0.6	1.00	8_1	0.00	$7_1 9_1$	55	A′	2290.9	0.0	1.6	0.73	$8_1 9_3$	0.17	$5_1 8_1 9_1$
5	A′	945.8	−0.1	0.0	0.90	5_1	0.09	9_2	56	A′	2316.4	−0.2	−0.8	0.51	$5_1 8_1 9_1$	0.18	$3_1 7_1$
6	A′	964.1	0.1	0.0	0.84	9_2	0.10	5_1	57	A′	2317.8	−0.3	0.0	0.31	$3_1 7_1$	0.31	$5_1 8_1 9_1$
7	A′	1040.1	0.0	−0.4	0.94	4_1	0.06	9_2	58	A′	2338.3	−0.4	−3.9	0.97	6_2	0.01	$3_1 7_1$
8	A″	1048.6	0.1	1.0	1.00	$7_1 9_1$	0.00	8_1	59	A″	2357.8	0.4	2.3	0.67	$5_1 9_3$	0.22	$5_2 9_1$
9	A′	1111.6	−0.3	0.5	1.00	7_2	0.00	6_1	60	A″	2372.4	−0.3	0.9	0.93	$5_1 7_1 8_1$	0.06	$7_1 8_1 9_2$
10	A′	1173.5	−0.1	−1.0	1.00	6_1	0.00	9_2	61	A″	2389.1	0.3	−1.1	0.76	$5_2 9_1$	0.18	$5_1 9_3$
11	A′	1367.6	−0.2	−0.7	0.99	$8_1 9_1$	0.00	4_1	62	A″	2398.1	0.3	2.0	0.81	$7_1 8_1 9_2$	0.07	$4_1 7_1 8_1$
12	A″	1413.5	0.1	1.4	0.81	9_3	0.12	$5_1 9_1$	63	A′	2406.5	0.1	−0.5	0.75	$4_1 8_1 9_1$	0.17	$7_1 9_4$
13	A″	1429.2	−0.2	0.0	0.99	$7_1 8_1$	0.00	9_3	64	A′	2409.3	1.4	10.1	0.66	$7_1 9_4$	0.14	$4_1 8_1 9_1$
14	A″	1442.3	0.2	−0.5	0.88	$5_1 9_1$	0.10	9_3	65	A′	2442.6	0.0	0.4	0.90	$5_2 7_1$	0.07	$5_1 7_1 9_2$
15	A′	1500.3	−0.2	0.6	0.92	$5_1 7_1$	0.08	$7_1 9_2$	66	A″	2444.2	−0.5	3.7	0.66	$4_1 9_3$	0.12	$4_2 9_1$
16	A′	1521.7	0.4	2.2	0.84	$7_1 9_2$	0.08	$5_1 7_1$	67	A″	2466.9	−0.1	−1.2	0.90	$4_1 7_1 8_1$	0.07	$7_1 8_1 9_2$
17	A″	1532.2	0.1	0.3	0.91	$4_1 9_1$	0.08	9_3	68	A′	2470.8	0.9	1.9	0.76	$5_1 7_1 9_2$	0.09	$5_2 7_1$
18	A′	1593.7	−0.1	−0.3	0.93	$4_1 7_1$	0.07	$7_1 9_2$	69	A″	2475.5	0.9	−0.6	0.77	$4_1 5_1 9_1$	0.09	$5_1 9_3$
19	A″	1606.9	0.0	1.9	0.99	$7_2 9_1$	0.00	$7_1 8_1$	70	A′	2482.0	0.0	2.2	0.95	$7_2 8_1 9_1$	0.01	$7_3 9_2$
20	A″	1660.9	−0.1	−1.1	0.99	$6_1 9_1$	0.01	9_3	71	A″	2529.1	0.8	9.7	0.74	$7_2 9_3$	0.16	$5_1 7_2 9_1$
21	A′	1669.7	−0.8	0.1	0.99	7_3	0.00	$6_1 7_1$	72	A′	2530.9	−0.6	0.0	0.83	$4_1 5_1 7_1$	0.08	$5_1 7_1 9_2$
22	A′	1723.1	−0.2	−0.5	0.94	$6_1 7_1$	0.04	3_1	73	A′	2534.6	−0.3	−1.0	0.98	$6_1 8_1 9_1$	0.01	$6_1 7_1 9_2$
23	A′	1730.0	−0.5	−1.5	0.55	8_2	0.40	3_1	74	A″	2543.4	−0.8	0.9	0.98	$7_3 8_1$	0.01	$7_2 9_3$
24	A′	1764.9	−0.3	0.0	0.56	3_1	0.43	8_2	75	A′	2555.7	1.3	2.9	0.68	$4_1 7_1 9_2$	0.13	$4_2 7_1$
25	A″	1818.2	−0.2	−0.1	0.93	$5_1 8_1$	0.07	$8_1 9_2$	76	A″	2557.6	0.8	1.8	0.83	$5_1 7_2 9_1$	0.13	$7_2 9_3$
26	A″	1841.1	−0.1	−0.8	0.85	$8_1 9_2$	0.07	$5_1 8_1$	77	A″	2566.3	0.7	−0.2	0.82	$4_2 9_1$	0.13	$4_1 9_3$
27	A′	1851.8	0.4	2.9	0.85	9_4	0.08	$4_1 9_2$	78	A″	2573.4	0.2	1.0	0.81	$6_1 9_3$	0.11	$5_1 6_1 9_1$
28	A′	1888.7	0.1	−0.2	0.89	5_2	0.09	$5_1 9_2$	79	A″	2585.9	−1.2	−3.4	0.54	8_3	0.44	$3_1 8_1$
29	A″	1913.5	−0.1	−1.6	0.92	$4_1 8_1$	0.06	$8_1 9_2$	80	A″	2595.5	−0.4	−0.5	0.97	$6_1 7_1 8_1$	0.01	8_3
30	A′	1913.7	0.3	−0.2	0.77	$5_1 9_2$	0.10	5_2	81	A″	2602.4	−0.1	−2.3	0.86	$5_1 6_1 9_1$	0.09	$6_1 9_3$
31	A′	1924.1	−0.1	0.8	0.97	$7_1 8_1 9_1$	0.01	$7_2 9_2$	82	A′	2614.2	−1.7	0.1	0.93	$5_1 7_3$	0.06	$7_3 9_2$
32	A″	1970.7	0.5	5.9	0.77	$7_1 9_3$	0.14	$5_1 7_1 9_1$	83	A′	2626.3	0.4	−1.4	0.83	$4_2 7_1$	0.13	$4_1 7_1 9_2$
33	A′	1977.9	−0.5	−0.3	0.84	$4_1 5_1$	0.08	$4_1 9_2$	84	A′	2638.4	−0.2	−0.9	0.95	1_1	0.03	$3_1 5_1$
34	A″	1985.5	−0.4	0.6	0.98	$7_2 8_1$	0.01	$7_1 9_3$	85	A′	2640.9	0.8	5.7	0.83	$7_3 9_2$	0.08	$4_1 7_3$
35	A″	1999.2	0.5	0.6	0.86	$5_1 7_1 9_1$	0.12	$7_1 9_3$	86	A″	2645.2	0.6	1.6	0.84	$4_1 7_2 9_1$	0.08	$7_2 9_3$
36	A′	1999.8	0.6	0.9	0.70	$4_1 9_2$	0.11	4_2	87	A″	2645.5	−1.1	0.0	0.52	$3_1 8_1$	0.41	8_3
37	A″	2045.7	−0.3	−1.0	0.99	$6_1 8_1$	0.00	$8_1 9_2$	88	A′	2660.1	−0.6	−1.0	0.88	$5_1 6_1 7_1$	0.07	$6_1 7_1 9_2$
38	A′	2056.4	−0.7	0.7	0.93	$5_1 7_2$	0.07	$7_2 9_2$	89	A′	2672.6	−0.7	−0.7	0.54	$5_1 8_2$	0.34	$3_1 5_1$
39	A′	2074.1	0.2	−1.4	0.85	4_2	0.11	$4_1 9_2$	90	A′	2677.8	1.9	9.1	0.86	9_6	0.09	$4_1 9_4$
40	A′	2080.6	0.7	4.2	0.84	$7_2 9_2$	0.07	$4_1 7_2$	91	A′	2680.9	0.3	1.4	0.82	$6_1 7_1 9_2$	0.07	$5_1 6_1 7_1$
41	A″	2087.9	0.4	1.1	0.90	$4_1 7_1 9_1$	0.08	$7_1 9_3$	92	A″	2684.1	−0.2	−0.6	0.57	$4_1 6_1 9_1$	0.33	$2_1 9_1$
42	A′	2110.5	−0.2	−1.4	0.89	$5_1 6_1$	0.09	$6_1 9_2$	93	A′	2696.1	−0.3	−0.8	0.45	$3_1 9_2$	0.39	$8_2 9_2$
43	A′	2128.5	0.1	−1.1	0.84	$6_1 9_2$	0.08	$5_1 6_1$	94	A′	2706.6	−0.9	−1.8	0.82	$4_1 7_3$	0.08	$7_3 9_2$
44	A′	2149.2	−0.3	−0.8	0.91	$4_1 7_2$	0.08	$7_2 9_2$	95	A′	2707.2	−0.4	1.0	0.50	$3_1 5_1$	0.34	$5_1 8_2$
45	A″	2166.9	−0.3	2.3	0.99	$7_3 9_1$	0.01	$7_2 8_1$	96	A″	2721.4	0.1	−0.9	0.63	$2_1 9_1$	0.32	$4_1 6_1 9_1$
46	A′	2195.8	−0.3	−1.4	0.58	$4_1 6_1$	0.34	2_1	97	A″	2728.6	−1.1	1.8	0.98	$7_4 9_1$	0.01	$7_3 8_1$
47	A″	2212.6	−0.1	0.1	0.96	$6_1 7_1 9_1$	0.02	$3_1 9_1$	98	A″	2730.6	0.3	3.7	0.78	$8_1 9_4$	0.08	$4_1 8_1 9_2$
48	A″	2223.0	−0.4	−1.1	0.51	$8_2 9_1$	0.46	$3_1 9_1$	99	A′	2731.4	−0.3	−0.8	0.43	$8_2 9_2$	0.41	$3_1 9_2$
49	A′	2229.7	−1.9	−1.0	0.98	7_4	0.01	$6_1 7_2$	100	A′	2746.6	−0.5	−1.4	0.63	$4_1 6_1 7_1$	0.27	$2_1 7_1$
50	A′	2232.5	0.0	−0.4	0.62	2_1	0.35	$4_1 6_1$	101	A″	2758.8	0.1	0.3	0.91	$5_2 8_1$	0.06	$5_1 8_1 9_2$
51	A″	2258.0	−0.4	−0.4	0.52	$3_1 9_1$	0.47	$8_2 9_1$	102	A″	2766.1	−0.3	1.1	0.94	$6_1 7_2 9_1$	0.04	$3_1 7_1 9_1$
52	A″	2273.2	1.0	5.4	0.86	9_5	0.09	$4_1 9_3$	103	A′	2767.6	−0.4	−2.3	0.50	$4_1 8_2$	0.41	$3_1 4_1$

continued

Table D.7 (continued)

					state 1		state 2							state 1		state 2	
No.	Γ	$E(6)$	Δ(4)	Δ(2)	P	Label	P	Label	No.	Γ	$E(6)$	Δ(4)	Δ(2)	P	Label	P	Label
104	A″	2777.7	−0.4	0.4	0.47	$3_1 7_1 9_1$	0.46	$7_1 8_2 9_1$	155	A′	3102.1	0.9	−2.9	0.77	4_3	0.16	$4_2 9_2$
105	A′	2785.7	0.0	0.2	0.69	$2_1 7_1$	0.27	$4_1 6_1 7_1$	156	A″	3102.9	−1.7	1.3	0.96	$7_4 8_1$	0.01	$7_3 9_3$
106	A″	2788.9	−0.1	−0.9	0.76	$5_1 8_1 9_2$	0.08	$4_1 5_1 8_1$	157	A′	3113.2	1.9	4.4	0.66	$4_1 7_2 9_2$	0.15	$4_2 7_2$
107	A′	2791.8	−3.7	−3.4	0.98	7_5	0.01	$6_1 7_3$	158	A″	3117.4	0.8	2.8	0.78	$5_1 7_3 9_1$	0.14	$7_3 9_3$
108	A′	2795.3	0.8	4.9	0.75	$5_1 9_4$	0.11	$5_2 9_2$	159	A″	3120.6	1.5	0.5	0.77	$4_2 7_1 9_1$	0.13	$4_1 7_1 9_3$
109	A′	2802.7	−0.3	−1.0	0.51	$3_1 4_1$	0.41	$4_1 8_2$	160	A″	3125.0	0.3	6.7	0.65	$6_1 7_1 9_3$	0.13	$1_1 9_1$
110	A″	2811.9	−0.4	0.1	0.48	$7_1 8_2 9_1$	0.43	$3_1 7_1 9_1$	161	A′	3128.6	−0.9	−1.9	0.59	$4_1 5_1 6_1$	0.23	$2_1 5_1$
111	A″	2822.1	−0.4	−3.4	0.91	$6_2 9_1$	0.04	$3_1 7_1 9_1$	162	A″	3129.1	0.0	−2.3	0.79	$1_1 9_1$	0.12	$6_1 7_1 9_3$
112	A′	2827.9	0.4	−0.6	0.88	5_3	0.06	$5_2 9_2$	163	A″	3138.3	−1.3	−1.9	0.49	$7_1 8_3$	0.45	$3_1 7_1 8_1$
113	A′	2828.4	−1.1	−0.9	0.88	$6_1 7_3$	0.09	$3_1 7_2$	164	A′	3140.2	−1.1	−0.6	0.52	$3_1 8_1 9_1$	0.45	$8_3 9_1$
114	A″	2829.4	3.1	16.7	0.83	$7_1 9_5$	0.08	$4_1 7_1 9_3$	165	A″	3146.0	−0.2	2.5	0.36	$3_1 9_3$	0.29	$8_2 9_3$
115	A′	2837.7	−1.0	−0.5	0.45	$7_2 8_2$	0.42	$3_1 7_2$	166	A″	3147.3	−0.7	−0.3	0.87	$6_1 7_2 8_1$	0.04	$7_1 8_3$
116	A′	2846.6	0.8	7.1	0.66	$7_1 8_1 9_3$	0.18	$5_1 7_1 8_1 9_1$	167	A′	3148.5	0.2	0.3	0.48	$4_1 6_1 9_2$	0.21	$2_1 9_2$
117	A″	2849.1	−0.6	−0.8	0.85	$4_1 5_1 8_1$	0.07	$5_1 8_1 9_2$	168	A′	3152.6	0.9	7.3	0.77	$8_1 9_5$	0.08	$4_1 8_1 9_3$
118	A′	2858.9	0.5	−0.7	0.71	$5_2 9_2$	0.09	$4_1 5_2$	169	A″	3154.4	0.1	−0.9	0.82	$5_1 6_1 7_1 9_1$	0.10	$6_1 7_1 9_3$
119	A′	2870.7	−0.5	0.4	0.43	$7_2 8_2$	0.36	$3_1 7_2$	170	A′	3168.3	0.2	−1.4	0.64	$2_1 5_1$	0.26	$4_1 5_1 6_1$
120	A′	2873.3	0.4	0.8	0.64	$5_1 7_1 8_1 9_1$	0.08	$7_1 8_1 9_3$	171	A″	3170.9	−0.5	−1.6	0.48	$5_1 8_2 9_1$	0.29	$3_1 5_1 9_1$
121	A″	2875.7	0.3	−0.6	0.67	$4_1 8_1 9_2$	0.12	$4_2 8_1$	172	A′	3173.9	−3.4	−1.6	0.92	$5_1 7_4$	0.05	$7_4 9_2$
122	A′	2878.2	−1.0	5.9	0.57	$4_1 9_4$	0.12	$4_2 9_2$	173	A′	3180.6	0.3	−2.2	0.80	$4_2 7_2$	0.14	$4_1 7_2 9_2$
123	A′	2883.6	−0.6	−2.4	0.85	$6_2 7_1$	0.06	$3_1 7_2$	174	A″	3180.7	−0.2	2.0	0.41	$8_2 9_3$	0.27	$3_1 9_3$
124	A′	2897.9	−0.7	−1.5	0.54	$6_1 8_2$	0.42	$3_1 6_1$	175	A′	3187.7	−0.3	0.3	0.94	$1_1 7_1$	0.03	$3_1 5_1 7_1$
125	A′	2912.2	0.0	−0.3	0.79	$4_1 5_2$	0.08	$5_2 9_2$	176	A′	3189.7	0.3	−0.4	0.64	$2_1 9_2$	0.22	$4_1 6_1 9_2$
126	A″	2913.6	1.2	6.9	0.62	$5_1 7_1 9_3$	0.25	$5_2 7_1 9_1$	177	A″	3197.1	−1.1	0.4	0.47	$3_1 7_1 8_1$	0.43	$7_1 8_3$
127	A″	2928.0	−0.6	1.6	0.92	$5_1 7_2 8_1$	0.05	$7_2 8_1 9_2$	178	A′	3202.9	0.3	6.1	0.81	$7_4 9_2$	0.09	$4_1 7_4$
128	A′	2934.1	−0.5	−1.6	0.54	$3_1 6_1$	0.44	$6_1 8_2$	179	A″	3204.4	0.5	1.4	0.88	$4_1 7_3 9_1$	0.09	$7_3 9_3$
129	A′	2941.7	1.3	0.2	0.59	$4_1 5_1 9_2$	0.14	$4_2 5_1$	180	A″	3206.4	−0.4	−1.3	0.41	$3_1 5_1 9_1$	0.36	$5_1 8_2 9_1$
130	A″	2945.7	0.9	0.3	0.71	$5_2 7_1 9_1$	0.19	$5_1 7_1 9_3$	181	A″	3208.1	−0.4	−2.1	0.90	$6_2 8_1$	0.04	$3_1 7_1 8_1$
131	A″	2946.7	0.2	−3.4	0.83	$4_2 8_1$	0.11	$4_1 8_1 9_2$	182	A′	3211.8	−1.2	−1.1	0.87	$5_1 6_1 7_2$	0.06	$6_1 7_2 9_2$
132	A″	2956.3	0.7	4.6	0.77	$7_2 8_1 9_2$	0.08	$4_1 7_2 8_1$	183	A″	3215.6	1.4	8.6	0.78	$5_1 9_5$	0.09	$4_1 5_1 9_3$
133	A′	2961.8	0.4	0.8	0.80	$4_1 7_1 8_1 9_1$	0.10	$7_2 9_4$	184	A′	3221.2	−0.5	−2.1	0.53	$4_2 6_1$	0.32	$2_1 4_1$
134	A′	2967.5	2.6	17.3	0.70	$7_2 9_4$	0.09	$4_1 7_2 9_2$	185	A′	3224.8	−0.8	0.4	0.49	$5_1 7_1 8_2$	0.35	$3_1 5_1 7_1$
135	A″	2980.0	−0.4	−0.4	0.91	$5_1 6_1 8_1$	0.06	$6_1 8_1 9_2$	186	A′	3231.2	1.1	4.2	0.37	$5_1 8_1 9_3$	0.35	$7_1 9_6$
136	A′	2998.2	−0.5	0.6	0.90	$5_2 7_2$	0.06	$5_1 7_2 9_2$	187	A′	3233.6	4.7	23.8	0.46	$7_1 9_6$	0.19	$5_1 8_1 9_3$
137	A″	2999.8	0.4	8.1	0.62	$4_1 7_1 9_3$	0.12	$4_1 5_1 7_1 9_1$	188	A′	3235.0	0.5	3.8	0.80	$6_1 7_2 9_2$	0.07	$4_1 6_1 7_2$
138	A″	3003.2	−0.1	−1.1	0.83	$6_1 8_1 9_2$	0.07	$4_1 6_1 8_1$	189	A″	3236.9	−0.2	0.2	0.62	$4_1 6_1 7_1 9_1$	0.26	$2_1 7_1 9_1$
139	A′	3004.1	−1.2	−1.3	0.75	$4_2 5_1$	0.12	$4_1 5_1 9_2$	190	A′	3250.9	−0.2	2.0	0.45	$3_1 7_1 9_2$	0.34	$7_1 8_2 9_2$
140	A′	3006.6	0.7	2.7	0.84	$6_1 9_4$	0.08	$4_1 6_1 9_2$	191	A′	3258.5	−0.4	0.8	0.48	$3_1 5_1 7_1$	0.38	$5_1 7_1 8_2$
141	A″	3022.1	−0.3	−1.2	0.88	$4_1 7_2 8_1$	0.07	$7_2 8_1 9_2$	192	A″	3261.0	−0.3	−1.3	0.44	$4_1 8_2 9_1$	0.43	$3_1 4_1 9_1$
142	A′	3028.6	1.5	1.2	0.44	$4_2 9_2$	0.17	$5_1 7_2 9_2$	193	A′	3262.6	−0.2	−1.8	0.68	$5_2 8_1 9_1$	0.23	$5_1 8_1 9_3$
143	A′	3029.3	1.7	3.7	0.56	$5_1 7_2 9_2$	0.13	$4_2 9_2$	194	A′	3266.1	−2.1	−4.0	0.88	$4_1 7_4$	0.09	$7_4 9_2$
144	A″	3031.2	1.6	0.5	0.74	$4_1 5_1 7_1 9_1$	0.09	$5_1 7_1 9_3$	195	A′	3269.3	−0.7	−2.9	0.77	$5_1 6_2$	0.10	$6_2 9_2$
145	A′	3041.3	−0.2	3.3	0.94	$7_3 8_1 9_1$	0.02	$7_4 9_2$	196	A′	3273.0	0.5	−1.3	0.55	$2_1 4_1$	0.31	$4_2 6_1$
146	A′	3044.7	−0.1	−2.4	0.86	$5_2 6_1$	0.09	$5_1 6_1 9_2$	197	A″	3276.7	0.2	0.5	0.69	$2_1 7_1 9_1$	0.25	$4_1 6_1 7_1 9_1$
147	A″	3063.2	−0.6	−1.1	0.47	$4_1 6_1 8_1$	0.45	$2_1 8_1$	198	A″	3282.3	3.6	15.1	0.50	$7_1 8_1 9_4$	0.19	$4_1 9_5$
148	A″	3065.5	3.3	14.6	0.86	9_7	0.09	$4_1 9_5$	199	A′	3284.0	−0.4	−2.5	0.40	$6_2 9_2$	0.25	$7_1 8_2 9_2$
149	A′	3069.4	−0.2	−2.3	0.75	$5_1 6_1 9_2$	0.09	$5_2 6_1$	200	A′	3289.3	0.1	0.3	0.41	$6_2 9_2$	0.20	$3_1 7_1 9_2$
150	A′	3080.3	−1.2	−2.8	0.49	$8_3 9_1$	0.46	$3_1 8_1 9_1$	201	A″	3292.3	−2.6	−0.1	0.97	$7_5 9_1$	0.01	$7_4 8_1$
151	A′	3085.9	−1.2	−0.3	0.72	$4_1 5_1 7_2$	0.12	$6_1 7_1 8_1 9_1$	202	A″	3294.9	−1.3	5.3	0.30	$4_1 9_5$	0.13	$5_2 9_3$
152	A′	3086.3	−0.4	0.3	0.82	$6_1 7_1 8_1 9_1$	0.10	$4_1 5_1 7_2$	203	A″	3296.7	−0.2	−1.4	0.36	$3_1 4_1 9_1$	0.34	$4_1 8_2 9_1$
153	A″	3089.0	0.7	11.7	0.71	$7_3 9_3$	0.18	$5_1 7_3 9_1$	204	A′	3299.1	−1.0	−1.8	0.66	$4_1 6_1 7_2$	0.22	$2_1 7_2$
154	A″	3098.8	0.0	−1.7	0.51	$2_1 8_1$	0.45	$4_1 6_1 8_1$	205	A″	3299.2	0.0	6.2	0.36	$5_2 9_3$	0.22	$5_3 9_1$

Estimation of missing A_u modes of symmetrically deuterated (FF)

Table D.8 The three A_u symmetric fundamentals (ν_{13}, ν_{15}, ν_{16}; for nomenclature see Table 2.2, p. 35) of the cyclic formic acid dimer (FF) are currently only available from low-resolution thermal gas phase spectroscopy [93, 118, 138]. The vibrational band centres are estimated by applying the deperturbed VPT2 deuteration shifts, computed on the QB-PES [23], to the available experimental band centres of the main isotopologue (from Table 7.5).

	ν_{13}			ν_{15}			ν_{16}		
Isotopologue	DVPT2	Exp.	Estimate	DVPT2	Exp.	Estimate	DVPT2	Exp.	Estimate
$(HCOOH)_2$	1065.3	1069.3		171.2	168.47		69.3	69.2	
$(DCOOH)_2$	892.2		896	145.0		142	69.7		70
$(HCOOD)_2$	1057.6		1062	163.7		161	70.3		70
$(DCOOD)_2$	895.3		899	139.5		137	69.4		69

Semi-experimental SOF+x band centres of excited vibrational states in (FF)

Table D.9 Semi-experimental SOF and SOF+x (Eq. 2.17, p. 17) band centres of binary (FF) states between 600 and 1500 cm^{-1}. The experimental fundamentals are from Tables 7.5 and D.8. The second-order anharmonicity constants are computed at the MP2/aVTZ level using default thresholds for deperturbation (see Chapter 2.1.2).

	$(HCOOH)_2$			$(DCOOH)_2$			$(HCOOD)_2$			$(DCOOD)_2$		
	Label	SOF	SOF+x	Label	SOF	SOF+x	Label	SOF	SOF+x	Label	SOF	SOF+x
A_g	$\nu_7+\nu_9$	842	842	$\nu_7+\nu_9$	834	834	$\nu_7+\nu_9$	784	784	$\nu_7+\nu_9$	780	779
A_g	$\nu_7+\nu_8$	875	874	$\nu_7+\nu_8$	867	866	$\nu_{14}+\nu_{16}$	788	788	$\nu_{14}+\nu_{16}$	781	781
A_g	$\nu_{23}+\nu_{24}$	972	968	$\nu_{23}+\nu_{24}$	960	956	$\nu_7+\nu_8$	821	820	$\nu_7+\nu_8$	815	814
A_g	$\nu_{14}+\nu_{16}$	1008	1009	$\nu_{13}+\nu_{16}$	966	966	$\nu_{14}+\nu_{15}$	879	871	$\nu_{14}+\nu_{15}$	849	841
A_g	$\nu_{14}+\nu_{15}$	1107	1101	$\nu_{14}+\nu_{16}$	1028	1028	$\nu_{11}+\nu_{12}$	910	900	$\nu_{11}+\nu_{12}$	879	869
A_g	$\nu_{13}+\nu_{16}$	1139	1138	$\nu_{13}+\nu_{15}$	1039	1037	$\nu_{23}+\nu_{24}$	916	911	$\nu_{23}+\nu_{24}$	906	901
A_g	$\nu_{11}+\nu_{12}$	1153	1139	$\nu_{14}+\nu_{15}$	1101	1091	$\nu_{13}+\nu_{16}$	1132	1132	$\nu_{13}+\nu_{16}$	969	969
A_g	$\nu_{13}+\nu_{15}$	1238	1232	$\nu_{10}+\nu_{12}$	1105	1103	$\nu_{13}+\nu_{15}$	1223	1220	$\nu_{13}+\nu_{15}$	1036	1035
A_g	$\nu_{10}+\nu_{12}$	1300	1297	$\nu_{11}+\nu_{12}$	1132	1119	$\nu_4+\nu_9$	1231	1228	$\nu_{10}+\nu_{12}$	1103	1102
A_g	$2\nu_7$	1362	1362	$\nu_5+\nu_9$	1159	1159	$2\nu_7$	1254	1253	$\nu_5+\nu_9$	1149	1149
A_g	$\nu_6+\nu_9$	1385	1384	$\nu_5+\nu_8$	1192	1191	$\nu_4+\nu_8$	1268	1264	$\nu_5+\nu_8$	1184	1183
A_g	$2\nu_{23}$	1415	1413	$\nu_{21}+\nu_{24}$	1262	1261	$\nu_{10}+\nu_{12}$	1292	1291	$\nu_{21}+\nu_{24}$	1237	1236
A_g	$\nu_6+\nu_8$	1418	1415	$2\nu_7$	1350	1350	$\nu_{20}+\nu_{24}$	1299	1296	$2\nu_7$	1246	1245
A_g	$\nu_{22}+\nu_{24}$	1498	1493	$\nu_6+\nu_9$	1397	1396	$2\nu_{23}$	1322	1318	$\nu_4+\nu_9$	1249	1246
A_g				$2\nu_{23}$	1404	1401	$2\nu_{11}$	1344	1326	$\nu_4+\nu_8$	1284	1281
A_g				$\nu_6+\nu_8$	1430	1427	$2\nu_{14}$	1436	1418	$2\nu_{23}$	1312	1308
A_g				$\nu_{22}+\nu_{24}$	1503	1499	$\nu_6+\nu_9$	1426	1424	$\nu_{20}+\nu_{24}$	1322	1320
A_g							$\nu_6+\nu_8$	1463	1460	$2\nu_{11}$	1338	1321
A_g										$2\nu_{14}$	1423	1403
A_g										$\nu_6+\nu_9$	1414	1412
A_g										$\nu_6+\nu_8$	1449	1447
B_g	$\nu_{16}+\nu_{23}$	777	776	$\nu_{16}+\nu_{23}$	772	771	$\nu_{16}+\nu_{23}$	731	731	$\nu_{16}+\nu_{23}$	725	726
B_g	$\nu_{15}+\nu_{23}$	876	875	$\nu_{15}+\nu_{23}$	844	843	$\nu_{15}+\nu_{23}$	822	820	$\nu_{15}+\nu_{23}$	793	791
B_g	$\nu_7+\nu_{12}$	923	922	$\nu_7+\nu_{12}$	887	887	$\nu_9+\nu_{11}$	829	826	$\nu_9+\nu_{11}$	826	822
B_g	$\nu_9+\nu_{11}$	1072	1069	$\nu_9+\nu_{10}$	1052	1052	$\nu_8+\nu_{11}$	866	860	$\nu_7+\nu_{12}$	833	832
B_g	$\nu_8+\nu_{11}$	1105	1097	$\nu_{16}+\nu_{21}$	1074	1074	$\nu_7+\nu_{12}$	865	865	$\nu_8+\nu_{11}$	861	856
B_g	$\nu_{14}+\nu_{24}$	1203	1193	$\nu_9+\nu_{11}$	1079	1075	$\nu_{14}+\nu_{24}$	973	964	$\nu_{14}+\nu_{24}$	962	952
B_g	$\nu_9+\nu_{10}$	1219	1218	$\nu_8+\nu_{10}$	1085	1085	$\nu_{16}+\nu_{20}$	1115	1114	$\nu_9+\nu_{10}$	1050	1050

continued

Table D.9 (continued)

	$(HCOOH)_2$			$(DCOOH)_2$			$(HCOOD)_2$			$(DCOOD)_2$		
	Label	SOF	SOF+x	Label	SOF	SOF+x	Label	SOF	SOF+x	Label	SOF	SOF+x
B_g	$\nu_8+\nu_{10}$	1252	1250	$\nu_8+\nu_{11}$	1112	1103	$\nu_{15}+\nu_{20}$	1205	1204	$\nu_{16}+\nu_{21}$	1056	1056
B_g	$\nu_{16}+\nu_{22}$	1303	1303	$\nu_{15}+\nu_{21}$	1146	1146	$\nu_9+\nu_{10}$	1211	1211	$\nu_8+\nu_{10}$	1085	1083
B_g	$\nu_{13}+\nu_{24}$	1333	1328	$\nu_{13}+\nu_{24}$	1154	1153	$\nu_8+\nu_{10}$	1248	1248	$\nu_{15}+\nu_{21}$	1124	1123
B_g	$\nu_{15}+\nu_{22}$	1402	1401	$\nu_{14}+\nu_{24}$	1217	1202	$\nu_7+\nu_{11}$	1299	1297	$\nu_{16}+\nu_{20}$	1141	1141
B_g	$\nu_{16}+\nu_{21}$	1441	1440	$\nu_5+\nu_{12}$	1212	1211	$\nu_4+\nu_{12}$	1312	1309	$\nu_{13}+\nu_{24}$	1149	1149
B_g	$\nu_6+\nu_{12}$	1466	1463	$\nu_{16}+\nu_{22}$	1314	1313	$\nu_{13}+\nu_{24}$	1317	1316	$\nu_5+\nu_{12}$	1202	1201
B_g	$\nu_{16}+\nu_{20}$	1476	1475	$\nu_{15}+\nu_{22}$	1387	1386	$\nu_{16}+\nu_{22}$	1337	1336	$\nu_{15}+\nu_{20}$	1209	1208
B_g				$\nu_{16}+\nu_{20}$	1451	1448	$\nu_{14}+\nu_{23}$	1379	1373	$\nu_7+\nu_{11}$	1292	1290
B_g				$\nu_6+\nu_{12}$	1450	1449	$\nu_{15}+\nu_{22}$	1428	1427	$\nu_4+\nu_{12}$	1302	1300
B_g							$\nu_{16}+\nu_{21}$	1461	1461	$\nu_{16}+\nu_{22}$	1326	1325
B_g										$\nu_{14}+\nu_{23}$	1368	1362
B_g										$\nu_{15}+\nu_{22}$	1393	1393
B_g										$\nu_6+\nu_{12}$	1467	1466
A_u	$\nu_7+\nu_{16}$	750	750	$\nu_7+\nu_{16}$	745	745	$\nu_7+\nu_{16}$	697	698	$\nu_7+\nu_{16}$	692	693
A_u	$\nu_7+\nu_{15}$	849	849	$\nu_7+\nu_{15}$	817	817	$\nu_7+\nu_{15}$	788	787	$\nu_7+\nu_{15}$	760	759
A_u	$\nu_{12}+\nu_{23}$	950	948	$\nu_{12}+\nu_{23}$	914	913	$\nu_9+\nu_{14}$	875	872	$\nu_{12}+\nu_{23}$	866	864
A_u	$\nu_9+\nu_{14}$	1100	1098	$\nu_9+\nu_{13}$	1055	1055	$\nu_{12}+\nu_{23}$	899	897	$\nu_9+\nu_{14}$	869	865
A_u	$\nu_8+\nu_{14}$	1133	1128	$\nu_5+\nu_{16}$	1070	1070	$\nu_8+\nu_{14}$	912	906	$\nu_8+\nu_{14}$	904	898
A_u	$\nu_{11}+\nu_{24}$	1175	1162	$\nu_8+\nu_{13}$	1088	1088	$\nu_{11}+\nu_{24}$	927	918	$\nu_{11}+\nu_{24}$	919	910
A_u	$\nu_9+\nu_{13}$	1230	1228	$\nu_9+\nu_{14}$	1118	1113	$\nu_4+\nu_{16}$	1144	1143	$\nu_9+\nu_{13}$	1056	1056
A_u	$\nu_8+\nu_{13}$	1263	1259	$\nu_8+\nu_{14}$	1151	1142	$\nu_9+\nu_{13}$	1219	1218	$\nu_5+\nu_{16}$	1061	1061
A_u	$\nu_6+\nu_{16}$	1293	1293	$\nu_5+\nu_{15}$	1142	1142	$\nu_4+\nu_{15}$	1235	1233	$\nu_8+\nu_{13}$	1091	1091
A_u	$\nu_{10}+\nu_{24}$	1322	1320	$\nu_{10}+\nu_{24}$	1151	1150	$\nu_8+\nu_{13}$	1256	1255	$\nu_5+\nu_{15}$	1129	1128
A_u	$\nu_6+\nu_{15}$	1392	1391	$\nu_{11}+\nu_{24}$	1178	1164	$\nu_{12}+\nu_{20}$	1282	1281	$\nu_{10}+\nu_{24}$	1143	1142
A_u	$\nu_5+\nu_{16}$	1444	1444	$\nu_{12}+\nu_{21}$	1216	1215	$\nu_{10}+\nu_{24}$	1309	1308	$\nu_4+\nu_{16}$	1161	1161
A_u	$\nu_{12}+\nu_{22}$	1476	1474	$\nu_6+\nu_{16}$	1308	1307	$\nu_{11}+\nu_{23}$	1333	1327	$\nu_{12}+\nu_{21}$	1197	1196
A_u	$\nu_4+\nu_{16}$	1499	1499	$\nu_6+\nu_{15}$	1380	1379	$\nu_6+\nu_{16}$	1339	1339	$\nu_4+\nu_{15}$	1229	1228
A_u				$\nu_{12}+\nu_{22}$	1457	1456	$\nu_7+\nu_{14}$	1345	1343	$\nu_{12}+\nu_{20}$	1282	1280
A_u				$\nu_4+\nu_{16}$	1488	1487	$\nu_6+\nu_{15}$	1430	1429	$\nu_{11}+\nu_{23}$	1325	1319
A_u							$\nu_5+\nu_{16}$	1452	1452	$\nu_6+\nu_{16}$	1326	1325
A_u										$\nu_7+\nu_{14}$	1335	1332
A_u										$\nu_6+\nu_{15}$	1394	1392
A_u										$\nu_{12}+\nu_{22}$	1467	1466
B_u	$\nu_9+\nu_{23}$	869	867	$\nu_9+\nu_{23}$	861	859	$\nu_{11}+\nu_{16}$	742	741	$\nu_{11}+\nu_{16}$	738	737
B_u	$\nu_8+\nu_{23}$	902	899	$\nu_8+\nu_{23}$	894	892	$\nu_9+\nu_{23}$	818	816	$\nu_{11}+\nu_{15}$	806	798
B_u	$\nu_7+\nu_{24}$	945	943	$\nu_7+\nu_{24}$	933	931	$\nu_{11}+\nu_{15}$	833	825	$\nu_9+\nu_{23}$	813	811
B_u	$\nu_{11}+\nu_{16}$	980	980	$\nu_{10}+\nu_{16}$	963	963	$\nu_8+\nu_{23}$	855	851	$\nu_8+\nu_{23}$	848	845
B_u	$\nu_{11}+\nu_{15}$	1079	1070	$\nu_{11}+\nu_{16}$	990	990	$\nu_7+\nu_{24}$	882	879	$\nu_7+\nu_{24}$	873	870
B_u	$\nu_{10}+\nu_{16}$	1127	1128	$\nu_{10}+\nu_{15}$	1035	1034	$\nu_{12}+\nu_{14}$	956	945	$\nu_{12}+\nu_{14}$	922	912
B_u	$\nu_{12}+\nu_{14}$	1181	1172	$\nu_{11}+\nu_{15}$	1062	1053	$\nu_{10}+\nu_{16}$	1124	1125	$\nu_{10}+\nu_{16}$	962	963
B_u	$\nu_{10}+\nu_{15}$	1226	1224	$\nu_{12}+\nu_{13}$	1108	1106	$\nu_9+\nu_{20}$	1201	1199	$\nu_{10}+\nu_{15}$	1030	1029
B_u	$\nu_{12}+\nu_{13}$	1311	1304	$\nu_{12}+\nu_{14}$	1171	1158	$\nu_{10}+\nu_{15}$	1215	1212	$\nu_{12}+\nu_{13}$	1109	1109
B_u	$\nu_7+\nu_{23}$	1389	1388	$\nu_9+\nu_{21}$	1163	1163	$\nu_8+\nu_{20}$	1238	1236	$\nu_9+\nu_{21}$	1144	1144
B_u	$\nu_9+\nu_{22}$	1395	1393	$\nu_8+\nu_{21}$	1196	1195	$\nu_7+\nu_{23}$	1288	1286	$\nu_8+\nu_{21}$	1179	1178
B_u	$\nu_8+\nu_{22}$	1428	1426	$\nu_5+\nu_{24}$	1258	1258	$\nu_{12}+\nu_{13}$	1300	1298	$\nu_9+\nu_{20}$	1229	1227
B_u	$\nu_6+\nu_{24}$	1488	1483	$\nu_7+\nu_{23}$	1377	1376	$\nu_4+\nu_{24}$	1329	1324	$\nu_5+\nu_{24}$	1242	1241
B_u				$\nu_9+\nu_{22}$	1404	1402	$\nu_{11}+\nu_{14}$	1390	1369	$\nu_8+\nu_{20}$	1264	1262
B_u				$\nu_8+\nu_{22}$	1437	1435	$\nu_9+\nu_{22}$	1424	1422	$\nu_7+\nu_{23}$	1279	1277
B_u				$\nu_6+\nu_{24}$	1496	1492	$\nu_8+\nu_{22}$	1461	1459	$\nu_4+\nu_{24}$	1342	1338
B_u										$\nu_{11}+\nu_{14}$	1381	1355
B_u										$\nu_9+\nu_{22}$	1414	1413
B_u										$\nu_8+\nu_{22}$	1449	1447

References

[1] Mata, R. A., Suhm, M. A., „Benchmarking Quantum Chemical Methods: Are We Heading in the Right Direction?“, *Angew. Chem. Int. Ed.* **2017**, *56*, 11011–11018.

[2] Born, M., Oppenheimer, R., „Zur Quantentheorie der Molekeln“, *Ann. Phys.* **1927**, *389*, 457–484.

[3] Hoy, A. R., Mills, I. M., Strey, G., „Anharmonic force constant calculations“, *Mol. Phys.* **1972**, *24*, 1265–1290.

[4] Christiansen, O., „Vibrational structure theory: new vibrational wave function methods for calculation of anharmonic vibrational energies and vibrational contributions to molecular properties“, *Phys. Chem. Chem. Phys.* **2007**, *9*, 2942–2953.

[5] Bowman, J. M., Carrington, T., Meyer, H.-D., „Variational quantum approaches for computing vibrational energies of polyatomic molecules“, *Mol. Phys.* **2008**, *106*, 2145–2182.

[6] Albert, S., Albert, K. K., Hollenstein, H., Tanner, C. M., Quack, M., „Fundamentals of Rotation-Vibration Spectra“, in *Handbook of High-resolution Spectroscopy*, (Eds.: F. Merkt, M. Quack), pp. 117–173, John Wiley & Sons, New York, **2011**.

[7] Császár, A. G., Fábri, C., Szidarovszky, T., Mátyus, E., Furtenbacher, T., Czakó, G., „The fourth age of quantum chemistry: molecules in motion“, *Phys. Chem. Chem. Phys.* **2012**, *14*, 1085–1106.

[8] Carrington Jr., T., „Perspective: Computing (ro-)vibrational spectra of molecules with more than four atoms“, *J. Chem. Phys.* **2017**, *146*, 120902.

[9] Sibert III, E. L., „Modeling vibrational anharmonicity in infrared spectra of high frequency vibrations of polyatomic molecules“, *J. Chem. Phys.* **2019**, *150*, 090901.

[10] Erfort, S., Tschöpe, M., Rauhut, G., „Toward a fully automated calculation of rovibrational infrared intensities for semi-rigid polyatomic molecules“, *J. Chem. Phys.* **2020**, *152*, 244104.

[11] Franke, P. R., Stanton, J. F., Douberly, G. E., „How to VPT2: Accurate and Intuitive Simulations of CH Stretching Infrared Spectra Using VPT2+K with Large Effective Hamiltonian Resonance Treatments“, *J. Phys. Chem. A* **2021**, *125*, 1301–1324.

[12] Schröder, B., Rauhut, G., „Incremental vibrational configuration interaction theory, iVCI: Implementation and benchmark calculations“, *J. Chem. Phys.* **2021**, *154*, 124114.

[13] Mathea, T., Petrenko, T., Rauhut, G., „Advances in vibrational configuration interaction theory - part 2: Fast screening of the correlation space“, *J. Comput. Chem.* **2022**, *43*, 6–18.

[14] *Vibrational Dynamics of Molecules*, (Ed.: J. M. Bowman), World Scientific, New Jersey, **2022**.

[15] Poblotzki, A., Gottschalk, H. C., Suhm, M. A., „Tipping the Scales: Spectroscopic Tools for Intermolecular Energy Balances“, *J. Phys. Chem. Lett.* **2017**, *8*, 5656–5665.

[16] Oswald, S., Suhm, M. A., „Soft experimental constraints for soft interactions: a spectroscopic benchmark data set for weak and strong hydrogen bonds“, *Phys. Chem. Chem. Phys.* **2019**, *21*, 18799–18810.

[17] Gottschalk, H. C., Poblotzki, A., Fatima, M., Obenchain, D. A., Pérez, C., Antony, J., Auer, A. A., Baptista, L., Benoit, D. M., Bistoni, G., Bohle, F., Dahmani, R., Firaha, D., Grimme, S., Hansen, A., Harding, M. E., Hochlaf, M., Holzer, C., Jansen, G., Klopper, W., Kopp, W. A., Krasowska, M., Kröger, L. C., Leonhard, K., Mogren Al-Mogren, M., Mouhib, H., Neese, F., Pereira, M. N., Prakash, M., Ulusoy, I. S., Mata, R. A., Suhm, M. A., Schnell, M., „The first microsolvation step for furans: New experiments and benchmarking strategies“, *J. Chem. Phys.* **2020**, *152*, 164303.

[18] Knizia, G., Adler, T. B., Werner, H.-J., „Simplified CCSD(T)-F12 methods: Theory and benchmarks“, *J. Chem. Phys.* **2009**, *130*, 054104.

[19] Hättig, C., Klopper, W., Köhn, A., Tew, D. P., „Explicitly Correlated Electrons in Molecules“, *Chem. Rev.* **2012**, *112*, 4–74.

[20] Rauhut, G., Knizia, G., Werner, H.-J., „Accurate calculation of vibrational frequencies using explicitly correlated coupled-cluster theory“, *J. Chem. Phys.* **2009**, *130*, 054105.

[21] Tew, D. P., Mizukami, W., „Ab Initio Vibrational Spectroscopy of *cis*- and *trans*-Formic Acid from a Global Potential Energy Surface“, *J. Phys. Chem. A* **2016**, *120*, 9815–9828.

[22] Richter, F., Carbonnière, P., „Vibrational treatment of the formic acid double minimum case in valence coordinates“, *J. Chem. Phys.* **2018**, *148*, 064303.

[23] Qu, C., Bowman, J. M., „An ab initio potential energy surface for the formic acid dimer: zero-point energy, selected anharmonic fundamental energies, and ground-state tunneling splitting calculated in relaxed 1–4-mode subspaces“, *Phys. Chem. Chem. Phys.* **2016**, *18*, 24835–24840.

[24] Käser, S., Meuwly, M., „Transfer learned potential energy surfaces: accurate anharmonic vibrational dynamics and dissociation energies for the formic acid monomer and dimer“, *Phys. Chem. Chem. Phys.* **2022**, *24*, 5269–5281.

[25] Rasheeda, D. S., Martín Santa Daría, A., Schröder, B., Mátyus, E., Behler, J., „High-dimensional neural network potentials for accurate vibrational frequencies: the formic acid dimer benchmark“, *Phys. Chem. Chem. Phys.* **2022**, Advance Article.

[26] Qu, C., Bowman, J. M., „High-dimensional fitting of sparse datasets of CCSD(T) electronic energies and MP2 dipole moments, illustrated for the formic acid dimer and its complex IR spectrum“, *J. Chem. Phys.* **2018**, *148*, 241713.

[27] Aerts, A., Carbonnière, P., Richter, F., Brown, A., „Vibrational states of deuterated *trans*- and *cis*-formic acid: DCOOH, HCOOD, and DCOOD“, *J. Chem. Phys.* **2020**, *152*, 024305.

[28] Nejad, A., Sibert III, E. L., „The Raman jet spectrum of *trans*-formic acid and its deuterated isotopologs: Combining theory and experiment to extend the vibrational database“, *J. Chem. Phys.* **2021**, *154*, 064301.

[29] Martín Santa Daría, A., Avila, G., Mátyus, E., „Variational vibrational states of HCOOH“, *J. Mol. Spectrosc.* **2022**, *385*, 111617.

[30] Aerts, A., Brown, A., Gatti, F., „Intramolecular vibrational redistribution in formic acid and its deuterated forms“, *J. Chem. Phys.* **2022**, *157*, 014306.

[31] Richardson, J. O., „Full- and reduced-dimensionality instanton calculations of the tunnelling splitting in the formic acid dimer“, *Phys. Chem. Chem. Phys.* **2017**, *19*, 966–970.

[32] Qu, C., Bowman, J. M., „Quantum approaches to vibrational dynamics and spectroscopy: is ease of interpretation sacrificed as rigor increases?“, *Phys. Chem. Chem. Phys.* **2019**, *21*, 3397–3413.

[33] Martín Santa Daría, A., Avila, G., Mátyus, E., „Fingerprint region of the formic acid dimer: variational vibrational computations in curvilinear coordinates“, *Phys. Chem. Chem. Phys.* **2021**, *23*, 6526–6535.

[34] Whittle, E., Dows, D. A., Pimentel, G. C., „Matrix Isolation Method for the Experimental Study of Unstable Species“, *J. Chem. Phys.* **1954**, *22*, 1943–1943.

[35] Toennies, J. P., Vilesov, A. F., „Superfluid Helium Droplets: A Uniquely Cold Nanomatrix for Molecules and Molecular Complexes“, *Angew. Chem. Int. Ed.* **2004**, *43*, 2622–2648.

[36] Albert, S., Albert, K. K., Quack, M., „High-Resolution Fourier Transform Infrared Spectroscopy“, in *Handbook of High-resolution Spectroscopy*, (Eds.: F. Merkt, M. Quack), pp. 965–1019, John Wiley & Sons, New York, **2011**.

[37] Levy, D. H., „Laser Spectroscopy of Cold Gas-Phase Molecules“, *Annu. Rev. Phys. Chem.* **1980**, *31*, 197–225.

[38] Herman, M., Georges, R., Hepp, M., Hurtmans, D., „High resolution Fourier transform spectroscopy of jet-cooled molecules“, *Int. Rev. Phys. Chem.* **2000**, *19*, 277–325.

[39] Snels, M., Horká-Zelenková, V., Hollenstein, H., Quack, M., „High-Resolution FTIR and Diode Laser Spectroscopy of Supersonic Jets“, in *Handbook of High-resolution Spectroscopy*, (Eds.: F. Merkt, M. Quack), pp. 1021–1067, John Wiley & Sons, New York, **2011**.

[40] Coolidge, A. S., „The vapor density and some other properties of formic acid“, *J. Am. Chem. Soc.* **1928**, *50*, 2166–2178.

[41] Nejad, A., Meyer, E., Suhm, M. A., „Glycolic Acid as a Vibrational Anharmonicity Benchmark“, *J. Phys. Chem. Lett.* **2020**, *11*, 5228–5233.

[42] Meyer, K. A. E., Nejad, A., „CC-stretched formic acid: isomerisation, dimerisation, and carboxylic acid complexation“, *Phys. Chem. Chem. Phys.* **2021**, *23*, 17208–17223.

[43] Schweer, S. M., Nejad, A., Suhm, M. A., „Coupled proton vibrations between two weak acids: the hinge complex between formic acid and trifluoroethanol“, *Phys. Chem. Chem. Phys.* **2022**, *24*, 26449–26457.

[44] Quack, M., Suhm, M. A., „Potential energy surfaces, quasiadiabatic channels, rovibrational spectra, and intramolecular dynamics of $(HF)_2$ and its isotopomers from quantum Monte Carlo calculations“, *J. Chem. Phys.* **1991**, *95*, 28–59.

[45] Mukhopadhyay, A., Xantheas, S. S., Saykally, R. J., „The water dimer II: Theoretical investigations“, *Chem. Phys. Lett.* **2018**, *700*, 163–175.

[46] Sibert III, E. L., Hynes, J. T., Reinhardt, W. P., „Fermi resonance from a curvilinear perspective“, *J. Phys. Chem.* **1983**, *87*, 2032–2037.

[47] Beck, M. H., Jäckle, A., Worth, G. A., Meyer, H.-D., „The multiconfiguration time-dependent Hartree (MCTDH) method: a highly efficient algorithm for propagating wavepackets“, *Phys. Rep.* **2000**, *324*, 1–105.

[48] Bowman, J. M., „The self-consistent-field approach to polyatomic vibrations“, *Acc. Chem. Res.* **1986**, *19*, 202–208.

[49] Norris, L. S., Ratner, M. A., Roitberg, A. E., Gerber, R. B., „Møller-Plesset perturbation theory applied to vibrational problems“, *J. Chem. Phys.* **1996**, *105*, 11261–11267.

[50] Christiansen, O., „Vibrational coupled cluster theory“, *J. Chem. Phys.* **2004**, *120*, 2149–2159.

[51] Schröder, B., Rauhut, G., „Vibrational Configuration Interaction Theory“, in *Vibrational Dynamics of Molecules*, (Ed.: J. M. Bowman), Chapter 1, pp. 1–40, World Scientific, New Jersey, **2022**.

[52] Bowman, J. M., Carter, S., Huang, X., „MULTIMODE: A code to calculate rovibrational energies of polyatomic molecules“, *Int. Rev. Phys. Chem.* **2003**, *22*, 533–549.

[53] Neff, M., Rauhut, G., „Toward large scale vibrational configuration interaction calculations“, *J. Chem. Phys.* **2009**, *131*, 124129.

[54] Werner, H.-J., Knowles, P. J., Manby, F. R., Black, J. A., Doll, K., Heßelmann, A., Kats, D., Köhn, A., Korona, T., Kreplin, D. A., Ma, Q., Miller III, T. F., Mitrushchenkov, A., Peterson, K. A., Polyak, I., Rauhut, G., Sibaev, M., „The Molpro quantum chemistry package“, *J. Chem. Phys.* **2020**, *152*, 144107.

[55] Mizukami, W., Tew, D. P., „A second-order multi-reference perturbation method for molecular vibrations“, *J. Chem. Phys.* **2013**, *139*, 194108.

[56] Sibaev, M., Crittenden, D. L., „PyVCI: A flexible open-source code for calculating accurate molecular infrared spectra“, *Comput. Phys. Commun.* **2016**, *203*, 290–297.

[57] Watson, J. K. G., „Simplification of the molecular vibration-rotation hamiltonian“, *Mol. Phys.* **1968**, *15*, 479–490.

[58] Changala, P. B., Baraban, J. H., „Ab initio effective rotational and rovibrational Hamiltonians for non-rigid systems via curvilinear second order vibrational Møller–Plesset perturbation theory“, *J. Chem. Phys.* **2016**, *145*, 174106.

[59] Hougen, J. T., Bunker, P. R., Johns, J. W. C., „The vibration-rotation problem in triatomic molecules allowing for a large-amplitude bending vibration“, *J. Mol. Spectrosc.* **1970**, *34*, 136–172.

[60] Tew, D. P., Handy, N. C., Carter, S., Irle, S., Bowman, J., „The internal coordinate path Hamiltonian; application to methanol and malonaldehyde“, *Mol. Phys.* **2003**, *101*, 3513–3525.

[61] Miller, W. H., Handy, N. C., Adams, J. E., „Reaction path Hamiltonian for polyatomic molecules“, *J. Chem. Phys.* **1980**, *72*, 99–112.

[62] Carrington Jr., T., Miller, W. H., „Reaction surface Hamiltonian for the dynamics of reactions in polyatomic systems“, *J. Chem. Phys.* **1984**, *81*, 3942–3950.

[63] Tew, D. P., Handy, N. C., Carter, S., „A reaction surface Hamiltonian study of malonaldehyde“, *J. Chem. Phys.* **2006**, *125*, 084313.

[64] Nielsen, H. H., „The Vibration-rotation Energies of Molecules and their Spectra in the Infra-red“, in *Atoms III – Molecules I*, (Ed.: S. Flügge), Encyclopedia of Physics 37/1, pp. 173–313, Springer, Berlin, **1959**.

[65] Califano, S., *Vibrational States*, John Wiley & Sons, London, **1976**.

[66] Papoušek, D., Aliev, M. R., *Molecular Vibrational-rotational Spectra: Theory and Applications of High Resolution Infrared, Microwave, and Raman Spectroscopy of Polyatomic Molecules*, Elsevier Scientific Publishing Company, Amsterdam, **1982**.

[67] Aliev, M. R., Watson, J. K. G., „Higher-order effects in the vibration-rotation spectra of semirigid molecules“, in *Molecular Spectroscopy: Modern Research*, *Vol. 3*, (Ed.: K. N. Rao), pp. 1–67, Academic Press, Orlando, Florida, **1985**.

[68] Sibert III, E. L., „VANVLK: An algebraic manipulation program for canonical Van Vleck perturbation theory“, *Comput. Phys. Commun.* **1988**, *51*, 149–160.

[69] Sibert III, E. L., „Theoretical studies of vibrationally excited polyatomic molecules using canonical Van Vleck perturbation theory“, *J. Chem. Phys.* **1988**, *88*, 4378–4390.

[70] Barone, V., „Anharmonic vibrational properties by a fully automated second-order perturbative approach“, *J. Chem. Phys.* **2005**, *122*, 014108.

[71] Krasnoshchekov, S. V., Isayeva, E. V., Stepanov, N. F., „Numerical-Analytic Implementation of the Higher-Order Canonical Van Vleck Perturbation Theory for the Interpretation of Medium-Sized Molecule Vibrational Spectra“, *J. Phys. Chem. A* **2012**, *116*, 3691–3709.

[72] Rosnik, A. M., Polik, W. F., „VPT2+K spectroscopic constants and matrix elements of the transformed vibrational Hamiltonian of a polyatomic molecule with resonances using Van Vleck perturbation theory“, *Mol. Phys.* **2014**, *112*, 261–300.

[73] Gong, J. Z., Matthews, D. A., Changala, P. B., Stanton, J. F., „Fourth-order vibrational perturbation theory with the Watson Hamiltonian: Report of working equations and preliminary results“, *J. Chem. Phys.* **2018**, *149*, 114102.

[74] Boyer, M. A., McCoy, A. B., „A flexible approach to vibrational perturbation theory using sparse matrix methods“, *J. Chem. Phys.* **2022**, *156*, 054107.

[75] Helgaker, T., Jørgensen, P., Olsen, J., *Molecular Electronic-Structure Theory*, John Wiley & Sons, Chichester, **2000**.

[76] Christiansen, O., „Møller-Plesset perturbation theory for vibrational wave functions“, *J. Chem. Phys.* **2003**, *119*, 5773–5781.

[77] Matthews, D. A., Vázquez, J., Stanton, J. F., „Calculated stretching overtone levels and Darling-Dennison resonances in water: a triumph of simple theoretical approaches“, *Mol. Phys.* **2007**, *105*, 2659–2666.

[78] White, E. T., Tang, J., Oka, T., „CH_5^+: The Infrared Spectrum Observed“, *Science* **1999**, *284*, 135–137.

[79] Ramakrishnan, R., Rauhut, G., „Semi-quartic force fields retrieved from multi-mode expansions: Accuracy, scaling behavior, and approximations“, *J. Chem. Phys.* **2015**, *142*, 154118.

[80] Karle, J., Brockway, L. O., „An Electron Diffraction Investigation of the Monomers and Dimers of Formic, Acetic and Trifluoroacetic Acids and the Dimer of Deuterium Acetate“, *J. Am. Chem. Soc.* **1944**, *66*, 574–584.

[81] Hocking, W. H., „The Other Rotamer of Formic Acid, *cis*-HCOOH“, *Z. Naturforsch. A* **1976**, *31*, 1113–1121.

[82] Winnewisser, M., Winnewisser, B. P., Stein, M., Birk, M., Wagner, G., Winnewisser, G., Yamada, K. M. T., Belov, S. P., Baskakov, O. I., „Rotational Spectra of *cis*-HCOOH, *trans*-HCOOH, and *trans*-$H^{13}COOH$“, *J. Mol. Spectrosc.* **2002**, *216*, 259–265.

[83] Pettersson, M., Lundell, J., Khriachtchev, L., Räsänen, M., „IR Spectrum of the Other Rotamer of Formic Acid, *cis*-HCOOH“, *J. Am. Chem. Soc.* **1997**, *119*, 11715–11716.

[84] Marushkevich, K., Khriachtchev, L., Lundell, J., Domanskaya, A. V., Räsänen, M., „Vibrational spectroscopy of *trans* and *cis* deuterated formic acid (HCOOD): Anharmonic calculations and experiments in argon and neon matrices“, *J. Mol. Spectrosc.* **2010**, *259*, 105–110.

[85] Lopes, S., Fausto, R., Khriachtchev, L., „Formic acid in deuterium and hydrogen matrices“, *Mol. Phys.* **2019**, *117*, 1708–1718.

[86] Meyer, K. A. E., *Carboxylic Acids Under Vibrational Scrutiny: Experimental Reference Data to Benchmark Quantum Chemical Calculations*, DOI 10.53846/goediss-8262, Niedersächsische Staats- und Universitätsbibliothek Göttingen, Göttingen, **2020**.

[87] Meyer, K. A. E., Suhm, M. A., „Stretching of *cis*-formic acid: warm-up and cool-down as molecular workout“, *Chem. Sci.* **2019**, *10*, 6285–6294.

[88] Baskakov, O. I., Horneman, V.-M., Lohilahti, J., Alanko, S., „High resolution FTIR spectra of the ν_9 vibrational band of *cis*-rotamers HCOOH and $H^{13}COOH$“, *J. Mol. Struct.* **2006**, *795*, 49–53.

[89] Meyer, K. A. E., Suhm, M. A., „Vibrational exciton coupling in homo and hetero dimers of carboxylic acids studied by linear infrared and Raman jet spectroscopy“, *J. Chem. Phys.* **2018**, *149*, 104307.

[90] Doney, K. D., Kortyna, A., Chan, Y.-C., Nesbitt, D. J., „Formation and detection of metastable formic acid in a supersonic expansion: High resolution infrared spectroscopy of the jet-cooled *cis*-HCOOH conformer“, *J. Chem. Phys.* **2022**, *156*, 204309.

[91] Nejad, A., Suhm, M. A., Meyer, K. A. E., „Increasing the weights in the molecular work-out of *cis*- and *trans*-formic acid: extension of the vibrational database via deuteration“, *Phys. Chem. Chem. Phys.* **2020**, *22*, 25492–25501.

[92] Millikan, R. C., Pitzer, K. S., „Infrared Spectra and Vibrational Assignment of Monomeric Formic Acid“, *J. Chem. Phys.* **1957**, *27*, 1305–1308.

[93] Bertie, J. E., Michaelian, K. H., „The Raman spectra of gaseous formic acid $-h_2$ and $-d_2$“, *J. Chem. Phys.* **1982**, *76*, 886–894.

[94] Freytes, M., Hurtmans, D., Kassi, S., Liévin, J., Vander Auwera, J., Campargue, A., Herman, M., „Overtone spectroscopy of formic acid“, *Chem. Phys.* **2002**, *283*, 47–61.

[95] Baskakov, O. I., Markov, I. A., Alekseev, E. A., Motiyenko, R. A., Lohilahti, J., Horneman, V.-M., Winnewisser, B. P., Medvedev, I. R., De Lucia, F. C., „Simultaneous analysis of rovibrational and rotational data for the 4^1, 5^1, 6^1, 7^2, 8^1, 7^19^1 and 9^2 states of HCOOH“, *J. Mol. Struct.* **2006**, *795*, 54–77.

[96] Perrin, A., Vander Auwera, J., Zelinger, Z., „High-resolution Fourier transform study of the ν_3 fundamental band of *trans*-formic acid“, *J. Quant. Spectrosc. Radiat. Transfer* **2009**, *110*, 743–755.

[97] Kelemen, A. K., Luber, S., „On the vibrations of formic acid predicted from first principles“, *Phys. Chem. Chem. Phys.* **2022**, *24*, 28109–28120.

[98] Luckhaus, D., Quack, M., Willeke, M., „Coupling Across Bonds: *Ab Initio* Calculations for the Anharmonic Vibrational Resonance Dynamics of the Coupled OH and CH Chromophores in Trans Formic Acid HCOOH“, *Z. Phys. Chem.* **2000**, *214*, 1087–1114.

[99] Demaison, J., Herman, M., Liévin, J., „Anharmonic force field of *cis*- and *trans*-formic acid from high-level *ab initio* calculations, and analysis of resonance polyads“, *J. Chem. Phys.* **2007**, *126*, 164305.

[100] Scribano, Y., Benoit, D. M., „Calculation of vibrational frequencies through a variational reduced-coupling approach“, *J. Chem. Phys.* **2007**, *127*, 164118.

[101] Lane, J. R., Kjaergaard, H. G., „XH-stretching overtone transitions calculated using explicitly correlated coupled cluster methods“, *J. Chem. Phys.* **2010**, *132*, 174304.

[102] Miliordos, E., Xantheas, S. S., „On the validity of the basis set superposition error and complete basis set limit extrapolations for the binding energy of the formic acid dimer“, *J. Chem. Phys.* **2015**, *142*, 094311.

[103] Mitra, H., Roy, T. K., „Comprehensive Benchmark Results for the Accuracy of Basis Sets for Anharmonic Molecular Vibrations“, *J. Phys. Chem. A* **2020**, *124*, 9203–9221.

[104] Käser, S., Boittier, E. D., Upadhyay, M., Meuwly, M., „Transfer Learning to CCSD(T): Accurate Anharmonic Frequencies from Machine Learning Models“, *J. Chem. Theory Comput.* **2021**, *17*, 3687–3699.

[105] Aerts, A., Schäfer, M. R., Brown, A., „Adaptive fitting of potential energy surfaces of small to medium-sized molecules in sum-of-product form: Application to vibrational spectroscopy“, *J. Chem. Phys.* **2022**, *156*, 164106.

[106] Hisatsune, I. C., Heicklen, J., „Are There 2 Structural Isomers of Formic-Acid?“, *Can. J. Spectrosc.* **1973**, *18*, 135–142.

[107] Hull, K., Wells, T., Billinghurst, B. E., Bunn, H., Raston, P. L., „Synchrotron-based infrared spectroscopy of formic acid: Confirmation of the reassignment of Fermi-coupled 8 μm states“, *AIP Adv.* **2019**, *9*, 015021.

[108] Nejad, A., Crittenden, D. L., „On the separability of large-amplitude motions in anharmonic frequency calculations“, *Phys. Chem. Chem. Phys.* **2020**, *22*, 20588–20601.

[109] Nejad, A., Meyer, K. A. E., Kollipost, F., Xue, Z., Suhm, M. A., „Slow monomer vibrations in formic acid dimer: Stepping up the ladder with FTIR and Raman jet spectroscopy“, *J. Chem. Phys.* **2021**, *155*, 224301.

[110] Goroya, K. G., Zhu, Y., Sun, P., Duan, C., „High resolution jet-cooled infrared absorption spectra of the formic acid dimer: A reinvestigation of the C−O stretch region“, *J. Chem. Phys.* **2014**, *140*, 164311.

[111] Dübal, H.-R., Quack, M., „Tridiagonal Fermi resonance structure in the IR spectrum of the excited CH chromophore in CF_3H“, *J. Chem. Phys.* **1984**, *81*, 3779–3791.

[112] Dübal, H.-R., Quack, M., „Vibrational overtone spectra and vibrational dynamics of $CFHCl_2$ and $(CH_3)_2CFH$“, *Mol. Phys.* **1984**, *53*, 257–264.

[113] Herman, M., Perry, D. S., „Molecular spectroscopy and dynamics: a polyad-based perspective“, *Phys. Chem. Chem. Phys.* **2013**, *15*, 9970–9993.

[114] Hurtmans, D., Herregodts, F., Herman, M., Liévin, J., Campargue, A., Garnache, A., Kachanov, A. A., „Spectroscopic and *ab initio* investigation of the ν_{OH} overtone excitation in *trans*-formic acid“, *J. Chem. Phys.* **2000**, *113*, 1535–1545.

[115] Madeja, F., Markwick, P., Havenith, M., Nauta, K., Miller, R. E., „Rotationally resolved infrared spectroscopy of h_2- and d_1-formic acid monomer in liquid He droplets“, *J. Chem. Phys.* **2002**, *116*, 2870–2878.

[116] Svoboda, V., Rakovský, J., Votava, O., „High-resolution spectra of $2\nu_{OH}$ overtone of *trans*-formic acid in the supersonic jet“, *J. Quant. Spectrosc. Radiat. Transfer* **2022**, *292*, 108319.

[117] Redington, R. L., „Vibrational spectra and normal coordinate analysis of isotopically labeled formic acid monomers“, *J. Mol. Spectrosc.* **1977**, *65*, 171–189.

[118] Bertie, J. E., Michaelian, K. H., Eysel, H. H., Hager, D., „The Raman–active O−H and O−D stretching vibrations and Raman spectra of gaseous formic acid–d_1 and –OD“, *J. Chem. Phys.* **1986**, *85*, 4779–4789.

[119] Xue, Z., *Raman Spectroscopy of Carboxylic Acid and Water Aggregates*, Logos Verlag Berlin, Berlin, **2011**.

[120] Madeja, F., Havenith, M., Nauta, K., Miller, R. E., Chocholoušová, J., Hobza, P., „Polar isomer of formic acid dimers formed in helium nanodroplets“, *J. Chem. Phys.* **2004**, *120*, 10554–10560.

[121] Meyer, K. A. E., Davies, J. A., Ellis, A. M., „Shifting formic acid dimers into perspective: vibrational scrutiny in helium nanodroplets“, *Phys. Chem. Chem. Phys.* **2020**, *22*, 9637–9646.

[122] Marushkevich, K., Khriachtchev, L., Lundell, J., Räsänen, M., „*cis-trans* Formic Acid Dimer: Experimental Observation and Improved Stability against Proton Tunneling“, *J. Am. Chem. Soc.* **2006**, *128*, 12060–12061.

[123] Marushkevich, K., Khriachtchev, L., Räsänen, M., „High-energy conformer of formic acid in solid neon: Giant difference between the proton tunneling rates of *cis* monomer and *trans-cis* dimer“, *J. Chem. Phys.* **2007**, *126*, 241102.

[124] Olbert-Majkut, A., Ahokas, J., Lundell, J., Pettersson, M., „Raman spectroscopy of formic acid and its dimers isolated in low temperature argon matrices“, *Chem. Phys. Lett.* **2009**, *468*, 176–183.

[125] Meyer, K. A. E., Suhm, M. A., „Formic acid aggregation in 2D supersonic expansions probed by FTIR imaging“, *J. Chem. Phys.* **2017**, *147*, 144305.

[126] Oswald, S., Meyer, E., Suhm, M. A., „Dinitrogen as a Sensor for Metastable Carboxylic Acid Dimers and a Weak Hydrogen Bond Benchmarking Tool“, *J. Phys. Chem. A* **2018**, *122*, 2933–2946.

[127] Balabin, R. M., „Polar (Acyclic) Isomer of Formic Acid Dimer: Gas-Phase Raman Spectroscopy Study and Thermodynamic Parameters“, *J. Phys. Chem. A* **2009**, *113*, 4910–4918.

[128] Chang, Y.-T., Yamaguchi, Y., Miller, W. H., Schaefer III, H. F., „An analysis of the infrared and Raman spectra of the formic acid dimer $(HCOOH)_2$“, *J. Am. Chem. Soc.* **1987**, *109*, 7245–7253.

[129] Georges, R., Freytes, M., Hurtmans, D., Kleiner, I., Vander Auwera, J., Herman, M., „Jet-cooled and room temperature FTIR spectra of the dimer of formic acid in the gas phase“, *Chem. Phys.* **2004**, *305*, 187–196.

[130] Nejad, A., Suhm, M. A., „Concerted Pair Motion Due to Double Hydrogen Bonding: The Formic Acid Dimer Case“, *J. Indian Inst. Sci.* **2020**, *100*, 5–19, note that the labels “12” and “24” must be interchanged in Fig. 7 for Hartree-Fock.

[131] Li, W., Evangelisti, L., Gou, Q., Caminati, W., Meyer, R., „The Barrier to Proton Transfer in the Dimer of Formic Acid: A Pure Rotational Study“, *Angew. Chem. Int. Ed.* **2019**, *58*, 859–865.

[132] Florio, G. M., Zwier, T. S., Myshakin, E. M., Jordan, K. D., Sibert III, E. L., „Theoretical modeling of the OH stretch infrared spectrum of carboxylic acid dimers based on first-principles anharmonic couplings“, *J Chem. Phys.* **2003**, *118*, 1735–1746.

[133] Smedarchina, Z., Fernandez-Ramos, A., Siebrand, W., „Calculation of the tunneling splitting in the zero-point level and CO-stretch fundamental of the formic acid dimer“, *Chem. Phys. Lett.* **2004**, *395*, 339–345.

[134] Luckhaus, D., „Concerted Hydrogen Exchange Tunneling in Formic Acid Dimer“, *J. Phys. Chem. A* **2006**, *110*, 3151–3158.

[135] Barnes, G. L., Sibert III, E. L., „The effects of asymmetric motions on the tunneling splittings in formic acid dimer“, *J. Chem. Phys.* **2008**, *129*, 164317.

[136] Luckhaus, D., „Hydrogen exchange in formic acid dimer: tunnelling above the barrier“, *Phys. Chem. Chem. Phys.* **2010**, *12*, 8357–8361.

[137] Mackeprang, K., Xu, Z.-H., Maroun, Z., Meuwly, M., Kjaergaard, H. G., „Spectroscopy and dynamics of double proton transfer in formic acid dimer“, *Phys. Chem. Chem. Phys.* **2016**, *18*, 24654–24662.

[138] Millikan, R. C., Pitzer, K. S., „The Infrared Spectra of Dimeric and Crystalline Formic Acid“, *J. Am. Chem. Soc.* **1958**, *80*, 3515–3521.

[139] Maréchal, Y., „IR spectra of carboxylic acids in the gas phase: A quantitative reinvestigation“, *J. Chem. Phys.* **1987**, *87*, 6344–6353.

[140] Zielke, P., Suhm, M. A., „Raman jet spectroscopy of formic acid dimers: low frequency vibrational dynamics and beyond“, *Phys. Chem. Chem. Phys.* **2007**, *9*, 4528–4534.

[141] Xue, Z., Suhm, M. A., „Probing the stiffness of the simplest double hydrogen bond: The symmetric hydrogen bond modes of jet-cooled formic acid dimer“, *J. Chem. Phys.* **2009**, *131*, 054301.

[142] Merker, U., Engels, P., Madeja, F., Havenith, M., Urban, W., „High-resolution CO-laser sideband spectrometer for molecular-beam optothermal spectroscopy in the 5-6.6 μm wavelength region“, *Rev. Sci. Instrum.* **1999**, *70*, 1933–1938.

[143] Ito, F., Nakanaga, T., „Jet-cooled infrared spectra of the formic acid dimer by cavity ring-down spectroscopy: observation of the O−H stretching region“, *Chem. Phys.* **2002**, *277*, 163–169.

[144] Madeja, F., Havenith, M., „High resolution spectroscopy of carboxylic acid in the gas phase: Observation of proton transfer in $(DCOOH)_2$“, *J. Chem. Phys.* **2002**, *117*, 7162–7168.

[145] Ito, F., „Jet-cooled infrared spectra of the formic acid dimer by cavity ring-down spectroscopy: Observation of the C−O stretching region and vibrational analysis of the Fermi-triad system“, *Chem. Phys. Lett.* **2007**, *447*, 202–207.

[146] Ortlieb, M., Havenith, M., „Proton Transfer in $(HCOOH)_2$: An IR High-Resolution Spectroscopic Study of the Antisymmetric C−O Stretch“, *J. Phys. Chem. A* **2007**, *111*, 7355–7363.

[147] Gutberlet, A., Schwaab, G., Havenith, M., „High resolution IR spectroscopy of the carbonyl stretch of $(DCOOD)_2$“, *Chemical Physics* **2008**, *343*, 158–167.

[148] Kollipost, F., Wugt Larsen, R., Domanskaya, A. V., Nörenberg, M., Suhm, M. A., „Communication: The highest frequency hydrogen bond vibration and an experimental value for the dissociation energy of formic acid dimer“, *J. Chem. Phys.* **2012**, *136*, 151101.

[149] Kollipost, F., *Schwingungsdynamik in O−H···O-verbrückten Aggregaten: FTIR-Spektroskopie vom Nah- bis zum Ferninfraroten*, DOI 10.53846/goediss-5302, Niedersächsische Staats- und Universitätsbibliothek Göttingen, Göttingen, **2015**.

[150] Zhang, Y., Li, W., Luo, W., Zhu, Y., Duan, C., „High resolution jet-cooled infrared absorption spectra of $(HCOOH)_2$, $(HCOOD)_2$, and HCOOH−HCOOD complexes in 7.2 μm region“, *J. Chem. Phys.* **2017**, *146*, 244306.

[151] Neill, J. L., *A New Generation of Chirped Pulse Rotational Spectroscopy with Applications to Structure Determination and Astrochemistry*, DOI 10.18130/V3VP1B, University of Virginia Library, Charlottesville, Virginia, **2011**.

[152] Roy, A. K., Thakkar, A. J., „Structures of the formic acid trimer“, *Chem. Phys. Lett.* **2004**, *386*, 162–168.

[153] Wilson Jr., E. B., Decius, J. C., Cross, P. C., *Molecular Vibrations: The Theory of Infrared and Raman Vibrational Spectra*, Dover Publications, New York, **1980**.

[154] Watson, J. K. G., „The vibration-rotation hamiltonian of linear molecules“, *Mol. Phys.* **1970**, *19*, 465–487.

[155] Eckart, C., „Some Studies Concerning Rotating Axes and Polyatomic Molecules“, *Phys. Rev.* **1935**, *47*, 552–558.

[156] Willetts, A., Handy, N. C., Green Jr., W. H., Jayatilaka, D., „Anharmonic corrections to vibrational transition intensities“, *J. Phys. Chem.* **1990**, *94*, 5608–5616.

[157] Vázquez, J., Stanton, J. F., „Simple(r) algebraic equation for transition moments of fundamental transitions in vibrational second-order perturbation theory“, *Mol. Phys.* **2006**, *104*, 377–388.

[158] Vázquez, J., Stanton, J. F., „Treatment of Fermi resonance effects on transition moments in vibrational perturbation theory“, *Mol. Phys.* **2007**, *105*, 101–109.

[159] Barone, V., Bloino, J., Guido, C. A., Lipparini, F., „A fully automated implementation of VPT2 Infrared intensities“, *Chem. Phys. Lett.* **2010**, *496*, 157–161.

[160] Carbonniere, P., Barone, V., „Coriolis couplings in variational computations of vibrational spectra beyond the harmonic approximation: implementation and validation“, *Chem. Phys. Lett.* **2004**, *392*, 365–371.

[161] Sarka, J., Poirier, B., Szalay, V., Császár, A. G., „On neglecting Coriolis and related couplings in first-principles rovibrational spectroscopy: Considerations of symmetry, accuracy, and simplicity. II. Case studies for H_2O isotopologues, H_3^+, O_3, and NH_3“, *Spectrochim. Acta Part A* **2021**, *250*, 119164.

[162] Heger, M., Andersen, J., Suhm, M. A., Wugt Larsen, R., „The donor OH stretching-libration dynamics of hydrogen-bonded methanol dimers in cryogenic matrices“, *Phys. Chem. Chem. Phys.* **2016**, *18*, 3739–3745.

[163] Heger, M., *Diagonal and Off-Diagonal Anharmonicity in Hydrogen-Bonded Systems*, DOI 10.53846/goediss-5641, Niedersächsische Staats- und Universitätsbibliothek Göttingen, Göttingen, **2016**.

[164] Puzzarini, C., Stanton, J. F., Gauss, J., „Quantum-chemical calculation of spectroscopic parameters for rotational spectroscopy“, *Int. Rev. Phys. Chem.* **2010**, *29*, 273–367.

[165] Schuurman, M. S., Allen, W. D., von Ragué Schleyer, P., Schaefer III, H. F., „The highly anharmonic BH_5 potential energy surface characterized in the *ab initio* limit“, *J. Chem. Phys.* **2005**, *122*, 104302.

[166] Suhm, M. A., Watts, R. O., „Quantum Monte Carlo studies of vibrational states in molecules and clusters“, *Phys. Rep.* **1991**, *204*, 293–329.

[167] Acioli, P. H., „Review of quantum Monte Carlo methods and their applications“, *J. Mol. Struct.: THEOCHEM* **1997**, *394*, 75–85.

[168] Frisch, M. J., Trucks, G. W., Schlegel, H. B., Scuseria, G. E., Robb, M. A., Cheeseman, J. R., Scalmani, G., Barone, V., Petersson, G. A., Nakatsuji, H., Li, X., Caricato, M., Marenich, A. V., Bloino, J., Janesko, B. G., Gomperts, R., Mennucci, B., Hratchian, H. P., Ortiz, J. V., Izmaylov, A. F., Sonnenberg, J. L., Williams-Young, D., Ding, F., Lipparini, F., Egidi, F., Goings, J., Peng, B., Petrone, A., Henderson, T., Ranasinghe, D., Zakrzewski, V. G., Gao, J., Rega, N., Zheng, G., Liang, W., Hada, M., Ehara, M., Toyota, K., Fukuda, R., Hasegawa, J., Ishida, M., Nakajima, T., Honda, Y., Kitao, O., Nakai, H., Vreven, T., Throssell, K., Montgomery, Jr., J. A., Peralta, J. E., Ogliaro, F., Bearpark, M. J., Heyd, J. J., Brothers, E. N., Kudin, K. N., Staroverov, V. N., Keith, T. A., Kobayashi, R., Normand, J., Raghavachari, K., Rendell, A. P., Burant, J. C., Iyengar, S. S., Tomasi, J., Cossi, M., Millam, J. M., Klene, M., Adamo, C., Cammi, R., Ochterski, J. W., Martin, R. L., Morokuma, K., Farkas, O., Foresman, J. B., Fox, D. J., Gaussian 16 Revision A.03, Gaussian Inc. Wallingford CT, **2016**.

[169] Barone, V., „Vibrational zero-point energies and thermodynamic functions beyond the harmonic approximation“, *J. Chem. Phys.* **2004**, *120*, 3059–3065.

[170] Stanton, J. F., Gauss, J., Cheng, L., Harding, M. E., Matthews, D. A., Szalay, P. G., CFOUR, Coupled-Cluster techniques for Computational Chemistry, a quantum-chemical program package, With contributions from A.A. Auer, R.J. Bartlett, U. Benedikt, C. Berger, D.E. Bernholdt, Y.J. Bomble, O. Christiansen, F. Engel, R. Faber, M. Heckert, O. Heun, M. Hilgenberg, C. Huber, T.-C. Jagau, D. Jonsson, J. Jusélius, T. Kirsch, K. Klein, W.J. Lauderdale, F. Lipparini, T. Metzroth, L.A. Mück, D.P. O'Neill, D.R. Price, E. Prochnow, C. Puzzarini, K. Ruud, F. Schiffmann, W. Schwalbach, C. Simmons, S. Stopkowicz, A. Tajti, J. Vázquez, F. Wang, J.D. Watts and the integral packages MOLECULE (J. Almlöf and P.R. Taylor), PROPS (P.R. Taylor), ABACUS (T. Helgaker, H.J. Aa. Jensen, P. Jørgensen, and J. Olsen), and ECP routines by A. V. Mitin and C. van Wüllen. For the current version, see http://www.cfour.de.

[171] Matthews, D. A., Cheng, L., Harding, M. E., Lipparini, F., Stopkowicz, S., Jagau, T.-C., Szalay, P. G., Gauss, J., Stanton, J. F., „Coupled-cluster techniques for computational chemistry: The CFOUR program package“, *J. Chem. Phys.* **2020**, *152*, 214108.

[172] Herzberg, G., *Molecular spectra and molecular structure. II. Infrared and Raman spectra of polyatomic molecules*, Van Nostrand Reinhold Company, New York, **1945**.

[173] Morse, P. M., „Diatomic Molecules According to the Wave Mechanics. II. Vibrational Levels“, *Phys. Rev.* **1929**, *34*, 57–64.

[174] Herzberg, G., *Molecular spectra and molecular structure. I. Spectra of diatomic molecules*, 2nd ed., D. Van Nostrand Company, New York, **1950**.

[175] Darling, B. T., Dennison, D. M., „The Water Vapor Molecule“, *Phys. Rev.* **1940**, *57*, 128–139.

[176] Martin, J. M. L., Lee, T. J., Taylor, P. R., François, J., „The anharmonic force field of ethylene, C_2H_4, by means of accurate *ab initio* calculations“, *J. Chem. Phys.* **1995**, *103*, 2589–2602.

[177] Krasnoshchekov, S. V., Isayeva, E. V., Stepanov, N. F., „Criteria for first- and second-order vibrational resonances and correct evaluation of the Darling-Dennison resonance coefficients using the canonical Van Vleck perturbation theory“, *J. Chem. Phys.* **2014**, *141*, 234114.

[178] Boyer, M. A., McCoy, A. B., „A wave function correction-based approach to the identification of resonances for vibrational perturbation theory“, *J. Chem. Phys.* **2022**, *157*, 164113.

[179] Lehmann, K. K., „Beyond the *x*-*K* relations“, *Mol. Phys.* **1989**, *66*, 1129–1137.

[180] Martin, J. M. L., Taylor, P. R., „Accurate ab initio quartic force field for *trans*-HNNH and treatment of resonance polyads“, *Spectrochim. Acta Part A* **1997**, *53*, 1039–1050.

[181] Fermi, E., „Über den Ramaneffekt des Kohlendioxyds“, *Z. Phys.* **1931**, *71*, 250–259.

[182] Borro, A. F., Mills, I. M., Venuti, E., „Quartic anharmonic resonances in acetylenes and haloacetylenes“, *J. Chem. Phys.* **1995**, *102*, 3938–3944.

[183] Plíva, J., „Molecular constants for the bending modes of acetylene $^{12}C_2H_2$“, *J. Mol. Spectrosc.* **1972**, *44*, 165–182.

[184] Miani, A., Hänninen, V., Horn, M., Halonen, L., „Anharmonic force field for methanol“, *Mol. Phys.* **2000**, *98*, 1737–1748.

[185] Begue, D., Carbonniere, P., Pouchan, C., „Calculations of Vibrational Energy Levels by Using a Hybrid ab Initio and DFT Quartic Force Field: Application to Acetonitrile“, *J. Phys. Chem. A* **2005**, *109*, 4611–4616.

[186] Sibaev, M., Crittenden, D. L., „The PyPES library of high quality semi-global potential energy surfaces“, *J. Comput. Chem.* **2015**, *36*, 2200–2207.

[187] Sibaev, M., Crittenden, D. L., „An efficient and numerically stable procedure for generating sextic force fields in normal mode coordinates“, *J. Chem. Phys.* **2016**, *144*, 214107.

[188] Császár, A. G., „Anharmonic molecular force fields“, *WIREs Comput. Mol. Sci.* **2012**, *2*, 273–289.

[189] Sibaev, M., Crittenden, D. L., „Balancing accuracy and efficiency in selecting vibrational configuration interaction basis states using vibrational perturbation theory“, *J. Chem. Phys.* **2016**, *145*, 064106.

[190] Baraille, I., Larrieu, C., Dargelos, A., Chaillet, M., „Calculation of non-fundamental IR frequencies and intensities at the anharmonic level. I. The overtone, combination and difference bands of diazomethane, H_2CN_2“, *Chem. Phys.* **2001**, *273*, 91–101.

[191] Handy, N. C., Carter, S., „Large vibrational variational calculations using ‘multimode’ and an iterative diagonalization technique“, *Mol. Phys.* **2004**, *102*, 2201–2205.

[192] Odunlami, M., Le Bris, V., Bégué, D., Baraille, I., Coulaud, O., „A-VCI: A flexible method to efficiently compute vibrational spectra“, *J. Chem. Phys.* **2017**, *146*, 214108.

[193] Scribano, Y., Benoit, D. M., „Iterative active-space selection for vibrational configuration interaction calculations using a reduced-coupling VSCF basis“, *Chem. Phys. Lett.* **2008**, *458*, 384–387.

[194] Carbonnière, P., Dargelos, A., Pouchan, C., „The VCI-P code: an iterative variation–perturbation scheme for efficient computations of anharmonic vibrational levels and IR intensities of polyatomic molecules“, *Theor. Chem. Acc.* **2010**, *125*, 543–554.

[195] Zielke, P., *Ramanstreuung am Überschallstrahl: Wasserstoffbrückendynamik aus neuer Perspektive*, Cuvillier, Göttingen, **2007**.

[196] Lüttschwager, N. O. B., *Raman Spectroscopy of Conformational Rearrangements at Low Temperatures: Folding and stretching of alkanes in supersonic jets*, Springer, Heidelberg, **2014**.

[197] Bocklitz, S., *Conformational spectroscopy of flexible chain molecules near the folding limit*, DOI 10.53846/goediss-6744, Niedersächsische Staats- und Universitätsbibliothek Göttingen, Göttingen, **2018**.

[198] Forsting, T., *Schwingungsspektroskopische Untersuchung der Aggregation und Isomerisierung von Modellpeptiden in der Jet-Expansion am Beispiel kleiner sekundärer Amide*, DOI 10.53846/goediss-8766, Niedersächsische Staats- und Universitätsbibliothek Göttingen, Göttingen, **2021**.

[199] Gawrilow, M., Suhm, M. A., „2-Methoxyethanol: harmonic tricks, anharmonic challenges and chirality-sensitive chain aggregation“, *Phys. Chem. Chem. Phys.* **2020**, *22*, 15303–15311.

[200] Gawrilow, M., *Ramanspektroskopische Untersuchung der Esterfaltung in Überschallexpansionen, Oder: Wie man bei der Suche nach der Haarnadel im Esterhaufen fünf auf einmal findet*, DOI 10.53846/goediss-9313, Niedersächsische Staats- und Universitätsbibliothek Göttingen, Göttingen, **2022**.

[201] Forsting, T., Suhm, M., Curry-Jet SETUP, see https://doi.org/10.6084/m9.figshare.6395840.v1, **2019**.

[202] Kramida, A., Yu. Ralchenko, Reader, J., NIST ASD Team, NIST Atomic Spectra Database (ver. 5.8), [Online]. Available: https://physics.nist.gov/asd [2021, August 9]. National Institute of Standards and Technology, Gaithersburg, MD. **2020**.

[203] Borho, N., *Chirale Erkennung in Molekülclustern: Maßgeschneiderte Aggregation von α-Hydroxyestern*, Cuvillier, Göttingen, **2005**.

[204] Suhm, M. A., Kollipost, F., „Femtisecond single-mole infrared spectroscopy of molecular clusters“, *Phys. Chem. Chem. Phys.* **2013**, *15*, 10702–10721.

[205] Gottschalk, H. C., *IR-Untersuchung von schwach gebundenen Molekülaggregaten im Überschallstrahl*, DOI 10.53846/goediss-8308, Niedersächsische Staats- und Universitätsbibliothek Göttingen, Göttingen, **2020**.

[206] Long, D. A., *The Raman effect: A unified treatment of the theory of Raman scattering by molecules*, Wiley, Chichester, **2002**.

[207] Placzek, G., „Rayleigh-Streuung und Raman-Effekt“, in *Quantenmechanik der Materie und Strahlung. II. Moleküle*, (Ed.: E. Marx), Handbuch der Radiologie 6, pp. 205–374, Akademische Verlagsgesellschaft, Leipzig, **1934**.

[208] Michalska, D., Wysokiński, R., „The prediction of Raman spectra of platinum(II) anticancer drugs by density functional theory“, *Chem. Phys. Lett.* **2005**, *403*, 211–217.

[209] Wassermann, T., *Umgebungseinflüsse auf die CC- und CO-Torsionsdynamik in Molekülen und Molekülaggregaten: Schwingungsspektroskopie bei tiefen Temperaturen*, Logos Verlag Berlin, Berlin, **2010**.

[210] Hollas, J. M., *High resolution spectroscopy*, 2nd ed., John Wiley & Sons, Chichester, **1998**.

[211] Gawrilow, M., Suhm, M. A., „Quantifying Conformational Isomerism in Chain Molecules by Linear Raman Spectroscopy: The Case of Methyl Esters“, *Molecules* **2021**, *26*, 4523.

[212] Hills, G. W., Foster, R. B., Jones, W. J., „Raman spectra of asymmetric top molecules. Part IV. Vibration-rotation selection rules and general band contours“, *Mol. Phys.* **1977**, *33*, 1571–1588.

[213] Chocholoušová, J., Vacek, J., Hobza, P., „Potential energy and free energy surfaces of the formic acid dimer: Correlated *ab initio* calculations and molecular dynamics simulations“, *Phys. Chem. Chem. Phys.* **2002**, *4*, 2119–2122.

[214] Roszak, S., Gee, R. H., Balasubramanian, K., Fried, L. E., „New theoretical insight into the interactions and properties of formic acid: Development of a quantum-based pair potential for formic acid“, *J. Chem. Phys.* **2005**, *123*, 144702.

[215] Kisiel, Z., “PROSPE - Programs for ROtational SPEctroscopy”, http://info.ifpan.edu.pl/~kisiel/prospe.htm.

[216] Ray, B. S., „Über die Eigenwerte des asymmetrischen Kreisels“, *Z. Phys.* **1932**, *78*, 74–91.

[217] Townes, C. H., Schawlow, A. L., *Microwave spectroscopy*, Dover Publications, New York, **1975**.

[218] Perrin, A., Flaud, J.-M., Bakri, B., Demaison, J., Baskakov, O., Sirota, S. V., Herman, M., Vander Auwera, J., „New High-Resolution Analysis of the ν_7 and ν_9 Fundamental Bands of *trans*-Formic Acid by Fourier Transform Infrared and Millimeter-Wave Spectroscopy“, *J. Mol. Spectrosc.* **2002**, *216*, 203–213.

[219] Baskakov, O. I., Demaison, J., „Spectroscopic Study of the $v_6 = 1$ and $v_8 = 1$ Vibrational States of Formic Acid, HCOOH: New Assignments of Laser Transitions“, *J. Mol. Spectrosc.* **2002**, *211*, 262–272.

[220] Domanskaya, A., Marushkevich, K., Khriachtchev, L., Räsänen, M., „Spectroscopic study of *cis*-to-*trans* tunneling reaction of HCOOD in rare gas matrices“, *J. Chem. Phys.* **2009**, *130*, 154509.

[221] Baskakov, O. I., Bürger, H., Jerzembeck, W., „The Coriolis-Coupled States $v_7 = 1$ and $v_9 = 1$ of *trans*-HCOOD and *trans*-DCOOD“, *J. Mol. Spectrosc.* **1999**, *193*, 33–45.

[222] Nejad, A., „Monomer-optimised formic acid Raman jet spectra“, *Göttingen Research Online / Data* **2022**, *version V1*, DOI: 10.25625/BIZQZ4.

[223] Shimanouchi, T., *Tables of Molecular Vibrational Frequencies Consolidated Volume I*, National Institute of Standards and Technology (NIST, formerly National Bureau of Standards), Washington, D.C., **1972**.

[224] A'dawiah, R., Tan, T. L., Ng, L. L., „The v_2 band of formic acid-d_1 (HCOOD) by high-resolution FTIR spectroscopy“, *J. Mol. Spectrosc.* **2018**, *349*, 43–48.

[225] Goh, K. L., Ong, P. P., Teo, H. H., Tan, T. L., „High resolution FTIR spectrum of the v_1 band of DCOOD“, *Spectrochim. Acta Part A* **2000**, *56*, 991–1001.

[226] Tan, T. L., Goh, K. L., Ong, P. P., Teo, H. H., „Rovibrational Analysis of v_2 and $2v_5$ Bands of DCOOH by High Resolution FTIR Spectroscopy“, *J. Mol. Spectrosc.* **1999**, *198*, 387–392.

[227] Goh, K. L., Ong, P. P., Tan, T. L., „The v_3 band of DCOOH“, *Spectrochim. Acta Part A* **1999**, *55*, 2601–2614.

[228] Baskakov, O. I., „FTIR Spectrum of the v_3 Band of HCOOD“, *J. Mol. Spectrosc.* **2002**, *213*, 1–7.

[229] Madeja, F., Hecker, A., Ebbinghaus, S., Havenith, M., „High resolution spectroscopy of the v_3 band of DCOOD“, *Spectrochim. Acta Part A* **2003**, *59*, 1773–1782.

[230] Luo, W., Zhang, Y., Li, W., Duan, C., „Jet-cooled infrared absorption spectrum of the v_4 fundamental band of HCOOH and HCOOD“, *J. Mol. Spectrosc.* **2017**, *334*, 22–25.

[231] Baskakov, O. I., Alanko, S., Koivusaari, M., „The Coriolis-Coupled States $v_6 = 1$ and $v_8 = 1$ of DCOOH“, *J. Mol. Spectrosc.* **1999**, *198*, 40–42.

[232] Tan, T. L., Goh, K. L., Ong, P. P., Teo, H. H., „Rovibrational Constants for the v_6 and $2v_9$ Bands of HCOOD by Fourier Transform Infrared Spectroscopy“, *J. Mol. Spectrosc.* **1999**, *198*, 110–114.

[233] Goh, K. L., Ong, P. P., Tan, T. L., Wang, W. F., Teo, H. H., „The High-Resolution Infrared Spectrum of the v_5 Band of Deuterated Formic Acid (DCOOH)“, *J. Mol. Spectrosc.* **1998**, *190*, 125–129.

[234] Baskakov, O. I., „The Vibrational State $v_5 = 1$ of HCOOD“, *J. Mol. Spectrosc.* **2001**, *208*, 194–196.

[235] Tan, T. L., Goh, K. L., Ong, P. P., Teo, H. H., „FTIR Spectrum of the v_4 Band of DCOOD“, *J. Mol. Spectrosc.* **1999**, *195*, 324–327.

[236] Baskakov, O. I., Lohilahti, J., Horneman, V.-M., „High resolution analysis of the v_7 and v_9 bands of DCOOH“, *J. Mol. Spectrosc.* **2003**, *219*, 191–199.

[237] Slaber, L., Zhao, J., Billinghurst, B. E., Raston, P. L., „Synchrotron-based infrared spectroscopy of the Coriolis perturbed v_6 and v_8 bands of *trans*-DCOOH“, *J. Mol. Spectrosc.* **2022**, *390*, 111718.

[238] Williams, V. Z., „Infra-Red Spectra of Monomeric Formic Acid and Its Deuterated Forms. II. Low Frequency Region ($2200 - 800\,\mathrm{cm}^{-1}$)“, *J. Chem. Phys.* **1947**, *15*, 243–251.

[239] Daunt, S. J., Shurvell, H. F., „The gas phase infrared band contours of s-triazine and s-triazine-d_3: The fundamentals of $C_3N_3H_3$ and $C_3N_3D_3$ and some overtone and combination bands of $C_3N_3H_3$“, *J. Mol. Spectrosc.* **1976**, *62*, 373–395.

[240] Maçôas, E. M. S., Lundell, J., Pettersson, M., Khriachtchev, L., Fausto, R., Räsänen, M., „Vibrational spectroscopy of *cis*- and *trans*-formic acid in solid argon“, *J. Mol. Spectrosc.* **2003**, *219*, 70–80.

[241] Wilmshurst, J. K., „Vibrational Assignment in Monomeric Formic Acid“, *J. Chem. Phys.* **1956**, *25*, 478–480.

[242] Ong, P. P., Goh, K. L., Teo, H. H., „Analysis of High-Resolution FTIR Spectrum of the v_6 Band of $H^{13}COOH$“, *J. Mol. Spectrosc.* **1999**, *194*, 203–205.

[243] Baskakov, O., Horneman, V.-M., Alanko, S., Lohilahti, J., „FTIR spectra of the v_6 and v_8 bands of ^{13}C formic acid molecule–Assignment of FIR-laser lines“, *J. Mol. Spectrosc.* **2008**, *249*, 60–64.

[244] Luiz, G. M. R. S., Scalabrin, A., Pereira, D., „Gas phase infrared Fourier transform spectra of $H^{12}COOH$ and $H^{13}COOH$“, *Infrared Phys. Technol.* **1997**, *38*, 45–49.

[245] Nemes, L., McKellar, A. R. W., Johns, J. W. C., „Laser-Stark and Fourier-transform spectroscopy of the ν_3 band of monodeuterated formic acid, HCOOD“, *J. Opt. Soc. Am. B* **1987**, *4*, 1165–1172.

[246] Goh, K. L., Ong, P. P., Teo, H. H., Tan, T. L., „Improved Rovibrational Constants for the ν_3 Infrared Band of HCOOD“, *J. Mol. Spectrosc.* **1999**, *197*, 322–323.

[247] Weber, W. H., Maker, P. D., Johns, J. W. C., Weinberger, E., „Sub-Doppler laser-Stark and high-resolution Fourier transform spectroscopy of the ν_3 band of formic acid“, *J. Mol. Spectrosc.* **1987**, *121*, 243–260.

[248] Gordon, I. E., Rothman, L. S., Hargreaves, R. J., Hashemi, R., Karlovets, E. V., Skinner, F. M., Conway, E. K., Hill, C., Kochanov, R. V., Tan, Y., Wcisło, P., Finenko, A. A., Nelson, K., Bernath, P. F., Birk, M., Boudon, V., Campargue, A., Chance, K. V., Coustenis, A., Drouin, B. J., Flaud, J.-M., Gamache, R. R., Hodges, J. T., Jacquemart, D., Mlawer, E. J., Nikitin, A. V., Perevalov, V. I., Rotger, M., Tennyson, J., Toon, G. C., Tran, H., Tyuterev, V. G., Adkins, E. M., Baker, A., Barbe, A., Canè, E., Császár, A. G., Dudaryonok, A., Egorov, O., Fleisher, A. J., Fleurbaey, H., Foltynowicz, A., Furtenbacher, T., Harrison, J. J., Hartmann, J.-M., Horneman, V.-M., Huang, X., Karman, T., Karns, J., Kassi, S., Kleiner, I., Kofman, V., Kwabia-Tchana, F., Lavrentieva, N. N., Lee, T. J., Long, D. A., Lukashevskaya, A. A., Lyulin, O. M., Makhnev, V. Y., Matt, W., Massie, S. T., Melosso, M., Mikhailenko, S. N., Mondelain, D., Müller, H. S. P., Naumenko, O. V., Perrin, A., Polyansky, O. L., Raddaoui, E., Raston, P. L., Reed, Z. D., Rey, M., Richard, C., Tóbiás, R., Sadiek, I., Schwenke, D. W., Starikova, E., Sung, K., Tamassia, F., Tashkun, S. A., Vander Auwera, J., Vasilenko, I. A., Vigasin, A. A., Villanueva, G. L., Vispoel, B., Wagner, G., Yachmenev, A., Yurchenko, S. N., „The HITRAN2020 molecular spectroscopic database“, *J. Quant. Spectrosc. Radiat. Transfer* **2022**, *277*, 107949.

[249] Perrin, A., Rinsland, C. P., Goldman, A., „Spectral parameters for the ν_6 region of HCOOH and its measurement in the infrared tropospheric spectrum“, *J. Geophys. Res.: Atmos.* **1999**, *104*, 18661–18666.

[250] A'dawiah, R., Tan, T. L., Ng, L. L., „High-resolution FTIR spectroscopy of $H^{13}COOD$: The ground state and $v_2 = 1$ state rovibrational constants“, *J. Mol. Spectrosc.* **2018**, *354*, 1–6.

[251] Baskakov, O. I., Alekseev, E. A., Motiyenko, R. A., Lohilahti, J., Horneman, V.-M., Alanko, S., Winnewisser, B. P., Medvedev, I. R., De Lucia, F. C., „FTIR and millimeter wave investigation of the 7^1 and 9^1 states of formic acid HCOOH and $H^{13}COOH$“, *J. Mol. Spectrosc.* **2006**, *240*, 188–201.

[252] Erfort, S., Tschöpe, M., Rauhut, G., Zeng, X., Tew, D. P., „*Ab initio* calculation of rovibrational states for non-degenerate double-well potentials: *cis-trans* isomerization of HOPO“, *J. Chem. Phys.* **2020**, *152*, 174306.

[253] *Global and Accurate Vibration Hamiltonians from High-Resolution Molecular Spectroscopy*, (Eds.: M. Herman, J. Lievin, J. Vander Auwera, A. Campargue), Advances in Chemical Physics 108, John Wiley & Sons, New York, **1999**.

[254] Allen, W. D., Császár, A. G., „On the ab initio determination of higher-order force constants at nonstationary reference geometries“, *J. Chem. Phys.* **1993**, *98*, 2983–3015.

[255] Allen, W. D., Császár, A. G., Szalay, V., Mills, I. M., „General derivative relations for anharmonic force fields“, *Mol. Phys.* **1996**, *89*, 1213–1221.

[256] Brontein, I. N., Semendjajew, K. A., Musiol, G., Mühlig, H., *Taschenbuch der Mathematik*, 10th ed., Europa-Lehrmittel, Haan-Gruiten, **2016**.

[257] Chung-Phillips, A., „Torsional energy levels and wave functions“, *J. Comput. Chem.* **1992**, *13*, 874–882.

[258] Medel, R., Springborn, J. R., Crittenden, D. L., Suhm, M. A., „Hydrogen Delocalization in an Asymmetric Biomolecule: The Curious Case of Alpha-Fenchol“, *Molecules* **2022**, *27*, 101.

[259] Miyazawa, T., Pitzer, K. S., „Internal Rotation and Infrared Spectra of Formic Acid Monomer and Normal Coordinate Treatment of Out-of-Plane Vibrations of Monomer, Dimer, and Polymer“, *J. Chem. Phys.* **1959**, *30*, 1076–1086.

[260] Schwartz, M. E., Hayes, E. F., Rothenberg, S., „Theoretical Study of the Barriers to Internal Rotation in Formic Acid“, *J. Chem. Phys.* **1970**, *52*, 2011–2014.

[261] Nejad, A., „Dimer-optimised formic acid Raman jet spectra“, *Göttingen Research Online / Data* **2022**, *version V1*, DOI: 10.25625/YT8NP2.

[262] Nejad, A., „Dimer-optimised formic acid FTIR jet spectra“, *Göttingen Research Online / Data* **2022**, *version V1*, DOI: 10.25625/TUSJO5.

[263] Yang, Q., Mendolicchio, M., Barone, V., Bloino, J., „Accuracy and Reliability in the Simulation of Vibrational Spectra: A Comprehensive Benchmark of Energies and Intensities Issuing From Generalized Vibrational Perturbation Theory to Second Order (GVPT2)“, *Front. Astron. Space Sci.* **2021**, *8*, 665232.

[264] Heger, M., Suhm, M. A., Mata, R. A., „Communication: Towards the binding energy and vibrational red shift of the simplest organic hydrogen bond: Harmonic constraints for methanol dimer“, *J. Chem. Phys.* **2014**, *141*, 101105.

[265] Franke, P. R., Brice, J. T., Moradi, C. P., Schaefer III, H. F., Douberly, G. E., „Ethyl+O_2 in Helium Nanodroplets: Infrared Spectroscopy of the Ethylperoxy Radical“, *J. Phys. Chem. A* **2019**, *123*, 3558–3568.

[266] Kalescky, R., Kraka, E., Cremer, D., „Accurate determination of the binding energy of the formic acid dimer: The importance of geometry relaxation“, *J. Chem. Phys.* **2014**, *140*, 084315.

[267] Florio, G. M., Sibert III, E. L., Zwier, T. S., „Fluorescence-dip IR spectra of jet-cooled benzoic acid dimer in its ground and first excited singlet states“, *Faraday Discuss.* **2001**, *118*, 315–330.

[268] Emmeluth, C., Suhm, M. A., Luckhaus, D., „A monomers-in-dimers model for carboxylic acid dimers“, *J. Chem. Phys.* **2003**, *118*, 2242–2255.

[269] Head-Gordon, M., Head-Gordon, T., „Analytic MP2 frequencies without fifth-order storage. Theory and application to bifurcated hydrogen bonds in the water hexamer“, *Chem. Phys. Lett.* **1994**, *220*, 122–128.

[270] Lee, C., Yang, W., Parr, R. G., „Development of the Colle-Salvetti correlation-energy formula into a functional of the electron density“, *Phys. Rev. B* **1988**, *37*, 785–789.

[271] Becke, A. D., „Density-functional thermochemistry. III. The role of exact exchange“, *J. Chem. Phys.* **1993**, *98*, 5648.

[272] Grimme, S., Antony, J., Ehrlich, S., Krieg, H., „A consistent and accurate ab initio parametrization of density functional dispersion correction (DFT-D) for the 94 elements H-Pu“, *J. Chem. Phys.* **2010**, *132*, 154104.

[273] Grimme, S., Ehrlich, S., Goerigk, L., „Effect of the damping function in dispersion corrected density functional theory“, *J. Comput. Chem.* **2011**, *32*, 1456–1465.

[274] Gauss, J., Stanton, J. F., „Analytic CCSD(T) second derivatives“, *Chem. Phys. Lett.* **1997**, *276*, 70–77.

[275] Werner, H.-J., Knowles, P. J., Knizia, G., Manby, F. R., Schütz, M., Celani, P., Györffy, W., Kats, D., Korona, T., Lindh, R., Mitrushenkov, A., Rauhut, G., Shamasundar, K. R., Adler, T. B., Amos, R. D., Bennie, S. J., Bernhardsson, A., Berning, A., Cooper, D. L., Deegan, M. J. O., Dobbyn, A. J., Eckert, F., Goll, E., Hampel, C., Hesselmann, A., Hetzer, G., Hrenar, T., Jansen, G., Köppl, C., Lee, S. J. R., Liu, Y., Lloyd, A. W., Ma, Q., Mata, R. A., May, A. J., McNicholas, S. J., Meyer, W., Miller III, T. F., Mura, M. E., Nicklass, A., O'Neill, D. P., Palmieri, P., Peng, D., Pflüger, K., Pitzer, R., Reiher, M., Shiozaki, T., Stoll, H., Stone, A. J., Tarroni, R., Thorsteinsson, T., Wang, M., Welborn, M., MOLPRO, version 2018.1, a package of ab initio programs, see https://www.molpro.net, **2018**.

[276] Werner, H.-J., Knowles, P. J., Knizia, G., Manby, F. R., Schütz, M., „Molpro: a general-purpose quantum chemistry program package“, *WIREs Comput. Mol. Sci.* **2012**, *2*, 242–253.

[277] Győrffy, W., Werner, H.-J., „Analytical energy gradients for explicitly correlated wave functions. II. Explicitly correlated coupled cluster singles and doubles with perturbative triples corrections: CCSD(T)-F12“, *J. Chem. Phys.* **2018**, *148*, 114104.

[278] Kendall, R. A., Dunning Jr., T. H., Harrison, R. J., „Electron affinities of the first-row atoms revisited. Systematic basis sets and wave functions“, *J. Chem. Phys.* **1992**, *96*, 6796–6806.

[279] Peterson, K. A., Adler, T. B., Werner, H.-J., „Systematically convergent basis sets for explicitly correlated wavefunctions: The atoms H, He, B–Ne, and Al–Ar“, *J. Chem. Phys.* **2008**, *128*, 084102.

[280] Simons, G., Parr, R. G., Finlan, J. M., „New alternative to the Dunham potential for diatomic molecules“, *J. Chem. Phys.* **1973**, *59*, 3229–3234.

[281] Forsting, T., Zischang, J., Suhm, M. A., Eckhoff, M., Schröder, B., Mata, R. A., „Strained hydrogen bonding in imidazole trimer: a combined infrared, Raman, and theory study“, *Phys. Chem. Chem. Phys.* **2019**, *21*, 5989–5998.

[282] Dai, S., Funk, L.-M., von Pappenheim, F. R., Sautner, V., Paulikat, M., Schröder, B., Uranga, J., Mata, R. A., Tittmann, K., „Low-barrier hydrogen bonds in enzyme cooperativity“, *Nature* **2019**, *573*, 609–613.

[283] Frisch, M. J., Trucks, G. W., Schlegel, H. B., Scuseria, G. E., Robb, M. A., Cheeseman, J. R., Scalmani, G., Barone, V., Mennucci, B., Petersson, G. A., Nakatsuji, H., Caricato, M., Li, X., Hratchian, H. P., Izmaylov, A. F., Bloino, J., Zheng, G., Sonnenberg, J. L., Hada, M., Ehara, M., Toyota, K., Fukuda, R., Hasegawa, J., Ishida, M., Nakajima, T., Honda, Y., Kitao, O., Nakai, H., Vreven, T., Montgomery, J. A., Jr., Peralta, J. E., Ogliaro, F., Bearpark, M., Heyd, J. J., Brothers, E., Kudin, K. N., Staroverov, V. N., Kobayashi, R., Normand, J., Raghavachari, K., Rendell, A., Burant, J. C., Iyengar, S. S., Tomasi, J., Cossi, M., Rega, N., Millam, J. M., Klene, M., Knox, J. E., Cross, J. B., Bakken, V., Adamo, C., Jaramillo, J., Gomperts, R., Stratmann, R. E., Yazyev, O., Austin, A. J., Cammi, R., Pomelli, C., Ochterski, J. W., Martin, R. L., Morokuma, K., Zakrzewski, V. G., Voth, G. A., Salvador, P., Dannenberg, J. J., Dapprich, S., Daniels, A. D., Farkas, Ö., Foresman, J. B., Ortiz, J. V., Cioslowski, J., Fox, D. J., Gaussian 09 Revision E.01, Gaussian Inc. Wallingford CT, **2009**.

[284] Fortenberry, R. C., Lee, T. J., „Vibrational and Rovibrational Spectroscopy Applied to Astrochemistry“, in *Vibrational Dynamics of Molecules*, (Ed.: J. M. Bowman), Chapter 7, pp. 235–295, World Scientific, New Jersey, **2022**.